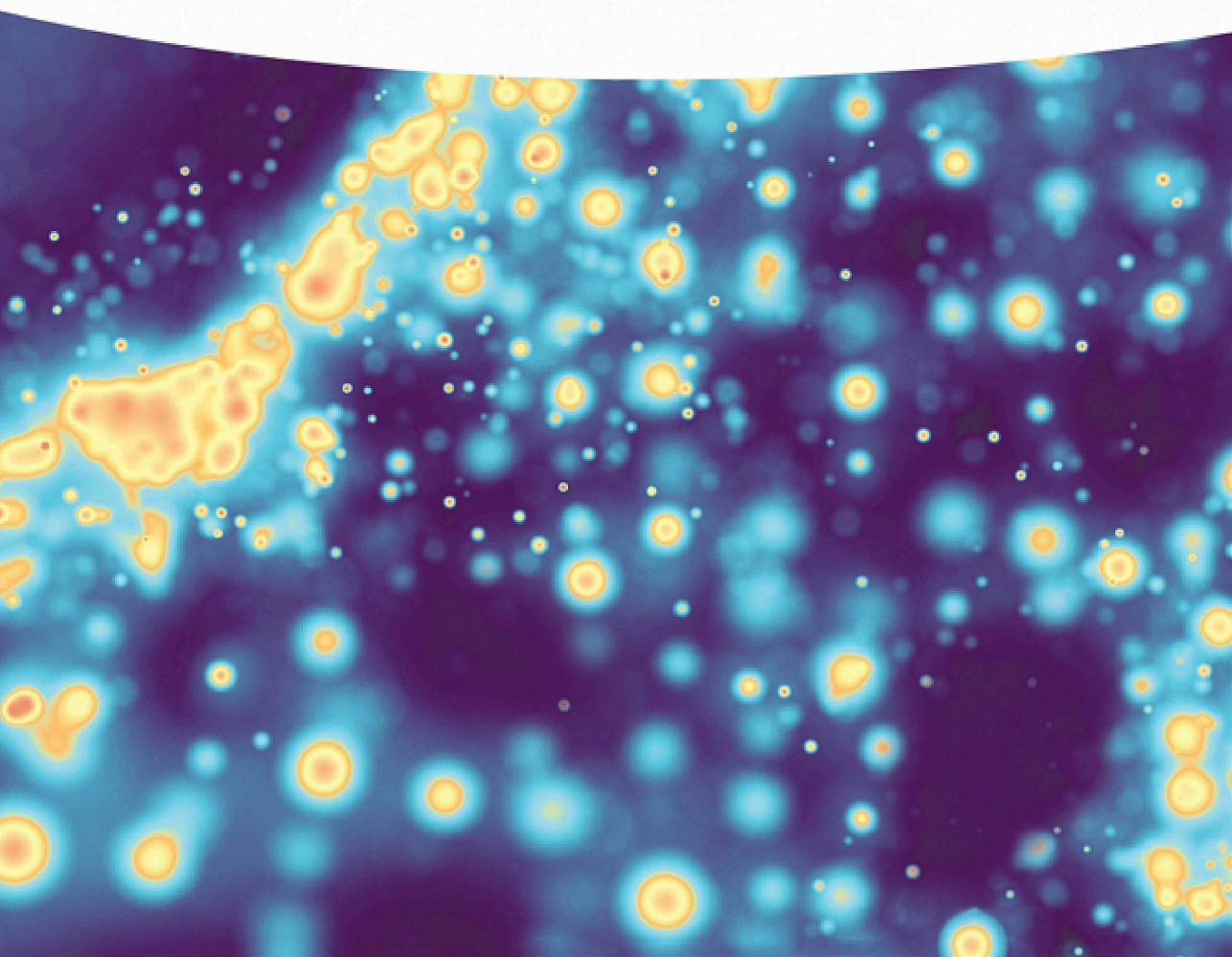


Abdollah Hajalilou, Mahmoud Tavakoli,
and Elahe Parvini

Magnetic Nanoparticles

Synthesis, Characterization, and Applications



Magnetic Nanoparticles

Magnetic Nanoparticles

Synthesis, Characterization, and Applications

Abdollah Hajalilou, Mahmoud Tavakoli, and Elahe Parvini

WILEY-VCH

Authors

Dr. Abdollah Hajalilou

Institute of Systems and Robotics (ISR)
Department of Electrical and Computer
Engineering
University of Coimbra
Coimbra 3030-290
Portugal

Prof. Mahmoud Tavakoli

Institute of Systems and Robotics (ISR)
Department of Electrical and Computer
Engineering
University of Coimbra
Coimbra 3030-290
Portugal

Dr. Elahe Parvini

Department of Physical Chemistry
Faculty of Chemistry
University of Tabriz
29 Bahman Blvd.
5166616471 Tabriz
Tabriz
Iran

Cover Image: © HaHanna/Shutterstock

■ All books published by **WILEY-VCH** are carefully produced. Nevertheless, authors, editors, and publisher do not warrant the information contained in these books, including this book, to be free of errors. Readers are advised to keep in mind that statements, data, illustrations, procedural details or other items may inadvertently be inaccurate.

Library of Congress Card No.: applied for

British Library Cataloguing-in-Publication Data

A catalogue record for this book is available from the British Library.

Bibliographic information published by the Deutsche Nationalbibliothek

The Deutsche Nationalbibliothek lists this publication in the Deutsche Nationalbibliografie; detailed bibliographic data are available on the Internet at <http://dnb.d-nb.de>.

© 2023 WILEY-VCH GmbH, Boschstraße 12,
69469 Weinheim, Germany

All rights reserved (including those of translation into other languages). No part of this book may be reproduced in any form – by photoprinting, microfilm, or any other means – nor transmitted or translated into a machine language without written permission from the publishers. Registered names, trademarks, etc. used in this book, even when not specifically marked as such, are not to be considered unprotected by law.

Print ISBN: 978-3-527-35097-1

ePDF ISBN: 978-3-527-84078-6

ePub ISBN: 978-3-527-84077-9

oBook ISBN: 978-3-527-84076-2

Typesetting Straive, Chennai, India

This book is offered to all students, scientists, and researchers who dedicate their lives to make an impact on society. I hope this book can make a positive and lasting impact on the lives of humans and science and new coming technologies for the next generations.

Last but not least, I would like to thank those who helped us to edit this book, especially Professor Liliana P. Ferreira and Professor Maria Margarida Cruz, and M. Estrela B. Melo Jorge, for their constant guidance, support, and encouragement. Words are not enough to express how thankful I am.

I would also like to thank all readers of the current book for sending us their ideas/suggestions for future editions for further improvement.

Abdollah Hajalilou, PhD

Contents

Preface *xiii*

1	Introduction to Magnetic Materials	1
1.1	Theory and Fundamentals of Magnetization	1
1.2	Type of Magnetism	2
1.2.1	Diamagnetism	3
1.2.2	Paramagnetism	3
1.2.3	Ferromagnetism	4
1.2.4	Antiferromagnetism	4
1.2.5	Ferrimagnetism	4
1.3	Extrinsic and Intrinsic Characteristics of Magnetic Materials	5
1.3.1	Intrinsic Properties	8
1.3.1.1	Saturation Magnetization (M_s)	8
1.3.1.2	Curie Temperature (T_C)	10
1.3.1.3	Magnetic Anisotropy	10
1.3.2	Extrinsic Properties	13
	References	14
2	Type and Characteristics of Magnetic Materials	17
2.1	Introduction	17
2.2	Soft and Hard Magnetic Materials	17
2.2.1	Soft Magnetic Materials	17
2.2.2	Hard Magnetic Materials	19
2.3	Hysteresis Loop	19
2.3.1	The Process of Hysteresis Loop Formation	19
2.3.2	Domain Orientation in Directions Favorable to the Applied Field	20
2.4	Magnetic Characteristic Measurements	21
2.4.1	M - H Hysteresis Loop	21
2.4.2	B - H Hysteresis Loop	22
2.5	Magnetic Losses	22
2.5.1	Eddy Current Losses	23
2.5.2	Residual Losses	25
2.5.3	Hysteresis Losses	25
	References	26

3	Insight into the Synthesis of Nanostructured Magnetic Materials	29
3.1	Introduction	29
3.2	Synthesis Process of the Magnetic Nanoparticles	30
3.3	Importance of the Synthesis and/or Preparation Methods	31
3.4	Dependency of Particle Size and Shape on Synthesize Route	32
3.5	Questions Related to the Selected Synthesis Route	33
3.6	Dependency of Magnetic Behaviors on Particle/Grain Size	38
3.7	Dependency of Magnetic Behaviors on Particle/Grain Shape	40
3.8	Introduction to Wet-Chemical Synthesis Route	41
3.8.1	Microemulsion	43
3.8.2	Hydrothermal Method	43
3.8.3	Co-precipitation	44
3.8.4	Sonochemical	44
3.8.5	Sol-Gel Method	44
3.8.6	Thermal Decomposition	45
3.8.7	Solvothermal	45
3.8.8	Microwave-Assisted Route	45
3.8.9	Green-Assisted Synthesis Route	45
3.9	Introduction to Solid-State Routes to Synthesize Magnetic Nanoparticles	46
3.9.1	A Standard Ceramic Route	46
3.9.2	Mechanical Alloying (MA) Process	46
3.10	Some Methods for Extraction of Iron Oxide Nanoparticles from Industrial Wastes	50
3.10.1	Magnetic Separation Technique (MST)	50
3.10.2	Curie Temperature Separation Technique	50
3.10.3	Oxidation of Wuestite	50
	References	51
4	Parallel Evolution of Microstructure-Magnetic Properties Relationship in Nanostructured Ferrites	59
4.1	Introduction	59
4.2	Insights into a Sintering Phenomenon	62
4.2.1	Magnetism-Microstructure Parallel Evolution in Yttrium Iron Garnet	68
4.2.2	Magnetism-Microstructure Parallel Evolution in Hard Ferrites	71
4.2.3	Magnetism-Microstructure Parallel Evolution in Soft Ferrites	80
4.3	Soaking or Sintering Time	84
4.4	Heating Rate	88
4.5	Trends of Sintering: Single-Sample and Multi-Sample Sintering	89
4.6	Conclusion and Perspective Outlook	91
	References	92

5	Surface Modification of Magnetic Nanoparticles	99
5.1	Introduction	99
5.2	Employed Technical Resources for Surface Modification	99
5.2.1	Plasma Treatment	99
5.2.2	Corona Discharge	100
5.2.3	Parylene Coating	101
5.2.4	Photolysis	101
5.2.5	Other Methods and Examples	101
5.3	Surface Modification of Magnetic Nanoparticles with Surfactant	103
5.4	Current Trends for Surface Modification of Nanomaterials	105
5.4.1	Chemical Functionalization	105
5.4.2	Physical Functionalization	106
5.5	Surface Modification Based on Organic Reactions	108
5.6	Surface Modification Based on Polymerization	109
5.7	Surface Modification with Inorganic Layers	110
5.8	Summary	111
	References	112
6	Insight into Superconducting Quantum Interference Devices (SQUID)	117
6.1	Introduction to SQUID	117
6.1.1	A Radio Frequency (RF) SQUID	117
6.1.2	A Direct Current (DC) SQUID	119
6.2	Superconducting Materials Used in SQUID	120
6.3	What Is the Basic Principle in SQUID VSM Magnetometer?	121
6.4	Superconductivity	121
6.4.1	Electron–Lattice Interaction	123
6.4.2	Cooper Pairs	124
6.4.3	Energy Gap	124
6.4.4	Coherence	125
6.4.5	Flux Quantization	125
6.5	Josephson Tunneling (JT) Phenomenon	125
6.6	Utilizations and Applications of SQUID	127
6.7	Advantage and Disadvantage of SQUID Compared to Other Techniques in Characterization of Magnetic Nanomaterials	128
	References	131
7	The Principle of SQUID Magnetometry and Its Contribution in MNPs Evaluation	135
7.1	Introduction	135
7.2	The Correct Procedure to Perform the Zero Field Cooling (ZFC) and Field Cooling (FC) Magnetic Study	136
7.3	The Concept of Merging Zero Field Cooled (ZFC) and Field Cooled (FC) Curve Completely with Each Other	137

7.4	Types of Information Obtained from the ZFC and FC Curves	138
7.4.1	Blocking Temperature	138
7.4.2	Néel Temperature	140
7.4.3	Types of Magnetism	140
7.4.4	Spin Glass (SG) and Superparamagnetic (SPM)	140
7.5	SQUID Magnetometry: Magnetic Measurements	141
7.5.1	Magnetization Versus Temperature, $M(T)$	141
7.5.1.1	Blocking Temperature (T_B) as a Function of Particle Size Distribution	141
7.5.1.2	Dependency of Blocking Temperature (T_B) on the Volume of Particles	144
7.5.1.3	The Field Dependence of the Blocking Temperature	144
7.5.1.4	The Blocking Temperature (T_B) Versus Applied Pressure, and Density	146
7.5.1.5	Effect of Heat Treatment on Blocking Temperature	147
7.5.2	Magnetization as a Function of Applied Magnetic Field	148
	References	149
8	Type of Interactions in Magnetic Nanoparticles	157
8.1	Introduction	157
8.2	Magnetic Dipole–Dipole Interaction Between Magnetic Nanoparticles	157
8.3	Exchange Interaction	158
8.3.1	Direct Exchange Interaction	159
8.3.2	Indirect Exchange Interaction	160
8.4	Super-Exchange Interaction	163
8.5	Dipolar Interactions	165
8.6	Spin–Orbit Interaction	165
	References	166
9	Insight into AC Susceptibility Measurements in Nanostructured Magnetic Materials	169
9.1	Introduction	169
9.2	AC Susceptibility Measurement	170
9.3	AC Susceptibility as a Probe of Magnetic Dynamics in a Wide Variety of Systems	172
9.3.1	AC Susceptibility as a Probe of Low-Frequency Magnetic Dynamics	172
9.3.2	AC Susceptibility as a Probe of High-Frequency Magnetic Dynamics	172
9.4	Information Obtained from Susceptibility Measurements	173
9.5	Insight into the Interaction Between Magnetic Nanoparticles and Used Models	174
9.5.1	Néel–Brown Model	174
9.5.2	Vogel–Fulcher Model	175

9.5.3	Conventional Critical Slowing Down Model	176
9.5.4	Power Law (P-L) Model	176
9.6	Examples of Evaluation of AC Susceptibility in MNPs	177
9.7	Using AC Susceptibility Measurements to Probe Transitions in Colloidal Suspensions	188
	References	191
10	Induced Effects in Nanostructured Magnetic Materials	197
10.1	Introduction	197
10.2	The Spin-Canted Effect	197
10.3	Spin-Glass-Like Behavior in Magnetic Nanoparticles	200
10.4	Reentrant Spin Glass (RSG) Behavior in Magnetic Nanoparticles	203
10.5	Finite Size Effects on Magnetic Properties	206
10.6	Surface Effect in Nanosized Particles	207
10.7	Memory Effect	208
	References	210
11	Insight into Superparamagnetism in Magnetic Nanoparticles	219
11.1	Introduction	219
11.2	Description of Superparamagnetism Based on Size of Particles and Magnetic Measurements	219
11.3	SPM Description Based on Magnetization Hysteresis Loop ($M-H$ or $B-H$)	228
11.4	SPM Detection Based on ZFC and FC Magnetization Curves	229
	References	230
12	Mössbauer Spectroscopy	233
12.1	Introduction to Mössbauer Spectroscopy	233
12.2	Observed Effects in Mössbauer	235
12.2.1	Mössbauer Effect	235
12.2.2	Recoil Effect	235
12.2.3	Doppler Effect	237
12.3	Hyperfine Interactions	238
12.3.1	Electric Monopole Interaction	238
12.3.1.1	S-Electron Density (Indirectly p and d-Electron Density)	240
12.3.1.2	Dependency of Isomer Shift on Spin State	241
12.3.1.3	Dependency of Isomer Shift on Strong Field Ligands	241
12.3.1.4	Dependency of Isomer Shift on Electronegativity of Ligands	241
12.3.2	Electric Quadrupole Interaction (Quadrupole Splitting)	242
12.3.3	Magnetic Dipole Interaction (Magnetic Splitting)	244
12.4	Mössbauer Spectroscopy Applied to Magnetism	246
12.4.1	Superparamagnetic Characterization	247

12.4.2	Mössbauer Spectroscopy Applied to Characterize the Effect of Synthesis Method on the MNPs Behavior	254
12.5	Phase Formation Evaluation Through Mössbauer Spectroscopy	274
12.6	Chemical Composition Evaluation Based on the Mössbauer Spectroscopy Spectra	281
	References	284
13	Application of Magnetic Nanoparticles	295
13.1	Introduction	295
13.2	Magnetic Nanoparticles: Application in Engineering	295
13.2.1	Mechanical and Materials Engineering: Magnetic Nanoparticles in Magnetorheological Fluids (MRF)	295
13.2.2	Environmental Engineering: Magnetic Nanoparticles in Wastewater Treatment	296
13.2.3	Surface Engineering	300
13.2.4	Tissue Engineering (TE)	300
13.3	Magnetic Nanoparticle Application in Energy	301
13.3.1	Supercapacitors and Batteries	301
13.3.2	Solar Cells	301
13.4	Magnetic Nanoparticles Application in Medical Science	302
13.4.1	Magnetic Resonance Imaging (MRI)	303
13.4.2	Drug Delivery	304
13.4.3	An Introduction to Hyperthermia (Therapy) in Cancer Treatment (Methods, Mechanisms, Constraints, and Role of Nanotechnology)	306
13.4.3.1	Magnetic Loss Processes Contributed to Magnetic Heating	307
13.4.3.2	Challenges of Magnetic Hyperthermia for Therapeutic Uses	309
13.5	Other General Applications of Magnetic Nanoparticles	313
	References	313

Index	321
--------------	------------

Preface

Magnetic materials are everywhere – from electrical motors and magnetorheological clutches to biomedicine. Since their introduction, scientists have always been enthusiastic to know more about the correlation between matter morphology and its magnetic properties. Advances in the field of nanomaterials as well gave birth to the field of nanomagnetism. That initiated many research works to understand the magnetic properties at the nanoscale. While significant advances were made in the last decades, additional research is necessary to better understand the nanostructured magnetic materials. It is known that when the size of particles reduces below 100 nm, their properties vary due to several factors such as increased surface-to-volume ratio, the spin-canted effect on the surface of nanoparticles, creation of some internal defects like grain boundaries and dislocation.

This book aims to provide an overview of magnetic nanostructured materials, especially focusing on the synthesis, characterization, and application of magnetic nanoparticles. Indeed, this book studies the recent progress in theory, synthesis, characterization, and application of magnetic materials. It focuses on the basic concept of magnetism in Chapters 1 and 2, followed by introducing methods for the synthesis of various magnetic nanoparticles in Chapters 3 and 4. It is believed that the synthesis routes have remarkable contributions to the size, shape, and other morphological characteristics of the magnetic nanoparticles that affect their magnetic properties. In Chapter 5, the functionalization of nanoparticles is considered due to the importance of reduction of some undesirable aspects of nanoparticles for particular applications, e.g. reducing their toxicity by coating them with some inert and/or environment-friendly materials such as silicon, silver, and gold. Chapters 6–12 further detail the characterization techniques and characteristics of nanostructures magnetic materials. This includes SQUID, magnetometry, AC susceptibility, and Mossbauer spectroscopy. Finally, the book discusses some of the applications of magnetic nanoparticles in Chapter 13.

This book addresses diverse groups of readers with a general background in physics and chemistry as well as medical and material science. Not only does it cover topics for the specialists in the field of magnetism, but it can also serve as a reference to provide a solid foundation for the topic for the students, scientists, and engineers working in the field of material science and condensed matter physics.

Instituto de Sistemas e Robótica (ISR)
Faculty of Sciences and Technology
of the University of Coimbra
Portugal
11 June 2022

Abdollah Hajalilou, PhD

1

Introduction to Magnetic Materials

1.1 Theory and Fundamentals of Magnetization

Almost everyone knows about magnetic materials and the magnetic force, but very few are familiar with the underlying mechanisms that cause the magnetic force. The existence of an inextricable correlation between electricity and magnetism is the key to understanding this phenomenon. In the nineteenth century, research on magnetism and electricity resulted in the discovery of electromagnetism theory by Faraday and Maxwell. They proposed that the magnetic field can be induced in a material in the presence of electric current, which attributes to the understanding of the origin of magnetism. Indeed, for any material volume, matter consists of electrons with their motion around atoms and their interaction, which indicates how magnetism is induced from matter. This simply means that the magnetism originates from the contribution of electron motion around their own axis, which is considered as spin magnetic moment (μ_s), and the motion of the electron around the nucleus of the atom, which is considered as orbital magnetic moment (μ_{orb}). The combination of these moments results in magnetic moment generation, which affects the type of magnetism for each element or material. According to Halliday et al. [1], the spin magnetic moment is an intrinsic property of the electron and is attributed to the spin angular momentum (S) as follows:

$$\mu_s = \frac{e}{m} S \quad (1.1)$$

where e is the electron charge and m is the electron mass. S is quantized and can only be $\pm 1/2$. Since only the z component of S is measurable, the z component of μ_s is given as [2]:

$$\mu_{s,z} = \pm \frac{eh}{4\pi m} \quad (1.2)$$

where h is Planck's constant. The positive value of this equation is equal to 9.27×10^{-24} J/T. This is considered as Bohr magneton (μ_B), which is the most basic unit of the magnetic moment in magnetism, and magnetic materials are elucidated based on this quantity.

The magnetic moment of solids normally arises from partially filled inner electron shells of transition metal atoms. In Hund's rules, the theory is closely related to the magnetism of free atoms or ions, which expect the orbital and spin moment as the role of the number of inner-shell electrons [3]. Indeed, some factors give rise to the origin of magnetism in ferrites, which are: (i) superexchange adjacent metal ions, (ii) unpaired electrons in 3d or 4f shells, and (iii) nonequivalence in the number of magnetic moments in tetrahedral and octahedral sites [4]. In oxide compounds such as ferrites, the orbital magnetic moment is typically quenched by the electronic fields induced by the surrounding oxygens around the metal ions [4]. The atomic magnetic moment then becomes equal to the electron spin moment as follows:

$$m = n\mu_B \quad (1.3)$$

where n is the number of unpaired electrons and μ_B is a Bohr magneton unit. For more details, the readers are referred to Ref. [5].

1.2 Type of Magnetism

In general, the magnetic materials in the micro or macroscopic scale are classified into five distinct groups based on their response to an externally applied magnetic field. They are diamagnetic, paramagnetic, ferromagnetic, anti-ferromagnetic, and ferromagnetic, which are briefly described below according to Refs. [5–8]. Additionally, Table 1.1 introduces the quantities and units that are taken into account in magnetism [4].

Table 1.1 Presented quantities and units considered in magnetism [5].

Quantity	Symbol	Gaussian unit	Conversion Factor	SI unit
Mass magnetization	σ, M	emu/g	1	Am ² /kg
Magnetic flux	Φ	Maxwell (Mx)	10 ⁻⁸	Weber (Wb)
Volume magnetization	$4\pi m$	G	10 ³ /4 π	A/m
Magnetic dipole moment	j	emu	4 $\pi \times 10^{-10}$	Wbm
Volume susceptibility	χ	Dimensionless	4 π	Dimensionless
Magnetic field strength	H	Oersted (Oe)	10 ³ /4 π	Ampere/m (A/m)
Mass susceptibility	χ_P	cm ³ /g	4 $\pi \times 10^{-3}$	m ³ /kg
Magnetic flux density, magnetic induction	B	Gauss (G)	10 ⁻⁴	Tesla (T)
Magnetic moment	m	Mu	10 ⁻³	Am ²

Source: Hajalilou et al. [5]/with permission of Springer Nature.

1.2.1 Diamagnetism

In this state, the atoms do not exhibit a magnetic moment in the absence or presence of an externally applied field. But, when the external field is applied, it causes an induced magnetic field in the opposite direction, which results in repulsive force. This simply means that the diamagnetic materials are repelled by a magnetic field. Indeed, the orbital velocity of the electrons, around their nuclei, would change in the presence of an applied magnetic field, which results in magnetic dipole moment variation in the opposite direction of the applied field [9]. In terms of electronic configuration, such characteristics occur in those materials with filled electronic sub-shells, in which, the magnetic moments are paired and overall cancel off each other [5].

1.2.2 Paramagnetism

In this state of magnetism, the materials represent a permanent magnetic dipole moment with an unpaired electron shell typically in the 3d or 4f shells [5, 9, 10]. Several theories have been suggested to explain such magnetism, which is only valid for a specific type of material. For instance, the Langevin model, which is considered for describing the non-interacting concentrated electrons' behavior, declares that the magnetic moment of each atom orientates in a random state because of thermal agitation [5]. The small alignment of these magnetic moments is caused by applying an external magnetic field, which accordingly gives rise to the creation of low magnetization in the applied field direction. Owing to the contribution of both the electron spin and the orbital angular moment to the magnetization, a positive susceptibility between 10^{-2} and 10^{-4} is obtained at room temperature. The magnetization (M) is proportional to the applied field (H) at relatively lower applied fields, but it deviates from proportionality at a higher applied field where saturation magnetization (M_s) initiates to occur. A slight alignment is taken into account by the inverse correlation of susceptibility (χ) with temperature (T), which is known as Curie law and is expressed as:

$$\chi = C/T \quad (1.4)$$

Based on this relation, the temperature would enhance at a relatively high applied magnetic field, which increases thermal agitation. Therefore, the alignment of the magnetic moment becomes very difficult. The Curie law also pronounces the positive susceptibility and is normally given through [11]:

$$\chi = \frac{C\mu_0 NM^2}{KT} \quad (1.5)$$

where N is the number of magnetic dipoles (M) per unit volume, C is a constant, K is the Boltzmann constant, T is the absolute temperature, and μ_0 is the permeability of the vacuum. Except for very low temperatures, typically less than 5 K, some paramagnetic materials track this equation at most temperatures. However, most paramagnetic materials follow the Curie–Weiss Law as:

$$\chi = \frac{C}{T - \theta_c} \quad (1.6)$$

where θ_c is a critical temperature and C is a Curie constant.

1.2.3 Ferromagnetism

In this state, the materials represent a powerful interaction with magnets like iron. Parallel alignment of the net moments of the same magnitude in these materials results in a remarkable net magnetization even in the absence of an externally applied field. Consequently, these materials have two key characteristics: (i) the presence of magnetic ordering temperature and (ii) spontaneous magnetization, which is the net magnetization existing inside of an even magnetized microscopic volume.

The susceptibility of a ferromagnetic material is typically large and positive in value. Moreover, it is a microstructure-dependent factor.

The atomic moments in these materials are produced by the electronic exchange force and give rise to the parallel alignment of atomic moments. A massive exchange force is equivalent to a field of about 1000 T.

Furthermore, the exchange force is a quantum mechanical phenomenon due to the orientation of the relative spins of two electrons. The electrons of neighboring atoms interact with one another in a process compared to the weaker diamagnetism and paramagnetism. This process is called exchange coupling [12]. If the material has a strong flux density and crystalline structure, a direct coupling between moments would occur (e.g. Fe, Ni, and Co) [9]. In the absence of an applied magnetic field, the aligned moment would yield spontaneous magnetization in the ferromagnetic material. Each material, which keeps permanent magnetization in the absence of an applied field, is considered a hard magnet.

1.2.4 Antiferromagnetism

This characteristic of magnetic materials can be observed once the two sub-lattices (namely tetrahedral and octahedral) are equally located in an opposite direction, which leads to zero net moments. Antiferromagnetic materials such as transition metal oxides present similar traits as ferromagnetic materials. A discrepancy is that the exchange interaction between the adjacent atoms gives rise to an anti-parallel alignment of the atomic magnetic moments. Hence, the magnetic moments cancel out each other, and the material would behave like low magnetization materials, i.e. paramagnetic. Susceptibility characteristics above the Néel temperature (T_N) are the clue to elucidate the antiferromagnetism property. Indeed, above T_N , a sufficient thermal energy results in equally but oppositely aligned atomic magnetic moments to cancel out each other. Thus, their long-range order vanishes due to the random fluctuation alignment, which is the behavior of a paramagnetic material [10].

1.2.5 Ferrimagnetism

In this case of magnetism, the distribution of atoms represents an opposite magnetic moment, as in antiferromagnetism; however, in ferrimagnetic materials, the opposing moments are unequal and a spontaneous magnetization remains [13]. This happens when the distribution consists of different materials or ions such as

Fe^{2+} and Fe^{3+} . Typically, within a magnetic domain, a net magnetic moment is induced from the anti-parallel arrangement of adjacent non-equivalent sublattices. Thus, the macroscopic property of ferrimagnetism is effectively a ferromagnetism behavior.

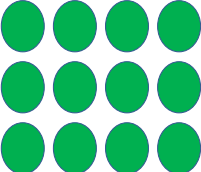
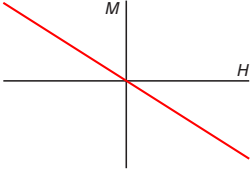
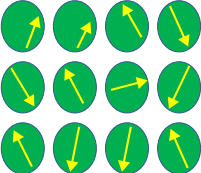
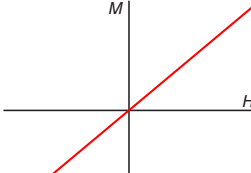
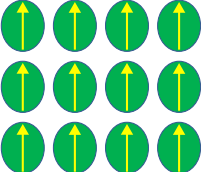
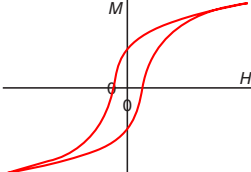
Ferrimagnetism is normally observed in ferrites such as Fe_3O_4 and magnetic garnets, and ionic compounds with more complex crystal structures. The oldest known magnetic substance, magnetite (Fe_3O_4), is a ferrimagnet; it was originally classified as a ferromagnet before Néel discovered ferrimagnetism and antiferromagnetism in 1948 [14]. Other known ferrimagnetic materials include yttrium iron garnet (YIG), cubic ferrites composed of iron oxides and other elements such as aluminum, cobalt, nickel, manganese, and zinc, and hexagonal ferrites such as $\text{PbFe}_{12}\text{O}_{19}$ and $\text{BaFe}_{12}\text{O}_{19}$, and pyrrhotite, Fe_{1-x}S [15].

In a ferrimagnet, the magnetic moments of one type of ion on one type of lattice site are aligned antiparallel to those of an ion on another lattice site. Since the magnetic moments are not of the same magnitude, they only partially cancel each other, and the material has a net magnetic moment. Ferrimagnetism has several similarities to ferromagnetism in which the cooperative alignment between magnetic dipoles leads to a net magnetic moment even in the absence of an applied field. Ferrimagnetism is lost above curie temperature (T_C), as it has the paramagnetic behavior above the T_C . Details and characteristics of the foregoing-mentioned magnetic states are given in Table 1.2.

1.3 Extrinsic and Intrinsic Characteristics of Magnetic Materials

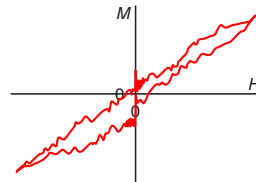
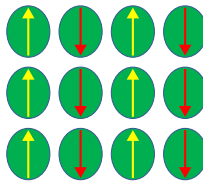
Understanding the concept of the intrinsic and extrinsic properties of magnetic materials is important to handle the microstructure and thus their application. It is believed that the ferrites' magnetic behavior relies not only on the intrinsic properties but also on the extrinsic behaviors. Therefore, understanding both of them is required to evaluate the magnetic behavior of a material. The intrinsic properties of a material are typically dependent on the chemistry and crystal structure such as crystal anisotropy, magnetostriction, and magnetostatic energy. While the extrinsic parameters such as pores, inclusions, and the nature of grain boundaries are highly microstructure sensitive. Atomic-scale quantum mechanics and relativistic effects have been modified to produce high-performance magnetic materials. Thus, due to the importance of ferrites in our daily lives, many attempts have been devoted to improving their versatility for various applications, e.g. from science to technology. In addition to the magnetic properties, the electrical properties are also important for describing their characteristics. Thus, it is necessary to correlate these properties with the relevant chemical, physical, and microstructural characteristics to improve their performance. Especially, for optimizing the properties of ferrimagnetic ceramics, it is necessary to understand both the intrinsic and extrinsic properties of a magnetic material. Intrinsic properties are those that are insensitive to variations in the microstructure feature of a sample [16]. Some characteristics of magnetic

Table 1.2 Characteristics of different types of magnetism.

Type	Atomic/magnetic behavior	Spin orientation	M–H curves	Example
Diamagnetism	<ul style="list-style-type: none">• Atoms have no magnetic movement• Susceptibility is small and negative, -10^{-6} to 10^{-5}			<ul style="list-style-type: none">➤ Inert gases, e.g. Ar, N₂;➤ Nonmetallic elements e.g. B, Si, P, S;➤ Many ions, e.g. Na⁺, Cl⁻ and their salts;➤ Diatomic molecules, e.g. H₂, N₂, H₂O;➤ Most organic compounds
Paramagnetism	<ul style="list-style-type: none">• Atoms have randomly oriented magnetic moments• Susceptibility is small and positive, $+10^{-5}$ to $+10^{-3}$			<ul style="list-style-type: none">➤ Some metals, e.g. Al;➤ Some diatomic gases, e.g. O₂ and NO;➤ Ions of transition metals and rare earth metals, and their salts;➤ Rare earth oxides
Ferromagnetism	<ul style="list-style-type: none">• Atoms have parallel aligned magnetic moments• Susceptibility is large (below T_C)			<ul style="list-style-type: none">➤ Transition metals, like Co, Ni, and rare earth with $64 \leq Z \leq 69$;➤ Alloys of ferromagnetic elements and some alloys of Mn, e.g. MnBi, Cu₂MnAl

Antiferromagnetism

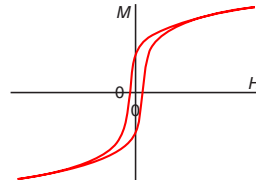
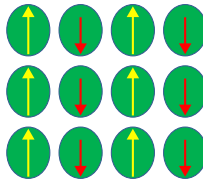
- Atoms have anti-parallel aligned magnetic moments
- Susceptibility is small and positive, $+10^{-5}$ to $+10^{-3}$



➤ Transition metals: Mn, Cr, Ni, Zn, and many of their compounds, e.g. MnO, CoO, NiO, Cr_2O_3 , MnS, MnSe, and CuCl_2

Ferrimagnetism

- Atoms have mixed parallel and antiparallel aligned magnetic moments
- Susceptibility is large (below T_C)



➤ Fe_3O_4 (magnetite);
 ➤ $\gamma\text{-Fe}_2\text{O}_3$ (maghemite);
 ➤ Mixed oxides of iron and other elements

materials such as spontaneous magnetization (M_o), saturation magnetization (M_s), crystal anisotropy or magnetocrystalline anisotropy (K), ferromagnetic resonance (FMR), and Curie temperature (T_C) are independent of the microstructure once the chemical composition of a material is fixed. As a result, it is useless to attempt to change, e.g. the curie temperature, by adjusting the microstructure. On the other hand, the extrinsic properties such as coercivity (H_c), remanence magnetization (M_r), permeability, hysteresis loop, and magnetic losses (hysteresis, eddy current, and residual) are highly microstructure sensitive. These parameters are influenced by the synthesis process, which affects the chemical homogeneity, crystallite or grain sizes, density, presence of nonmagnetic inclusions, and distribution of pores. From the physicochemical point of view, however, it is very difficult to fully separate the intrinsic and extrinsic properties of a material, and some of them are distinguishable based on the microstructural characteristics.

1.3.1 Intrinsic Properties

The intrinsic or intensive behaviors of magnetic materials, such as saturation, magnetization, anisotropy, Curie temperature, and magnetostriction, are those traits that belong to the material's characteristics and are not influenced by the microstructure, i.e. crystallite/grain, porosity size, and their distribution [9]. Intrinsic properties normally describe the atomic origin of magnetism and quantum phenomena such as exchange, crystal-field interaction, interatomic bonding, and spin-orbital coupling [17, 18]. The following sub-subsections deal with the details of intrinsic properties.

1.3.1.1 Saturation Magnetization (M_s)

Saturation magnetization (M_s) is given as the net magnetic moment per unit volume of a material. The saturation state only takes place in the situation wherein no further increase in magnetization happens by increasing the externally applied field. In this case, all domains would favor to line up in the same direction of the applied field. Increasing the externally applied field intensity enhances the domain alignment. The variation of magnetization with particle size as a result of temperature variation can be given as [19, 20]:

$$M_s = 8.1661 \exp(3T/1000) \quad (1.7)$$

where T is temperature.

The net M_s is equivalent to the vector of the magnetization of A and B sublattices in spinel ferrite, as:

$$M_s = |M_B - M_A| \quad (1.8)$$

The exchange interaction among the electrons' ions would yield various magnetization values in A and B sites. Typically, the interaction between magnetic ions of A and B sublattices is the strongest in the state of the A-B configuration. B-B configuration is the weakest and A-A interaction is the intermediate state. The dominant A-B

configuration leads to either a partial (noncompensated) or fully ferrimagnetism in magnetic materials. Typically, the magnetic moment value in A-lattice is much smaller than that in B-lattice, which results in the above-mentioned equation [21]. As mentioned, saturation magnetization (M_s) refers to the net magnetic moment per unit volume of a given material. This can be associated with the formula:

$$M_s = \frac{n_B \mu_B N}{M} d \quad (1.9)$$

where n_B is the number of Bohr magnetons per atom or ion (number of unpaired electron spins per atom or ion), μ_B is the value of a Bohr magneton (1.1654×10^{-29} Vsm), N is the Avogadro number (6.025×10^{23} atoms per mole or molecules per mole), M is the molecular weight, and d is the density. This formula is used for converting the moment in Bohr magnetons per atom or ion to units of bulk magnetization, M in emu/cm³ or emu/g, where $n \times \mu_B$ is the moment of the atom or ion in emu. As is known, Bohr magneton is the fundamental unit of the magnetic moment in Bohr theory, and it has been found that the magnetic moment is associated with the spin moment, which is almost identically equal to one Bohr magneton. The magnetic moment or magnetization is usually measured at 0 K to allow the correlation with the number of Bohr magnetons [22]. As shown in Figure 1.1, the magnetization of the sample follows the magnetization field. The slope of the curve in each region, from the origin to a point on the curve, or the ratio M/H is defined as magnetic susceptibility. The magnetization curve is divided into three major divisions. The lower section is for a reversible domain wall movement and rotation, which is considered as the initial susceptibility region. Being reversible means that after changing the magnetization slightly with an increase in the applied field, the original magnetization condition returns, once the field intensity is reduced to the original value. The second division of the magnetization curve is the one in which the irreversible domain wall motion occurs, and the slope increases greatly. The third section of the curve is the irreversible domain rotations. In this section, the slope is very flat, indicating that a large amount of energy is required to rotate the remaining domain magnetization in line with the magnetic field.

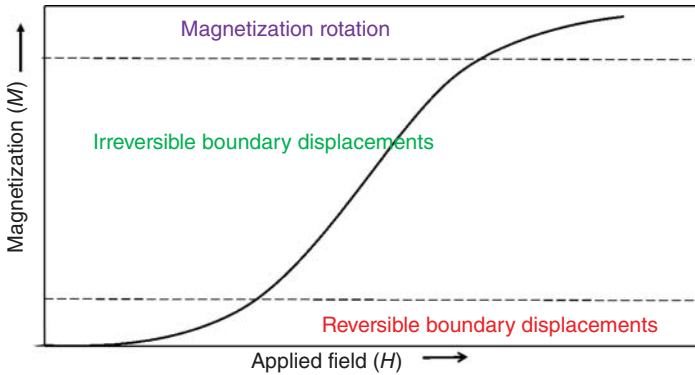


Figure 1.1 Divisions on the M – H curve based on domain magnetization.

1.3.1.2 Curie Temperature (T_C)

Curie temperature is a critical temperature where the magnetic behavior of a material or type of magnetization varies. Below this temperature, the ordered magnetic moment is dominant. At the Curie temperature, magnetic moments would change their directions. Above the Curie temperature, disorder magnetic moments occur, and ferromagnetic materials lose their spontaneous magnetization and hence behave similarly to paramagnetic materials. In fact, by increasing the temperature above the Curie point, thermal agitation causes a weaker alignment of the magnetic moments and leads to the net magnetization reduction. Hence, the increased thermal motion of the atoms tends to randomize the directions of any moments that may be aligned. In this circumstance, the atomic thermal motions counteract the coupling forces between the adjacent atomic dipole moment, causing some dipole misalignment without being affected by the presence of an external field. This results in saturation magnetization reduction. The saturation magnetization is maximum at 0 K, at which the thermal vibrations are in a minimum state. With the increase in temperature, the saturation magnetization diminishes gradually and then abruptly drops to zero, at what is called the Curie temperature (T_C). At T_C , the mutual spin coupling forces are destroyed in such a way that the ferromagnetic materials behave as paramagnetic at temperatures above T_C .

1.3.1.3 Magnetic Anisotropy

The variation of magnetic properties concerning the magnetic moment orientation is well known as magnetic anisotropy. In other words, it refers to the dependence of the internal energy on the magnetization direction. That is, the spins of the magnetic ions are bound to a specific crystallographic direction. In crystalline materials, the magnetic moments tend to align more readily along certain crystallographic axes called easy magnetization directions. The source of this magnetic anisotropy is the interaction of magnetic ions with the electrostatic field formed typically by the first nearest neighbors of oxygen. Magnetic anisotropy is the energy of a magnetic solid related to the orientation of magnetization regarding the crystal axes. Magnetic anisotropy is typically used to discuss the dependence of the internal energy on the direction of spontaneous magnetization in ferromagnetic materials. Magnetic anisotropy affects the shape of the hysteresis loops when measured in different directions. Each permanent magnet requires a high magnetic anisotropy to retain magnetism on every magnet in the required direction. Soft magnets contained a very low anisotropy because of the easy change of their magnetization. Different types of anisotropy are as follows:

- Magnetocrystalline anisotropy,
- Shape anisotropy,
- Stress anisotropy,
- Exchange anisotropy, and
- Surface anisotropy.

These magnetic anisotropies play an important role in a variety of magnetic properties such as coercive force, hysteresis losses, magnetization processes, domain structure, shape of the hysteresis loop, and magnitudes of permeability [14].

Magnetocrystalline Anisotropy Magnetocrystalline anisotropy is an intrinsic property and is induced by the interaction between orbit and spin known as spin–orbit coupling. This is used to study the modification of magnetic properties along various crystal axes. Different types of crystal axes are easy, intermediate, and hard axes, which display the highest, intermediate, and lowest magnetic moment at the applied magnetic field, respectively. Indeed, there are a set of directions in all ferromagnetic substances in which the magnetization tends to be oriented in the desired direction, depending on the amount and direction of an applied field. Anisotropy of materials describes the competition between the electrostatic crystal–field interaction and spin–orbit coupling. When an applied field adjusts the spin of an electron, its orbit shows a resistance, since the orientation of the electron’s orbit is strongly fixed to the crystal lattice. The magnetocrystalline anisotropy energy is the required energy for breaking the spin–orbit coupling to magnetize a material by reorienting its spin direction.

The magnetization process is different when the field is applied along with different crystallographic directions, and the anisotropy reflects the crystal symmetry. Its origin is in the crystal–field interaction and spin–orbit coupling, or else the inter-atomic dipole–dipole interaction.

Magnetocrystalline anisotropy is the energy necessary to deflect the magnetic moment from the easy to an arbitrary direction. The magneto anisotropy energy (E_K) for the uniaxial crystals is evaluated based on the direction in which the magnetization is rotated. Its value is obtained by considering some constants:

$$E_K = K_1 \sin^2 \theta + K_2 \sin^4 \theta + \dots \quad (1.10)$$

where θ is the angle between M_s and the easy axis.

The magnetization inclines to locate along with fixed crystallographic directions, which are called easy directions or easy axes due to the influence of magnetocrystalline anisotropy. This all happens because of the spontaneous domain magnetization directions of a crystalline material in the demagnetized state. There is cubic symmetry of the easy axes in the $\langle 100 \rangle$ direction for body-centered cubic (BCC) and $\langle 111 \rangle$ for the face-centered cubic (FCC) lattices in the crystals. A variety of crystal directions for a cubic crystal are shown in Figure 1.2 [23]. The situation is more complete in the case of hexagonal crystals when the easy direction may lie either along the c axis of the crystal, or on the basal plane, or even in a cone about the c axis.

For spinel ferrite, magneto anisotropy energy is more formally stated as follows [9]:

$$E_K = K_1 (\alpha_1^2 \alpha_2^2 + \alpha_2^2 \alpha_3^2 + \alpha_3^2 \alpha_1^2) + K_2 (\alpha_1^2 \alpha_2^2 \alpha_3^2) + \dots \quad (1.11)$$

where K_1 and K_2 are the constants of anisotropy and α_1 , α_2 , and α_3 are the angles between M_s and cubic axes of a , b , and c , respectively [14]. Commonly the first

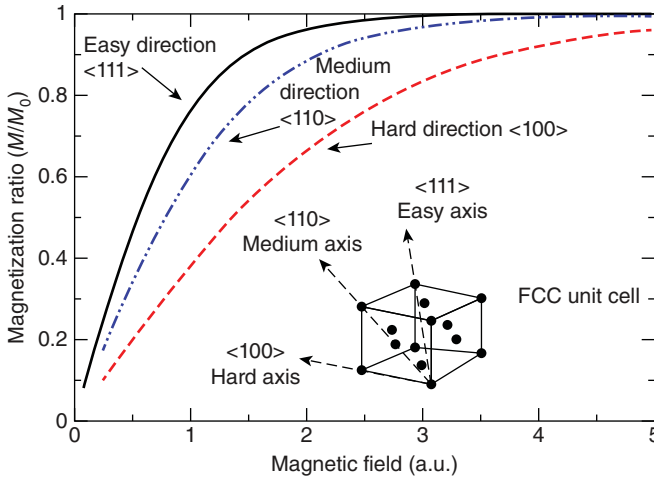


Figure 1.2 Various possible axes of magnetization in a cubic FCC crystal. In this example, (111) is the easy axis, and (100) is the hard axis. Source: Fernando [23]/with permission of Elsevier.

constant of anisotropy (K_1) has a key role and is dominant. Except for CoFe_2O_4 , in other spinel ferrites, K_1 has a negative value. Therefore, in most spinel ferrites, the easy direction is the cubic diagonal [111]. In soft magnetic ferrite, K_1 should be as minimum as possible in absolute magnitude.

For polycrystalline materials of cubic symmetry, the average magnetostriction or deformation (λ_s) is given by:

$$\lambda_s = \frac{2}{5}\lambda_{100} + \frac{3}{5}\lambda_{111} \quad (1.12)$$

where λ_{100} and λ_{111} are the maximum linear deformation with a field in the [100] and [111] crystallographic directions, respectively. In most ferrites, the body diagonal [111] is the easy direction except for cobalt ferrite, which exhibits an easy direction of magnetization along the cube edges at [100], and a single crystal of iron tends to magnetize in the directions of the cube edges at [100] [13]. The induced anisotropy energy is given as:

$$E = K_U \sin^2(\theta - \theta_U) \quad (1.13)$$

where $(\theta - \theta_U)$ is the angle of the measuring field (θ) relative to the annealing field (θ_U) and K_U is the induced anisotropy constant.

Shape Anisotropy Shape anisotropy derives from the demagnetizing field which relies on the direction of magnetization in the sample, and it is not an intrinsic property of the material.

Shape anisotropy is the force that orders the magnetization throughout a certain particle axis. Shape anisotropy happens in extended particles. A polycrystalline sample has no macroscopic crystal anisotropy, and its grains have no specific orientation. If the sample is spherical, the direction of an applied field will not affect

its magnetization. If a magnetic sample is not spherical, it will be magnetized along the long axis than the short one. This is because the demagnetizing field along the short axis is stronger, and thus, a longer field is needed to create the same true field inside the sample.

Stress Anisotropy This kind of anisotropy occurs due to the change in physical dimensions when the sample is subjected to an externally applied field. The effect is associated with a fractional change in length and is called magnetostriction (λ_s). Stress anisotropy is also affected by external or internal stresses caused by rapid cooling, application of external pressure, etc. It may also be induced by annealing a sample in a magnetic field, plastic deformation, or ion beam irradiation [24].

Magnetostriction (λ) results from the fractional variation in length (or dimension) of a material, which is called a strain, in relevance with the constants of anisotropy (variation of magnetization). The reduction in length occurs in all ferrites during magnetization, except for ferrous ferrites. This variation can be related to the energy sensitivity to mechanical stress, which happens during the synthesis and operation process. The control of such stresses is somehow difficult. To achieve the desired quality of soft ferrites, magnetostriction should be as low as possible. In magnetostrictive materials, however, magnetostriction and magnetocrystalline are the intrinsic behavior, and through a selection of proper crystal structure and chemistry, they can affect the magnetic factors for certain utilization.

Exchange Anisotropy The exchange anisotropy is almost a new phenomenon, which is produced by an interaction between an antiferromagnetic and ferromagnetic material [25]. The source of the interaction that lines up the spins in the magnetic system is a result of the exchange interaction. The occurrence of such anisotropy has been considered to have a fundamental role in information storage technology.

Surface Anisotropy The contribution of surface anisotropy in magnetic particles occurs once their sizes reduce to a nanosized scale. It mostly seems to appear in grain boundaries and has a crystal field nature [26].

1.3.2 Extrinsic Properties

Extrinsic or extensive properties of magnetic materials depend on the quantity of matter (for example, weight). Some examples of the extrinsic properties of magnetic materials are hysteresis loop, magnetic loss, and permeability. These properties are influenced by microstructure characteristics [9]. However, chemical microstructure may possess deleterious influences; sometimes taking benefit of chemical aspects is carried out to develop microstructural as well as properties such as electrical and magnetic properties. Undoubtedly, the microstructure conundrums are the most crucial issues that must be considered to achieve a desirable property and reproduce a high quality of ferrites. To improve the property of ferrite to be used in high-frequency applications, the control of microstructure characteristics,

i.e. pores, sintered density, grain size, and distribution, is more crucial than the choice of chemistry [20, 27–35]. Indeed, the porosity as well as grain size and their distribution, as a microstructure feature, are the two main factors that affect magnetic properties such as initial permeability [20, 36, 37]. Recent studies on nickel ferrite and nickel-zinc ferrite, for example, revealed that grain size has a more key role in initial permeability than porosity. In soft ferrites, sometimes, the effects of these parameters on permeability become more complicated. Therefore, the importance of controlling the microstructure characteristics becomes more evident. However, the experimental effects of grain size are well known, and a systematical science about physical phenomena has not been completely developed. In fine-structured materials, normally there is no domain wall within the grain; thus, the permeability is accomplished by the means of the rotational process. However, in the single-domain state, one cannot easily determine the critical grain size. As the size of the grain enhances, the domain walls within the grains would increase. They may either be nailed at intergranular pores or grain boundaries. Porosities have an important role in the restriction of the domain wall movement as well as in the contribution of the demagnetizing field. Therefore, the domain wall motion is sensitive to porosity distribution and grain size as well. The existence of porosity at the grain boundaries and within the grains can affect the hysteresis, coercivity, and permeability.

References

- 1 Halliday, D., Resnick, R., and Walker, J. (1997). *Fundamentals of Physics, Extended*, 5e. Wiley.
- 2 Foot, C.J. (2004). *Atomic physics*, vol. 7, 331. Department of Physics Christopher, Oxford University Press.
- 3 Kittel, C., McEuen, P., and McEuen, P. (1996). *Introduction to Solid State Physics*. New York: Wiley.
- 4 Wenzel, M.J. and Steinle-Neumann, G. (2007). Nonequivalence of the octahedral sites of cubic Fe_3O_4 magnetite. *Physical Review B* 75: 214430.
- 5 Hajalilou, A., Mazlan, S.A., Lavvafi, H., and Shameli, K. (2016). *Field Responsive Fluids as Smart Materials*. Springer.
- 6 Gilleo, M. (1980). Ferromagnetic insulators: garnets. In: *Handbook of Ferromagnetic Materials*, vol. 2, 1–53. Elsevier [https://doi.org/10.1016/S1574-9304\(05\)80102-6](https://doi.org/10.1016/S1574-9304(05)80102-6).
- 7 Morrish, A.H. (2001). *The Physical Principles of Magnetism*. Wiley.
- 8 Moskowitz, B. M. (1991). Hitchhiker's guide to magnetism. *Environmental Magnetism Workshop (IRM)*, Institute for Rock Magnetism University of Minnesota, Minneapolis, Minnesota, p. 48.
- 9 Goldman, A. (2012). *Handbook of Modern Ferromagnetic Materials*. Springer Science & Business Media.
- 10 Winkler, G. (1981). *Magnetic Garnets*, Vieweg Tracts in Pure and Applied Physics. Braunschweig/Wiesbaden: Vieweg.

- 11 Jakubovics, J.P. (1987). *Magnetism and Magnetic Materials*. London: Institute of Metals, Carlton House Terrace.
- 12 Goldman, A. (1999). *Handbook of Modern Ferromagnetic Materials*. Boston: Kluwer Academic Publishers.
- 13 Spaldin, N.A. (2010). *Magnetic Materials: Fundamentals and Applications*. Cambridge University Press.
- 14 Néel, L. (1948). Propriétés magnétiques des ferrites; ferrimagnétisme et antiferromagnétisme. *Annales de Physique* 12 (3): 137–198.
- 15 Klein, C. and Dutrow, B. (2009). *Manual de ciência dos minerais*. Bookman Editora.
- 16 Ghate, B.B. and Goldman, A. (2006). Ferrimagnetic ceramics, Chapter 13. In: *Materials Science and Technology*, 681–726. Wiley <https://doi.org/10.1002/9783527603978.mst0129>.
- 17 Brooks, H. (1940). Ferromagnetic anisotropy and the itinerant electron model. *Physical Review* 58: 909.
- 18 Heisenberg, W. (1985). Zur theorie des ferromagnetismus. In: *Original Scientific Papers Wissenschaftliche Originalarbeiten*, 580–597. Springer.
- 19 Abdollah, H., Mansor, H., Reza, E.-K., and Taghi, M.M. (2015). Effect of milling atmosphere on structural and magnetic properties of Ni–Zn ferrite nanocrystalline. *Chinese Physics B* 24: 048102.
- 20 Hajalilou, A., Hashim, M., Kamari, H.M., and Masoudi, M.T. (2015). Effects of milling atmosphere and increasing sintering temperature on the magnetic properties of nanocrystalline $\text{Ni}_{0.36}\text{Zn}_{0.64}\text{Fe}_2\text{O}_4$. *Journal of Nanomaterials* 16: 232.
- 21 Hajalilou, A. and Mazlan, S.A. (2016). A review on preparation techniques for synthesis of nanocrystalline soft magnetic ferrites and investigation on the effects of microstructure features on magnetic properties. *Applied Physics A* 122: 1–15.
- 22 Hajalilou, A., Mazlan, S.A., and Shila, S.T. (2016). Magnetic carbonyl iron suspension with Ni–Zn ferrite additive and its magnetorheological properties. *Materials Letters* 181: 196–199.
- 23 Fernando, G.W. (2008). Magnetic anisotropy in transition metal systems, Chapter 4. In: *Handbook of Metal Physics* (ed. G.W. Fernando), 89–110. Elsevier.
- 24 Kakeshita, T. (2012). *Progress in Advanced Structural and Functional Materials Design*. Springer Science & Business Media.
- 25 Berkowitz, A., Lahut, J., and VanBuren, C. (1980). Properties of magnetic fluid particles. *IEEE Transactions on Magnetics* 16: 184–190.
- 26 Varadan, V.K., Chen, L., and Xie, J. (2008). *Nanomedicine: Design and Applications of Magnetic Nanomaterials, Nanosensors and Nanosystems*. Wiley.
- 27 Hajalilou, A., Hashim, M., Ebrahimi-Kahrizsangi, R., and Mohamed Kamari, H. (2015). Influence of evolving microstructure on electrical and magnetic characteristics in mechanically synthesized polycrystalline Ni-ferrite nanoparticles. *Journal of Alloys and Compounds* 633: 306–316.
- 28 Hajalilou, A., Hashim, M., Ebrahimi-Kahrizsangi, R., and Sarami, N. (2015). Influence of CaO and SiO_2 co-doping on the magnetic, electrical properties and microstructure of a Ni–Zn ferrite. *Journal of Physics D: Applied Physics* 48: 145001.

- 29 Hajalilou, A., Kianvash, A., Lavvafi, H., and Shameli, K. (2018). Nanostructured soft magnetic materials synthesized via mechanical alloying: a review. *Journal of Materials Science: Materials in Electronics* 29: 1690–1717.
- 30 Rezaie, E., Rezanezhad, A., Ghadimi, L.S., Hajalilou, A., and Arsalani, N. (2018). Effect of calcination on structural and supercapacitance properties of hydrothermally synthesized plate-like $\text{SrFe}_{12}\text{O}_{19}$ hexaferrite nanoparticles. *Ceramics International* 44: 20285–20290.
- 31 Pourzaki, M., Kavkhani, R., Kianvash, A., and Hajalilou, A. (2019). Structure, magnetic and transmission characteristics of the Co substituted Mg ferrites synthesized via a standard ceramic route. *Ceramics International* 45: 5710–5716.
- 32 Ismail, M.A.N., Hashim, M., Hajalilou, A. et al. (2014). Magnetic properties of mechanically alloyed cobalt-zinc ferrite nanoparticles. *Journal of Superconductivity and Novel Magnetism* 27: 1293–1298.
- 33 Hajalilou, A., Hashim, M., and Mohamed Kamari, H. (2014). Effects of additives and sintering time on the microstructure of Ni–Zn ferrite and its electrical and magnetic properties. *Advances in Materials Science and Engineering* 2014: 6. doi.org/10.1155/2014/138789.
- 34 Mirzazadeh, A., Kianvash, A., and Hajalilou, A. (2018). Plating of Cu and Ni metals on Mg-ferrite sintered bodies by an electroless method and an investigation of magnetic behavior. *Journal of Materials Science: Materials in Electronics* 29: 5753–5760.
- 35 Kavkhani, R., Pourzaki, M., Kianvash, A., and Hajalilou, A. (2021). Effect of sintering temperature and soaking time on the magnetic properties and transmission behavior of nano crystalline $\text{Mg}_{0.8}\text{Mn}_{0.2}\text{Al}_{0.1}\text{Fe}_{1.9}\text{O}_4$. *Journal of Sol-Gel Science and Technology* 99 (2): 444–454.
- 36 Kingery, W.D., Bowen, H.K., and Uhlmann, D.R. (1976). *Introduction to Ceramics*. Wiley.
- 37 Hajalilou, A., Kamari, H.M., and Shameli, K. (2017). Dielectric and electrical characteristics of mechanically synthesized Ni–Zn ferrite nanoparticles. *Journal of Alloys and Compounds* 708: 813–826.

2

Type and Characteristics of Magnetic Materials

2.1 Introduction

In general, magnetic materials in the polycrystalline state can be composed of a large number of minute crystals and are categorized into different groups in terms of type and crystal structure (Table 2.1).

Among them, ferrites are a large class of magnetic oxides with remarkable characteristics, which have been investigated and applied in various applications during the last ~50 years. Their multiple functionalities arise from several positive points such as the combination of electrical insulators and magnetic materials with remarkable flexibility in controlling their properties. These features enable them to be used in applications ranging from mankind's body protection, i.e. life science, e.g. cancer treatment, to daily-used devices such as electronic devices.

It is believed that the application of magnetic materials is mainly dependent upon the type of magnetic materials, e.g. being either soft or hard ones. Thus, this chapter briefly describes the characteristics of soft and hard magnetic materials by taking into account their hysteresis loop formation. Their hysteresis loops are derived from either magnetization as a function of the magnetic field ($M-H$) for powder- or liquid-form samples and/or induction as a function of the magnetic field ($B-H$), which is obtained from bulk, pellet, or toroid-shaped samples. This is followed by studying the types of magnetic losses in magnetic materials.

2.2 Soft and Hard Magnetic Materials

Spinel ferrites, based on their ability to maintain hysteresis or magnetization/demagnetization, can be divided into two categories: soft and hard.

2.2.1 Soft Magnetic Materials

In general, the chemical formula for such materials is AB_2O_4 , where metal ions tend to occupy the A and B sites, which are called as tetrahedral and octahedral sites, respectively. Materials such as Ni ferrite, Zn ferrite, Ni-Zn ferrites, Fe_3O_4 , and

Table 2.1 Classification of ferrite materials in terms of the general formula, crystal structure, and replacements.

Serial number	Types	Crystal structure	General formula	Replacements
1	Garnet	Cubic	$\text{Ln}^{\text{III}}_3\text{Fe}_5\text{O}_{12}$	Ln^{III} : Eu, Gd, Tb, Tm, Lu, Y, Dy, Ho, Er, Sm, etc.
2	Spinel	Cubic	$\text{A}^{\text{II}}\text{Fe}_2\text{O}_4$	A^{II} : Zn, Mn, Ni, Mg, Co, etc.
3	Magnetoplumbite	Hexagonal	$\text{A}^{\text{II}}\text{Fe}_{12}\text{O}_{19}$	A^{II} : Ba, Sr, Pb, etc.
4	Orthoferrite	Perovskite	$\text{Ln}^{\text{II}}\text{FeO}_3$	Ln^{II} : Ho, Er, Tm, Lu, Eu, Gd, Tb, Dy, Y, Sm, etc.

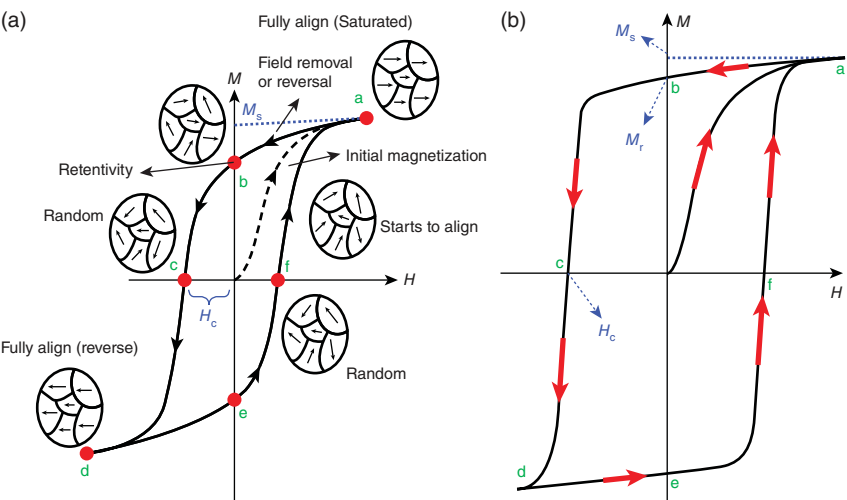


Figure 2.1 M - H hysteresis loop of (a) soft and (b) hard magnetic materials.

Mn-Zn ferrites [1–10] are considered soft magnets, as they are easily magnetized in the presence of an applied magnetic field and demagnetized when the applied magnetic field is removed. In such materials, coercivity is small (usually less than 1000 A/m) (Figure 2.1a). The main characteristic of these materials is that they have a low density of crystal defects and lattice strain, which causes easy domain wall movement.

These soft magnetic materials have versatile technological applications due to the involvement of remarkable magnetic properties such as high electrical resistivity, high permeability, low power loss at high frequency, high Curie temperature, and low hysteresis losses. Such characteristics result in their use in high-frequency utilizations such as microwave communication, as core materials for transformers and inductors, and in other applications, e.g. medical science, bioengineering, and environment.

2.2.2 Hard Magnetic Materials

Hard magnetic materials are those materials that maintain their magnetism even after the elimination of the external magnetic field. This simply means that they exhibit high resistance against demagnetization. For this reason, they are also considered as permanent magnetic materials. In these materials, due to the presence of crystalline defects and phase boundaries, the movement of domains is difficult. Therefore, there are hardly any rotation of domains and the movement of domain walls. These kinds of materials have an intrinsic coercivity greater than about 10 kA/m and include a wide hysteresis loop (Figure 2.1b).

2.3 Hysteresis Loop

The magnetization of materials that are plotted schematically as a function of magnetized and demagnetized fields is known as a hysteresis loop. They are given either as $M-H$ or $B-H$ hysteresis loop, where the $M-H$ hysteresis curve is obtained from the powder or liquid form of sample measurement, while the $B-H$ hysteresis curve is achieved from a pellet or toroid-shaped sample. The integrated area in the corresponding hysteresis loop is a measure of the hysteresis loss that is strongly attributed to irreversible domain rotation and domain wall motion. The shape of the loop relies on both intrinsic and extrinsic magnetic properties of a sample. The correlation between magnetization (M) and induction (B) can be given as:

$$B = \mu_0(M + H) \quad (2.1)$$

where $\mu_0 = 4\pi \times 10^{-7}$ H/m is the permeability of the vacuum and H is the applied field.

2.3.1 The Process of Hysteresis Loop Formation

It is believed that, in the absence of a magnetic field (zero field), the magnetic moments in a material are randomly oriented around or along the easy axes. This means that there is no specific magnetic moments alignment. This state is considered a “virgin state.” When a small magnetic field is applied, the magnetic moments are slowly oriented in the direction of the magnetic field and increase magnetization (dashed line in Figure 2.1a). With the further increase in the magnetic field, the magnetization increases and reaches a point where no further increase in the value is obtained. This maximum magnetization is called saturation magnetization (M_s in the $M-H$ curve and B_s in the $B-H$ curve) (point a in Figure 2.1). It is expected that by removing the applied magnetic field, the curve returns to point O, but it rarely happens. This means that the flux density/magnetic induction would not relax back to zero magnetization (“virgin state”). Thus, a reverse magnetic field is applied for the magnetic moments initiated to demagnetize and lose their alignment along with the preferred crystallographic ordinates of easy axes. In this circumstance, however, the amount of the applied magnetic field is identical to

the one used for magnetization, but in an opposite direction. It is thought that all the magnetic moments lose their alignment along the easy axes and return to the “virgin state” at zero field. Some of the magnetic moments retain in the direction of hard axes even though there is no magnetic field applied to the materials. The value of the magnetization at this moment is known as the remanence or retentive value (point b). At this point, the magnetization force is zero, but some magnetic fluxes remain in the material, which is considered remanence or retentivity. It presents residual magnetization in the material in the absence of an externally applied field. These remaining magnetic moments are held by magnetocrystalline anisotropy. A large amount of energy – magnetocrystalline anisotropy energy – is needed to align all the magnetic moments back to the original position. To decrease the flux to zero, a small reverse magnetic field is applied, and the curves shift to point “c.” The amount of magnetic field used to align the magnetic moments in the direction of easy axes is known as coercivity. The domains have been flipped enough by the reversed magnetizing force in such a way that the net flux through the material is zero. The force required to eliminate the residual magnetism from the sample is known as coercive force. With further enhancement in the magnetic field in the negative direction, the sample would be magnetically saturated again but in the inverse direction (point “d”).

Upon reversal of the field direction from point a to point d, the changes in the domain structure also reverse. The single domain is rotated with the reverse field, which is followed by the domains having magnetic moments aligned with the new field formation and growth at the expense of the former domains. Crucial to this description is the resistance to the domain wall movement that takes place in response to the increase in the magnetic field in the opposite direction that gives the lag of M with H or hysteresis. When the applied field reaches zero, there is still some net volume fraction of domains oriented in the former direction, which emphasizes the existence of the remanence. This is followed by a coercive force (H_c) at point c. Upon continuation of the applied field in the reverse direction, saturation is finally completed in the opposite sense, which is attributed to point d. A second reversal of the field to the point of initial saturation (point a) completes the symmetrical hysteresis loop and yields both negative remanence ($-M_r$) and positive coercivity ($+H_c$).

By removing the magnetic field, the curve moves to point “e,” which creates the same level of residual magnetism obtained in the other direction. The graph did not return to its original shape due to the requirement of some forces to eliminate the residual magnetism. The loop tends to be completed when the curve traverses various paths from point “f” back to the saturation.

2.3.2 Domain Orientation in Directions Favorable to the Applied Field

Figure 2.2 indicates an initially magnetized curve (dashed line) in the M – H or B – H curve. The magnetization (M) enhances slowly at the beginning of an applied field, and then more quickly, and finally leveling off and becoming independent of H . Subsequently, a state is reached where further increase in the applied magnetic field does not lead to further magnetization occurrence in the sample; this state is

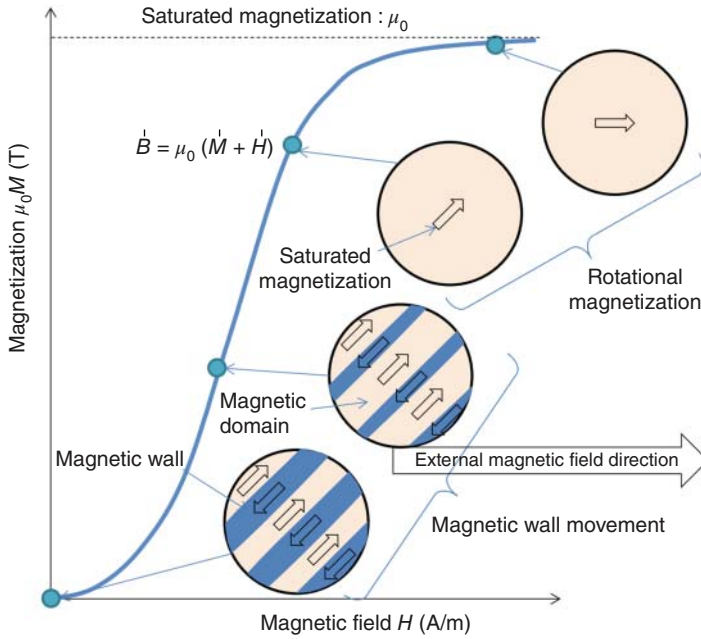


Figure 2.2 Magnetic domain structure and magnetization process. Source: Fujisaki [11]/with permission of Elsevier.

considered as saturation magnetization (M_s) or saturation flux density (B_s) in the B - H hysteresis loop. Since the permeability (μ) refers to the slope of the M - H curve based on the equation: $M = \mu H$, the slope of the M - H curve at $H = 0$ is stated as a material property, which is termed as the initial permeability (μ_i). The domain size and shape variation can be seen by the movement of domain boundaries when the magnetic field is applied. The figure shows a schematic representation of domain configurations during several stages of magnetization along the M - H curve. Initially, the moments of the domains are randomly oriented because there is no net M (or B) field. In the presence of an externally applied magnetic field, the domains that are oriented in directions favorable to the applied field grow at the expense of those that are unfavorably oriented. This process continues with the increase in field strength until the macroscopic sample becomes a single domain, which is nearly aligned with the field. Saturation is achieved as this domain becomes oriented with the field by rotation.

2.4 Magnetic Characteristic Measurements

2.4.1 M - H Hysteresis Loop

A vibrating sample magnetometer (VSM) is typically used to characterize the magnetic behavior of the samples. The VSM traits, based on Faraday's law of induction, indicate the generation of the electric field as a result of a varying

magnetic field. The principle performance of VSM is firstly established by placing the sample in a constant magnetic field. This constant magnetic field tends to magnetize the sample by lining up the magnetic domains or the individual magnetic spins with the field if the sample is magnetic. A larger magnetization will occur if the constant field is stronger. A magnetic field around the sample is created as a result of the magnetic dipole moment, which is well known as a magnetic stray field. As the sample is shifted up and down, the magnetic stray field varies as a function of time, and it is sensed by a set of pick-up coils.

The hysteresis loops obtained, by using a VSM or superconducting quantum interference device (SQUID), are considered as M - H hysteresis curves or loops. Automatic measurement of the fundamental magnetization curve is provided by this equipment. Furthermore, it provides magnetic hysteresis graphs under the static state of magnetic materials and precise measurement of static magnetic behavior parameters such as coercivity (H_c), saturation magnetization (M_s), and remanence (M_r). Magnetization in terms of applied field measurements is a time-dependent measurement of the magnetic moment of a sample as the magnetism is enhanced and declined in a hysteretic fashion. In general, the M - H curve yields information about an intrinsic amount of magnetic moment. It does not measure the effect of the field. For the room-temperature measurement for obtaining the hysteresis loop, for instance, first, the magnetic field is ramped to 1 kOe in 100 Oe accretions, continued by ramping to 10 kOe in 1 kOe enhancements. The reversion magnetic field is applied at an identical state of field spacings to -10 kOe. Eventually, the magnetic field is elevated to, e.g. 12 kOe, to carry out a complete measurement of the hysteresis loop. The M_s is identified by scrutinizing the magnetic moment of the sample at the largest applied magnetic field. H_c and M_r are estimated by placing the point on the x -axis and y -axis, respectively, where the magnetization is zero in an applied field [12].

2.4.2 B - H Hysteresis Loop

B - H hysteresis loop can be attained by performing, e.g. a Linkjoin Technology MATS 2010 Static Hysteresisgraph. From the B - H curve, the main parameters that can be obtained include coercivity (H_c), saturation induction (B_s), flux density (B_r), and magnetic losses. The measurement is accomplished on the toroid-shaped samples at room temperature. The sample is prepared by rounding a sample with a copper wire with 60 turns for the secondary turn (N_2) and with 10 turns for the primary turn (N_1). Then, the samples are connected to a B - H hysteresis graph, and the curve data are shown on the monitor. The B - H curve yields information about an extrinsic characteristic of a material, and the contribution of the field is considered. Thus, for engineering applications, the B - H would give more accurate information or details.

2.5 Magnetic Losses

When the magnetic materials are subjected to an external magnetic field, some of the energy is lost in the form of heat. Generally, the three main mechanisms of energy losses in those materials are as follows:

- (i) Eddy current loss, also known as dielectric loss, is induced by the electric induction current flowing through the ferrite.
- (ii) Residual loss which resulted from intrinsic damping.
- (iii) Hysteresis loss which is caused by an irreversible jump of the domain walls.

The overall power loss (P_y) of ferrites is achieved by the combination of (i), (ii), and (iii) based on the following relation:

$$P_y = P_e + P_r + P_h \quad (2.2)$$

where the three terms on the right-hand side are eddy current loss, residual magnetic loss, and hysteresis loss, respectively.

Magnetic losses in ferrites can be classified into residual losses, hysteresis losses, and eddy current losses. For the ferrite core losses (R) per unit frequency (f) and inductance (L), it can be expressed as:

$$\frac{R}{fL} = ef + hH + r \quad (2.3)$$

where H is the field strength and e , h , and r are eddy current, hysteresis, and residual coefficients, respectively [13]. Core losses are the low losses in the core at high levels of induction and are used in power applications of ferrites such as hard drives. Separation of the losses can be accomplished by plotting R/fL versus f for different field strengths or R/fL versus H at different frequencies and solving for e , h , and r from the intercepts and slopes.

2.5.1 Eddy Current Losses

The eddy current loss mechanism is due to the resistive losses that are created by the current induced in ferromagnetic materials, when subjected to an alternating magnetic field. To obstruct the flow of eddy currents and consequently diminish their losses, normally silicon-iron is laminated in most electrical tools. The eddy current losses increase with the square of frequency at high frequencies. When an alternating magnetic field is applied to a magnetic material, an electromotive force (emf) is induced in the material itself according to Faraday's law of electromagnetic induction. Since the magnetic material is a conducting material, the emf circulates currents within the body of the material. These circulating currents are called eddy currents. Eddy currents occur when the conductor experiences a change in the magnetic field. As these currents are not responsible for useful work, they will produce a loss in the magnetic material, known as eddy current losses. Eddy current losses (P_e) may occur in all types of materials but are higher in magnetic materials due to their higher permeability and a greater change in induction, ΔB [13]. The eddy current loss factor $(\tan \delta_e)/\mu$ is directly related to the reciprocal of resistivity, ρ . The eddy current effect is strongly dependent on the resistivity of the material, which affects the resistance in the eddy current loop [14]. Since the ferrites have high resistivity, the eddy currents will be reduced. However, as the frequency is increased, the eddy current losses will be greater and therefore considerably reduce the performance of magnetic materials.

The voltage induced during the cyclic magnetization of materials, which is in the inverse direction of the alternating magnetic field, results in magnetic current generation. The circular current occurs in the material due to the induced value and gives rise to magnetic fields in the opposite direction of the original magnetic field. The induced voltage is a rate of induction (B) variation with time. The effect of eddy current typically relies on the material's resistivity, which can affect the resistance of the eddy current loop. This is expressed by [15]:

$$P_e = CB^2 \frac{f}{\rho} \quad (2.4)$$

where P_e is the eddy current losses, f is the frequency, ρ is the resistivity, B is the flux density, and C is the proportionality constant. This equation suggests that these losses are crucial as well as dominant compared to other losses at high frequencies. These losses are reduced by increasing the resistivity of the material. They would decline with the increase in the resistivity of the sample.

The eddy currents generated by the alternating magnetic field are restricted by their high intrinsic resistivities. It is believed that the losses by the eddy current are inversely proportional to the electrical resistivity of the spinel ferrite [16]. The chemical and microstructure characteristics of ferrites can significantly modify their electrical resistivity. Its value varies with the changes in experimental conditions and usually ranges from 10 to $10^{11} \Omega \text{ cm}$. A resistivity of $10 \Omega \text{ cm}$ was reported for Ni-Zn ferrites when they contained 0.42% by weight of ferrous oxide [17]. The influence of microstructure on resistivity can be often described in terms of the composite behavior of ferrites. The electrons' flow resistance varies from grain interior to grain boundaries. The grain boundaries would show trait as an insulator and impede electron flow, while grains would behave as a semiconductor. Thus, it is expected that the electrical resistivity of ferrite materials will be reduced with the number of grain boundaries reduced by the means of grain growth [18]. A reduction in the electrical resistivity of Ni-Zn ferrite can also be attributed to the divalent ions of iron formed by zinc loss at high sintering temperature, resulting in enhanced conductivity and decreased resistivity.

Electrical conduction in spinel ferrite takes place by the polaron-hopping mechanism. This simply means that the electron movement with its corresponding elastic distortion field causes electrical conduction. Electron hopping occurs between various cations of the same atom situated at a crystallographically equivalent lattice site [19]. Thus, attention must be paid to cations in the lattice that present multivalent behavior. In Ni-Zn ferrite, the multivalent character has been distinguished for iron cations based on the following reaction:



Consequently, to achieve a high resistivity in Ni-Zn ferrites, the Fe^{2+} cations must be closely controlled and kept at a minimum. This is achieved by low sintering temperature and high-pressure oxygen sintering [18–20].

2.5.2 Residual Losses

Residual loss is concerned with magnetic relaxations and resonances in magnetic materials. Magnetic relaxations contributing to these losses are due to the domain wall excitations. Magnetic resonance may occur in two ways: as a rotational resonance and as a domain wall resonance. These kinds of losses become more important in the low magnetic field and low-frequency field. Normally, for high-frequency applications, they can be ignored. Residual losses (P_r) play a key role in falling power loss in the MHz range as they claim over 80% of the total core loss at frequencies above 500 kHz [13].

To reduce the residual loss, the grain size in ferrites should be reduced as much as possible [13]. Small grains can be achieved by using ultrafine powders and sintering at a lower temperature during shorter periods.

These kinds of losses are microscopically observable from the position of the moment in the magnetic material. Magnetic resonance is an example of this intrinsic factor, which includes energy absorption preceded by energy dissipation to the lattice structure in the form of heat. Typically, residual losses are damping losses, and they are induced by the occurrence of the diffusion process in the lattice.

2.5.3 Hysteresis Losses

Hysteresis is a nonlinear behavior of ferromagnetic materials. Indeed, the area within a hysteresis loop represents the losses in the material during the cyclic magnetization process. At high induction levels, as utilized in power applications, the displacement of domain walls takes place and leads to hysteresis losses. In other words, hysteresis losses are due to energy losses from irreversible wall motion. This energy loss is manifested as heat that is generated within the magnetic sample. These kinds of losses are due to the required dissipating energy to rotate the domains and to move the domain walls back and forth during the magnetization and demagnetization of materials. These losses are dependent on the magnetic anisotropies (K_1 , K_u , and λ_s) and shape anisotropy, which includes extrinsic properties such as porosity, nonmagnetic inclusion, grain size, and internal strain distribution. Hysteresis losses can be minimized by reducing hindrance to the domain wall movement by reducing their concentration and their influence [13]. This can be achieved by a low-volume fraction of crystalline defects per unit volume, i.e. pores, impurities, and dislocations. In addition, a low level of stress, small magnetocrystalline anisotropy, small magnetostriction, and high saturation magnetization are also necessary. In other words, to reduce hysteresis loss, all these factors must be decreased, except for M_s . The M_s is affected by chemical composition and density. Moreover, uniform grain growth and low porosity are also desired for hysteresis losses.

Hysteresis losses are typically dependent on frequency; therefore, they linearly enhance with frequency. They are closely attributed to coercivity; hence,

processing a material to lessen coercivity results in the reduction of hysteresis losses. However, hysteresis losses are not the only loss or dissipative mechanism in alternating current utilization.

References

- 1 Hajalilou, A. and Mazlan, S.A. (2016). A review on preparation techniques for synthesis of nanocrystalline soft magnetic ferrites and investigation on the effects of microstructure features on magnetic properties. *Applied Physics A* 122: 1–15.
- 2 Hajalilou, A., Hashim, M., and Kamari, H.M. (2015). Structure and magnetic properties of $\text{Ni}_{0.64}\text{Zn}_{0.36}\text{Fe}_2\text{O}_4$ nanoparticles synthesized by high-energy milling and subsequent heat treatment. *Journal of Materials Science: Materials in Electronics* 26: 1709–1718.
- 3 Hajalilou, A., Hashim, M., Abbasi, M. et al. (2015). A comparative study on the effects of different milling atmospheres and sintering temperatures on the synthesis and magnetic behavior of spinel single phase $\text{Ni}_{0.64}\text{Zn}_{0.36}\text{Fe}_2\text{O}_4$ nanocrystals. *Journal of Materials Science: Materials in Electronics* 26: 7468–7483.
- 4 Hajalilou, A., Hashim, M., Ebrahimi-Kahrizsangi, R. et al. (2014). Parametric optimization of NiFe_2O_4 nanoparticles synthesized by mechanical alloying. *Materials Science-Poland* 32: 281–291.
- 5 Hajalilou, A., Hashim, M., and Masoudi, M.T. (2015). A comparative study of in-situ mechanochemically synthesized $\text{Mn}_{0.5}\text{Zn}_{0.5}\text{Fe}_2\text{O}_4$ ferrite nanoparticles in the $\text{MnO}/\text{ZnO}/\text{Fe}_2\text{O}_3$ and $\text{MnO}_2/\text{Zn}/\text{Fe}_2\text{O}_3$ systems. *Ceramics International* 41: 8070–8079.
- 6 Hajalilou, A., Hashim, M., Ebrahimi-Kahrizsangi, R., and Kamari, H.M. (2015). Thermal evolution of the Ni-ferrite nanoparticles obtained by mechanical alloying as probed by differential scanning calorimetry. *Journal of Thermal Analysis and Calorimetry* 119: 995–1000.
- 7 Hajalilou, A., Mazlan, S.A., Shilan, S.T., and Abouzari-Lotf, E. (2017). Enhanced magnetorheology of soft magnetic carbonyl iron suspension with binary mixture of Ni–Zn ferrite and Fe_3O_4 nanoparticle additive. *Colloid and Polymer Science* 295: 1499–1510.
- 8 Ogholbeyg, A.B., Kianvash, A., Hajalilou, A. et al. (2018). Cytotoxicity characteristics of green assisted-synthesized superparamagnetic maghemite ($\gamma\text{-Fe}_2\text{O}_3$) nanoparticles. *Journal of Materials Science: Materials in Electronics* 29: 12135–12143.
- 9 Hajalilou, A., Abouzari-Lotf, E., Abbasi-Chianeh, V. et al. (2018). Inclusion of octahedron-shaped ZnFe_2O_4 nanoparticles in combination with carbon dots into carbonyl iron based magnetorheological suspension as additive. *Journal of Alloys and Compounds* 737: 536–548.
- 10 Kanagesan, S., Hashim, M., Tamilselvan, S. et al. (2013). Synthesis, characterization, and cytotoxicity of iron oxide nanoparticles. *Advances in Materials Science and Engineering* 2013: 1–7.

- 11 Fujisaki, K. (2019). Fundamental concept of magnetic material for electrical engineer. In: *Magnetic Material for Motor Drive Systems: Fusion Technology of Electromagnetic Fields* (ed. K. Fujisaki), 27–44. Singapore: Springer Singapore.
- 12 Roodbar Shojaei, T., Hajalilou, A., Tabatabaei, M. et al. (2019). Characterization and evaluation of nanofiber materials. In: *Handbook of Nanofibers* (ed. A. Barhoum, M. Bechelany and A.S.H. Makhlouf), 491–522. Springer International Publishing https://doi.org/10.1007/978-3-319-53655-2_15.
- 13 Wohlfarth, E.P. (1986). *Handbook of Magnetic Materials*. Elsevier.
- 14 Goldman, A. (2006). *Modern Ferrite Technology*. Springer Science & Business Media.
- 15 Felicetti, R., Abrahamsson, C.J.D., and Lundin, U. (2020). The influence of eddy currents on the excitation winding impedance of solid and laminated salient pole synchronous machines. *Electrical Engineering* 102 (4): 2553–2566.
- 16 Snelling, E.C. (1969). *Soft Ferrites: Properties and Applications*. London: Iliffe Books.
- 17 Koops, C. (1951). On the dispersion of resistivity and dielectric constant of some semiconductors at audiofrequencies. *Physical Review* 83: 121.
- 18 Van Groenou, A.B., Bongers, P., and Stuyts, A. (1969). Magnetism, microstructure and crystal chemistry of spinel ferrites. *Materials Science and Engineering* 3: 317–392.
- 19 Mitoff, S. (1966). Electrical conduction mechanisms in oxides. *Progress in Ceramic Science* v4: 217–264.
- 20 Globus, A., Pascard, H., and Cagan, V. (1977). Distance between magnetic ions and fundamental properties in ferrites. *Le Journal de Physique Colloques* 38 (C1): 163–168. <https://doi.org/10.1051/jphyscol:1977132>.

3

Insight into the Synthesis of Nanostructured Magnetic Materials

3.1 Introduction

Nanotechnology is making a transformative impact in material science, leading to new applications, and more efficient devices. Several scientific and technological efforts have largely been directed toward improving the properties of nanocrystalline materials and developing their performance [1–3]. Indeed, the research in nanoscience focuses on the synthesis of advanced materials, and on understanding and correlating the phenomena attributed to them [2, 3].

Nanostructured materials are often considered materials in which the size of the particles is below 100 nm in at least one or more dimensions. At this length scale, a huge fraction of the atoms exists at or close to the surface of particles which yields unique characteristics to such materials. In particular, it can be said that the term “nano” is just a fraction that presented one billionth of a unit quantity until recently; however, the same is re-defining the understanding of the science matter at an extraordinary pace every day [3, 4]. For producing different self-assembly materials with size- and shape-controlled nanostructures (wires, tubes, cubes, and fibers), controlled properties to be used in various applications are under meticulous research.

At the nanoscale, these materials behave differently compared with their bulk or even micron-size counterparts. At the nanoscale, there is a significant increase in the surface-to-volume ratio, enhanced surface chemistry, a higher reactivity, and a high density of impurities in their structure. These features, considered microstructural imperfections, would act as the short-circuit paths to facilitate the diffusivity, which contributes to the synthesis of magnetic nanoparticles (MNPs) at low temperatures. These features can result in improved properties compared to their corresponding bulk (micro-sized) ones [2–10]. In addition, they can facilitate synthesizing MNPs at relatively low temperatures and short time span. In other words, unexpected behaviors concerning their chemical and physical properties can be observed in the nanoscale regimes accompanied by exhibiting unique and desirable electrical, electronic, and magnetic behaviors [11–13].

3.2 Synthesis Process of the Magnetic Nanoparticles

Generally, there are two approaches for making nanoparticles: (i) Top-down (from bulk [macro- or micro-sized] to nano-sized scale) and (ii) Bottom-up (from atom- to nano-sized scale). Figure 3.1 schematically represents how nanoparticles are produced using these methods. Examples of the top-down method are ball milling, electrochemical etching, and ultrasonic cutting. Examples of the second method include sol-gel, chemical vapor deposition (CVD), physical vapor deposition (PVD), laser ablation, and thermal plasma. The comparison of these processes for the synthesis of nanoparticles is given in Table 3.1.

There are several sub-categories of these processes such as wet-chemical or dry solid-state routes, which are used for the synthesis of magnetic or any other advanced materials nanoparticles. The preparation of MNPs has been studied for many years. A variety of methods have been developed and employed to produce

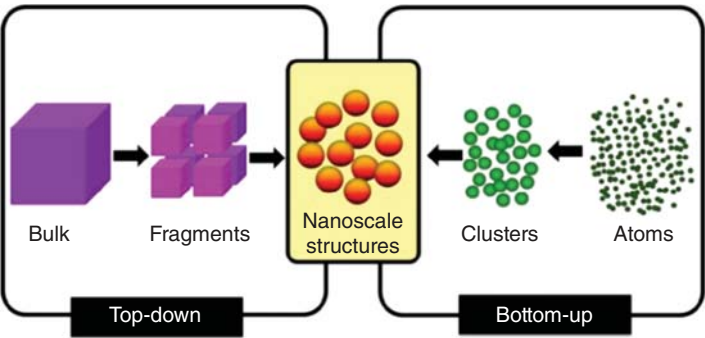


Figure 3.1 Schematic representation of bottom-up and top-down processes for the synthesis of nanoparticles. Source: Rawat [14]/IOP Publishing/Public Domian CC BY.

Table 3.1 Comparison of top-down and bottom-up processes for the synthesis of nanoparticles.

Top-down approach	Bottom-up approach
It involves particle size reduction to nano size	This involves the growth of nanoparticles from atomic size particles
All particles of the precursor may not break down to the required particle size	More control over particle size
The process is used only for hard, and brittle materials	The process is used for gas, liquids, and solids as well
The nanocrystalline materials prepared by this process may be contaminated by milling tools and the atmosphere	Fewer chances of contamination
e.g. Ball milling	e.g. Sol-gel, gas condensation method

the desired sample with the best characteristics depending on the application. For example, the synthesis methods can be divided into physical (e.g. ball milling and film deposition, laser ablation) and chemical routes (e.g. sol-gel, hydrothermal, etc.). Recently, a combination of these methods (e.g. mechanochemical) is considered in nanoscience as well. Each of these techniques has its own pros and cons. For example, it is possible to produce very fine powder particles at relatively low temperatures by employing the wet chemical routes; however, these methods have exhibited some drawbacks such as relatively complex procedure, pH sensitivity, low production rate, and expensive precursors. Generally, they are not environment-friendly. Moreover, they can mostly be utilized in the synthesis of nanopowders on laboratory scales.

Hence, the synthesis of inorganic compounds, especially magnetic materials, remains a big challenge in chemistry and chemical engineering. The idea of employing solid-state reactions to avoid dissolving steps, fusion, or sintering of the reactants in the course of synthesis has always been attractive [2, 3]. However, inadequate mixing of the reaction components, low contact surface, and strong diffusion resistance make the application of solid-state reaction difficult. Formation of the complex oxides with the spinel structure using the conventional solid-state reaction between simple oxides proceeds slowly and requires prolonged exposure at noticeably elevated temperatures [15–18]. Besides, the particles are large and non-uniform in their shape, size, and distribution [19, 20]. A high sintering temperature is required in solid-state methods, making them uneconomical due to their needs for equipment, such as highly expensive furnaces. Moreover, some elements like Zn, e.g. in Ni-Zn ferrite, and Mn-Zn ferrite may evaporate and cause unfavorable properties in the sample [21–26]. Thus, the combination of the solid-state method with other methods such as high-energy ball milling may eliminate their limitations and make them more suitable for large-scale production.

3.3 Importance of the Synthesis and/or Preparation Methods

The choice of synthesis route is very important, mainly due to aspects related with:

- (i) Cost and complexity; save time and energy.
- (ii) Eco-friendly nature.
- (iii) Performance and application.

Regarding the latter one, one should consider two main factors, i.e. the size and shape of as-synthesized nanoparticles. These parameters are remarkably influenced by the synthesis route, which gives rise to different magnetic properties and therefore to different performances and applications. In below sections, we briefly describe how the synthesis route affects the size and shape of the particles, thereby impacting the magnetic properties and performance of the material.

3.4 Dependency of Particle Size and Shape on Synthesize Route

The preparation methods are important because they influence a particle's morphology, shape, size, and distribution. Tuning the size of nanoparticles can be achieved by exercising control over nucleation and growth rates, as schematically illustrated in Figure 3.2. Fast nucleation provides a high concentration of nuclei, ultimately yielding smaller nanocrystals, whereas slow nucleation provides a low concentration of seeds consuming the same amount of precursors, thereby resulting in larger nanocrystals or particle formation.

Aspects of nanoparticle growth in a solution can be based on the following factors.

- (i) *Arrested precipitation*: Precipitation under starving conditions, where a large number of nucleation centers are formed by vigorous mixing of the reactant solution. If a concentration growth is kept small, nuclei growth is stopped due to lack of material. Thus, the particles have to be protected from Ostwald ripening by stabilizers.
- (ii) *Ostwald ripening*: It is the growth mechanism where small particles dissolve and are consumed by larger particles. As a result, the average size of the nanoparticles increases with time, and their concentration decreases with time. As particles increase in size, solubility decreases.

It can be generally said that parameters that are mainly affecting particle growth/shape/structure, are:

- Type of capping agent/stabilizer
- Reducing agent
- Type and concentration of the reactants
- pH value of the solution
- Experimental conditions, such as time, temperature, and stirring.
- Method employed.

The following factors are mainly considered to control [27] the particle growth/shape/structure:

- (i) The average particle size, which is strongly affected by reductant concentration, stirring rate, and temperature.

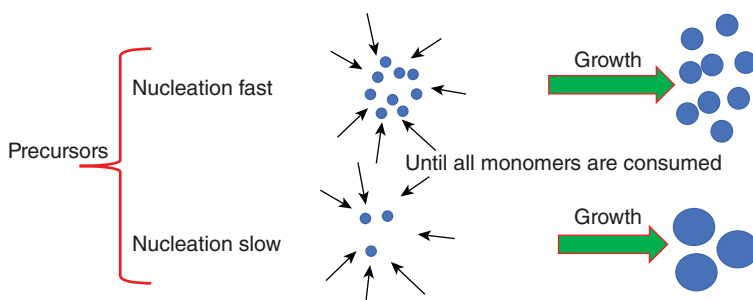


Figure 3.2 Schematic representation of nucleation and growth.

- (ii) The size distribution is normally influenced by the rate of reductant addition, stirring rate, and fresh filtered solutions.
- (iii) The stabilization is usually affected by solution composition.
- (iv) The shape of particles, where the pH, surfactant, and employed method are the main determinants.

3.5 Questions Related to the Selected Synthesis Route

Many times, the choice of synthesis route becomes a dilemma for some researchers. Some questions that have to be asked and answered before making a choice include:

- (i) Why do the employed wet-chemical routes need low temperature for the synthesis? Why the obtained particles are relatively small compared to the solid-state route?

To answer this question, one must first know the concepts of nucleation and growth. In nucleation, the first nanocrystals are formed in a solution. Very small particles or nuclei of the new phases appear and then grow. In general, there are two types of nucleation:

1. *Homogenous nuclei*: they form simultaneously and uniformly through the solution.
2. *Heterogenous nuclei*: they are nucleated at different times.

In summary, nucleation is the creation of nuclei upon which growth can occur. Indeed,

- nucleation plays an important role in controlling the properties of the final product, size distribution, and nature of the phase.
- nanoparticles need strong nucleation and slow growth.
- highly monodisperse nanoparticles are formed if the processes of nucleation and growth can be successfully separated.

The growth of the nanocrystals in a solution involves two important processes, nucleation and the growth of the nanocrystals [28].

The process of nucleation and growth is illustrated by the LaMer plot in Figure 3.3 [29, 31]. According to the plot, colloidal nanoparticle formation can be accomplished through three main stages: stage I: induction period, which is before the nucleation period. In this stage, the concentration of atoms steadily increases with time to supersaturation levels. The state of supersaturation is essential for nucleation. Depending on the solute concentration levels, three major zones are proposed. The zone below the saturation level (i.e. the solubility curve) is called the stable (unsaturated) zone, where nucleation is impossible. Ostwald introduced the terms “metastable” and “labile” supersaturation to specify two stages of a supersaturated solution [32, 33]. The metastable (supersaturated) zone lies between the saturation level and the minimum critical supersaturation level (super solubility curve) above which uncontrolled spontaneous nucleation commences. In this metastable zone, spontaneous nucleation is improbable. However, seed-mediated growth

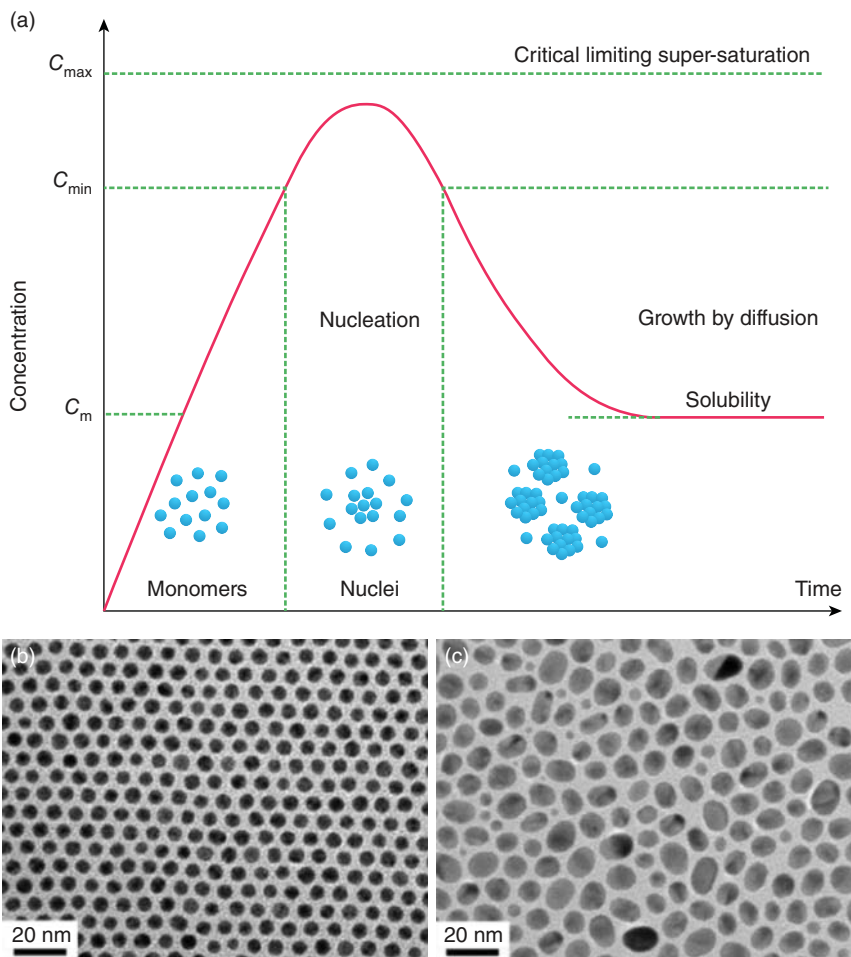


Figure 3.3 (a) A typical plot of the LaMer model describing nucleation and growth of colloidal particles, and (b) Monodispersed, and (c) Polydispersed particles formation. Source: [34], B.-H. Wu et al. (2013), ELSEVIER.

would be possible in the metastable concentration zone. The labile or unstable (supersaturated) zone lies above the metastable zone, where spontaneous nucleation is probable. The location of the minimum critical supersaturation level (super solubility curve) is not as specific as the saturation level (solubility curve). Many factors affect the value of the metastable zone's width, such as temperature, agitation, presence of impurities or additives, the rate at which the supersaturation is generated, and so on. Therefore, the induction period is related to the metastable zone width and the nucleation rate.

Stage II is the nucleation period. In this stage, atoms concentration reaches a critical limit of supersaturation, and rapid nucleation occurs forming critical nuclei by the aggregation of atoms. When the concentration of atoms falls below the minimum critical supersaturation level, nucleation ceases.

Stage III is the growth period. In this stage, the atoms continuously deposit on the preexisting nuclei, which leads to a gradual increase in the particle size and a decrease in the atom concentration until an equilibrium state is reached between the atoms on the surface of the nanocrystal and the atoms in the solution [34]. Distribution of the monodispersed and polydispersed nanoparticles is shown in Figure 3.3b. It is clear that if all nuclei form simultaneously, they will have homogenous nucleation, which results in monodispersed nanoparticle formation. If the nucleation occurs at different times, it results in polydispersed particle formation.

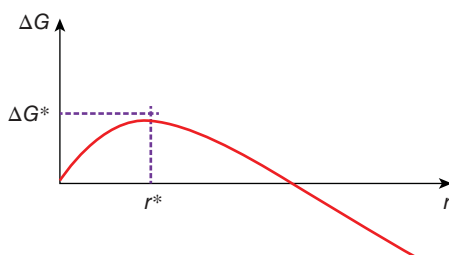
The free energy changes (ΔG) are used to describe the nucleation and particle formation during the synthesis process. When the metallic precursor such as a salt of chloride or nitrate or sulfate that contains metals like Co, Fe, Ni, Zn, and so on, are dissolved in water in the aim of the synthesis of MNPs, they would decompose or reduce, which results in the “clusters” or the so-called “embryos” or “monomers” formation the formation of MNPs. In this state, the monomer concentration increases up to the minimal nucleation concentration ($C_{\min, \text{nu}}$) that marks the beginning and the end of the nucleation step. In other words, when the salts of initial materials are dissolved in the solvent, some embryos are spontaneously formed. Now, if a suitable condition is provided for them ($\Delta G < \Delta G^*$, where * mark shows critical state), e.g. exposing temperature, these embryos will initiate to nucleate (Figure 3.4). It means that they enter the second stage, i.e. the nucleation stage. In this case, the interface between nuclei and solution is formed, which gives rise to surface energy.

Furthermore, there are changes in free energy per unit volume between solute atoms in solution and bulk crystal. Thus, according to the classical theory of nucleation, the free energy (i.e. excess free energy) changes associated with the process of homogeneous nucleation (by considering spherical nuclei) are given as:

$$\Delta G_r = \Delta G_r^{\text{volume}} + \Delta G_r^{\text{interface}} = \frac{4}{3}\pi r^3 \cdot \Delta G + 4\pi r^2 \gamma = \frac{-4}{3}\pi r^3 \cdot \frac{RT \ln S}{V_m} + 4\pi r^2 \gamma \quad (3.1)$$

where r is the radius of the cluster or embryo; γ is the surface free energy per unit area; R is the ideal gas constant; T is the reaction temperature; V_m is the molar volume of bulk crystal, and S is the supersaturation ratio, given

Figure 3.4 ΔG versus r (radius of an embryo).



by the ratio of solute concentration in the solution to that in the equilibrium saturation at the same temperature.

A differential from Eq. (3.1) in terms of “ r ,” yields the critical r for nuclei as:

$$r^* = -\frac{2\gamma}{\Delta G_v} = \frac{2\gamma V_m}{RT \ln S} \quad (3.2)$$

Then,

$$\Delta G^* = \frac{16\pi\gamma^3}{3(\Delta G_v)^2} = \frac{4\pi\gamma r_c^2}{3} \quad (3.3)$$

According to Figure 3.4, if $r < r^*$, the nuclei would dissolve to decrease the free energy. Whereas, if $r > r^*$, nuclei are thermodynamically stable and can lower the free energy of the system through continuous growth.

The relationship between spherical particles with a radius of “ r ” with the total number of atoms (n_0) is as follows:

$$n_r = n_0 \exp\left(\frac{-\Delta G_r}{k_B T}\right) \quad (3.4)$$

where n_r is the number of nuclei; k_B is the Boltzmann constant, and T is the temperature. In the case of homogeneous nucleation, the nucleation rate (N) is given by:

$$N = fC_0 \exp\left(\frac{-\Delta G_{\text{hom}}^*}{RT}\right) \quad (3.5)$$

where f is the frequency of joining a nucleus to a particle, and C_0 is the number of total atoms per unit volume, and R is constant. A schematic representation of nucleation and growth is given in Figure 3.5.

- (ii) As mentioned, the solid-state route can be employed for producing large-scale (tonnages) powder but the question is: how can find a solution to synthesize the MNPs at relatively low temperature? In other words, how can we produce large tonnages of fine powder at relatively low temperatures while considering the affordability of the product? “Mechanical alloying,” (MA) is a technique that addresses this challenge to some extent. MA is a good replacement for the

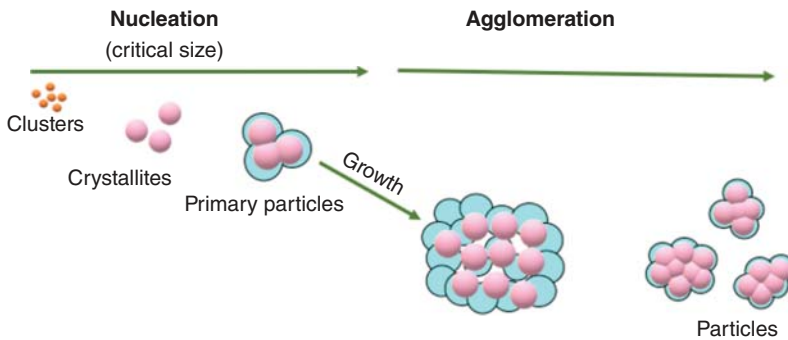


Figure 3.5 Schematic representation of nucleation and growth.

solid-state method with the additional advantages of producing the nanosized powder during the milling process or, at least, by heating the milled powders at relatively low temperatures. This technique is utilized not only for producing various types of magnetic nanostructured materials [2, 3, 21–26, 35, 36], but also for the speedy preparation of nanocomposites, advanced ceramics, amorphous alloys, and metastable materials, because of its relative simplicity and availability [2, 3, 21–26, 35–38].

MA is a powder metallurgy technique, in which initial raw materials are subjected to the milling process under different conditions depending on the aim and final products obtained. This technique involves a chemical reaction during milling and is frequently considered a mechano-synthesis or mechano-chemical synthesis as well [8, 37–40]. In this process, a frequent fracturing and re-welding of powder particles give rise to plastic deformation, resulting in the creation of lattice imperfections or defects. These short-circuit paths derived by the formation of defects provide faster diffusion, which results in the mass transformed during the milling process. Thus, these characteristics open new doors for the room-temperature production of commercial compounds. In this method, the desired product characteristics are strongly dependent on various variable parameters of the process, such as milling atmosphere, grinding media, rotation speed or rotation per minute (RPM), ball-to-powder ratio (BPR), and milling time. Hence, optimizing these parameters saves time and energy [39, 40]. In other words, controlling the variable parameters of the process allows for controlling the microstructure of the sample as well.

Furthermore, both the non-equilibrium and equilibrium nature of the mechanically alloyed materials pave the way to produce powder particles with controlled size and shape [35] with novel and/or improved magnetic, electrical, and physical characteristics in large quantities or industrial scales. This is while the internal strains induced during the process would affect the characteristics of the powders by lowering their magnetic properties such as saturation magnetization (M_s).

- (iii) The micron-sized magnetic particles typically present better magnetic properties, e.g. high permeability, and, saturation magnetization, compared to their nanostructure counterparts (this will be further discussed in Section 3.6). So, the question arises why the synthesis of MNPs is preferred as compared to their corresponding bulk ones in recent years.

We would answer this question by mentioning an example of the utilization of soft magnetic materials, e.g. Ni–Zn ferrite, Mn–Zn ferrite, etc. in electronic and electrical industries owing to their desirable electromagnetic characteristics, such as relatively high electrical resistivity and low eddy current loss at high frequencies. From an industrial point of view, once the size of particles or grains is in a micron-sized regime, their performance is narrowed to only a few megahertz frequencies, because of their higher conductivity and domain wall resonance. Therefore, one way to remedy this matter and expand the application of these materials at high-frequency utilizations is to reduce the size of the



grains from micron to sub or nanoscale before they are subjected to compact for sintering. In this aspect, several methods, as discussed in this chapter, are employed to synthesize these nanoparticles.

3.6 Dependency of Magnetic Behaviors on Particle/Grain Size

Before describing the effect of grain/particle size on magnetic properties, some methods that can be employed to compute the grain/particle size are given below:

- (i) from the field emission scanning electron microscope (FESEM), high-resolution transmission electron microscopy (HRTEM) micrographs
 - *The intercept technique*: Draw a random straight line through the micrograph and count the number of grain boundaries intersecting the line. The average grain size is calculated by the division of the number of intersections by the actual line length.
 - Average grain size = $1/\text{number of intersections/actual length of the line}$.
 - Actual line length = Measured length/magnification.
 - The average grain size can be calculated by the formula:

$$D = \frac{0.5L}{NM} \quad (3.6)$$

where M is the magnification; N is the total number of intercepts; L is the total test line length; D is the average grain size.

- Using Image J software analyzer.
- Directly from particle size analyzer equipment.
- Based on the size distribution histogram, which is determined using the method described by Lavorato et al. [41]. The size dispersion is fitted with a log-normal function $f(D) = (1/\sqrt{2\pi\sigma D})\exp[-\ln^2(D/D_0)/2\sigma^2]$ and then the median diameter (D_0) and dispersion (σ) are determined.

It is well-known that nanometer-sized grains of ferrites display a much higher coercivity compared to micron-sized grains [3, 26]. Inui and Ogasawara [42] found an inverse relationship between H_c and grain size for multi-domain grains. This is because the larger grains possess greater domain walls and, thus, an enhancement is achieved in the contribution of wall movement to magnetization and demagnetization, which needs less energy than domain rotation. The smaller grains are, therefore, expected to have a higher H_c [26, 43].

It has been stated that, according to the well-accepted $1/D$ law, coercivity would reduce by increasing the grain size in large-grained polycrystalline soft magnetic materials [26, 44]. Concerning Herzer's random anisotropy model [45], grain size has a fundamental effect on coercivity. Based on the Herzer's D^6 law, coercivity tends to decline sharply with a reduction in grain size in case of grain sizes smaller than the length of magnetic exchange (i.e. $L_{\text{exchang}} \sim 40\text{--}50\text{ nm}$).

Herzer's random anisotropy and the classic models can be used to explain variations in the values of coercivity concerning the size of the crystalline. In Ref. [26],



none of the three-synthesized samples in different atmospheres, coercivity did obey Herzer's random anisotropy model ($H_c \propto D^6$). The reason for this unexpected behavior might lie in the residual stress induced during the milling process or in the high densities of the structural imperfections. Since this model cannot capture the influence of residual stress, it cannot be applied to the milled powder, either. As it is not possible to avoid residual stresses during the milling process, Shen et al. modified Herzer's random anisotropy model to account for the effects [46]. According to this modified version, the creation of lattice imperfections, like dislocations, contributes mainly to the residual stresses during the milling process. In this way, the model predicts that coercivity in the case of $D < L_{\text{exchang}}$ in the milled nanocrystalline magnetic materials depends on both crystallite size and dislocation density (residual stress). The proposed model can be articulated as follows:

State 1: $|M_s| \rightarrow 0$, dislocation $\rightarrow 0$, $H_c \propto D^6$

State 2: $|M_s| \rightarrow 0$, dislocation $\gg 0$, $H_c \propto D^6$

State 3: $|M_s| \gg 0$, dislocation $\rightarrow 0$, $H_c \propto D^6$

State 4: $|M_s| \gg 0$, dislocation $\rightarrow 0$, $H_c \propto D^{1/2}$

It has been stated that grain boundaries are the most crucial factors contributing to coercivity in the case of large-grained polycrystalline nanomaterials ($d > L_{\text{exchang}}$). Therefore, fine-grained soft magnetic materials are often magnetically harder than coarse-grained soft ones with identical compositions. As a result, coercivity would tend to decline since the grain size increases, according to the well-accepted $1/d$ law [44].

Goldman in 1999 found that the coercivity of soft magnetic materials is sensitive to microstructural characteristics such as grain size, porosity, and anisotropy [47]. Pal et al. [48] reported high coercivity in soft spinel ferrite materials with nano-sized dimensions as compared to that in micron-sized ones. Inui and Ogasawara [42] found the inverse proportion of coercivity to grain size in multidomain grains. This is because the enlargement of the grains takes place by increasing the sintering temperature, in such a way that the larger grains contain more domain walls, enhancing the wall movement contribution to magnetization or demagnetization [26, 43]. Wall movement requires lower energy than in the rotation of domains. Consequently, a lower coercivity is expected in large grains [26]. Ladislaus [49] and George et al. [50] reported that a single-domain state dominates below a critical grain size and H_c reaches its maximum value in the range of critical grain size.

In terms of the coherent polycrystal model [51], the volume fraction of the grain boundaries (f_{gb}) can be evaluated by the following equation:

$$f_{\text{gb}} = 1 - \frac{(D - t)^3}{D^3} \quad (3.7)$$

where t is the effective grain boundary thickness, which comprises two to three atomic layers [52] and D is the average grain size. Interplanar spacing for this (311) set of planes is assumed here to estimate the effective grain boundary thickness.



Furthermore, according to magnetic permeability, the complex permeability can be expressed as:

$$\mu = \mu' - j\mu'' \quad (3.8)$$

where μ' , μ'' , and j refer to the real permeability, the loss factor/imaginary permeability, and the unit imaginary vector, respectively. Permeability typically declines with the reduction of average grain size and sintering density [43]. The permeability is associated with two main magnetization mechanisms, domain wall motion and spin rotation by the following correlation [53];

$$\mu_i = 1 + X_{\text{spin}} + X_w \quad (3.9)$$

where X_{spin} and X_w are the intrinsic rotational and domain wall susceptibility, respectively. These two factors can also be written as:

$$X_{\text{spin}} = \frac{2\pi M_s^2}{K} \quad (3.10)$$

and

$$X_w = \frac{3\pi M_s^2 D}{4\gamma} \quad (3.11)$$

where M_s is the saturation magnetization. γ is the domain wall energy; D is the average grain size, and K designates the total anisotropy. These equations suggest that the domain walls' motion is affected by the grain size and is enhanced with grain growth. The initial permeability is thus a function of magnetization and grain size [26, 43, 54]. Normally, larger grains consist of a huge number of domain walls; as their number increase, their contribution to magnetization also increases.

3.7 Dependency of Magnetic Behaviors on Particle/Grain Shape

The particles/grains' shape is another main factor that would affect the magnetic behavior of the sample, but this is not considered as much as "the particles/grains size" effect by most researchers. Here, we describe the importance of this factor, and its impact on the magnetic behaviors in nanostructured materials. Several researchers synthesized various types of nanostructured magnetic materials with different shapes (morphologies), including but not limited to Refs. [35, 55, 56]. However, the influence of particles' shape on magnetic behaviors has not been studied systematically and has remained a question mark. Regardless of the size of the as-synthesized nanoparticles and used raw materials for the synthesis, but in the same material with identical composition, the spherical particles exhibited the lowest magnetic properties, i.e. saturation magnetization (M_s) compared to other shaped particles such as cubic, rod, polyhedron, etc. [35, 55–57]. The reason for this phenomenon is not discussed in the literature. From our understanding, this can be based on spin rotational and domain wall movement, as two main factors of the magnetization mechanism [2, 43], the effect of particles' shape on the magnetic properties can be explained in terms of the representation illustrated in Figure 3.6



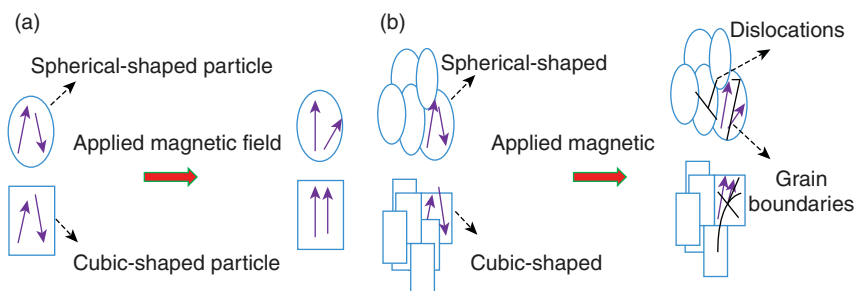


Figure 3.6 Effect of particle shape on spin rotation: (a) randomly orientation of spins in spherical and cubic-shaped particles in single-domain particles, (b) when an external magnetic field is applied, the spins can easily orientate with the field in the cubic-shaped particles compared to the spherical-shaped particles in the polycrystalline state, and (c) it shows the effect of defects such as grain boundaries and dislocation on the spin orientation in both spherical, and cubic-shaped particles in polycrystalline materials. Source: Hajalilou et al. [2]/with permission of Elsevier.

Regardless of the particle size, and assuming different particle shapes with the same spin inside, it can be said that the spin rotation inside a spherical shape particle needs more energy in the presence of an applied magnetic field. This is due to their relatively lower surface-to-volume area compared to other particle shapes [2]. On the other hand, the coercivity of the samples does not show a sequence among the different shapes of nanoparticles.

3.8 Introduction to Wet-Chemical Synthesis Route

The general process of the chemical route to synthesize MNPs is given in Figure 3.7. The most common raw materials are nitrite, chloride, or sulfate of iron oxides in the presence of reducing agents and capping agents. Some examples of the

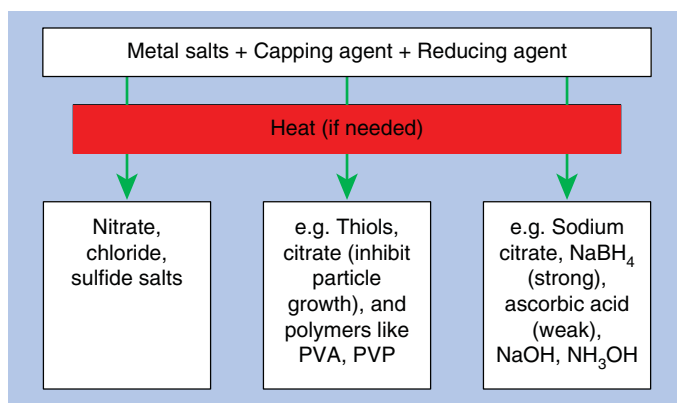


Figure 3.7 General process of chemical routes usually employed for the synthesis of nanoparticles.



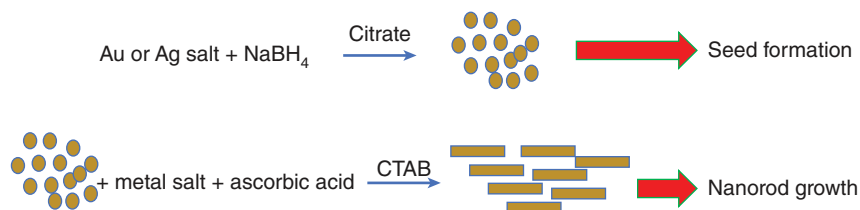


Figure 3.8 Synthesis of nanoparticles with different shapes (CTAB, rod-like template).

chemical routes for the synthesis of MNPs include microemulsion, co-precipitation of ferrous and ferric ions in alkaline medium, hydrothermal, sonochemical, and so on.

Capping agents are stabilizing agents that can also be called ligands or passivating agents that play important roles as:

- Allow particle solubility in various solvents.
- Control particle size.
- Control particle growth rate.
- Prevent particle aggregation.
- Prevent uncontrollable growth of particles.

An example of particle shape formation in the presence of the above-mentioned parameters is shown in Figure 3.8.

Generally, it can be said that besides the type of capping agents/stabilizers, other parameters such as reducing agent (controlling the pH of solution), the types of used reactants, and their concentrations, duration, and heating temperature are the main parameters that influence the particle growth, shape, size, and structure, which will affect the sample properties. For example, it was stated that the reductant concentration, stirring rate, and temperature are the factors that allow controlling the particles' size, while their distribution mainly depends on the rate of reductant addition, stirring rate, and filtering solutions, which are followed by their stabilization by the solution composition [17, 58].

There are two ways to stabilize the nanoparticles against aggregation:

1. *Electrostatic stabilization*: Adsorption of ions to the surface creates an electrical double layer which results in a Coulombic repulsion force between individual particles (Figure 3.9a).

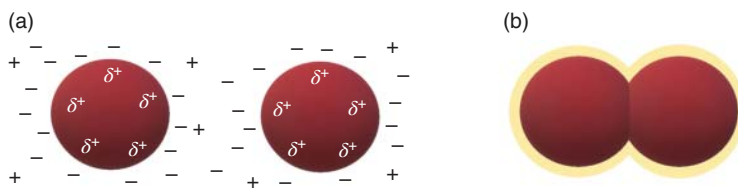


Figure 3.9 Schematic representation of (a) Electrostatic stabilization and (b) Steric stabilization.



2. *Steric stabilization*: Surrounding the metal center by layers of material that are sterically bulky (Figure 3.9b). Examples are polymers, surfactants, and so on.

3.8.1 Microemulsion

A microemulsion is a simple method that involves the process of trapping a micron droplet of aqueous phase inside an assembly of surfactant molecules in a continuous oil phase. The surfactants limit the growth, nucleation, and agglomeration of the particles. The homogeneity and the size of the particles are controllable by controlling the relative amounts of surfactant and solvent and the ratio of a polar solvent to the surfactant [59]. Hence, the particles obtained from the microemulsion method are well defined and their properties are well controlled. For example, iron oxide nanoparticles with sizes ranging from 2 to 10 nm were obtained using 21.5 wt% of Synperonic 10/6 (surfactant) and 14 wt% of hexane plus iron(III) 2-ethyl hexanoate with 2 wt% of concentration Fe in the solution as the oil phase. The iron oxide nanoparticles magnetization was obtained at about ~ 35 emu/g with negligible coercivity [60]. It was stated that a very small uniform size in the range of 1–2 nm of iron oxide possessed superparamagnetic behavior that was produced by using the microemulsion method and the properties of the iron oxide were affected by the type of surfactant used [61]. However, the microemulsion is an expensive technique and requires a large number of liquids yet yielded a very low amount of sample [62].

3.8.2 Hydrothermal Method

The hydrothermal method has been developed to synthesize the control-shaped nanoparticles with an almost homogeneous size distribution. This method requires an adiabatic system, including a sealed autoclave with high pressure, but a temperature range, normally, of 100–250 °C. Indeed, the As-prepared solution of the raw materials is transferred into a sealed autoclave and heated at relatively low temperatures, e.g. below 250 °C for a few hours, e.g. 1–24 hours, which results in the desired phase formation with a narrow size distribution. For example, Takami et al. studied the hydrothermal preparation of iron oxide nanoparticles by heating iron sulfate (FeSO_4) at 473 K with *n*-decanoic acid and *n*-decylamine (organic reagent) [63]. They could synthesize single-phase and found that the crystallinity and shape of iron oxide nanoparticles were affected by the organic reagent. This suggests the reliability and reproducibility problems of the method. In our study, smaller particle sizes have been found as compared to using the sol-gel method in the case of the synthesis of Co-ferrite nanoparticles with the hydrothermal method [9]. This method was found easy-going also for the synthesis of hard magnetic materials such as Sr-ferrite nanoparticles [64]. In our previous study, synthesizing the superparamagnetic iron oxide nanoparticles (IONPs) revealed that the samples synthesized with the hydrothermal route yielded a bigger particle size compared to the samples synthesized with the coprecipitation method [65]. Furthermore, types of reducing agents used in the hydrothermal route, such as NaOH, NH_4OH , NH_3 , etc. can affect the MNPs' characteristics due to their effect on the shape, size of particles, and their distribution [66].



3.8.3 Co-precipitation

The co-precipitation method is the simplest chemical method to produce MNPs. The MNPs are prepared by adding an alkali into an iron salt solution until the black or dark-brown precipitation of MNPs is formed under several conditions. High yield production of MNPs could be obtained by using co-precipitation as a preparation method; however, the MNPs possessed high agglomeration and very wide size distributions which are affected by the synthesis conditions, such as pH value and ionic strength of precipitation medium, $\text{Fe}^{+2}/\text{Fe}^{+3}$ molar ratio, temperature, and time. Therefore, the co-precipitation method involves the formation of a solid precipitate followed by the separation of the solids with a filtration step. This method needs co-precipitation agents which are a solution of inorganic or organic salt. The parameters such as the heating temperature, pH, precursors, etc. are the most important factors to transfer the precipitates into crystalline phases with the desired structure. The precipitates can be in the form of hydroxides, chlorides, nitrates, oxalates, or carbonates and all of which can be thermally decomposed into corresponding oxides. Numerous examples of the synthesis of MNPs via co-precipitation are reported in the literature. For example, several works include, but are not limited to Refs. [67–69].

3.8.4 Sonochemical

Sonochemical is a simple process, in which a chemical reaction of molecules takes place at the ambient temperature under the influence of powerful ultrasound radiation. The particle size and crystallinity of MNPs are affected by the temperature and the intensity of radiation. It is proven that the particle size and crystallinity of iron oxide nanoparticles have a strong correlation with the temperature of ultrasonic radiation [70]. For example, increasing the intensity of ultrasonic radiation caused a reduction in the particle size of iron oxide from ~24 to 19 nm. In another study, Dolores and Adianez stated that the frequency of ultrasonic radiation did not affect the particle size of iron oxide nanoparticles, but it did affect the thickness of the coating layer on the surface of iron oxide nanoparticles [71]. The nanoparticles obtained from the sonochemical method were a mixture of superparamagnetic magnetite and maghemite with a M_s value of 60 emu/g. Using this method, nanoparticles could be inserted into the mesoporous structure and deposited on ceramic and polymeric surfaces. Unfortunately, the amount of the product obtained was very low and highly agglomerated [72]. The agglomeration state of the nanoparticles was improved by modification of their surface with biocompatible materials such as PEG-400.

3.8.5 Sol–Gel Method

In the sol–gel method, small colloidal particles are first formed in solution by hydrolysis and condensation reaction. They then link to form a gel which is converted into the desired oxide(s) by drying and firing. In most cases of the processes, the reactants are solutions of metal alkoxy compounds. Most of the alkoxides can be easily prepared or are commercially available and can be readily purified for further use.



The significant advantage of the sol–gel method is the homogeneous compositions prepared at much lower temperatures than those prepared at conventional powder processes [9, 73, 74]. Furthermore, the reactants used in the sol–gel method are available in very high purities, which allows the formation of high-purity powders of crystalline ceramics.

3.8.6 Thermal Decomposition

By controlling the heating temperature and rate, it is possible to achieve the MNPs with homogeneous, narrow size distribution and controlled shape without agglomeration. In this method, organometallic precursors such as metallic acetylacetonates and carbonyls are decomposed, which causes some environmental toxicity. This means that one can synthesize very homogeneous MNPs with the desired shape and size distribution. The only disadvantage of the method is associated with the toxicity of the used materials, which results in environmental pollution.

3.8.7 Solvothermal

In the solvothermal method, wet or dry solvents are used. The properties of the product differ by changing some parameters such as time, temperature, solvent, and surfactant. Controlling the size and the shape of the particles is simple with solvothermal [75, 76].

3.8.8 Microwave-Assisted Route

The use of emerging microwave-assisted chemistry techniques in conjunction with benign reaction media is dramatically reducing chemical waste and reaction timespan in several organic syntheses and chemical transformations [77].

This is a relatively novel method for synthesizing magnetic nanomaterials in which heat is produced by transferring electromagnetic energy to thermal energy [78, 79]. This method for the synthesis of NPs has gained importance in the field of synthetic technology because of its faster, cleaner, and more cost-effective nature than of other conventional and wet chemical methods for the preparation of metal oxide nanoparticles [80].

3.8.9 Green-Assisted Synthesis Route

The development of materials and chemical synthesis methods for nanoparticles has raised some environmental concerns. Green chemistry is a set of alternative techniques that are clean, non-toxic, and environmentally friendly, meaning that green-assisted synthesis methods are a safer alternative to natural chemical and physical methods for the synthesis of MNPs, due to their being environmentally friendly and cost-effective [81]. Synthesis of nanoparticles by green chemistry was remarked since 1990. Using greenery in this method is somehow exciting



and unfamiliar. The extract of many plants can be used as a capping agent or stabilizer agent in this method. Recently, the green-assisted route has attracted the interest of not only material science researchers [2, 25, 65, 81, 82], but also medical scientists [83–85]. This is mainly because of requests for nontoxic materials for biomedical applications. Thus, the synthesis of MNPs with the assistance of the extract of natural plants as a capping agent has attracted the interest of researchers. For instance, the Fe_3O_4 NPs have been recently synthesized via green-assisted routes in the presence of mango leaves [85], pomegranate, and zucchini extract [82], starch [86], egg white [65, 87], green tea [88], and honey [89]. It has been reported that the interaction of metal precursor ions with reducing agents, and capping agent interface with metal nanoparticles greatly influence the size, shape, stability, and physicochemical properties of the NPs [83, 90]. Capping agents affect the synthesis of MNPs through different mechanisms, including depletion stabilization, stabilization by hydration forces, electrostatic stabilization, steric stabilization, and stabilization using van der Waals forces. A combination of some of these mechanisms may be at work for certain capping agents, such as branched polyethyleneimine (BPEI) [91]. The choice of a capping agent for the synthesis of MNPs is crucial because the capping agent often influences various properties of the NPs, including their size, shape, and interactions with the surrounding solvent. Therefore, the type of the capping agent plays a vital and critical role in the synthesis of MNPs, and as a result in their magnetic and microstructure characteristics. Furthermore, the green-assisted route can result in the interdisciplinary link between nanotechnology and biotechnology, which gives rise to a new discipline, namely “nanobiotechnology,” which specifically deals with production, enhanced potential, and utilization of material at the nanoscale for advanced research [65, 92].

3.9 Introduction to Solid-State Routes to Synthesize Magnetic Nanoparticles

3.9.1 A Standard Ceramic Route

In this method, initial raw materials (powders) are compacted (pressed into pellet or toroid shapes), and then, are subject to thermal treatment at relatively high temperatures. The reaction is completed based on different mechanisms such as diffusion. Since the use of starting materials in this circumstance is normally in a micron-sized state, to obtain the nanostructured of the desired material, they are subjected to mechanical milling, e.g. high-energy ball milling to produce a nanosized powder. One given example in this regard is a synthesis of the Co-substituted Mg ferrites, which was synthesized through this method [93].

3.9.2 Mechanical Alloying (MA) Process

In this process, the employed raw materials are chosen based on a molar ratio or atomic percentage and are employed by considering desired variable parameters [7, 21–26, 36–40, 94]. This technique paves the way to produce any advanced



materials with both equilibrium and non-equilibrium states. In other words, to obtain desired powder particles, the raw materials are firstly mixed and then subjected to the grinding media and ball-milling or other types of the milling process. Afterward, the milled powder may be heated at a certain temperature for a different purpose, to increase the crystallinity, reduce the lactic strain of the sample induced during the milling process, to improve the properties of the sample, e.g. magnetic, conductivity, etc. Some important features of MA can be [3]:

1. The process is feasible from small to several tonnage scales.
2. Synthesis of advanced material with the desired composition and controlled microstructure.
3. Producing alloy systems that are hard to produce by conventional melting techniques.
4. Synthesis and development of amorphous phases.
5. Inducement of chemical (displacement) reactions at low temperatures.
6. Fabrication of quasicrystalline and/or novel crystalline phases.
7. Refinement of crystallite size down to nanometer scale.
8. Proper distribution of second phase particles in the matrix (usually oxides).

High-energy ball milling (HEBM) is an example of a MA process where a mixture of powders is ground in vials with the presence of high mechanical energy impacted on the powders by the collision of heavy balls and powders [7, 21–26, 36–40, 94]. The conversion of large particles of powders into fine particles during the HEBM process involves a complex mixture of fracturing, grinding, welding, cold welding, thermal shock, and mixing. Several works have reported diffusion occurring during HEBM, hence alloying/phase transformation process happened due to the thermal energy generated [7, 21–26, 36–40, 94]. A new metastable interface region tends to be formed due to the fracturing, welding, and cold-welding process. In addition, HEBM introduced a high amount of lattice strain, defects, and atom dislocations that enhance the rate of diffusion through the formed phases. However, the sintering process is sometimes needed to complete the growth of the product phase through the reactant phase. HEBM is very sensitive to the grinding condition. Many factors affect the product such as milling speed, milling time, BPR, and milling container [39]. The simplicity and efficiency of HEBM come along with some advantages. The final microstructure of the products is adjustable depending on the HEBM process conditions [39]. The plastic deformation and disordering of the iron oxide nanoparticles lattice occur under the influence of high energy during grinding [4, 95]. The changes in microstructural characteristics such as crystallite size and lattice strain are affected by many factors including milling time and the speed of milling. Also, HEBM without a proper selection of milling media as well as without optimization of HEBM process conditions, some impurities could be introduced during HEBM due to the high collision of heavy balls and vials [3, 96]. This method also is cost-effective and more environmentally friendly than other processes. This method allows exceptional control over particle morphology and purity at lower temperatures. Table 3.2 shows some examples of the forgoing-mentioned methods that have been employed in the synthesis of MNPs.



Table 3.2 Summary of the preparation method, and coating process on some morphological characteristics of magnetite.

Methods	Coating	Phase analysis	Particle size analysis	Magnetic analysis	References
Coprecipitation	Aldehyde dextran	The cubic inverse spinel structure	20 nm	Superparamagnetic, $M_s > 20$ emu/g	[67]
Coprecipitation	Oleic acid, hexanoic acid	Cubic spinel structure Eight ferric ions at tetrahedral sites, eight ferric ions, and eight ferrous ions at octahedral sites	10–40 nm	Superparamagnetic, M_s with oleic acid 33.29 emu/g, M_s with hexanoic acid 58.72 emu/g, bare magnetite 57.2 emu/g	[97]
Coprecipitation	Oleic acid	Cubic spinel structure	Average size 9.1 nm	Superparamagnetic, M_s 3.6 emu/g	[98]
Coprecipitation	—	—	Average size 26.78 nm	Superparamagnetic, M_s 90 emu/g	[99]
Coprecipitation	—	Cubic spinel structure	8 nm	—	[100]
Coprecipitation	—	Cubic structure	20 nm	—	[101]
Coprecipitation	sodium oleate, polyethylene glycol	Cubic structure	Spherical, 8.0, 8.5 nm	Superparamagnetic, M_s 41.60–49.42 emu/g	[102]
Electrochemical	Amine	Spinel structure	20–30 nm	Ferromagnetic, M_s 70 emu/g	[103]
Microemulsion	Iron salts	Spinel structure	2–10 nm	Superparamagnetic, M_s decreases as the size decreases, 135–173 emu/g	[104]



Reverse micelle	Sodium bis(2-ethylhexyl) sulfosuccinate (AerosolOT)	Cubic spinel structure	4 nm	0.41 emu/g at 0 K temperature	[105]
Reverse micelle	Silica	Cubic structure	5–20 nm	Superparamagnetic at 300 K temperature with 20 emu/g M_S , Ferromagnetic at 2 K temperature with 30 emu/g M_S	[106]
Reverse micelle	Polyaniline (PANI)	Cubic structure	10 nm	Superparamagnetic 30 emu/g	[107]
Hydrothermal	—	Cubic structure	10 nm	Superparamagnetic, 60 emu/g	[107]
Hydrothermal	Ascorbic acid	Face centered cubic structure	5.2 nm	Superparamagnetic, M_S 5.2 emu/g	[108]
Thermal decomposition	Oleic acid	Cubic structure	7 nm, 9 nm	Ferromagnetic	[109]
High energy ball milling	Graphite–molybdenum disulfide	Cubic structure	2 μ m	—	[110]
High energy ball milling	—	Cubic spinel structure	12–20 nm	Superparamagnetic, M_S 217 emu/g	[111]
Milling	3%, 10%, 50% methyl-alcohol	Cubic spinel structure	6–10 nm	Ferrimagnetic, M_S 0.7, 15, 35 emu/g Coercivity 100 Oe	[112]
Milling	Oleic acid	Cubic spinel structure	Average size 8.7 nm	Superparamagnetic M_S 13.9 emu/g	[98]



3.10 Some Methods for Extraction of Iron Oxide Nanoparticles from Industrial Wastes

3.10.1 Magnetic Separation Technique (MST)

This process is used to remove impurities contained in the mill scales. The mill scales powder is added to the glass tube filled with deionized water and imposed with an external, e.g. 1 T, magnetic field. Deionized water is used to ensure there is no reaction of the magnetic particle with a water molecule that might affect their ionic bonds. The crushed mill scales are then stirred in deionized water to separate impurities from magnetic particles. Impurities with high density will submerge at the bottom of the glass tube. The impurities that are of lower density will float on the surface of the glass tube. Magnetic particles are attracted to the applied magnetic field and stick to the surface of the tube near the poles. Floating impurities are removed by using filter paper, while the heavy impurities can be taken out by opening the stopper and letting them flow out into the beaker. After all the impurities are removed, the magnetic field is then turned off and the magnetic materials are taken out. The magnetic slurry is then filtered and dried in an oven.

3.10.2 Curie Temperature Separation Technique

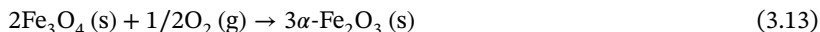
Curie Temperature Separation Technique (CTST) is used to separate the Wüstite compound from the mill scales which consist of Wüstite and magnetite. During the CTST process, the mill scales powder (magnetic separation technique [MST]) is again poured into the glass tube filled with 100 °C of deionized water. The glass tube is shaken vertically along the 1 T magnetic field to ensure all the magnetic particles are imposed by a magnetic field. As the temperature of deionized water reaches 100 °C, the magnetic particles with high Curie temperature can stick to the magnet. This is because the ionic bonding of magnetic particles with high Curie temperature is very strong. Whereas the magnetic particles with a temperature lower than 100 °C will lose their magnetic properties and thus will be submerged at the bottom of the glass tube. Magnetic particles that fall to the bottom of the tube are assumed to be Wüstite, FeO. Wüstite has weak susceptibility to ferromagnetic particles and has a lower Curie temperature of 71 °C which is below the boiling point of deionized water. The magnetic particles which are submerged in the bottom of a glass tube and stick to the magnet are taken out and dried. To confirm the identities of magnetic particles, both magnetic particles are required to be subjected to structural characterization through, e.g. XRD and XRF measurement. The magnetic particles that stick to the magnet are estimated as magnetite. The magnetite particles are removed because the magnet has lower resistance and high conductivity that can generate an eddy current on the material.

3.10.3 Oxidation of Wuestite

Once the magnetic slurry is dried completely, Wüstite is oxidized, e.g. at 500 °C for several hours, e.g. 10 hours in the air. The purpose of oxidation of Wüstite



is to convert the phase of Wüstite (FeO) and magnetite (Fe₃O₄) into hematite (α -Fe₂O₃) as:



References

- 1 Kuchibhatla, S.V., Karakoti, A., Bera, D., and Seal, S. (2007). One dimensional nanostructured materials. *Progress in Materials Science* 52: 699–913.
- 2 Hajalilou, A. and Mazlan, S.A. (2016). A review on preparation techniques for synthesis of nanocrystalline soft magnetic ferrites and investigation on the effects of microstructure features on magnetic properties. *Applied Physics A* 122: 1–15.
- 3 Hajalilou, A., Kianvash, A., Lavvafi, H., and Shameli, K. (2018). Nanostructured soft magnetic materials synthesized via mechanical alloying: a review. *Journal of Materials Science: Materials in Electronics* 29: 1690–1717.
- 4 Suryanarayana, C. (2001). Mechanical alloying and milling. *Progress in Materials Science* 46: 1–184.
- 5 Kodama, R.H., Berkowitz, A.E., McNiff, E. Jr., and Foner, S. (1996). Surface spin disorder in NiFe₂O₄ nanoparticles. *Physical Review Letters* 77: 394.
- 6 Chinnnasamy, C., Narayanasamy, A., Ponpandian, N. et al. (2001). Mixed spinel structure in nanocrystalline NiFe₂O₄. *Physical Review B* 63: 184108.
- 7 Hajalilou, A., Hashim, M., and Kamari, H.M. (2015). Structure and magnetic properties of Ni_{0.64}Zn_{0.36}Fe₂O₄ nanoparticles synthesized by high-energy milling and subsequent heat treatment. *Journal of Materials Science: Materials in Electronics* 26: 1709–1718.
- 8 Adli, R.G., Kianvash, A., Hosseini, M.G. et al. (2018). Mechanochemically synthesized NiCo₂O₄/Vulcan/PANI nanocomposite and investigation of its electrochemical behavior as a supercapacitor. *Ceramics International* 44: 20049–20057.
- 9 Hajalilou, A., Mazlan, S.A., Abbasi, M., and Lavvafi, H. (2016). Fabrication of spherical CoFe₂O₄ nanoparticles via sol–gel and hydrothermal methods and investigation of their magnetorheological characteristics. *RSC Advances* 6: 89510–89522.
- 10 Hajalilou, A., Abouzari-Lotf, E., Etemadifar, R. et al. (2018). Fabrication by electrophoretic deposition of nano-Fe₃O₄ and Fe₃O₄@SiO₂ 3D structure on carbon fibers as supercapacitor materials. *Journal of Minerals, Metals and Materials* 70: 1404–1410.
- 11 Tao, S., Gao, F., Liu, X., and Sørensen, O.T. (2000). Preparation and gas-sensing properties of CuFe₂O₄ at reduced temperature. *Materials Science and Engineering B* 77: 172–176.
- 12 Misra, R., Gubbala, S., Kale, A., and Egelhoff, W. Jr. (2004). A comparison of the magnetic characteristics of nanocrystalline nickel, zinc, and manganese



- ferrites synthesized by reverse micelle technique. *Materials Science and Engineering B* 111: 164–174.
- 13 Hajalilou, A., Etemadifar, R., Abbasi-Chianeh, V., and Abouzari-Lotf, E. (2018). Electrophoretically-deposited nano- Fe_3O_4 @carbon 3D structure on carbon fiber as high-performance supercapacitors. *Journal of Electronic Materials* 47: 4807–4812.
 - 14 Rawat, R. (2015). Dense plasma focus-from alternative fusion source to versatile high energy density plasma source for plasma nanotechnology. In: *Journal of Physics: Conference Series* (Vol. 591, No. 1, p. 012021), 012021. IOP Publishing.
 - 15 Parker, R., Rigden, C., and Tinsley, C. (1969). Solid-state reaction between zinc oxide and ferric oxide. *Transactions of the Faraday Society* 65: 219–224.
 - 16 Hill, R.J., Craig, J.R., and Gibbs, G. (1979). Systematics of the spinel structure type. *Physics and Chemistry of Minerals* 4: 317–339.
 - 17 Navrotsky, A. and Kleppa, O. (1968). Thermodynamics of formation of simple spinels. *Journal of Inorganic and Nuclear Chemistry* 30: 479–498.
 - 18 Schmalzried, H. (1981). *Solid State Reactions*, 254. Verlag Chemie.
 - 19 Jadhav, S. (2001). Magnetic properties of Zn-substituted Li–Cu ferrites. *Journal of Magnetism and Magnetic Materials* 224: 167–172.
 - 20 Chinnasamy, C., Narayanasamy, A., Ponpandian, N. et al. (2002). Grain size effect on the Néel temperature and magnetic properties of nanocrystalline NiFe_2O_4 spinel. *Journal of Magnetism and Magnetic Materials* 238: 281–287.
 - 21 Hajalilou, A., Hashim, M., Abbasi, M. et al. (2015). A comparative study on the effects of different milling atmospheres and sintering temperatures on the synthesis and magnetic behavior of spinel single phase $\text{Ni}_{0.64}\text{Zn}_{0.36}\text{Fe}_2\text{O}_4$ nanocrystals. *Journal of Materials Science: Materials in Electronics* 26: 7468–7483.
 - 22 Hajalilou, A., Mazlan, S.A., and Shameli, K. (2016). A comparative study of different concentrations of pure Zn powder effects on synthesis, structure, magnetic and microwave-absorbing properties in mechanically-alloyed Ni–Zn ferrite. *Journal of Physics and Chemistry of Solids* 96: 49–59.
 - 23 Hajalilou, A., Hashim, M., and Masoudi, M.T. (2015). A comparative study of in-situ mechanochemically synthesized $\text{Mn}_{0.5}\text{Zn}_{0.5}\text{Fe}_2\text{O}_4$ ferrite nanoparticles in the $\text{MnO}/\text{ZnO}/\text{Fe}_2\text{O}_3$ and $\text{MnO}_2/\text{Zn}/\text{Fe}_2\text{O}_3$ systems. *Ceramics International* 41: 8070–8079.
 - 24 Abdollah, H., Mansor, H., Reza, E.-K., and Taghi, M.M. (2015). Effect of milling atmosphere on structural and magnetic properties of Ni–Zn ferrite nanocrystalline. *Chinese Physics B* 24: 048102.
 - 25 Hajalilou, A., Kamari, H.M., and Shameli, K. (2017). Dielectric and electrical characteristics of mechanically synthesized Ni–Zn ferrite nanoparticles. *Journal of Alloys and Compounds* 708: 813–826.
 - 26 Hajalilou, A., Hashim, M., Kamari, H.M., and Masoudi, M.T. (2015). Effects of milling atmosphere and increasing sintering temperature on the magnetic properties of nanocrystalline $\text{Ni}_{0.36}\text{Zn}_{0.64}\text{Fe}_2\text{O}_4$. *Journal of Nanomaterials* 16: 232.
 - 27 Hayat, M.A. (2012). *Colloidal Gold: Principles, Methods, and Applications*. Elsevier.



- 28 Rao, C., Thomas, P., and Kulkarni, G. (2007). *Nanocrystals, Synthesis, Properties and Applications*. Berlin: Springer.
- 29 LaMer, V.K. and Dinegar, R.H. (1950). Theory, production and mechanism of formation of monodispersed hydrosols. *Journal of the American Chemical Society* 72: 4847–4854.
- 30 Wu, B.-H., Yang, H.-Y., Huang, H.-Q. et al. (2013). Solvent effect on the synthesis of monodisperse amine-capped Au nanoparticles. *Chinese Chemical Letters* 24: 457–462.
- 31 Sau, T.K. and Rogach, A.L. (2012). *Complex-Shaped Metal Nanoparticles: Bottom-Up Syntheses and Applications*. Wiley Online Library.
- 32 Ashfield, L. (2013). Complex-shaped metal nanoparticles: bottom-up syntheses and applications. *Platinum Metals Review* 57: 123–126.
- 33 Vedantam, S. and Ranade, V.V. (2013). Crystallization: key thermodynamic, kinetic and hydrodynamic aspects. *Sadhana* 38: 1287–1337.
- 34 (a) Mullin, J. (2001). *Crystallization*, 4e. Elsevier. (b) Ge, X., Song, S.Y., and Zhang, H.J. (2012). Co_2GeO_4 nanoplates and nano-octahedrons from low-temperature controlled synthesis and their magnetic properties. *CrystEngComm* 14 (21): 7306–7311.
- 35 Shilan, S.T., Mazlan, S.A., Ido, Y. et al. (2016). A comparison of field-dependent rheological properties between spherical and plate-like carbonyl iron particles-based magneto-rheological fluids. *Smart Materials and Structures* 25: 095025.
- 36 Shafie, M., Hashim, M., Ismail, I. et al. (2014). Magnetic M–H loops family characteristics in the microstructure evolution of $\text{BaFe}_{12}\text{O}_{19}$. *Journal of Materials Science: Materials in Electronics* 25: 3787–3794.
- 37 Hajalilou, A., Hashim, M., Ebrahimi-Kahrizsangi, R. et al. (2014). Synthesis of titanium carbide and TiC-SiO_2 nanocomposite powder using rutile and Si by mechanically activated sintering. *Advanced Powder Technology* 25: 1094–1102.
- 38 Hajalilou, A., Hashim, M., Nahavandi, M., and Ismail, I. (2014). Mechanochemical carboaluminothermic reduction of rutile to produce $\text{TiC-Al}_2\text{O}_3$ nanocomposite. *Advanced Powder Technology* 25: 423–429.
- 39 Hajalilou, A., Hashim, M., Ebrahimi-Kahrizsangi, R. et al. (2014). Parametric optimization of NiFe_2O_4 nanoparticles synthesized by mechanical alloying. *Materials Science-Poland* 32: 281–291.
- 40 Hajalilou, A., Hashim, M., Ebrahimi-Kahrizsangi, R., and Sarami, N. (2014). Synthesis and structural characterization of nano-sized nickel ferrite obtained by mechanochemical process. *Ceramics International* 40: 5881–5887.
- 41 Lavorato, G.C., Lima, E. Jr., Tobia, D. et al. (2014). Size effects in bimagnetic $\text{CoO/CoFe}_2\text{O}_4$ core/shell nanoparticles. *Nanotechnology* 25: 355704.
- 42 Inui, T. and Ogasawara, N. (1977). Grain-size effects on microwave ferrite magnetic properties. *IEEE Transactions on Magnetics* 13: 1729–1744.
- 43 Hajalilou, A., Hashim, M., Ebrahimi-Kahrizsangi, R., and Sarami, N. (2015). Influence of CaO and SiO_2 co-doping on the magnetic, electrical properties and microstructure of a Ni–Zn ferrite. *Journal of Physics D: Applied Physics* 48: 145001.



- 44 Gignoux, D., Schlenker, M., and de Lacheisserie, É.D.T. (2002). *Magnetism: Materials and Applications*. Kluwer Academic Publishers.
- 45 Buschow, K.H.J. and Boer, F.R. (2003). *Physics of Magnetism and Magnetic Materials*. Springer.
- 46 Shen, T., Schwarz, R., and Thompson, J. (2005). Soft magnetism in mechanically alloyed nanocrystalline materials. *Physical Review B* 72: 014431.
- 47 Goldman, A. (2012). *Handbook of Modern Ferromagnetic Materials*. Springer Science & Business Media.
- 48 Pal, M., Brahma, P., Chakravorty, D. et al. (1996). Nanocrystalline nickel–zinc ferrite prepared by the glass-ceramic route. *Journal of Magnetism and Magnetic Materials* 164: 256–260.
- 49 Ladislaus, M. (1980). *Advances in Electronics and Electron Physics*, 1e. London, UK: Academic Press.
- 50 George, M., John, A.M., Nair, S.S. et al. (2006). Finite size effects on the structural and magnetic properties of sol–gel synthesized NiFe_2O_4 powders. *Journal of Magnetism and Magnetic Materials* 302: 190–195.
- 51 Song, H., Guo, S., and Hu, Z. (1999). A coherent polycrystal model for the inverse Hall–Petch relation in nanocrystalline materials. *Nanostructured Materials* 11: 203–210.
- 52 Greneche, J. and Ślawska-Waniewska, A. (2000). About the interfacial zone in nanocrystalline alloys. *Journal of Magnetism and Magnetic Materials* 215: 264–267.
- 53 Nakamura, T. (1997). Low-temperature sintering of NiZnCu ferrite and its permeability spectra. *Journal of Magnetism and Magnetic Materials* 168: 285–291.
- 54 Hossain, A.A., Mahmud, S., Seki, M. et al. (2007). Structural, electrical transport, and magnetic properties of $\text{Ni}_{1-x}\text{Zn}_x\text{Fe}_2\text{O}_4$. *Journal of Magnetism and Magnetic Materials* 312: 210–219.
- 55 Hajalilou, A., Abouzari-Lotf, E., Abbasi-Chianeh, V. et al. (2018). Inclusion of octahedron-shaped ZnFe_2O_4 nanoparticles in combination with carbon dots into carbonyl iron based magnetorheological suspension as additive. *Journal of Alloys and Compounds* 737: 536–548.
- 56 Shan, A., Wu, X., Lu, J. et al. (2015). Phase formations and magnetic properties of single crystal nickel ferrite (NiFe_2O_4) with different morphologies. *CrystEngComm* 17: 1603–1608.
- 57 Arief, I. and Mukhopadhyay, P. (2014). Preparation of spherical and cubic $\text{Fe}_{55}\text{Co}_{45}$ microstructures for studying the role of particle morphology in magnetorheological suspensions. *Journal of Magnetism and Magnetic Materials* 360: 104–108.
- 58 Frens, G. (1973). Controlled nucleation for the regulation of the particle size in monodisperse gold suspensions. *Nature Physical Science* 241: 20–22.
- 59 Blaney, L. (2007). Magnetite (Fe_3O_4): properties, synthesis, and applications. *Lehigh Review* 5: 33–81.
- 60 Okoli, C., Sanchez-Dominguez, M., Boutonnet, M. et al. (2012). Comparison and functionalization study of microemulsion-prepared magnetic iron oxide nanoparticles. *Langmuir* 28: 8479–8485.



- 61 Santra, S., Tapeç, R., Theodoropoulou, N. et al. (2001). Synthesis and characterization of silica-coated iron oxide nanoparticles in microemulsion: the effect of nonionic surfactants. *Langmuir* 17: 2900–2906.
- 62 Capek, I. (2004). Preparation of metal nanoparticles in water-in-oil (w/o) microemulsions. *Advances in Colloid and Interface Science* 110: 49–74.
- 63 Takami, S., Sato, T., Mousavand, T. et al. (2007). Hydrothermal synthesis of surface-modified iron oxide nanoparticles. *Materials Letters* 61: 4769–4772.
- 64 Rezaie, E., Rezanezhad, A., Ghadimi, L.S. et al. (2018). Effect of calcination on structural and supercapacitance properties of hydrothermally synthesized plate-like $\text{SrFe}_{12}\text{O}_{19}$ hexaferrite nanoparticles. *Ceramics International* 44: 20285–20290.
- 65 Hajalilou, A., Ferreira, L.P., Jorge, M.E.M. et al. (2021). Superparamagnetic Ag- Fe_3O_4 composites nanoparticles for magnetic fluid hyperthermia. *Journal of Magnetism and Magnetic Materials* 537: 168242. <https://doi.org/10.1016/j.jmmm.2021.168242>.
- 66 Kavkhani, R., Hajalilou, A., Abouzari-Lotf, E. et al. (2022). CTAB assisted synthesis of $\text{MnFe}_2\text{O}_4@\text{SiO}_2$ nanoparticles for magnetic hyperthermia and MRI application. *Materials Today Communications* 31: 103412.
- 67 Hong, R., Li, J., Qu, J. et al. (2009). Preparation and characterization of magnetite/dextran nanocomposite used as a precursor of magnetic fluid. *Chemical Engineering Journal* 150: 572–580.
- 68 Maaz, K., Karim, S., Mumtaz, A. et al. (2009). Synthesis and magnetic characterization of nickel ferrite nanoparticles prepared by co-precipitation route. *Journal of Magnetism and Magnetic Materials* 321: 1838–1842.
- 69 Wu, S., Sun, A., Zhai, F. et al. (2011). Fe_3O_4 magnetic nanoparticles synthesis from tailings by ultrasonic chemical co-precipitation. *Materials Letters* 65: 1882–1884.
- 70 Hassanjani-Roshan, A., Vaezi, M.R., Shokuhfar, A., and Rajabali, Z. (2011). Synthesis of iron oxide nanoparticles via sonochemical method and their characterization. *Particuology* 9: 95–99.
- 71 Dolores, R., Raquel, S., and Adianez, G.-L. (2015). Sonochemical synthesis of iron oxide nanoparticles loaded with folate and cisplatin: effect of ultrasonic frequency. *Ultrasonics Sonochemistry* 23: 391–398.
- 72 Khalil, H., Mahajan, D., Rafailovich, M. et al. (2004). Synthesis of zerovalent nanophase metal particles stabilized with poly(ethylene glycol). *Langmuir* 20: 6896–6903.
- 73 Kavkhani, R., Pourzaki, M., Kianvash, A. et al. (2021). Effect of sintering temperature and soaking time on the magnetic properties and transmission behavior of nano crystalline $\text{Mg}_{0.8}\text{Mn}_{0.2}\text{Al}_{0.1}\text{Fe}_{1.9}\text{O}_4$. *Journal of Sol-Gel Science and Technology* 99 (2): 444–454.
- 74 Ghadimi, L.S., Arsalani, N., Ahadzadeh, I. et al. (2019). Effect of synthesis route on the electrochemical performance of CoMnFeO_4 nanoparticles as a novel supercapacitor electrode material. *Applied Surface Science* 494: 440–451.



- 75 Zhang, H., Wu, J.-R., Wang, X. et al. (2019). One-pot solvothermal synthesis of Carboxylatopillar[5]arene-modified Fe_3O_4 magnetic nanoparticles for ultrafast separation of cationic dyes. *Dyes and Pigments* 162: 512–516.
- 76 Madrid, S.I.U., Pal, U., and Sanchez-De Jesus, F. (2014). Controlling size and magnetic properties of Fe_3O_4 clusters in solvothermal process. *Advances in Nano Research* 2: 187.
- 77 Polshettiwar, V., Nadagouda, M.N., and Varma, R.S. (2009). Microwave-assisted chemistry: a rapid and sustainable route to synthesis of organics and nanomaterials. *Australian Journal of Chemistry* 62: 16–26.
- 78 Ertürk, A.S. and Elmacı, G. (2018). PAMAM dendrimer functionalized manganese ferrite magnetic nanoparticles: microwave-assisted synthesis and characterization. *Journal of Inorganic and Organometallic Polymers and Materials* 28: 2100–2107.
- 79 Xiao, W., Gu, H., Li, D. et al. (2012). Microwave-assisted synthesis of magnetite nanoparticles for MR blood pool contrast agents. *Journal of Magnetism and Magnetic Materials* 324: 488–494.
- 80 Lagashetty, A., Havanoor, V., Basavaraja, S. et al. (2007). Microwave-assisted route for synthesis of nanosized metal oxides. *Science and Technology of Advanced Materials* 8: 484.
- 81 Faried, M., Shameli, K., Miyake, M. et al. (2016). Synthesis of silver nanoparticles via green method using ultrasound irradiation in seaweed *Kappaphycus alvarezii* media. *Research on Chemical Intermediates* 42: 7991–8004.
- 82 Etemadifar, R., Kianvash, A., Arsalani, N. et al. (2018). Green synthesis of superparamagnetic magnetite nanoparticles: effect of natural surfactant and heat treatment on the magnetic properties. *Journal of Materials Science: Materials in Electronics* 29: 17144–17153.
- 83 Rezanezhad, A., Hajalilou, A., Eslami, F. et al. (2021). Superparamagnetic magnetite nanoparticles for cancer cells treatment via magnetic hyperthermia: effect of natural capping agent, particle size and concentration. *Journal of Materials Science: Materials in Electronics* 32: 24026–24040.
- 84 Jalili, H., Aslibeiki, B., Hajalilou, A. et al. (2022). Bimagnetic hard/soft and soft/hard ferrite nanocomposites: structural, magnetic and hyperthermia properties. *Ceramics International* 48: 4886–4896.
- 85 Bali Ogholbeyg, A., Kianvash, A., Hajalilou, A. et al. (2018). Cytotoxicity characteristics of green assisted-synthesized superparamagnetic maghemite ($\gamma\text{-Fe}_2\text{O}_3$) nanoparticles. *Journal of Materials Science: Materials in Electronics* 29: 12135–12143.
- 86 Ghaseminezhad, S.M. and Shojaosadati, S.A. (2016). Evaluation of the antibacterial activity of $\text{Ag}/\text{Fe}_3\text{O}_4$ nanocomposites synthesized using starch. *Carbohydrate Polymers* 144: 454–463.
- 87 Hajalilou, A., Mazlan, S.A., Shilan, S.T., and Abouzari-Lotf, E. (2017). Enhanced magnetorheology of soft magnetic carbonyl iron suspension with binary mixture of Ni–Zn ferrite and Fe_3O_4 nanoparticle additive. *Colloid and Polymer Science* 295: 1499–1510.



- 88 Huang, L., Weng, X., Chen, Z. et al. (2014). Synthesis of iron-based nanoparticles using oolong tea extract for the degradation of malachite green. *Spectrochimica Acta, Part A: Molecular and Biomolecular Spectroscopy* 117: 801–804.
- 89 Hajalilou, A., Kianvash, A., Shameli, K., and Lavvafi, H. (2017). Carbonyl iron based magnetorheological effects with silver nanoparticles via green-assisted coating. *Applied Physics Letters* 110: 261902.
- 90 Hajalilou, A., Ferreira, L., Jorge, M.M. et al. (2021). Superparamagnetic Ag-Fe₃O₄ composites nanoparticles for magnetic fluid hyperthermia. *Journal of Magnetism and Magnetic Materials* 537: 168242.
- 91 El Badawy, A.M., Scheckel, K.G., Suidan, M., and Tolaymat, T. (2012). The impact of stabilization mechanism on the aggregation kinetics of silver nanoparticles. *Science of the Total Environment* 429: 325–331.
- 92 Stan, M., Popa, A., Toloman, D. et al. (2015). Enhanced photocatalytic degradation properties of zinc oxide nanoparticles synthesized by using plant extracts. *Materials Science in Semiconductor Processing* 39: 23–29.
- 93 Pourzaki, M., Kavkhani, R., Kianvash, A., and Hajalilou, A. (2019). Structure, magnetic and transmission characteristics of the Co substituted Mg ferrites synthesized via a standard ceramic route. *Ceramics International* 45: 5710–5716.
- 94 Hajalilou, A., Hashim, M., Ebrahimi-Kahrizsangi, R., and Kamari, H.M. (2015). Thermal evolution of the Ni-ferrite nanoparticles obtained by mechanical alloying as probed by differential scanning calorimetry. *Journal of Thermal Analysis and Calorimetry* 119: 995–1000.
- 95 Arbain, R., Othman, M., and Palaniandy, S. (2011). Preparation of iron oxide nanoparticles by mechanical milling. *Minerals Engineering* 24: 1–9.
- 96 Jeong, Y.K., Nakahira, A., Morgan, P.E., and Niihara, K. (1997). Effect of milling conditions on the strength of alumina–silicon carbide nanocomposites. *Journal of the American Ceramic Society* 80: 1307–1309.
- 97 Petcharoen, K. and Sirivat, A. (2012). Synthesis and characterization of magnetite nanoparticles via the chemical co-precipitation method. *Materials Science and Engineering B* 177: 421–427.
- 98 Almásy, L., Creanga, D., Nadejde, C. et al. (2015). Wet milling versus co-precipitation in magnetite ferrofluid preparation. *Journal of the Serbian Chemical Society* 80: 367–376.
- 99 Rajendran, K., Balakrishnan, G.S., and Kalirajan, J. (2015). Synthesis of magnetite nanoparticles for arsenic removal from ground water pond. *International Journal of PharmTech Research* 8: 670–677.
- 100 Giraldo, L., Erto, A., and Moreno-Piraján, J.C. (2013). Magnetite nanoparticles for removal of heavy metals from aqueous solutions: synthesis and characterization. *Adsorption* 19: 465–474.
- 101 Santoyo-Salazar, J., Castellanos-Roman, M., and Gómez, L.B. (2007). Structural and magnetic domains characterization of magnetite nanoparticles. *Materials Science and Engineering C* 27: 1317–1320.
- 102 Sun, J., Zhou, S., Hou, P. et al. (2007). Synthesis and characterization of biocompatible Fe₃O₄ nanoparticles. *Journal of Biomedical Materials Research Part A* 80: 333–341.



- 103 Cabrera, L., Gutierrez, S., Menendez, N. et al. (2008). Magnetite nanoparticles: electrochemical synthesis and characterization. *Electrochimica Acta* 53: 3436–3441.
- 104 Lee, Y., Lee, J., Bae, C.J. et al. (2005). Large-scale synthesis of uniform and crystalline magnetite nanoparticles using reverse micelles as nanoreactors under reflux conditions. *Advanced Functional Materials* 15: 503–509.
- 105 Iida, H., Nakanishi, T., Takada, H., and Osaka, T. (2006). Preparation of magnetic iron-oxide nanoparticles by successive reduction–oxidation in reverse micelles: effects of reducing agent and atmosphere. *Electrochimica Acta* 52: 292–296.
- 106 Lee, J., Lee, Y., Youn, J.K. et al. (2008). Simple synthesis of functionalized superparamagnetic magnetite/silica core/shell nanoparticles and their application as magnetically separable high-performance biocatalysts. *Small* 4: 143–152.
- 107 Yao, Y., Jiang, H., Wu, J. et al. (2012). Synthesis of Fe_3O_4 /polyaniline nanocomposite in reversed micelle systems and its performance characteristics. *Procedia Engineering* 27: 664–670.
- 108 Xuan, S., Hao, L., Jiang, W. et al. (2007). Preparation of water-soluble magnetite nanocrystals through hydrothermal approach. *Journal of Magnetism and Magnetic Materials* 308: 210–213.
- 109 Zhang, L., He, R., and Gu, H.-C. (2006). Oleic acid coating on the monodisperse magnetite nanoparticles. *Applied Surface Science* 253: 2611–2617.
- 110 Österle, W., Orts-Gil, G., Gross, T. et al. (2013). Impact of high energy ball milling on the nanostructure of magnetite–graphite and magnetite–graphite–molybdenum disulphide blends. *Materials Characterization* 86: 28–38.
- 111 De Carvalho, J., De Medeiros, S., Morales, M. et al. (2013). Synthesis of magnetite nanoparticles by high energy ball milling. *Applied Surface Science* 275: 84–87.
- 112 Goya, G.F. (2004). Handling the particle size and distribution of Fe_3O_4 nanoparticles through ball milling. *Solid State Communications* 130: 783–787.



4

Parallel Evolution of Microstructure-Magnetic Properties Relationship in Nanostructured Ferrites

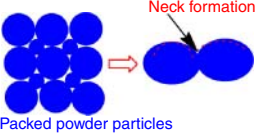

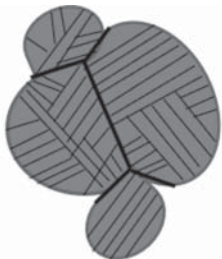
4.1 Introduction

With a combination of electrical and magnetic properties, magnetic ferrite ceramics have become high-potential candidates for electronic materials applications. During the last decades, more attention has been focused on the synthesis of the materials, particularly via solid-state sintering at relatively high temperatures. In fact, a large and growing body of literature has investigated either material synthesis or the final microstructures and properties of those products. However, there is a relatively small body of literature that investigated the effect of microstructural changes from the nanometric (a mixture of amorphous and polycrystalline state) to micrometric (complete polycrystalline state) on the magnetic properties of these materials. For instance, what is not yet clear is the impact of microstructural changes obtained during gradual sintering conditions, e.g. sintering from low to elevated temperatures with small steps, on the magnetic properties. This indicates a need to fully understand the relationship between microstructures and materials' properties from nanometric grain size up to micrometric grain size. The purpose of this chapter is to provide a reference to guide researchers who want to develop a theoretical model which can be utilized for structure–property relationship studies in future research.

In general, ferrites are hard, brittle, and brown- or black-colored ceramic materials [1, 2], which are normally composed of iron oxides [3, 4] and/or with a combination of other metallic elements such as zinc [5], nickel [6], manganese [7], strontium [8], cobalt [9], magnesium [10], and barium [11]. In the polycrystalline state, they can be composed of a large number of minute crystals and are categorized into distinct groups in terms of type and crystal structure, as mentioned in Chapter 2, Table 4.1. Ferrites are a large class of magnetic oxides with remarkable characteristics, which have been investigated and applied during the last ~50 years. Their multiple functionalities arise from several positive points such as the combination of electrical insulators and magnetic materials characteristics with remarkable flexibility in controlling their properties. These features enable them to be used in applications ranging from mankind's body protection, i.e. life science, e.g. cancer treatment [2, 12–14], to daily-used devices such as in electronic devices [15]. For example, to utilize these materials at high frequency applications, it is essential that the size of



Table 4.1 Characteristics of the sintering process stages.

Stages	Characteristics	Schematic representations
First	The powder particles are packed and subjected to sintering The rough surface of the particles is smoothed, and neck formation takes place. Thus, the stage is well known as neck formation	
Second or intermediate	Densification and pore shrinkage. If grain boundaries are created after the first stage, these are a new source of atoms for filling up the concave areas, which reduce the outer surface of the particle	
Third or final	Grain growth occurs, the pores break up and form closed spherical bubbles	

particles should be as small as possible. Furthermore, to expand their applications, the particles should be uniform and nonagglomerated. To achieve these properties, many investigations have been shifted toward developing these materials at the nanoscale regime. In fact, magnetic nanomaterials, where their size, in at least in one dimension, is in the range of 10^{-9} – 10^{-7} m (from 1 to 100 nm), have proven that their magnetic and physical attributes significantly differ from those exposed by either atoms or bulk counterpart [16]. This has attracted the interest of magnetic materials researchers due to the novel and unexpected behaviors found by particles placed between the bulk solids and isolated atoms. These behaviors make them interesting, both from the technological and application point of view, and the scientific knowledge to understand the properties of these materials. In nanostructured materials, it is possible to manipulate vital behaviors of materials, such as their charge capacity, magnetic characteristic, melting temperature, and even their color, without modification in the material’s chemical composition, which results in new and high-performance technologies that were not possible before or observed in micron-sized bulk materials. Furthermore, nanostructured materials’ behaviors sometimes are unpredictable in terms of chemical or physical behaviors compared to their bulk counterpart [17, 18]. This is not only associated with continuous modification of characteristics with size reduction but also with the emergence



of totally new phenomena such as the predominance of interfacial phenomena, wave-like transport, and quantum size confinement [19, 20]. Thus, these phenomena pave a new way for the fundamental science in electrical engineering, solid-state physics and/or chemistry, condensed matter physics, biology, materials science, and other disciplines.

Furthermore, there is a strong dependency of these characteristics on microstructural variations, which consequently alter their performance [18, 21, 22]. So far, magnetic properties' dependency on microstructural features, i.e. grain size and porosity, in polycrystalline ferrites having submicron or micron grain size has been broadly considered [16, 23]. For example, Goldman indicated that the magnetic permeability of ferrites is strongly dependent on grain size [24]. Complex behavior of the grain size effect on the initial permeability has been observed in Ref. [25]. In this study on Ni-Zn ferrite, a critical grain size of about 15 μm was detected at which, the initial permeability shows a maximum value [24]. Such a maximum occurs when half of the grains have included pores. The domain walls' movement is restricted by the pores. Indeed, defects like pores or other imperfections pin the domain walls inside of the grains resulting in the reduction of permeability. A basic property of any magnetic material is explored by taking into account the relation between magnetization (M) or flux density (B) and field strength, i.e. the M - H or B - H hysteresis loop. The area of the hysteresis loops is a measure of the energy loss due to hysteresis in a unit volume during one cycle of magnetization. The loop shape would vary gradually because of eddy current loss and residual loss at high frequencies. Hence, the losses at small amplitudes cannot be inferred, and therefore, the loop area is only an indication of the high amplitude low-frequency loss [26]. A precise understanding of what factors fundamentally shape M - H and B - H hysteresis loops is still ambiguous. Irreversible effects are derived by the hysteresis [27]. However, their behaviors are understandable both in small magnetic fields regarding the coercive field and very strong fields near saturation, and the phenomena that occur within the major loop have yet to be unveiled. Several types of research deal with hysteresis properties [7, 28–31], e.g. a theoretical theory for a sigmoid-shaped ferromagnetic hysteresis curve is given in Ref. [28]. Nevertheless, only a few studies focused on the parallel evolution of magnetic behaviors changes, e.g. B - H hysteresis shape changes due to the microstructure changes when a sample is subjected to sintering from relatively low to high temperatures [8, 11, 17, 18, 21, 32–34]. These studies reveal that most of the undertaken cause-and-effect sequences in the ferrite research literature are experimental sequences dedicated mainly to producing the final outcome. This indicates that little attention has been given from the fundamental line of scientific inquiry point of view for several decades since the beginning of research on ferrites. In other words, the parallel evolution of magnetic properties in polycrystalline materials with grain sizes in the range of several nanometers and microns has yet to be ventured. Therefore, in this chapter, it is attempted to unveil the phenomena that can be evolved in the microstructure-properties relationship in parallel evolution of polycrystalline magnetic materials by considering sintering from relatively low to high temperatures. Besides the sintering temperature, both the soaking time and



the heating rate are the other two main factors of the sintering process, which are curtailed in this regard. Some other factors such as type of furnace and heating environment may also be considered. Thus, in this chapter, it is attempted to spark a light on those three important factors on the parallel evolution of microstructure and magnetism relationship in magnetic materials. This is because of the strong dependency of polycrystalline magnetic materials characteristics on those parameters, which are achieved at different sintering conditions. In other words, the microstructural characteristics of the ferrites, such as grain size, pores, and grain boundaries, strongly affect their magnetic behaviors, depending on the different sintering conditions. For example, sintering temperature varies the microstructure features such as density and grain size, which results in variation in the magnetic behavior of a sample. Thus, these parameters are described by giving some examples in Sections 4.2.1–4.2.3. Moreover, some ideas for controlling the magnetic properties of a material as a consequence of changes in their microstructural characteristics, when they are exposed to intermediate sintering temperatures, soaking time, and heating rate, are given in the current chapter. This idea further can be applied to other engineering or advanced materials. Thus, the possibility of using ferrites or any other materials for desired applied purposes (e.g. electrical, dielectric, optic, mechanical, magnetic, and medical) increases by a proper choice of microstructural factors. In fact, the effect of the sintering process parameters such as temperature, soaking time, and heating rate on the microstructural changes and as a result on magnetic properties in magnetic materials are briefly considered and discussed in the following text.

4.2 Insights into a Sintering Phenomenon

The concept of the sintering process has been already reported in the literature and some textbooks [35–38]. It simply signifies the heating of the compacted powders at a certain temperature(s) to achieve the desired microstructure. Sintering is defined as the thermal treatment of fine-grained material at a temperature below the melting point of the main constituent to bond the particles together by increasing the size of grains and strengthening the materials at the expense of reducing the porosities. Indeed, the compacted powders of magnetic materials are subjected to the sintering process to (i) form a desired phase or remove any other undesired phases, e.g. to form a single phase of spinel ferrite [39] and (ii) improve the properties of the materials as a consequence of microstructure improvement through the elimination of the internal defects induced from the preparation stage, with enhancement of grain size and reduction of porosity [40]. These phenomena can be accomplished through three main stages: necking formation, intermediate stage, and final stage, as given in Table 4.1 and with different mechanisms (Figure 4.1a). The necking stage occurs at relatively low sintering temperatures so that the particles would rearrange and form a dumbbell-shaped state (neck formation). This phenomenon causes the pore channels to close and the density of the powder compact starts to improve by about 60–65% with the sintering time. With the increase in temperature or time, the second



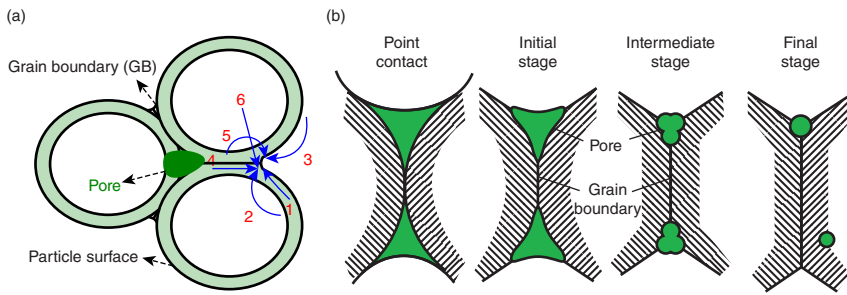


Figure 4.1 Schematic representation of (a) the matter transport paths in the sintered particles and (b) contact point is highlighted for different stages. 1. Surface diffusion; 2. Lattice diffusion from the lattice; 3. Vapor transport; 4. Grain boundary diffusion; 5. Lattice diffusion from the GB; 6. Plastic flow.

stage of sintering can be observed based on the microstructural images, where the pores initiate to become round in shape, where the most shrinkage occurs, and relative density is increased by about 90%. With the further increase in sintering time or temperature, single round-shaped pores form, which is considered the third stage of sintering. This stage involves a final omission of porosity in the sample through diffusion of vacancies along grain boundaries. Therefore, the pores closer to the grain boundaries remain after sintering. At this stage, the motion of grain boundaries and growth of grain may be faster than the elimination of pores, and single pores may remain inside the grains. With the continued growth of these grains, the pores are separated from grain boundaries, and their elimination probability is reduced. This suggests that the interaction between pores and grain boundaries is a key factor in the assessment of the final microstructure. Thus, to achieve the maximum elimination of porosities, the rate of grain growth should be controlled.

Depending on the stages of sintering and the nature of pores, grain boundaries and pores interact differently, i.e. pores can inhibit grain growth, grain boundaries can drag pores, or pores can break free from the moving grain boundaries. In the last situation, when pores get trapped inside grains, the density of material decreases. Hence, the selection of a high sintering temperature is avoided. Although faster sintering is possible at high temperatures, which gives rise to rapid grain growth and the breakaway of pores from the grain boundaries. All these stages occur with a matter of transport with different mechanisms including one or a combination of them (Figure 4.1). The main observed mechanisms in polycrystalline materials are: diffusion through the grains, their boundaries, surfaces, dislocations motion, and vapor transport (evaporation/condensation). All these phenomena would contribute to the accomplishment of sintering stages and the matter transport with two main mechanisms: densifying and nondensifying. The densifying mechanism is where atoms are moved from the bulk to the surface of pores thereby eliminating porosity and increasing the density of the sample [35, 36, 38, 40, 41]. For example, the lattice diffusion from the grain boundary as well as the grain boundary diffusion to the neck (contact point) is the most important densifying mechanism in polycrystalline ceramics. The neck would grow and shrinkage



(densification) would occur as a result of diffusion from the grain boundaries to the pores. Furthermore, a plastic flow by dislocation motion gives rise to neck growth and densification with the assistance of particle deformation or creep in response to the sintering stress. On the other hand, a rearrangement of atoms and moving on the surface of the part of the same particle or the surface of other particles result in the nondensifying mechanism. Moreover, surface diffusion, lattice diffusion, and vapor transport from the surface of particles to the neck also cause neck growth and coarsening of particles without densification.

The grain growth in polycrystalline materials occurs to reduce the free energy of the system at the expense of grain boundaries reduction. In fact, since the grain boundaries have more energy than that of grains, they would reduce the free energy of a system by grain growth once the material is subjected to the heat treatment/sintering process. This occurs in such a way that the atoms/ions would diffuse from one side of the boundary to the other side and align inside a grain, which results in grain boundary movement. If the provided heat is as enough, the grain will grow at the expense of its neighbor and reduce the total free energy of the system. In this circumstance, the concave grain gains atoms with the result that the boundary moves toward its center of curvature, and the convex grain loses atoms. Once the grain growth occurs with the rise in pore size, it is considered "Grain growth coarsening," which gives rise to a reduction in the driving force of a system and an enhancement in diffusion distance for matter transport. This results in the reduction of the rate of sintering. Thus, the suppression of coarsening mechanisms becomes a crucial factor in obtaining a high density. During the process, the grains may be growing in a normal or abnormal state. In the case of normal growth, the mean grain size increases with time, but the grain size distribution remains self-similar (invariant in time). A few large grains grow rapidly at the expense of the smaller grains in the case of abnormal grain growth, which leads to discontinuous growth occurring and the grain size distribution being bimodal. This behavior is sometimes considered as exaggerated grain growth. Anisotropic grain growth is a type of abnormal grain growth in which the abnormal grains grow in an elongated manner, commonly faceted, and straight sides. This kind of growth in porous ceramics is complemented by the breakaway of the boundaries from the pores and is not favorable if high densities are to be attained. As mentioned above, variation in the sintering conditions, i.e. sintering temperature, soaking time, and the heating rate, would result in grain growth with different mechanisms, yielding various magnetic properties due to variation in the microstructure feature of the samples. Typically, the main cause of grain growth in polycrystalline materials is the reduced free energy (ΔG) due to the reduced total grain boundary energy. However, this does not usually occur in the majority of nanostructured materials unless the temperature rises above one-half of their absolute melting point [42]. In nanostructured materials, the grain boundary diffusion [43], second phase (Zener) drag [44], grain boundary segregation [45], and solute drag [46] influence the kinetic of grain boundary motion and kinetics of growth. The effect of sintering temperature on microstructural-magnetic behavior changes is described in the following text.



The grain growth activation energy from the behavior of the particle growth is given based on the Arrhenius equation as follows [47, 48]:

$$d(\ln k)/dT = Q/RT^2 \quad (4.1)$$

where Q is the activation energy, T is the absolute temperature (K), k is the specific reaction rate constant, and R is the ideal gas constant. The value of k is directly associated with grain size, which yields [17]:

$$\text{Log } D = (-Q/2.303R)(1/T) + A \quad (4.2)$$

where A is the intercept, D is the grain size, and R and T are mentioned above. Plotting the $\log D$ versus $1/T$ determines both the activation energy value and the dominant mechanism during the sintering process. The slope of the line is equal to $-Q/2.303R$, where Q is the value of activation energy of grain growth [47]. For example, the plot of $\log D$ as a function of the reciprocal of absolute temperature for the Ni-Zn ferrite samples, which were sintered from 600 to 1200 °C with only 25 °C increments, is given in Figure 4.2 [49]. However, the Q values exhibited some fluctuations with the increase in temperature. It is expected the Q decreases by increasing sintering temperature as a result of an increase in diffusion (D) according to the following equation:

$$D = D_0 \exp\left(\frac{-Q}{RT}\right) \quad (4.3)$$

Overall, the Q obtained was much lower than that of the values reported for Ni-Zn ferrite produced via a conventional ceramic route [50]. This implies that the diffusion process is more probably completed through the surface area and grain

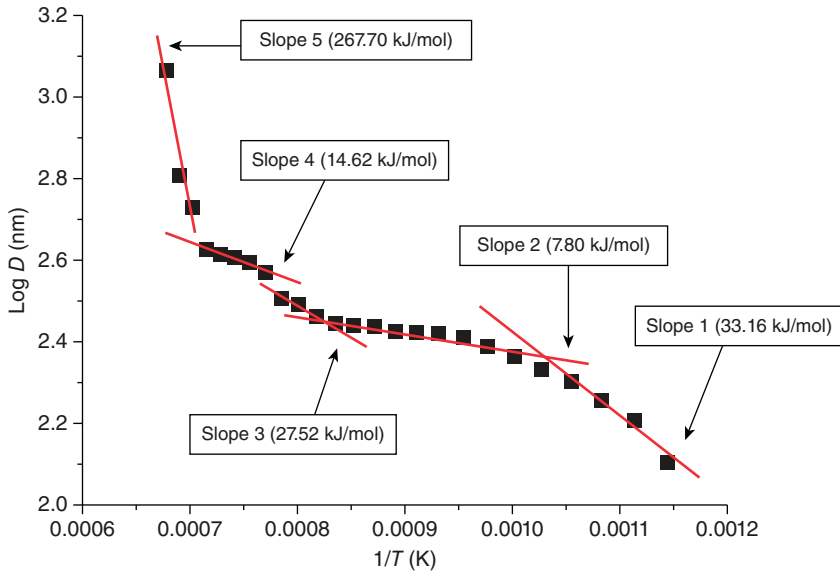


Figure 4.2 Plots of $\log D$ versus the reciprocal of absolute temperature ($1/T$ (K)). Source: Syazwan et al. [49]/with permission of Elsevier.



boundaries in the ball-milled-sintered Ni–Zn ferrites samples [17]. The nanosized starting powder particles, which were obtained from the ball-milled powders, contribute to the achievement of low activation energy. In fact, the ball milling process increases the surface area of the particles, which results in the reduction of activation energy [17].

Based on this plot (Figure 4.2), the mechanism of sintering can be divided into different stages:

Slope 1 is attributed to the initial stage; sintering at relatively low temperatures: the surface diffusion dominates the mass transport mechanism because of the low crystallinity, high reactivity, and low activation energy of the as-synthesized nanoparticles. It seems that the diffusion tries to occur through the surface area since the particles do not have much crystallinity because of the amorphous or dead layer that exists at/or close to the surface of particles. The diffusion speed is low, which becomes faster in the range of 700–800 °C sintering. As their corresponding X-ray diffraction (XRD) patterns indicate (Figure 4.3), the crystallinity increases by increasing the sintering temperature. This suggests that the particles recover their crystallinity and contribute to rapid diffusion through the surface area (Step 2). Since the diffusion in polycrystalline materials is accomplished in the sequence of:

$$D(\text{surface}) > D(\text{grain boundaries}) > D(\text{dislocation}) > D(\text{lattice}) \quad (4.4)$$

the lower value of Q in the range of 700–800 °C suggests that diffusion is accomplished through the surface. During the intermediate stage of the sintering process (range between 800 and 1000 °C), there is fluctuation in Q values, according to slopes 2 and 3. This is more probably associated with grain boundary formation, which facilitates the diffusion process, in particular at a temperature range that belongs to slope 4. By sintering at relatively high temperatures, above 1000 °C, the value of Q increases, and the slope becomes sharper (slope 5). This indicates that the diffusion process through the lattice dominates other mechanisms. In this stage, the grains initiate to grow and become much large in size at a high sintering temperature of 1200 °C.

In nanostructured materials, the dependency of activation energy and the particle or grain size can be explained based on the following function [51]:

$$\frac{E_a}{E_\phi} = \left[1 - \left(1 - \frac{Z_a}{Z_\phi} \right) \frac{N_s}{N_t} \right] \quad (4.5)$$

where N_s and N_t are the numbers of particles in the surface and bulk, respectively. Z_ϕ and Z_a are the atomic coordination numbers in the crystal lattice of bulk and nanoparticles, respectively. E_ϕ and E_a are the activation energy for a bulk and nanoparticle, respectively. This equation indicates that the value of N_s/N_t approaches 1 by increasing the N_s value. Thus, the E_a/E_ϕ value will be declined, which results in the simultaneous reduction in activation energy in polycrystalline materials.

Furthermore, magnetic characteristics of polycrystalline ferrites are considerably dependent not only on intrinsic but also on extrinsic behaviors, e.g. dependency of complex permeability on microstructure [52, 53]. The magnetic behaviors of



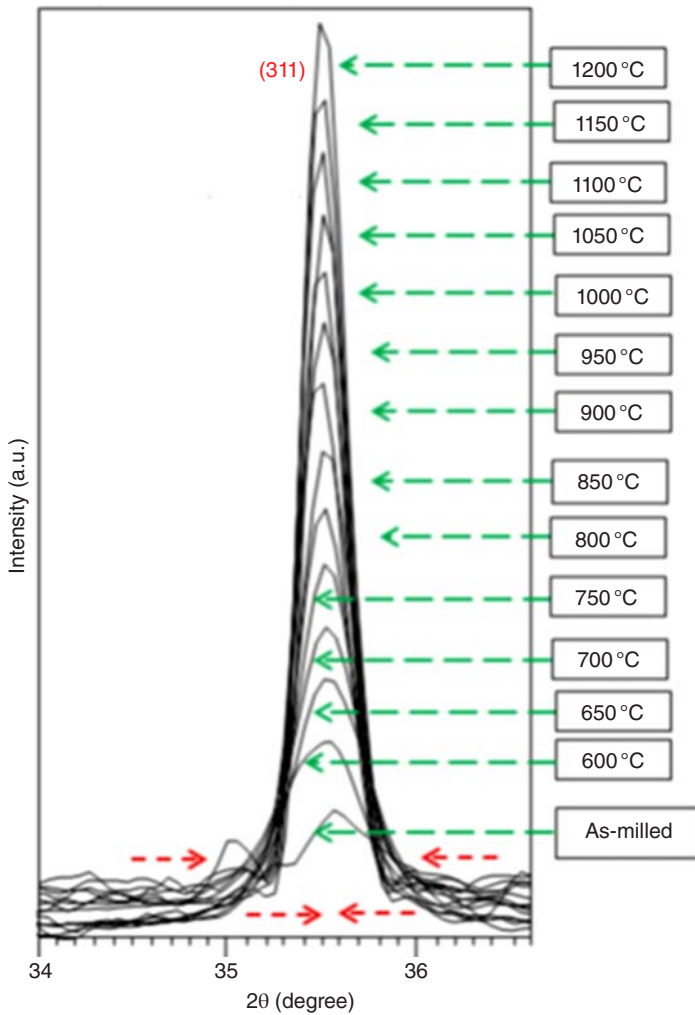


Figure 4.3 XRD pattern of the sintered samples, indicating increasing crystallinity by increasing sintering temperature. Source: Syazwan et al. [49]/with permission of Elsevier.

ferrites such as the initial magnetic permeability, the coercivity, and the shape of the hysteresis loop are not only determined by the intrinsic properties, such as the magnetostriction constant (λ) and magnetocrystalline anisotropy constant (K_1), but also by the microstructural features, including defects, crystalline volume fraction, pore size, and grain size [54].

Generally speaking, microstructural evolution caused by elevating sintering temperatures would affect the magnetic behaviors. Explicitly, a larger grain size forms at the relatively higher sintering temperature, the porosities eliminate, and the number of grain boundaries declines, which makes it easier for magnetic domain walls to move. Their easier movement gives rise to the achievement of higher magnetic permeability which corresponds to the higher efficiency of the magnetic materials [55].



Therefore, with this in mind, one may ask why we should consider the parallel evolution of the magnetic-microstructure relationship from low to higher sintering temperatures. To answer this, we refer the readers to the given examples below.

4.2.1 Magnetism-Microstructure Parallel Evolution in Yttrium Iron Garnet

Rodziah et al. [56] by sintering the ball-milled samples, which were sintered from 600 to 1400 °C, reported that elevating the sintering temperature causes grain growth, which resulted in augmentation of both the saturation induction and magnetization. This is associated with an increase in crystallinity and a reduction of demagnetizing fields in the grains. Furthermore, the change in coercivity is attributed to anisotropy field changes within the samples due to grain size variations. Specifically, the starting appearance of room temperature ferromagnetic order observed by the sigmoid-shaped $B-H$ loops relies on large magnetic domain-containing grains having been formed in the microstructure. Based on the grain size distribution and phase purity, three groups with different magnetism-type dominance were observed in the corresponding hysteresis curves. Later on, in 2018, the same authors focused on the parallel evolutions of magnetic and microwave loss dependence on microstructural changes in several polycrystalline yttrium iron garnets (YIGs) [34]. Increasing sintering temperature from 600 to 800 °C with 100 °C increments indicated an increase of M_s value with an increase in grain size. This is associated with the increase in the crystallinity of the grains. Further studies of the magnetic behavior of the samples revealed a transition from disordered-to-ordered magnetism in $M-H$ curves, which belonged to the formation of different magnetically dominant stages. The sigmoid-shaped loops suggested a ferromagnetic state at room temperature, which seems to be due to the formation of large magnetic domains, phase purity, and crystallinity. Furthermore, transmission loss increased with the increase in grain size. This is more probably associated with loss contribution enhancement from hysteresis and domain wall resonance of the samples. In particular, the variations in transmission loss and ferromagnetic linewidth of the samples are induced by the associated processes of microwave resonance and relaxation due to the domain wall movements and damping of spin rotation contribution as well as the changes in crystallinity and microstructure. In another study [33], the 2-hours ball-milled $Y_3Fe_5O_{12}$ samples were subjected to sintering from 600 to 1400 °C with a temperature step of 100 °C for 10 hours (Table 4.2). By increasing the sintering temperature from 600 to 1400 °C, the average crystallite size increased from 0.20 to 3.09 μm , which was accompanied by their density increments from 4.37 to 4.86 g/cm^3 with a relative density of 84.5–94%. Meanwhile, the porosity of the samples was reduced from 15.5% to 6%. This indicates a reverse relationship between porosity and density. Since the intermediate stage of the sintering process would take place at the relative density of 65–90% [58], it can be concluded that this stage took place at the temperature range of 800–1200 °C. In fact, the higher interparticle interface activates the matter transport, which gives rise to a higher number of neck formation between the particles. This results in increasing the diffusion of the matter on interface and evaporation condensation



Table 4.2 Characteristics of the XRD patterns associated with the YIG samples sintered from 500 to 1400 °C [57].

Sintering temperature (°C)	<i>hkl</i>	Phase	%	Space group	Peak position (°)	FWHM (°)	<i>a</i> (Å)
Before sintering	104	Fe ₂ O ₃	100	<i>R-3c</i>	33.091	0.6336	5.038
500	104	Fe ₂ O ₃	84	<i>R-3c</i>	33.128	0.1948	5.038
500	222	Y ₂ O ₃	16	<i>la-3</i>	29.19	0.2598	10.604
600	104	Fe ₂ O ₃	50	<i>R-3c</i>	33.259	0.2273	5.038
600	121	YFeO ₃	43.3	<i>pnma</i>	33.259	0.2273	5.596
600	222	Y ₂ O ₃	7.0	<i>la-3</i>	29.304	0.2598	10.604
700	104	Fe ₂ O ₃	50	<i>R-3c</i>	33.093	0.2598	5.038
700	121	YFeO ₃	44	<i>pnma</i>	33.093	0.2598	5.596
700	222	Y ₂ O ₃	6.0	<i>la-3</i>	27.170	0.3572	10.604
800	104	Fe ₂ O ₃	50	<i>R-3c</i>	33.055	0.2273	5.038
800	121	YFeO ₃	47	<i>pnma</i>	33.055	0.2273	5.596
800	222	Y ₂ O ₃	3	<i>la-3</i>	29.076	0.3897	10.604
900	024	YIG	100	<i>la-3d</i>	32.354	0.1299	12.375
1000	024	YIG	100	<i>la-3d</i>	32.275	0.1188	12.375
1100	024	YIG	100	<i>la-3d</i>	32.368	0.1980	12.375
1200	024	YIG	100	<i>la-3d</i>	32.474	0.1188	12.375
1300	024	YIG	100	<i>la-3d</i>	32.649	0.1584	12.375
1400	024	YIG	100	<i>la-3d</i>	32.397	0.1188	12.375

Source: Azis et al. [57]/with permission of Springer Nature.

and consequently bulk densification. By elevating the annealing temperature from 1200 to 1400 °C, the grain size increased rapidly, and densification slowed down. This caused the relative density to be reached more than 90%, indicating the final sintering stage occurred.

The magnetic properties study of the Y₃Fe₅O₁₂ samples revealed an obvious jump in the complex permeability (μ^*) values in the permeability, which was resulted from increasing the sintering temperature from 900 to 1100 °C. This phenomenon is described based on three different magnetic categories:

- (i) *Group 1*: weak ferromagnetism dominance, where the samples were sintered at 600–900 °C, and the average grain size distribution ranged in 0.20–0.25 μm . The formation of a paramagnetic-like behavior in the amorphous grain boundary is the main source of the weak ferromagnetism phase. Such materials with weakly ferromagnetic properties consist of less than 50% multidomain grains. Therefore, samples with grain size less than 0.25 μm obtained at sintering temperatures below 900 °C are dominated by spin rotation. Superparamagnetic along with some weak ferromagnetic phases, i.e. yttrium orthoferrite and amorphous phase of YIG exist as well, which contribute to a small value of μ' .



- (ii) *Group 2*: moderately strong ferromagnetism dominance, where the samples were sintered from 1000 to 1100 °C, having the mean grain size distribution from 0.28 to 0.80 μm . This could be due to the fine ferromagnetic crystalline grain size with a large content of the paramagnetic grain-boundary phase of the yttrium orthoferrite and YIG phase. The volume fraction of the crystalline grains increased with increasing the sintering temperature – indicating the formation of higher magnetic mass – which would exhibit stronger ferromagnetism behavior arising from the YIG phase formation. Samples with multidomain grains of more than 50% show moderately ferromagnetic behavior. Therefore, the permeability value variation of the samples sintered from 1000 to 1100 °C was due to the combination of magnetic moment rotation and domain wall motion. Moreover, by increasing the grain size distribution and reduction of the porosity above 1100 °C, a higher value of real permeability (μ') was obtained.
- (iii) *Group 3*: strong ferromagnetic dominance, where the sintering temperature was between 1200 and 1400 °C and the average grain size distribution of samples was between 1.25 and 3.09 μm . Strong ferromagnetic behavior with eliminated paramagnetic phase was observed in the samples due to the highly crystalline YIG phase and large grain size. Moreover, 100% of the grains were ranged in the multidomain grains regime, which was counted as strongly ferromagnetic behavior. Therefore, the permeability of the samples sintered from 1200 °C upward was dominated by domain wall movement. As a consequence, the strong exchange interaction between magnetic moments within domains led to a high real permeability (μ').

Notably, studying the Curie temperature in the parallel evolution of the magnetic-microstructure relationship in polycrystalline YIG revealed the independency of Curie temperature on microstructural changes with sintering from 600 to 1400 °C. The Curie temperature remained relatively stable, unaffected by the microstructure evolutions.

In 2018, Azis et al. [57], in the parallel evolution of magnetic-microstructure properties relationship study, focused on the structural, electrical, and microwave properties of YIG, which were sintered from 500 to 1400 °C with 100 °C increments. The characteristics of the XRD intense peaks in the sintered samples from 500 to 1400 °C are given in Table 4.3. This indicates the dependence of crystal and phase formation on the sintering temperature. It also reveals that the single-phase formation was found by sintering at 900 °C with a space group of *La-3d*.

The density of the samples increased from 4.67 to 5.11 g/cm³ with a relative density of 90.319% and 98.859%, respectively, by increasing the sintering temperature from 500 to 1400 °C. As shown in Figure 4.4, their corresponding grain growth was increased from 0.032 to 6.325 μm accordingly. The initial stage of sintering was concluded to occur in the range of 500–800 °C, which is involved in a strong bond or neck formation at the contact point between particles and rearrangement of the powder particles. The intermediate stage of sintering would take place by sintering at the range of 800–1100 °C, which involves neck growth, grain boundaries formation, and



Table 4.3 Details of the magnetic behavior of the sintered Ba-ferrite samples [11].

T (°C)	Phases	H_c (G)	M_r (emu/g)	M_s (emu/g)	Grain size (nm)	Magnetic moment (μ_B)
400	Fe_2O_3 , $BaCo_3$	364.6	0.1043	0.612	55.2	0.121
500	Fe_2O_3 , $BaCo_3$	479.69	0.106	0.563	87.4	0.112
600	Fe_2O_3 , $BaCo_3$	909.13	0.104	0.696	90.8	0.138
700	Fe_2O_3 , $BaCo_3$	566.88	16.826	0.544	122.5	0.108
800	Fe_2O_3 , $BaFe_{12}O_{19}$	2686.8	22.073	36.75	123.2	7.313
900	$BaFe_{12}O_{19}$	3436.7	25.677	42.468	142.9	8.451
1000	$BaFe_{12}O_{19}$	4435.8	27.529	45.102	219.29	8.975
1100	$BaFe_{12}O_{19}$	3994.7	28.849	47.371	322.19	9.427
1200	$BaFe_{12}O_{19}$	2778.4	28.396	51.004	542.2	10.15
1300	$BaFe_{12}O_{19}$	1014.9	20.131	56.54	916.2	11.251
1400	$BaFe_{12}O_{19}$	201.25	5.3787	52.122	9270.6	10.372

Source: Shafie et al. [11]/with permission of Springer Nature.

porosity reduction. The last stage of sintering, sintering at 1200–1300 °C, caused the pores to reduce and slowly disappear by the diffusion of vacancies from the pores along the grain boundaries.

The magnetic characteristics revealed that transmission loss would increase with the increase in the sintering temperature; thus, this variation was with a small rate at low sintering temperatures (≤ 900 °C) and with a high rate at high sintering temperatures. This is associated with the high crystallinity obtained with the increase in the sintering temperature so that a high crystallinity with high purity of crystal structure obtained at temperatures higher than 900 °C contributes more to spin contribution at high-frequency range [16, 22, 59]. The resonance frequency is found to shift at a higher frequency as the sintering temperature increases. This phenomenon is associated with the crystallographic anisotropy of the static magnetization of YIG crystals. Furthermore, the transmission loss variation with temperature was in accordance with the inverse relationship with linewidth by increasing sintering temperature. This is associated with grain growth and porosity reduction with temperature [47].

4.2.2 Magnetism-Microstructure Parallel Evolution in Hard Ferrites

A series of 12-hours ball-milled polycrystalline $BaFe_{12}O_{19}$ bulk samples were subjected to sintering from 700 to 1300 °C with 100 °C increments to find out the parallel evaluation of the magnetic-microstructure relationship [60]. The results revealed that the magnetic B - H hysteresis loop relies on the grain size variation. In fact, this is because of the phase crystallinity enhancement by increasing sintering temperature that would affect the magnetic characteristics of the sample. Three different groups of samples based on their magnetic behaviors were found: (i) paramagnetic state with the grain size distribution ranging in 0.30–0.39 μm ,



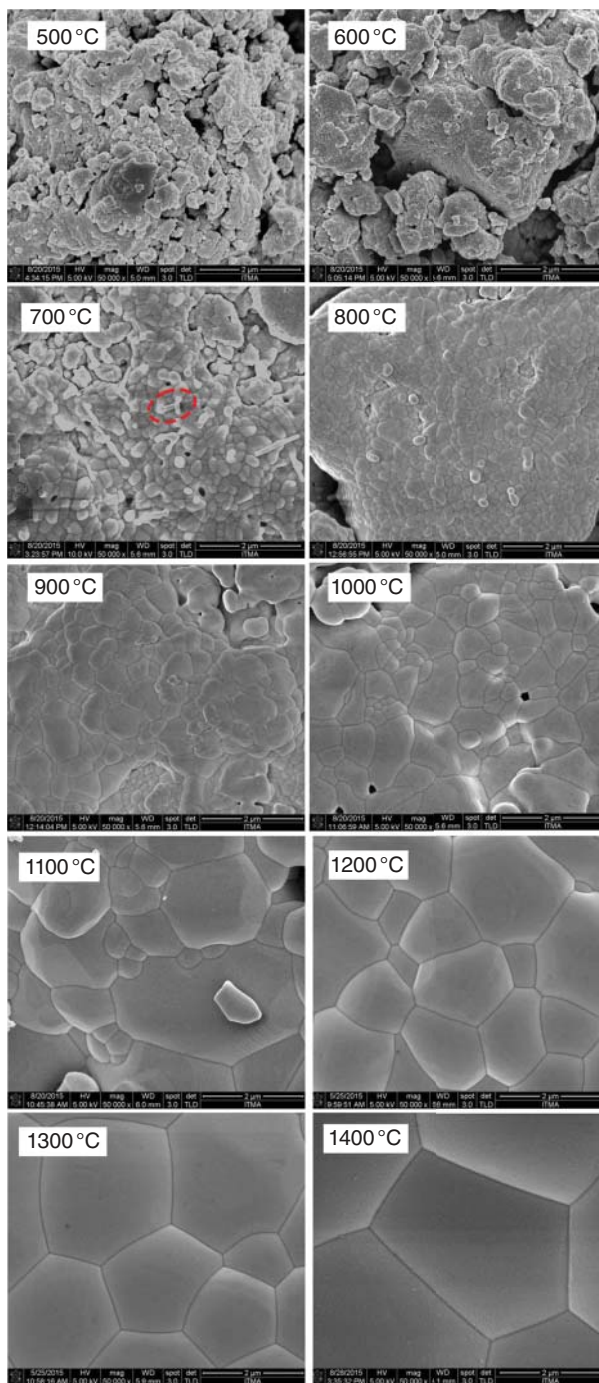


Figure 4.4 FESEM images of YIG samples sintered at different temperatures. The images are given in a scale bar of 2 μm. Source: Azis et al. [57], Springer Nature.



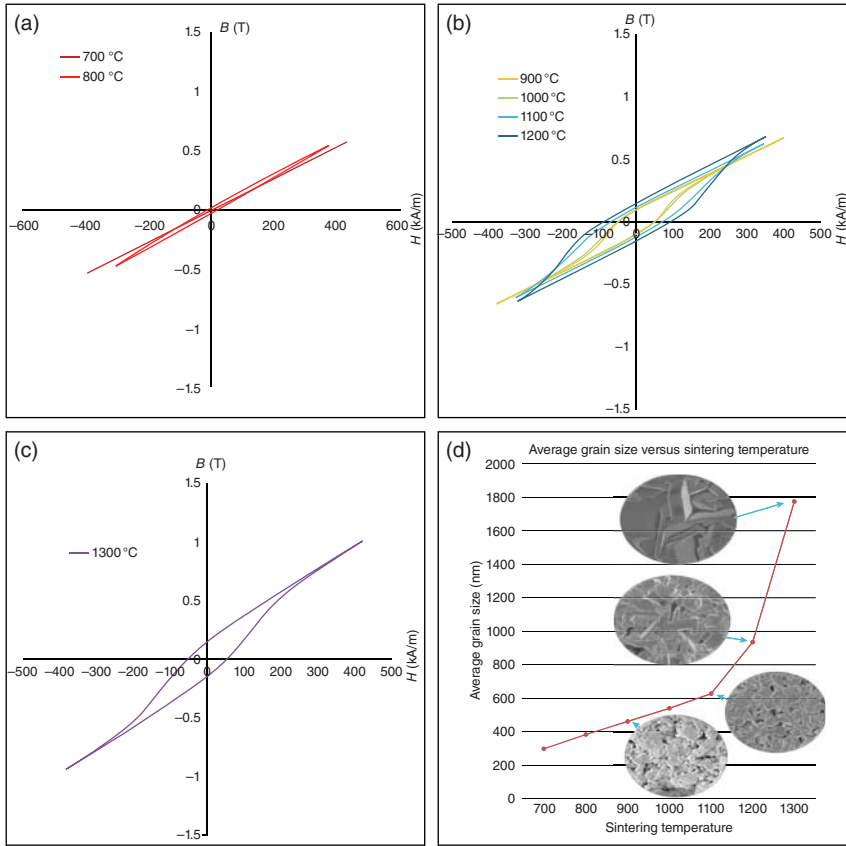


Figure 4.5 B - H hysteresis curves of the $\text{BaFe}_{12}\text{O}_{19}$ samples sintered at different temperatures (a-c), and representation of the mean grain size versus sintering temperature (d). Source: Huang et al. [60], Springer Nature.

(ii) intermediate ferromagnetic state with the grain size distribution ranging in $0.46\text{--}0.94\text{ }\mu\text{m}$, and (iii) strong ferromagnetic state with the grain size distribution greater than $1.78\text{ }\mu\text{m}$. For the smaller size of the grain, the B - H hysteresis loop more looks like a linear curve, proving the paramagnetic behavior (Figure 4.5a) [61]. A slanting-sigmoid hysteresis loop for the second group indicates the mixture of para- and ferromagnetic behavior of the samples (Figure 4.5b). Eventually, by sintering at $1300\text{ }^{\circ}\text{C}$, a sigmoid-shaped hysteresis loop (Figure 4.5c) suggests a high crystalline phase and as a result the ferromagnetic behavior of the sample. The variation in the mean grain size as a function of sintering temperature is given in Figure 4.5d. It indicates that the grain growth is slower at low temperatures, and it becomes faster at high temperatures due to the fact that the matter transport via diffusion mechanism facilitates by increasing the sintering temperature.

Figure 4.6 shows the variation of normalized inductance (L_Q) as a function of temperature (T). Using this data, the Curie temperature of the samples is determined. A null value was found for the samples sintered at 700 and $800\text{ }^{\circ}\text{C}$.



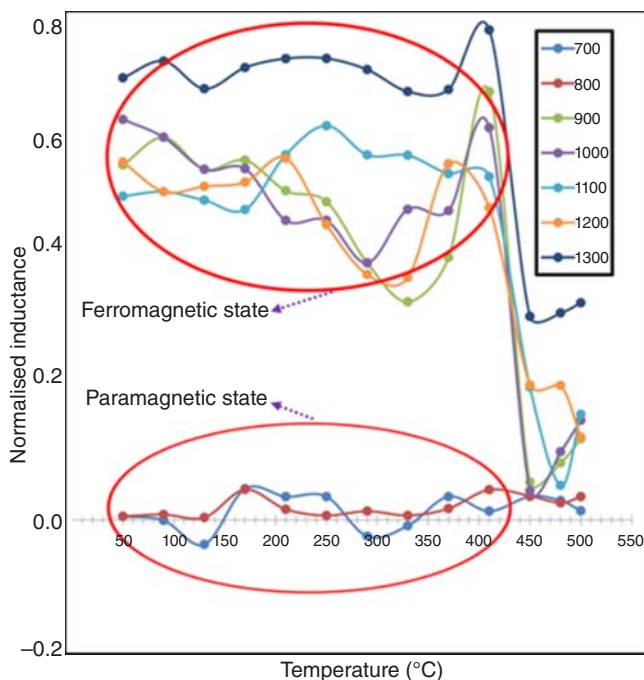


Figure 4.6 Determination of Curie temperatures based on L_Q versus T plot for the samples sintered at different temperatures. Source: Huang et al. [60], Springer Nature.

According to the paramagnetic behavior of the samples in this range of temperature, the random orientation of magnetic moments occurred, and there were no strong exchange interactions between adjacent moments. By sintering onward 900 °C, the Curie temperature increased by increasing the sintering temperature. This is because the neighboring magnetic moments' distances decreased, the interactions strengthen, and higher thermal energy is needed to cause a paramagnetic state.

Shafie et al. in 2014 [60] tried to figure out the variation of magnetic properties of $\text{BaFe}_{12}\text{O}_{19}$ against its evolving microstructure. The 12-hours milled barium carbonate and iron oxide powders were pressed and sintered from 400 to 1400 °C with 100 °C increments for 10 hours. The phase formation and structural changes were determined via XRD patterns, as shown in Figure 4.7. The results showed that a crystalline ferrite phase was formed by sintering the milled powders at 1000 °C. In other words, there was no trace of the barium ferrite phase by sintering the milled samples at the temperature range of 400–700 °C, but by increasing the sintering temperature up to 1000 °C, the ferrite phase with some other secondary phases was detected. A well-crystallized $\text{BaFe}_{12}\text{O}_{19}$ formation at above 1200 °C suggests that lower sintering temperatures are not able to provide enough energy for neither high purity phase formation nor crystallinity in Ba-ferrite samples.

The effect of sintering temperature from 400 to 1400 °C on microstructural properties of samples is shown in FESEM images given in Figure 4.8. The grains are in the range of 41–80 nm with an average size of ~55 nm for the sintered sample



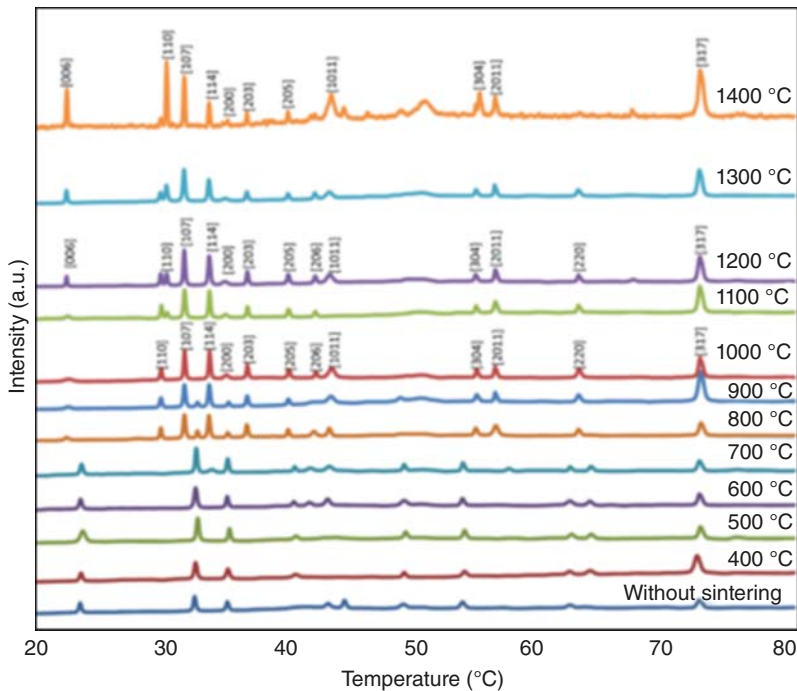


Figure 4.7 The effect of sintering temperature on the XRD pattern of the Ba-ferrite samples. Source: Shafie et al. [11]/with permission of Springer Nature.

at 400 °C, in the range of 81–120 nm with the average size of ~87 nm at 500 °C; the dominating sizes are 81–120 nm with the average size of ~90 nm by sintering at 600 °C and 81–160 nm with the average size of ~122 nm at 700 °C. As compared to 700 °C, almost the same-sized grains but with a well-formed morphology were observed by sintering at 800 °C, which suggests that the necking process seems to occur. At this temperature, the grains were ranged in 81–120 nm with an average size of ~123 nm. It is evident from the corresponding XRD patterns that Bragg peaks of the Ba-ferrite phase are observed in the sample sintered at 800 °C, although other phases were not fully vanished. In other words, single-phase formation is not completed yet by sintering at 800 °C. The grain growth is also observable in the samples sintered at 900 and 1100 °C, where the grain sizes ranged in 121–160 (average size of ~142 nm) and 191–300 nm (average size of ~219 nm), respectively. By sintering at 1100 °C, well-textured grains with an average size of ~322 nm were observed. The neighbor grains coalesce and form larger grains by sintering at 1200 °C. The block-like columnar structures can be seen in the morphology of the 1200 °C sintered sample, suggesting strong growth anisotropy with grains growing in different directions to yield a very elongated branched structure. This kind of structure would lead to the formation of the pores between the grains in samples sintered at 1300 and 1400 °C, which weakens the hard magnetic properties of the samples.

The study of the magnetic properties of the samples revealed that the magnetic hysteresis loops fall into three distinct groups based on the sintering temperature



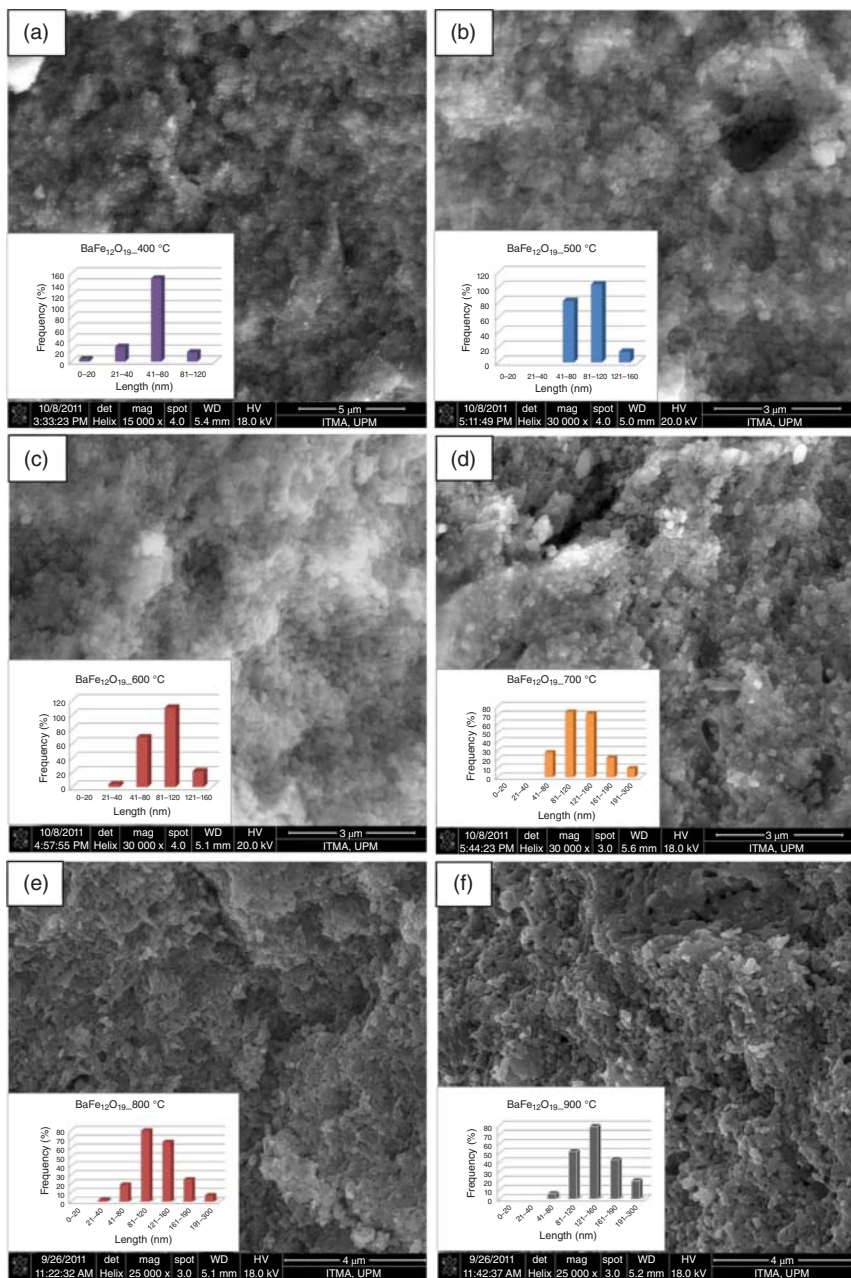


Figure 4.8 FESEM images of the Ba-ferrite samples sintered from 400 to 1400 °C; (a–k), respectively. Source: [36], M. Shafie et al. (2018), Springer Nature.



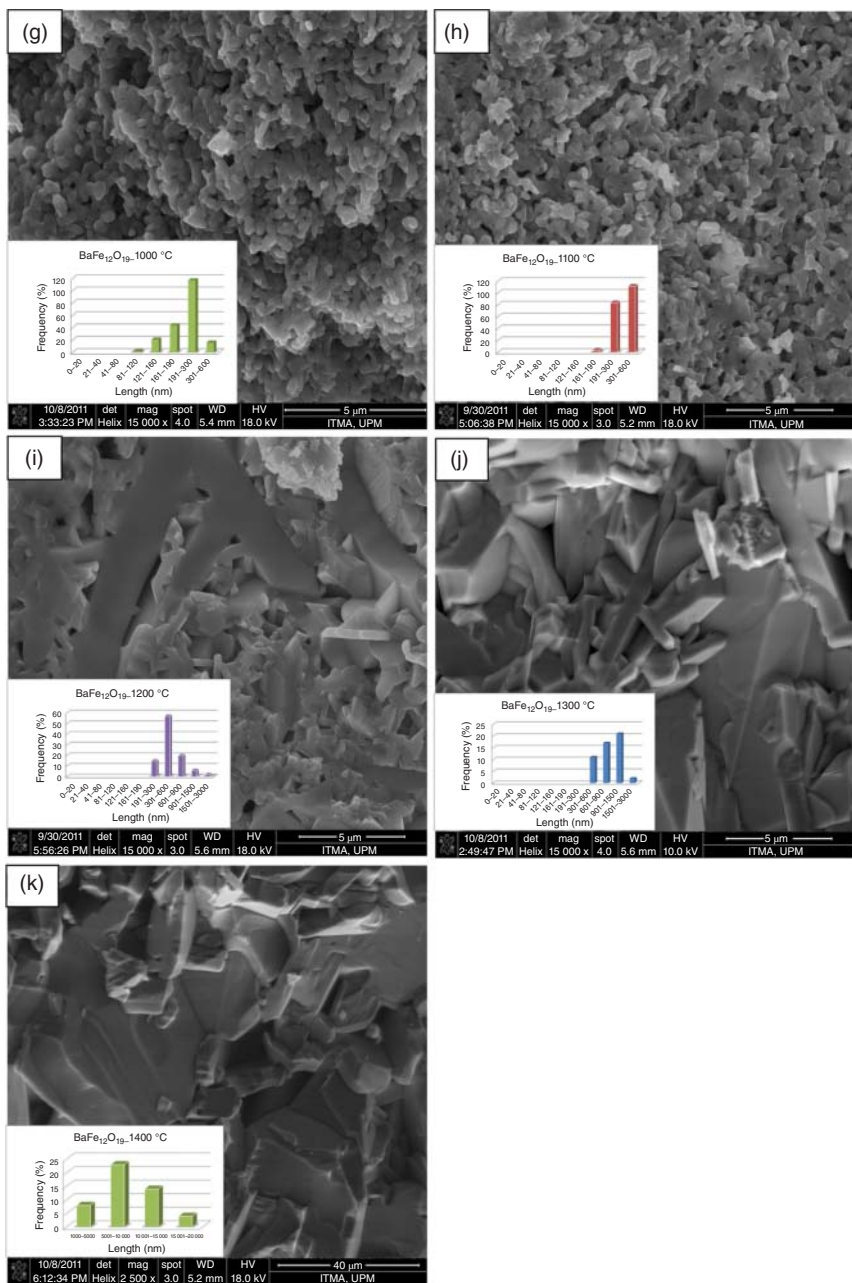


Figure 4.8 (Continued)



and grain size distribution, ranging in 400–700, 800–1000, and 1200–1400 °C. Observation of the different $M-H$ loop behaviors for the three hysteresis loop groups suggests microstructure-dependent states of magnetism.

Sintering at 400–700 °C indicated $M-H$ curves with a slim hysteresis pattern (Figure 4.9a). These linear-like curves suggest the paramagnetic behavior of the samples. In fact, M_s is almost zero, indicating a very weak ferromagnetic behavior in the samples. By increasing the sintering temperature, ranging from 800 to 1100 °C, a higher magnetic ordering was obtained. This is concluded from their broader hysteresis loops with higher M_s values (Figure 4.9b). By sintering above 1200 °C (third group), the further increase in M_s value (Figure 4.9c) suggests a strongly ordered magnetism in those samples. Noticeably, by further enhancement in the sintering temperature from 1300 to 1400 °C, the M_s value decreased, which is more probably associated with the oxidation of iron oxide and formation of maghemite. Furthermore, according to their corresponding FESEM images, abnormal grain growth and poorly arranged crystallites in microstructure were observed. This occurs due to the high thermal energy provided at the high sintering temperature, which results in the ready occurrence of anisotropy growth. Details of the magnetic behavior of the samples are given in Table 4.3. It is evident that for the samples sintered above 1300 °C, the coercivity and remanence are deteriorated due to the disordered microstructure.

The effect of the grain size on the variation of coercivity is given in Figure 4.10a. It indicates that by elevating the sintering temperature the grains grow; however, the coercivity reveals different behaviors. The coercivity first increases sharply with the increase in grain size and then shows a downward trend with further grain growth. This phenomenon suggests, according to Figure 4.10b as well [61], a transition from single-domain grains to a multidomain regime in polycrystalline materials. The temperature, grain size, and coercivity related to this regime are considered as critical temperature, grain size, and coercivity, respectively [11, 18, 55]. These critical values were obtained at about 219 nm for Ba-ferrite samples [11].

A rapid increase in H_c value with enhancement in the sintering temperature from 400 to 1000 °C is associated with grain growth, which obeys Herzer's random anisotropy model ($H_c \propto D^6$) [55]. In fact, the fine starting powder is so reactive that a quick grain growth would easily occur. In this stage of sintering, strong super-exchange interactions inside the domains may lead to a high magnetocrystalline anisotropy according to their $M-H$ curves (Figure 4.9); three groups of samples are reported in which each group with a particular grain size shows different magnetic strength. The reduction of coercivity with grain size can be described in terms of Herzer's random anisotropy model ($H_c \propto D^6$), where coercivity has a direct relationship with grain size, as consequence with temperature [21]. On the other hand, the reduction in coercivity values with further grain growth, by sintering from 1000 to 1400 °C, is associated with the lattice imperfections elimination, and the relaxation of residual stress was dominant [21]. The obtained results from the parallel evolution of the magnetic-microstructural properties of Ba-ferrite samples suggest a new and good idea to improve and develop the permanent-magnet materials in the industry for different purposes.



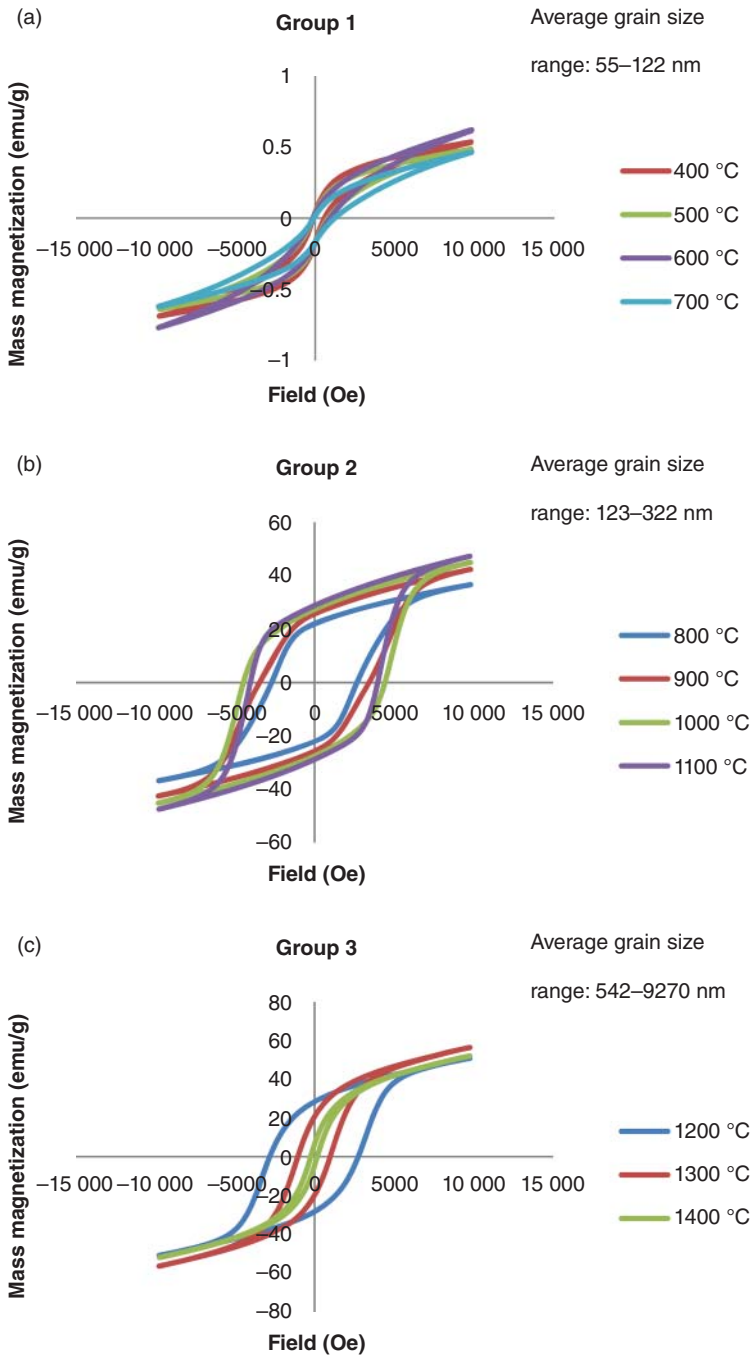


Figure 4.9 Room temperature M – H curves of the sintered Ba-ferrite samples [11]; where the curves can be divided into three groups based on the average grain size obtained at different sintering temperatures: (a) group 1 suggesting paramagnetic or very weak ferromagnetic behavior, (b) group 2: strong ferromagnetic behavior, and (c) group 3: moderate ferromagnetic behavior of the samples. Source: Shafie et al. [11]/with permission of Springer Nature.



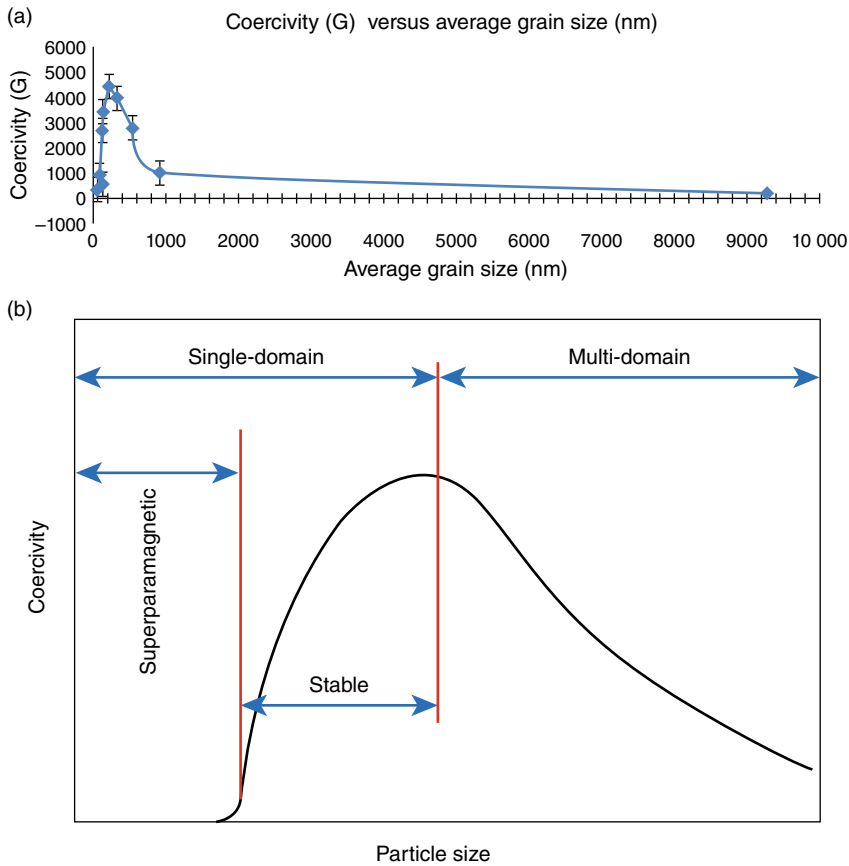


Figure 4.10 Coercivity versus grain size in (a) $\text{BaFe}_{12}\text{O}_{19}$ samples. Source: Shafie et al. [11], Springer Nature and (b) schematic representation of H_c versus particle size in single-domain and multi-domain magnetic particles. Source: Hajalilou et al. [61]/with permission of Springer Nature.

4.2.3 Magnetism-Microstructure Parallel Evolution in Soft Ferrites

Soft ferrites are extensively employed in electronic electromagnetic devices because of their outstanding characteristics, i.e. relatively high electrical resistivity and low eddy current loss at high frequencies [17, 55, 62, 63]. From an industrial point of view, the performance of spinel ferrite is only narrowed to a few megahertz frequencies in the state of a micron-sized scale, due to their higher conductivity and domain wall resonance [62]. Hence, one way to remedy this matter and employ these materials in high-frequency applications is to use powders with nanosized grains which show higher resistivity [62, 64].

Soft spinel ferrites, with the general chemical formula $(\text{A})[\text{B}_2]\text{O}_4$ where A is a divalent and B stands as a trivalent cation, have a close-packed fcc array of anions with sites partly filled by the A and B cations [7, 17, 18, 62, 65]. In terms of cation



distribution, spinel structure can be normal or inverse, depending on the type of A and B cations, synthesis method, composition, sintering temperature, and so on [16]. In other words, to emphasize the microstructural aspects of soft ferrites, their chemical formula is generally given by $(M^{2+}_{1-x}Fe^{3+}_x)_A[M^{2+}_xFe^{3+}_{2-x}]_BO^{2-}_4$, in which M is one or any divalent cations. Here, x represents the degree of inversion, and A and B denote tetrahedral and octahedral sites, respectively [23]. Single-phase Ni-ferrite and Ni-Zn, and Mn-Zn ferrites are examples of the most technologically used materials due to their high permeability, low eddy current loss, and high electrical resistivity. These properties enable them to be appropriate candidates in core materials for power transformation, recording media, microwave devices, loading coil applications, and telecommunication systems antenna rods [66].

In a similar manner to other ferrites, most of the previously published works focused only on the final products' microstructure or magnetic properties. Few works, as given in examples below, considered a parallel evolution study in soft magnetic materials. Ni-ferrite samples: the 30-hours ball-milled Ni ferrite samples sintered from 900 to 1300 °C, are given as a first example [18]. The FESEM images of these samples accompanied by their particle size distribution in the inset of images are shown in Figure 4.11. It was found that almost 97% of the particles ranged in a single domain state by sintering at 900 °C. For a sample sintered at 1300 °C the grains consist of multi-domain. As mentioned before, the coercivity (H_c) plot verse grain size, determines a critical value, so that below that value the particles are in a single-domain limit and above that all the particles are multi-domain. At 1100 °C sintering temperature, the grain size was about 211 nm, which was considered a critical temperature and grain size. However, the magnetic properties, i.e. saturation magnetization in the M - H curve or saturation induction in the B - H curve increased by increasing the sintering temperature, three different groups with various magnetic behaviors are suggested based on M - H or B - H curves. The paramagnetic accompanied by superparamagnetic behavior was detected by sintering up to 1000 °C. This is more probably associated with the small size of the grains, where the cation distribution is in a nonequilibrium state [67] and/or the arrangement of the spins in the structure is in the canted state [68]. These phenomena lead to the reduced connecting numbers of magnetic $Fe^{+3}(A)-O^{2-}-Fe^{+3}[B]$ and finally result in the debilitated superexchange interaction of the primary (A)-O-[B] binds [18, 68]. The M - H hysteresis loops are roughly lined up with a magnetic field for the 30-hours milled samples sintered at 900 and 1000 °C, implying the presence of both the paramagnetic (from amorphous phase) and superparamagnetic (from crystalline phase) behaviors in those samples. On the other hand, a narrowly bulging but linear-looking curve for the sample sintered at 1100 °C indicates that the paramagnetic phase dominates over a ferromagnetic phase in the samples. According to the corresponding FESEM images and the grain size distribution histograms, the average grain size is located in the single-domain region for the samples sintered at 900 and 1000 °C. At this temperature interval, a strong necking process occurs, and the crystalline structure is not completely formed. During the necking process, the shape anisotropy occurs in somewhat small and elongated



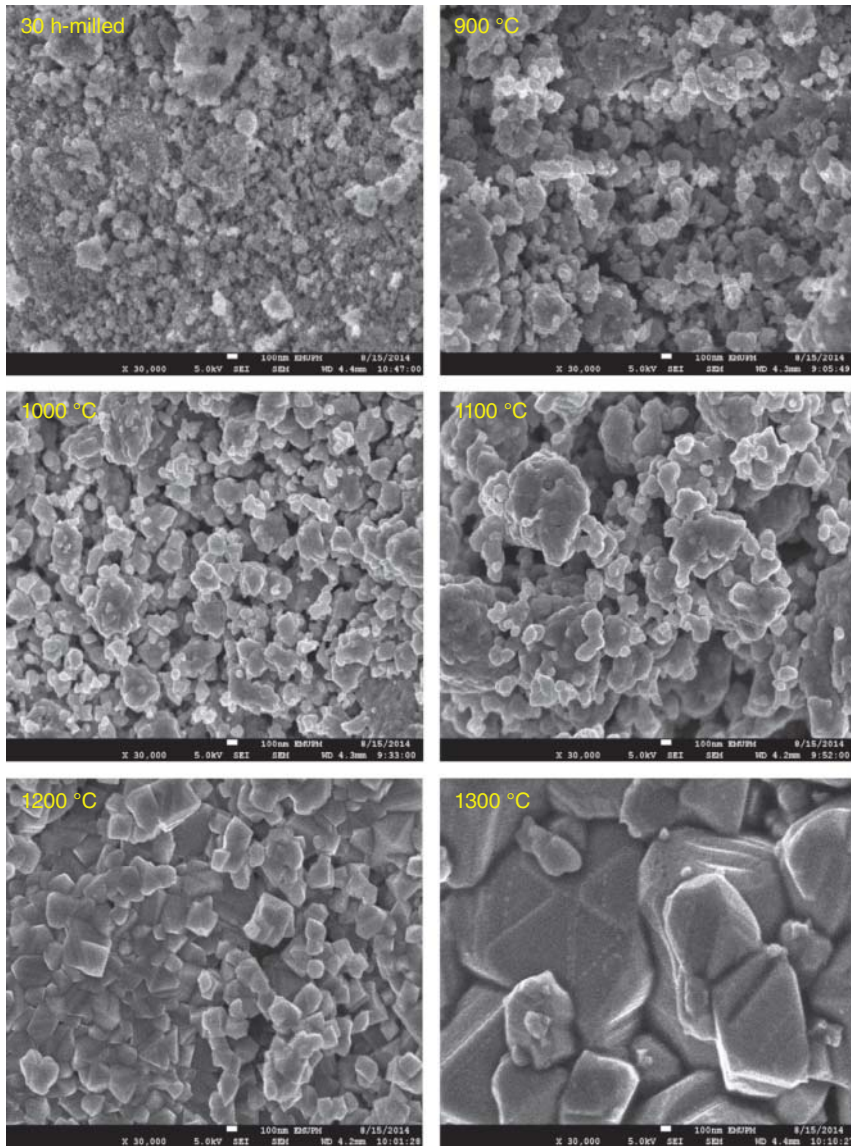


Figure 4.11 FESEM images of the sintered nickel ferrite samples at various temperatures, accompanied by their corresponding grain size distribution histograms and $M-H$ curves. Source: [37], A. Hajalilou et al. (2015), ELSEVIER.

grains, which results in a higher value of coercivity is obtained. The sigmoid-shaped loops were observed for those samples that were sintered at high temperatures of 1200 and 1300 °C. This shows a strong ferromagnetic property of the samples. This is because the domain wall motion becomes easier at large grains, as results in its contribution to magnetization and demagnetization increases, which needs less energy than domain rotation [22].



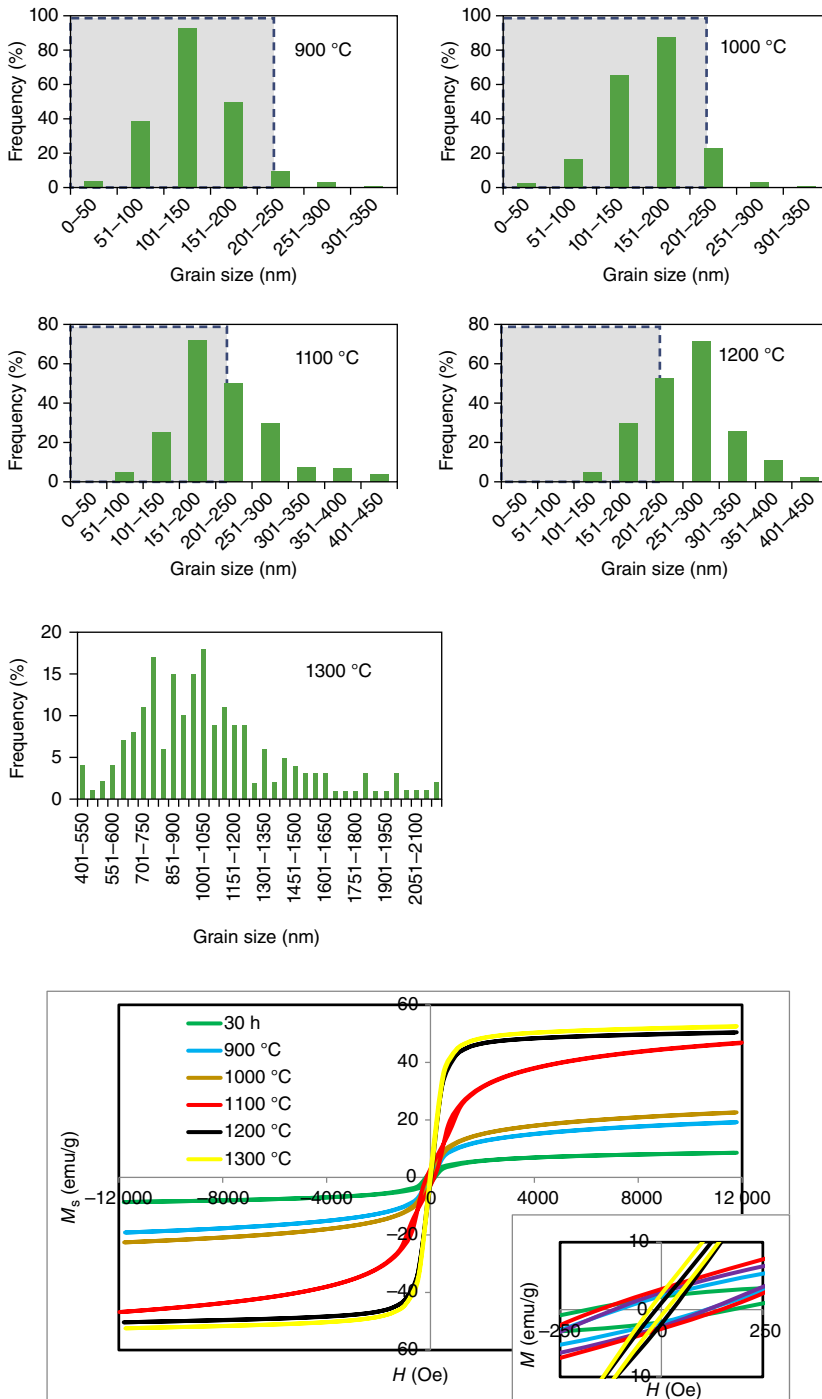


Figure 4.11 (Continued)



4.3 Soaking or Sintering Time

The sintering temperature is the most focused parameter in the sintering process of spinel ferrites [69–72], while studies on soaking time are scarcely found in the literature on those ceramic magnetic materials. Thus, to better understand the role of sintering time, a nonmagnetic TiO_2 nanoparticle as an example is taken into account, which will be followed by given examples of magnetic materials. Buesser et al. [73] investigated the sintering rate and mechanism of 3-nm TiO_2 nanoparticles sintered at 1800 K. They studied the effect of the surface area of the sintered particles at various times and simulated through molecular dynamics (MD). The results revealed that highly mobile ions from the particle surface fill in the initially concave space between nanoparticles (surface diffusion) forming the final, fully coalesced, spherical-like particle with minimal displacement of inner Ti and O ions (grain boundary diffusion), revealing also the significance and sequence of these two sintering mechanisms of TiO_2 . A sintering rate for TiO_2 nanoparticles is extracted that is much faster than that in the literature but nicely converges to it for increasing particle size. It indicates that the two particles approach each other and somewhat rotate to accommodate their lattice planes at the beginning (10^{-5} – 10^{-3} ns). This has been detected by MD simulation [75], and experimentally [76] on noble metals such as Au nanoparticles as well. In fact, the time evolution of the gyration radii during the particle coalescence evaluated via MD, defined as $R_\alpha = 1/N \sum_{i=1}^N \alpha_i^2$, where $\alpha = x, y, z$ are the molecule coordinates and N total number of the simulated molecules, is reported in Figure 4.12a for two particles of 20 Å radius and an initial temperature of 895 K. A typical transient can be characterized by two main stages. A very fast first phase can be distinguished where a neck forms between the two particles and its growth rate is following a power law in time (Figure 4.12b) as given in equation:

$$xR_p^n = BtR_p^m \quad (4.6)$$

where R_p is the initial particle radius, x the neck radius, t the time, and B is a constant depending on the temperature. If grain boundary diffusion or surface diffusion is

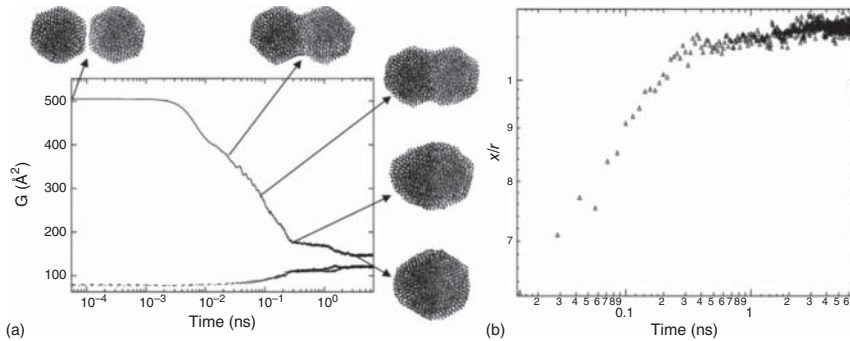


Figure 4.12 (a) Time evolution of the gyration radii in the three directions x (continuous line), y , z (dashed lines) during the sintering of two nanoparticles: $r=20$ Å, $T=895$ K. (b) Time evolution of the neck during the sintering of two nanoparticles: $r=20$ Å, $T=895$ K. Source: Adapted from Arcidiacono et al. [75].



dominant Eq. (4.6) becomes [93]

$$t = x r_p^6 r_p^4 R T C w D \sigma_{sv} \Omega \quad (4.7)$$

where C is a constant, R is the universal gas constant, D is the grain boundary or surface diffusion coefficient, σ_{sv} is the solid-vapor surface tension, Ω is the molar volume, and w is the surface or grain boundary layer width, estimated as $\Omega^{1/3}$ [94].

This is a sign of an oriented attachment mechanism [77] in those nanoparticles, where highly mobile particles would translate and rotate to reach energetically favorable contact points in order to lessen the total free energy of the system. In this state, the total surface area might even rise to some extent by deformation occurring by their ion interactions [73]. The surface energy would decline after the sintering process at three different stages [78]: neck formation and their initial growth of about 6–7% at a sintering time range of 10^{-3} –0.01 ns. The oval-shaped structures about 1–2% are formed in the second stage at a time range of 0.01–1 ns. In this stage of sintering, the sinter neck becomes comparable to the diameter of particles. Finally, full coalescence occurs by forming spherical-shaped particles at the expense of surface area reduction of about 10% at the sintering time range of 1–100 ns. This is considered as the third stage of sintering, where the slope of this region in the given figure is comparable to that of the phenomenological model [74] with the characteristic sintering time based on the following equation [73]:

$$\tau = 7.44 \times 10^{16} d_p^4 T \exp\left(\frac{258\,000}{RT}\right) \quad (4.8)$$

where T is temperature, R is the universal gas constant, and d_p denotes the primary diameter of particles. Early deviations between the two simulations arise from the surface area reduction due to the particles' connection and neck formation at the first stage of sintering.

Those few works are mentioned in Refs. [69–72] mostly focused on the cation distribution between tetrahedral and octahedral sites [79, 80]. For example, an investigation by ESR spectra on the cation distribution in Co–Zn ferrite revealed that the Fe^{2+} content in the octahedral site decreases by increasing soaking time, and consequently, the cation distribution changes in A and B sublattices. The soaking time was also found to affect electrical mobility. Tashtous et al. reported that the electrical resistivity would decline with the rise in soaking time due to the formation of more ferric ions (Fe^{3+}) at octahedral sites. In fact, by considering the general formula for mixed spinel ferrites such as Co–Zn and Ni–Zn ferrites, as ABFe_2O_4 , where A and B stand for A and B sites, respectively, that can be written as $\text{A}^{2+}_x\text{Fe}^{3+}_{1-x}(\text{B}^{2+}_{1-x}\text{Fe}^{3+}_{1+x})\text{O}_4$ [81]. As the soaking time increases, more ferrous ions (Fe^{2+}) would transform to Fe^{3+} ions at B sites by the oxidation process.

The activation energy required to transfer an electron between ferrous and ferric ions is affected by strong B–B exchange interaction. Since the cations such as Zn have preferences to occupy the A sites, the strength of A–A and A–B interactions decreases owing to the migration of ferric ions to B sites [82]. Hence, by increasing soaking time and then increasing the number of ferric ions in the B sublattice, the B–B exchange interaction is strengthened. Also, the increase of ferric ions in B sites, due to soaking time, increases the conductivity of the ferrite sample [83].



According to their physical properties, the lattice constant decreased while the experimental density increased by increasing Fe^{3+} (due to the oxidation of Fe^{2+}) due to increasing the sintering/soaking time. These Fe^{3+} ions would reside in the B sites, which have a higher effective magnetic moment than Fe^{2+} . Furthermore, more spins would be generated and form domain walls by elevating the soaking time [79].

In the foregoing-mentioned work, however, the density constantly increased, and porosity decreased. The critical density or porosity may be considered by the parallel evolution of microstructure study with sintering soaking time. In other words, there is a possibility that increasing soaking time results in grain growth until a critical grain size, which results in an increment of density and reduction of porosity. But after that, both characters show revelry. In fact, increasing the soaking time would give rise to an increase in the concentration of structural vacancies, which provides an opportunity to increase the diffusion coefficient through the increment of oxygen vacancies in the crystal lattice. As the coefficient diffusion is faster, the grains grow easily and rapidly. Thus, more pores are accumulated in the larger grain size area, which results in a reduction in the density of a sample. The pores would isolate and sink in the grains as the sintering process further proceeds. The pores' growth cannot easily take place in the case of their isolation from grain boundaries. Thus, this reduction in porosity will increase the density of a sample. This suggests that a systematic study for the determination of critical physical characteristics with soaking time is required in magnetic materials, which will have various effects on magnetic behaviors. In fact, it is believed that the effective magnetic moments of metal ions in tetrahedral (A site) and octahedral (B site) in cubic spinels, cause three interaction mechanisms, i.e. A–A, A–B, and B–B through the separating oxygen ions. So, with elevating the soaking time, the net magnetic moment increases as the pores reduce, which results in an increment of the exchange interaction strength in the ferrimagnetic interval below Curie temperature (T_C). This leads to a reduction in domain wall motion. Ismail et al. [32] by using magnetic hysteresis loops and phase transition studies reported the effect of soaking time on the magnetic-microstructure properties relationship in the mechanically alloyed Ni–Zn ferrite. The FESEM images of the sintered samples at 800 °C for soaking times of 1, 5, 10, 20, 30, 40, and 96 hours are shown in Figure 4.13. The images indicate that the necking process is observable which suggests the grain growth phenomenon occurrence, increasing their size from 0.14 to 0.25 μm . This small variation in the grain size indicates the slow rate of microstructural evolution of the samples. The other structural and microstructural variations with soaking time are given in Table 4.4. The densification of the samples is attributed to the arrangement of the particle in the first step of the sintering process due to the lattice diffusion [84]. Indeed, the necking phenomenon in the sintering process is associated with the surface and grain boundary diffusion occurrence between the nano-sized particles.

The dependence of magnetic properties of the Ni–Zn ferrite samples on soaking time, which were sintered at 800 °C, is shown in Figure 4.14. The initial magnetization curve indicates that as the crystalline phase develops, more



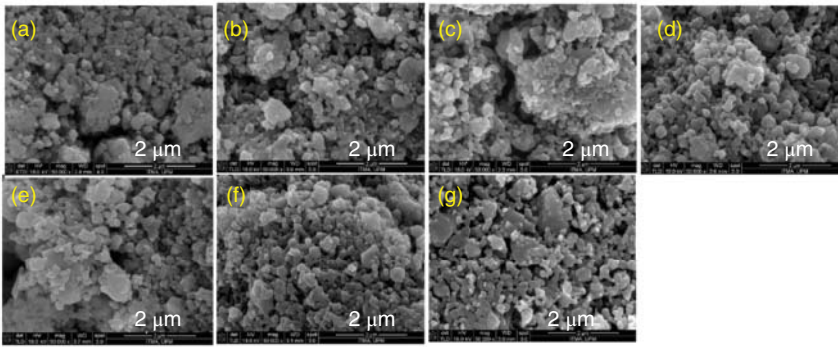


Figure 4.13 FESEM images of the 800 °C sintered samples at (a) 1, (b) 5, (c) 10, (d) 20, (e) 30, (f) 40, and (g) 96 hours; redrawn from the scale bar of 2 μm . Source: [33], I. Ismail et al. (2012), with permission from ELSEVIER.

Table 4.4 The effect of soaking time on microstructural properties of Ni–Zn ferrite samples [32].

Soaking time (h)	Average grain size (μm)	Density (g/cm^3)	Theoretical density (%)	Porosity (%)	A (\AA)	Volume (\AA^3)	Intensity peak (counts)
1	0.14(0)	4.51(1)	84	16	8.40	592.16	1851.00
5	0.15(8)	4.61(6)	86	14	8.39	591.49	2207.00
10	0.19(7)	4.66(0)	87	13	8.39	591.51	2583.06
20	0.21(0)	4.69(8)	88	12	8.39	591.18	2618.58
30	0.23(2)	4.70(1)	88	12	8.39	591.47	2750.00
40	0.25(0)	4.72(2)	88	12	8.39	591.55	2365.00
96	0.25(6)	4.92(0)	92	8	8.39	591.85	2943.00

Source: Ismail et al. [32]/with permission of Elsevier.

super-exchange interaction transpired which reflected the increase of the magnetization (Figure 4.14a). The relative permeability in terms of soaking time is given in Figure 4.14b. It indicates that the magnetic moment would easily align in the direction of the external field due to the increase of magnetic moment with the grain growth as a result of increasing the soaking time. A little variation in relative permeability was observed in the samples subjected to a soaking time of one and five hours. This is because the formation of multidomains is negligible and needs more soaking time. The saturation induction (B_s) and remanence magnetization (B_r) as a function of soaking time are shown in Figure 4.14c,d, respectively. Both of them would increase with the increase in soaking time. Indeed, these extrinsic properties rely on the inter- and intra-granular porosity, grain size, and distribution. The enhancement in M_s and B_s suggests that an increase of ordered magnetic moment within the samples is subjected to the longer soaking time and external field.



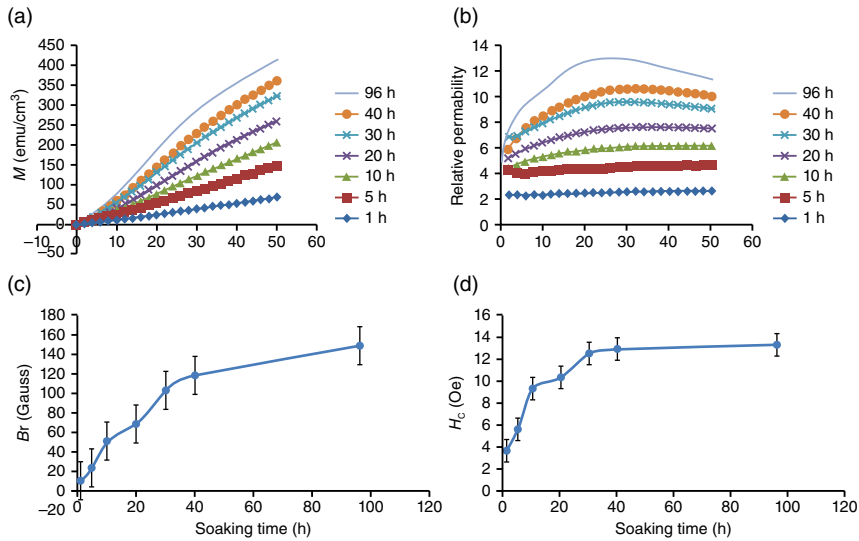


Figure 4.14 The 800 °C sintered Ni–Zn ferrite samples were subjected to different soaking times, (a) magnetization curve, (b) relative permeability (μ_r), (c) remanence magnetization (B_r), and (d) effect of soaking time on coercivity. Source: Ismail et al. [32]/with permission of Elsevier.

The phase composition study of the iron oxide samples, from ferrous carbonate, which was sintered at 500 °C for different soaking times of 0, 30, and 60 minutes indicated that the formation of alpha ferric oxide (“S-2, S-3, S-5, S-6, and S-9”) increases by increasing the soaking time. The formation of this phase results in the variation of magnetic properties, lowering both the saturation magnetization and coercivity values [85].

4.4 Heating Rate

The importance of synthesis methods with lower heating rate is that in these routes, the required time for high crystallization of sample is provided, which also increases the magnetic behavior and M_s . A detailed study on magnetic properties of CoFe_2O_4 nanoparticles showed an increment in M_s from 10 to 57 emu/g by reducing the heating rate from 20 to 5 °C/min [86].

Narasimhan et al. [85] investigated the effect of heating rate in the synthesis of gamma ferric oxide by thermal decomposition of ferrous carbonate. Their results revealed that short residence time and faster heating rate would form the desired oxides with outstanding magnetic behaviors, representing a saturation magnetization of 64 emu/g and coercivity of around 360 Oe. The effect of heating rate on phase formation based on the XRD pattern results is given in Table 4.5. It is worth mentioning that all the samples were heated at 500 °C.

The results indicate that a faster heating rate promotes the gamma ferric oxide formation (“S-4, S-7, and S-8”), while this phase accompanied by alpha ferric oxide



Table 4.5 The effect of heating rate and soaking time on the formation of gamma ferric oxide by thermal decomposition of ferrous carbonate [85].

Sample code	Heating rate (°C/min)	Soaking time (min)	Phase composition	Remarks
S-1	2	0	$\gamma\text{-Fe}_2\text{O}_3$ + $\alpha\text{-Fe}_2\text{O}_3$	Weak diffraction lines of $\alpha\text{-Fe}_2\text{O}_3$
S-2	2	30	$\gamma\text{-Fe}_2\text{O}_3$ + $\alpha\text{-Fe}_2\text{O}_3$	Slightly strong diffraction lines of $\alpha\text{-Fe}_2\text{O}_3$
S-3	2	60	$\gamma\text{-Fe}_2\text{O}_3$ + $\alpha\text{-Fe}_2\text{O}_3$	Stronger diffraction lines of $\alpha\text{-Fe}_2\text{O}_3$
S-4	5	0	$\gamma\text{-Fe}_2\text{O}_3$	Sharp diffraction lines of $\gamma\text{-Fe}_2\text{O}_3$
S-5	5	30	$\gamma\text{-Fe}_2\text{O}_3$ + $\alpha\text{-Fe}_2\text{O}_3$	Weak diffraction lines of $\alpha\text{-Fe}_2\text{O}_3$
S-6	5	60	$\gamma\text{-Fe}_2\text{O}_3$ + $\alpha\text{-Fe}_2\text{O}_3$	Slightly strong diffraction lines of $\alpha\text{-Fe}_2\text{O}_3$
S-7	10	0	$\gamma\text{-Fe}_2\text{O}_3$	Distinct diffraction lines of $\gamma\text{-Fe}_2\text{O}_3$
S'-7	10	0	Fe_3O_4	Distinct diffraction lines of Fe_3O_4
S-8	10	30	$\gamma\text{-Fe}_2\text{O}_3$	Distinct diffraction lines of $\gamma\text{-Fe}_2\text{O}_3$
S-9	10	60	$\gamma\text{-Fe}_2\text{O}_3$ + $\alpha\text{-Fe}_2\text{O}_3$	Weak diffraction lines of $\alpha\text{-Fe}_2\text{O}_3$
S-10	10	0	$\alpha\text{-Fe}_2\text{O}_3$	Distinct diffraction lines of $\alpha\text{-Fe}_2\text{O}_3$

Source: Narasimhan et al. [85]/with permission of Elsevier.

(S-1) is formed at a slow heating rate. Thus, to produce a pure single phase with great magnetic properties, rapid heating of ferrous carbonate is required. Such heating condition has also been adopted to form gamma ferric oxide from ferrous oxalate dihydrate decomposition at 300 °C in 15–20 minutes [87]. Studying the effect of heating rate on magnetic properties of the samples revealed that iron oxide samples, “S-4, S-7, and S-8” would represent the saturation magnetization values of 56.5, 64.0, and 58.5 emu/g and coercivity values of 324, 363, and 323 Oe, respectively, when compared with samples “S-1, S-2, S-3, S-5, S-6, and S-9.”

4.5 Trends of Sintering: Single-Sample and Multi-Sample Sintering

Two different sintering methods are used in preparing magnetic materials, which are named as a single-sample sintering scheme and a multi-sample sintering scheme [88, 89]. Generally, a multi-sample sintering scheme is a more common method employed for synthesizing polycrystalline materials [90, 91].



In both states, the as-prepared initial powder is compacted and subjected to sintering at desired temperatures. With a difference that in a multi-sample sintering scheme, one sample is made for each sintering temperature, but in an adopted single-sample sintering scheme, one sample is subjected to sintering at all temperatures. This will obviously result in the obtainment of various morphological features, which alters the magnetic properties as well. In other words, the single-sample sintering scheme has only one single compact with a definite starting point and one particular particle size distribution where only one sample is sintered at different temperatures. These characteristics make this scheme economically reasonable when compared to raw materials and the synthesis process. Therefore, the obtained data could be more useful in the scientific interpretation of the evolution study. Ibrahim et al. [88] in the parallel evolution of the magnetic-microstructure relationship in $\text{Ni}_{0.3}\text{Zn}_{0.7}\text{Fe}_2\text{O}_4$ samples considered two trends of multi-sample and single-sample sintering from 600 to 1400 °C. Their comparison results for both samples are given in Table 4.6.

The results reveal that the single-sample sintering had better microstructure features such as higher density and lower porosity as compared to the multi-sample sintering. It suggests that this sample would have a better magnetic behavior compared to another trend. Based on the H_c versus grain size diagram, for both the trends, the critical grain size was found to be between 0.20 and 0.25 μm for multi-sample sintering and in the range of 0.20–0.25 μm for single-sample sintering. This simply means that by elevating the sintering temperature, the grain growth occurs so that for the case of multi-sample sintering, all the grains are located in a multidomain area after

Table 4.6 Structural parameters of single-sample ferrite and multi-sample as a function of sintering temperature [88].

T (°C)	a		ρ_{xrd}		ρ_{exp}		P	
	S	M	S	M	S	M	S	M
600	8.3800 (2)	8.3700 (5)	5.40	5.42	4.23	3.48	21.6	35.8
700	8.4290 (1)	8.4330 (1)	5.30	5.30	4.49	3.62	15.4	31.7
800	8.4186 (4)	8.4277 (5)	5.32	5.31	4.62	3.70	13.2	30.3
900	8.4156 (3)	8.4167 (3)	5.33	5.33	4.73	3.98	11.3	25.3
1000	8.4150 (3)	8.4149 (5)	5.33	5.33	4.78	4.02	10.3	24.6
1100	8.4100 (3)	8.4161 (5)	5.34	5.33	4.81	4.20	9.9	21.2
1200	8.4098 (3)	8.4144 (2)	5.34	5.33	4.91	4.64	8.1	13.0
1300	8.3990 (3)	8.4138 (5)	5.36	5.33	4.93	4.73	8.0	11.3
1400	8.3961 (4)	8.4120 (1)	5.37	5.34	4.88	4.56	9.1	14.6

M, multi-sample; S, single-sample; a , lattice parameters (Å); ρ_{xrd} , theoretical density (X-ray density) (g/cm^3); ρ_{exp} , experimental density ($\pm 2\%$ g/cm^3); porosity (%) (P), $[1 - (\rho_{\text{exp}}/\rho_{\text{xrd}})] \times 100\%$.

Source: Ibrahim et al. [88]/with permission of Elsevier.



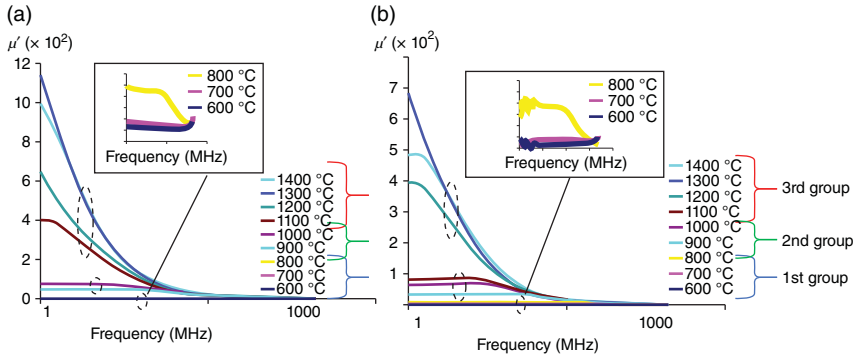


Figure 4.15 Frequency dependence of real permeability for Ni–Zn ferrite, (a) multi-sample sintering, and (b) single-sample sintering. Source: Ibrahim et al. [88]/with permission of Elsevier.

sintering at 1100 °C, but the single-sample sintering happens at a temperature above 1200 °C.

The frequency dependence of μ' in the range of 1–1.8 GHz for both sintering routes is given in Figure 4.15. In general, two different mechanisms affect the real part of permeability: (i) domain wall motion and (ii) magnetic moments rotation [92]. Typically, at higher frequencies, domain walls are damped, and moment rotation happens. Based on Snoek's law, the resonance frequency (f_R) is related to initial permeability (μ_i) as follows [22]:

$$f_R = (1/\mu_i) \times 10^9 \text{ Hz} \quad (4.9)$$

This designates that the lower the initial permeability values, the higher the frequency will be with the occurrence of the resonance phenomenon. It was found that at lower sintering temperatures of 600 and 700 °C, the value of the real part of permeability is independent of frequency in the measured frequency region for both the sintering scheme. The resonance frequency is observed in samples exiting a single Ni–Zn ferrite phase and sintered at temperatures of 800–1000 °C. In both cases, samples sintered at above 1100 °C show coarsened grains in the microstructure, which would result in a lower frequency ferromagnetic resonance; thus, f_R is higher than the utilized frequency region in Figure 4.15.

4.6 Conclusion and Perspective Outlook

Sintering or heating of magnetic materials dates to a long time ago to produce the desired material and improve its microstructure for various applications. But, most of the last decades' research mostly focused on the final outputs; by sintering at high temperatures and by neglecting the parallel evolution of microstructure and property relationship at various intermediate sintering conditions, i.e. temperature, time, and rate. Consequently, systematic studies on microstructure-magnetic evolution in the nanometer grain size regime are absent. This suggests that much possible



essential information has been neglected, which diminishes the capabilities of producing fundamental scientific knowledge that lies behind the parallel evolution of the microstructure-magnetic relationship. This is evident not only in magnetic properties but also in the parallel evolution in microstructure and other properties such as mechanical, physical, and electrical. The information obtained from this chapter could be considered as a reference to guide the researcher in the development of the new general theoretical model for in-depth understanding of the microstructure-property relationship in future research.

References

- 1 Goldman, A. (2006). *Modern Ferrite Technology*. Springer Science & Business Media.
- 2 Bali Ogholbeyg, A., Kianvash, A., Hajalilou, A. et al. (2018). Cytotoxicity characteristics of green assisted-synthesized superparamagnetic maghemite ($\gamma\text{-Fe}_2\text{O}_3$) nanoparticles. *Journal of Materials Science: Materials in Electronics* 29: 12135–12143.
- 3 Hajalilou, A., Mazlan, S.A., Shilan, S.T., and Abouzari-Lotf, E. (2017). Enhanced magnetorheology of soft magnetic carbonyl iron suspension with binary mixture of Ni–Zn ferrite and Fe_3O_4 nanoparticle additive. *Colloid and Polymer Science* 295: 1499–1510.
- 4 Kanagesan, S., Hashim, M., Tamilselvan, S. et al. (2013). Synthesis, characterization, and cytotoxicity of iron oxide nanoparticles. *Advances in Materials Science and Engineering* 2013: 710432. <https://doi.org/10.1155/2013/710432>.
- 5 Hajalilou, A., Abouzari-Lotf, E., Abbasi-Chianeh, V. et al. (2018). Inclusion of octahedron-shaped ZnFe_2O_4 nanoparticles in combination with carbon dots into carbonyl iron based magnetorheological suspension as additive. *Journal of Alloys and Compounds* 737: 536–548.
- 6 Hajalilou, A., Hashim, M., Ebrahimi-Kahrizsangi, R., and Sarami, N. (2014). Synthesis and structural characterization of nano-sized nickel ferrite obtained by mechanochemical process. *Ceramics International* 40: 5881–5887.
- 7 Hajalilou, A., Hashim, M., and Masoudi, M.T. (2015). A comparative study of in-situ mechanochemically synthesized $\text{Mn}_{0.5}\text{Zn}_{0.5}\text{Fe}_2\text{O}_4$ ferrite nanoparticles in the $\text{MnO}/\text{ZnO}/\text{Fe}_2\text{O}_3$ and $\text{MnO}_2/\text{Zn}/\text{Fe}_2\text{O}_3$ systems. *Ceramics International* 41: 8070–8079.
- 8 Rezaie, E., Rezanezhad, A., Ghadimi, L.S. et al. (2018). Effect of calcination on structural and supercapacitance properties of hydrothermally synthesized plate-like $\text{SrFe}_{12}\text{O}_{19}$ hexaferrite nanoparticles. *Ceramics International* 44: 20285–20290.
- 9 Hajalilou, A., Mazlan, S.A., Abbasi, M., and Lavvafi, H. (2016). Fabrication of spherical CoFe_2O_4 nanoparticles via sol–gel and hydrothermal methods and investigation of their magnetorheological characteristics. *RSC Advances* 6: 89510–89522.



- 10 Aslibeiki, B., Varvaro, G., Peddis, D., and Kameli, P. (2017). Particle size, spin wave and surface effects on magnetic properties of MgFe_2O_4 nanoparticles. *Journal of Magnetism and Magnetic Materials* 422: 7–12.
- 11 Shafie, M., Hashim, M., Ismail, I. et al. (2014). Magnetic M–H loops family characteristics in the microstructure evolution of $\text{BaFe}_{12}\text{O}_{19}$. *Journal of Materials Science: Materials in Electronics* 25: 3787–3794.
- 12 Jalili, H., Aslibeiki, B., Hajalilou, A. et al. (2022). Bimagnetic hard/soft and soft/hard ferrite nanocomposites: structural, magnetic and hyperthermia properties. *Ceramics International* 48: 4886–4896.
- 13 Hajalilou, A., Ferreira, L.P., Jorge, M.E.M. et al. (2021). Superparamagnetic $\text{Ag-Fe}_3\text{O}_4$ composites nanoparticles for magnetic fluid hyperthermia. *Journal of Magnetism and Magnetic Materials* 537: 168242. <https://doi.org/10.1016/j.jmmm.2021.168242>.
- 14 Rezanezhad, A., Hajalilou, A., Eslami, F. et al. (2021). Superparamagnetic magnetite nanoparticles for cancer cells treatment via magnetic hyperthermia: effect of natural capping agent, particle size and concentration. *Journal of Materials Science: Materials in Electronics* 32: 24026–24040.
- 15 Hajalilou, A., Silva, A.F., Lopes, P.A. et al. (2022). Biphasic liquid metal composites for sinter-free printed stretchable electronics. *Advanced Materials Interfaces* 9: 2101913.
- 16 Hajalilou, A., Kianvash, A., Lavvafi, H., and Shameli, K. (2018). Nanostructured soft magnetic materials synthesized via mechanical alloying: a review. *Journal of Materials Science: Materials in Electronics* 29: 1690–1717.
- 17 Hajalilou, A., Kamari, H.M., and Shameli, K. (2017). Dielectric and electrical characteristics of mechanically synthesized Ni–Zn ferrite nanoparticles. *Journal of Alloys and Compounds* 708: 813–826.
- 18 Hajalilou, A., Hashim, M., Ebrahimi-Kahrizsangi, R., and Kamari, H.M. (2015). Influence of evolving microstructure on electrical and magnetic characteristics in mechanically synthesized polycrystalline Ni-ferrite nanoparticles. *Journal of Alloys and Compounds* 633: 306–316.
- 19 Stucky, G.D. and Mac Dougall, J.E. (1990). Quantum confinement and host/guest chemistry: probing a new dimension. *Science* 247: 669–678.
- 20 Myndyk, M. (2010). Nanocrystalline oxides prepared by mechanochemical reactions. Dissertation. Technische Universität Braunschweig, Braunschweig.
- 21 Hajalilou, A., Hashim, M., Kamari, H.M., and Masoudi, M.T. (2015). Effects of milling atmosphere and increasing sintering temperature on the magnetic properties of nanocrystalline $\text{Ni}_{0.36}\text{Zn}_{0.64}\text{Fe}_2\text{O}_4$. *Journal of Nanomaterials* 2015: 615739.
- 22 Hajalilou, A., Hashim, M., Ebrahimi-Kahrizsangi, R., and Sarami, N. (2015). Influence of CaO and SiO_2 co-doping on the magnetic, electrical properties and microstructure of a Ni–Zn ferrite. *Journal of Physics D: Applied Physics* 48: 145001.
- 23 Hajalilou, A. and Mazlan, S.A. (2016). A review on preparation techniques for synthesis of nanocrystalline soft magnetic ferrites and investigation on the effects of microstructure features on magnetic properties. *Applied Physics A* 122: 1–15.



- 24 Goldman, A. (1999). *Handbook of Modern Ferromagnetic Materials*. Boston: Kluwer Academic Publishers.
- 25 Igarashi, H. and Okazaki, K. (1977). Effects of porosity and grain size on the magnetic properties of NiZn ferrite. *Journal of the American Ceramic Society* 60: 51–54.
- 26 Mangalaraja, R.V., Ananthakumar, S., Manohar, P., and Gnanam, F.D. (2003). Magnetic hysteresis studies of $\text{Ni}_{1-x}\text{Zn}_x\text{Fe}_2\text{O}_4$ prepared by non-conventional techniques. *Materials Letters* 57: 2666–2669.
- 27 De Lacheisserie, E.d.T., Gignoux, D., and Schlenker, M. (2005). *Magnetism*. Springer Science & Business Media.
- 28 Jiles, D.C. and Atherton, D.L. (1986). Theory of ferromagnetic hysteresis. *Journal of Magnetism and Magnetic Materials* 61: 48–60.
- 29 Bean, C. (1955). Hysteresis loops of mixtures of ferromagnetic micropowders. *Journal of Applied Physics* 26: 1381–1383.
- 30 Mirzazadeh, A., Kianvash, A., and Hajalilou, A. (2018). Plating of Cu and Ni metals on Mg-ferrite sintered bodies by an electroless method and an investigation of magnetic behavior. *Journal of Materials Science: Materials in Electronics* 29: 5753–5760.
- 31 Namvari, M., Kianvash, A., and Hajalilou, A. (2018). Influence of Ca–La and Cr-addition on the structure and magnetic characteristics of nanocrystalline Sr-hexaferrite powder. *Journal of Materials Science: Materials in Electronics* 29: 1435–1443.
- 32 Ismail, I., Hashim, M., Amin Matori, K. et al. (2012). Dependence of magnetic properties and microstructure of mechanically alloyed $\text{Ni}_{0.5}\text{Zn}_{0.5}\text{Fe}_2\text{O}_4$ on soaking time. *Journal of Magnetism and Magnetic Materials* 324: 2463–2470.
- 33 Nazlan, R., Hashim, M., Ibrahim, I.R. et al. (2016). Influence of microstructural evolution on the magnetically group dominance in polycrystalline $\text{Y}_3\text{Fe}_5\text{O}_{12}$ multi-samples. In: *Materials Science Forum*, 366–374. Trans Tech Publications.
- 34 Nazlan, R., Ismail, I., Abbas, Z. et al. (2018). Dependence of magnetic and microwave loss on evolving microstructure in yttrium iron garnet. *Journal of Materials Science: Materials in Electronics* 29: 8688–8700.
- 35 Lakshmanan, A. (2012). *Sintering of Ceramics: New Emerging Techniques*. BoD – Books on Demand.
- 36 German, R.M. (1996). *Sintering Theory and Practice*, 568. Wiley.
- 37 De Jonghe, L.C. and Rahaman, M.N. (2003). 4.1 Sintering of ceramics, Chapter 4. In: *Handbook of Advanced Ceramics* (ed. S. Sōmiya, F. Aldinger, N. Claussen, et al.), 187–264. Oxford: Academic Press.
- 38 Rahaman, M.N. (2003). *Ceramic Processing and Sintering*. CRC Press.
- 39 Hajalilou, A., Hashim, M., and Kamari, H.M. (2015). Structure and magnetic properties of $\text{Ni}_{0.64}\text{Zn}_{0.36}\text{Fe}_2\text{O}_4$ nanoparticles synthesized by high-energy milling and subsequent heat treatment. *Journal of Materials Science: Materials in Electronics* 26: 1709–1718.
- 40 Jalaly, M., Enayati, M.H., Karimzadeh, F., and Kameli, P. (2009). Mechano-synthesis of nanostructured magnetic Ni–Zn ferrite. *Powder Technology* 193: 150–153.



- 41 De Jonghe, L.C. and Rahaman, M.N. (2003). 4.1 Sintering of ceramics. In: *Handbook of Advanced Ceramics: Materials, Applications, Processing and Properties*, vol. 2 (ed. S. Somiya, F. Aldinger, R.M. Spriggs, et al.), 187.
- 42 Mallow, T. and Koch, C. (1996). *Synthesis and Processing of Nanocrystalline Materials*, 33. Warrandale, PA: TMS.
- 43 Gleiter, H. (2000). Nanostructured materials: basic concepts and microstructure. *Acta Materialia* 48: 1–29.
- 44 Boylan, K., Ostrander, D., Erb, U. et al. (1991). An in-situ tem study of the thermal stability of nanocrystalline Ni–P. *Scripta Metallurgica et Materialia* 25: 2711–2716.
- 45 Seah, M. and Hondros, E. (1973). Grain boundary segregation. *Proceedings of the Royal Society of London. A. Mathematical and Physical Sciences* 335: 191–212.
- 46 Michels, A., Krill, C., Ehrhardt, H. et al. (1999). Modelling the influence of grain-size-dependent solute drag on the kinetics of grain growth in nanocrystalline materials. *Acta Materialia* 47: 2143–2152.
- 47 Goldman, A. (2012). *Handbook of Modern Ferromagnetic Materials*. Springer Science & Business Media.
- 48 Coble, R.L. (1961). Sintering crystalline solids. I. Intermediate and final state diffusion models. *Journal of Applied Physics* 32: 787–792.
- 49 Syazwan, M.M., Hapishah, A.N., Azis, R.S. et al. (2018). Grain growth effects on magnetic properties of $\text{Ni}_{0.6}\text{Zn}_{0.4}\text{Fe}_2\text{O}_4$ material prepared using mechanically alloyed nanoparticles. *Results in Physics* 9: 842–850.
- 50 Rao, B.P., Rao, P.S., and Rao, K. (1997). Densification, grain growth and microstructure of Ni–Zn ferrites. *Le Journal de Physique IV* 7: C1–241–C1–242.
- 51 Phuoc, T.X. and Chen, R.-H. (2012). Modeling the effect of particle size on the activation energy and ignition temperature of metallic nanoparticles. *Combustion and Flame* 159: 416–419.
- 52 Joseyphus, R., Narayanasamy, A., Nigam, A., and Krishnan, R. (2006). Effect of mechanical milling on the magnetic properties of garnets. *Journal of Magnetism and Magnetic Materials* 296: 57–64.
- 53 Zaspalis, V., Sklari, S., and Kolenbrander, M. (2007). The effect of heating rate on the microstructure and properties of high magnetic permeability MnZn-ferrites. *Journal of Magnetism and Magnetic Materials* 310: 28–36.
- 54 Yu, R., Basu, S., Zhang, Y. et al. (1999). Pinning effect of the grain boundaries on magnetic domain wall in FeCo-based magnetic alloys. *Journal of Applied Physics* 85: 6655–6659.
- 55 Abdollah, H., Mansor, H., Reza, E.-K., and Taghi, M.M. (2015). Effect of milling atmosphere on structural and magnetic properties of Ni–Zn ferrite nanocrystalline. *Chinese Physics B* 24: 048102.
- 56 Rodziah, N., Hashim, M., Idza, I.R. et al. (2012). Dependence of developing magnetic hysteresis characteristics on stages of evolving microstructure in polycrystalline yttrium iron garnet. *Applied Surface Science* 258: 2679–2685.
- 57 Azis, R., Syazwan, M., Shahrani, N. et al. (2018). Influence of sintering temperature on the structural, electrical and microwave properties of yttrium iron garnet (YIG). *Journal of Materials Science: Materials in Electronics* 29: 8390–8401.



- 58 Kim, J.-S. and Ham, C.-W. (2009). The effect of calcining temperature on the magnetic properties of the ultra-fine NiCuZn-ferrites. *Materials Research Bulletin* 44: 633–637.
- 59 Hajalilou, A., Hashim, M., and Mohamed Kamari, H. (2014). Effects of additives and sintering time on the microstructure of Ni–Zn ferrite and its electrical and magnetic properties. *Advances in Materials Science and Engineering* 2014: 138789.
- 60 Huang, L.Z., Hashim, M., Ismail, I. et al. (2015). Development of magnetic B–H hysteresis loops through stages of microstructure evolution of bulk BaFe₁₂O₁₉. *Journal of Superconductivity and Novel Magnetism* 28: 3075–3086.
- 61 Hajalilou, A., Mazlan, S.A., Lavvafi, H., and Shameli, K. (2016). *Field Responsive Fluids as Smart Materials*. Springer.
- 62 Faried, M., Shameli, K., Miyake, M. et al. (2016). Synthesis of silver nanoparticles via green method using ultrasound irradiation in seaweed *Kappaphycus alvarezii* media. *Research on Chemical Intermediates* 42: 7991–8004.
- 63 Kingery, W.D., Bowen, H.K., and Uhlmann, D.R. (1976). *Introduction to Ceramics*. Wiley.
- 64 Adli, R.G., Kianvash, A., Hosseini, M.G. et al. (2018). Mechanochemically synthesized NiCo₂O₄/Vulcan/PANI nanocomposite and investigation of its electrochemical behavior as a supercapacitor. *Ceramics International* 44: 20049–20057.
- 65 Hajalilou, A., Hashim, M., Abbasi, M. et al. (2015). A comparative study on the effects of different milling atmospheres and sintering temperatures on the synthesis and magnetic behavior of spinel single phase Ni_{0.64}Zn_{0.36}Fe₂O₄ nanocrystals. *Journal of Materials Science: Materials in Electronics* 26: 7468–7483.
- 66 Snelling, E.C. and Giles, A.D. (1983). *Ferrites for Inductors and Transformers*. Letchworth, Hertfordshire/New York: Research Studies Press, Wiley.
- 67 Šepelák, V., Baabe, D., Mienert, D. et al. (2003). Evolution of structure and magnetic properties with annealing temperature in nanoscale high-energy-milled nickel ferrite. *Journal of Magnetism and Magnetic Materials* 257: 377–386.
- 68 Kodama, R.H. and Berkowitz, A.E. (1999). Atomic-scale magnetic modeling of oxide nanoparticles. *Physical Review B* 59: 6321.
- 69 Reddy, M.P., Shakoor, R., Mohamed, A. et al. (2016). Effect of sintering temperature on the structural and magnetic properties of MgFe₂O₄ ceramics prepared by spark plasma sintering. *Ceramics International* 42: 4221–4227.
- 70 Thakur, P., Sharma, R., Sharma, V., and Sharma, P. (2017). Structural and optical properties of Mn_{0.5}Zn_{0.5}Fe₂O₄ nano ferrites: effect of sintering temperature. *Materials Chemistry and Physics* 193: 285–289.
- 71 Hcini, S., Kouki, N., Omri, A. et al. (2018). Effect of sintering temperature on structural, magnetic, magnetocaloric and critical behaviors of Ni–Cd–Zn ferrites prepared using sol–gel method. *Journal of Magnetism and Magnetic Materials* 464: 91–102.
- 72 Praveena, K., Sadhana, K., Matteppanavar, S., and Liu, H.-L. (2017). Effect of sintering temperature on the structural, dielectric and magnetic properties of Ni_{0.4}Zn_{0.2}Mn_{0.4}Fe₂O₄ potential for radar absorbing. *Journal of Magnetism and Magnetic Materials* 423: 343–352.



- 73 Buesser, B., Grohn, A., and Pratsinis, S.E. (2011). Sintering rate and mechanism of TiO_2 nanoparticles by molecular dynamics. *The Journal of Physical Chemistry C* 115: 11030–11035.
- 74 Koch, W. and Friedlander, S. (1990). The effect of particle coalescence on the surface area of a coagulating aerosol. *Journal of Colloid and Interface Science* 140: 419–427.
- 75 Arcidiacono, S., Bieri, N., Poulikakos, D., and Grigoropoulos, C. (2004). On the coalescence of gold nanoparticles. *International Journal of Multiphase Flow* 30: 979–994.
- 76 Iijima, S. and Ajayan, P. (1991). Substrate and size effects on the coalescence of small particles. *Journal of Applied Physics* 70: 5138–5140.
- 77 Barnard, A. (2010). Modelling of nanoparticles: approaches to morphology and evolution. *Reports on Progress in Physics* 73: 086502.
- 78 Collins, D., Harrison, N., and Forester, T. (1997). Molecular dynamics study of the high temperature fusion of TiO_2 nanoclusters. *Journal of Materials Chemistry* 7: 2543–2546.
- 79 Tashtoush, N., Hemeda, O., and Tawfik, A. (2003). Effect of the soaking time on the diffusion and resonant frequency of CoZn ferrite transducer. *Journal of Magnetism and Magnetic Materials* 256: 168–173.
- 80 Hemeda, O. and El-Ati, M.A. (2001). Spectral studies of $\text{Co}_{0.6}\text{Zn}_{0.4}\text{Fe}_2\text{O}_4$ at different soaking times. *Materials Letters* 51: 42–47.
- 81 Ahmed, M. (1989). Electrical properties of Co–Zn ferrites. *Physica Status Solidi (a)* 111: 567–572.
- 82 Tawfik, A. (1989). Effect of magnetic order on the conductivity in Co–Zn ferrites. *Journal of Thermal Analysis and Calorimetry* 35: 141–145.
- 83 El-Ati, M.A. (1994). Dependence of electrical conductivity and tawfik coefficient on the soaking time of $\text{Co}_{0.6}\text{Zn}_{0.4}\text{Fe}_2\text{O}_4$ ferrite. *Phase Transitions: A Multinational Journal* 50: 193–198.
- 84 Sameshima, S., Higashi, K., and Hirata, Y. (2000). Sintering and grain growth of rare earth-doped Ceria particles. In: *Proceedings of the Korea Association of Crystal Growth Conference*, 65–86. The Korea Association of Crystal Growth.
- 85 Narasimhan, B., Prabhakar, S., Manohar, P., and Gnanam, F. (2002). Synthesis of gamma ferric oxide by direct thermal decomposition of ferrous carbonate. *Materials Letters* 52: 295–300.
- 86 Sangmanee, M. and Maensiri, S. (2009). Nanostructures and magnetic properties of cobalt ferrite (CoFe_2O_4) fabricated by electrospinning. *Applied Physics A* 97: 167–177.
- 87 Rao, V., Shashimohan, A., and Biswas, A. (1974). Studies on the formation of $\gamma\text{-Fe}_2\text{O}_3$ (maghemite) by thermal decomposition of ferrous oxalate dihydrate. *Journal of Materials Science* 9: 430–433.
- 88 Ibrahim, I.R., Hashim, M., Nazlan, R. et al. (2014). Grouping trends of magnetic permeability components in their parallel evolution with microstructure in $\text{Ni}_{0.3}\text{Zn}_{0.7}\text{Fe}_2\text{O}_4$. *Journal of Magnetism and Magnetic Materials* 355: 265–275.
- 89 Ibrahim, I.R., Hashim, M., Nazlan, R. et al. (2015). A comparative study of different sintering routes effects on evolving microstructure and B–H magnetic



- hysteresis in mechanically-alloyed Ni–Zn ferrite, $\text{Ni}_{0.3}\text{Zn}_{0.7}\text{Fe}_2\text{O}_4$. *Journal of Materials Science: Materials in Electronics* 26: 59–65.
- 90 Shirsath, S.E., Kadam, R., Gaikwad, A.S. et al. (2011). Effect of sintering temperature and the particle size on the structural and magnetic properties of nanocrystalline $\text{Li}_{0.5}\text{Fe}_{2.5}\text{O}_4$. *Journal of Magnetism and Magnetic Materials* 323: 3104–3108.
- 91 Huang, C.-C., Hung, Y.-H., Huang, J.-Y., and Kuo, M.-F. (2014). Impact of stoichiometry and sintering temperature on magnetic properties of $\text{Y}_3\text{Mn}_x\text{Al}_{0.83-x}\text{Fe}_{4.17}\text{O}_{12}$ ferrites. *IEEE Transactions on Magnetics* 50: 1–4.
- 92 Nakamura, T. (1997). Low-temperature sintering of NiZnCu ferrite and its permeability spectra. *Journal of Magnetism and Magnetic Materials* 168: 285–291.
- 93 Coblenz, W.S., Dynys, J.M., Cannon, R.M., and Coble, R.L. (1980). Initial stage solid state sintering models. A critical analysis and assessment. *Sintering Processes. Materials Science Research* 13: 141–157.
- 94 Kruis, F.E., Kusters, K.A., Pratsinis, S.E., and Scarlett, B. (1993). A simple model for the evolution of the characteristics of aggregate particles undergoing coagulation and sintering. *Aerosol science and technology* 19 (4): 514–526.



5

Surface Modification of Magnetic Nanoparticles

5.1 Introduction

Surface modification is the act of modifying the surface of particles by physical, chemical, or biological characteristics different from the ones originally found on the surface of the particles. The main aims of surface modification include:

- Enhancing anticorrosive properties.
- Improving the electrical conductivities and optical properties.
- Increasing bioactivities.
- Improving adhesion properties.
- Improving component lifetime and resistance to aggressive environments.
- Producing biocompatibility.
- Creating permanent wettability.
- Producing hydrophobic characteristics.

Some benefits of surface medication are given in Figure 5.1a; how and by which properties one can analyze surface modification are represented in (Figure 5.1b).

5.2 Employed Technical Resources for Surface Modification

However, there are several technical resources for surface modification, some of the widely used resources are (i) plasma treatment, (ii) corona discharge, (iii) parylene coating, and (iv) photolysis.

5.2.1 Plasma Treatment

Plasma is a reactive treatment process in which positive and negative ions, electrons, and radicals react and collide as long as an electric potential difference exists. Plasma surface treatment is extremely versatile and is used in a range of industries. It can enhance biocompatibility, prevent moisture absorption through hydrophobic treatments, and improve functionalization and adhesion – all from a value-driven, green alternative to harsh chemical techniques. It even extends the treatment lifetime from

Magnetic Nanoparticles: Synthesis, Characterization, and Applications, First Edition.

Abdollah Hajalilou, Mahmoud Tavakoli, and Elahe Parvini.

© 2023 WILEY-VCH GmbH. Published 2023 by WILEY-VCH GmbH.



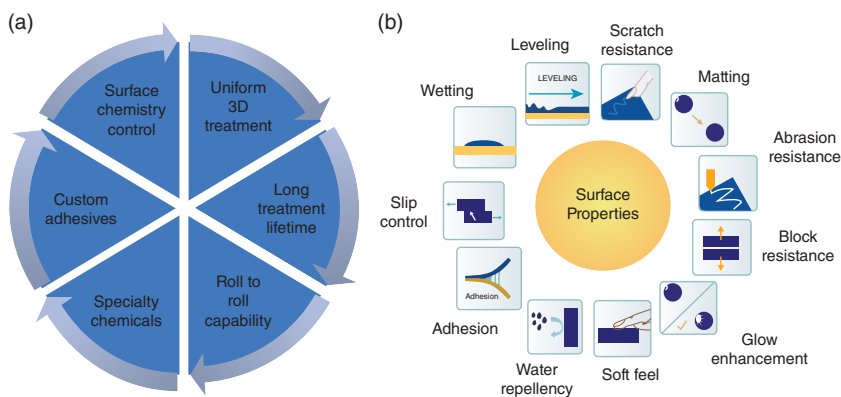


Figure 5.1 (a) Benefits of surface modification, and (b) How and by which properties one can analyze surface modification.

days to years. Its advantages include, but are not limited to surface chemistry, which is highly selective and has the unique ability to treat a three-dimensional (3D) material and control the treatment conditions by controlling gas flow, pressure, and concentration. On the other hand, high plasma system prices and low rate of production (large chamber size and high power) limit its application.

5.2.2 Corona Discharge

Corona discharge is plasma at standard atmospheric pressure. This plasma is produced by high voltage and the proximity of two metal plates (electrodes) in the atmosphere (Figure 5.2).

It modifies the properties of a surface to provide a longer lifespan, improve surface bonding, and improve corrosion resistance. The cons and pores of the process include:

(i) Advantages:

- Ease of use.
- Systems are robust and easy to maintain.
- Price of purchasing a system for in-house treatment.

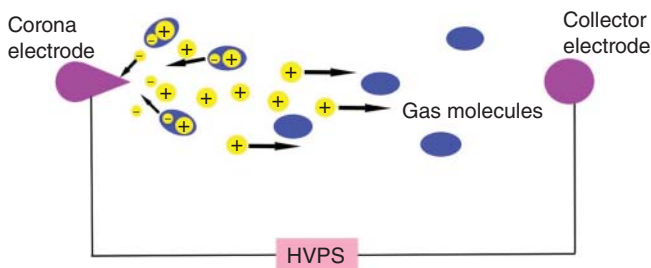


Figure 5.2 Schematic representation of corona discharge. HVPS, high-voltage power supply.



(ii) Disadvantages:

- Most corona systems are designed to operate in open-air conditions.
- Lack of surface chemistry selectivity.
- Limited polymer choice.
- Treatment is two-dimensional.

5.2.3 Parylene Coating

It is a conformal surface coating that protects sensitive devices by providing a barrier layer against environmental contaminants. It remarkably improves the performance and durability of manufacturing components by extending the lifetime coating to a decade or even longer. Parylene coating improves device longevity because it:

- Offers excellent thermal stability in high temperatures.
- Improves lubricity through low friction.
- Provides a barrier against leaching or blooming.
- Strengthens molded plastic magnetic components.
- Reduces surface tack and stickiness.
- Resists flaking, abrasion chemicals, solvents, and moisture.
- Remains chemically and biologically inert.

5.2.4 Photolysis

It combines principles of corona and plasma. Such systems use high voltage to excite the gas in an emitter, which then radiates to the surface of a polymer. Radiation is then fine-tuned to chemically modify a polymer to receive most adhesives, paints, coatings, and inks. Its benefits include:

- Moderate costs related to the size of the system.
- Systems can be easily designed to fit on nearly any conveyor system.
- Electrically or charge-sensitive devices are easily and safely treated.
- High throughput treatment of stable polymers and elastomers.
- Efficient and effective due to the specific wavelength emitted by the radiation source.
- Offers very selective surface chemistry.
- Line-of-sight (or two-dimensional) design.

It should be noted that the standard atmospheric condition is required for photolysis.

5.2.5 Other Methods and Examples

There are many methods to modify the surface of magnetic nanoparticles. One of them is a non-seeded method, where an external force such as stirring, mixing, or ultrasonic wave is employed to modify the surface of particles. By stirring the particles in the coating solution, the speed of stirring provides high force and energy that allows inelastic collision between the surface of magnetic nanoparticles and coating materials, causing attachment of the coating material to the surface of particles.



Baker and coworkers reported the synthesis of iron oxide nanoparticles (IONPs) via microemulsion, which was followed by surface modification (PC) [1]. The particle size distribution was found to be about 8–20 nm. The hydrophobic van der Waals interaction between the hydrophobic tail of PC and the hydrophobic surface of IONPs formed a thermodynamic bilayer structure surrounding each particle of IONPs. The presence of PC on the surface of IONPs would reduce the saturation magnetization (M_s) value due to the additional mass of non-magnetic PC in the samples. In other investigations, surface modification of IONPs was studied by modifying the nanoparticle surface with hexanoic acid and oleic acid using the co-precipitation method [2]. New bands detected in the Fourier transform infrared (FTIR) spectra are attributed to C–H and carboxyl group, suggesting the bonding of the coating agent on the surface of IONPs. No significant changes were obtained from the X-ray diffraction (XRD) patterns of IONPs modified with hexanoic acid and oleic acid as compared to the XRD patterns of IONPs without surface modification. The size of coated IONPs obtained from a scanning electron microscope (SEM) was larger than that of IONPs due to the coating on the surface of IONPs. The M_s value of IONPs was higher than that of IONPs modified with oleic acid because the non-magnetic layer of oleic acid reduced the magnetic interaction between the particles. In another study, the IONPs were modified with silica and 3-(4-methoxybenzylideneamino)-2-thioxothiazolidin-4-one by chemical precipitation [3]. The average spherical particle size of IONPs was found to be about 26 nm with some agglomerated state, which increased to 38 nm in the IONPs-Silica with a low agglomerated state. Inclusion of (4-methoxybenzylideneamino)-2-thioxothiazolidin-4-one onto the surface of iron oxide-silica nanoparticles, the agglomeration was found to be absent. FTIR results indicated bands of Fe–O at 625 and 575 cm^{-1} wavenumbers for the IONPs sample. The Fe–O–Si band could not be seen through the FTIR spectrum because the band that appeared at 580 cm^{-1} was overlapped with the Fe–O band. However, the vibration of Si–O–H and Si–O–Si bands were observed, confirming the presence of silica on the IONPs' surface. Also, vibration bands of C–H, C–N, and N–H were detected on the surface of the iron oxide-silica nanoparticles. Their corresponding transmission electron microscope (TEM) images are shown in Figure 5.3.

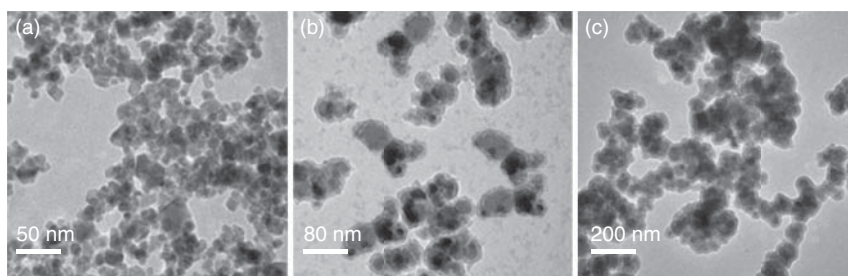


Figure 5.3 TEM images of (a) iron oxide nanoparticles coated with (b) Silica and (c) (4-methoxybenzylideneamino)-2 thioxothiazolidin-4-one. Source: [3], H. Bagheri et al. (2012), ELSEVIER.



Polyethylene glycol (PEG) and 3-amino propyltriethoxysilane (APTES) were also employed to modify the IONPs using the co-precipitation method [4]. The XRD patterns revealed the desired phase formation. The Si–O, N–H, and NH_2 vibration bands were detected which confirmed the presence of APTES in the IONPs. The band of $-\text{C}(\text{C}=\text{O})-\text{N}-\text{H}$ appeared at 1540 cm^{-1} , which confirmed the existence of PEG on the surface of the IONPs-APTES sample. The average particle size was found to be about 124 nm with a spherical shape [4]. APTES is an amino-silane linker frequently used in the surface modification of magnetic nanoparticles (MNPs) [5–7]. The formation of a monolayer of amino silane eases the linking of a specific drug through the tail side amino groups ($-\text{NH}_2$). These amino groups form the imine bond ($\text{C}=\text{N}$) between the carbonyl group of the drug and the amine group of MNS-APTES and assist the drug conjugation process [8].

In another study, surface modification of IONPs modified with cetyltrimethyl ammonium bromide (CTAB) suggested superparamagnetic behavior with a diameter of less than 5 nm [9]. Their corresponding XRD patterns indicated the cubic spinel structure of IONPs. The vibration of Fe–O appeared at bands 620, 588, and 412 cm^{-1} , and the observed bands at 2853 and 2923 cm^{-1} were attributed to the C–H band of CTAB. The presence of CTAB contributed to the well-monodispersed of IONPs-CTAB in a matrix with no agglomeration. In our studies [10, 11], superparamagnetic IONPs were modified with a sugar loaf (sugar cube). The prepared solution was subjected to vigorous stirring for 10 minutes, and then transferred to a sealed autoclave and kept at 180°C for 4 hours, which resulted in the formation of $\text{Fe}_3\text{O}_4@\text{C}$ nanoparticles. It was found that the coating process increased the magnetic properties of the sample [10]. This is why modification of Fe_3O_4 nanoparticles with SiO_2 reduces the magnetic properties from ($\sim 11.26\text{ emu/g}$) for $\text{Fe}_3\text{O}_4@\text{SiO}_2$ powder compared with Fe_3O_4 powder ($\sim 13.30\text{ emu/g}$) [11]. In another study, carbonyl iron (CI) particles were modified with Ag nanoparticles via the precipitation method, which results in reduction saturation magnetization as well [12]. In another study, plating of Cu and Ni metals on Mg-ferrite sintered bodies by an electroless method was considered and the magnetic behavior of the samples was examined [13]. The results indicated that the plating of Cu and Ni metals on the ferrite results in a negligible variation in M_s value as compared to Mg ferrite. On the other hand, the H_{cJ} was reduced from 12 to 8 Oe, which enables them to be promising candidates as inductors and transformer materials for high-frequency applications.

5.3 Surface Modification of Magnetic Nanoparticles with Surfactant

The term *surfactant* comes from the word *surface active agent*. They are amphiphilic molecules and are thus absorbed in the air-water interface. Surfactant tends to be attached to the surface of materials due to their amphiphilic nature (hydrophobic and hydrophilic) (Figure 5.4). Headgroup dissolves in polar solvents. Further, the tail, which is composed of a long hydrocarbon chain, dissolves in non-polar solvents.





Figure 5.4 Amphiphilic nature of surfactant.

The main advantages of surfactants are their tendency to adsorb at the surface and reduce the surface tension of particles. Surface tension is the free energy per unit area on the surfaces of particles. The surface tension reduces when the surface of the particles is covered by surfactant molecules. The denser the surfactant layer on the surface, the larger the surface tension will be reduced. Different types of surfactants are oleic acid [14–17], citric acid (CA) [18], and so on. Surfactants come in four different types: anionic, nonionic, cationic, and amphoteric. The attractive electrostatic and van der Waals interaction between IONPs and surfactants contributes to surface modification [19]. Role of surfactant becomes very important when the magnetic nanoparticles are coated with other materials such as SiO_2 , Al_2O_3 , Ag, Au, etc., for making stable suspension with the coated nanoparticles for different purposes. For example, for making stable suspension of superparamagnetic IONPs in water, CA was used as a surfactant [18]. By studying different factors such as the concentration of CA, pH value, and temperature on the stability of nanoparticles in the suspension, it was found that the highest stable IONPs in water-based fluid obtain once pH is about 5. In this state, two carboxyl groups are dissociated. Once the pH value is increased to about 10, all three carboxyl groups of the CA are in a dissociated state [20].

The selection of CTAB is due to its composition which consists of a positive charge of the hydrophilic head group with a long chain of the alkyl group (hydrophobic tail). In another study, Desai and Banat in 1997 [21] reported that CTAB contains cations that could reduce surface tension between liquid, solids, and gases. It is also associated with the substances in the solution. CTAB is a cationic surfactant that dissociated in water into amphiphilic cation and anion. There are electrostatic interactions between the substrate's surface and the cationic headgroups of the surfactant, coating the IONPs [22]. The characteristic of IONPs modified with CTAB is shown in Figure 5.5.

Surfaces grafted with biomolecules are also vital for life science and modern biotechnology. For instance, processes through surface-activated nanoparticles contain multi detection systems based on biosensors in array formats (biochips) [24–27], magnetic separation [28–30], and liquid chromatography [31]. These are all examples of technologies where the controlled and optimized attachment of biomolecules to solid surfaces plays a critical role in their ultimate utility. In this regard, Bruce and Sen modified the surface of magnetic nanoparticles with alkoxysilanes for bioseparations application [24]. They stated that careful manipulation of solvent conditions, such as time and temperature is important for optimal silanization of the nanoparticles. The efficiency of the oligonucleotide-modified particles in the capture experiments was found to be directly associated with the original density of amine groups present at the surface of the support. This suggests that surface engineering of the magnetic nanoparticles is possible by silanization



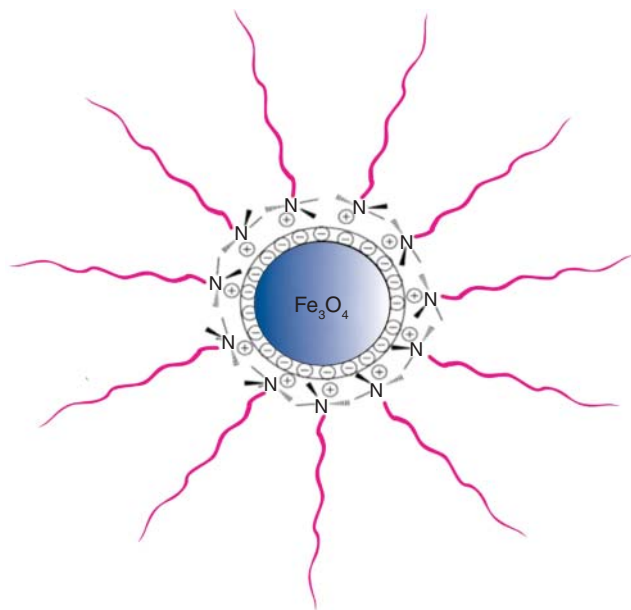


Figure 5.5 Schematic representation of iron oxide nanoparticles modified with CTAB.
Source: Kavkhani et al. [23]/with permission of Elsevier.

under-defined and optimized conditions. This approach could be developed for the activation of such surfaces and other materials with other functional groups.

5.4 Current Trends for Surface Modification of Nanomaterials

Functionalization is referred to as the process of attaching functional groups to the nanomaterials (such as fullerene, carbon nanodots, carbon nanotubes [CNTs], graphene, etc.) surface with molecular moieties possessing suitable properties that are essential for the realization of new molecular hybrid materials with novel/enhanced functions. Functionalization methods can either be non-covalent functionalization of nanomaterials which is typically based on physical adsorption of functional unites on nanomaterials via $\pi-\pi$ stacking, hydrophobic interaction, or electrostatic interaction, or covalent functionalization between nanomaterials and functional units via condensation reaction (amidation or ester formation) and acid treatments. Two types of $\pi-\pi$ interactions occur between the electron-rich and electron-poor regions, which influence its interaction with other molecules or nanomaterials. Different types of functionalization are given in Figure 5.6.

5.4.1 Chemical Functionalization

The functionalization is based on the covalent linkage of functional entities onto, e.g. carbon scaffold of carbon-based nanomaterials like CNTs, graphene, reduced



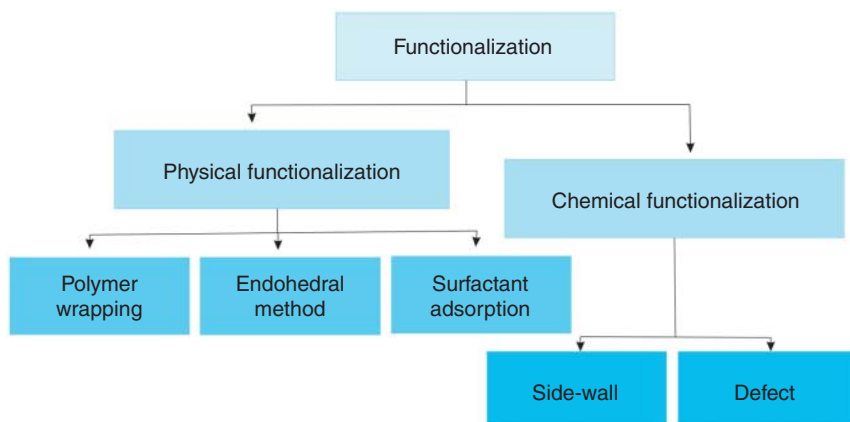


Figure 5.6 Methods for functionalization.

graphene oxide (rGO), etc. The direct covalent side-wall functionalization is associated with a change of hybridization from sp^2 to sp^3 and a simultaneous loss of π -conjugation system on the graphene layer. Defects and side-wall are types of chemical functionalization. Indeed, in defect functionalization, defect sites can be at the open ends and/or holes in the sidewalls, pentagon, or heptagon irregularities in the hexagon graphene framework. For instance, oxygenated sites can be also considered as defects. The defects can be created on the sidewalls as well as at the open ends of carbon black nanoparticles by an oxidative process with strong acids, such as HNO_3 , H_2SO_4 , or a mixture of them, or with strong oxidants such as $KMnO_4$, ozone, or reactive plasma.

5.4.2 Physical Functionalization

Functionalization of carbon black nanoparticles using the covalent method can provide useful functional groups onto the carbon black cloud surface. Non-covalent functionalization is a method for turning the interfacial properties of nanotubes. For example, the suspension of CNTs in the presence of polymers, such as polystyrene, leads to the wrapping of polymer around the CNTs to form supermolecular complexes of CNTs. The physical adsorption of surfactant on the CNTs surface lowers the surface tension of nanotubes, effectively preventing the formation of aggregates. The efficiency of this method is strongly dependent on the properties of surfactants, medium chemistry, and polymer matrix. Examples of this functionalization can be surfactant adsorption, polymer wrapping, and the endohedral method. For example, in the endohedral method, guest atoms or molecules are stored in the inner cavity of CNTs through the capillary effect. The insertion often takes place at defect sites localized at the ends or on the sidewalls. The insertion of inorganic nanoparticles into the tubes, such as C_{60} , Ag, Au, and Pt, is a typical example of endohedral functionalization. Small biomolecules, such as proteins, DNA, can also be entrapped in the inner hollow channel of nanotubes by simple adsorption, forming natural nano-test tubes. The combination of these two materials, i.e. CNTs and guest molecules, is particularly useful to integrate the properties of the two



components in hybrid materials for use in catalysis, energy storage, nanotechnology, and molecular-scale devices.

The terms “adsorption” and “absorption” are typically used in the physical or chemical state of nanoparticle functionalization. Before describing the terms of adsorption, one should know the difference between “adsorption” and “absorption.” Figure 5.7 clearly shows their concept.

Figure 5.7 Schematic representation of “adsorption” and “absorption” phenomena.

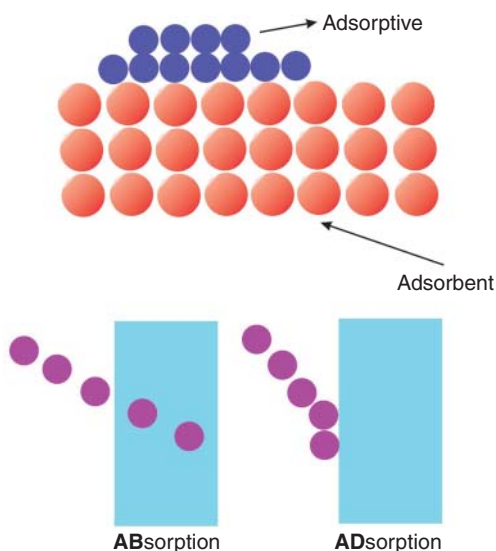


Table 5.1 Comparison between physical and chemical adsorption.

Physical adsorption	Chemical adsorption
The forces operating, in this case, are van der Waals forces	The forces operating are chemical bonds (ionic or covalent bonds)
The heat of adsorption is low about 20–40 kJ/mol	The heat of adsorption is high about 40–400 kJ/mol
It does not require any activation energy	It requires activation energy
It takes place at a low temperature and decreases with an increase in the temperature	This type of adsorption increases with an increase in temperature
It is not specific in nature that all gases adsorb on all solids to the same extent	It is highly specific in nature that adsorption occurs only by the possibility of the formation of chemical bonds
It forms a multi-molecular layer	It forms a uni-molecular layer
It increases with the increase in surface area	It also increases with the increase in surface area
The process is reversible, adsorption can occur by increasing temperature or decreasing pressure	The process is irreversible Efforts to free the adsorbed gas give different compounds



Physical adsorption (physisorption) is among the methods that are conceptually straightforward in the surface modification of nanoparticles for good stability and hydrophilicity in suspensions. Chemical adsorption (chemisorption) involves a chemical reaction between the surface and the adsorbate by the generation of new chemical bonds (Table 5.1).

5.5 Surface Modification Based on Organic Reactions

There are four main purposes of surface modification of NPs: (i) to improve or change the dispersion of MNPs; (ii) to improve the surface activity of MNPs; (iii) to enhance the physicochemical and mechanical properties; and (iv) to improve the biocompatibility of MNPs. There are mainly four magnetic iron oxide nanocomposites (Figure 5.8) [33].

Direct grafting through chemical adsorption has been employed for the nanoparticle's surface modification, having strong covalent bonds with functional molecules. For instance, other bonds generated between dextran nanoparticles and aliphatic or aromatic groups are applied to make the surface hydrophobic. Silanization is one such method where the silanol group on silane coupling agents (SCAs) reacts with surface species. Hydrolysis and polycondensation of $-\text{Si}-(\text{C}_x\text{H}_y)_3$ itself and with surface hydroxyl groups are a powerful combination for creating new coating layers [34].

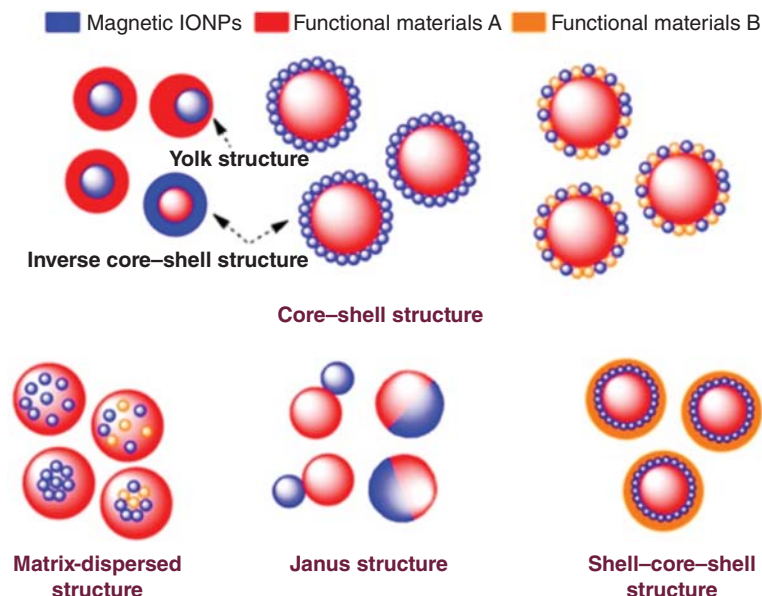


Figure 5.8 Typical morphologies of magnetic composite nanomaterials. Source: Wu et al. [32]/Taylor & Francis/Public Domain CC BY.



5.6 Surface Modification Based on Polymerization

Polymerization is any process in which relatively small molecules, called monomers, combine chemically to produce a very large chainlike or network molecule, called a polymer. The monomer molecules may be all alike, or they may represent two, three, or more different compounds. Different polymerization methods are applied for the nanoparticle's surface modification. Suitable types of reactions are free radical or ionic polymerization. Mainly, nanostructures of metals, metal alloys, metal oxides, and other materials have been modified with polymers. In recent years, polymer-coated magnetic nanoparticles have drawn much more attention owing to their widespread applications in various research areas including nanomedicine. Post-annealing and *in situ* coating are two common approaches to synthesizing, e.g. polymer-coated IONPs [35]. The former approach is further polymer functionalized based on previously prepared IONPs. *In situ* coating is coating the polymer onto the surface of IONPs during the synthesis process [36]. Some polymers such as polyethylenimine (PAMAM), polyacid polyetherimide, polyvinylpyrrolidone (PVP), polyethylenimine, polysaccharide, polydopamine (PDA), polyvinyl alcohol (PVA), polyethylene glycol (PEG), alginate, dextran, and chitosan are the most commonly used polymers for the surface modification of IONPs (Table 5.2).

Table 5.2 Polymers used for coating IONPs and their applications [33].

Polymer	Source/Production/Preparation	Applications
Lipids	In nature, animal food and nuts	Gene therapy, dual-modal imaging
Amino acids	In nature	Adsorbent, radio-labeling, biosensors, and cancer detection
Flavonoids	Found in some common plant foods like fruits, vegetables, beans, and tea	Cell imaging, nano-carrier; nano-drug
Polyphenol	Found in some common plant foods like cocoa beans, tea, and vegetables	Magnetic hyperthermia
Chitosan	Extracted from shellfish or fungi cell wall	Hyperthermia, tissue engineering
Dextran	Produced by lactic acid bacteria	<i>In vivo</i> cancer drug carriers, MRI contrast agents
Polyvinyl alcohol (PVA)	Polymerization of vinyl acetate, then saponification of polyvinyl acetate	<i>In vivo</i> imaging, drug delivery, biosensor
Polyethylene glycol (PEG)	Produced by the interaction of ethylene oxide with water, ethylene glycol, or ethylene glycol oligomers	Magnetic resonance imaging (MRI) contrast agents for <i>in vivo</i> cancer imaging, biosensors
Polyvinylvinyl pyrrolidone (PVP)	Made from the monomer <i>N</i> -vinylpyrrolidone	Targeted killing of breast cancer cells, MRI contrast agents

Source: Zhu et al. [33]/with permission of Elsevier.



5.7 Surface Modification with Inorganic Layers

The rapid agglomeration, oxidation, and un-biocompatibility of magnetic nanoparticles' surfaces limit their applications due to a reduction in their magnetic properties. Thus, the appropriate surface modification of magnetic nanoparticles can conquer these barriers with improved physicochemical properties, e.g. using inorganic materials and noble metals such as Fe_3O_4 , Ag, etc. [11, 12, 33, 37]. Inorganic materials are chosen to improve stability and to introduce new electronic, photonic, magnetic, mechanical, and surface chemical properties in the desired particles. Common choices of inorganic layers include zirconia, titania, silica, and other metal oxides that are readily obtainable through solution-phase approaches. Silica is the most common and widely used agent for surface modification of IONPs [38–40]. Silica coating has the following advantages: low agglomeration, enhancing stability, and reducing the cytotoxic effects of MNPs. Therefore, silica has demonstrated good biocompatibility, hydrophilicity, and stability [41]. Recently, researchers have described the procedure to control the size and thickness of the silica-coated NPs [42]. Generally, there are four main approaches to preparing IONP@SiO_2 (Table 5.3) [33].

The Stöber method is the most common approach to synthesizing IONP@SiO_2 , in which the IONPs are uniformly dispersed in an ethanol solution, followed by the addition of tetraethoxysilane (TEOS), then finally the aqueous ammonia solution is admixed to the mixed solution [32, 43]. As a basic catalyst, ammonia can not only control the particle size but also inhibit hydrolysis to form particles with regular morphology. Zhao Li et al. found that the size of silica particles increases with the concentration of ammonia, water, and TEOS in the reaction solution. At the same time, they found that an increase in the reaction temperature accelerated the ripening of the silica particles, causing the particle size to increase slightly [44]. This method can be applied to coat a SiO_2 layer directly onto the surface of Fe_3O_4 . Malvindi et al. studied the toxicity of silica-coated IONPs in an *in vitro* model. They used the A549 and HeLa lines and incubated cells with surface-modified $\text{Fe}_3\text{O}_4\text{@SiO}_2$ as well as bare NPs. They reported that the naked NPs show higher toxicity due to their

Table 5.3 Summary of synthesis methods for silica-coated IONPs [33].

Synthesis methods	Advantages	Disadvantages
Stöber method	Controllable silica shell and uniform size, high crystallinity	Lack of understanding of its kinetics and mechanism
Methods based on sodium silicate solution	Control of crystallinity and surface area	Depends on the preparation method
Microemulsion	Control of the particle size, high homogeneous	Poor yield, large amounts of solvent required, and time-consuming
Aerosol pyrolysis	Hermetically-coated	Complex experimental conditions

Source: Zhu et al. [33]/with permission of Elsevier.



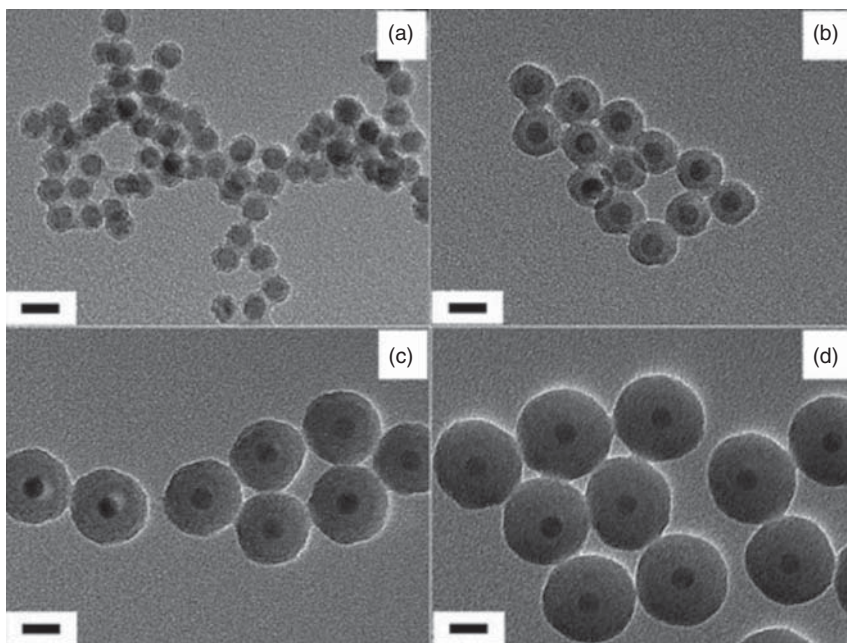


Figure 5.9 Transmission electron microscope (TEM) image of 12.2-nm $\text{Fe}_3\text{O}_4@\text{SiO}_2$ nanoparticles (NPs) with shell thicknesses of (a) 2.0 nm, (b) 6.3 nm, (c) 14.1 nm, and (d) 19.8 nm. Scale bar = 20 nm. Source: [47], H. Ding et al. (2012), American Chemical Society.

stronger in situ degradation [45]. Uribe Madrid et al. demonstrated the synthesis of $\text{Fe}_3\text{O}_4@\text{mSiO}_2$ core-shell structures with high specific surface area and different mesoporous silica (mSiO_2) shell thicknesses. This composite nanoparticle synthesized via the modified Stöber method shows excellent drug release performance, and it is ideal for targeted drug delivery *in vivo* [46]. They systematically studied the factors affecting the core size and shell thickness of $\text{Fe}_3\text{O}_4@\text{SiO}_2$ NPs. They found that shell thickness increased with an increasing amount of ammonia and TEOS. Meanwhile, the small aqueous domain is suitable for ultrathin silica shell, while the large aqueous domain is essential for a thicker shell. Single-core $\text{Fe}_3\text{O}_4@\text{SiO}_2$ NPs with different shell thicknesses are shown in Figure 5.2 and the surface coating mechanism is depicted in Figure 5.9 [47]. The CTAB-assisted synthesis of $\text{MnFe}_2\text{O}_4@\text{SiO}_2$ nanoparticles for magnetic hyperthermia and magnetic resonance imaging (MRI) application was prepared in a similar method with some modifications, as given in Ref. [23].

5.8 Summary

Finally, we summarize the reasons that describe the potentials and advantages that surface engineering of nanoparticles brings to the field:

- Surface modification improves the surface of nanoparticles in terms of functionality, compatibility, etc.



- Surface properties determine the interaction among the components as well as the solubility and agglomeration behavior in different solvents.
- Surface modifications of nanoparticles assist to tune their properties for different applications in the field of nanotechnology.
- Nanoparticles help in gaining hydrophilic, hydrophobic, conductive, optical, and anticorrosive properties.

References

- 1 Zhang, G., Liao, Y., and Baker, I. (2010). Surface engineering of core/shell iron/iron oxide nanoparticles from microemulsions for hyperthermia. *Materials Science and Engineering: C* 30: 92–97.
- 2 Petcharoen, K. and Sirivat, A. (2012). Synthesis and characterization of magnetite nanoparticles via the chemical co-precipitation method. *Materials Science and Engineering B* 177: 421–427.
- 3 Bagheri, H., Afkhami, A., Saber-Tehrani, M., and Khoshsafar, H. (2012). Preparation and characterization of magnetic nanocomposite of Schiff base/silica/magnetite as a preconcentration phase for the trace determination of heavy metal ions in water, food and biological samples using atomic absorption spectrometry. *Talanta* 97: 87–95.
- 4 Behbahani, N.S., Rostamizadeh, K., Yaftian, M.R. et al. (2014). Covalently modified magnetite nanoparticles with PEG: preparation and characterization as nano-adsorbent for removal of lead from wastewater. *Journal of Environmental Health Science and Engineering* 12: 1–12.
- 5 Ding, W. and Guo, L. (2013). Immobilized transferrin $\text{Fe}_3\text{O}_4@ \text{SiO}_2$ nanoparticle with high doxorubicin loading for dual-targeted tumor drug delivery. *International Journal of Nanomedicine* 8: 4631.
- 6 He, Y., Wang, S., Li, C. et al. (2005). Synthesis and characterization of functionalized silica-coated Fe_3O_4 superparamagnetic nanocrystals for biological applications. *Journal of Physics D: Applied Physics* 38: 1342.
- 7 Giri, S., Trewyn, B.G., Stellmaker, M.P., and Lin, V.S.Y. (2005). Stimuli-responsive controlled-release delivery system based on mesoporous silica nanorods capped with magnetic nanoparticles. *Angewandte Chemie International Edition* 117: 5166–5172.
- 8 Karade, V., Sharma, A., Dhavale, R. et al. (2021). APTES monolayer coverage on self-assembled magnetic nanospheres for controlled release of anticancer drug Nintedanib. *Scientific Reports* 11: 1–12.
- 9 Guivar, J.A.R., Sanches, E.A., Magon, C.J., and Fernandes, E.G.R. (2015). Preparation and characterization of cetyltrimethylammonium bromide (CTAB)-stabilized Fe_3O_4 nanoparticles for electrochemistry detection of citric acid. *Journal of Electroanalytical Chemistry* 755: 158–166.
- 10 Hajalilou, A., Etemadifar, R., Abbasi-Chianeh, V., and Abouzari-Lotf, E. (2018). Electrophoretically-deposited nano- $\text{Fe}_3\text{O}_4@$ carbon 3D structure on carbon



- fiber as high-performance supercapacitors. *Journal of Electronic Materials* 47: 4807–4812.
- 11 Hajalilou, A., Abouzari-Lotf, E., Etemadifar, R. et al. (2018). Fabrication by electrophoretic deposition of Nano- Fe_3O_4 and $\text{Fe}_3\text{O}_4@ \text{SiO}_2$ 3D structure on carbon fibers as supercapacitor materials. *JOM* 70: 1404–1410.
 - 12 Hajalilou, A., Kianvash, A., Shameli, K., and Lavvafi, H. (2017). Carbonyl iron based magnetorheological effects with silver nanoparticles via green-assisted coating. *Applied Physics Letters* 110: 261902.
 - 13 Mirzazadeh, A., Kianvash, A., and Hajalilou, A. (2018). Plating of Cu and Ni metals on Mg-ferrite sintered bodies by an electroless method and an investigation of magnetic behavior. *Journal of Materials Science: Materials in Electronics* 29: 5753–5760.
 - 14 Hajalilou, A., Mazlan, S.A., and Shila, S.T. (2016). Magnetic carbonyl iron suspension with Ni–Zn ferrite additive and its magnetorheological properties. *Materials Letters* 181: 196–199.
 - 15 Shilan, S.T., Mazlan, S.A., Ido, Y. et al. (2016). A comparison of field-dependent rheological properties between spherical and plate-like carbonyl iron particles-based magneto-rheological fluids. *Smart Materials and Structures* 25: 095025.
 - 16 Hajalilou, A., Mazlan, S.A., Shilan, S.T., and Abouzari-Lotf, E. (2017). Enhanced magnetorheology of soft magnetic carbonyl iron suspension with binary mixture of Ni–Zn ferrite and Fe_3O_4 nanoparticle additive. *Colloid and Polymer Science* 295: 1499–1510.
 - 17 Hajalilou, A., Abouzari-Lotf, E., Abbasi-Chianeh, V. et al. (2018). Inclusion of octahedron-shaped ZnFe_2O_4 nanoparticles in combination with carbon dots into carbonyl iron based magnetorheological suspension as additive. *Journal of Alloys and Compounds* 737: 536–548.
 - 18 Kralj, S., Makovec, D., Čampelj, S., and Drofenik, M. (2010). Producing ultra-thin silica coatings on iron-oxide nanoparticles to improve their surface reactivity. *Journal of Magnetism and Magnetic Materials* 322: 1847–1853.
 - 19 Sodipo, B.K. and Aziz, A.A. (2016). Recent advances in synthesis and surface modification of superparamagnetic iron oxide nanoparticles with silica. *Journal of Magnetism and Magnetic Materials* 416: 275–291.
 - 20 Campelj, S., Makovec, D., and Drofenik, M. (2008). Preparation and properties of water-based magnetic fluids. *Journal of Physics: Condensed Matter* 20: 204101.
 - 21 Desai, J.D. and Banat, I.M. (1997). Microbial production of surfactants and their commercial potential. *Microbiology and Molecular Biology Reviews* 61: 47–64.
 - 22 Peetla, C. and Labhasetwar, V. (2009). Effect of molecular structure of cationic surfactants on biophysical interactions of surfactant-modified nanoparticles with a model membrane and cellular uptake. *Langmuir* 25: 2369–2377.
 - 23 Kavkhani, R., Hajalilou, A., Abouzari-Lotf, E. et al. (2022). CTAB assisted synthesis of $\text{MnFe}_2\text{O}_4@ \text{SiO}_2$ nanoparticles for magnetic hyperthermia and MRI application. *Materials Today Communications* 31: 103412.



- 24 Bruce, I.J. and Sen, T. (2005). Surface modification of magnetic nanoparticles with alkoxysilanes and their application in magnetic bioseparations. *Langmuir* 21: 7029–7035.
- 25 Cutler, P. (2003). Protein arrays: the current state-of-the-art. *Proteomics* 3: 3–18.
- 26 Lee, Y.-S. and Mrksich, M. (2002). Protein chips: from concept to practice. *Trends in Biotechnology* 20: s14–s18.
- 27 Phelan, M.L. and Nock, S. (2003). Generation of bioreagents for protein chips. *Proteomics* 3: 2123–2134.
- 28 Bucak, S., Jones, D.A., Laibinis, P.E., and Hatton, T.A. (2003). Protein separations using colloidal magnetic nanoparticles. *Biotechnology Progress* 19: 477–484.
- 29 Karumanchi, R.S., Doddamane, S.N., Sampangi, C., and Todd, P.W. (2002). Field-assisted extraction of cells, particles and macromolecules. *Trends in Biotechnology* 20: 72–78.
- 30 Saiyed, Z., Telang, S., and Ramchand, C. (2003). Application of magnetic techniques in the field of drug discovery and biomedicine. *BioMagnetic Research and Technology* 1: 1–8.
- 31 Leonard, M. (1997). New packing materials for protein chromatography. *Journal of Chromatography B: Biomedical Sciences and Applications* 699: 3–27.
- 32 Wu, W., Wu, Z., Yu, T. et al. (2015). Recent progress on magnetic iron oxide nanoparticles: synthesis, surface functional strategies and biomedical applications. *Science and Technology of Advanced Materials* 16: 023501.
- 33 Zhu, N., Ji, H., Yu, P. et al. (2018). Surface modification of magnetic iron oxide nanoparticles. *Nanomaterials* 8: 810.
- 34 Shen, R. and Yang, H. (2010). Surface modifications and applications of magnetic and selective nonmagnetic nanoparticles. *Annual Review of Nano Research* 3: 83–147.
- 35 Laurent, S., Forge, D., Port, M. et al. (2008). Magnetic iron oxide nanoparticles: synthesis, stabilization, vectorization, physicochemical characterizations, and biological applications. *Chemical Reviews* 108: 2064–2110.
- 36 Shaterabadi, Z., Nabiyouni, G., and Soleymani, M. (2017). High impact of in situ dextran coating on biocompatibility, stability and magnetic properties of iron oxide nanoparticles. *Materials Science & Engineering C, Materials for Biological Applications* 75: 947–956.
- 37 Hajalilou, A., Ferreira, L.P., Jorge, M.E.M. et al. (2021). Superparamagnetic Ag-Fe₃O₄ composites nanoparticles for magnetic fluid hyperthermia. *Journal of Magnetism and Magnetic Materials* 168242.
- 38 Maleki, A. (2012). Fe₃O₄/SiO₂ nanoparticles: an efficient and magnetically recoverable nanocatalyst for the one-pot multicomponent synthesis of diazepines. *Tetrahedron* 68: 7827–7833.
- 39 Kiasat, A.R. and Davarpanah, J. (2013). Fe₃O₄@silica sulfuric acid nanoparticles: an efficient reusable nanomagnetic catalyst as potent solid acid for one-pot solvent-free synthesis of indazolo [2, 1-*b*] phthalazine-triones and pyrazolo [1, 2-*b*] phthalazine-diones. *Journal of Molecular Catalysis A: Chemical* 373: 46–54.



- 40 Sun, H., Zeng, X., Liu, M. et al. (2012). Synthesis of size-controlled $\text{Fe}_3\text{O}_4@\text{SiO}_2$ magnetic nanoparticles for nucleic acid analysis. *Journal of Nanoscience and Nanotechnology* 12: 267–273.
- 41 Abbas, M., Rao, B.P., Islam, M.N. et al. (2014). Highly stable-silica encapsulating magnetite nanoparticles ($\text{Fe}_3\text{O}_4/\text{SiO}_2$) synthesized using single surfactantless-polyol process. *Ceramics International* 40: 1379–1385.
- 42 Xin, C., Jing, Y., and Yang-Long, H. (2015). Surface modification of magnetic nanoparticles in biomedicine. *Chinese Physics B* 24: 014704.
- 43 Hui, C., Shen, C., Tian, J. et al. (2011). Core-shell $\text{Fe}_3\text{O}_4@\text{SiO}_2$ nanoparticles synthesized with well-dispersed hydrophilic Fe_3O_4 seeds. *Nanoscale* 3: 701–705.
- 44 Zhao, L., Yu, J.-G., Cheng, B., and Zhao, X.-J. (2003). Preparation and formation mechanisms of monodispersed silicon dioxide spherical particles. *Acta Chimica Sinica – Chinese Edition* 61: 562–566.
- 45 Malvindi, M.A., De Matteis, V., Galeone, A. et al. (2014). Toxicity assessment of silica coated iron oxide nanoparticles and biocompatibility improvement by surface engineering. *PLoS One* 9: e85835.
- 46 Madrid, S.I.U., Pal, U., Kang, Y.S. et al. (2015). Fabrication of $\text{Fe}_3\text{O}_4@m\text{SiO}_2$ core-shell composite nanoparticles for drug delivery applications. *Nanoscale Research Letters* 10: 1–8.
- 47 Ding, H., Zhang, Y., Wang, S. et al. (2012). $\text{Fe}_3\text{O}_4@\text{SiO}_2$ core/shell nanoparticles: the silica coating regulations with a single core for different core sizes and shell thicknesses. *Chemistry of Materials* 24: 4572–4580.





6

Insight into Superconducting Quantum Interference Devices (SQUID)

6.1 Introduction to SQUID

The term SQUID stands for a Superconducting Quantum Interference Device. It works based on a Josephson junction effect, which is employed to record extremely small changes in magnetic flux. Normally, as shown in Figure 6.1, a SQUID is a ring of superconductors interrupted by one or more Josephson junctions. Several previous works have explained this phenomenon in detail [1–5].

A superconducting quantum interference device is a very sensitive magnetometer, which is utilized to determine the magnetic behavior of the samples as well as to measure extremely subtle magnetic fields. This is accomplished in terms of superconducting loops comprising the Josephson junction. Extremely weak signals such as subtle variations in the human body's electromagnetic energy field are possibly measured through SQUID. In fact, it detects an energy variation by using the Josephson junction effect, which is 100 billion times weaker than the electromagnetic energy that moves a compass needle. The effect consists of two superconductors separated by an insulating layer so thin that electrons can pass through it. In detail, a SQUID is made of tiny loops of superconductors using Josephson junctions to obtain superposition: each electron moves simultaneously in both directions. The electrons can perform as qubits as the current moves in two opposite directions (that theoretically could be used to enable quantum computing).

SQUID devices can be generally divided into two categories: (i) radio frequency (RF) SQUID and (ii) Direct current (DC) SQUID. These two types are also having various types, e.g. high-temperature RF SQUID (HTS), low-temperature RF SQUID (LTS), high-temperature DC SQUID (HTS), VSM magnetometer squid, and quantum design's magnetic property measurement system (QD-MPMS). Several works of literature, such as Refs. [5–7], describe the theory of different types of SQUIDs in more detail.

6.1.1 A Radio Frequency (RF) SQUID

An RF SQUID is made up of a single Josephson junction, which is mounted on a superconducting ring. As shown in Figure 6.2a, flux is inductively coupled into the



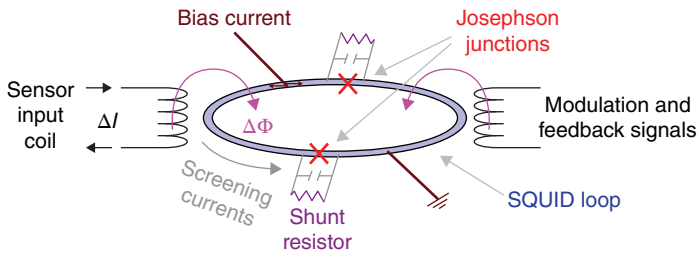


Figure 6.1 Schematic representation of dual junction (DC) SQUID loop. Source: Fagaly [1]/with permission of AIP Publishing.

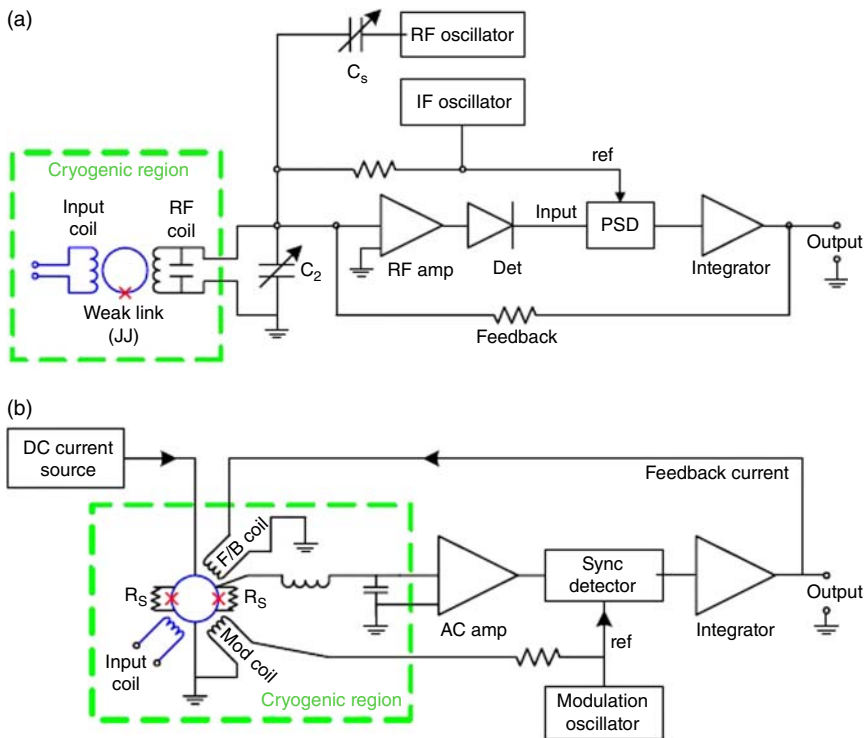


Figure 6.2 Schematic representation of (a) RF SQUID, and (b) DC SQUID. PSD; power spectral density. Source: Fagaly [1]/with permission of AIP Publishing.

SQUID loop via an input coil, connecting the SQUID to the experiment. An “RF” coil, which is part of a high-Q resonant (tank) circuit, is employed to record the variations of current in the SQUID loop. In other words, an oscillating current is applied to an external circuit, whose voltage changes as an effect of the interaction between the electric *circuit* and the ring. The magnetic flux is then measured.



6.1.2 A Direct Current (DC) SQUID

A DC SQUID, which is much more sensitive, consists of two Josephson junctions employed in parallel so that electrons tunneling through the junctions demonstrate quantum interference, depending upon the strength of the magnetic field within a loop. DC SQUIDS demonstrate resistance in response to even tiny variations in a magnetic field, which is the capacity that enables the detection of such minute changes. The DC SQUID offers lower noise in comparison with an RF SQUID, which is why it is widely used for commercial purposes. The DC SQUID offers clear advantages over the RF SQUID for many applications with modern thin-film fabrication techniques and improvements in control electronics design.

Noteworthy differences between HTS and LTS DC SQUIDS are related to the materials used in their design, which affect their performances. Ductile materials such as NbTi and Nb₃Sn are used in LTS. Moreover, the use of Nb₃Sn provides an opportunity to use the detection coils in high field cases. This is while the actual LTS SQUID sensor can be employed in a low field environment. Furthermore, moisture degrades the HTS structure, while the LTS materials are stable in air. Thus, to remedy the issue that occurred in HTS, they are required to be coated or passivated. Although LTS materials have superior properties, the main advantage of HTS devices is the operation ability of HTS devices under liquid nitrogen rather than under liquid helium, which provides remarkable operational benefits and cannot be discounted.

Some limitations of the SQUID Technology can be summarized as [1]:

- (1) A 180° rotation would sweep out a total field variation of $\sim 100 \mu\text{T}$ for a pure magnetometer that performs in the Earth's magnetic field. It simply means that the SQUID magnetometers are vector magnetometers. For example, for the magnetometer with $10 \text{ fT}/\sqrt{\text{Hz}}$ sensitivity, a dynamic range of $100 \mu\text{T}/10 \text{ fT} = 200 \text{ dB}$ is required to track the total field variation, which is well beyond the capabilities of current electronics. Moreover, the rotational speed must not lead the current flowing through the SQUID sensor to exceed its slew rate limitations. Pure gradiometers are insensitive to even fields and do not have this dynamic range limitation.
- (2) According to the voltage versus current curve (Figure 6.3a), SQUIDS are sensitive to relative (field or current) variations only. This is because the output voltage of a SQUID is a periodic function (Figure 6.3b) of the flux penetrating the SQUID loop. The SQUID is "flux-locked" on an arbitrary point on the $V-\Phi$ curve and the SQUID output is dependent upon flux variations relative to this lock point.
- (3) The existence of $1/f$ noise is another limitation. The use of alternating current (AC) biasing in HTS-SQUIDS confines their maximum bandwidth to less than half of the bias reversal frequency. For example, the noise would be induced, owing to voltage spikes in the transformer-coupled preamplifier input circuit,



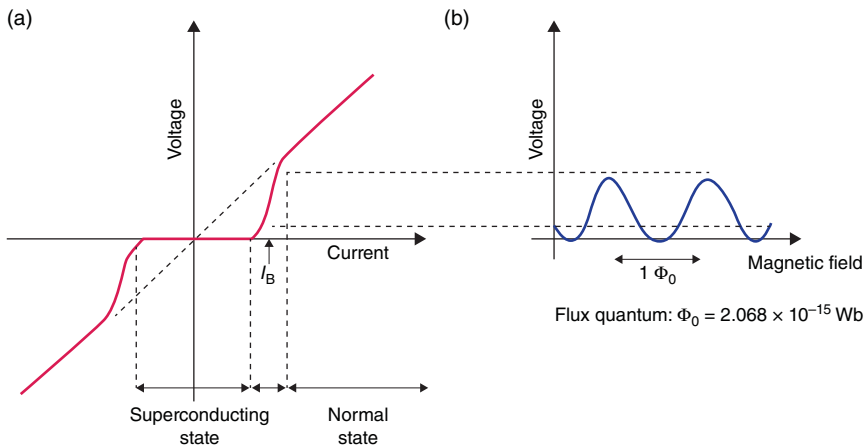


Figure 6.3 (a) Voltage–current curve to indicate bias point for Josephson junction, and (b) voltage as a function of an externally applied flux. Source: Fagaly [2]/with permission of AIP Publishing.

if the bias reversal frequency is too high. Due to this fact, the maximum bandwidth of commercially available HTS-SQUIDs is typically restricted to ~ 50 kHz. Thus, the AC bias is not used in the case of MHz bandwidths; however, there will be excess noise below 1 kHz. Although the SQUID has an intrinsic bandwidth of several GHz, the maximum usable bandwidth of most commercially available electronics is typically 50–100 kHz when they are performed with standard flux-locked loop electronics using AC flux modulation.

6.2 Superconducting Materials Used in SQUID

Niobium (Nb) or lead alloys with 10% indium (In) or gold are traditionally used as superconducting materials for SQUIDs. The composite materials are often consisting of the tunnel barrier sandwiched between a base electrode of niobium and the top electrode of lead alloy. Pure lead is rarely used due to its instability with temperature variations. Recently, carbon nanotube (CNT)-SQUID sensors, which are made of an aluminum loop and a single-walled CNT, are employed in Josephson junctions [8]. The sensors operate at 1 K or below and are a few 100 nm in size. These characteristics enable them to count spins [9]. More recently, the high-temperature SQUID sensors are remarkably considered in practical applications due to their superior properties such as crystalline chemical compounds, which are well known for displaying high-temperature superconductivity. For example, Yttrium barium copper oxides (YBCOs) become superconducting above the boiling point of liquid nitrogen (77 K) at about 92 K. They are also cooled by liquid nitrogen, which is cheaper and more easily handled than liquid helium. Moreover, they are less sensitive than conventional low-temperature SQUIDs but good enough for many applications.



6.3 What Is the Basic Principle in SQUID VSM Magnetometer?

In any SQUID-based measuring instrument, the signal of interest is coupled to the SQUID by a superconducting flux transformer containing a pick-up loop and an input coil tightly coupled to SQUID. Any variation in magnetic flux through the pick-up loop, due to flux quantization in superconducting rings, gives rise to a flow of screening current in the flux transformer coupling magnetic flux through the SQUID loop, and the SQUID responds by generating a proportional output voltage. In a conventional SQUID magnetometer, the sample is repeatedly transported across a superconducting pick-up loop in the form of a first- or second-order gradiometer, which is followed by the SQUID output voltage recorded in terms of sample position in the form of a flux profile. Fitting the measured flux profile to that expected for a point dipole yields magnetization of the sample. Measurements over an extended range of temperature (T) and field (H) tend to take a long time because a full flux profile has to be recorded at each value of T and H .

6.4 Superconductivity

To identify and fully understand the crucial characteristics of the Josephson junction effect, it is first needed to grasp the straightforward concepts of superconductivity. Superconductors are elements, intermetallic alloys, or compounds (maybe organic) that lose their electrical resistance below a certain temperature. This temperature is considered a critical (or transition) temperature (T_c) to define either the non or superconductive state of the materials, as shown in Figure 6.4. In other words, if the alloys or metals are cooled to a very low temperature (e.g. below absolute zero), a phase transition would occur. This is considered as “critical temperature” (T_c), where a transition occurs from the “resistive” state to the superconducting state. In fact, it is considered as the resistance-less state (Figure 6.4),

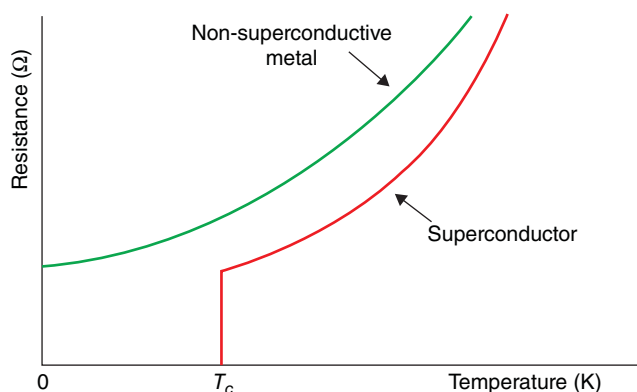


Figure 6.4 Resistance versus temperature to indicate the transition temperature in superconductors.



where the electrons become paired in the metal. Below the critical temperature (T_c), the overall interaction between two electrons becomes attractive, due to the interaction of electrons with the ionic lattice of the metal. This is while the net interaction between two electrons is repulsive above the critical temperature. In fact, two phenomena may occur below T_c : (i) resistance-less supercurrent and (ii) Meissner effect. In other words, in those materials, the current is carried not only by single electrons but also by pairs of electrons with opposite spins called Cooper pairs. These are quantum mechanical entities. For $T < T_c$, the binding energy of the Cooper pairs is large in comparison with the thermal energy scattering. Consequently, Cooper pairs propagate through the material, and current flow without any resistance.

Three different phenomena could be observed if a superconductor material is subjected to an externally applied magnetic field and cooled below its transition temperature: normal state, which is non-superconducting and happens at $T > T_c$, flux expulsion, and persistent current, which is representative of superconducting behavior. As shown in Figure 6.5a, the magnetic flux lines penetrate through the material in the normal state. For a hypothetical perfectly conducting (zero resistance material), the currents induced by attempts to alter the magnetic field would hinder variations in the magnetic field within the conductor. On the other hand, flux lines could not occur within the superconducting region in the superconducting states, except for a shallow surface layer, which is called the penetration depth (λ). As the material becomes superconducting, the magnetic flux is expelled (Figure 6.5b) unlike a perfect conductor that traps the flux. This flux expulsion is given as the Meissner effect, which is a consequence of the fundamental character of the superconducting state. In other words, the Meissner effect is the exclusion of magnetic flux from the superconductor. This is due to the electric currents known as the screening currents owing on the surface of the superconductor. The screening currents flow in such a direction to produce a field equal and opposite to the applied field. This causes zero induction ($B = 0$) inside the superconductor. Superconductors expel the field even if they are cooled into the superconducting state in the presence

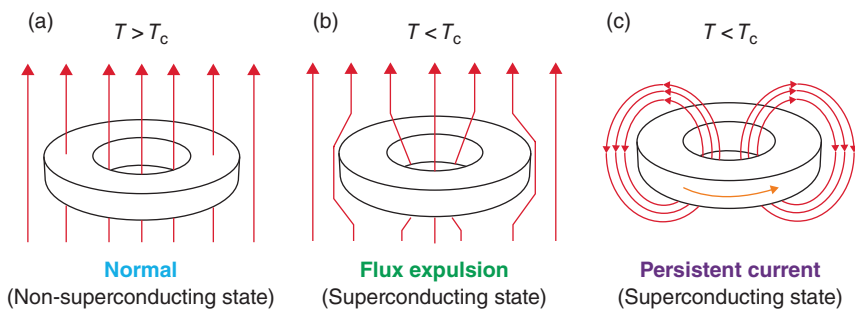


Figure 6.5 Schematic representation of Meissner effect in a superconducting ring cooled in an externally applied magnetic field. (a) Normal state (non-superconducting state), (b) flux expulsion (superconducting state), and (c) persistent current (superconducting state). Source: Fagaly [2]/with permission of AIP Publishing.



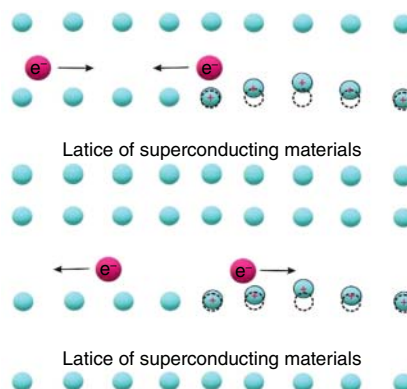
of an applied field. In the case of a ring formation in the superconducting material, the flux interior to the ring is trapped when the ring becomes superconducting (Figure 6.5b) rather than expelled as in a continuous solid. If the magnetic field is then turned off, a current, which circulates the ring keeping the magnetic flux ($\Phi = \int B dA$) inside the ring constant, is induced (Figure 6.5c). The current in a ring made of a normal (non-superconducting) metal will quickly decay due to the electrical resistance. The current decay is exponential with a time constant that is attributed to the inductance (L) of the ring and resistance (R) as $I(t) = I_0 e^{-tR/L}$. In a superconducting ring, where R is zero, there would be no decay of the current, which will result in the establishment of a persistent current ($I = -\Phi/L$). The circulation of current would continue as long as the ring is kept below T_c .

According to the Bardeen–Cooper–Schrieffer (BCS) theory, superconductivity can be explained as follows:

6.4.1 Electron–Lattice Interaction

According to the BCS theory, superconductivity occurs because of the existence of an attractive force between conduction electrons in metals. Due to this attraction the bound pairs of electrons form. These pairs of electrons are called Cooper pairs, which can move in the crystal structure without resistance. In the electron–lattice interaction state, an electron moves in a crystal and experiences an attractive Coulomb force due to the positive ions. This interaction will lead to distortion of the lattice (Figure 6.6). Supposing that another electron comes by that time then the distorted lattice will interact with the second electron. So two electrons are interacting with each other via the lattice distortion. This lattice distortion is also known as a phonon. Indeed, there is an electron–lattice–electron interaction resulting in the attractive force between two electrons. This interaction is strongest when the two electrons have equal and opposite momenta and opposite spins. It may exceed the Coulomb repulsive interaction between the electrons at low temperatures. Pair of such electrons that interact attractively is called Cooper pair. At temperature below a critical temperature, the electron–lattice–electron interaction is stronger than the

Figure 6.6 Electron–lattice interaction.



electron–electron Colombian repulsion force and so a pair of electrons are formed. The Cooper pair of electrons has the property to move smoothly through lattice without ever-changing energy between them. This means that the Cooper pair is not scattered and hence shows infinite conductivity. At high temperatures due to lattice vibration, the Cooper pairs do not form. The Cooper pair of electrons is formed with electrons having equal but opposite momenta; hence, any change in momentum due to one electron will be counterbalanced by the other.

The Cooper pair moves through the material without resistance.

6.4.2 Cooper Pairs

They are two coupled electrons with opposite momenta and spin at low temperatures. The American physicist Leon Cooper showed that an arbitrarily small attraction between electrons in a metal can give rise to a paired state of electrons to have lower energy than the Fermi energy, which implies that the pair is bound. Their characteristics can be Boson-like, resistance-less (does not scatter), and energetically favorable in the superconducting state.

6.4.3 Energy Gap

A very slight attraction of two electrons below the critical temperature allows them to drop into a lower energy state, generating an energy “gap” (Figure 6.7). Thus, the electrons move and result in a current that can flow without being scattered by the ions of the lattice due to the energy gap and the lower energy state. Electrical resistance in metals could be induced once the ions scatter electrons. In the case of a superconductor state, there is no energy loss since there is no electrical resistance in a superconductor. A maximum supercurrent that can flow is considered as the critical current, where the material behaves as normal above this current. The other characteristic is that once a metal goes into the superconducting state, it expels all magnetic fields, as long as the magnetic fields are not too large.

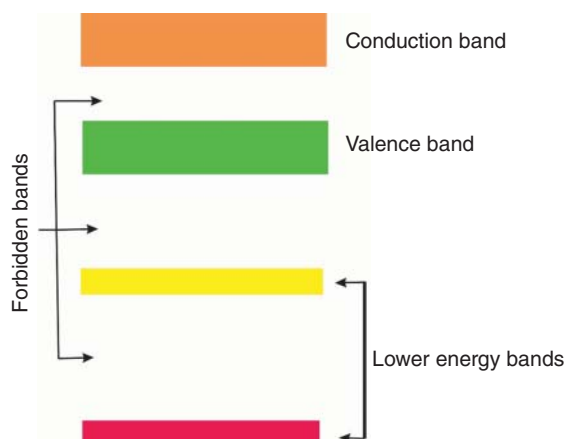


Figure 6.7 Schematic representation of energy gap. Source: Ciftja [10]/with permission of IOP Publishing.



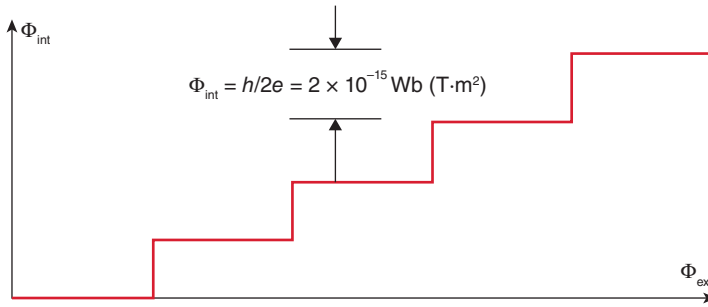


Figure 6.8 Schematic representation of flux quantization. Source: Fagaly [1]/with permission of AIP Publishing.

6.4.4 Coherence

Based on coherence characteristics, one can calculate phase and amplitude at any point on the wave and one wave equation describes all Cooper pairs.

6.4.5 Flux Quantization

The magnetic flux within a superconducting ring remains trapped as long as it remains superconducting. This trapped flux has some very unusual characteristics as (i) the level of magnetic flux cannot be continually changed in the ring and (ii) only the discrete levels of the magnetic flux can be trapped (Figure 6.8). In other words, the magnetic flux is quantized [11] and exists only in multiples of the flux quantum $\Phi_0 = 2.07 \times 10^{-15} \text{ Wb}$; $1 \text{ Wb/m}^2 = 1 \text{ T}$. Equivalently, the field inside the ring can only exist in discrete steps of $2.068 \times 10^{-11} \text{ T}$ for a ring with an area of 1 cm^2 .

6.5 Josephson Tunneling (JT) Phenomenon

A Josephson junction is composed of sandwiching a nonsuperconducting thin layer material (on the order of 30 \AA thick or less) between two layers of the superconducting material. The device is named after Brian Josephson, with the prediction tunneling the pairs of superconducting electrons right through the nonsuperconducting barrier from one superconductor to another (Figure 6.9a). Moreover, the exact form of the current and voltage relations for the junction is proposed. This was in good consistent with experimental work, which results in Nobel Prize being awarded to Josephson in 1973.

In the case of an insulator barrier, its thickness should be on the order of 30 \AA thick or less, while it may vary to several microns thick in the case of a metal barrier (nonsuperconducting). Until a critical current is reached, a supercurrent can flow across the barrier; electron pairs can tunnel across the barrier without any resistance. But when the critical current is exceeded, another voltage will develop across the junction. That voltage will depend on time, that is, it is an AC voltage. This in turn causes a lowering of the junction's critical current, giving rise to an even more normal current to flow, and a larger AC voltage (Figure 6.9b).



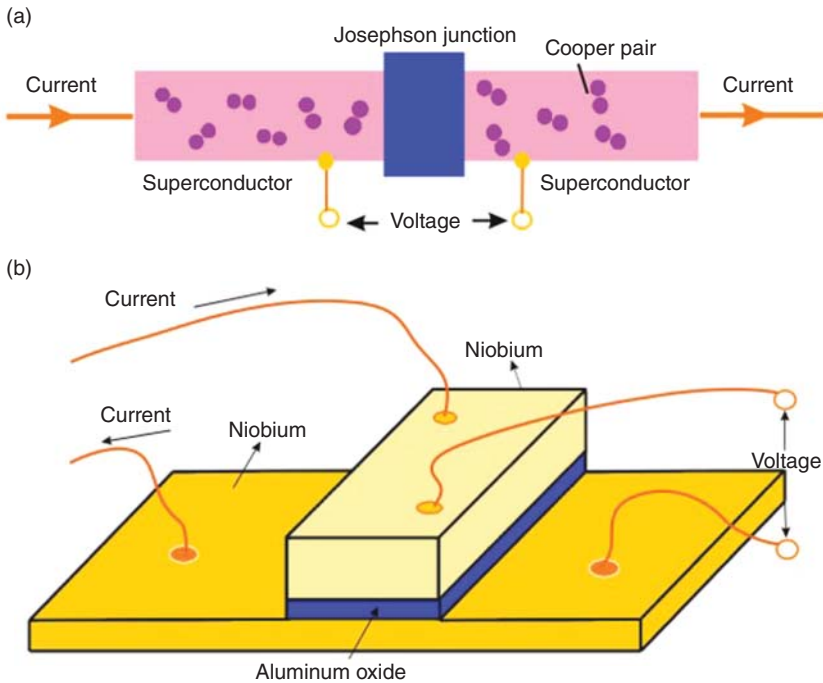


Figure 6.9 (a) Schematic representation of Josephson tunneling phenomenon, and (b) set up of Josephson junction.

The Josephson junction can be made by different states and designs, i.e. superconducting-insulator-superconducting (SIS) barrier such as a point contact, a normal metal (superconducting-normal-superconducting [SNS]), a microbridge where the current flowing through a small constriction exceeds J_c only in the region of the microbridge, a thin-film tunnel junction (the barrier can either be an insulating (SIS), or a normal metal (SNS) material), bicrystal, step edge grain boundary, step edge superconductor-normal superconductor, and ramp edge superconductor-normal superconductor with a $\text{PrBa}_2\text{Cu}_3\text{O}_{7-\delta}$ barrier [1, 2].

This Josephson tunneling (JT) effect can be described in terms of (i) Josephson Junction – the small gap between two superconductors, (ii) Cooper pairs, and (iii) Critical current. Indeed, in 1962, Josephson [12] proposed a model that there is the possibility of electrons tunneling from one superconducting region to another. They are separated by a resistive insulating barrier, often denoted as a “weak link” or “Josephson Junction.” The Cooper pairs could tunnel through the resistive barrier, and the superconducting current could penetrate the resistive barrier with no voltage drop in the cases of (i) for distances less than the coherence length (ξ) of the superconducting material (Table 6.1) and (ii) currents less than a critical current (I_c) that is characteristic of the weak link. The I_c is equal to $\sin\Delta\phi/(I_s)$, where I_s is supercurrent, and $\Delta\phi$ is due to a phase difference across the junction. This indicates that the phase change can be due to current, magnetic field, and Josephson Junctions.



Table 6.1 Some characteristics of superconducting materials.

Material	T_c (K)	Δ_0 (meV)	λ_0 (nm)	ξ_0 (nm)	H_{c0} (T)	H_{c1} (T)	H_{c2} (T)
HTS							
$\text{Ba}_{0.6}\text{K}_{0.4}\text{BiO}_3$	30						
MgB_2	39		140	2.5		18	6.5
$\text{La}_{1.8}\text{Sr}_{0.5}\text{CuO}_4$	40						
$\text{YBa}_2\text{Cu}_3\text{O}_{7-\delta}$	95		150	0.7		>100	4
$\text{Bi}_2\text{Sr}_2\text{Ca}_2\text{Cu}_3\text{O}_{10}$	110		150	0.2		>100	4.5
$\text{Tl}_2\text{Bi}_2\text{Ca}_2\text{Cu}_3\text{O}_{10}$	125						
$\text{HgBa}_2\text{Ca}_2\text{Cu}_3\text{O}_{8+\delta}$	134						
LTS							
Nb_3Sn	18.1	3.4	65	3			24.5
NbTi	9.50	1.5	240	4			15
Niobium	9.25	1.50		40		0.198	0.268
Mercury	4.153				0.0412		
Lead	7.193	1.35			0.0803		

Source: Adapted from [1, 2].

6.6 Utilizations and Applications of SQUID

SQUIDS have been used for a variety of testing purposes that demand extreme sensitivity, including engineering, medical, and geological equipment. They are not only used in applications associated with materials science but also in several other areas of science such as biology, medical, and clinical environment. For example, it is employed in magnetogastrography to record the weak magnetic fields of the stomach due to the extreme sensitivity that makes it a very desirable technique for these kinds of applications. In the clinical environment, the SQUIDS are employed in cardiology for magnetic field imaging (MFI), which detects the magnetic field of the heart for diagnosis and risk stratification. Furthermore, it is employed to perform magnetic resonance imaging (MRI) in the human body. Indeed, in the research laboratories, scanning SQUID microscopes are used for this purpose; a SQUID is scanned across the surface of a part of the body, and variations in magnetism at the surface of the body produce an image. Another new application of SQUID in medical science would be the magnetic marker monitoring method, which is utilized to trace the path of orally applied drugs. Since the brain operates electrically, one can monitor the activity of the brain or the heart by sensing the magnetic fields created by neurological currents.

Another application is the scanning SQUID microscope, which uses a SQUID immersed in liquid helium as the probe. The use of SQUIDS in oil prospecting mineral exploration, earthquake prediction, submarine detection, geothermal



energy surveying, and geological research for detecting remnants of past geophysical changes of the earth's field in rocks is becoming more widespread as superconductor technology develops. This is sometimes accompanied by using precision movement sensors in a variety of scientific applications to detect, for example, gravitational waves, where the sensor in each of the four gyroscopes is employed on Gravity Probe B to test the limits of the theory of general relativity.

Furthermore, in materials science, SQUID is widely utilized to characterize the magnetic nanoparticles in terms of magnetization as a function of an applied field and magnetization versus temperature [13, 14], which will be systematically described in the following Chapter 7.

6.7 Advantage and Disadvantage of SQUID Compared to Other Techniques in Characterization of Magnetic Nanomaterials

It has been proven that a DC-detected high-frequency electron paramagnetic resonance (HF-EPR) is a desirable technique for the characterization of magnetic materials [15–21]. Generally, there are two configurations for its performance: (i) locating the sample within a resonant cavity and measuring the variation in the resonant frequency of the cavity yields the real part or in-phase (x'), or measurement the variation in quality factor (Q) yields the imaginary part or out-of-phase susceptibility (x'') [16, 20, 21] and (ii) mounting the sample inside a waveguide and measuring the variation in transmitted radiation power versus the swept magnetic field, which is considered as a single-pass or transmission measurement [16, 17, 22]. The case of (i) has the benefit of discrete observation of x' and x'' and high sensitivity, while the case of (ii) has the benefit of ease of use and broadband measurements. Discrete line shape analysis of the transmission technique is unfortunately prevented by admixtures of dispersive and absorptive signals as well as by the effects associated with microwave propagation [22].

In general, for an exchange-coupled spin system, the EPR signal tends toward a Lorentzian line shape. Following Pake and Purcell [23] in Figure 6.10, Cage and Russek investigated the complex magnetic susceptibility (χ) as a function of the dimensionless parameter x . Indeed, χ is equal to $\chi = x' + ix''$ and x is equal to $2(H_0 - H)/\Delta H_{1/2}$ where H , H_0 , and $\Delta H_{1/2}$ denote the swept field, resonance field, and the full width at half maximum in units of A/m on the abscissa, respectively [23]. On the ordinate, the product of the volume static susceptibility χ_0 , the angular frequency (ω) in Hz, and the transverse spin lifetime T_2 in seconds was plotted [23]. The traces are offset, and the baseline signifies the zero for each trace. The line shape for the imaginary part in the absence of magnetic field modulation is illustrated in Figure 6.10a. The line position would be manifested by the field at which the maximum is indented. This relative signal shape has also been proven to be representative of the Hall-bar detected EPR suppression of the magnetic moment and superconducting quantum interference device SQUID-detected [24–26]. As shown in Figure 6.10b, the absorptive signal emerges as the first



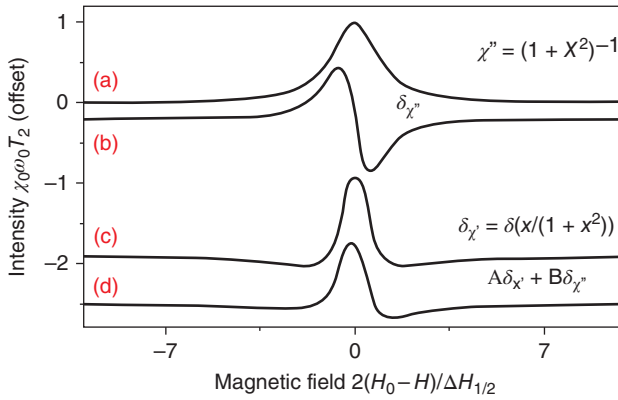


Figure 6.10 Simulated spectra in terms of a Lorentzian line shape and Bloch formalism. Source: Cage et al. [19]/with permission of AIP Publishing.

derivative in the presence of field modulation, which yields the line position at the zero crossings. Figure 6.10c indicates the first derivative of the reactive signal, and the line position is manifested as the maximum. These components can be discretely separated through resonant cavity measurements in conjunction with automatic frequency control that compensates for the variation in resonant cavity frequency. However, the line is commonly a superposition of these two components in the case of transmission measurements using an over-molded waveguide. This gives rise to a mixed spectrum (Figure 6.10d), where it is not clear a priori where the line position should be signed or even whether a single peak is present.

The methods in use to spark light this issue are (i) post-experimental analytic fitting of the line, (ii) iterative adjustments of the frequency or phase of the excitation radiation during the experiment until the line shape emerges either absorptive or dispersive, and (iii) a combination of both [22]. These methods, unfortunately, involve a certain amount of operator judgment and assumptions as to the signal shape. The propagation effects are the other issues related to RF-detected transmission techniques. This would exist once the sample dimension is close to the exciting radiation wavelength [22]. These propagation effects are influenced by the radiation frequency, magnetic field, sample thickness, and any other perturbations of the refractive index [19, 22].

The spectra of a single-aligned crystal of Fe8 obtained with a conventional transmission HF-EPR system at 141 GHz and 4 K are illustrated in Figure 6.11a. The lower trace suggests the spectrum after iterative operator adjustments of the frequency until the spectrum emerges to contain as few dispersive elements as possible. The upper trace indicates a spectrum with no operator influence. Figure 6.11b displays the magnetization data of this sample in the absence of super curved and the presence of slower curved microwave irradiation at 4 K and 141 GHz. A series of dips in the magnetization would come out upon irradiation. These dips are associated with electron paramagnetic resonant absorption of microwave power between adjacent



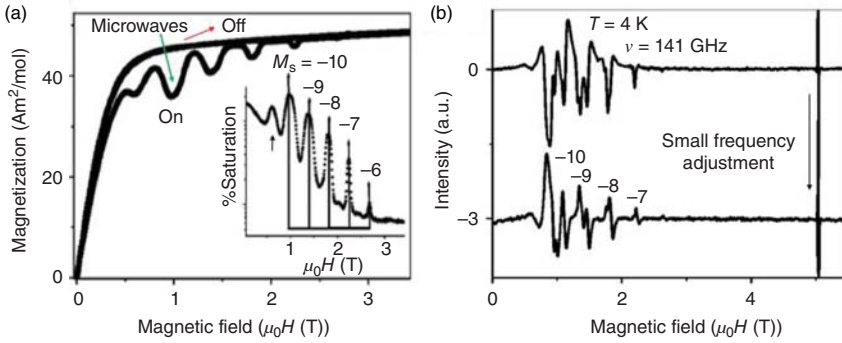


Figure 6.11 (a) HF-EPR system for Fe8 at 141 GHz and 4 K, and (b) M - T curve for the same sample. Source: Cage et al. [19]/ with permission of AIP Publishing.

M_s levels. The presence of saturation is shown in the inset of Figure 6.11b. This is equal to

$$(1 - M_{\text{on}}/M_{\text{off}}) \times 100 \quad (6.1)$$

where M_{off} and M_{on} designate the z -axis magnetization (M_z) in the absence and presence of microwave irradiation. These peak amplitudes signify quantitative knowledge of the degree of saturation of the magnetization as a function of M_s . This type of quantitative knowledge is not easily obtained by conventional HF-EPR. In other words, SQUID-based HF-EPR gives information about quantitative determination of the DC magnetic moment of nanomagnetic materials as a function of known microwave irradiation power and eliminates uncertainties in the line positions and line shapes that occur in standard single-pass transmission HF-EPR. Thus, it can be concluded that separation of the dispersive and absorptive elements for questionable spectra would be possible by performing an RF-detected reflection EPR experiment followed by a SQUID-based EPR experiment.

Magnetoencephalography (MEG) is a functional nerve imaging technique for mapping brain activities by recording magnetic fields generated by electrical currents, which occur naturally in the brain, are very sensitive to magnetometers. MEG applications include initial research in cognitive and brain processes, areas affected by preoperative pathology, determining the function of different parts of the brain, and neurofeedback. It can be used to measure brain activity in a clinical setting to find abnormal locations as well as in a laboratory environment to do image analysis.

MEG signals were first measured through the induction coil of the copper detector by David Cohen, a physicist at the University of Illinois in 1968 prior to accessing SQUID. To reduce the noise of the magnetic field, measurements were taken in a protected magnetic room. The coil detector was almost susceptible enough to result in a weak MEG and a noise that was difficult to use. Subsequently, Cohen built a better protector at MIT and used one of the first SQUID detectors designed by James Zimmerman, a researcher at Ford Motor Company, to record MEG signals. The signals obtained were almost as large as electroencephalograms (EEGs).



This prompted physicists who were looking to use the SQUID. Subsequently, various types of self-stimulating MEGs were measured.

Recent advances are in the effort to increase the portability of the MEG scanner using a magneto-sensor spin exchange relaxation-free (SERF). SERF magnets are relatively small because they do not require a large cooling system to perform. They have similar sensitivity to SQUIDs at the same time. Later on, it was found that the MEG can operate on a chip scale with an atomic magnetometer (CSAM, type SERF). More recently, in 2017, researchers produced a prototype that utilizes a SERF magnetometer mounted on a three-dimensional print.

The basis of the MEG signals is summarized in the fact that synchronous neural currents create a weak magnetic field. Brain magnetic fields have a size equal to 10 femtotesla (fT) for cortical activity and 103 fs for human alpha rhythms, which is much less than the magnetic noise of the environment in urban environments, which is about 108 fT or 0.1 μ T. Thus, a big issue of biomagnets is the weakness of the signal relative to the sensitivity of detectors and the competition with environmental noise. Electromyography (EMG) and EEG signals are generated by ionic fluid flows in dendritic neurons during synaptic transmission. According to the Maxwell equations, each electric current produces a magnetic field, and this field is measured. Network flows can be considered as bipolar flows, for example, flow with position, orientation, and size, but without any spatial dimension. According to the law of the right hand, a bipolar current causes the magnetic field to be located around the axis of its vector component.

The challenge caused by MEG determines the location of the electrical activity inside the brain from the magnetic field caused by its outside. Problems such as those model parameters (location of activity) must be estimated from measured data (SQUID signal). As a problem of inverting in comparison with previous problems model parameters, such as the place of activities, are known and the data, e.g. the field at a given distance must be estimated. The main problem is that the inverting is not a unique solution (that is, there are many answers as the correct answer) and the problem of defining the best solution can itself be a subject of intensive research. The solution may be to use models that are derived from previous knowledge of brain activity.

References

- 1 Fagaly, R. (2005). SQUID instruments and applications. *The Review of Scientific Instruments* 77.
- 2 Fagaly, R. (2006). Superconducting quantum interference device instruments and applications. *Review of Scientific Instruments* 77: 101101.
- 3 Goree, W. and Fuller, M. (1976). Magnetometers using RF-driven squids and their applications in rock magnetism and paleomagnetism. *Reviews of Geophysics* 14: 591–608.
- 4 Clarke, J. and Braginski, A. (2006). *The SQUID Handbook: Applications of SQUIDs and SQUID Systems*, vol. II. Weinheim: Wiley.



- 5 Giffard, R., Webb, R., and Wheatley, J. (1972). Principles and methods of low-frequency electric and magnetic measurements using an rf-biased point-contact superconducting device. *Journal of Low Temperature Physics* 6: 533–610.
- 6 Van Duzer, T. and Turner, C.W. (1981). *Principles of Superconductive Devices and Circuits*, 369. Edward Arnold, London; ISBN 0 7131 3432 1, 13(1); 7(1).
- 7 Orlando, T.P. and Delin, K.A. (1991). *Foundations of Applied Superconductivity*. Upper Saddle River, NJ: Prentice Hall, ISBN: 0201183234.
- 8 Cleuziou, J.-P., Wernsdorfer, W., Bouchiat, V. et al. (2006). Carbon nanotube superconducting quantum interference device. *Nature Nanotechnology* 1: 53–59.
- 9 Aprili, M. (2006). The nanoSQUID makes its debut. *Nature Nanotechnology* 1: 15–16.
- 10 Ciftja, O. (2013). Understanding electronic systems in semiconductor quantum dots. *Physica Scripta* 88: 058302.
- 11 Feynman, R.P., Leighton, R.B., and Sands, M. (1965). The feynman lectures on physics; vol. i. *American Journal of Physics* 33: 750–752.
- 12 Josephson, B.D. (1962). Possible new effects in superconductive tunnelling. *Physics Letters* 1: 251–253.
- 13 Jalili, H., Aslibeiki, B., Hajalilou, A. et al. (2022). Bimagnetic hard/soft and soft/hard ferrite nanocomposites: structural, magnetic and hyperthermia properties. *Ceramics International* 48: 4886–4896.
- 14 Hajalilou, A., Ferreira, L.P., Melo Jorge, M.E. et al. (2021). Superparamagnetic Ag-Fe₃O₄ composites nanoparticles for magnetic fluid hyperthermia. *Journal of Magnetism and Magnetic Materials* 537: 168242.
- 15 Mola, M., Hill, S., Goy, P., and Gross, M. (2000). Instrumentation for millimeter-wave magneto-electrodynamic investigations of low-dimensional conductors and superconductors. *Review of Scientific Instruments* 71: 186–200.
- 16 Hassan, A., Pardi, L., Krzystek, J. et al. (2000). Ultrawide band multifrequency high-field EMR technique: a methodology for increasing spectroscopic information. *Journal of Magnetic Resonance* 142: 300–312.
- 17 Muller, F., Hopkins, M., Coron, N. et al. (1989). A high magnetic field EPR spectrometer. *Review of Scientific Instruments* 60: 3681–3684.
- 18 Cage, B., Hassan, A.K., Pardi, L. et al. (1997). 375 GHz EPR measurements on undiluted Cr(V) salts. The role of exchange effects and g-strain broadening in determining resolution in high-field EPR spectroscopy of S = 12 paramagnets. *Journal of Magnetic Resonance* 2: 495–498.
- 19 Cage, B., Russek, S.E., Zipse, D., and Dalal, N.S. (2005). Advantages of superconducting quantum interference device-detected magnetic resonance over conventional high-frequency electron paramagnetic resonance for characterization of nanomagnetic materials. *Journal of Applied Physics* 97: 10M507.
- 20 Hill, S., Dalal, N., and Brooks, J. (1999). A multifrequency-resonator-based system for high-sensitivity high-field EPR investigations of small single crystals. *Applied Magnetic Resonance* 16: 237–245.
- 21 Lynch, W.B., Earle, K.A., and Freed, J.H. (1988). 1-mm wave ESR spectrometer. *Review of Scientific Instruments* 59: 1345–1351.



- 22 Brunel, L., Caneschi, A., Dei, A. et al. (2002). How and why the characterization of magnetic materials can give directions in the methodological development in high field-high frequency EPR. *Research on Chemical Intermediates* 28: 215–229.
- 23 Pake, G. and Purcell, E. (1948). Line shapes in nuclear paramagnetism. *Physical Review* 74: 1184.
- 24 Cage, B. and Russek, S. (2004). Design for a multifrequency high magnetic field superconducting quantum interference device-detected quantitative electron paramagnetic resonance probe: spin-lattice relaxation of cupric sulfate pentahydrate ($\text{CuSO}_4 \cdot 5\text{H}_2\text{O}$). *Review of Scientific Instruments* 75: 4401–4405.
- 25 Bal, M., Friedman, J.R., Suzuki, Y. et al. (2004). Photon-induced magnetization reversal in the Fe_8 single-molecule magnet. *Physical Review B* 70: 100408.
- 26 Wernsdorfer, W., Müller, A., Mailly, D., and Barbara, B. (2004). Resonant photon absorption in the low-spin molecule V15. *EPL (Europhysics Letters)* 66: 861.





7

The Principle of SQUID Magnetometry and Its Contribution in MNPs Evaluation

7.1 Introduction

A SQUID is a superconducting quantum interference device. It is a very sensitive magnetometer used to measure extremely subtle magnetic fields, based on superconducting loops containing Josephson junctions.

The model MPMS sample magnetometer is currently used in research laboratories worldwide and is specified for experimental and material characterization that require the highest detection sensitivities over a broad temperature range and in applied magnetic fields to 7 T. It is configured to detect the magnetic moment of a sample of material, from which the magnetization and magnetic susceptibility can be determined. For the MPMS, superconductivity is the critical enabling technology that provides for both the production of large, very stable magnetic fields and the ability to measure changes in those fields which are 14 orders of magnitude smaller than that of the foregoing-mentioned value.

In the case of the practical operation of SQUID, the sample is moved through an external magnetic field. A pickup coil links to a superconducting detector loop with parallel Josephson junctions. Any magnetic flux from the moving sample interrupts the superconducting loops. An applied bias current re-establishes the superconducting loop and indicates the magnetism of the sample. A SQUID setup and detection mechanism are schematically shown in Figure 7.1. A sample is moved through a coil-set (second-order gradiometer), giving rise to a voltage function of characteristic shape, whose amplitude is proportional to the net magnetic moment of the sample. In other words, the sample is mounted at the end of the sample holder and is passed in a vertical state. The voltage signals induced through the detection coils are transferred to the SQUID sensor. The characteristic shape of the response function, from which the net magnetic moment is induced in the sample, is attributed to the detection-coil configuration geometry.

To operate the SQUID, the SQUID device is firstly refilled with liquid helium at 2.4 K. A computer reports the progress of the filling (the rate should be slow at about 2.5% per minute), which is followed by setting a magnetic field, e.g. 500 Oe. Then, different conditions establish for measurement. For example, it can be programmed to measure magnetism as the temperature is changed from 350 to 10 K, establishes a 50 Oe field and then scan from 10 to 350 K.



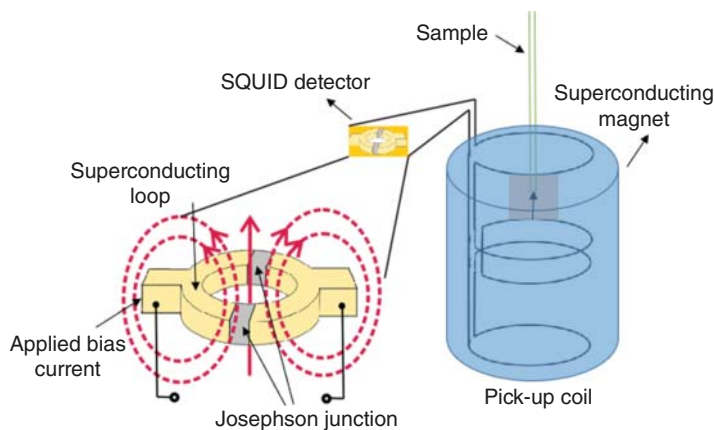


Figure 7.1 Schematic representation of SQUID setup and detection mechanism.

7.2 The Correct Procedure to Perform the Zero Field Cooling (ZFC) and Field Cooling (FC) Magnetic Study

The Zero Field Cooling (ZFC) curve shows magnetism over-temperature by applying a small external magnetic field of about 50 Oe as an example. This simply means that the sample is cooled from a high temperature, e.g. 400 K to a low temperature, e.g. 5 K, then a small magnetic field, e.g. 50 Oe is applied, and the measurement is accomplished in the warming mode. It should mention that the temperature range of 5–400 K can be varied depending on the aim and information required. In short, in the ZFC mode, the measurement is carried out as:

1. Switch off the magnetic field ($H = 0$)
2. Cool down the sample to e.g. $T = 5$ K.
3. At $T = 5$ K, switch on the magnetic field and a small field is applied, e.g. 50 Oe.
4. Perform the measurements of magnetization in terms of temperature, $M(T)$, e.g. from 5 to 400 K.

In the case of Field Cooling (FC) circumstance, which is followed by ZFC measurement, the same applied magnetic field of 50 Oe is kept, and the measurement is carried out in two modes: FCC or FCW.

- (i) Field cooled cooling (FCC) data are collected during the cooling state, e.g. from 400 to 5 K. Indeed, in the FC process, the data are collected during the cooling sample from 400 to 5 K. It simply means that from the last step of ZFC, the field is kept on at the same field of ZFC ($H = 50$ Oe), and the temperature declines from 400 to 5 K to record $M(T)$ data.
- (ii) Field cooled warming (FCW): Similar to ZFC, the sample is cooled from 400 to 5 K, but under an applied magnetic field of 50 Oe, and the data are then collected during the warming mode from 5 to 400 K.



There is a slight difference between the magnetization FCC and FCW modes during measuring magnetization in terms of temperature, which can be accounted for by:

- the calculation based on flux density profile,
- the existence of the quenching effect, which will cause the FCC and FCW modes to be not, particularly in the vicinity of the blocking temperature.

For those modes to be identical:

- One must change the applied magnetic field or give more relaxation time at every temperature before performing the measurement.
- The specimen should be heated above T_c after each measurement to erase the thermo-magnetic history.

In ZFC experiments, as the name implies, no external field is applied. However, in practice, we apply a small external field, e.g. 50 Oe. This is because when the external field is zero, particles are randomly oriented and when cooled, these particles remain oriented and become immobilized. Now, by applying the field, the response will be related to the anisotropy of the particles. If there is strong anisotropy, it would increase at low temperatures; therefore, the field for magnetic saturation becomes very large. However, if the sample is cooled in the presence of a magnetic field, the situation becomes different. For example, at room temperature, the spins would be oriented by the magnetic field and if cooled in the applied field, the spins have less chance to disorient. So, under this condition, magnetic saturation is attained. In other words, when one cools the particles under the presence of the field, the moments freeze as well. In FC, depending on the cooling field, the particle's direction of magnetization will be frozen in a direction other than the easy axis; thus, texture effects will be introduced.

7.3 The Concept of Merging Zero Field Cooled (ZFC) and Field Cooled (FC) Curve Completely with Each Other

In the case of bifurcation or merging of the ZFC and FC curves depends on several factors such as how much external magnetic field is applied, the size of magnetic particles, and measurement temperature. It is also important to confirm whether this bifurcation is related to the glass phase (which will be explained later on), or it is only due to anisotropy present in the system. The difference is not revealing the glassy magnetism. There are some other methods and measurements for concluding the presence of spin glass.

Furthermore, if the ZFC and FC are identical, then there are no nanoparticles (NPs) in the sample. If they are different, there is a nanoparticle in the sample and the maximum point of the ZFC curve is called blocking temperature (T_B). One can use T_B to calculate the size of the particles.



In the case of superparamagnetic nanoparticles (SPMNs), the process is irreversible and the FC and ZFC curves are separate. The magnetic moment plotted against the magnetic field is also not a straight line.

Moreover, the divergence of ZFC and FC suggests some kinds of magnetic frustration, either due to coexisting ferro- and antiferromagnetic phases or due to non-interacting SPMNs. If an $M-H$ hysteresis is with a finite coercive field, then most probably, the system is a spin or a cluster glass kind of system. But one needs to do temperature and frequency-dependent AC susceptibility measurements for verifying that.

7.4 Types of Information Obtained from the ZFC and FC Curves

One can get various information from these curves depending on the interest and aim. Some are:

7.4.1 Blocking Temperature

The blocking temperature (T_B) is normally indicative of the energy barrier distribution. One can obtain the difference between the field cooled susceptibility and the zero-field susceptibility, which provides a direct measurement for the blocking temperature distribution. In general, it can be attained by considering the ZFC-FC susceptibility as a function of temperature. Some theoretical models that need to consider the magnetic characteristics of magnetic nanoparticles would be found in Refs. [1–3] according to Néel, Brown, Bean, and Livingston, respectively. According to them, the atomic magnetic moments within the particles act coherently and their magnetic moments can be denoted by a single vector with a magnitude as follows:

$$\mu = N\mu_0 \quad (7.1)$$

where μ_0 is the average magnetic moment of an atom and N is the number of atoms in the particle. By taking into account that the relaxation time (τ) is a function of temperature (T) and anisotropy barrier (E_a), we can express:

$$\frac{1}{\tau} = f_0 \exp\left(\frac{-E_a}{k_B T}\right) \quad (7.2)$$

where f_0 is a frequency factor on the order of 10^9 s^{-1} and k_B is Boltzmann's constant [2]. E_a is determined by $E_a = KV$ where K is the anisotropy energy density constant, and V is the particle volume [4–6].

Normally, the blocking region is wide; therefore, a representative T_B value of the sample may not be well defined. However, there are several different criteria employed to determine a representative T_B from ZFC-FC data. Some studies suggest the inflection point (IP) criterion [7, 8], while others consider the maximum ZFC magnetization temperature [9–11]. Both criteria are still under



debate [8, 12–14]. Some other approaches have been considered as alternative approaches, e.g. proposing a route in which the T_B distribution is measured from the T derivative of the difference between ZFC and FC curves [15–17]. In this case, the maximum peak that emerged in the ZFC curve is not indicating T_B . The T_B is given by $T_{\max} = \beta \langle T_B \rangle$, where β is reported to be in the range of 1–2.5 [18]. The smaller the particle size distribution, the closer the value of β to 1. For determining the β value and the average blocking temperature $\langle T_B \rangle$, the $\Delta M = M^{\text{FC}} - M^{\text{ZFC}}$ versus temperature (T) is plotted, as shown in Figure 7.2. Whatever the curve is sharper, the value of β is small. Thus, the distribution of nanoparticle blocking temperatures will be narrower [15, 20, 21]. By deriving the ΔM curve as temperature, the distribution of blocking temperatures is achieved [18], which is shown in the inset of Figure 7.2. The Fe_3O_4 (F) NPs present two peaks (two blocking temperatures) that can be due to the presence of maghemite ($\gamma\text{-Fe}_2\text{O}_3$) as the second phase in the NPs structure, which cannot be seen in the FTIR and X-ray diffraction (XRD) diagrams due to the overlap of their peaks with Fe_3O_4 . As expected, only one blocking temperature is observed in the CoFe_2O_4 NPs (C sample) while in the $\text{Fe}_3\text{O}_4/\text{CoFe}_2\text{O}_4$ NPs (F/C sample) and $\text{CoFe}_2\text{O}_4/\text{Fe}_3\text{O}_4$ NPs (C/F sample), two peaks are observable. In the F/C sample, some uncoated F NPs with lower blocking temperatures may coexist with shell/core NPs, while the small peak in C/F NPs

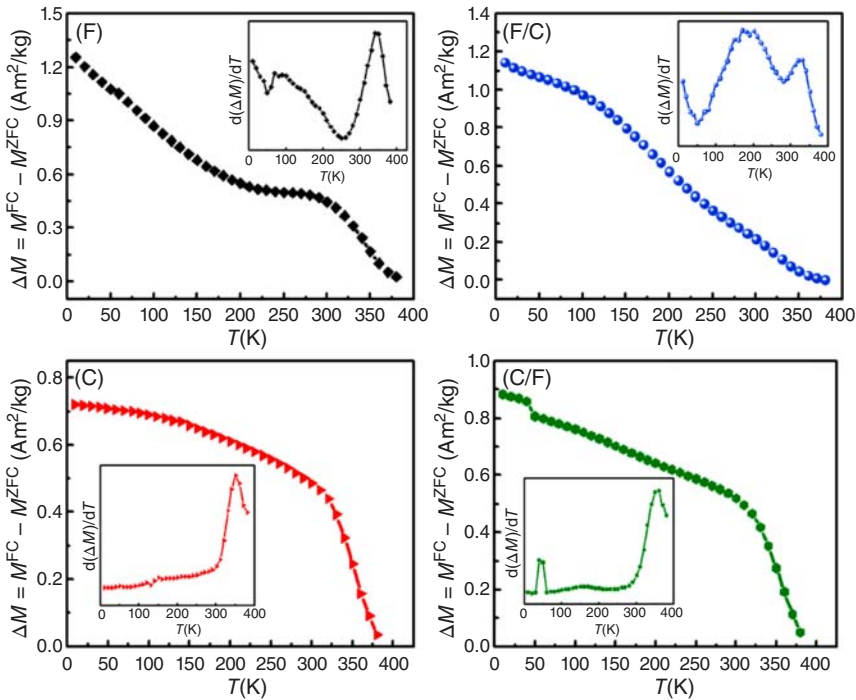


Figure 7.2 Schematic representation of $\Delta M = M^{\text{FC}} - M^{\text{ZFC}}$ as a function of temperature. The inset of the figure shows the distribution of the blocking temperatures of the sample fitted with a Gaussian function. Source: Jalili et al. [19]/with permission of Elsevier.



at 50 K reflects a discontinuity in ZFC behavior that can hint at the presence of adsorbed oxygen and is not associated with the NPs [22, 23].

T_B shifts to a higher temperature in the ZFC curve in the case of performance of the samples in powder form due to the presence of big dipolar interactions between the particles [24–26], which would not be neglected. In this circumstance, the temperature at which the ZFC curve has the maximum is proposed to yield the upper limit for T_B .

7.4.2 Néel Temperature

The Néel temperature or magnetic ordering temperature (T_N) is the temperature above which an antiferromagnetic material becomes paramagnetic – that is, the thermal energy becomes large enough to destroy the microscopic magnetic ordering within the material.

Both ZFC and FC curves show some differences below the Néel temperature where the first and/or second derivatives of the free energy play an important role in magnetic properties variation.

7.4.3 Types of Magnetism

Diverse types of magnetism such as para, ferro, antiferro, and superparamagnetism are differentiated from FCC–ZFC measured data, especially ferro with Curie temperature (T_C), and antiferromagnetism by Néel temperature (T_N).

The ZFC–FC curves are generally measured for static magnetization and can be characterized by an open-loop (in the case of a ferromagnet) or closed-loop (superparamagnet) or linear M – H (paramagnetism) or zero spontaneous magnetization (antiferromagnet) or negative magnetization (diamagnet), etc.

7.4.4 Spin Glass (SG) and Superparamagnetic (SPM)

In the case of thermo-magnetic irreversibility, i.e. the existence of a difference between ZFC and FC curves, a spin glass or superparamagnetic phase is predicted. However, only ZFC and FC curves cannot confirm that, and to confirm the real phase, AC magnetization measurement is required as well. Frequency dependence of real and imaginary susceptibility provides information on the real magnetic phase.

If the corresponding peak to magnetic transition temperature increases or decreases by increasing frequency, then the change is plotted as a function of frequency, and depending on some fitting parameters, either spin glass or superparamagnetic transition is predicted. AC susceptibility measurements can provide more information about the spin-glass state: χ' (real part) and χ'' (imaginary or dissipative part). Their dependence on frequency (f) yields information on the relaxation process based on Arrhenius law.

For purely ferromagnetic transition, no thermomagnetic irreversibility is expected. However, for a weak ferromagnet or a frustrated system with a mixed



antiferromagnetic–ferromagnetic (AFM–FM) phase, the irreversibility is seen. But, in general, these transitions are not a frequency-dependent factor. However, for spin-glass systems, the ZFC susceptibility shows a large peak at T_{sg} , and when the sample is cooled under the same field (FC), the static susceptibility curve is not reversible; it shows a plateau or a step because of a quenched part of magnetic moments under the field.

7.5 SQUID Magnetometry: Magnetic Measurements

7.5.1 Magnetization Versus Temperature, $M(T)$

To understand deeply the correlation between magnetization (M) and temperature (T), it is essential to ponder the thermal fluctuation effect that allows transition between stable configurations. In doing so, it is possible to simulate M as a function of T experiments as the extensively performed ZFC–FC routine. In other words, the $M(T)$ measurement is accomplished using a DC magnetic field to figure out where magnetic transitions occur. As mentioned above, in general, there are three protocols for making $M(T)$ measurements: ZFC, FCW, and FCC. These curves provide information on the magnetic transitions within the samples, the interparticle interactions, and the size distribution of the nanoparticles. The ZFC curve also yields a desirable idea on T_B , which is related to the apparent freezing, within the measuring time of the magnetometer, of the magnetic moments of the nanoparticles as the temperature decreases [27].

In the case of a noninteracting magnetic nanoparticles sample, a narrow temperature region exists in which the system performs a transition between reversible and irreversible regimes. The thermal energy (KT) is initially much smaller than the anisotropy barrier (KV) once the sample is subjected to heating under an applied field. Thus, the magnetization remains null. When KT is equal to KV , the magnetization grows quickly up to its thermodynamic equilibrium value due to the exponential dependence of the Néel relaxation time with temperature [3], which determines the above-mentioned transition regime. T_B can be expressed as the inflection point (IP) of this growth, and its experimental determination is a key factor in the characterization of the magnetic nanoparticles.

The magnetic relaxation is slower than that of the measurement time at low temperatures. Thus, the magnetic domains are unable to vary their orientation in the measurement time window and the magnetic moments are blocked. The transition between the two regimes, superparamagnetic and blocked, is associated with a maximum in ZFC curves, determining the blocking temperature (T_B), which is dependent on several parameters as:

7.5.1.1 Blocking Temperature (T_B) as a Function of Particle Size Distribution

A size dispersion is always available in the areal sample, which is typically well-described by a log-normal distribution [8, 19, 27]. It is believed that the size of nanoparticles is one of the main parameters of nanostructured materials that affect



the magnetic characteristics, such as saturation magnetization (M_s), coercivity (H_c), and in particular T_B of the sample. It simply means that once the size of particles becomes ultrafine, their surface-to-volume aspect ratio increases considerably [28]. This, in turn, affects the distribution of blocking temperature, power, and type of interactions, as well as how the system responds to the external field of operation.

Different particle sizes imply a different anisotropy barrier (KV), and therefore, a different T_B for each size fraction is expected in real ZFC–FC experiments. T_B is where the transition from the blocked to superparamagnetic regimes occurs during the warming process. This transition is determined by a peak in the ZFC curve. The breadth of this peak serves as an indicator of the size distribution of the nanoparticles within various samples; a broader peak indicates a larger size distribution than that of a narrower peak [29]. This is due to the fact that as the size of the nanoparticles varies, the temperature where magnetic blocking takes place changes as well. It has been reported that the smaller nanoparticles tend to have a lower T_B , while larger nanoparticles tend to have a higher T_B , e.g. as shown in Figure 7.3. Therefore, a wider range of blocking temperatures and a broader peak in the ZFC curve would emerge if there were a wide size distribution. Strong magnetic dipolar interactions between nanoparticles can also broaden the maximum of the ZFC curve and flatten out the FCW curve [31].

The temperature below which the ZFC and FCW curves begin to separate from each other is signed as the irreversibility temperature (T_{irr}), which is frequently concerned with the magnetic blocking of the largest particles. Systems where T_{irr} is much higher than T_B often show a large particle size distribution [27, 32–38]. Above T_{irr} , the system enters a superparamagnetic regime with minimal interactions. It can be seen from Figure 7.3 that both samples undergo a transition from the blocked state to the superparamagnetic state with an increase in temperature. The broadening of the ZFC $M(T)$ curve observed for 12-nm Fe_3O_4 nanoparticles points to the system with stronger dipolar interparticle interactions, whereas the narrow shape of the ZFC $M(T)$ curve observed for 6-nm- Fe_3O_4 nanoparticles is associated with the perspective of an assembly of weakly interacting single domain (SD) particles [37].

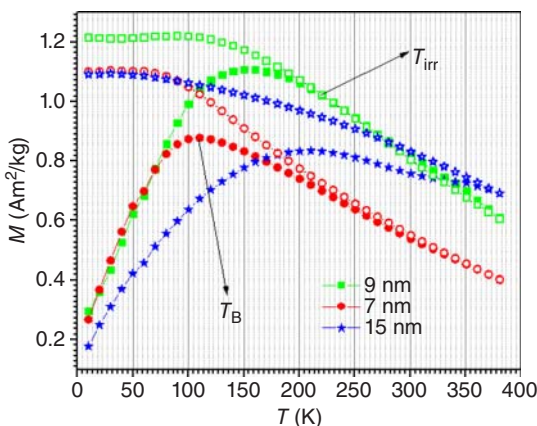


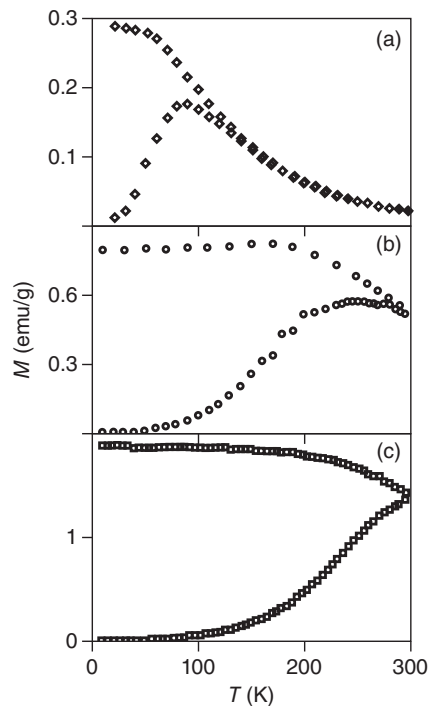
Figure 7.3 Zero-field cooled and field cooled warming magnetization versus temperature curves of magnetite with different particle sizes; ZFC curves (closed signs), and FC curves (open signs). Source: Hajalilou et al. [30]/with permission of Elsevier.



In some cases, the aforementioned statement may not be valid for comparing large and small nanoparticles for T_B evaluation. It can be due to a difference in the strength of inter-particle interactions in the two samples. Inter-particle interactions are factors that affect the particle blocking temperature. Experience has shown that the more inter-particle interactions are, the greater the locking temperature is [39]. This phenomenon is justified by the direct connection of the energy barrier between the equilibrium magnetization states and the strength of magnetic interactions. Whatever the interactions are stronger, the energy barrier increases and the possibility of rotation of the superspin of the nanoparticle decreases with heat flushes. Thus, the magnetic moment of the particle is located in a locked state. To exit from the blocked state and to find the superparamagnetic feature, higher temperatures will be needed. One of the common methods for investigating the power of inter-particle interactions is the study of the dynamic behavior of magnetism and the measurement of magnetic permeability [40–43].

The $M(T)$ for ZFC and FC curves for Co-ferrite nanoparticles with different particle sizes of about 3, 5, and 6 nm are shown in Figure 7.4 [44]. It was found that the T_B to be about 85 and 250 K for the 3- and 5-nm sized particles, respectively, but it is above room temperature for the 6-nm-sized particles. The shape of the FC curve suggests that a noninteracting phenomenon is a good approximation in the 3-nm-sized particles [45]. It is not the case for the 5-nm-sized particles where the corresponding curve is rather flat. In fact, a temperature-independent FC curve would be due to sizable interactions or aggregation effects [46]. The magnetic interactions must

Figure 7.4 ZFC–FC magnetization curves for (a) 3 nm, (b) 5 nm, and (c) 6 nm for Co-ferrite nanoparticles. Source: [44]/with permission of AIP Publishing.



be stronger in the case of the 5-nm-sized particles because the net moment is about three to four times larger than that of the 3-nm-sized particles; assuming that the mean interparticle distance is the same in all the samples. Thus, the peak temperature (T_g) in the 5-nm-sized particles must be increased with respect to its value in the absence of interactions. Nevertheless, by comparing the ratios of the T_g (≈ 3) and the mean volumes $\langle V \rangle$ (≈ 4) for the 5 and 3-nm-sized particles and taking into account the fact that T_g for the 5-nm-sized particles is overestimated, one can say that the anisotropy constants (K) in the two-particle sets must be of the same order of magnitude (within a factor of 2).

7.5.1.2 Dependency of Blocking Temperature (T_B) on the Volume of Particles

Based on the Néel–Brown model, T_B as a function of volume for noninteracting particles is given as:

$$T_B = \frac{K_{\text{eff}} V}{k_B \ln \left(\frac{\tau}{\tau_0} \right)} \quad (7.3)$$

where τ is the characteristic measuring time and τ_0 is the particle relaxation time ($\tau_0 \sim 10^{-9}$ – 10^{-11} seconds, e.g. is of the order of 10^{-10} seconds for ferro- or ferrimagnetic materials), K_{eff} is the effective magnetocrystalline anisotropy energy density, k_B is the Boltzmann constant, and V is the particle volume. The K_{eff} consists of the K_v , which is related to the volume of the particle (V) as $K_v = V_0 \exp(4.5\sigma_d^2)$, where σ_d is a standard deviation and the K_s is the surface contributions as $6K_s/d$, d is the linear particle size. Equation (7.3) indicates that the T_B would increase with the increase in the volume of the particles.

In the quasi-static magnetic measurements ($\tau \sim 10^{1-2}$ seconds), the T_B is proportional to the effective anisotropy (K_{eff}) and volume of the magnetic particle (V) via

$$T_B \approx \frac{K_{\text{eff}} V}{25k_B} \quad (7.4)$$

where k_B is the Boltzmann constant [27, 47–49].

On the other hand, in the case of the interactions between particles, T_B as a function of V is given as:

$$T_B = \frac{(K_v + 6K_s/d)V + U_{\text{int}}}{k_B \ln \left(\frac{\tau}{\tau_0} \right)} \quad (7.5)$$

In interparticle interactions, T_B would increase [40, 50–54], which tends to have less contribution to the K_{eff} proportional to the interaction energy U_{int} . Both the equations reveal that T_B has a direct relationship with V for both the isolated and interacted particles.

7.5.1.3 The Field Dependence of the Blocking Temperature

To determine a blocking temperature (T_B) and magnetic field (H) correlation, the effective magnetic anisotropy constant (K_{eff}) for magnetic nanoparticles upon weak interparticle interactions is required to be considered. The $M(T)_{\text{ZFC}}$ dependence of



H for noninteracting particles in a sufficiently weak applied field can be expressed through [42, 49, 54–56]:

$$\frac{M(T)}{H} = \frac{M_s^2}{3K_{\text{eff}}} \left[\ln \left(\frac{\tau}{\tau_0} \right) \int_0^T \frac{T_B}{T} f(T_B) dT_B + \int_T^\infty f(T_B) dT_B \right] \quad (7.6)$$

where M_s is the saturation magnetization of a sample and $f(T_B)$ is the blocking temperature distribution function. Studies have proven that the lognormal distribution is properly employed to describe the size characteristics of nanoparticles [49, 57]. Thus, the lognormal distribution as a blocking temperature distribution function of particles is given as:

$$f(T_B) = (T_B \cdot S \cdot (2\pi)^{1/2})^{-1} \exp \left\{ -\frac{[\ln(T_B/n)]^2}{2S^2} \right\} \quad (7.7)$$

with a dispersion of $\ln(T_B) = S^2$ and an average value of $\langle T_B \rangle = n \cdot \exp(S^2)$.

Furthermore, the field dependence of T_B for noninteracting particles is given by the classical relation as follows:

$$T_B(H) = \frac{K_{\text{eff}} V}{k_B \ln \left(\frac{\tau}{\tau_0} \right)} \left[1 - \frac{M_s H}{2K_{\text{eff}}} \right]^{3/2} \quad (7.8)$$

On the other hand, a modified random anisotropy model (RAM) [58], which is developed in [59, 60] can be employed in the case of interacting particles. This model deals not with an isolated particle, but with a cluster of a larger size, which involves a certain number of particles depending on volume concentration (x). The correlation length (L_H) of such a cluster depends on the external field as:

$$L_H = \sqrt{\frac{2A_{\text{eff}}}{M_s H + C}} + d \quad (7.9)$$

Here, A_{eff} is attributed to the interparticle interaction intensity and has the meaning of volume constant and C is responsible for the interaction intensity variation with particle concentration and plays a key role only in fields close to zero [59, 60]. In this case, the anisotropy constant also modifies as:

$$K \rightarrow \frac{K}{\sqrt{N}} = \frac{K}{\sqrt{1 + \frac{x(L_H^3 - d^3)}{d^3}}} \quad (7.10)$$

where N is the number of particles in a cluster, which, in turn, can be expressed through the correlation length. As a result, the dependence of T_B on H is modified as:

$$T_B(H) = \frac{K_{\text{eff}} [d^3 + x(L_H^3 - d^3)]}{k_B \ln \left(\frac{\tau_m}{\tau_0} \right) \sqrt{1 + \frac{x(L_H^3 - d^3)}{d^3}}} \times \left[1 - \frac{HM_s \sqrt{1 + \frac{x(L_H^3 - d^3)}{d^3}}}{2K_{\text{eff}}} \right]^{3/2} \quad (7.11)$$

This expression is given for cubic particles ($V = d^3$).

The temperature dependence of ZFC and FC curves measured at different magnetic fields is exhibited in Figure 7.5. FC data show a sharp increase at a certain



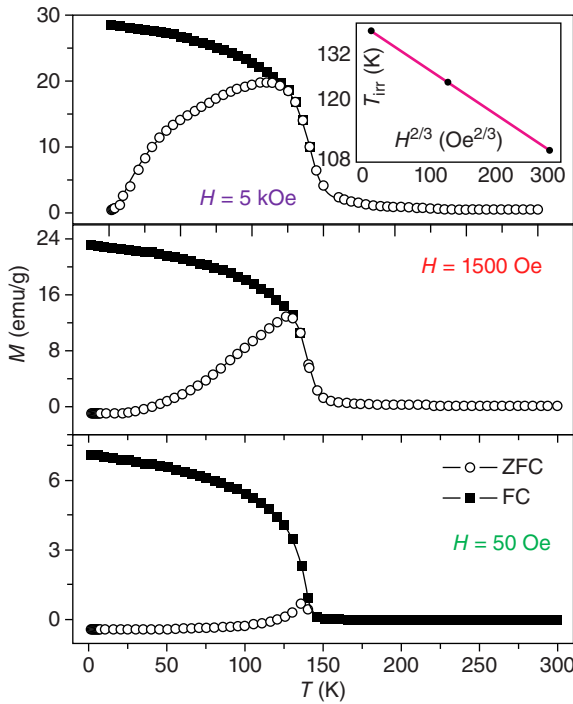


Figure 7.5 M versus T for ZFC and FC curves at different magnetic fields. The inset shows the plot of irreversibility temperature (T_{irr}) against $H^{2/3}$ following the AT relation. Source: Maiti et al. [61]/with permission of AIP Publishing.

temperature, suggesting the ferromagnetic transition. This is associated with FM superexchange of the order $\text{Co}^{2+}-\text{O}^{2-}-\text{Mn}^{4+}$ pair [62]. From the inverse susceptibility ($1/\chi_{\text{FC}}$), the ferromagnetic Curie temperature was found to be 139 K. The ZFC and FC data indicate large thermomagnetic irreversibility with irreversibility temperature (T_{irr}) being close to T_{C} . A large difference between the FC and ZFC data suggests that the samples have short-range FM interactions. In a low field, $M(T)$ in ZFC mode shows a sharp peak. With the increase in the magnetic field, this peak becomes broader and shifts to lower temperatures, and, simultaneously, T_{irr} is shifted to lower temperatures. The inset of Figure 7.5 shows the plot of T_{irr} against $H^{2/3}$ which fits satisfactorily with the Almeida–Thouless (AT) relation viz., $T_{\text{irr}} \propto H^{2/3}$ over a range between 50 Oe and 5 kOe [63].

7.5.1.4 The Blocking Temperature (T_{B}) Versus Applied Pressure, and Density

The variation of T_{B} due to pressure can be described based on changes in the distance of particles as well as the sample density. It simply means that once the distance between particles varies, it will spontaneously affect the interparticle interaction. This, in turn, will give rise to the variation of the magnetic characteristics, e.g. T_{B} . In other words, to identify the causes of the T_{B} variation, one may take into account the variations in density of a sample as a result of the interparticle distance and interaction, or the change in shape or size of particles. Figure 7.6a indicates that T_{B} increases by increasing the compressing pressure. This is because by compressing the sample, the distance among the particles decreases, resulting in higher density [64–71], and consequently higher blocking temperature. In the following, we will



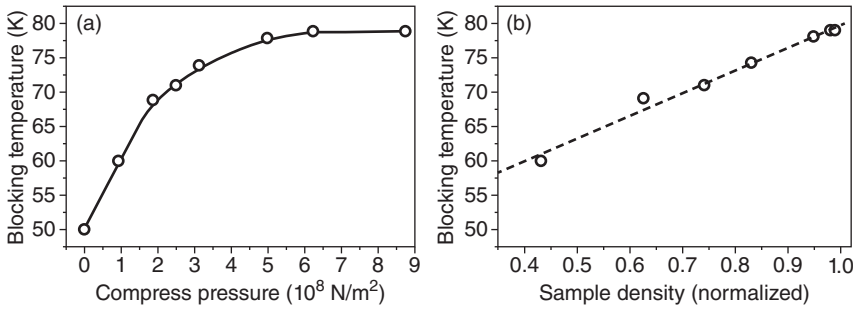


Figure 7.6 (a) T_B versus compress pressure, and (b) T_B versus D . Source: Dai et al. [5]/with permission of American Physical Society.

discuss how a change in interparticle distance is the main reason for the increase in T_B .

By considering the dipole–dipole interaction as the main coupling mechanism between magnetic particles, for two identical particles with the magnetic moment of M , interaction is given as [5, 72–74]:

$$E_{\text{int}} \propto \frac{M^2}{r^3} (3 \cos \psi_1 \cdot \cos \psi_2 - \cos \alpha) \quad (7.12)$$

where α is the angle between the two moments, r is the distance between the particles, and ψ_1 and ψ_2 are the angles between r and the two moments, respectively. Compressing alters the density of the sample and declines the average distance between particles (r), which gives rise to increased interaction among the particles. According to the following equation:

$$T_B = \frac{(E_a + E_{\text{int}})}{k_B \ln(tf_0)} \quad (7.13)$$

where E_a is the anisotropy energy barrier, E_{int} is the interaction energy, f_0 is a frequency factor on the order of 10^9 s^{-1} , k_B is Boltzmann's constant, and t is the experimental measuring time [2, 74, 75], an enhanced T_B is expected. Once only the anisotropy energy barrier (E_a) is taken into an account, the T_B of an ideal superparamagnetic particle system can be described as [6, 76]:

$$T_B = \frac{E_a}{k_B \ln(tf_0)} \quad (7.14)$$

Now, by taking into account the density (D) as a function of particle distance (r), $D \propto r^{-3}$, from Eqs. (7.12), (7.13), and (7.14) it can be found that the T_B has a linear function with D ; that is $T_B \propto D$. This phenomenon is exhibited in Figure 7.6b for iron oxide nanoparticles [5].

7.5.1.5 Effect of Heat Treatment on Blocking Temperature

This phenomenon is described by considering the heating temperature on particle size and distribution. Furthermore, the relation between M_s and temperature can be given as in Refs. [70, 77]:

$$M_s = 8.1661 \exp\left(\frac{3T}{1000}\right) \quad (7.15)$$



In terms of coercivity, it would reduce with the increase in particle size in large-grained polycrystalline soft magnetic materials according to the well-accepted $1/D$ law [78, 79]. This suggests that by increasing the heating temperature the particle growth occurs, which results in an increase in M_s and a decrease in H_c values. Since the results of the research have shown that T_B would increase by increasing the size of particles [26, 29, 32–38, 44, 45], it is expected that the increasing temperature would cause particle growth and as a result increase in the T_B . One example is given based on Cruz et al.'s investigation by considering the heating temperature of T_B in the synthesis of the ferrite nanoparticles [26]. Their results revealed that the T_B value is 320 K for a sample heated at 175 °C and 355 K for a sample heated at 230 °C. In the case of the nanoparticles prepared by the standard hydrothermal method, the maxima of the ZFC curves are above 390 K, higher than 175 and 230 °C-heated samples, in agreement with their larger particle size distribution. The corresponding ZFC curve exhibited a maximum between 300 and 400 K, indicating that a significant part of the nanoparticle distribution is in the superparamagnetic state and explaining the low coercivities obtained in the hysteresis curves at this temperature (Figure 7.7). A similar result was observed for other ferrites such as Mn ferrite. They finally reported that as T_B is closely associated with the size of nanoparticles, the higher value obtained for the samples heated at higher temperatures is associated with the higher diameters of these ferrite nanoparticles. This is in good agreement with other work's results [23, 80].

7.5.2 Magnetization as a Function of Applied Magnetic Field

This measurement can be established based on $M-H$ (for powder and liquid form samples), and $B-H$ hysteresis curves (for pellet or toroid shape samples). It normally gives information about M_s , remanence (M_r), coercivity (H_c), and energy stored by considering the area of the hysteresis loop. The magnetic moment as a function of

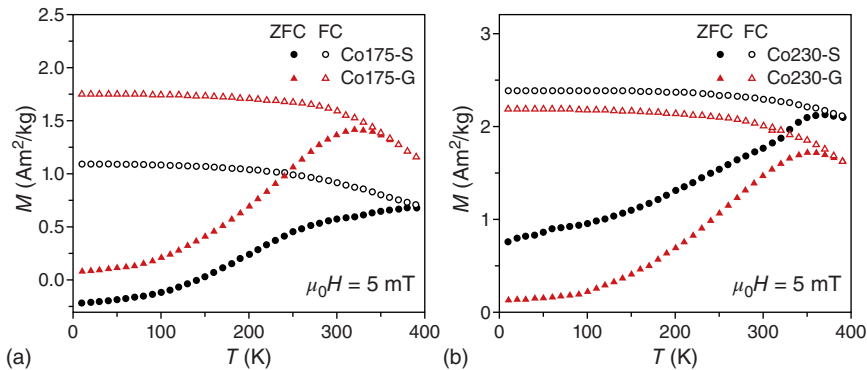


Figure 7.7 M as a function of temperature for Co ferrite samples synthesized at (a) 175 °C with standard (S) and in the presence of gelatin (G), and (b) 230 °C with standard (S) and in the presence of gelatin (G). Source: Ferreira et al. [25]/with permission of Royal Society of Chemistry.



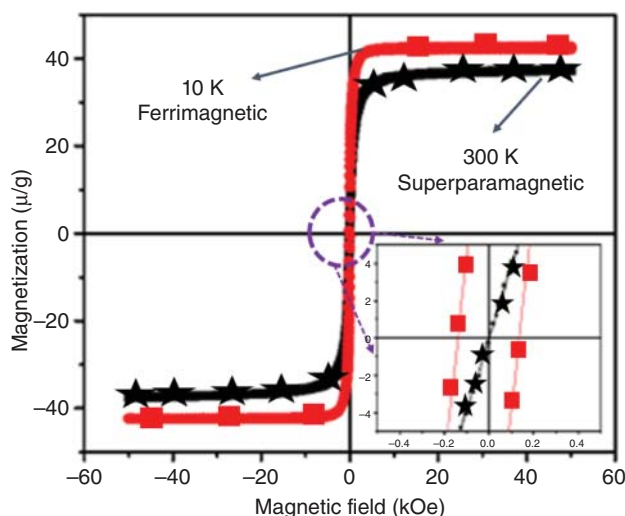


Figure 7.8 M - H hysteresis curves of Ni-ferrite NPs in the case of superparamagnetic (300 K) and ferrimagnetic state (10 K).

the applied DC magnetic field is recorded to further probe the sample. The magnetic moment of a sample is recorded as the external magnetic field is altered from positive to negative values. It has been proven that in the case of a ferromagnetic blocked state ($T < T_B$), the maximum magnetization and the coercivity would enhance as temperature declines [27, 81], as shown in Figure 7.8. At 300 K, the 7-nm-sized particles do not exhibit any trace of hysteresis or remnant magnetization and coercivity, which is a characteristic feature of the superparamagnetic state, while for the 7-nm-sized particles at 10 K, the curve exhibits a clear hysteresis with an $H_c = 138$ Oe, which is a characteristic of the blocked states of ferromagnetic particles.

The fluctuation for coercivity (H_c) values with particle size has been reported below blocking temperature. The H_c first declined with a reduction in particle size from 150 to 11 nm but increased sharply for the smallest particles of 4 nm [40]. In another study, a slight enhancement in H_c value was observed once the particle size declined from 12 to 6 nm and a sudden increase for 4 nm Fe_3O_4 nanoparticles [82]. It can be concluded that a remarkable increase of H_c for 4-nm-sized particles is attributed to the strong decline of maximum magnetization due to a huge surface spin disorder presented in the samples.

References

- 1 Néel, L. (1949). Influence des fluctuations thermiques sur l'aimantation de grains ferromagnétiques très fins. *Comptes Rendus Hebdomadaires Des Seances De L Academie Des Sciences* 228: 664–666.
- 2 Brown, W.F. Jr. (1963). Thermal fluctuations of a single-domain particle. *Physical Review* 130: 1677.



- 3 Bean, C. and Livingston, J.D. (1959). Superparamagnetism. *Journal of Applied Physics* 30: S120–S129.
- 4 Dimitrov, D. and Wysin, G. (1996). Magnetic properties of superparamagnetic particles by a Monte Carlo method. *Physical Review B* 54: 9237.
- 5 Dai, J., Wang, J.-Q., Sangregorio, C. et al. (2000). Magnetic coupling induced increase in the blocking temperature of γ -Fe₂O₃ nanoparticles. *Journal of Applied Physics* 87: 7397–7399.
- 6 El-Hilo, M., O'grady, K., and Chantrell, R. (1992). Susceptibility phenomena in a fine particle system: I. Concentration dependence of the peak. *Journal of Magnetism and Magnetic Materials* 114: 295–306.
- 7 Schmitz-Antoniak, C. (2015). X-ray absorption spectroscopy on magnetic nanoscale systems for modern applications. *Reports on Progress in Physics* 78: 062501.
- 8 Bruvera, I., Mendoza Zélis, P., Pilar Calatayud, M. et al. (2015). Determination of the blocking temperature of magnetic nanoparticles: the good, the bad, and the ugly. *Journal of Applied Physics* 118: 184304.
- 9 Sankar, S., Berkowitz, A., Dender, D. et al. (2000). Magnetic correlations in non-percolated Co–SiO₂ granular films. *Journal of Magnetism and Magnetic Materials* 221: 1–9.
- 10 De la Presa, P., Luengo, Y., Velasco, V. et al. (2015). Particle interactions in liquid magnetic colloids by zero field cooled measurements: effects on heating efficiency. *The Journal of Physical Chemistry C* 119: 11022–11030.
- 11 Hajalilou, A., Ferreira, L.P., Jorge, M.E.M. et al. (2021). Superparamagnetic Ag-Fe₃O₄ composites nanoparticles for magnetic fluid hyperthermia. *Journal of Magnetism and Magnetic Materials* 537: 168242. <https://doi.org/10.1016/j.jmmm.2021.168242>.
- 12 Respaud, M., Broto, J., Rakoto, H. et al. (1998). Surface effects on the magnetic properties of ultrafine cobalt particles. *Physical Review B* 57: 2925.
- 13 Mamiya, H., Nakatani, I., Furubayashi, T., and Ohnuma, M. (2002). Analyses of superparamagnetism-magnetic properties of isolated iron-nitride nanoparticles. *Transactions of the Magnetism Society of Japan* 2: 36–48.
- 14 Tournus, F. and Tamion, A. (2011). Magnetic susceptibility curves of a nanoparticle assembly II. Simulation and analysis of ZFC/FC curves in the case of a magnetic anisotropy energy distribution. *Journal of Magnetism and Magnetic Materials* 323: 1118–1127.
- 15 Hansen, M.F. and Mørup, S. (1999). Estimation of blocking temperatures from ZFC/FC curves. *Journal of Magnetism and Magnetic Materials* 203: 214–216.
- 16 Mamiya, H., Ohnuma, M., Nakatani, I., and Furubayashim, T. (2005). Extraction of blocking temperature distribution from zero-field-cooled and field-cooled magnetization curves. *IEEE Transactions on Magnetics* 41: 3394–3396.
- 17 Micha, J., Dieny, B., Régnard, J. et al. (2004). Estimation of the Co nanoparticles size by magnetic measurements in Co/SiO₂ discontinuous multilayers. *Journal of Magnetism and Magnetic Materials* 272: E967–E968.



- 18 Gittleman, J., Abeles, B., and Bozowski, S. (1974). Superparamagnetism and relaxation effects in granular Ni-SiO₂ and Ni-Al₂O₃ films. *Physical Review B* 9: 3891.
- 19 Jalili, H., Aslibeiki, B., Hajalilou, A. et al. (2022). Bimagnetic hard/soft and soft/hard ferrite nanocomposites: structural, magnetic and hyperthermia properties. *Ceramics International* 48: 4886–4896.
- 20 Cannas, C., Musinu, A., Piccaluga, G. et al. (2006). Magnetic properties of cobalt ferrite-silica nanocomposites prepared by a sol-gel autocombustion technique. *The Journal of Chemical Physics* 125: 164714.
- 21 Aslibeiki, B., Kameli, P., and Salamati, H. (2016). The effect of dipole-dipole interactions on coercivity, anisotropy constant, and blocking temperature of MnFe₂O₄ nanoparticles. *Journal of Applied Physics* 119: 063901.
- 22 Jalili, H., Aslibeiki, B., Hajalilou, A. et al. (2022). Bimagnetic hard/soft and soft/hard ferrite nanocomposites: structural, magnetic and hyperthermia properties. *Ceramics International* 48: 4886–4896.
- 23 Kavkhani, R., Hajalilou, A., Abouzari-Lotf, E. et al. (2022). CTAB assisted synthesis of MnFe₂O₄@SiO₂ nanoparticles for magnetic hyperthermia and MRI application. *Materials Today Communications* 31: 103412.
- 24 Artus, M., Tahar, L.B., Herbst, F. et al. (2011). Size-dependent magnetic properties of CoFe₂O₄ nanoparticles prepared in polyol. *Journal of Physics: Condensed Matter* 23: 506001.
- 25 Ferreira, L., Cruz, M., Oliveira, M. et al. (2016). CoFe₂O₄ nanoparticles synthesized with natural templates. *RSC Advances* 6: 73506–73516.
- 26 Cruz, M., Ferreira, L., Ramos, J. et al. (2017). Enhanced magnetic hyperthermia of CoFe₂O₄ and MnFe₂O₄ nanoparticles. *Journal of Alloys and Compounds* 703: 370–380.
- 27 Repa, K.L.S. (2016). Confinement effects and magnetic interactions in magnetic nanostructures. Doctoral dissertation. University of South Florida.
- 28 Hajalilou, A., Hashim, M., and Masoudi, M.T. (2015). A comparative study of in-situ mechanochemically synthesized Mn_{0.5}Zn_{0.5}Fe₂O₄ ferrite nanoparticles in the MnO/ZnO/Fe₂O₃ and MnO₂/Zn/Fe₂O₃ systems. *Ceramics International* 41: 8070–8079.
- 29 Ferreira, L.P., Reis, C.P., Robalo, T.T. et al. (2022). Assisted synthesis of coated iron oxide nanoparticles for magnetic hyperthermia. *Nanomaterials* 12 (11): 1870.
- 30 Hajalilou, A., Ferreira, L.P., Melo Jorge, M.E. et al. (2021). Superparamagnetic Ag-Fe₃O₄ composites nanoparticles for magnetic fluid hyperthermia. *Journal of Magnetism and Magnetic Materials* 537: 168242.
- 31 Aalaye, S., Kameli, P., Salamati, H., and Arabi, H. (2019). Preparation and investigation of magnetic properties of pure MnFe₂O₄ ferrite nanoparticles and those dispersed in SiO₂ matrix. *Iranian Journal of Physics Research* 12: 361–369.
- 32 Kirschning, M. and Jansen, R.H. (1982). Accurate model for effective dielectric constant of microstrip with validity up to millimetre-wave frequencies. *Electronics Letters* 18: 272–273.



- 33 Baker-Jarvis, J., Vanzura, E.J., and Kissick, W.A. (1990). Improved technique for determining complex permittivity with the transmission/reflection method. *IEEE Transactions on Microwave Theory and Techniques* 38: 1096–1103.
- 34 Yamashita, E. (1968). Variational method for the analysis of microstrip-like transmission lines. *IEEE Transactions on Microwave Theory and Techniques* 16: 529–535.
- 35 Farrar, A. and Adams, A. (1974). Multilayer microstrip transmission lines (short papers). *IEEE Transactions on Microwave Theory and Techniques* 22: 889–891.
- 36 Massé, D. and Pucel, R. (1972). Microstrip propagation on magnetic substrates – part II: experiment. *IEEE Transactions on Microwave Theory and Techniques* 20: 309–313.
- 37 Wheeler, H.A. (1964). Transmission-line properties of parallel wide strips by a conformal-mapping approximation. *IEEE Transactions on Microwave Theory and Techniques* 12: 280–289.
- 38 Svacina, J. (1992). Analysis of multilayer microstrip lines by a conformal mapping method. *IEEE Transactions on Microwave Theory and Techniques* 40: 769–772.
- 39 Aslibeiki, B., Kameli, P., Ehsani, M. et al. (2016). Solvothermal synthesis of MnFe_2O_4 nanoparticles: the role of polymer coating on morphology and magnetic properties. *Journal of Magnetism and Magnetic Materials* 399: 236–244.
- 40 Goya, G., Berquo, T., Fonseca, F., and Morales, M. (2003). Static and dynamic magnetic properties of spherical magnetite nanoparticles. *Journal of Applied Physics* 94: 3520–3528.
- 41 Desautels, R., Skoropata, E., Rowe, M., and van Lierop, J. (2015). Investigating nanoparticle interactions from interparticle-to-nanocomposite. *Journal of Applied Physics* 117: 17C755.
- 42 Nadeem, K., Krenn, H., Traußnig, T. et al. (2011). Effect of dipolar and exchange interactions on magnetic blocking of maghemite nanoparticles. *Journal of Magnetism and Magnetic Materials* 323: 1998–2004.
- 43 Bedanta, S. (2006). Supermagnetism in magnetic nanoparticle systems. Doctoral dissertation. Universität Duisburg-Essen, Fakultät für Physik.
- 44 Ngo, A., Bonville, P., and Pileni, M. (2001). Spin canting and size effects in nanoparticles of nonstoichiometric cobalt ferrite. *Journal of Applied Physics* 89: 3370–3376.
- 45 Ngo, A., Bonville, P., and Pileni, M. (1999). Nanoparticles of: synthesis and superparamagnetic properties. *The European Physical Journal B – Condensed Matter and Complex Systems* 9: 583–592.
- 46 Tronc, E., Prene, P., Jolivet, J. et al. (1995). Magnetic behaviour of $\gamma\text{-Fe}_2\text{O}_3$ nanoparticles by Mössbauer spectroscopy and magnetic measurements. *Hyperfine Interactions* 95: 129–148.
- 47 Stojak, K., Srikanth, H., Mukherjee, P. et al. (2012). *Size- and Shape-Variant Magnetic Nanoparticles: Synthesis and Characterisation for Biomedical Applications*. Wiley.



- 48 Stojak Repa, K., Israel, D., Alonso, J. et al. (2015). Superparamagnetic properties of carbon nanotubes filled with NiFe_2O_4 nanoparticles. *Journal of Applied Physics* 117: 17C723.
- 49 Balaev, D., Semenov, S., Dubrovskiy, A. et al. (2017). Superparamagnetic blocking of an ensemble of magnetite nanoparticles upon interparticle interactions. *Journal of Magnetism and Magnetic Materials* 440: 199–202.
- 50 Russier, V. (2016). Blocking temperature of interacting magnetic nanoparticles with uniaxial and cubic anisotropies from Monte Carlo simulations. *Journal of Magnetism and Magnetic Materials* 409: 50–55.
- 51 Allia, P., Barrera, G., Tiberto, P. et al. (2014). Fe_3O_4 nanoparticles and nanocomposites with potential application in biomedicine and in communication technologies: nanoparticle aggregation, interaction, and effective magnetic anisotropy. *Journal of Applied Physics* 116: 113903.
- 52 Carpenter, E.E., Sangregorio, C., and O'Connor, C.J. (1999). Effects of shell thickness on blocking temperature of nanocomposites of metal particles with gold shells. *IEEE Transactions on Magnetics* 35: 3496–3498.
- 53 Vestal, C.R., Song, Q., and Zhang, Z.J. (2004). Effects of interparticle interactions upon the magnetic properties of CoFe_2O_4 and MnFe_2O_4 nanocrystals. *The Journal of Physical Chemistry B* 108: 18222–18227.
- 54 Denardin, J., Brandl, A., Knobel, M. et al. (2002). Thermoremanence and zero-field-cooled/field-cooled magnetization study of $\text{Co}_x(\text{SiO}_2)_{1-x}$ granular films. *Physical Review B* 65: 064422.
- 55 Muscas, G., Concas, G., Laureti, S. et al. (2018). The interplay between single particle anisotropy and interparticle interactions in ensembles of magnetic nanoparticles. *Physical Chemistry Chemical Physics* 20: 28634–28643.
- 56 Pankrats, A., Vorotynov, A., Tugarinov, V. et al. (2018). Magnetic resonance studies of mixed chalcospinel $\text{CuCr}_2\text{S}_x\text{Se}_{4-x}$ ($x = 0; 2$) and $\text{Co}_x\text{Cu}_{1-x}\text{Cr}_2\text{S}_4$ ($x = 0.1; 0.2$) nanocrystals with strong interparticle interactions. *Journal of Magnetism and Magnetic Materials* 452: 297–305.
- 57 Berger, R., Kliava, J., Bissey, J.-C., and Baïetto, V. (2000). Magnetic resonance of superparamagnetic iron-containing nanoparticles in annealed glass. *Journal of Applied Physics* 87: 7389–7396.
- 58 Alben, R., Becker, J., and Chi, M. (1978). Random anisotropy in amorphous ferromagnets. *Journal of Applied Physics* 49: 1653–1658.
- 59 Knobel, M., Nunes, W., Winnischofer, H. et al. (2007). Effects of magnetic interparticle coupling on the blocking temperature of ferromagnetic nanoparticle arrays. *Journal of Non-Crystalline Solids* 353: 743–747.
- 60 Nunes, W., Socolovsky, L., Denardin, J. et al. (2005). Role of magnetic interparticle coupling on the field dependence of the superparamagnetic relaxation time. *Physical Review B* 72: 212413.
- 61 Maiti, R., Mitra, M., and Chakravorty, D. (2014). Ferromagnetic superexchange interaction and spin glass behaviour in $\text{Sm}_2\text{CoMnO}_6$ nanoparticles. In: *AIP Conference Proceedings*, 390–392. American Institute of Physics.
- 62 Dass, R. and Goodenough, J. (2003). Multiple magnetic phases of $\text{La}_2\text{CoMnO}_{6-\delta}$ ($0 < \delta < 0.05$). *Physical Review B* 67: 014401.



- 63 de Almeida, J.R. and Thouless, D.J. (1978). Stability of the Sherrington–Kirkpatrick solution of a spin glass model. *Journal of Physics A: Mathematical and General* 11: 983.
- 64 Hajalilou, A., Hashim, M., Ebrahimi-Kahrizsangi, R., and Kamari, H.M. (2015). Influence of evolving microstructure on electrical and magnetic characteristics in mechanically synthesized polycrystalline Ni-ferrite nanoparticles. *Journal of Alloys and Compounds* 633: 306–316.
- 65 Hajalilou, A., Hashim, M., and Mohamed Kamari, H. (2014). Effects of additives and sintering time on the microstructure of Ni–Zn ferrite and its electrical and magnetic properties. *Advances in Materials Science and Engineering* 2014: 138789. <https://doi.org/10.1155/2014/138789>.
- 66 Hajalilou, A., Kamari, H.M., and Shameli, K. (2017). Dielectric and electrical characteristics of mechanically synthesized Ni–Zn ferrite nanoparticles. *Journal of Alloys and Compounds* 708: 813–826.
- 67 Ismail, M.A.N., Hashim, M., Hajalilou, A. et al. (2014). Magnetic properties of mechanically alloyed cobalt-zinc ferrite nanoparticles. *Journal of Superconductivity and Novel Magnetism* 27: 1293–1298.
- 68 Hajalilou, A. and Mazlan, S.A. (2016). A review on preparation techniques for synthesis of nanocrystalline soft magnetic ferrites and investigation on the effects of microstructure features on magnetic properties. *Applied Physics A* 122: 1–15.
- 69 Hajalilou, A., Hashim, M., Abbasi, M. et al. (2015). A comparative study on the effects of different milling atmospheres and sintering temperatures on the synthesis and magnetic behavior of spinel single phase $\text{Ni}_{0.64}\text{Zn}_{0.36}\text{Fe}_2\text{O}_4$ nanocrystals. *Journal of Materials Science: Materials in Electronics* 26: 7468–7483.
- 70 Hajalilou, A., Hashim, M., Kamari, H.M., and Masoudi, M.T. (2015). Effects of milling atmosphere and increasing sintering temperature on the magnetic properties of nanocrystalline $\text{Ni}_{0.36}\text{Zn}_{0.64}\text{Fe}_2\text{O}_4$. *Journal of Nanomaterials* 16: 232.
- 71 Etemadifar, R., Kianvash, A., Arsalani, N. et al. (2018). Green synthesis of superparamagnetic magnetite nanoparticles: effect of natural surfactant and heat treatment on the magnetic properties. *Journal of Materials Science: Materials in Electronics* 29: 17144–17153.
- 72 Malkinski, L.M., Wang, J.-Q., Dai, J. et al. (1999). Thickness dependence of magnetic properties of granular thin films with interacting particles. *Applied Physics Letters* 75: 844–846.
- 73 Ashcroft, N.W. and Mermin, N.D. (1976). *Solid State Physics*. New York/London: Holt, Rinehart and Winston.
- 74 Dormann, J.L., Spinu, L., Tronc, E. et al. (1998). Effect of interparticle interactions on the dynamical properties of $\gamma\text{-Fe}_2\text{O}_3$ nanoparticles. *Journal of Magnetism and Magnetic Materials* 183: L255–L260.
- 75 Dormann, J., Fiorani, D., and El Yamani, M. (1987). Field dependence of the blocking temperature in the superparamagnetic model: H^{23} coincidence. *Physics Letters A* 120: 95–99.
- 76 Leslie-Pelecky, D.L. and Rieke, R.D. (1996). Magnetic properties of nanostructured materials. *Chemistry of Materials* 8: 1770–1783.



- 77 Hajalilou, A., Hashim, M., and Kamari, H.M. (2015). Structure and magnetic properties of $\text{Ni}_{0.64}\text{Zn}_{0.36}\text{Fe}_2\text{O}_4$ nanoparticles synthesized by high-energy milling and subsequent heat treatment. *Journal of Materials Science: Materials in Electronics* 26: 1709–1718.
- 78 Abdollah, H., Mansor, H., Reza, E.-K., and Taghi, M.M. (2015). Effect of milling atmosphere on structural and magnetic properties of Ni–Zn ferrite nanocrystalline. *Chinese Physics B* 24: 048102.
- 79 Hajalilou, A., Hashim, M., Ebrahimi-Kahrizsangi, R., and Sarami, N. (2015). Influence of CaO and SiO_2 co-doping on the magnetic, electrical properties and microstructure of a Ni–Zn ferrite. *Journal of Physics D: Applied Physics* 48: 145001.
- 80 Pereira, C., Pereira, A.M., Fernandes, C. et al. (2012). Superparamagnetic MFe_2O_4 (M = Fe, Co, Mn) nanoparticles: tuning the particle size and magnetic properties through a novel one-step coprecipitation route. *Chemistry of Materials* 24: 1496–1504.
- 81 Cullity, B. (1972). *Introduction to Magnetic Materials*. Reading: Addison-Wesley Pub. Co.
- 82 Dutta, P., Pal, S., Seehra, M. et al. (2009). Size dependence of magnetic parameters and surface disorder in magnetite nanoparticles. *Journal of Applied Physics* 105: 07B501.





8

Type of Interactions in Magnetic Nanoparticles

8.1 Introduction

The magnetization characteristics of the magnetic materials, which are of a typical type of magnetic ordering, can be described based on exchange interaction changes occurring between octahedral and tetrahedral sub-lattices [1–3]. However, in all systems that involve magnetic nanoparticles, there are several types of magnetic interactions between nanoparticles and the strength of these interactions is different depending on the type of system.

8.2 Magnetic Dipole–Dipole Interaction Between Magnetic Nanoparticles

This interaction, also named dipolar coupling, refers to the direct interaction between two magnetic dipoles. If we consider two magnetic dipole moments of m_1 and m_2 that are far enough apart that they can be treated as point dipoles in calculating their interaction energy, the potential energy (H) of the interaction is then given by:

$$H = -(3[(m_1 \cdot \hat{r}) \cdot (m_2 \cdot \hat{r})] - [m_1 - m_2]) \frac{\mu_0}{4\pi|r|^3} + \frac{2\mu_0 m_1}{3} \cdot m_{2\delta(r)} \quad (8.1)$$

where \hat{r} is a unit vector parallel to the line joining the centers of the two dipoles, $|r|$ is the distance between the centers of m_1 and m_2 , and μ_0 is the magnetic constant. Alternatively, if we consider γ_1 and γ_2 as gyromagnetic ratios of two particles with spin quanta S_1 and S_2 , respectively, then:

$$H = -(3[(S_1 \cdot \hat{r}) \cdot (S_2 \cdot \hat{r})] - [S_1 \cdot S_2]) \frac{\mu_0 \gamma_1 \gamma_2 \hbar^2}{4\pi|r|^3} \quad (8.2)$$

where \hat{r} is a unit vector in the direction of the line joining the two spins, and $|r|$ is the distance between them. Finally, the interaction energy is given as the dot product of the moment of either dipole into the field from the other dipole:

$$H = -m_1 \cdot B_2(r_1) = -m_2 \cdot B_1(r_2) \quad (8.3)$$



where $B_2(r_1)$ is the field that dipole 2 produces at dipole 1, and $B_1(r_2)$ is the field that dipole 1 produces at dipole 2. The force F arising from the interaction between m_1 and m_2 is given by:

$$F = (3[(m_1 \cdot \hat{r})m_2 + (m_2 \cdot \hat{r})m_1 - 2\hat{r}(m_1 \cdot m_2) + (5\hat{r}(m_1 \cdot \hat{r})(m_2 \cdot \hat{r}))]) \frac{3\mu_0}{4\pi|r|^4} \quad (8.4)$$

This type of interaction is long-range order and anisotropic; the strength of interaction depends on the distance, the size of the moments, and their orientation. The magnitude order of the energy of the interaction of atomic moments that have a 1 nm distance from each other, is of the order of 1 K. Also, the dipole interaction is much weaker than the interaction that leads to the formation of the order in most magnetic materials. Because most magnetic materials attain a magnetic order at temperatures exceeding 1 K. However, in the systems of magnetic nanoparticles whose magnetic moments are of magnitude 10^3 – 10^5 magnets Bohr, this energy can lead to ordering at several dozen Kelvin temperatures and therefore becomes important. In other words, the most obvious interaction between magnetic ions is the effect of the magnetic field of a dipole on a neighboring dipole. But this interaction is very weak, except at very low temperatures. So it can be said that it is so small that it cannot be responsible for creating a magnetic order. At a distance d of a dipole with intensity m_m , the intensity of the field H is equal to $m_m/(4\pi d^3)$. As a result, the amount of dipolar magnetic energy in the field H is equal to:

$$M_m B = \mu_0 m_m H = \mu_0 m_m^2 / (4\pi d^3) \quad (8.5)$$

If m_m is as large as the magneton Bohr ($0.9 \times 10^{-23} \text{ Am}^2$) and d is the inter-atomic distance ($\sim 0.3 \text{ nm}$), this energy is approximately $3 \times 10^{-25} \text{ J}$. This energy is equivalent to thermal energy KT at a temperature of about 10^{-2} K . As a result, the torque orientation of this magnetic interaction can take place only at very low temperatures [4].

8.3 Exchange Interaction

Exchange interactions are of quantum origin. These types of interactions are the source of high-level magnetic ordering. When the electrons of the neighboring magnetic atoms engage in exchange interaction, this kind of exchange is called a direct exchange. Hence, the role of those nanoparticles whose surfaces are in contact with each other becomes important in the direct exchange interaction. There are other interchangeable interactions, where a nonmagnetic ion-like O^{2-} acts as an intermediate between two magnetic ions. These interactions have been observed in various compositions, including metal oxides. An example of this kind of interaction is the exchange clouds interact with a dual exchange, which is the origin of the ferromagnetic and antiferromagnetic phases in magnetic compounds [5, 6].

Exchange interaction simply means interaction among the individual moments. In some materials, each moment may act independent from the others, giving rise



to non-interaction. Diamagnets and paramagnets are examples of such kinds of materials. On the other hand, the magnetic moments coupled with one another make magnetically ordered states in some materials such as iron or nickel. The coupling, which is quantum mechanical in nature, is known as the exchange interaction and is rooted in the overlap of electrons in conjunction with Pauli's exclusion principle. Whether it is a ferrimagnet, antiferromagnet, or ferromagnet, the exchange interaction between the neighboring magnetic ions will force the individual moments into antiparallel (antiferromagnetic) or parallel (ferromagnetic) alignment with their neighbors. In other words, in a simple two-electron picture, exchange gives rise to $\uparrow\uparrow$ (ferromagnetic) or $\uparrow\downarrow$ (antiferromagnetic) coupling between spins. There are two types of exchanges. The atomic moments can be explained by an interatomic exchange and an intra-atomic exchange between neighboring magnetic atoms. The result of interatomic exchange can be observed in a ferromagnet, the long-range magnetic order is recognized. The interparticle distance in magnetic particles can form a different kind of interaction. When the particles are close to each other, they represent reprisal behavior, which is called exchange interaction between neighboring particles, and they tend to align with each other. Nonetheless, exchange interactions, especially the dipolar interactions induced by Coulomb force, reduce the distance between the particles from each other. Thus, it can be concluded that there are several types of exchange interactions that manifest long-range order in magnetic materials, with two main types: direct exchange and indirect exchange [7]. The direct exchange comes about when magnetic materials are in close enough contact for the electrons of neighboring magnetic atoms to interact with one another [7–9]. The indirect exchange appears in many forms such as superexchange and Ruderman, Kittel, Kasuya, and Yoshida (RKKY) interactions, which will be described in Section 8.3.2. A very special type of exchange between nanoparticles, in which the particles are only a few nanometers apart from each other is considered Tunnel Exchange Interaction (TEI) [10, 11].

8.3.1 Direct Exchange Interaction

As discussed above, the dipole–dipole interactions cannot individually respond to the magnetism of magnetic materials; therefore, other interactions should be considered in this regard. This was first analyzed by Heisenberg [12, 13]. The prime imperative of par excellence is a spin-dependent force that includes the spin exclusion principle. This force is a powerful exchange force since it is of the same magnitude as the Coulomb force. For example, the hydrogen molecule is considered, where two electrons are moving at the Coulomb field in the core of the molecule. There are two possibilities for arranging the spins of these electrons. Either spin is parallel or anti-parallel. If the spins are parallel, the principle of exclusion requires that the electrons be far from each other, and if the spins are anti-parallel, the electrons may be interconnected, and their wave functions overlap substantially. These two spin arrangements have different energies. When the electrons approach each other, energy increases due to the Coulomb repulsion force between them. This case solely makes the spins parallel to the preferred state. But there are other things to



do that will ultimately favor the anomalies. Which mode exists depends on which item overcomes the other. In a hydrogen molecule, the base state corresponds to the anti-parallel supply, i.e. the non-magnetic mode.

8.3.2 Indirect Exchange Interaction

It is the dominant exchange interaction in metals, where there is little or no direct overlap between neighboring electrons. It means that the indirect exchange couples moments occur relatively at large distances among the electrons. Indirect exchange interaction couples moments over relatively large distances. It is the dominant exchange interaction in metals, where there is little or no direct overlap between neighboring electrons. It therefore acts through an intermediary, which in metals are the condelectrons (itinerant electrons). This type of exchange is termed as the RKKY interaction. This type of interaction is especially relevant for the rare earth metals with the unfilled 4f shell.

The indirect exchange theory of magnetism in disordered metals (amorphous magnetic materials) with a small amount of magnetic impurities, which are randomly distributed in the system was studied by Kaneyoshi [14]. In general, as the disorder of a system increases, a single isolated band becomes broader, and the nature of the electronic wave function changes. Therefore, the absence of long-range structural order in amorphous materials not only makes the characteristic properties of their electronic structure differ from those of their perfect crystals but also may severely affect the range of indirect exchange interaction. It is believed that there are two characteristic energies in the band in a disordered system, which separate the regions of localized states from those of extended states: (i) the mean free path of the extended states is reduced [15], and (ii) as the randomness increases, more and more localized states are created, and the characteristic energies (or mobility edges) move inward in the band. Thus, the form of the indirect exchange interaction in an amorphous magnet may be severely different from that of the Ruderman–Kittel interaction, especially for a system with the Fermi energy near a mobility edge. In which, their effective indirect interactions may not be applied to a system with the Fermi energy near a mobility edge for a system with a finite mean free path [16]. To address this issue, Kaneyoshi proposed a general theory by the use of a one-electron Green function for taking into account indirect exchange interaction in a disordered magnet. For a model Green function, an exact expression of the effective indirect interaction is obtained and evaluated numerically for some degrees of disorder, for more details the readers refer to Ref. [14].

There is a kind of indirect exchange interaction (commonly known as the RKKY interaction) that is used to justify the behavior of rare earth metals with magnetic moments. In a system of metal nanoparticles that are spread over a metal substrate, RKKY interaction occurs. RKKY stands for four names of the scientist who discovered this kind of interaction with the name: Ruderman–Kittel–Kashua and Yoshida [17–19]. This kind of interaction has a relation as $1/d_{ij}^3$ with particle distance d_{ij} . Such interactions take an advantage of spin polarization in conduction electrons of metallic media. They originate from the direct consequence of



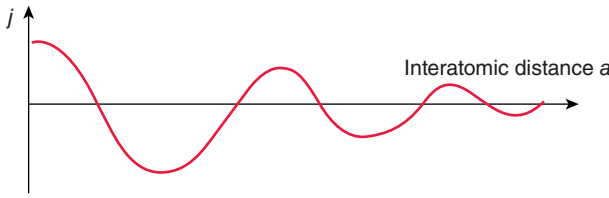


Figure 8.1 The RKKY exchange coefficient (j) versus the interatomic spacing a . Source: Shakil et al. [20]/with permission of Elsevier.

free-electron approximation [14]. Double exchange arises when magnetic ions in a molecule exhibit different valence states. As shown in Figure 8.1, the RKKY exchange coefficient (j) oscillates from positive to negative as the separation of the ion changes and has a damped oscillatory nature. Thus, their magnetic coupling can be antiferromagnetic or ferromagnetic, depending on the separation between a pair of ions. A magnetic ion induces a spin polarization in the conduction electrons in its neighborhood. This spin polarization in the itinerant electrons is felt by the moments of other magnetic ions within the range, which gives rise to an indirect coupling. This suggests that the indirect exchange interaction depends on the characteristic nature of the electronic states in the system.

In rare-earth metals, whose magnetic electrons in the 4f shell are shielded by the 5s and 5p electrons, a direct exchange is rather an indirect exchange through the conduction electrons leads to magnetic order in these materials.

Jalbout and Chen [21] employed Monte Carlo simulations using a three-dimensional lattice model to study the RKKY effect in the Co-doped in ZnO films. Their results revealed that the RKKY interaction in Co-doped ZnO film is long-ranged order and its magnitude is proportional to R^{-1} (inverse of the distance R from a central Co^{2+} ion). The sign oscillates with a frequency that depends on the concentration of the carrier. The long-distance sum of the RKKY indirect exchange energies is positive, indicating the ferromagnetic nature of these materials. In another study, it was found that the polarization of the conduction electrons in the n-type $\text{Zn}_{1-x}\text{Co}_x\text{O}$ gives rise to an s-d exchange process [22, 23], in good agreement with the previous work.

According to Heisenberg's theory, it can be shown that the energy of the interaction between the spins of the electrons of atoms i and j is as follows:

$$E_{\text{ex}} = -2J_{\text{ex}}S_iS_j \cos(\theta_{ij}) \quad (8.6)$$

where θ_{ij} is the angle between the spin torque direction; S is the spin vector for these two atoms, and J refers to the exchange integral.

Figure 8.2 shows the exchange integral of J in terms of D/d , where D is the atomic radius of the 3d layer. If this integral is positive, a material is ferromagnetic, and the energy will be at a minimum once $\theta_{ij} = 0$. If the exchange integral is negative, then the energy of the interaction is at its lowest value, and the angle between the neighbors' spins is 180° , i.e. the direction of the electron spin of the adjacent magnetic atoms is in a reverse state that is a behavior of antiferromagnetic materials. In fact, the size and symbol of the J -exchange integral depend on D/d . According to Figure 8.1, if the $D/d = 1.5$, the sign of the exchange interaction will be negative.



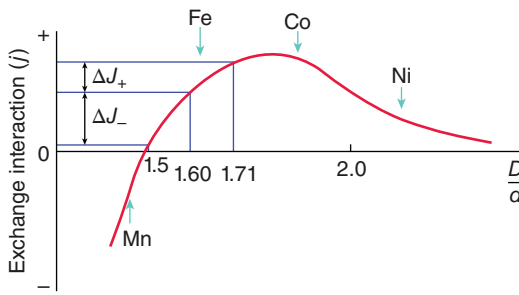


Figure 8.2 Slater-Bethe curve for representing the size and symbol of the J -exchange integral versus D/d , where D is the atomic separation and d is the diameter of the 3d orbital. Source: McHenry et al. [24]/with permission of Elsevier.

Being higher than that, it becomes positive and will reach the highest value for $D/d = 1.8$. Then, with the increase in this ratio, the strength of the interaction is reduced, but it remains a positive sign.

In spinel ferrites, the amount of D/d is approximately 2.5, which, according to the above curve, expects a poorly positive interaction (direct type) between the magnetic cations in the sub-lattice of A (tetrahedral) and B (octahedral). However, the empirical observations show that these interactions are strong and indirect, and the J sign is negative. The reason for this is the difference in the structure of metal oxides with magnetic metals and the presence of oxygen-ion intermediates among the cations. In other words, the indirect interaction between metal ions due to the presence of oxygen among them (intermediate), has produced such a strong interaction. To justify the strong negative interaction, where oxygen plays as a mediator, a model of super-exchange interaction has been suggested [25]. This suggests that “ j ” can be positive or negative for direct inter-atomic exchange, depending on the balance between the Coulomb and kinetic energies.

One can simply take into account that the direct exchange occurs between moments that are close enough to have sufficient overlap of their wavefunctions. It yields a powerful but short-range coupling, which declines quickly as the ions are separated. An easy way to understand the direct exchange concept is to consider two atoms with one electron each (Figure 8.3). The Coulomb interaction is in the minimal state when the atoms are very close together, where the electrons spend most of their time in between the nuclei. Due to the necessity of being electrons at the same place in space at the same time, Pauli’s exclusion principle requires that they possess opposite spins. When the interatomic distance is small, the electrons spend most of their time in between neighboring atoms according to Bethe and Slater. This results in antiparallel alignment with a negative exchange, which is the characteristic of antiferromagnetic materials (Figure 8.3a). On the other hand, if the atoms are far away, the electrons are away from each other as well to minimize the electron–electron repulsion. This results in parallel alignment with positive exchange (Figure 8.3b), which is the characteristic of ferromagnetism.

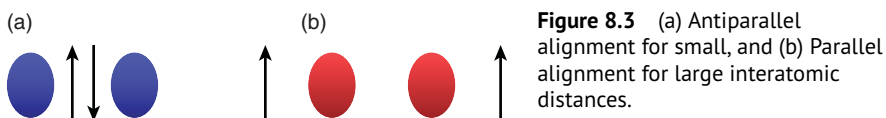


Figure 8.3 (a) Antiparallel alignment for small, and (b) Parallel alignment for large interatomic distances.



8.4 Super-Exchange Interaction

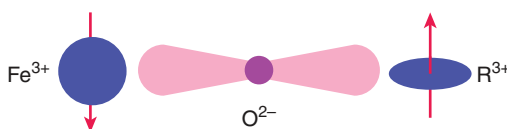
Although exchange interactions generally take place over short distances, super-exchange takes place over magnetic ions that are next-nearest neighbors. Super-exchange is mediated through a non-magnetic ion that locates between the magnetic ions.

In crystalline magnetic materials, including oxides and ferrites, as a magnetic component, the oxygen anions, which are the main configuration of the structure, and metal cations, like Fe^{+2} and Fe^{+3} , fill the empty spaces between the anions. In this case, the interactions between the magnetic cations whose electrons are not overlapping are accomplished through electrons in the non-magnetic anions that act as mediators. This kind of interaction is known as the superconducting interaction, and it determines the order of magneto of these types of structures. In a magnetic structure, when one metal cation is placed in the auxiliary lattices A and another cation in the sub-lattice B and oxygen ions between them, the overlapping of 2p-oxygen and 3d-metal-cathode-wave functions overlaps is possible only with the same spins. Because in the stable state of oxygen, the ion has twice the negative, and the assignment of one or three times the negative is not correct. This type of overlap in the superconducting interaction causes the magnetic ordering of the sub-lattices A and B, which results in the formation of the antiferromagnetic order in most of the magnetic oxides [26].

It can be said that super-exchange describes the interaction between moments on ions that are too far to be coupled by the direct exchange but are connected over a relatively long distance through a non-magnetic material like oxygen. Figure 8.4 shows an example of the super-exchange state through the coupling between the moments on a pair of metal cations separated by a diatomic anion. The Fe^{3+} has a half-filled 3d shell, which gives rise to a spherically symmetric charge distribution (S state ion). The R^{3+} (R is a rare-earth ion) is not symmetric and its charge distribution is coupled to its moment, which results in strong spin-orbit coupling (SOC). Thus, turning the iron moment varies the overlap of the R cation in the molecule, which results in the connection of ion moments through superexchange. Due to this phenomenon, the magnitude of both the Coulomb and exchange interactions between the cations would change and be coupled, depending on the moment orientation.

The yttrium iron garnet (YIG), as an example, is taken into account to describe super-exchange interaction in more detail. The magnetic moment, at 0 K, for YIG is found to be slightly less (5%) than $5 \mu_B$, μ_B is Bohr magneton [27]. The origin of this moment is associated with the result of the super-exchange antiferromagnetic interaction between trivalent iron ions, in which there are three in tetrahedral coordination, and two in octahedral coordination with oxygen ions. Each Fe^{3+} ion is in a $3d^5$ electronic configuration and has a moment of $5 \mu_B$, thus the difference

Figure 8.4 Schematic representation of super-exchange interaction state in $\text{Fe}^{3+}-\text{Re}^{3+}$ in a garnet.



in iron sublattice moments is $5 \mu_B$. Explicitly, to form the Fe^{3+} ion, firstly, two $4s$ electrons are removed followed by the one $3d$ electron that gives rise to five unpaired electrons in $3d$. These unpaired electrons lead to a net magnetic moment and are proportional to the number of unpaired electron spins. Each unpaired spin produced $1 \mu_B$, and thus the Fe^{3+} has $5 \mu_B$. The importance of this superexchange interaction in transition-metal oxides is recognized by Kramers [28] and Néel [29] stated that ferrimagnetism results from the super-exchange interactions. Subsequent work by Gilleo and Geller [30] placed the magnetic moment of YIG within a fraction of a percent of $5 \mu_B$. Prince [31] confirmed that the ferrimagnetism of YIG is due to the octahedral iron moments that are antiparallel to the tetrahedral moments by the neutron diffraction experiments. Figure 8.5 shows the super-exchange linkage geometry of iron ions in octahedral coordination (Fe_a^{3+}) and iron ions in tetrahedral coordination (Fe_d^{3+}) with oxygen ions. The included angle in this linkage is 125.9° while the distance of the octahedral site to the surrounding oxygen ions is 2.01 \AA and the distance of the tetrahedral site to the surrounding oxygen ions is 1.87 \AA . The angle of yttrium-oxygen-iron and iron-oxygen-iron linkages in YIG are presented in Table 8.1. Besides the $(a)-(d)$ linkage which exhibits the strongest for super-exchange interaction, there are one other $(a)-(a)$ linkage and four other $(d)-(d)$ linkages, which lead to an antiferromagnetic interaction in the (a) and (d) sublattices. These sublattice interactions become important when the tetrahedral or octahedral iron is substantially depleted by non-magnetic ion substitution [29, 33].

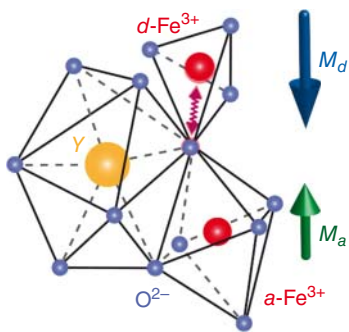


Figure 8.5 The coordination of Y^{3+} ion in 24(c), Fe^{3+} ion in 16(a), and Fe^{3+} ion in 24(d) with oxygen ion in YIG. Source: Maehrlein et al. [32].

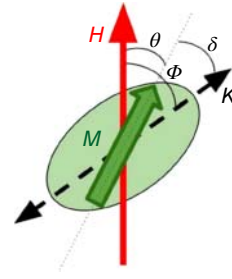
Table 8.1 The angle of yttrium-oxygen-iron and iron-oxygen-iron linkages in YIG.

Ions	Angles ($^\circ$)	Ions	Angles ($^\circ$)
$\text{Fe}^{3+}(a)\text{-O}^{2-}\text{-Fe}^{3+}(d)$	125.9	$\text{Fe}^{3+}(a)\text{-O}^{2-}\text{-Fe}^{3+}(a)^c$	147.2
$\text{Fe}^{3+}(a)\text{-O}^{2-}\text{-Y}^{3+}(a)$	102.8	$\text{Fe}^{3+}(d)\text{-O}^{2-}\text{-Fe}^{3+}(d)^c$	86.6
$\text{Fe}^{3+}(a)\text{-O}^{2-}\text{-Y}^{3+}(b)$	104.7	$\text{Fe}^{3+}(d)\text{-O}^{2-}\text{-Fe}^{3+}(d)^c$	78.8
$\text{Fe}^{3+}(d)\text{-O}^{2-}\text{-Y}^{3+}(a)$	123.0	$\text{Fe}^{3+}(d)\text{-O}^{2-}\text{-Fe}^{3+}(d)^c$	74.7
$\text{Fe}^{3+}(d)\text{-O}^{2-}\text{-Y}^{3+}(b)$	92.2	$\text{Fe}^{3+}(d)\text{-O}^{2-}\text{-Fe}^{3+}(d)^c$	74.6
$\text{Y}^{3+}\text{-O}^{2-}\text{-Y}^{3+}$	104.7		

- a) $\text{Y}^{3+}\text{-O}^{2-}$ distance = 2.43 \AA .
b) $\text{Y}^{3+}\text{-O}^{2-}$ distance = 2.37 \AA .
c) The longer $\text{Fe}^{3+}\text{-O}^{2-}$ distances.



Figure 8.6 The angle δ between M and the easy axis K , and θ between the M and H indicate the energy. The $\phi = \theta + \delta$ between K and H is employed instead of δ for the calculation simplicity. Source: Bruvera et al. [36]/AIP Publishing.



8.5 Dipolar Interactions

Dipolar interactions are long-range interactions that arise from the fundamental dipolar nature of magnetic moments [9, 34]. Energy arising from dipolar interactions is described by the following equation,

$$E_{\text{dip},ij} = - \left(\frac{\mu_0}{4\pi} \right) \frac{\mu_i \mu_j}{r^3} [3\cos^2\theta_{ij} - 1] \quad (8.7)$$

where μ_0 is the permeability of free space, μ_i and μ_j are point dipoles with an angle of θ_{ij} between them and r is the distance between the point dipoles [8]. If the magnetic nanoparticles are fixed in the matrix and separated from each other by a distance $d > 3V^{1/3}$, dipolar interactions can be neglected [35, 36] and the energy of the system can be expressed as the sum of the anisotropy energy ($E_K = KV\sin^2\delta$) and the Zeeman energy ($E_H = -MH\cos\theta$) as:

$$E = E_K + E_H \quad (8.8)$$

where θ is the angle between H and M (Figure 8.6). This configuration is usually called the Stoner–Wohlfarth (SW) system in reference to these authors' publication of work [36] in which they perform a numerical calculation of M versus H curves of ordered systems with different orientations, i.e. systems of identical magnetic nanoparticles (MNPs) with a single value of θ , and of the M versus H curve of a disordered system, i.e. with a uniform distribution of θ values. Since no thermal agitation was considered by Stoner and Wohlfarth, their calculations were made just by finding the positions θ_i of the minima of Eq. (8.8) for each value of H .

8.6 Spin–Orbit Interaction

The physical origin of the magnetic anisotropy energy is the interaction of the mean exchange field and the orbital angular momenta of the atoms (ions) in the lattice. This interaction is referred to as SOC.

As discussed in Chapter 1, magnetocrystalline anisotropy is an intrinsic property. The magnetization process is different when the field is applied along with different crystallographic directions, and the anisotropy reflects the crystal symmetry. Its origin is in the crystal–field interaction and SOC, or else the interatomic dipole–dipole interaction.

The term magnetocrystalline anisotropy which is induced from the interaction between orbit and spin known as the orbital–spin coupling is used to study the



modification of magnetic properties along various crystal axes. The different types of crystal axes are easy, intermediate, and hard axes which display the highest, intermediate, and lowest magnetic moment, respectively, at the applied magnetic field.

The spin–orbit interaction is the primary source of magnetocrystalline anisotropy. It is basically the orbital motion of the electrons that couples with the crystal electric field giving rise to the first-order contribution to magnetocrystalline anisotropy. The second-order arises due to the mutual interaction of the magnetic dipoles. In other words, the anisotropic exchange interaction (also known as the Dzyaloshinsky–Moriya interaction) arises from the spin–orbit interaction in the magnetic ions to form an exchange interaction between the excited state of one ion and the ground state of another.

From a property perspective, magnetocrystalline anisotropy (MCA) intrinsically associated with SOC turns out to be an important ingredient in spintronics. Large MCA offers thermal stability as well as a small switching current in practical applications. In summary, anti-ferromagnetic (AFM) materials with large MCA would be highly prospective as reported in several experiments [37–39] and also from theoretical work [40–42].

References

- 1 Hajalilou, A., Hashim, M., and Kamari, H.M. (2015). Structure and magnetic properties of $\text{Ni}_{0.64}\text{Zn}_{0.36}\text{Fe}_2\text{O}_4$ nanoparticles synthesized by high-energy milling and subsequent heat treatment. *Journal of Materials Science: Materials in Electronics* 26: 1709–1718.
- 2 Hajalilou, A., Hashim, M., Abbasi, M. et al. (2015). A comparative study on the effects of different milling atmospheres and sintering temperatures on the synthesis and magnetic behavior of spinel single phase $\text{Ni}_{0.64}\text{Zn}_{0.36}\text{Fe}_2\text{O}_4$ nanocrystals. *Journal of Materials Science: Materials in Electronics* 26: 7468–7483.
- 3 Hajalilou, A. and Mazlan, S.A. (2016). A review on preparation techniques for synthesis of nanocrystalline soft magnetic ferrites and investigation on the effects of microstructure features on magnetic properties. *Applied Physics A* 122: 1–15.
- 4 Jiles, D. (2015). *Introduction to Magnetism and Magnetic Materials*. CRC Press.
- 5 Aslibeiki, B., Kameli, P., and Salamati, H. (2009). Reentrant spin glass behavior in $\text{La}_{0.8}\text{Sr}_{0.2}\text{Mn}_{1-x}\text{Ti}_x\text{O}_3$ manganites. *Solid State Communications* 149: 1274–1277.
- 6 Aslibeiki, B., Kameli, P., and Salamati, H. (2019). The effect of Ti substitution in Mn sites on the structural and electrical properties of $\text{La}_{0.8}\text{Sr}_{0.2}\text{MnO}_3$ manganite. *Iranian Journal of Physics Research* 10: 9–16.
- 7 Blundell, S. (2001). *Oxford Master Series in Condensed Matter Physics*. Oxford: Oxford University Press.
- 8 Majetich, S. and Sachan, M. (2006). Magnetostatic interactions in magnetic nanoparticle assemblies: energy, time and length scales. *Journal of Physics D: Applied Physics* 39: R407.



- 9 Repa, K.L.S. (2016). Confinement effects and magnetic interactions in magnetic nanostructures. Doctoral dissertation. University of South Florida.
- 10 Kondratyev, V. and Lutz, H. (1998). Shell effect in exchange coupling of transition metal dots and their arrays. *Physical Review Letters* 81: 4508.
- 11 Scheinfein, M., Schmidt, K., Heim, K., and Hembree, G. (1996). Magnetic order in two-dimensional arrays of nanometer-sized superparamagnets. *Physical Review Letters* 76: 1541.
- 12 Mankovsky, S., Polesya, S., and Ebert, H. (2020). Extension of the standard Heisenberg Hamiltonian to multispin exchange interactions. *Physical Review B* 101: 174401.
- 13 Li, X., Yu, H., Lou, F. et al. (2021). Spin Hamiltonians in magnets: theories and computations. *Molecules* 26: 803.
- 14 Kaneyoshi, T. (1975). Indirect exchange interaction in a disordered magnet. *Journal of Physics F: Metal Physics* 5: 1014.
- 15 Economou, E. and Ngai, K. (2007). Surface plasma oscillations and related surface effects in solids. In: *Advances in Chemical Physics*, 265–354. Wiley.
- 16 De Gennes, P., Hartmann-Boutron, F., Pincus, P., and Saint-James, D. (1962). Contribution of static crystal-field effects to the line-width in rare earth-doped yttrium iron garnet. *Physics Letters* 1: 273–274.
- 17 Ruderman, M.A. and Kittel, C. (1954). Indirect exchange coupling of nuclear magnetic moments by conduction electrons. *Physical Review* 96: 99.
- 18 Kasuya, T. (1956). A theory of metallic ferro-and antiferromagnetism on Zener's model. *Progress of Theoretical Physics* 16: 45–57.
- 19 Yosida, K. (1957). Magnetic properties of Cu–Mn alloys. *Physical Review* 106: 893.
- 20 Shakil, M., Hussain, A., Zafar, M. et al. (2018). Ferromagnetism in GaN doped with transition metals and rare-earth elements: a review. *Chinese Journal of Physics* 56: 1570–1577.
- 21 Jalbout, A.F., Chen, H., and Whittenburg, S.L. (2002). Monte Carlo simulation on the indirect exchange interactions of Co-doped ZnO film. *Applied Physics Letters* 81: 2217–2219.
- 22 Ueda, K., Tabata, H., and Kawai, T. (2001). Magnetic and electric properties of transition-metal-doped ZnO films. *Applied Physics Letters* 79: 988–990.
- 23 Sinha, K.P. and Kumar, N. (1980). *Interactions in Magnetically Ordered Solids*. USA: Oxford University Press.
- 24 McHenry, M.E., Willard, M.A., and Laughlin, D.E. (1999). Amorphous and nanocrystalline materials for applications as soft magnets. *Progress in Materials Science* 44: 291–433.
- 25 Kingery, W.D., Bowen, H.K., and Uhlmann, D.R. (1976). *Introduction to Ceramics*. Wiley.
- 26 Morrow, R. (2015). *Competing Superexchange Interactions in Double Perovskite Osmates*. The Ohio State University.
- 27 Geller, S. and Gilleo, M. (1957). The crystal structure and ferrimagnetism of yttrium-iron garnet, $\text{Y}_3\text{Fe}_2(\text{FeO}_4)_3$. *Journal of Physics and Chemistry of Solids* 3: 30–36.



- 28 Kramers, H. (1934). L'interaction entre les atomes magnétogènes dans un cristal paramagnétique. *Physica* 1: 182–192.
- 29 Néel, L. (1948). Propriétés magnétiques des ferrites; ferrimagnétisme et antiferromagnétisme. *Annales de Physique* 12: 137–198.
- 30 Gilleo, M. and Geller, S. (1958). Magnetic and crystallographic properties of substituted yttrium-iron garnet, $3Y_2O_3 \cdot xM_2O_3(5-x)Fe_2O_3$. *Physical Review* 110: 73.
- 31 Prince, E. (1957). Crystal and magnetic structure of copper chromite. *Acta Crystallographica* 10: 554–556.
- 32 Maehrlein, S.F., Radu, I., Maldonado, P. et al. (2018). Dissecting spin-phonon equilibration in ferrimagnetic insulators by ultrafast lattice excitation. *Science Advances* 4: eaar5164.
- 33 Anderson, P.W. (1950). Antiferromagnetism. Theory of superexchange interaction. *Physical Review* 79: 350.
- 34 Griffiths, D.J. (2005). Introduction to Electrodynamics. *Journal of Physics* 73: 574. <https://doi.org/10.1119/1.4766311>.
- 35 Wońska, M., Szczytko, J., Majhofer, A. et al. (2013). Magnetic interactions in an ensemble of cubic nanoparticles: a Monte Carlo study. *Physical Review B* 88: 144421.
- 36 Bruvera, I., Mendoza Zélis, P., Pilar Calatayud, M. et al. (2015). Determination of the blocking temperature of magnetic nanoparticles: the good, the bad, and the ugly. *Journal of Applied Physics* 118: 184304.
- 37 Martí, X., Park, B.G., Wunderlich, J. et al. (2012). Electrical measurement of antiferromagnetic moments in exchange-coupled IrMn/NiFe stacks. *Physical Review Letters* 108: 017201.
- 38 Moriyama, T., Matsuzaki, N., Kim, K.-J. et al. (2015). Sequential write-read operations in FeRh antiferromagnetic memory. *Applied Physics Letters* 107: 122403.
- 39 Wadley, P., Howells, B., Železný, J. et al. (2016). Electrical switching of an antiferromagnet. *Science* 351: 587–590.
- 40 Odkhuu, D., Rhim, S., and Hong, S. (2018). Thickness effect on magnetocrystalline anisotropy of MnPt(001) film. *Journal of Magnetism and Magnetic Materials* 467: 69–73.
- 41 Zheng, G., Ke, S.-H., Miao, M. et al. (2017). Electric field control of magnetization direction across the antiferromagnetic to ferromagnetic transition. *Scientific Reports* 7: 1–9.
- 42 Jekal, S., Rhim, S., Hong, S.C. et al. (2015). Surface-termination-dependent magnetism and strong perpendicular magnetocrystalline anisotropy of an FeRh(001) thin film. *Physical Review B* 92: 064410.



9

Insight into AC Susceptibility Measurements in Nanostructured Magnetic Materials

9.1 Introduction

Alternating current (AC) magnetic measurement, in which the sample moment is measured under the application of an AC field applied, is a fundamental technique for determining the magnetic characteristics of many materials, especially in magnetic nanoparticles (MNPs). The design of AC susceptibility (AC magnetic measurements) is originally focused on the thermometry measurements at different temperatures; however, it is also extensively used to determine other phenomena such as superparamagnetism, spin glass (SG) phenomena, superconducting transitions, magnetic phase transitions, and vortex dynamics. Indeed, even though the AC magnetic measurements have been broadly used for the characterization of high-temperature superconductors [1–4], the possible superparamagnetic-super-spin-glass phase transition has been investigated in many cases including MNPs dispersed in different matrices, either a solid or liquid [5].

Both the M – H and ZFC–FC studies discussed in the Chapters 1, 2, and 7 are direct current (DC) magnetic measurements, where a constant magnetic field is applied to determine the equilibrium value of the magnetization in the sample [6–10]. Since the induced magnetic moment in the sample is time-dependent, an AC susceptibility measurement is required to characterize the magnetization dynamics of the nanostructured magnetic materials. In an AC susceptibility measurement, the magnetization of a sample typically does not follow the DC magnetization curve because of the magnetic dynamic effects in the sample, and the magnetization may lag behind the external field. Hence, the AC susceptibility is composed of two components. The real component (χ'), signifies the component of the susceptibility that is in phase with the applied AC field; the imaginary component (χ'') indicates the component that is out of phase [11, 12]. Indeed, susceptibility (χ) is representative of sample magnetization and is defined as $\chi = M/H_{\text{DC}}$, where M is the magnetization (magnetic moment per unit volume) and H_{DC} is the applied DC field. This indicates that the susceptibility (ratio of the magnetization to the magnetic field) is the slope of the $M(H)$ curve. The sample moment is constant during the measurement time in this state. It simply means that the equilibrium value of the magnetization in a sample is obtained by a constant magnetic field and the magnetic moment of the sample is recorded, yielding a DC magnetization curve $M(H)$. In comparison with DC, AC



susceptibility measurement involves the application of an alternating magnetic field (H_{AC}) to the sample and recording the response of the sample by a sensitive winding. In this case, $\chi = dM/dH_{AC}$. This indicates that the magnetic moment of the sample varies in response to the applied field. Thus, this method can be used to evaluate the dynamic magnetic properties of a system. The other characteristics of the AC susceptibility measurements would be:

- The induced moment is time-dependent, meaning that the field of the time-dependent moment induces a current in the pickup coils, which provides measurement without sample motion. The detection circuitry is configured to sense only in a narrow frequency band, typically at the fundamental frequency (that of the AC drive field). In other words, in AC magnetic measurements, a small oscillating magnetic field applied leads to a time-dependent moment in the sample. The field of the time-dependent moment induces a current in the pick-up coils, allowing measurement without sample motion.
- AC field is small; a low field is required to get data. In this state, the induced AC moment is equivalent to $M_{AC} = \chi \cdot H_{AC} \sin(\omega t)$, where ω is the driving frequency, H_{AC} is the amplitude of the driving field, and $\chi = dM/dH$ is the susceptibility as well as the slope of the $M(H)$ curve at very small fields where the magnetization is still reversible. H_{AC} is usually around 10 Oe, where the susceptibility is still in the linear regime.
- Low frequencies are required to record data, meaning that the measurement is most like DC magnetometry.
- Critical current density is a function of temperature (T), field, and frequency using AC susceptibility measurements.
- The measurement is very sensitive to small changes in magnetization as a function of an applied field, $M(H)$. Since the AC measurement is dependent on the slope of $M(H)$ and not on the absolute value, small magnetic shifts can be noticed even when the absolute moment is large.

9.2 AC Susceptibility Measurement

Different types of machines can be also designed and used for the susceptibility measurement of the magnetic samples. More recently, the moment is measured by induction techniques. Inductive measurements are completed by moving the sample relative to a set of pickup coils, either by vibration or one-shot extraction. For example, in conventional inductive magnetometers, the voltage induced by means of the magnetic moment movement in the sample is measured by a set of copper pickup coils. The most important variables are the applied magnetic field, temperature range, and frequency. In detail, the system's components include a temperature control unit, a central control unit, and a lock amplifier. Controlling and transferring information to different parts of the system is accomplished by using a computer and software named ACS. After measurement, the data stored with this software are analyzed to chart them in a graph. The symbolic image of this



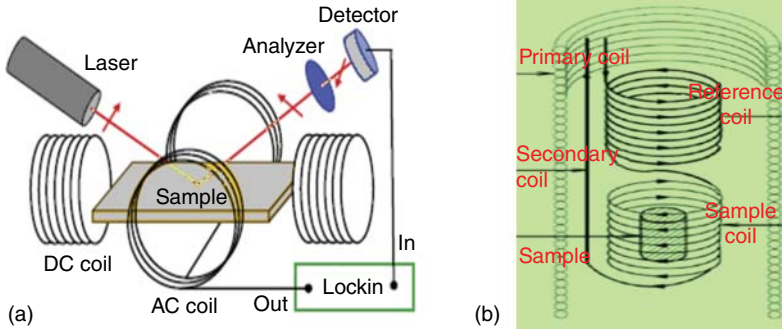


Figure 9.1 (a) The symbolic image of AC susceptibility, (b) schematic representation of putting sample within the sample coil with primary and secondary coils.

device is shown in Figure 9.1a. The sample is placed inside the device compartment, and then an alternating field with a small amplitude is applied to the sample. Charge changes generated by the sample are received by the winding around the sample and the induction voltage is detected. This voltage is proportional to the time derivative of the sample magnetization. Using the concept of interpenetration, we can obtain a relation for χ in terms of measurable quantities.

In brief, a sample inserted into one sensing coil of a susceptometer (see Figure 9.1b) will induce voltage that can be measured with the use of a lock-in amplifier as described by Nikolo [13]. The total magnetic flux from a sample filling the N_s turn sensing coil of radius r_s is given by

$$\Phi = \mu_0 \pi r_s^2 N_s M(t) \quad (9.1)$$

where $M(t)$ is the magnetic induction of the sample per unit volume and the flux from the applied field has been canceled due to the oppositely wound coils. By using $v = -\frac{d\Phi}{dt}$, the voltage is directly related to the magnetic induction by

$$v(t) = -\mu_0 \pi r_s^2 N_s dM(t)/dt \quad (9.2)$$

The AC magnetic susceptibility is complex and comprises real, X'_n , and imaginary, X''_n , components of multiple harmonics n which can be seen from a Fourier expansion of $M(t)$ as:

$$M(t) = \sum_{n=1}^{\infty} H_0 (X'_n \cos(n\omega t) + X''_n \sin(n\omega t)) \quad (9.3)$$

Combining Eqs. (9.2) and (9.3) and setting the prefactors to v_0 we have

$$v(t) = v_0 \sum_{n=1}^{\infty} n (X'_n \sin(n\omega t) - X''_n \cos(n\omega t)) \quad (9.4)$$

We only need to consider the fundamental, $n = 1$, harmonic though as higher harmonics are the result of flux entering and exiting the sample [13]. A lock-in amplifier can be used to measure this voltage and also the phase relative to a reference signal at the same frequency; in this case the current in the primary coil generating H_{AC} .



In this way, it is also able to resolve this into the real and imaginary components of the susceptibility directly [14].

$$v_1 = v_0 (X'_1 \sin(\omega t) - X''_1 \cos(\omega t)) \quad (9.5)$$

$$= v_y \sin(\omega t) - v_x \cos(\omega t) \quad (9.6)$$

Thus, root mean square voltages, v_y and v_x , measured by the lock-in amplifier are related to the susceptibilities X'_1 and X''_1 respectively by v_0 , which is equivalent to the prefactors from $v = (1/\alpha)\mu_0 V f H \chi$. It must be noted that in the above, the self-induced flux from the sensing coil has been neglected as the current will be negligible due to the lock-in amplifier's high impedance [15, 16]. Also, in practice no matter how careful the construction, it is unlikely for two sensing coils to be identical, and as such, there will always be a small voltage from the susceptometer when no sample is presently representing this imbalance. This mismatch may be corrected in several ways. One method involves canceling it by connecting a variable ratio transformer in series or using the lock-in amplifier's internal offset; however, the imbalance voltage will change based on field and temperature (due to uneven thermal expansion of components) which will require constant adjustments throughout a measurement. Alternatively, the sample can be moved between the sensing coils by the use of a motor to average its voltage response and cancel out this imbalance [13, 17].

9.3 AC Susceptibility as a Probe of Magnetic Dynamics in a Wide Variety of Systems

9.3.1 AC Susceptibility as a Probe of Low-Frequency Magnetic Dynamics

The experimental technique of AC susceptibility can be employed as a probe of magnetic dynamics in a wide variety of systems. Its use is restricted to the low-frequency regime, and hence, it is sensitive to relatively slow processes. Rather than measuring the dynamics of single spins, AC susceptibility can be employed to probe the dynamics of collective objects, such as vortex matter in superconductors or domain walls in ferromagnets. In some frustrating systems such as spin glasses (SGs), the complex interactions give rise to the substantial spectral weight of fluctuations in the low-frequency regime, and thus, AC susceptibility can play a unique role. The theory underlying the technique and magnetic dynamics more generally has a review in Ref. [18] and gives applications of AC susceptibility to a wide variety of experimental situations.

9.3.2 AC Susceptibility as a Probe of High-Frequency Magnetic Dynamics

At higher frequencies, the dynamic effects of the material come into play and the AC moment deviates from the DC magnetization curve. That is why AC susceptibility is often known as dynamic susceptibility. In the higher frequency range, the magnetization of the sample may lag behind the applied AC field; this effect is detected by the magnetometry circuitry. Therefore, the AC susceptibility



measurement produces two quantities; the magnitude of the susceptibility χ and the phase shift ϕ (relative to the drive signal). In other words, at relatively high frequencies, the AC moment of the sample does not track along the reversible part of the DC magnetization curve because of dynamic effects in the sample. Essentially, the rotation of the magnetic moment cannot keep up with the alternating magnetic field. In these frequency states, the magnetization of the sample may lag behind the drive field. This effect is identified by the physical property measurement system (PPMS) AC susceptibility using mutual inductance circuitry. Thus, the AC magnetic susceptibility (often known as the dynamic susceptibility) measurement yields two quantities: the phase shift (ϕ) relative to the drive signal and the magnitude of the susceptibility (χ). Alternatively, the susceptibility yields an in-phase or real component, which is assigned as χ' and an out-of-phase or imaginary part, which is assigned as χ'' . These two terms have a relationship with susceptibility and phase shift as follows:

$$\chi' = \chi \cos \phi \quad (9.7)$$

$$\chi'' = \chi \sin \phi \quad (9.8)$$

$$\phi = \text{Arctang} \left(\frac{\chi''}{\chi'} \right) \quad (9.9)$$

$$\chi = \sqrt{\chi'^2 + \chi''^2} \quad (9.10)$$

In the limit of low frequency where the AC measurement is not different from the DC measurement, the real component is equal to the susceptibility of the sample, $\chi' \approx \chi$ [19]. The χ'' designates dissipative processes in the sample. In ferromagnets, a nonzero imaginary susceptibility can indicate irreversible domain wall movement or absorption due to a permanent moment. Also, both χ' and χ'' are very sensitive to thermodynamic phase changes and are often used to measure transition temperatures. Furthermore, the high-frequency AC susceptibility can enhance a strong dipole–dipole interaction effect in MNPs [20], which will be discussed in the following.

9.4 Information Obtained from Susceptibility Measurements

- Quantitative measurements of the χ provide insights into the structure of materials, providing bonding and energy levels.
- Phase transition (para, ferro, antiferro, etc.), where for para, ferro, and ferri, anti-ferri susceptibility is positive, $\chi > 0$. On the other hand, in the case of diamagnetic, the susceptibility is negative ($\chi < 0$); meaning that the magnetic field in the material is weakened by the induced magnetization.
- Relaxation properties of the magnetic materials are achieved by susceptibility measurements. In fact, χ' and χ'' parts of AC magnetic susceptibility are normally measured in AC magnetic field at different frequencies to determine:
 - Strength and type of interaction between magnetic particles.
 - Dynamic-relaxation behavior of magnetic particles.



There is a practical parameter, Φ , to determine the dynamic behavior of the blocking/freezing process with a value of ~ 0.1 – 0.13 for superparamagnetic particles and ~ 0.005 – 0.05 for spin glass [21], which is given as:

$$\Phi = \frac{\Delta T_B}{T_B \Delta \log_{10}(f)} \approx 0.005 \quad (9.11)$$

where ΔT_B is the difference between blocking temperatures, T_B is a blocking temperature measured in the $\Delta \log_{10}(f)$ frequencies. The Φ value given by Eq. (9.11) probably exhibits the spin-glass behavior, although it is often difficult to experimentally distinguish between spin glass and superparamagnetic behavior [22].

9.5 Insight into the Interaction Between Magnetic Nanoparticles and Used Models

Different models have been suggested to investigate the interaction between magnetic nanoparticles as follows:

9.5.1 Néel–Brown Model

This model describes an inter-particle interaction, especially non-interaction (isolated) nanoparticles behavior. The frequency dependence of blocking temperature (T_B) follows the Néel–Brown model as [23]:

$$\tau = \tau_0 \exp \left(\frac{E_a}{k_B T_B} \right) \quad (9.12)$$

where τ is associated with measurement frequency as $\tau = 1/2\pi f$, and $\tau_0 = \rho N_0 h / 2K_{\text{eff}} V$, in which, ρ , N_0 , and h are the density, the Avogadro's number, and the Planck's constant, respectively. For superparamagnetic particles, τ_0 is given in the range of 10^{-9} – 10^{-13} seconds [24]. k_B is Boltzmann constant. The energy barrier (E_a) is assumed to be proportional to particle volume (V) in the absence of an external magnetic field. In this state: $E_a = K_{\text{eff}} V$, where K_{eff} is the effective magnetic anisotropy constant. Eq. (9.12) also indicates a direct relation between T_B and relaxation time (inverse of applied frequency) for non-interacting nanoparticles [25], due to the non-interacting behavior of superparamagnetic nanoparticles (SPMNs). Thus, the AC susceptibility measurements are useful, especially for their characterization. As originally theorized by Néel and Brown [25], the particles are assumed to be noninteracting and the blocking temperature is given by

$$T_B = \frac{\Delta E}{\ln \left(\frac{\tau}{\tau_0} \right) k_B} \quad (9.13)$$

where ΔE is the energy barrier to magnetization reversal in a single particle, τ is the measurement time, and k_B is the Boltzmann constant. $1/\tau_0$ is called the attempt frequency, and it describes how fast a particle reverses its magnetization. Typically, this value falls in the range of 10^{-9} – 10^{-10} seconds. Rearranging the equation above yields the typical form of the Néel–Arrhenius (NA) relation as Eq. (9.12).



The peaks observed from graphs of both χ' and χ'' correspond to the blocking temperature at the transition from ferromagnetism to superparamagnetism. Since T_B depends on the measurement frequency, the peak in χ'' versus T occurs at different temperatures for different frequencies. From such measurement, one can check that the particles are truly noninteracting by verifying the dependence of T_B on measurement time as given by the Néel–Brown theory. Departures from this theory indicate interparticle interactions, for example, dipole–dipole or interparticle exchange interactions. The frequency-dependent peak in χ'' versus T exhibited by superparamagnetic particles is a characteristic similar to spin glasses. However, spin glasses show a cooperative phase transition while superparamagnets show a gradual blocking of particles. Take note that the Néel–Arrhenius relation is limited to the magnetization reversal of a non-interacting single domain particle over an anisotropy barrier, E_a .

9.5.2 Vogel–Fulcher Model

This model describes the inter-particle interaction, in particular, in weakly interacting magnetic nanoparticles. The temperature dependence of the relaxation time, as well as the frequency dependence of T_B based on this model, is given as [26–28]:

$$\tau = \tau_0 \exp \left(\frac{E_a}{K(T_B - T_0)} \right) \quad (9.14)$$

where T_0 is an effective temperature, which indicates the existence of interactions among MNPs, and T_B is the characteristic temperature, representing the onset of the blocking process (i.e. the temperature of peak position in the real or imaginary parts of AC magnetic susceptibility). The typical value of τ_0 is 10^{-9} – 10^{-12} seconds for weakly interacting magnetic nanoparticles. If its value is zero, the non-interacting state is dominant between magnetic nanoparticles. If the obtained or measured value of τ_0 is less than that of the typical value, there is a strong interaction between magnetic nanoparticles.

The Vogel–Fulcher (VF) model cannot be used for highly agglomerated nanoparticle systems as well. Kura et al. [29] reported that there is a strong dipole–dipole interaction in agglomerated α -Fe nanoparticles and the energy barrier for the agglomerates per one nanoparticle could not be estimated from the Néel–Brown model and its modified models (Vogel–Fulcher model) [30]. This indicates that in the case of assemblies with considerable dipole–dipole or exchange interactions, the magnetic relaxation has been explained by Vogel–Fulcher (VF) law [31], which is a modification of the Néel–Brown theory.

In general, for an assembly of interacting magnetic nanoparticles, $T_{\max} \propto E_{\text{eff}}$, in which the E_{eff} is an effective energy barrier between equilibrium states and is given by

$$E_{\text{eff}} = E_d + E_h + E_{\text{ex}} + E_a \quad (9.15)$$

where E_d is dipole–dipole interaction energy, E_h is the Zeeman term, and E_{ex} is the exchange interaction energy in a system [32]. The $E_a = K_v V + K_s S$ is



anisotropy energy, where V is volume, S is the surface of nanoparticles, and K_v and K_s are volume and surface anisotropy constants, respectively [33, 34]. For weakly interacting NPs, Eq. (9.15) can be expressed by $E_{\text{eff}} = K_{\text{eff}}V$, where E_{eff} is the effective anisotropy constant.

9.5.3 Conventional Critical Slowing Down Model

This model is employed to evaluate the super spin glass (SSG) behavior (strongly interacting nanoparticles). The characteristic relaxation time (τ) diverges at the transition temperature according to strong interactions between superspins [35, 36]:

$$\tau = \tau_0 \left(\frac{T_B}{T_0 - 1} \right)^{-Z\nu} \quad (9.16)$$

where τ_0 is related to the relaxation time of the individual particle magnetic moment, T_0 is the value of T_B in the zero-frequency limit, ν is the critical exponent of correlation length as $\xi = (T_B/T_0 - 1)^{-\nu}$ and z relates τ and ξ as $\tau \propto \xi^z$ [28, 37]. The divergence of the correlation length or equally, relaxation time near T_0 , suggests the presence of a true equilibrium thermodynamic phase transition. The typical values of τ_0 and $Z\nu$ for spin glass systems are in the range of 10^{-9} – 10^{-13} seconds and 4–12 seconds, respectively [38, 39], while for interacting nanoparticle systems the smaller values are also reported. For nanoparticles of $\text{Nd}_{0.7}\text{Ba}_{0.3}\text{MnO}_3$ with a particle size of 20 nm, the values of $\tau_0 \approx 10^{-6}$ and $Z\nu = 6.03$ have been reported [40]. For interacting nanoparticles of $\gamma\text{-Fe}_2\text{O}_3$ the values of $\tau_0 \approx 10^{-11}$ and $Z\nu = 7.6$ [41] and in the case of the spin cluster in amorphous Fe_2O_3 the values of $\tau_0 \approx 10^{-11}$ and $Z\nu = 5.3$ have been reported [42]. For NiO core-shell nanoparticles, the values of $\tau_0 \approx 10^{-12}$ and $Z\nu = 8$ [43] and for $\text{Co}_{50}\text{Ni}_{50}$ nanoparticles embedded in the amorphous SiO_2 host with 10% volume fraction, the values of $\tau_0 \approx 10^{-9}$ and $Z\nu = 7.4$ [44] also have been reported. Such values of $Z\nu$ and τ_0 indicate the spin-glass behavior of the systems and could suggest the existence of a phase transition related to an SSG state below the peak temperature. This type of SSG-like behavior has been reported very recently in oleic acid-coated $\text{Mn}_{0.5}\text{Zn}_{0.5}\text{Fe}_2\text{O}_4$ ferrite nanoparticles by Parekh and Upadhyay [27].

9.5.4 Power Law (P-L) Model

This model has been widely used to study the strongly interacting systems which show disordered spin-glass behavior at low temperatures [30]. An increase in magnetic interaction strength by pressure creates doubt about the presence of SSG state in the samples. Thus, the power-law (P-L) model is employed to study the strong interaction between magnetic nanoparticles, as follows [30, 34, 45, 46]:

$$\tau = \tau_0 \left(\frac{T_p}{T_g} - 1 \right)^{-Z\nu} \quad (9.17)$$

where T_g is the glass temperature, T_p is the phase transition temperature, parameter z relates τ and correlation length (ξ) as $\tau \propto \xi^z$, and the parameter ν is a critical



exponent related to correlation length and reduced temperature as [30]:

$$\xi \propto \left(\frac{T_p}{T_g} - 1 \right)^{-\nu} \quad (9.18)$$

The divergence of the correlation length or equally relaxation time near T_g indicates the presence of a true equilibrium thermodynamic phase transition.

Furthermore, the possibility of spin-glass behavior can be evaluated by the power equation as follows:

$$f = f_0 \varepsilon^{z\nu} \quad (9.19)$$

where $\varepsilon = (T_B - T_g)/T_g$ is the reduced temperature, f is the frequency, z is the dynamic scaling exponent, and ν is the correlation length scaling exponent. For spin-glass, typical values of $\tau_0 = 1/f_0$ are within the range of 10^{-11} – 10^{-12} seconds [47]. The obtained parameters for Ni-Zn ferrite are $\tau_0 = 8.14 \times 10^{-21}$ seconds, $z\nu = 14.4$ and $T_g = 265$ K [48]. These values imply that spin-glass interaction does not exist in this system.

9.6 Examples of Evaluation of AC Susceptibility in MNPs

An observation of a maximum mountain-like peak, which is corresponded to transition temperature (T_p), in the curve of χ' versus temperature (T) in AC susceptibility in the given field and frequency indicates the superparamagnetic behavior of the sample (Figure 9.2). The value of T_p relies on several factors such as field and frequency amplitude, shape, particle size, and distribution, magnetic and shape anisotropies, and interactions strength. It has been proven that T_p is not identical to blocking temperature (T_B) [34, 49, 50], but it is a symptom of the average T_B of the nanoparticles. There are some errors in the values of E_a and τ_0 by considering T_p identical to T_B . For example, the value obtained for τ_0 was almost 1 order of magnitude smaller than the correct values or even extremely small in

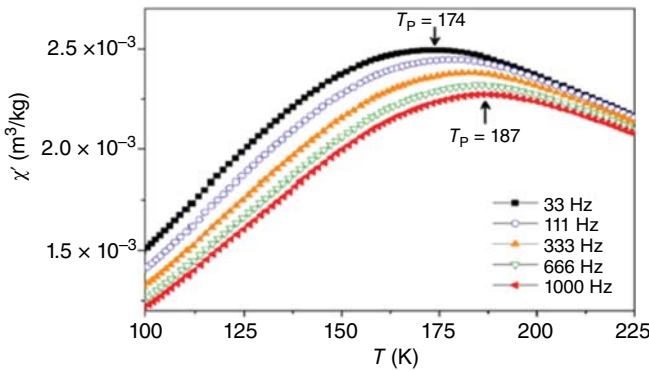


Figure 9.2 Frequency-dependent AC susceptibility at different frequencies in a field of 10 Oe. Source: Aslibeiki et al. [34]/with permission of AIP Publishing.



other studies [34]. This suggests that the nanoparticles are frequency-dependent, and interaction would exist between or among them. The frequency dependency of T_p in nanoparticles is a characteristic of superparamagnetic behavior and glassy systems [22, 32, 51, 52]. The T_p would shift towards higher frequencies by the increase in temperatures in $\chi'(T)$ curve, as shown in Figure 9.2. If there is an interaction between nanoparticles, the Vogel–Fulcher law would be a better choice to describe this dependency [53, 54]. Otherwise, the relationship between T_p and relaxation time is described based on the Néel–Brown law for noninteracting particles [25, 55]. Indeed, the Vogel–Fulcher model is an improved and modified state of the Néel–Brown model that gives a reasonable value to fit parameters.

To further study the dependency of χ' and χ'' as a function of temperature (T) for the nanoparticles of the same material heated at two different temperatures of 300 and 350 °C, their corresponding AC susceptibility measurements are shown in Figure 9.3a,b at 333 Hz and 10 Oe. Some significant differences are observed for those nanoparticles in their corresponding χ' and $\chi''(T)$. The hump emerged, which corresponds to T_p , was observed at about 140 K in the sample heated at 300 °C, but it appeared at about 190 K for the sample heated at 350 °C as well as at higher χ' and χ'' values. If we explain this phenomenon based on the heating temperature effect, one can say that since the heating temperature has a direct effect on magnetic properties,

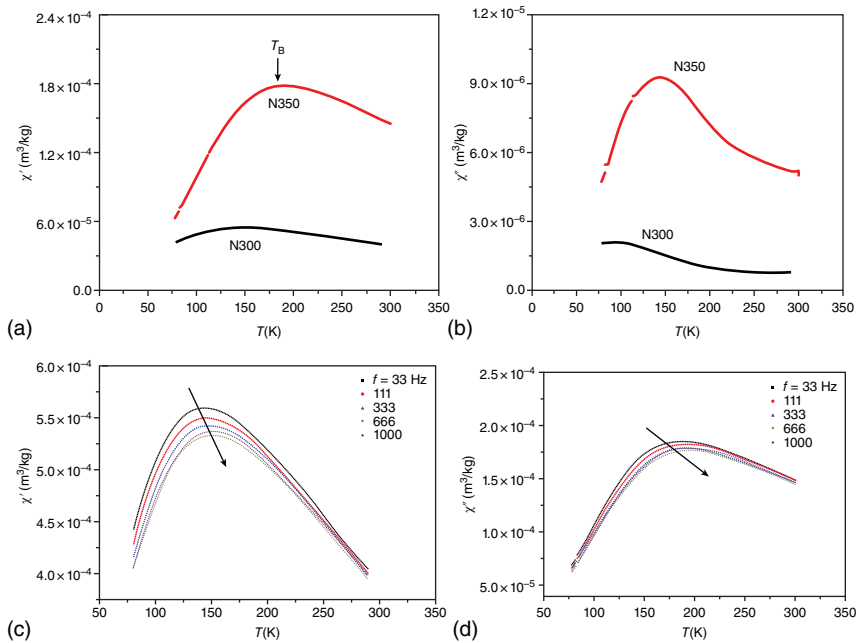


Figure 9.3 (a) Real and (b) imaginary parts of AC susceptibility of the samples versus temperature in the frequency of 333 Hz and AC field of 10 Oe, (c, d) Frequency dependence of real part of AC susceptibility for the samples heated at (c) 300 °C, and (d), 350 °C in the frequency of 333 Hz and field of 10 Oe. Source: Aslibeiki et al. [36]/with permission of Elsevier.



i.e. saturation magnetization (M_s), according to $M_s = 8.1661 \exp(3T/1000)$ [56–60], the T_p would increase by increasing the heating temperature.

If we consider based on the size of nanoparticles, since the heating process gives rise to particle growth, it is expected that the larger particle size to have a higher T_p . In general, this indicates that the average particle size, which is affected by the heating temperature, has a remarkable influence on T_p . In the same manner, as mentioned above, the T_p shifts to a higher temperature by increasing the applied frequency (Figure 9.3c,d).

To further study the inter-particle interaction behaviors, the Néel–Brown model [25, 36] was employed to describe the non-interacting state of nanoparticles and the Vogel–Fulcher law for the explanation of weakly interactions between nanoparticles [61], and the conventional critical slowing down model for strong interactions between superspins (SSG behavior) [35].

By fitting susceptibility data with those three relations (Figure 9.4), the calculated values of τ_0 (given in Table 9.1), indicate that the computed values of τ_0 are too large for an ensemble of weakly interacting nanoparticles. Thus, the Vogel–Fulcher model cannot be considered for this state. Furthermore, since the SEM images of those nanoparticles exhibited agglomerated state for those nanoparticles, it suggests that the Vogel–Fulcher model cannot be a choice to fit them as well. This statement

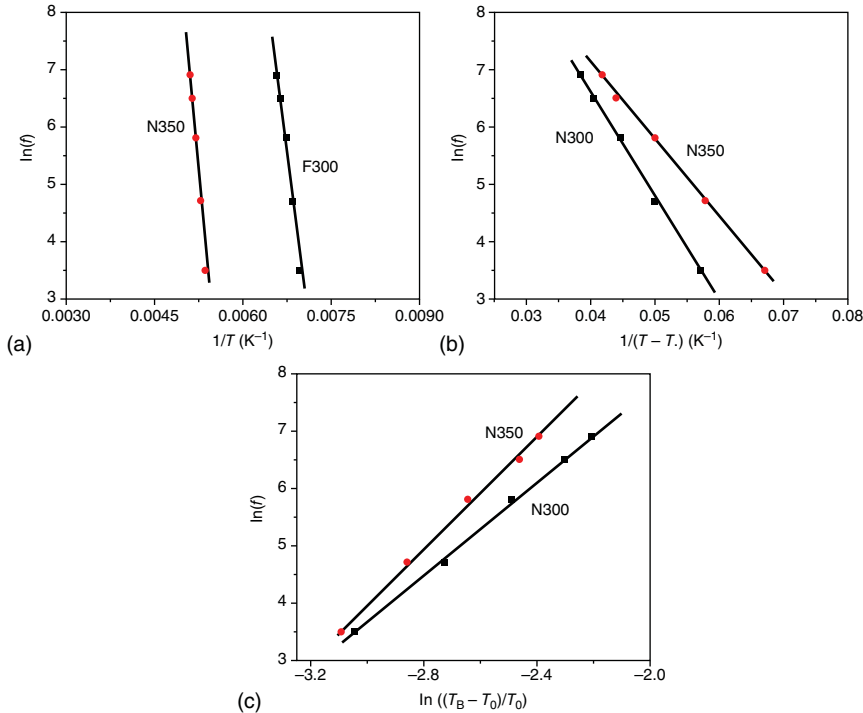


Figure 9.4 The best fits of AC magnetic susceptibility data for the samples heated at 300 and 350 °C using (a) Néel–Brown model, (b) Vogel–Fulcher, and (c) critical slowing down model. Source: Aslibeiki et al. [36]/with permission of Elsevier.



Table 9.1 C parameter and fitting data of three models.

Model	Parameter	N300	N350
Model-independent	C	0.039	0.035
Néel–Brown	τ_0 (s)	1.04×10^{-28}	9.85×10^{-34}
	E_a/k_B (K)	8741	13 521
Vogel–Fulcher	τ_0 (s)	1.16×10^{-6}	3.94×10^{-6}
	E_a/k_B (K)	138	133
	T_0 (K)	126	177
Critical slowing down	τ_0 (s)	1.12×10^{-7}	1.57×10^{-8}
	$z\nu$	4.11	4.81
	T_0 (K)	137	178

Source: Aslibeiki et al. [36]/with permission of Elsevier.

comes from the idea that there is strong dipole–dipole interaction in agglomerated α -Fe nanoparticles and the energy barrier for the agglomerates per one nanoparticle could not be identified from the Néel–Brown model and its modified models (Vogel–Fulcher model) [29, 30, 36]. This suggests that the SSG behavior should be sought in agglomerated as well as strongly interacting nanoparticles; strong interactions between superspins. This behavior can be described based on the conventional critical slowing down model [35]. The divergence of the correlation length or equally, relaxation time near T_0 , indicates the presence of a true equilibrium thermodynamic phase transition. The log–log plot of the external frequency (f) versus reduced temperature, $(T_p - T_0)/T_0$, for the given samples in Figure 9.5, shows an excellent linear dependence. The estimated values of T_0 , τ_0 , and $z\nu$ are given in Table 9.1; for those two samples heated at 300 and 350 °C based on those three models. For spin-glass systems, $z\nu$ and τ_0 are in the range of 4–12 and 10^{-11} – 10^{-13} [38, 39]. On the other hand, for interacting nanoparticle systems, smaller values are also reported, as mentioned above.

In spin-glass systems, the C parameter as ($C = \Delta T_p / T_p \Delta(\log f)$) is used to confirm the validity of the results. Herewith, ΔT_p is the difference between T_p , measured at

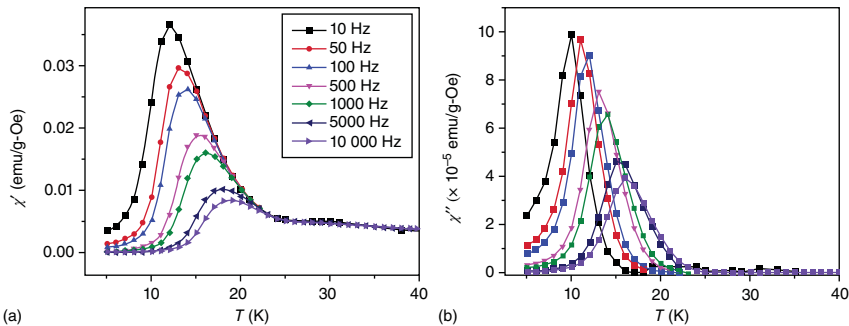


Figure 9.5 Frequency and temperature dependence of (a) χ' and (b) χ'' components of AC susceptibility. Source: Chandra [62].



the frequency $\Delta(\log_{10}f)$ interval, and T_p is the mean value of maximum temperature in the range of experimental frequencies. C is a model-independent parameter and is used to determine the type of interactions between superspins [63]. Based on the obtained values of C , there are three different types of dynamical behavior for non-interacting particles, $0.13 < C$, in the medium interaction regime, $0.05 < C < 0.13$, and for strongly interacting spins (spin glasses), $0.005 < C < 0.05$ [30, 63]. In Table 9.1, the given values of C indicate that the values decline by increasing particle size. This is because the magnetic moment increases by increasing the size of particles and consequently, the dipole–dipole interaction increases, and the C value decreases. By comparing the values of C for the samples in Table 9.1 with the above-mentioned values, one may claim the presence of SSG behavior in nanoparticles of Fe_3O_4 that are in the range of ~ 10 nm sizes.

Figure 9.5 shows the $\chi'(T)$ and $\chi''(T)$ curves for a nanoparticle ensemble, taken using the AC measurement system (ACMS) probe in the frequency range of 10 Hz to 10 kHz, and with an AC applied field of 10 Oe [62]. The ACMS option can detect the phase shift (θ) and measure the in-phase (real part) component χ' as well as the out-of-phase (imaginary part) component χ'' . The real component of AC susceptibility represents the slope of the $M(H)$ curve in the low-frequency limit, and it is sensitive to changes in the magnetic state of a material, exhibiting peaks at magnetic phase transitions or magnetic blocking in the case of nanostructures. The imaginary component reflects the loss in magnetic energy and is proportional to the area of the $M(H)$ hysteresis loop carved in one period of an AC cycle. For metallic or conductive samples, a non-zero χ'' represents dissipation due to eddy current. On the other hand, the presence of finite χ'' in the case of ferromagnets is indicative of irreversible domain wall motion or absorption due to a permanent moment. In the case of a nanoparticle ensemble with glassy dynamics, or a conventional spin glass system, a nonzero χ'' can arise due to magnetic relaxation, because the decoupling of spins from the lattice in the relaxation process can cause absorption of energy.

As can be seen in Figure 9.5, the peak in the $\chi'(T)$ and $\chi''(T)$ curves shifts to higher temperatures with the increase in the measurement frequency. Typically, in the case of MNPs, the development of such peaks can be associated with magnetic freezing phenomena or magnetic blocking [64]. By changing the frequency ($\omega = 2\pi f$), deliberately changing the probe time ($\tau = 1/f$) allows us to probe the relaxation of particles in different time windows. A systematic investigation of the evolution of peak shift in χ' is carried out. The peak shift in χ' can be quantified by $\Gamma = \frac{\Delta T_p}{T_p \Delta(\log \omega)}$, and it is empirically known that for SPMNPs, Γ ranges from 0.1 to 0.13 whereas for SSG systems $\Gamma < 0.06$ [65]. Further, the nature of peak shift can be tested using the Néel–Arrhenius (NA) relation for a non-interacting particle ensemble, or the Vogel–Fulcher (VF) relation for a weakly interacting particle system [65]. The peak temperature is plotted as a function of frequency, to which the relations mentioned are applied. In the VF relation, T_0 is the characteristic temperature, which gives a qualitative measure of the inter-particle interaction energy. Depending on the nature of the fit, and values of the fitting parameters obtained, one can deduce information about particle interactions, and magnetization dynamics as given in the following examples of MNP systems.



Figure 9.6 shows the χ' and χ'' parts of the AC susceptibility as a function of temperature at different frequencies and 5 Oe for the nanostructured block copolymers (BCPs) materials composited with different percentages of cobalt (Co); 13%, 66%, and 100% [66]. The results indicate that the χ' declines with an increase in frequency for all those three samples, which is consistent with other interacting magnetic systems, like spin glasses [67, 68].

The χ' component enhances with temperature and no peaks are evident in the temperature range considered, which distinguishes the magnetic behavior of this system from that of canonical spin-glass systems. The peak in χ' observed in spin glass systems is often interpreted as a phase transition between different magnetic states [67, 68]. Although the lack of peaks in the χ' curves prevents the determination of the intrinsic relaxation times and energy barriers by an Arrhenius plot, the χ' increases continuously with temperature for the 100% Co sample (Figure 9.6a), whereas saturation in χ' as a function of temperature is seen in the case of 13% and 66% Co samples (Figure 9.6b,c). Additionally, the saturation temperature for the 66% Co sample (~ 300 K) is higher than that of the 13% Co sample (~ 225 K). It has been reported that the peak in the χ' curve shifts toward higher temperatures with the increase in dipolar interactions [20, 69]. Although no peak in χ' is seen in the BCPs/Co systems, the χ' saturation temperatures followed the same trend. With decreasing cobalt density in the cylindrical domains, the dipolar interactions decline as well. This is confirmed by a decrease in the χ' saturation temperature, which is following the results obtained from the $M-H$ and ZFC-FC studies [66]. In another magnetic composite, polyaniline/ Fe_3O_4 nanostructures, the AC susceptibility study revealed that the peak position of the AC susceptibility of the nanocomposites shifts to a higher temperature (>245 K) compared with that of pure Fe_3O_4 nanoparticles (190–200 K). These results suggest that interactions between the polymer matrix and magnetic NPs take place in these nanocomposites [70].

To further investigate the influence of interparticle interactions on the magnetic relaxation in the Cyano-Bridged Magnetic Nanoparticles system, Clavel et al. performed AC susceptibility measurements with varying nanoparticle concentrations and thus with varying interparticle interaction strength [71]. The temperature dependence of the AC susceptibility for the $\text{Cu}_3[\text{Fe}(\text{CN})_6]_2/[\text{BMIM}][\text{BF}_4]$ sample was measured for three different concentrations of 1.4×10^{-6} , 7.4×10^{-7} , and 1.8×10^{-7} m. With decreasing concentration, the peaks of the χ' and χ'' components were shifted to lower temperatures (Figure 9.7), which suggests that the blocking temperature, and most likely the energy barrier, decreases with decreasing interparticle interactions.

In addition, the Arrhenius law fitting of the thermal variation of the relaxation time performed for this series of samples indicated that the energy barrier Δ/k_B decreases with decreasing interaction strength. These features are in accord with the studies performed on strongly interacting particles in frozen ferrofluids [72]. On the other hand, the thermal variation of the relaxation time of the most diluted sample (1.8×10^{-7} m) cannot be satisfactorily fitted with a power law, visibly suggesting that the decrease of interparticle interactions within the series of concentrations leads to the change of the magnetic regime from spin-glass-like dynamics to a superparamagnetic regime modified by interparticle interactions [73].



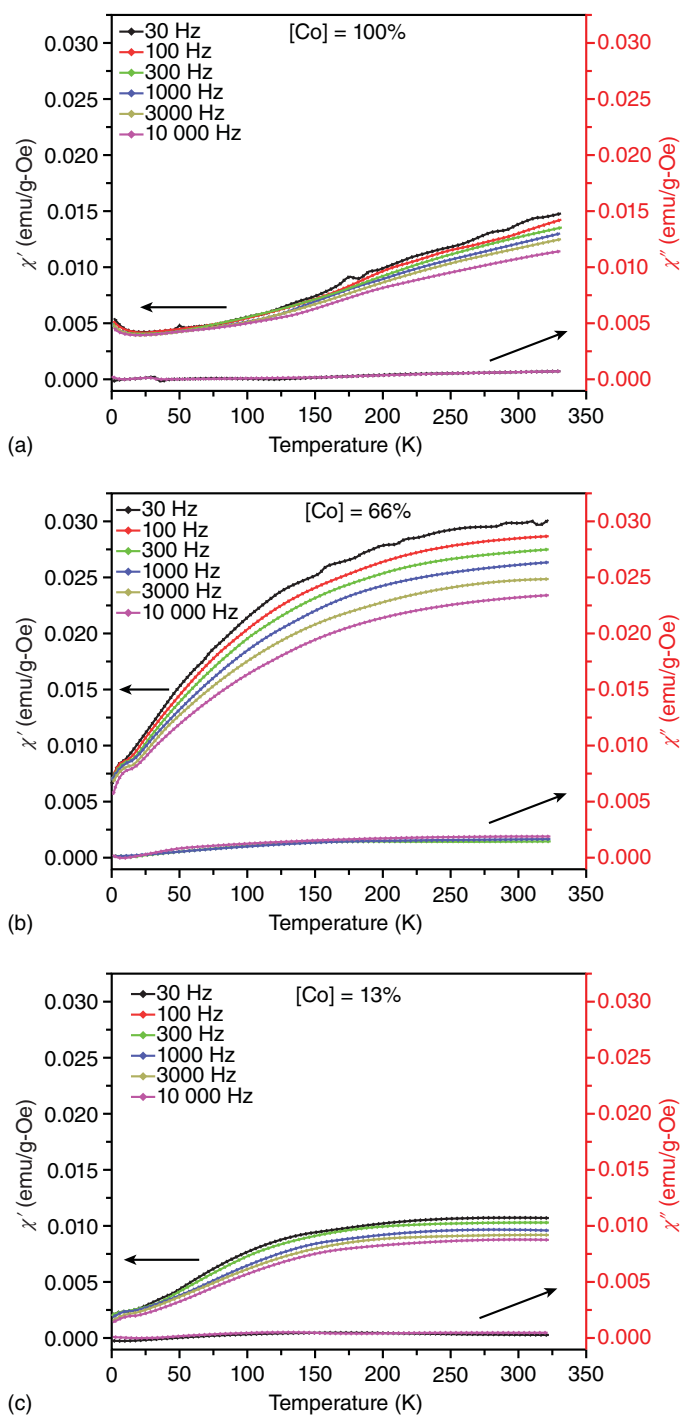


Figure 9.6 Temperature dependence of the χ' and χ'' of the AC susceptibility, measured at various frequencies (30–10 000 Hz) with an AC field of 5 Oe, for the nanostructured BCPs/Co materials with (a) 100%, (b) 66%, and (c) 13% Co units in the cylindrical domains. Source: Zha et al. [66]/American Chemical Society.



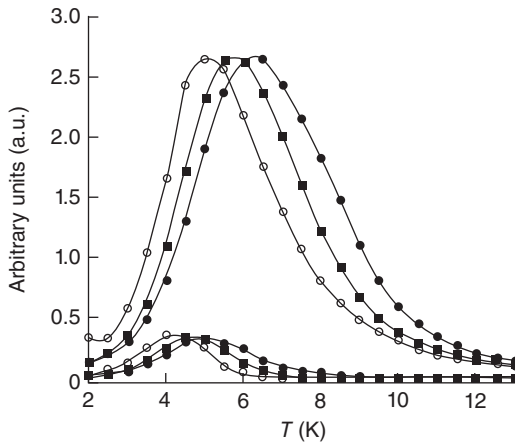


Figure 9.7 Temperature dependence of the χ' and χ'' components of the AC susceptibility measured with the frequency of 1 Hz for a colloid system with varying concentrations: 1.4×10^{-6} m (●), 7.4×10^{-7} m (■), and 1.8×10^{-7} m (○). Source: Clavel et al. [71]/with permission of John Wiley & Sons.

The χ' and χ'' parts as a function of temperature for the magnetic nanoparticles in $\text{Co}_{80}\text{Fe}_{20}/\text{Al}_2\text{O}_3$ multilayers, where the susceptibility measured in the frequency range $0.01 \leq f \leq 100$ Hz at an AC amplitude of 0.05 mT, are shown in Figure 9.8a [74]. It is evident that the peaks of both χ' and χ'' shift toward lower temperatures upon the frequency (f) lessening or, equivalently, enhancing the observation time $t = 1/\omega$, where $\omega = 2\pi f$. A peak in χ' (or in the low-field DC-magnetization M/H) refers to the situation where the observation time (t) equals the relaxation time (τ) of the system. Thus, useful information on the relaxational dynamics can be obtained from the variation of the peak position, T_m , of $\chi'(T)$ at different frequencies. In case of a collection of noninteracting nanoparticles with randomly distributed anisotropy axes, the relaxation time follows an Arrhenius law, $\tau \equiv 1/\omega = \tau_0 \exp\left(\frac{KV}{k_B T_m}\right)$, within the framework of the Néel–Brown model [55]. Here, τ_0 is the angular inverse attempt frequency, K is the anisotropy constant, V is the volume of the particle, and k_B is the Boltzmann constant. Figure 9.8b shows a plot of $\log_{10}(\tau)$ versus $1/T_m$, which yields $KV = 2.4 \times 10^{-20}$ J and $\tau_0 = 10^{-23}$ seconds when fitted to the Arrhenius law (solid line). While the value of anisotropy energy KV appears reasonable, the rather unphysical value of τ_0 indicates that the relaxational dynamics of the system cannot be adequately described by the Néel–Brown model.

Alternatively, the data are very well described by assuming critical dynamics of a spin glass with a finite static glass temperature T_g as shown in Figure 9.8c [22]. Indeed, the best fit of the data to the power-law $\tau = \tau^*(T_m/T_g - 1)^{-z\nu}$ yields $T_g = 61 \pm 2$ K, a dynamic critical exponent $z\nu = 10.2 \pm 2.6$, and a relaxation time of individual particle moment $\tau^* = 10^{-8}$ seconds. It should be noted that the fairly large values of τ^* refers to the single superspin dynamics, which obeys Néel–Brown behavior, $\tau^* = \tau_0 \exp(KV/k_B T)$, with $\tau_0 \approx 10^{-10}$ seconds, and $KV \approx 10^{-20}$ J [75]. The values of $z\nu$ and τ^* are very close to those reported previously on a similar system [76]. Another useful quantity that can be obtained from AC susceptibility is the relative shift of T_m at different frequencies, $k = \Delta T_m / T_m \cdot \Delta \log \omega$, found in this system to be 0.04 which comes close to those found in classic spin-glass systems [22]. These properties give very strong hints at a collective rather than a single-particle low-temperature behavior of the $\text{Co}_{80}\text{Fe}_{20}/\text{Al}_2\text{O}_3$ NPs system.



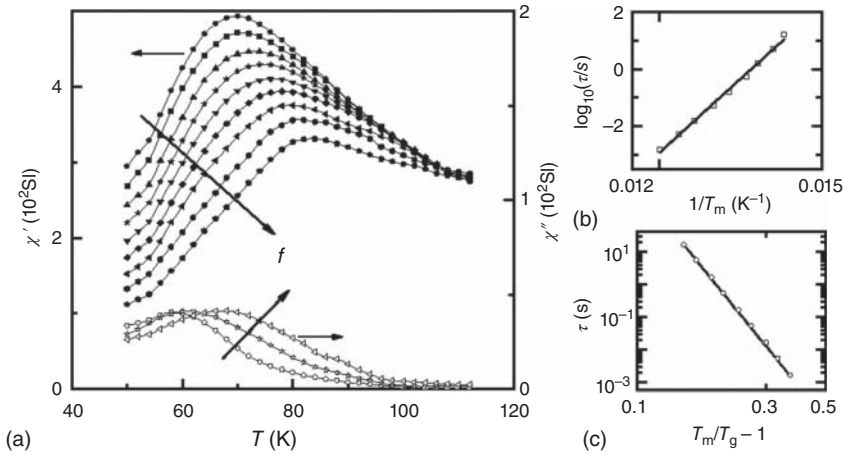


Figure 9.8 (a) The χ' and χ'' parts as a function of temperature for the MNPs in $\text{Co}_{80}\text{Fe}_{20}/\text{Al}_2\text{O}_3$ multilayers at $f = 0.01, 0.03, 0.1, 0.3, 1, 3, 10, 30$, and 100 Hz and $f = 0.01, 0.3$, and 10 Hz, respectively. (b) $\log_{10}(\tau/s)$ versus $1/T_m$ and the best fit to an Arrhenius law (straight line). (c) Double logarithmic plot of τ versus $T_m/T_g - 1$, and best fit to a power law (straight line). Source: Sahoo et al. [74]/with permission of AIP Publishing.

The frequency (f) dependence of the in-phase (χ') and the out-phase (χ'') AC susceptibility in the frequency range of 100–7000 Hz and under a magnetic excitation field with amplitude $H_{ac} = 10$ Oe for the $\text{CoFe}_2\text{O}_4/\text{Ag}$ composites NPs is shown in Figure 9.9a [77]. In the χ' data, a peak observed at $T_{\max} \approx 225$ K shifts to higher temperatures with the increase of frequency. Two peaks were observed at 42 and 200 K in the χ'' data at 7000 Hz. To examine the cusps at T_{\max} as a function of frequency, the Néel–Brown model, $\tau = \tau_0 \exp\left(\frac{E_a}{k_B T}\right)$, where E_a is the activation anisotropy energy of each particle, τ_0 is the attempt time, and k_B is the Boltzmann constant [35, 36] has been considered to evaluate an ensemble of non-interacting single domain MNPs with their super moments relaxing with a period of $\tau = 1/f$ in the presence of a thermal bath at T absolute temperature. The experimental data for $\ln(f)$ and the peak temperature are shown in Figure 9.9b, with an attempt time of $\tau_0 = 2.52 \times 10^{-25}$ seconds and $E_a/k_B = 11\,871$ K. The attempt time is significantly less than the expected values of $\tau_0 = 10^{-9}$ – 10^{-12} seconds, and so, it has no physical significance. As a result, the Néel–Brown model is ineffective for studying AC susceptibility data; instead, the system must be subjected to interacting forces that slow down magnetic moment relaxation. The parameter ψ , which is the relative variation of the freezing temperature (T_{\max}) per frequency decade, has been taken into account to further explicate the true magnetic state of the sample. This equation is defined as $\psi = \frac{\Delta T_{\max}}{T_{\max} \Delta(\log_{10} f)}$.

It is known that for the strong interaction regime (homogeneous freezing) ψ takes the values $0.005 < \psi < 0.02$, for the weak interaction regime (inhomogeneous freezing) the values are $0.03 < \psi < 0.06$, and for non-interacting particles it holds the values between $0.1 < \psi < 0.13$ [37]. The computed value of ψ is approximately 0.04 for the $\text{CoFe}_2\text{O}_4/\text{Ag}$ composites NPs. This indicates the sample is in a spin



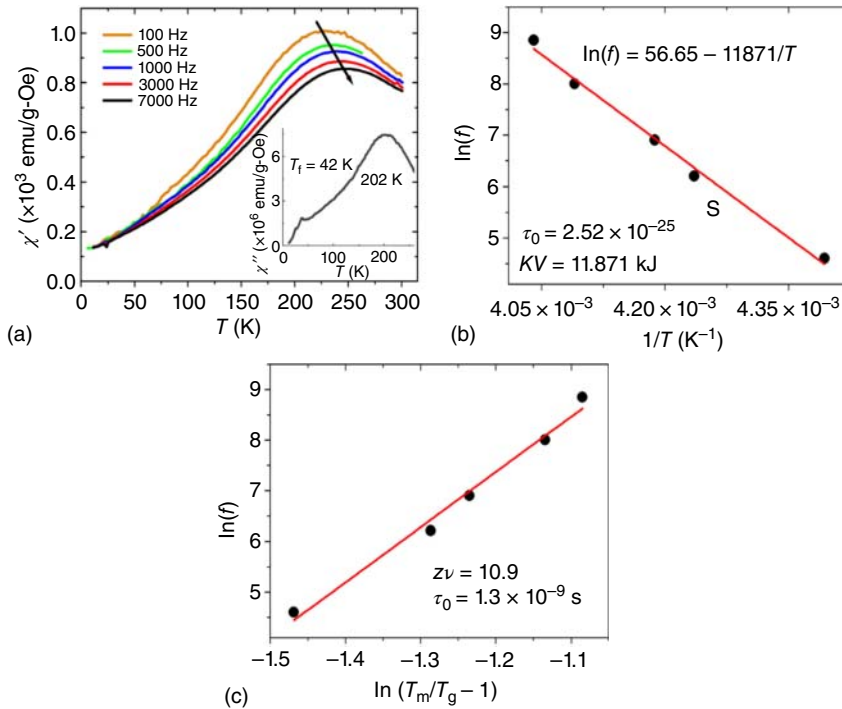


Figure 9.9 Frequency dependence of the in-phase AC susceptibility of $\text{CoFe}_2\text{O}_4/\text{Ag}$ composites NPs in the frequency range 100–7000 Hz under magnetic field excitation with amplitude $H_{AC} = 10$ Oe; The inset shows the χ'' signal for a frequency of 7000 Hz, (b) Fitting of graph $\ln(f) \times 1/T$ to the Néel–Brown model, and (c) Fitting of graph $\ln(f) \times \ln(T_m/T_g - 1)$ to the scaling law. Source: Pinheiro et al. [77]/with permission of Elsevier.

glass regime with weak interactions. The data were examined using the dynamic scaling law to learn more about the sample's spin glass state. In this model, the characteristic relaxation time τ diverges when the temperature approaches the glass transition as $\tau = \tau_0(T_m/T_g - 1)^{-z\nu}$, where T_g is the glass temperature and z and ν are the critical exponents, and τ_0 is the characteristic time scale of the system [38, 39]. The fit is shown in Figure 9.9c, along with their fitting parameters. Hence, the values of τ_0 and $z\nu$ are 1.3×10^{-9} seconds and 10.9, respectively. These values are within the expected range for spin-glass systems, $z\nu$ (6–12) and τ_0 (10^{-7} – 10^{-13}) [37–39]. As a result, random frozen superparamagnetic moments are most likely to give rise to the emergence of spin-glass behavior [40]. For the χ'' data, the peak at $T_f = 42$ K is considered to be the freezing of moments present in the disordered surface layer of the as-synthesized MNPs. These moments occur as a result of their small size or oxygen vacancies that influence the exchange interactions. The oxygen vacancies are associated with the Ag-doping CoFe_2O_4 NPs. Since the Ag^{1+} ionic radius is larger than that of the Fe^{2+} or Co^{2+} ionic radius, the migration of Ag^{1+} ions to the particle boundaries may take place and as a result, hinder the particle's growth.

The χ' and χ'' AC susceptibility measurements for the carbon nanotubes (CNTs)/ Fe_3O_4 composite NPs at different frequencies are shown in Figure 9.10a,b [79].



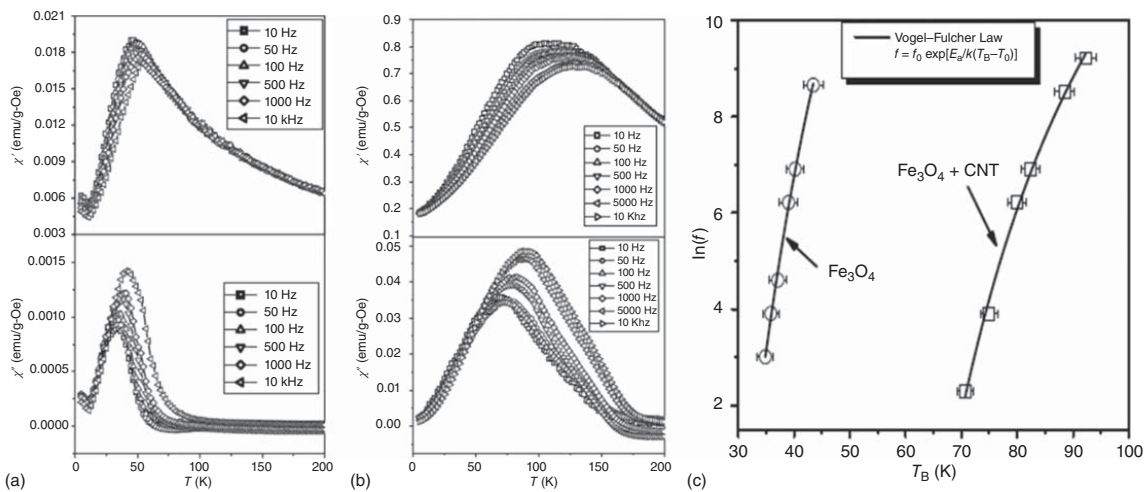


Figure 9.10 AC susceptibility graphs of (a) Fe_3O_4 NPs and (b) CNTs filled with Fe_3O_4 NPs, and (c) Vogel-Fulcher fitting data of Fe_3O_4 NPs (o) and CNTs filled with Fe_3O_4 NPs (\square). Source: Pal et al. [78] with permission of IOP Publishing.



It indicates that the χ' peaks are situated at a temperature higher than that for χ'' peaks for both the pristine Fe_3O_4 , and CNTs/ Fe_3O_4 composite NPs. Furthermore, the blocking temperature (T_B), which is estimated from the χ'' curve, could shift to higher temperature as frequency is enhanced. This phenomenon is also observed in other systems NPs [79]. Thus, in this case, the frequency dependence of the peaks in χ'' can be employed to fit based on the Neel-Arrhenius model ($\tau = \tau_0 \exp(E_a/kT_B)$ – where τ is the relaxation time, $\tau = 1/f$; f is the frequency), τ_0 is the microscopic flipping time of the fluctuating spins, E_a is the thermal activation energy, T_B is the blocking temperature, and T_0 is the characteristic temperature with thermal energy dominating for $T > T_0$ and interaction energy for $T < T_0$, but the fitting parameters obtained are unphysical ($\tau_0 = 1.49 \times 10^{-14}$ seconds and $E_a/k = 1003$ K for Fe_3O_4 NPs and $\tau_0 = 6.48 \times 10^{-15}$ seconds and $E_a/k = 2141$ K for CNTs/ Fe_3O_4 NPs).

Based on the Vogel-Fulcher (VF) scaling law ($\tau = \tau_0 \exp[E_a/k(T_B - T_0)]$) fitting, the model fits well the $\chi''(T)$ data (see Figure 9.10c) with acceptable fit parameters ($\tau_0 = 1.09 \times 10^{-12}$ seconds, $E_a/k = 698$ K, and $T_0 = 7$ K for Fe_3O_4 NPs and $\tau_0 = 4.78 \times 10^{-10}$ seconds, $E_a/k = 711$ K, and $T_0 = 34$ K for CNTs/ Fe_3O_4). This reveals that the present samples belong to the class of interacting particle systems [80, 81].

9.7 Using AC Susceptibility Measurements to Probe Transitions in Colloidal Suspensions

Variations in the constant-frequency AC susceptibility in terms of temperature can be used to determine and interpret the data obtained from AC susceptibility in colloidal samples. To make data interpretation easier, two limiting examples of the Debye model with infinite frequency susceptibility, provided by the equations below, can be employed.

$$\chi' = \chi_\infty + \frac{\chi_0 - \chi_\infty}{1 + \Omega^2 \tau^2}; \quad \chi'' = \frac{(\chi_0 - \chi_\infty) \Omega \tau}{1 + \Omega^2 \tau^2} \quad (9.20)$$

where χ_0 , χ_∞ , τ , and Ω refer to the initial susceptibility, infinite susceptibility, relaxation time, and the field frequency, respectively.

The real component (χ') of monodisperse suspensions decreases monotonically with increasing frequency, whereas the imaginary component (χ'') peaks at $\Omega\tau = 1$. Shifts in the peak position in NP suspensions with thermally inhibited magnetic dipoles can be linked to changes in particle diameter caused by analyte attachment. This is the foundation for an MNP-based sensor [82–87]. This cannot essentially be the case for the polydisperse suspensions or suspensions evaluated by multiple relaxation times, therefore the impact of multiple relaxation times or the size distribution should be thought about.

By considering the low-frequency limit of Eq. (9.20), expanding the χ' and χ'' components of the susceptibility in powers of the field frequency and keeping terms



quadratic in the frequency yields:

$$\chi' = \chi_\infty + (\chi_0 - \chi_\infty)(1 - \Omega^2 \tau^2); \quad \chi'' \approx (\chi_0 - \chi_\infty)\Omega\tau \quad (9.21)$$

According to this theory, monitoring a sample's low-frequency AC susceptibility offers information on the initial susceptibility (χ_0) and relaxation time (τ) changes in response to an external stimulus. For those particles with a thermally blocked magnetic dipoles behavior, the relaxation mechanism is Brownian and the relaxation time relies on the hydrodynamic diameter of particles, and the viscosity of the surrounding fluid in accordance with the following Eq. (9.22). This can be used for noninteracting particles in a Newtonian fluid.

$$\tau = \frac{\tau_B \tau_N}{\tau_B + \tau_N}; \quad \tau_B = \frac{3V_h \eta_0}{kT}; \quad \tau_N = \tau_0 \exp\left(\frac{kV_m}{kT}\right) \quad (9.22)$$

where τ is the “spin-lattice” relaxation time which follows the Arrhenius law for a thermal activation over the anisotropy energy barrier kV_m (k the anisotropy energy density and V_m is the volume of the particle), τ_0 is within the range 10^{-10} – 10^{-12} seconds, T is the temperature and k_B is the Boltzmann constant. The rotational hydrodynamic resistance of the NPs arises from the Brownian relaxation time in general. Variations in the relaxation time (as a result of changes in the AC susceptibility) reveal information about colloidal particle structure and aggregation state.

The temperature dependence of the initial and infinite frequency susceptibilities is usually inverse. Furthermore, assuming the assumptions of Eq. (9.22) are accurate, the Brownian relaxation time has an explicit inverse relationship with temperature and an implicit relationship with changes in the viscosity of the surrounding fluid. Thus, the relaxation time declines for most fluids with the increase in temperature. When this is combined with the temperature dependency of the initial and high-frequency susceptibilities, it is reasonable to predict that, in the absence of any changes in particle size or aggregation state, both components of the susceptibility should decrease as the temperature rises. The relaxation time varies dramatically depending on particle size or aggregation state. The Brownian relaxation period for well-dispersed colloidal NPs (monodispersed state), where particle-particle interactions are negligible, has a cubic relationship with hydrodynamic diameter. As a result, even a little increase (reduction) in hydrodynamic diameter leads to a significant rise (decrease) in relaxation time. When particles are aggregated, Eq. (9.22) no longer applies; yet, due to close contact hydrodynamic (lubrication) pressures, aggregation causes a rise in the rotating hydrodynamic resistance coefficient of the particles. As a result, aggregation (dispersion) should cause Brownian relaxation time to significantly increase (decrease). A sharp rise (reduction) in the relaxation period causes a sharp decrease (increase) in the χ' part of the low-frequency susceptibility and an increase (decrease) in the χ'' portion. It is possible to expand the real (χ') and imaginary (χ'') parts of the susceptibility in powers of the inverse field frequency and keep terms quadratic in the inverse frequency by using the high-frequency limit of Eq. (9.20) as:

$$\chi' \approx \chi_\infty + \frac{\chi_0 - \chi_\infty}{\Omega^2 \tau^2}; \quad \chi'' \approx \frac{(\chi_0 - \chi_\infty)}{\Omega\tau} \quad (9.23)$$



For monodispersed colloidal suspensions, the real part of the AC susceptibility could rise or fall based on the respective magnitudes of the two terms on the right-hand side of Eq. (9.23), with the first decreasing and the second increasing with temperature. The imaginary part of AC susceptibility, on the other hand, remains largely constant, with variation based on variations in medium viscosity. Sharp changes in the high-frequency susceptibility could be observed in suspensions with a sharp change in the hydrodynamic diameter of non-interacting particles or a change in the state of aggregation. In this situation, increasing (decreasing) the relaxation time results in a significant drop (increase) in both susceptibility components. As an example, Figure 9.11 shows the χ' and χ'' part of the AC susceptibility for the covalently-attached poly(*N*-isopropyl acrylamide) (pNIPAM) coated cobalt ferrite NPs [88]. It indicates a sharp reversible transition at about 30 °C for both components. As discussed above, for the case of the low-frequency limit, a decline in particle hydrodynamic diameter results in a reduction in the Brownian relaxation time. In that case, an enhancement in the χ' part and a reduction in the χ'' part of the AC susceptibility could be observed. Figure 9.11 shows the inverse behavior, exhibiting a process that increases the hydrodynamic rotational resistance, resulting in a dramatic rise in the relaxation time and MNP aggregation.

The complex susceptibility of several magnetic core-shell nanoparticle suspensions was tested and compared to theoretical models in the frequency range of 100 Hz to 1 MHz. In accordance with theory, the spectrum of the imaginary part of the AC susceptibility measured on aqueous suspensions of multicore magnetite nanoparticles with large distributions of core and hydrodynamic diameters comprises contributions from Brownian and Néel relaxation. Furthermore, the magnetic field dependency of the Brownian relaxation time may be used to infer the core size distribution from measurements on magnetic nanoparticle suspensions, whereas the mean hydrodynamic diameter can be calculated from the Brownian peak in the imaginary part of the AC susceptibility in zero fields. A second maximum in the imaginary part of the AC susceptibility below the Brownian peak with a resonant-like look was discovered for higher concentrated nanoparticle suspensions where magnetic dipole-dipole interactions are expected [89].

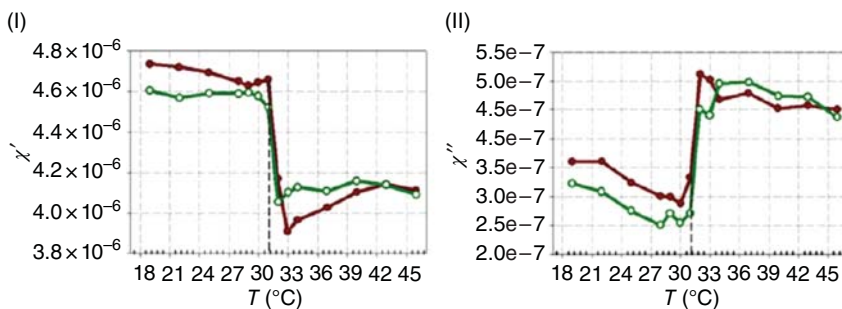


Figure 9.11 The χ' and χ'' parts as a function of temperature for the pNIPAM-coated cobalt ferrite NPs in heating (●) and cooling (○) states. Source: Herrera et al. [88]/with permission of Elsevier.



References

- 1 Gömöry, F. (1997). Characterization of high-temperature superconductors by AC susceptibility measurements. *Superconductor Science and Technology* 10: 523.
- 2 Frischherz, M., Sauerzopf, F., Weber, H. et al. (1995). Comparative study of experimental techniques for irreversibility lines and critical current densities in high-temperature superconductors. *Superconductor Science and Technology* 8: 485.
- 3 Perez, F., Obradors, X., Fontcuberta, J. et al. (1994). Intergranular flux penetration and creep in strongly connected $\text{YBa}_2\text{Cu}_3\text{O}_7$ ceramics. *Physica C: Superconductivity* 235: 2941–2942.
- 4 Senoussi, S. (1992). Review of the critical current densities and magnetic irreversibilities in high T_c superconductors. *Journal de Physique III* (2): 1041–1257.
- 5 Cador, O., Grasset, F., Haneda, H., and Etourneau, J. (2004). Memory effect and super-spin-glass ordering in an aggregated nanoparticle sample. *Journal of Magnetism and Magnetic Materials* 268: 232–236.
- 6 Hajalilou, A., Hashim, M., Ebrahimi-Kahrizsangi, R., and Sarami, N. (2015). Influence of CaO and SiO_2 co-doping on the magnetic, electrical properties and microstructure of a Ni–Zn ferrite. *Journal of Physics D: Applied Physics* 48: 145001.
- 7 Hajalilou, A., Ferreira, L.P., Melo Jorge, M.E. et al. (2021). Superparamagnetic Ag- Fe_3O_4 composites nanoparticles for magnetic fluid hyperthermia. *Journal of Magnetism and Magnetic Materials* 537: 168242.
- 8 Hajalilou, A., Hashim, M., and Mohamed Kamari, H. (2014). Effects of additives and sintering time on the microstructure of Ni–Zn ferrite and its electrical and magnetic properties. *Advances in Materials Science and Engineering* 2014: 138789. <https://doi.org/10.1155/2014/138789>.
- 9 Jalili, H., Aslibeiki, B., Hajalilou, A. et al. (2022). Bimagnetic hard/soft and soft/hard ferrite nanocomposites: Structural, magnetic and hyperthermia properties. *Ceramics International* 48: 4886–4896.
- 10 Kavkhani, R., Hajalilou, A., Abouzari-Lotf, E. et al. (2022). CTAB assisted synthesis of $\text{MnFe}_2\text{O}_4@ \text{SiO}_2$ nanoparticles for magnetic hyperthermia and MRI application. *Materials Today Communications* 31: 103412. <https://doi.org/10.1016/j.mtcomm.2022.103412>.
- 11 Giapintzakis, J., Neiman, R., Ginsberg, D., and Kirk, M. (1994). Multiple peaks in the ac susceptibility of untwinned Y–Ba–Cu–O single crystals: A manifestation of the peak effect. *Physical Review B* 50: 16001.
- 12 Akhmeteli, A.M., Gavrilin, A.V., Marshall, W., and Tran, L. (2006). Superconducting and resistive tilted coil magnets. Magnetic and mechanical aspects. In: *Superconductivity, Magnetism and Magnets* (ed. L.K. Tran), 139–172. Nova Publishers.
- 13 Nikolo, M. (1995). Superconductivity: a guide to alternating current susceptibility measurements and alternating current susceptometer design. *American Journal of Physics* 63: 57–65.



- 14 McCann, D.M. (2017). AC susceptibility studies under hydrostatic pressure. The University of Edinburgh, Physics thesis and dissertation collection, <http://hdl.handle.net/1842/23642>.
- 15 Chen, D.-X., Sanchez, A., Puig, T. et al. (1990). AC susceptibility of grains and matrix for high-T_c superconductors. *Physica C: Superconductivity* 168: 652–667.
- 16 Gömöry, F. and Lobotka, P. (1988). Determination of shielding current density in bulk cylindrical samples of high-T_c superconductors from AC susceptibility measurements. *Solid State Communications* 66: 645–649.
- 17 Goldfarb, R.B. and Minervini, J. (1984). Calibration of ac susceptometer for cylindrical specimens. *Review of Scientific Instruments* 55: 761–764.
- 18 Topping, C. and Blundell, S. (2018). AC susceptibility as a probe of low-frequency magnetic dynamics. *Journal of Physics: Condensed Matter* 31: 013001.
- 19 Morales, M.B. (2009). Magnetization dynamics and interparticle interactions in ferrofluids and nanostructures.
- 20 Jonsson, T., Nordblad, P., and Svedlindh, P. (1998). Dynamic study of dipole–dipole interaction effects in a magnetic nanoparticle system. *Physical Review B* 57: 497.
- 21 Goya, G. and Sagredo, V. (2001). Spin-glass ordering in Zn_{1-x}Mn_xIn₂Te₄ diluted magnetic semiconductor. *Physical Review B* 64: 235208.
- 22 Mydosh, J.A. (1993). *Spin Glasses: An Experimental Introduction*. CRC Press.
- 23 Singh, V., Seehra, M., and Bonevich, J. (2009). ac susceptibility studies of magnetic relaxation in nanoparticles of Ni dispersed in silica. *Journal of Applied Physics* 105: 07B518.
- 24 Goya, G., Berquo, T., Fonseca, F., and Morales, M. (2003). Static and dynamic magnetic properties of spherical magnetite nanoparticles. *Journal of Applied Physics* 94: 3520–3528.
- 25 Brown, W.F. Jr., (1963). Thermal fluctuations of a single-domain particle. *Physical Review* 130: 1677.
- 26 Tadic, M., Kusigerski, V., Markovic, D. et al. (2009). High concentration of hematite nanoparticles in a silica matrix: structural and magnetic properties. *Journal of Magnetism and Magnetic Materials* 321: 12–16.
- 27 Parekh, K. and Upadhyay, R.V. (2010). Static and dynamic magnetic properties of monodispersed Mn_{0.5}Zn_{0.5}Fe₂O₄ nanomagnetic particles. *Journal of Applied Physics* 107: 053907.
- 28 Aslibeiki, B., Kameli, P., Salamati, H. et al. (2010). Superspin glass state in MnFe₂O₄ nanoparticles. *Journal of Magnetism and Magnetic Materials* 322: 2929–2934.
- 29 Kura, H., Takahashi, M., and Ogawa, T. (2010). Extreme enhancement of blocking temperature by strong magnetic dipoles interaction of α-Fe nanoparticle-based high-density agglomerate. *Journal of Physics D: Applied Physics* 44: 022002.
- 30 Dormann, J., Fiorani, D., and Tronc, E. (1999). On the models for interparticle interactions in nanoparticle assemblies: comparison with experimental results. *Journal of Magnetism and Magnetic Materials* 202: 251–267.
- 31 Shtrikman, S. and Wohlfarth, E. (1981). The theory of the Vogel–Fulcher law of spin glasses. *Physics Letters A* 85: 467–470.



- 32 Aslibeiki, B., Kameli, P., and Salamati, H. (2012). The effect of grinding on magnetic properties of agglomerated MnFe_2O_4 nanoparticles. *Journal of Magnetism and Magnetic Materials* 324: 154–160.
- 33 Thakur, M., De, K., Giri, S. et al. (2006). Interparticle interaction and size effect in polymer coated magnetite nanoparticles. *Journal of Physics: Condensed Matter* 18: 9093.
- 34 Aslibeiki, B., Kameli, P., and Salamati, H. (2016). The effect of dipole–dipole interactions on coercivity, anisotropy constant, and blocking temperature of MnFe_2O_4 nanoparticles. *Journal of Applied Physics* 119: 063901.
- 35 Ogielski, A.T. and Morgenstern, I. (1985). Critical behavior of three-dimensional Ising spin-glass model. *Physical Review Letters* 54: 928.
- 36 Aslibeiki, B., Kameli, P., Manouchehri, I., and Salamati, H. (2012). Strongly interacting superspins in Fe_3O_4 nanoparticles. *Current Applied Physics* 12: 812–816.
- 37 Jonsson, P.E. (2004). Superparamagnetism and spin glass dynamics of interacting magnetic nanoparticle systems. *Advances in Chemical Physics* 128: 191–248.
- 38 Jonason, K., Mattsson, J., and Nordblad, P. (1996). Dynamic susceptibility of a reentrant ferromagnet. *Physical Review B* 53: 6507.
- 39 Nam, D., Jonason, K., Nordblad, P. et al. (1999). Coexistence of ferromagnetic and glassy behavior in the $\text{La}_{0.5}\text{Sr}_{0.5}\text{CoO}_3$ perovskite compound. *Physical Review B* 59: 4189.
- 40 Roy, B. and Das, S. (2008). Magnetic cluster glass behavior and grain boundary effect in $\text{Nd}_{0.7}\text{Ba}_{0.3}\text{MnO}_3$ nanoparticles. *Journal of Applied Physics* 104: 103915.
- 41 Fiorani, D., Testa, A., Lucari, F. et al. (2002). Magnetic properties of maghemite nanoparticle systems: surface anisotropy and interparticle interaction effects. *Physica B: Condensed Matter* 320: 122–126.
- 42 Mukadam, M., Yusuf, S., Sharma, P. et al. (2005). Dynamics of spin clusters in amorphous Fe_2O_3 . *Physical Review B* 72: 174408.
- 43 Winkler, E., Zysler, R., Mansilla, M.V. et al. (2008). Surface spin-glass freezing in interacting core–shell NiO nanoparticles. *Nanotechnology* 19: 185702.
- 44 Thakur, M., Patra, M., Majumdar, S., and Giri, S. (2009). Coexistence of superparamagnetic and superspin glass behaviors in $\text{Co}_{50}\text{Ni}_{50}$ nanoparticles embedded in the amorphous SiO_2 host. *Journal of Applied Physics* 105: 073905.
- 45 Suzuki, M., Fullem, S.I., Suzuki, I.S. et al. (2009). Observation of superspin-glass behavior in Fe_3O_4 nanoparticles. *Physical Review B* 79: 024418.
- 46 Alonso, J., Fdez-Gubieda, M., Barandiarán, J. et al. (2010). Crossover from superspin glass to superferromagnet in $\text{Fe}_x\text{Ag}_{100-x}$ nanostructured thin films ($20 \leq x \leq 50$). *Physical Review B* 82: 054406.
- 47 Idzikowski, B., Rössler, U., Eckert, D. et al. (1999). Spin-glass–like ordering in giant magnetoresistive CuCo. *EPL (Europhysics Letters)* 45: 714.
- 48 Jalaly, M., Enayati, M., and Karimzadeh, F. (2009). Investigation of structural and magnetic properties of nanocrystalline $\text{Ni}_{0.3}\text{Zn}_{0.7}\text{Fe}_2\text{O}_4$ prepared by high energy ball milling. *Journal of Alloys and Compounds* 480: 737–740.
- 49 Gittleman, J., Abeles, B., and Bozowski, S. (1974). Superparamagnetism and relaxation effects in granular Ni– SiO_2 and Ni– Al_2O_3 films. *Physical Review B* 9: 3891.



- 50 Madsen, D.E., Hansen, M.F., and Mørup, S. (2008). The correlation between superparamagnetic blocking temperatures and peak temperatures obtained from ac magnetization measurements. *Journal of Physics: Condensed Matter* 20: 345209.
- 51 Bedanta, S. and Kleemann, W. (2008). Supermagnetism. *Journal of Physics D: Applied Physics* 42: 013001.
- 52 Fischer, K.H. and Hertz, J.A. (1993). *Spin Glasses*. Cambridge University Press.
- 53 Masunaga, S.H., Jardim, R.d.F., Fichtner, P.F.P., and Rivas, J. (2009). Role of dipolar interactions in a system of Ni nanoparticles studied by magnetic susceptibility measurements. *Physical Review B* 80: 184428.
- 54 Dormann, J., Bessais, L., and Fiorani, D. (1988). A dynamic study of small interacting particles: superparamagnetic model and spin-glass laws. *Journal of Physics C: Solid State Physics* 21: 2015.
- 55 Néel, L. (1949). Théorie du trainage magnétique des ferromagnétiques en grains fins avec applications aux terres cuites. *Annals of Géophysics* 5: 99–136.
- 56 Hajalilou, A., Hashim, M., and Kamari, H.M. (2015). Structure and magnetic properties of $\text{Ni}_{0.64}\text{Zn}_{0.36}\text{Fe}_2\text{O}_4$ nanoparticles synthesized by high-energy milling and subsequent heat treatment. *Journal of Materials Science: Materials in Electronics* 26: 1709–1718.
- 57 Hajalilou, A., Hashim, M., Kamari, H.M., and Masoudi, M.T. (2015). Effects of milling atmosphere and increasing sintering temperature on the magnetic properties of nanocrystalline $\text{Ni}_{0.36}\text{Zn}_{0.64}\text{Fe}_2\text{O}_4$. *Journal of Nanomaterials* 16: 232.
- 58 Hajalilou, A., Hashim, M., Ebrahimi-Kahrizangi, R., and Kamari, H.M. (2015). Influence of evolving microstructure on electrical and magnetic characteristics in mechanically synthesized polycrystalline Ni-ferrite nanoparticles. *Journal of Alloys and Compounds* 633: 306–316.
- 59 Hajalilou, A., Kamari, H.M., and Shameli, K. (2017). Dielectric and electrical characteristics of mechanically synthesized Ni–Zn ferrite nanoparticles. *Journal of Alloys and Compounds* 708: 813–826.
- 60 Hajalilou, A., Hashim, M., Abbasi, M. et al. (2015). A comparative study on the effects of different milling atmospheres and sintering temperatures on the synthesis and magnetic behavior of spinel single phase $\text{Ni}_{0.64}\text{Zn}_{0.36}\text{Fe}_2\text{O}_4$ nanocrystals. *Journal of Materials Science: Materials in Electronics* 26: 7468–7483.
- 61 Rault, J. (2000). Origin of the Vogel–Fulcher–Tammann law in glass-forming materials: the α – β bifurcation. *Journal of Non-Crystalline Solids* 271: 177–217.
- 62 Chandra, S. (2013). Magnetization dynamics and related phenomena in nanostructures.
- 63 Tronc, E. (1997). Magnetic relaxation in fine-particle systems. *Advances in Chemical Physics* 283: 283–449.
- 64 O’handley, R.C. (1999). *Modern Magnetic Materials: Principles and Applications*, 768. Wiley ISBN: 978-0-471-15566-9.
- 65 Chandra, S., Khurshid, H., Li, W. et al. (2012). Spin dynamics and criteria for onset of exchange bias in superspin glass $\text{Fe}/\gamma\text{-Fe}_2\text{O}_3$ core-shell nanoparticles. *Physical Review B* 86 (1): 014426.



- 66 Zha, Y., Thaker, H.D., Maddikeri, R.R. et al. (2012). Nanostructured block-random copolymers with tunable magnetic properties. *Journal of the American Chemical Society* 134: 14534–14541.
- 67 Mydosh, J. (1996). Disordered magnetism and spin glasses. *Journal of Magnetism and Magnetic Materials* 157: 606–610.
- 68 Vincent, E., Yuan, Y., Hammann, J. et al. (1996). Glassy dynamics of nanometric magnetic particles. *Journal of Magnetism and Magnetic Materials* 161: 209–219.
- 69 Jonsson, T., Mattsson, J., Djurberg, C. et al. (1995). Aging in a magnetic particle system. *Physical Review Letters* 75: 4138.
- 70 Long, Y., Chen, Z., Duvail, J.L. et al. (2005). Electrical and magnetic properties of polyaniline/Fe₃O₄ nanostructures. *Physica B: Condensed Matter* 370: 121–130.
- 71 Clavel, G., Larionova, J., Guari, Y., and Guérin, C. (2006). Synthesis of cyano-bridged magnetic nanoparticles using room-temperature ionic liquids. *Chemistry – A European Journal* 12 (14): 3798–3804.
- 72 Dormann, J.L., Spinu, L., Tronc, E. et al. (1998). Effect of interparticle interactions on the dynamical properties of γ -Fe₂O₃ nanoparticles. *Journal of Magnetism and Magnetic Materials* 183: L255–L260.
- 73 Dormann, J., Cherkaoui, R., Spinu, L. et al. (1998). From pure superparamagnetic regime to glass collective state of magnetic moments in γ -Fe₂O₃ nanoparticle assemblies. *Journal of Magnetism and Magnetic Materials* 187: L139–L144.
- 74 Sahoo, S., Petravic, O., Kleemann, W. et al. (2003). Cooperative versus superparamagnetic behavior of dense magnetic nanoparticles in Co₈₀Fe₂₀/Al₂O₃ multilayers. *Applied Physics Letters* 82: 4116–4118.
- 75 Hansen, M.F., Jönsson, P.E., Nordblad, P., and Svedlindh, P. (2002). Critical dynamics of an interacting magnetic nanoparticle system. *Journal of Physics: Condensed Matter* 14: 4901.
- 76 Sahoo, S., Petravic, O., Binek, C. et al. (2002). Superspin-glass nature of discontinuous Co₈₀Fe₂₀/Al₂O₃ multilayers. *Physical Review B* 65: 134406.
- 77 Pinheiro, A., da Silva, R., Morales, M. et al. (2020). Exchange bias and superspin glass behavior in nanostructured CoFe₂O₄-Ag composites. *Journal of Magnetism and Magnetic Materials* 497: 165940.
- 78 Pal, S., Chandra, S., Phan, M.-H. et al. (2009). Carbon nanostraws: nanotubes filled with superparamagnetic nanoparticles. *Nanotechnology* 20: 485604.
- 79 Pal, S., Morales, M., Mukherjee, P., and Srikanth, H. (2009). Synthesis and magnetic properties of gold coated iron oxide nanoparticles. *Journal of Applied Physics* 105: 07B504.
- 80 Likodimos, V., Glenis, S., Guskos, N., and Lin, C. (2003). Magnetic and electronic properties of multiwall carbon nanotubes. *Physical Review B* 68: 045417.
- 81 Majetich, S. and Sachan, M. (2006). Magnetostatic interactions in magnetic nanoparticle assemblies: energy, time and length scales. *Journal of Physics D: Applied Physics* 39: R407.
- 82 Chung, S., Hoffmann, A., Bader, S. et al. (2004). Biological sensors based on Brownian relaxation of magnetic nanoparticles. *Applied Physics Letters* 85: 2971–2973.



- 83 Chung, S.-H., Hoffmann, A., Guslienko, K. et al. (2005). Biological sensing with magnetic nanoparticles using Brownian relaxation. *Journal of Applied Physics* 97: 10R101.
- 84 Fornara, A., Johansson, P., Petersson, K. et al. (2008). Tailored magnetic nanoparticles for direct and sensitive detection of biomolecules in biological samples. *Nano Letters* 8: 3423–3428.
- 85 Nutting, J., Antony, J., Meyer, D. et al. (2006). The effect of particle size distribution on the usage of the ac susceptibility in biosensors. *Journal of Applied Physics* 99: 08B319.
- 86 Connolly, J. and St Pierre, T.G. (2001). Proposed biosensors based on time-dependent properties of magnetic fluids. *Journal of Magnetism and Magnetic Materials* 225: 156–160.
- 87 DdelC, V.C., Rinaldi, C., and Zahn, M. (2006). Magnetic fluid and magnetic nanoparticle based sensors. *Encyclopedia of Sensors* 5: 389–401.
- 88 Herrera, A.P., Barrera, C., Zayas, Y., and Rinaldi, C. (2010). Monitoring colloidal stability of polymer-coated magnetic nanoparticles using AC susceptibility measurements. *Journal of Colloid and Interface Science* 342: 540–549.
- 89 Ludwig, F. (2010). Characterization of magnetic core-shell nanoparticle suspensions using AC susceptibility for frequencies up to 1 MHz. In: *AIP Conference Proceedings*, 249–254. American Institute of Physics.



10

Induced Effects in Nanostructured Magnetic Materials

10.1 Introduction

From the microscopic point of view, nanomaterials are mostly considered as materials in which the size of the particles is below 100 nm in at least one or more dimensions. Due to this reduction in the size of particles, the surface-to-volume ratio increases, which gives rise to the existence of a huge fraction of the atoms at/or close to the surface of particles. This characteristic results in achieving amazing and even different properties as compared to their corresponding bulk counterparts [1–5]. In most cases, it has been observed that the magnetic characteristics of the nanosized samples, e.g. saturation magnetization, decrease in comparison with their corresponding bulk (micron-sized) counterparts [6–10]. On the other hand, some other properties improved in the case of nanostructured magnetic materials. Several factors that can affect the variation in the magnetic characteristics of nanosized particles are briefly described in this chapter.

10.2 The Spin-Canted Effect

There are some compelling reasons to expect surface spin disorder in magnetic nanoparticles:

- Variations in the coordination of surface cations, resulting in a distribution of net exchange fields, both negative and positive concerning a cation's sublattice, namely tetrahedral and octahedral sites.
- The size effect means that the reduced coordination and a large number of broken exchange bonds of surface atoms lead to magnetic surface anisotropy, magnetic frustration, and spin disorder.
- Since the interaction is mediated by an intervening oxygen ion, exchange bonds are broken if an oxygen ion is missing from the surface.
- If organic molecules are bonded to the surface, the electrons involved can no longer contribute to the superexchange. Thus, the effective coordination of the surface cations reduces due to both types of broken exchange bonds. It has been stated that broken exchange bonds are sufficient to induce surface spin disorder [11].



- Competing exchange interactions in an incomplete coordination shell for surface ions in core/shell structure would also cause a spin disorder effect in magnetic nanoparticles.
- The superexchange is very sensitive to bond angles and lengths, which would likely be modified near the surface. For example, some antiferromagnetic (AFM) materials represent a nonzero magnetic moment at a temperature near absolute zero. This effect is attributed to spin canting, a phenomenon through which spins are tilted by a small angle about their axis rather than being exactly co-parallel (Figure 10.1).

In fact, the spin canting effect is mainly due to two factors contrasting each other: exactly antiparallel alignment of spins due to isotropic exchange, and the alignment of spins at 90° to each other due to antisymmetric exchange arising from relativistic effects (spin–orbit coupling). The net result is a small perturbation, the extent of which depends on the relative strength of these effects [12].

- The surface effect, where reduced exchange allows spins closest to the nanoparticle surface to deviate locally from collinear structures, causes a spin-canted effect in magnetic nanoparticles as well.

These forgoing-mentioned phenomena are somehow correlated to each other. It simply means that either one or some of them contribute to spin-canted effect observation in magnetic nanoparticles.

Generally speaking, surface spin canting due to crystallographic changes, surface spin disordering, broken symmetry, and nonmagnetic dead layers at the surface of magnetic nanoparticles can be the main reasons for the reduction in magnetic properties, such as reduction in saturation magnetization (M_s) and permeability compared to their corresponding bulk counterpart [6–10, 13]. This notably would decline the practical efficiency and sensitivity of such nanoparticles [14–18]. So far, challenging efforts have been taken into account to recognize and understand the surface spin structure of magnetic nanoparticles from both the consideration of fundamental science and improvements in the synthesis procedure's point of view [19–25]. Research is actively being chased to identify the surface spin geometry for various nano-dimensional systems, and several novel experimental techniques have been developed in the recent past to attain such information [26–36].

One may ask how it is possible to identify the spin-canted effect based on the magnetic materials characterization techniques. Herein, we are going to introduce some simple routes:

- (a) Based on the M – H or B – H curves: The value of magnetization (M) on the positive and negative sides are not equal, e.g. in Figure 10.2 [37, 38].

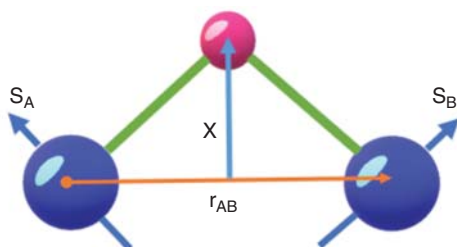


Figure 10.1 Perpendicular alignment of spins to each other due to antisymmetric exchange.



- (b) Based on the superconducting quantum interference device (SQUID) results: A few percentage changes in a moment upon field cooling (Figure 10.3) arises from changes in the surface spin configuration in the $M(T)$ curve; in the case of field-cooled (FC) and zero-field-cooled (ZFC) measurements [11].
- (c) Based on ^{57}Fe Mössbauer spectroscopy: It is employed to identify the size and canting effect on the local properties of the magnetic nanoparticles. The Mössbauer effect at a low temperature (4.2 K) and in the presence of an external magnetic field parallel to the γ -ray direction can provide valuable information about surface spin canting on the atomic scale in such nanoparticles as well as on the type of oxide phases and lattice sites [39–41].

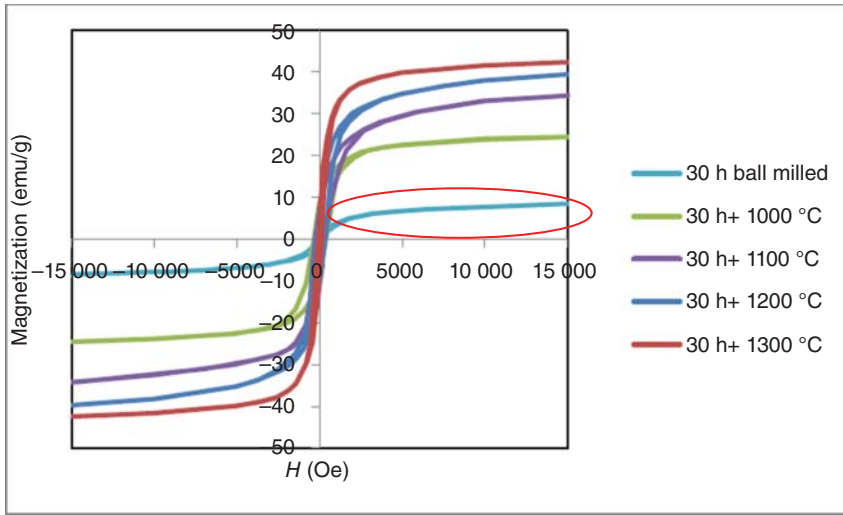


Figure 10.2 Detection of the spin-canted effect based on the M – H hysteresis curve. Source: Adapted from Šepelák et al. [37].

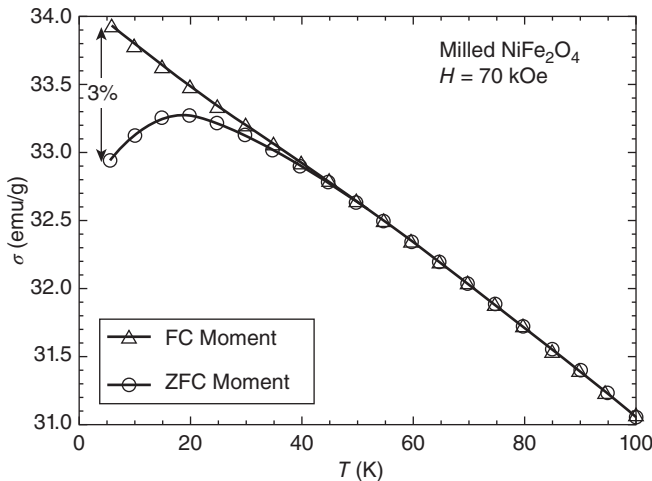


Figure 10.3 Detection of the spin-canted effect based on the M – T curve following ZFC-FC measurement. Source: Kodama et al. [11]/with permission of American Physical Society.



10.3 Spin-Glass-Like Behavior in Magnetic Nanoparticles

Spin glass is a metastable state that emerges in a material because of the randomness and frustration of spins. It means that once the system is not homogeneous, the disordered state of a system results in a spin glass. When we consider the low-energy configuration of the system (ground state), diverse types of atoms or molecules arrangement can be observed (Figure 10.4). In a crystal state, the atoms are distributed homogeneously, but in the state of glass, their distribution is not, moving around themselves. The spins in the ferromagnet are aligned in the direction of the applied field, but they become frustrated (randomly distributed) in a spin-glass state. As a classical area in condensed matter physics, low-temperature dynamics study results in spin-glass-like behaviors in magnetic nanoparticles [42–47]. In fact, a spin glass is a kind of disordered and frustrated magnetic system. The disorder originates from a structural disorder, in analogy to conventional glass, or some random doping of magnetic ions into a certain material. The frustration often leads to the absence of a unique ground energy state, which designates that there may be a variety of similar low energy states that makes a nonminimization of the energy impossible. In other words, similar to a classical spin glass, the frustration means there are many possible ground states, and none of them is most favorable. The frustration of super spins in nanoparticles can be attributed to the competition between the local anisotropy (the easy axes of the individual particles) and the inter-particle dipole–dipole interactions when the inter-particle interactions become comparable with the anisotropy energy of nanoparticles.

The story of spin glasses starts from the research of dilute magnetic alloys in experiments. These are materials in which a very small concentration of magnetic elements, e.g. iron or manganese, is doped into a nonmagnetic metallic host such as copper, silver, or gold. When the concentration is low enough (a few tenths of 1%), the magnetic moments are sufficiently far apart such that their effect on one another

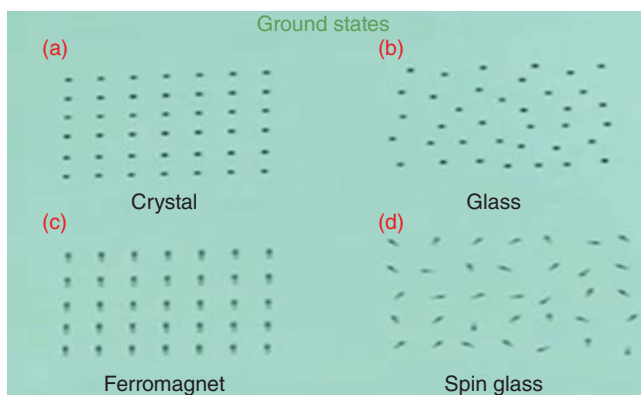
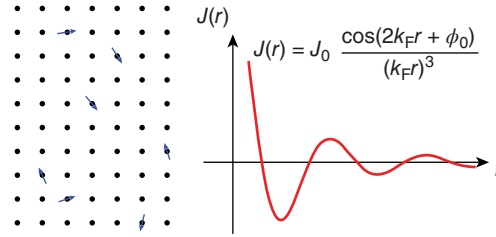


Figure 10.4 Atom distribution in (a) crystal and (b) glass, and spin arrangement in (c) ferromagnet and (d) spin glass.



Figure 10.5 Schematic representation of the RKKY theory. Source: Adapted from Refs. [49, 50].



is negligible, resulting in the well-known Kondo effect [48]. But when the concentration gets to a few percent, the interaction of those magnetic moments leads to some observable effects such as the exceedingly slow relaxation and memory effects that are now characterized by the name spin glasses. The mechanisms that give rise to spin-glass behavior can be described by the Ruderman–Kittel–Kasuya–Yosida (RKKY) theory. Owing to the placing of the magnetic impurities within a conducting matrix, the magnetic interaction is typically RKKY type (Figure 10.5). Thus, some spin–spin interactions may be negative, resulting in an antiparallel alignment, while others may be positive (favoring parallel alignment) due to the random placements of the spins in the host metal. This leads to magnetic frustration. This theory suggests that the effective coupling (or bond) strength $J(r)$ between magnets in metallic hosts has the form $J(r) = J_0 [\cos(2rK_F + \phi_0)/(K_F r)^3]$, where J_0 , ϕ_0 , and K_F is constants and r is the distance between two interacting magnets. This is a fast oscillation function of distance r since the inverse of K_F is the order of interatomic spacing.

Two features of spin glass models emerge immediately from this theory. The first one is the random fashion of coupling strength. Since the magnets are randomly doped into the host, the interaction between any pair of magnets should be random, with a roughly equal probability to be positive and negative. The second one is that the coupling between any pair of magnets is quenched since the migration of magnets in the metallic host is negligible in the experimental time scale. Any model that tries to describe the spin-glass behavior must share these two features [48]. In general, spin glasses may primarily be (i) canonical spin glass, (ii) cluster glass, and (iii) surface spin glass. A canonical spin glass is typically formed by the incorporation of noble metals such as Cu, Pt, Ag, and Au, which are weakly doped with 3d transition metal ions such as Mn or Fe [51]. The RKKY theory well describes this state. In the case of cluster glass, ferromagnetic (FM) clusters grow within an AFM matrix, and there is a possibility that FM domains interact with one another resulting in a glassy state that is considered a cluster glass type. The average FM cluster size determines the glassy dynamics in such materials. The influence of other factors such as external magnetic fields should not be neglected. It is believed that once the size of nanoparticles reduces to a few nanometers, the surface of the nanoparticles plays an important role in the magnetic behavior of the sample. Thus, the broken symmetry of the surface spins results in magnetic frustration, which is considered as a surface spin-glass [52–55]. In other words, the exchange interaction between the surface spins and the core moments (below the glass transition temperature) of the nanostructures triggers the exchange bias effect. Several theories such as the fractal-cluster model, the droplet model, the hierarchical model, the



Edwards–Anderson (EA) model, and the Sherrington–Kirkpatrick (SK) model have been suggested to identify the spin-glass behavior [56, 57]. Moreover, the different classes of spin glass can be distinguished by considering the relaxation time characteristic based on the Neel–Arrhenius and the Vogel–Fulcher models.

The competition between the nearest neighbor and next-nearest neighbor interactions or uncompensated spins can cause magnetic frustration in a material. Figure 10.6 shows an intrinsically frustrated AFM triangular lattice. Energetically, the orientation of the third spin in the “up” or “down” direction is indistinguishable. Thus, the degeneracy in the energy ground state is the presence and the system is magnetically frustrated.

In the case of the inclusion of impurities into nonmagnetic material, the systems would behave as magnetically disordered due to the random positioning of the magnetic atoms as a result of impurities interactions with varied strengths. By lowering the temperature of the system, the magnetic spins enter into an irreversible state (i.e. the magnetization reversal becomes critically slow), which is associated with cooperative spin freezing, below a certain temperature. This temperature for material is considered as its spin glass transition temperature. Below this temperature, the glassy nature of the material is thought to emerge owing to the independent slowing down of the spins, and the consequent formation of locally correlated units called droplets, clusters, or domains.

For a given example as illustrated in Figure 10.6a, there are four spins placed on a square lattice. If we suppose that the interaction between the nearest-neighbor spins prefers to be antiparallel, on the square lattice as shown in Figure 10.6a, it is easy to satisfy the requirement that the nearest-neighbor spins should be antiparallel. However, if the spins are put on a triangular lattice, the case will be far more complex. As shown in Figure 10.6b, if two adjacent spins are placed antiparallel and the third one is on vertex angle, it is impossible to find a ground state. Regardless of whether the spin is up or down, one of the two antiparallel spins will not have its energy minimized. Therefore, the system cannot achieve a unique ground state with the lowest energy infinite time. This is called frustration.

The concept of spin glass in bulk (micron-sized particles) materials is understood by taking into account atomic spins, while in the case of nanostructured materials, the atomic spins are replaced by “superspins.” In other words, for nanoparticle systems, the randomness and the frustration will be different from the classical spin-glass system. Firstly, the random size distribution of nanoparticles will cause randomness. For a single domain nanoparticle, in a first-order approximation, the

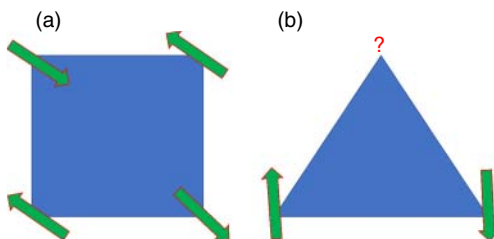


Figure 10.6 Antiferromagnetic nearest-neighbor interaction on (a) superlattice and (b) triangular lattice.



magnetic moment is proportional to the volume of the particles. Obviously, the different sizes will cause different magnetic moments in magnitude, which could result in a random dipolar interaction. On the other hand, a random position of nanoparticles would also be able to induce randomness. As we discussed above, the dipolar interaction is proportional to $1/r^3$; therefore, a random inter-particle distance could result in a random dipolar interaction in magnitude. On the other hand, the random distribution of position in space could also induce a random interaction coupling (FM or AFM interaction).

For instance, there are two identical particles with interspacing r between them. It is assumed that they have the same magnetic moment both in magnitude and orientation. If the direction of the moment is perpendicular to the vector r , the dipole–dipole interaction will be $E_D^{(i,j)} = \mu^2/r^3$. However, if the direction of their moments is parallel to r , the dipolar interaction energy will be $E_D^{(i,j)} = -2\mu^2/r^3$.

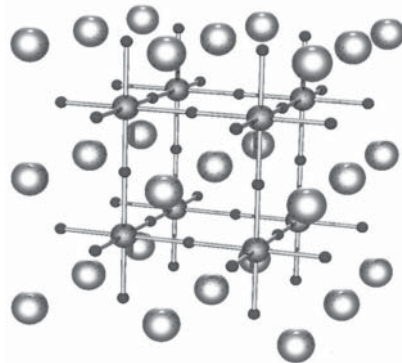
The random position of nanoparticles will give a random dipolar interaction both in strength and sign. Also, the random orientation of the uniaxial anisotropy axis (easy axis) could cause randomness. To simplify the issue, the dipole–dipole interaction could be written as $E_D^{(i,j)} = \vec{\mu}_i \cdot \vec{\mu}_j / r^3 = (\mu_i \mu_j / r^3) \cos \theta$, where θ is the angle between the two moments ranging from 0 to 180°, where $\cos \theta$ could be positive or negative. Therefore, the random distribution of the anisotropy axis could also result in a random dipolar interaction both in magnitude and sign.

From above, we can find that, in nanoparticle systems, the random size distribution, the random position, and the random distribution of easy axes would possibly result in randomness and frustration, which will give a chance to the formation of a spin-glass-like phase.

10.4 Reentrant Spin Glass (RSG) Behavior in Magnetic Nanoparticles

The reentrant spin glass (RSG) behavior is mainly attributed to an increase of disorder in the FM matrix induced by the random substitution of impurity in the “B” site in perovskite magnetic materials (Figure 10.7). The general chemical formula for perovskite compounds is given as ABX_3 , where “A” and “B” stand for two cations of

Figure 10.7 Crystal structure of perovskites materials (ABX_3). The very small spheres are X atoms (usually oxygens), the medium spheres are B atoms (a smaller metal cation such as Ti^{4+}), and the hollow spheres are the A atoms (a larger metal cation, such as Ca^{2+}). Pictured is the undistorted cubic structure; the symmetry is lowered to orthorhombic, tetragonal, or trigonal in many perovskites.



very different sizes, and X is an anion that bonds to both. The “A” atoms are larger than the “B” atoms. The ideal cubic structure has the A cation in 12-fold cuboctahedral coordination and the B cation in 6-fold coordination, surrounded by an octahedron of anions. The relative ion size requirements for stability of the cubic structure are quite stringent; therefore, slight buckling and distortion can form several lower-symmetry distorted versions, in which the coordination numbers of A cations, B cations, or both are declined.

A variety of disordered magnetic materials may represent reentrant behavior. Thus, there is a competition between long-range ferro or ferrimagnetic ordering and spin-glass ordering. For example, in a system, a majority of ferro or ferrimagnetic couplings exist between the individual spins but an adequately large number of ferro or ferrimagnetic couplings create substantial frustration. When the temperature is lowered in such a system, it exhibits a transition from the paramagnetic to a FM phase. By further lowering the temperature, a typical spin glass with RSG behavior emerges.

Aslibeiki et al. studied the temperature dependency of the real (X') and imaginary (X'') parts of ac susceptibility for $\text{La}_{0.8}\text{Sr}_{0.2}\text{Mn}_{1-x}\text{Ti}_x\text{O}_3$ with different composition; considering x as 0, 0.01, 0.025, 0.05, and 0.075 [58]. They found that all the samples exhibit the paramagnetic–ferromagnetic (PM–FM) transition and the transition temperature (T_c) declines as the Ti content enhances (Figure 10.8). By further increasing the Ti doping level, a new peak is created above T_c for sample $x = 0.05$. For $x \geq 0.05$, there is a remarkable reduction in the real part of the samples at low temperatures, with a difference that a new peak was also observed at high temperatures for $x = 0.05$.

An imaginary part of AC susceptibility represented a peak that indicates a PM–FM transition for the low-doped samples ($x < 0.05$). A second new peak close to the first peak and a third peak (at low temperatures) were observed for $x \geq 0.05$. This suggests the formation of the clusters above T_c [60–62]. This is in harmony with the sharp decline of the real part around the same temperature region. This peak is frequency-dependent and shifts toward higher temperatures with the increase in frequency (Figure 10.9c). Therefore, the possibility of the formation of orbital domains

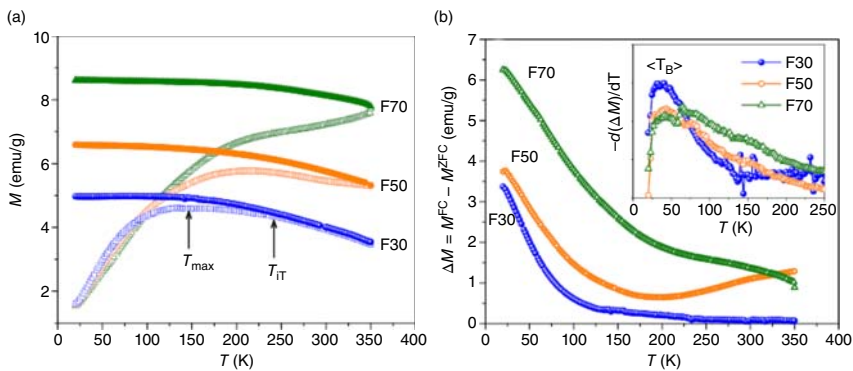


Figure 10.8 (a) M versus T and (b) ΔM plots versus temperature. Source: Aslibeiki et al. [59]/with permission of IOP Publishing.



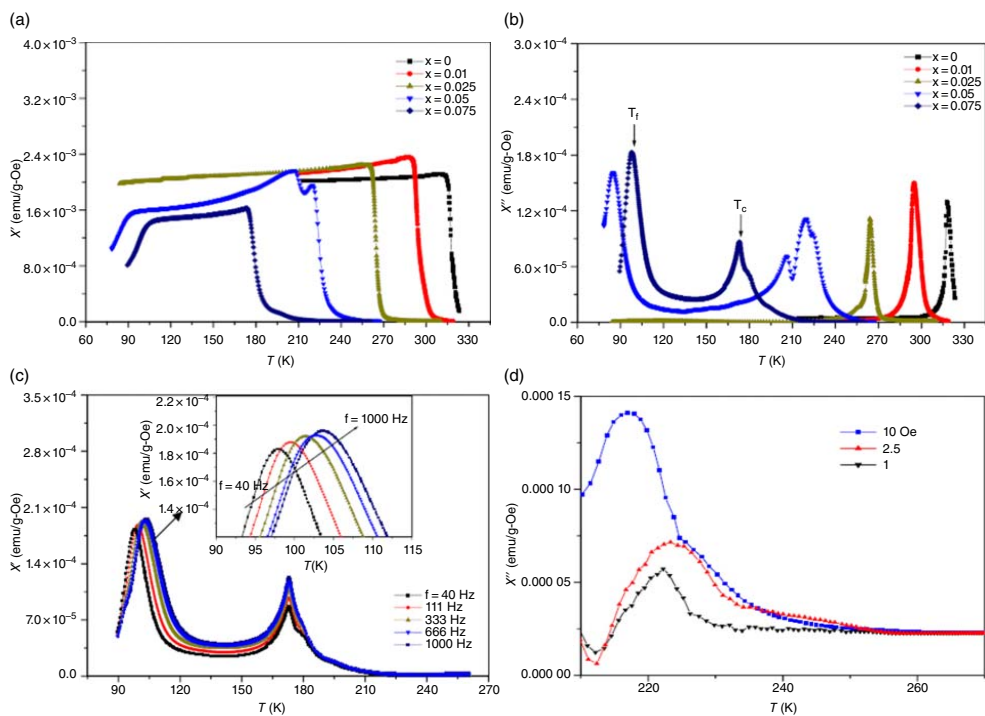


Figure 10.9 (a) Real part and (b) imaginary part as a function of temperature at an AC field of 5 Oe and frequency of 333 Hz for $\text{La}_{0.8}\text{Sr}_{0.2}\text{Mn}_{1-x}\text{Ti}_x\text{O}_3$ samples, (c) imaginary part for the $x = 0.075$ samples at different frequencies in the ac field of 5 Oe, and (d) for $x = 0.05$ sample in the ac fields of 1, 2.5, and 10 Oe, and frequency of 333 Hz. Source: Aslibeiki et al. [58]/with permission of Elsevier.



is ruled out for these samples. Similar behavior is also obtained by substituting Mn with Ga, Cr, and other cations in manganites [63, 64]. This is normally related to the existence of a RSG phase in these samples. To further clarify the nature of observed the new peaks, the imaginary part for $x = 0.05$ was measured at different amplitudes of the AC field (Figure 10.9d). The peak intensity increased with the increase in the ac field amplitude. It is well known that the imaginary component of ac susceptibility reflects the AC losses in magnetic systems. Therefore, the variation of this peak with ac field amplitude is related to the variation of cluster size. It seems that with the increase in AC field amplitude the FM cluster size increases and consequently the amount of ac loss increases.

10.5 Finite Size Effects on Magnetic Properties

The various properties of magnetic nanoparticles such as saturation magnetization and remanence, and coercivity are determined from the $M-H$ or $B-H$ hysteresis curve. The specific saturation magnetization of the nanosized magnetic ferrites is found to decline with a reduction in grain/particle size [2–10]. The linear reduction in M_s value is accompanied by an enhancement in the specific surface area of particles in the ultrafine regime. The findings of various researchers with regard to M_s are at variance [11, 65–69]. Most of the findings suggest that the reduction in M_s is attributed to the small grains/particles [27, 28]. From this point, one cannot definitely say that the decrease in grain size results in lowering M_s value. For example, ref. [65] stated an increase in M_s value with a decrease in grain size. Thus, it can be concluded that the observed decrease or increase can be associated with several factors or their combination effects, i.e. the formation of the spin-glass structure, the existence of surface spins, cation redistribution, etc., in nano- or submicron-sized grains/particles. This, in turn, depends upon the employed method to synthesize them. This is because once the size of particles reduces to only a few nanometers, the inversion degree of cation distribution between tetrahedral (A) and octahedral (B) sites would also be changed [4, 70]. This simply means that the cations would occupy lattice sites by a certain degree against their preference for micron-sized grains (bulk materials), and this inversion degree is dependent on the particle size in the nanometer scale regime [4]. Moreover, the presence of a dead layer has also been found to be one of the reasons for the reduced magnetization in the ultrafine regime [68]. A core-shell like structure model has been used to describe the theory of dead layer with respect to M_s reduction with particle size decreases [68]. It is assumed that a nonmagnetic layer shields the magnetic particles in this model. However, the Mössbauer spectroscopy findings ruled out the possibility of the existence of a dead layer in magnetization [11, 66].

Anomalous results in magnetization variation are also associated with cation redistribution [65]. In fact, in the usual structural model, for a ferrite, the magnetization of tetrahedral (A) sublattice is antiparallel to that of octahedral (B) sublattice. However, in some cases, for instance, ultrafine nickel ferrites exhibited a noncollinear magnetic structure on the surface layer [71]. The reduction in



particle size gives rise to an enhancement in the noncollinear magnetic structure proportion, in which magnetic moments are not aligned with the direction of the external magnetic field. This increment in the proportion of noncollinear structure declines the M_s . In ultrafine particles, since the surface-to-volume ratio becomes so large that the surface becomes a predominant factor in the determination of the characteristics, the small magnetic particles would possess lower M_s . Furthermore, a reduction in M_s value in the small magnetic nanoparticles is associated with a higher amount of noncollinear surface spins present in the surface of the ultrafine particles. As the particle size upsurges, this contribution becomes less, and hence, the M_s value reaches the theoretical limit as per Neel's two sub-lattices models.

On the other hand, the coercivity (H_c) with particle size variation would be described based on the anisotropy of the crystal, critical diameter, and domain structure [72–74]. Assuming that a crystallite breaks up into several domains, to reduce the large magnetization energy, the ratio of the energies before and after division into domains varies as $D^{1/2}$, where “ D ” is the average diameter of particles. Hence, the energy reduction becomes smaller, as “ D ” becomes smaller. This indicates that the crystallite prefers to remain in the single domain for very small D . In the single domain region as the particle size declines, the coercivity reduces as well due to thermal effects. In this state, the H_c in the single domain region is expressed as:

$$H_c = g - \frac{h}{D^2} \quad (10.1)$$

where g and h are constants, while in the multi-domain region, the variation of coercivity with grain size can be expressed as:

$$H_c = a + \frac{b}{D} \quad (10.2)$$

Herewith, the parameter of “ D ” is the average particle diameter, and “ a ” and “ b ” are constants [51]. Thus, the H_c would decline as the particle diameter enhances in the multi-domain region. For magnetic nanoparticles having no interaction between them, the coercivity H_c is given by [75].

$$H_c = H_{co} \left(1 - \frac{T}{T_B} \right)^{1/2} \quad (10.3)$$

where H_{co} is the coercivity at $T = 0$ K, T is the temperature of measurement and T_B is the critical blocking temperature, below which hysteresis appears and superparamagnetism disappears, and this explains the decrease in coercivity of magnetic nanoparticles as the temperature increases. As the temperature of measurement (T) decreases, the critical grain size (D_{cir}) of the fine particles decreases as follows [73]:

$$\left(\frac{D_{cir}}{D} \right)^{3/2} = \left(\frac{T}{T_B} \right)^{1/2} \quad (10.4)$$

10.6 Surface Effect in Nanosized Particles

The surface effect plays an important role in the variation of magnetic nanoparticles' behavior once their size approaches the finite size [76, 77]. In this regard, the



magnetic interaction between nanoparticles attracts more attention and becomes a motivating subject [78–83]. To fully understand the surface effect, it is assumed that a single domain nanoparticle is composed of core and shell, as core-shell-like structures. The core magnetic moment of a nanoparticle has a large value (10^3 – 10^4 Bohr magnetons), which is considered as “superspin.” Owing to this large moment value, most of the investigations have been focused on characteristics of interacting nanoparticles based on the assumption that the main interaction energy arises from dipole–dipole interactions [80–84]. This is while more complex properties can be observed at the surface with randomly oriented spins. Indeed, the role of surface exchange interactions becomes important besides the dipole–dipole interactions in the magnetic response of magnetic materials. Particularly, once the nanoparticles are in almost direct contact, e.g. in the case of agglomerated nanoparticles, cations on the surface of particles have exchange interactions such as direct exchange and superexchange interactions with neighbors’ particles. One given example in this regard is nanostructured thin films of $\text{Fe}_x\text{Ag}_{100-x}$, where the direct exchange interactions overcome the dipolar magnetic interactions and eventually give rise to super FM behavior in the system by increasing the Fe content [85, 86].

In the case of synthesis of magnetite nanoparticles from the chloride salts of iron two and three via coprecipitation at three different temperatures of 30, 50, and 70 °C, the blocking temperature was found to be 150, 214, and >350 K for those samples, accordingly [59]. This increase in blocking temperature is associated with the surface layer effect, polydispersity size, anisotropy constant, interparticle interactions, and an increase in particle size [59, 87]. According to their ZFC-FC curves (Figure 10.9a), as discussed in Chapter 6, the T_{max} obtained is not an accurate blocking temperature of all the NPs [88]. Indeed, the mean blocking temperature $\langle T_B \rangle$ of a nanoparticle assembly is found to be less than the T_{max} , which is determined by $T_{\text{max}} = \beta \langle T_B \rangle$, where β is a constant and its value depends on strength of interparticle interactions and distribution of blocking temperatures [88–91].

The $\Delta M = M_{\text{FC}} - M_{\text{ZFC}}$ curves versus temperature can be plotted to estimate the $\langle T_B \rangle$ of the samples (Figure 10.9b). The slope of the curves yields the distribution of blocking temperature. In the inset of Figure 10.9b, the $-d(\Delta M)/dT$ curves indicate the blocking temperature distribution and the $\langle T_B \rangle$ of the samples. The $\langle T_B \rangle$ was obtained at 35, 44, and 55 K for the mentioned samples, accordingly. The obtained values for β were more than those reported for the NPs assembly (1–2.5), probably because of the strong interparticle interactions [88, 92]. The temperature below which the M_{FC} and M_{ZFC} curves show an irreversible behavior (T_{irr}) is associated with the blocking of the biggest particles [92]. Furthermore, a flat state of FC curves suggests a distinctive behavior of the interacting nanoparticle systems [93–95].

10.7 Memory Effect

As an inherent characteristic of a spin glass, the memory effect can be employed for characterizing spin-glass-like behaviors in nanomagnetic particles. For memory, a “negative temperature cycle” experiment is often performed. The sample is cooled

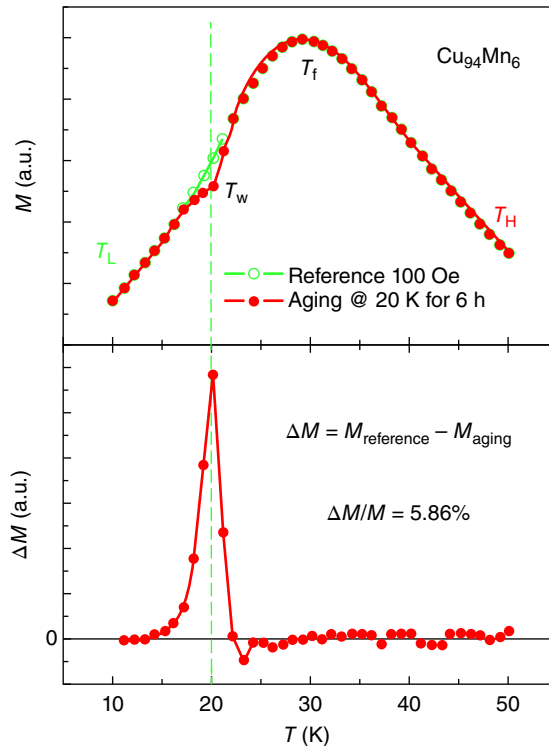


down with a certain cooling rate from a higher temperature (T_H) above the freezing temperature (T_f) to a lower temperature (T_L) far below (T_f) under zero field. At $T = T_L$, a small probing magnetic field (generally tens of Oersted) is applied and then the magnetization is recorded with the temperature increasing. To obtain the aging curve, at first, the sample is cooled down from T_H to T_w with the same cooling rate under zero field. At $T = T_w$, the temperature is kept for a long time (typically several hours). After that, the sample is further cooled down to T_L . And then, the same magnetic field as the reference one is applied, and the magnetization versus temperature curve is recorded.

A typical spin-glass material CuMn with a random spatial distribution of Mn ions in a Cu matrix is given as an example to explore the memory effect, as shown in Figure 10.10. An obvious difference between the reference and the aging curve can be found just around the waiting temperature (T_w). To see the difference more clearly, the aging curve is subtracted from the reference, and ΔM versus temperature is extracted. An obvious peak can be found near the waiting temperature, called the “memory dip.” The memory dip experiment is a quite simple and distinct approach for a spin glass characterization.

As proposed by the Saclay group [46, 96–98], a hierarchical organization of the metastable states in free energy surface as a function of temperature can provide a good explanation for the rejuvenation upon cooling and the memory effect upon heating. A schematic picture of the hierarchical model is shown in Figure 10.11.

Figure 10.10 (a) M as a function of T for $\text{Cu}_{94}\text{Mn}_6$, indicating the reference and aging curve, and (b) representation of memory effect. Source: Zhang [46].



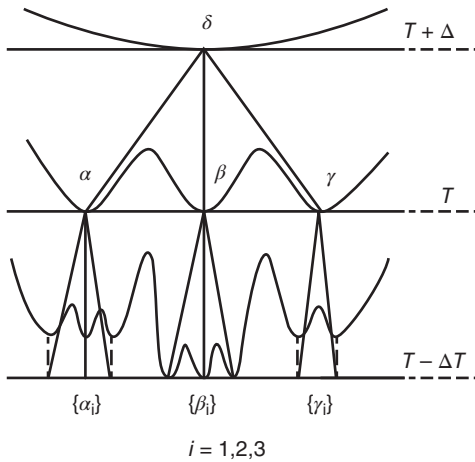


Figure 10.11 A schematic picture of the hierarchical structure of the metastable state as a function of temperature. Source: Vincent et al. [97]/with permission of Springer Nature.

In this model, with temperature decreasing from $T + \Delta T$ to T , a multivalley structure is organized on the free energy surface. With the further temperature decreasing to $T - \Delta T$, these free energy valleys (metastable states) will split into some new sub-valleys. While the temperature increases back to T , these subvalleys merge, and the free energy organization returns to a state identical to the previous one at temperature T . Indeed, the memory effect can be explained by this hierarchical model. At first, the free energy surface would split into some main valleys at temperature T with the decrease in temperature. If the temperature is kept at T over a certain period for the system aging, the relaxation will occur between these main valleys, and the magnetization of the whole system will decrease gradually. With a further decrease in temperature from T to $T - \Delta T$, these main valleys will split again into some new subvalleys. If ΔT is large, the thermal energy at the lower temperature $T - \Delta T$ will not be sufficient for the spins to overcome the barrier between the main valleys during the finite waiting time. The relaxation between the main valleys would be forbidden and only the one between sub-valleys is allowed. Therefore, the relative occupation of the magnetic spins or so-called spin configurations between the main valleys will remain unchanged. When the temperature increases back to T , the new sub-valleys will appear at $T - \Delta T$ which will merge back just to the previous main valleys. The free energy landscape or the related occupation between the main valleys would be identical to before. Therefore, a sudden drop of magnetization occurs near T and it appears that the system does remember the waiting or aging at the temperature T during the cooling process, which is called the memory effect.

References

- 1 Faried, M., Shameli, K., Miyake, M. et al. (2016). A green approach for the synthesis of silver nanoparticles using ultrasonic radiation's times in sodium alginate media: characterization and antibacterial evaluation. *Journal of Nanomaterials* 2016: 4941231.



- 2 Hajalilou, A., Abouzari-Lotf, E., Abbasi-Chianeh, V. et al. (2018). Inclusion of octahedron-shaped ZnFe_2O_4 nanoparticles in combination with carbon dots into carbonyl iron based magnetorheological suspension as additive. *Journal of Alloys and Compounds* 737: 536–548.
- 3 Hajalilou, A., Hashim, M., Ebrahimi-Kahrizsangi, R., and Sarami, N. (2015). Influence of CaO and SiO_2 co-doping on the magnetic, electrical properties and microstructure of a Ni-Zn ferrite. *Journal of Physics D: Applied Physics* 48: 145001.
- 4 Hajalilou, A. and Mazlan, S.A. (2016). A review on preparation techniques for synthesis of nanocrystalline soft magnetic ferrites and investigation on the effects of microstructure features on magnetic properties. *Applied Physics A* 122: 1–15.
- 5 Ogholbeyg, A.B., Kianvash, A., Hajalilou, A. et al. (2018). Cytotoxicity characteristics of green assisted-synthesized superparamagnetic maghemite ($\gamma\text{-Fe}_2\text{O}_3$) nanoparticles. *Journal of Materials Science: Materials in Electronics* 29: 12135–12143.
- 6 Hajalilou, A., Hashim, M., Abbasi, M. et al. (2015). A comparative study on the effects of different milling atmospheres and sintering temperatures on the synthesis and magnetic behavior of spinel single phase $\text{Ni}_{0.64}\text{Zn}_{0.36}\text{Fe}_2\text{O}_4$ nanocrystals. *Journal of Materials Science: Materials in Electronics* 26: 7468–7483.
- 7 Hajalilou, A., Hashim, M., and Kamari, H.M. (2015). Structure and magnetic properties of $\text{Ni}_{0.64}\text{Zn}_{0.36}\text{Fe}_2\text{O}_4$ nanoparticles synthesized by high-energy milling and subsequent heat treatment. *Journal of Materials Science: Materials in Electronics* 26: 1709–1718.
- 8 Shafie, M., Hashim, M., Ismail, I. et al. (2014). Magnetic M–H loops family characteristics in the microstructure evolution of $\text{BaFe}_{12}\text{O}_{19}$. *Journal of Materials Science: Materials in Electronics* 25: 3787–3794.
- 9 Hajalilou, A., Kamari, H.M., and Shameli, K. (2017). Dielectric and electrical characteristics of mechanically synthesized Ni-Zn ferrite nanoparticles. *Journal of Alloys and Compounds* 708: 813–826.
- 10 Ismail, M.A.N., Hashim, M., Hajalilou, A. et al. (2014). Magnetic properties of mechanically alloyed cobalt-zinc ferrite nanoparticles. *Journal of Superconductivity and Novel Magnetism* 27: 1293–1298.
- 11 Kodama, R.H., Berkowitz, A.E., McNiff, E. Jr., and Foner, S. (1996). Surface spin disorder in NiFe_2O_4 nanoparticles. *Physical Review Letters* 77: 394.
- 12 Winpenny, R. (2011). *Molecular Cluster Magnets*. World Scientific.
- 13 Hajalilou, A., Hashim, M., and Mohamed Kamari, H. (2014). Effects of additives and sintering time on the microstructure of Ni-Zn ferrite and its electrical and magnetic properties. *Advances in Materials Science and Engineering* 2014: 138789.
- 14 Linderoths, S., Hendriksen, P.V., Bødker, F. et al. (1994). On spin-canting in maghemite particles. *Journal of Applied Physics* 75: 6583–6585.
- 15 Morales, M., Serna, C., Bødker, F., and Mørup, S. (1997). Spin canting due to structural disorder in maghemite. *Journal of Physics: Condensed Matter* 9: 5461.
- 16 Parker, F., Foster, M., Margulies, D., and Berkowitz, A. (1993). Spin canting, surface magnetization, and finite-size effects in $\gamma\text{-Fe}_2\text{O}_3$ particles. *Physical Review B* 47: 7885.



- 17 Kubickova, S., Niznansky, D., Morales Herrero, M. et al. (2014). Structural disorder versus spin canting in monodisperse maghemite nanocrystals. *Applied Physics Letters* 104: 223105.
- 18 Coey, J.M.D. (1971). Noncollinear spin arrangement in ultrafine ferrimagnetic crystallites. *Physical Review Letters* 27: 1140.
- 19 Laurent, S., Forge, D., Port, M. et al. (2008). Magnetic iron oxide nanoparticles: synthesis, stabilization, vectorization, physicochemical characterizations, and biological applications. *Chemical Reviews* 108: 2064–2110.
- 20 Lu, A.H., Salabas, E.e.L., and Schüth, F. (2007). Magnetic nanoparticles: synthesis, protection, functionalization, and application. *Angewandte Chemie International Edition* 46: 1222–1244.
- 21 Deng, H., Li, X., Peng, Q. et al. (2005). Monodisperse magnetic single-crystal ferrite microspheres. *Angewandte Chemie* 117: 2842–2845.
- 22 Frey, N.A., Peng, S., Cheng, K., and Sun, S. (2009). Magnetic nanoparticles: synthesis, functionalization, and applications in bioimaging and magnetic energy storage. *Chemical Society Reviews* 38: 2532–2542.
- 23 Huber, D.L. (2005). Synthesis, properties, and applications of iron nanoparticles. *Small* 1: 482–501.
- 24 Kolhatkar, A.G., Jamison, A.C., Litvinov, D. et al. (2013). Tuning the magnetic properties of nanoparticles. *International Journal of Molecular Sciences* 14: 15977–16009.
- 25 Park, J., An, K., Hwang, Y. et al. (2004). Ultra-large-scale syntheses of monodisperse nanocrystals. *Nature Materials* 3: 891–895.
- 26 Negi, D., Loukya, B., Ramasamy, K. et al. (2015). Spatially resolved quantitative magnetic order measurement in spinel CuCr_2S_4 nanocrystals. *Applied Physics Letters* 106: 182402.
- 27 Verbeeck, J., Schattschneider, P., Lazar, S. et al. (2011). Atomic scale electron vortices for nanoresearch. *Applied Physics Letters* 99: 203109.
- 28 Gazeau, F., Boué, F., Dubois, E., and Perzynski, R. (2003). Static and quasi-elastic small angle neutron scattering on biocompatible ionic ferrofluids: magnetic and hydrodynamic interactions. *Journal of Physics: Condensed Matter* 15: S1305.
- 29 Schattschneider, P., Ennen, I., Löffler, S. et al. (2010). Circular dichroism in the electron microscope: progress and applications. *Journal of Applied Physics* 107: 09D311.
- 30 Loukya, B., Zhang, X., Gupta, A., and Datta, R. (2012). Electron magnetic chiral dichroism in CrO_2 thin films using monochromatic probe illumination in a transmission electron microscope. *Journal of Magnetism and Magnetic Materials* 324: 3754–3761.
- 31 Loukya, B., Negi, D., Dileep, K. et al. (2015). Effect of Bloch wave electron propagation and momentum-resolved signal detection on the quantitative and site-specific electron magnetic chiral dichroism of magnetic spinel oxide thin films. *Physical Review B* 91: 134412.



- 32 Wollan, E. and Koehler, W. (1955). Neutron diffraction study of the magnetic properties of the series of perovskite-type compounds $[(1 - x)\text{La}, x\text{Ca}]\text{MnO}_3$. *Physical Review* 100: 545.
- 33 Verbeeck, J., Tian, H., and Schattschneider, P. (2010). Production and application of electron vortex beams. *Nature* 467: 301–304.
- 34 Wiedenmann, A. (2005). Polarized SANS for probing magnetic nanostructures. *Physica B: Condensed Matter* 356: 246–253.
- 35 Disch, S., Wetterskog, E., Hermann, R.P. et al. (2012). Quantitative spatial magnetization distribution in iron oxide nanocubes and nanospheres by polarized small-angle neutron scattering. *New Journal of Physics* 14: 013025.
- 36 Dmitrienko, V., Ovchinnikova, E., Collins, S. et al. (2014). Measuring the Dzyaloshinskii–Moriya interaction in a weak ferromagnet. *Nature Physics* 10: 202–206.
- 37 Šepelák, V., Feldhoff, A., Heitjans, P. et al. (2006). Nonequilibrium cation distribution, canted spin arrangement, and enhanced magnetization in nanosized MgFe_2O_4 prepared by a one-step mechanochemical route. *Chemistry of Materials* 18: 3057–3067.
- 38 Hajalilou, A., Hashim, M., Ebrahimi-Kahrizsangi, R., and Kamari, H.M. (2015). Influence of evolving microstructure on electrical and magnetic characteristics in mechanically synthesized polycrystalline Ni-ferrite nanoparticles. *Journal of Alloys and Compounds* 633: 306–316.
- 39 Darbandi, M., Stromberg, F., Landers, J. et al. (2012). Nanoscale size effect on surface spin canting in iron oxide nanoparticles synthesized by the microemulsion method. *Journal of Physics D: Applied Physics* 45: 195001.
- 40 Tuček, J., Zboril, R., and Petridis, D. (2006). Maghemite nanoparticles by view of Mössbauer spectroscopy. *Journal of Nanoscience and Nanotechnology* 6: 926–947.
- 41 Vandenbergh, R.E. and De Grave, E. (1989). Mössbauer effect studies of oxidic spinels. In: *Mössbauer Spectroscopy Applied to Inorganic Chemistry*, vol. 3, 59–182. Boston, MA: Springer.
- 42 Mamiya, H., Nakatani, I., and Furubayashi, T. (1998). Blocking and freezing of magnetic moments for iron nitride fine particle systems. *Physical Review Letters* 80: 177.
- 43 Luo, W., Nagel, S.R., Rosenbaum, T., and Rosensweig, R. (1991). Dipole interactions with random anisotropy in a frozen ferrofluid. *Physical Review Letters* 67: 2721.
- 44 Dormann, J., Bessais, L., and Fiorani, D. (1988). A dynamic study of small interacting particles: superparamagnetic model and spin-glass laws. *Journal of Physics C: Solid State Physics* 21: 2015.
- 45 Mørup, S. and Tronc, E. (1994). Superparamagnetic relaxation of weakly interacting particles. *Physical Review Letters* 72: 3278.
- 46 Zhang, B. (2011). Spin-glass-like behaviors in magnetic nanoparticles. Doctoral dissertation. Hong Kong University of Science and Technology.



- 47 Jönsson, P., Hansen, M.F., and Nordblad, P. (2000). Nonequilibrium dynamics in an interacting Fe-C nanoparticle system. *Physical Review B* 61: 1261.
- 48 Stein, D.L. and Newman, C.M. (2013). *Spin Glasses and Complexity*. Princeton University Press.
- 49 Sethna, J.P., Kartha, S., Castán, T., and Krumhansl, J.A. (1992). Tweed in marten-sites: a potential new spin glass. *Physica Scripta* 1992: 214.
- 50 Flint, R. and Senthil, T. (2013). Chiral RKKY interaction in $\text{Pr}_2\text{Ir}_2\text{O}_7$. *Physical Review B* 87: 125147.
- 51 Blügel, S. (1995). Magnetism of 4d and 5d transition metal adlayers on Ag (001): dependence on the adlayer thickness. *Physical Review B* 51: 2025.
- 52 Xu, M., Zhong, W., Yu, J. et al. (2010). Exchange-bias-like behavior from disordered surface spins in $\text{Li}_4\text{Mn}_5\text{O}_{12}$ nanosticks. *The Journal of Physical Chemistry C* 114: 16143–16147.
- 53 Nadeem, K., Krenn, H., Traussing, T., and Letofsky-Papst, I. (2011). Distinguishing magnetic blocking and surface spin-glass freezing in nickel ferrite nanoparticles. *Journal of Applied Physics* 109: 013912.
- 54 Jaffari, G.H., Ali, S.R., Hasanain, S. et al. (2010). Stabilization of surface spin glass behavior in core-shell $\text{Fe}_{67}\text{Co}_{33}$ - CoFe_2O_4 nanoparticles. *Journal of Applied Physics* 108: 063921–063925.
- 55 Chandra, S. (2013). *Magnetization Dynamics and Related Phenomena in Nanostructures*. University of South Florida.
- 56 Edwards, S.F. and Anderson, P.W. (1975). Theory of spin glasses. *Journal of Physics F: Metal Physics* 5: 965.
- 57 Binder, K. and Young, A.P. (1986). Spin glasses: experimental facts, theoretical concepts, and open questions. *Reviews of Modern Physics* 58: 801.
- 58 Aslibeiki, B., Kameli, P., and Salamati, H. (2009). Reentrant spin glass behavior in $\text{La}_{0.8}\text{Sr}_{0.2}\text{Mn}_{1-x}\text{Ti}_x\text{O}_3$ manganites. *Solid State Communications* 149: 1274–1277.
- 59 Aslibeiki, B., Ehsani, M., Nasirzadeh, F., and Mohammadi, M. (2017). The effect of interparticle interactions on spin glass and hyperthermia properties of Fe_3O_4 nanoparticles. *Materials Research Express* 4: 075051.
- 60 De Teresa, J., Ibarra, M., Algarabel, P. et al. (2002). Magnetic versus orbital polarons in colossal magnetoresistance manganites. *Physical Review B* 65: 100403.
- 61 Mukherjee, K. and Banerjee, A. (2009). Selective substitution in orbital domains of a low doped manganite: an investigation from Griffiths phenomenon and modification of glassy features. *Journal of Physics: Condensed Matter* 21: 106001.
- 62 Pekała, M., Mucha, J., Vertruyen, B. et al. (2006). Effect of Ga doping on magneto-transport properties in colossal magnetoresistive $\text{La}_{0.7}\text{Ca}_{0.3}\text{Mn}_{1-x}\text{Ga}_x\text{O}_3$ ($0 < x < 0.1$). *Journal of Magnetism and Magnetic Materials* 306: 181–190.
- 63 Khan, H.U., Rabia, K., Mumtaz, A., and Hasanain, S.K. (2007). Non-linear susceptibility studies of $\text{La}_{0.85}\text{Ca}_{0.15}\text{Mn}_{0.95}\text{Fe}_{0.05}\text{O}_3$. *Journal of Physics: Condensed Matter* 19: 106202.
- 64 Dho, J., Kim, W., and Hur, N. (2002). Reentrant spin glass behavior in Cr-doped perovskite manganite. *Physical Review Letters* 89: 027202.



- 65 Chinnasamy, C., Narayanasamy, A., Ponpandian, N. et al. (2001). Mixed spinel structure in nanocrystalline NiFe_2O_4 . *Physical Review B* 63: 184108.
- 66 Kodama, R.H. and Berkowitz, A.E. (1999). Atomic-scale magnetic modeling of oxide nanoparticles. *Physical Review B* 59: 6321.
- 67 Vestal, C.R. and Zhang, Z.J. (2002). Synthesis of CoCrFeO_4 nanoparticles using microemulsion methods and size-dependent studies of their magnetic properties. *Chemistry of Materials* 14 (9): 3817–3822.
- 68 Zheng, M., Wu, X., Zou, B., and Wang, Y. (1998). Magnetic properties of nano-sized MnFe_2O_4 particles. *Journal of Magnetism and Magnetic Materials* 183: 152–156.
- 69 George, M., John, A.M., Nair, S.S. et al. (2006). Finite size effects on the structural and magnetic properties of sol-gel synthesized NiFe_2O_4 powders. *Journal of Magnetism and Magnetic Materials* 302: 190–195.
- 70 Hajalilou, A., Kianvash, A., Lavvafi, H., and Shameli, K. (2018). Nanostructured soft magnetic materials synthesized via mechanical alloying: a review. *Journal of Materials Science: Materials in Electronics* 29: 1690–1717.
- 71 Morrish, A. and Haneda, K. (1983). Surface magnetic properties of fine particles. *Journal of Magnetism and Magnetic Materials* 35: 105–113.
- 72 Chikazumi, S. and Graham, C.D. (2009). *Physics of Ferromagnetism*, 2e. Oxford University Press on Demand.
- 73 Cullity, B. (1972). *Introduction to Magnetic Materials*. Reading: Addison/Wiley.
- 74 Hadjipanayis, G.C. and Siegel, R.W. (2012). *Nanophase Materials: Synthesis-Properties-Applications*. Springer Science & Business Media.
- 75 Banerjee, S., Roy, S., Chen, J., and Chakravorty, D. (2000). Magnetic properties of oxide-coated iron nanoparticles synthesized by electrodeposition. *Journal of Magnetism and Magnetic Materials* 219: 45–52.
- 76 Komorida, Y., Mito, M., Deguchi, H. et al. (2009). Surface and core magnetic anisotropy in maghemite nanoparticles determined by pressure experiments. *Applied Physics Letters* 94: 202503.
- 77 Fita, I., Markovich, V., Mogilyansky, D. et al. (2008). Size- and pressure-controlled ferromagnetism in LaCoO_3 nanoparticles. *Physical Review B* 77: 224421.
- 78 Hansen, M.F. and Mørup, S. (1998). Models for the dynamics of interacting magnetic nanoparticles. *Journal of Magnetism and Magnetic Materials* 184: L262–L274.
- 79 Dormann, J., Fiorani, D., and Tronc, E. (1999). On the models for interparticle interactions in nanoparticle assemblies: comparison with experimental results. *Journal of Magnetism and Magnetic Materials* 202: 251–267.
- 80 Masunaga, S.H., Jardim, R.d.F., Fichtner, P.F.P., and Rivas, J. (2009). Role of dipolar interactions in a system of Ni nanoparticles studied by magnetic susceptibility measurements. *Physical Review B* 80: 184428.
- 81 Kasyutich, O., Desautels, R., Southern, B., and Van Lierop, J. (2010). Novel aspects of magnetic interactions in a macroscopic 3D nanoparticle-based crystal. *Physical Review Letters* 104: 127205.



- 82 Nunes, W., Socolovsky, L., Denardin, J. et al. (2005). Role of magnetic interparticle coupling on the field dependence of the superparamagnetic relaxation time. *Physical Review B* 72: 212413.
- 83 Pramanik, A. and Banerjee, A. (2010). Interparticle interaction and crossover in critical lines on field-temperature plane in $\text{Pr}_{0.5}\text{Sr}_{0.5}\text{MnO}_3$ nanoparticles. *Physical Review B* 82: 094402.
- 84 García-Otero, J., Porto, M., Rivas, J., and Bunde, A. (2000). Influence of dipolar interaction on magnetic properties of ultrafine ferromagnetic particles. *Physical Review Letters* 84: 167.
- 85 Alonso, J., Fdez-Gubieda, M., Barandiarán, J. et al. (2010). Crossover from superspin glass to superferromagnet in $\text{Fe}_x\text{Ag}_{100-x}$ nanostructured thin films ($20 \leq x \leq 50$). *Physical Review B* 82: 054406.
- 86 Aslibeiki, B., Kameli, P., and Salamati, H. (2012). The effect of grinding on magnetic properties of agglomerated MnFe_2O_4 nanoparticles. *Journal of Magnetism and Magnetic Materials* 324: 154–160.
- 87 Meiorin, C., Londono, O.M., Muraca, D. et al. (2016). Magnetism and structure of nanocomposites made from magnetite and vegetable oil based polymeric matrices. *Materials Chemistry and Physics* 175: 81–91.
- 88 Gittleman, J., Abeles, B., and Bozowski, S. (1974). Superparamagnetism and relaxation effects in granular Ni-SiO_2 and $\text{Ni-Al}_2\text{O}_3$ films. *Physical Review B* 9: 3891.
- 89 Hajalilou, A., Ferreira, L.P., Melo Jorge, M.E. et al. (2021). Superparamagnetic $\text{Ag-Fe}_3\text{O}_4$ composites nanoparticles for magnetic fluid hyperthermia. *Journal of Magnetism and Magnetic Materials* 537: 168242.
- 90 Jalili, H., Aslibeiki, B., Hajalilou, A. et al. (2022). Bimagnetic hard/soft and soft/hard ferrite nanocomposites: structural, magnetic and hyperthermia properties. *Ceramics International* 48: 4886–4896.
- 91 Kavkhani, R., Hajalilou, A., Abouzari-Lotf, E., Ferreira, L.P., Cruz, M.M., Yusefi, M., Parvini, E., Ogholbeyg, A.B. and Ismail, U.N., 2022. CTAB assisted synthesis of $\text{MnFe}_2\text{O}_4@ \text{SiO}_2$ nanoparticles for magnetic hyperthermia and MRI application. *Materials Today Communications*, 31, p. 103412. <https://doi.org/10.1016/j.mtcomm.2022.103412>.
- 92 Hansen, M.F. and Mørup, S. (1999). Estimation of blocking temperatures from ZFC/FC curves. *Journal of Magnetism and Magnetic Materials* 203: 214–216.
- 93 Aslibeiki, B., Kameli, P., and Salamati, H. (2016). The effect of dipole–dipole interactions on coercivity, anisotropy constant, and blocking temperature of MnFe_2O_4 nanoparticles. *Journal of Applied Physics* 119: 063901.
- 94 Nadeem, K., Krenn, H., Traußnig, T. et al. (2011). Effect of dipolar and exchange interactions on magnetic blocking of maghemite nanoparticles. *Journal of Magnetism and Magnetic Materials* 323: 1998–2004.
- 95 Peddis, D., Orrù, F., Ardu, A. et al. (2012). Interparticle interactions and magnetic anisotropy in cobalt ferrite nanoparticles: influence of molecular coating. *Chemistry of Materials* 24: 1062–1071.



- 96 Refregier, P., Vincent, E., Hammann, J., and Ocio, M. (1987). Ageing phenomena in a spin-glass: effect of temperature changes below T_g . *Journal de Physique* 48: 1533–1539.
- 97 Vincent, E., Hammann, J., Ocio, M. et al. (1997). Slow dynamics and aging in spin glasses. In: *Complex Behaviour of Glassy Systems*, 184–219. Berlin, Heidelberg: Springer.
- 98 Komori, T., Yoshino, H., and Takayama, H. (1995). *Philosophical Magazine B* 71: 489, (2000). *Journal of the Physical Society of Japan*, 69, pp. 1192–1201.





11

Insight into Superparamagnetism in Magnetic Nanoparticles

11.1 Introduction

Research in nanoparticle/nanocrystalline materials can be structured around three major goals, as addressed in the book's early chapters: synthesis, knowledge of new advanced materials, and correlations between them. Nanomaterials are materials with particle sizes of less than 100 nm in at least one or more dimensions, as defined by their nanometric equivalents. A large number of atoms exist at or near the surface of particles at this length scale, giving the materials their particular properties. Nanomaterials have a high surface-to-volume ratio; hence, they typically have extraordinary properties that aren't found in bulk materials [1–6]. By transition from micron-size to nano-size particles, the variations in the surface-to-volume ratio as well as changing the distribution of cations and consequently changing the structural characteristics are obtained. Such variations result in the fact that the nanostructured materials show different behaviors compared to bulk samples. One of the well-known phenomena to occur in magnetic nanoparticles is considered “superparamagnetism.” Such behavior can be calculated and measured with different tools and methods. Among the methods for characterizing nanostructured magnetic materials are direct current (DC) and alternating current (AC), residual curve measurements in fields, and zero field-cooled (ZFC) and field-cooled (FC) magnetization curves in terms of temperature in modes, as well as measuring magnetic susceptibility at different temperatures and frequencies, and studying the Henkel curve at different temperatures. These measurements can accurately determine the magnetic state of nanoparticles and their physical properties. A set of magnetic nanoparticles at different temperatures may have different magnetic states, including anisotropic superparamagnet, anisotropic superpromagnet, locked state, and super-spin glass and ferromagnetic glass phases.

11.2 Description of Superparamagnetism Based on Size of Particles and Magnetic Measurements

The superparamagnetism phenomenon is observed when the size of particles approaches to the single domain area in such a way that they behave as

Magnetic Nanoparticles: Synthesis, Characterization, and Applications, First Edition.

Abdollah Hajalilou, Mahmoud Tavakoli, and Elahe Parvini.

© 2023 WILEY-VCH GmbH. Published 2023 by WILEY-VCH GmbH.



ferromagnetic materials below Curie temperature (T_C). This is because they have rather large susceptibilities, which are saturated in moderate magnetic fields, exhibiting remanence and coercivity. Above T_C , superparamagnetic (SP) materials exhibit paramagnetic behavior but with no hysteresis [7]. The spin orientation in superparamagnetic materials in the presence and absence of an applied field is shown in Figure 11.1a. Two mechanisms, namely Brownian rotation and Neel rotation, are taken into account to describe the alignment of the superparamagnetic particles with an applied magnetic field. The Neel rotation means stationary revolving of particle magnetic moment in a solid or liquid, while the Brownian rotation occurs only in the case of physically revolving of a particle toward the applied field direction in a fluid [8, 9].

Ultrafine ferromagnetic particles have very short relaxation times, even at room temperature, and they behave superparamagnetically [10–14]; however, their magnetization values are typical of ferromagnetic substances. The individual particles have normal ferromagnetic movements but very short relaxation times, enabling them to rapidly follow directional changes in an applied field. A schematic diagram of a single domain particle is shown in Figure 11.1b. Without an external field, the spins of the atoms in the particle will spontaneously align along the easy axes ($\theta = 0$ or π). An external field is usually required to rotate the moment of the particle out from its easy axes to overcome the anisotropy energy field. Indeed, the induced single domains are immediately aligned in the direction of the applied field and rapidly distorted once the applied field is removed. Thus, there is no noticeable coercivity in their M – H or B – H hysteresis curves.

Once the size of magnetic nanoparticles reduces to less than 10 nm, they become single-domain (SD) particles. In the state of this size of particles and at temperature below T_C , the thermal energy is able to overcome the coupling force between adjacent atoms, which is enough to alter the direction of magnetization through the whole crystallite. This phenomenon causes the average magnetic moment to become zero, resulting in uniform magnetization in superparamagnetic particles along an easy axis. The thermal energy causes the magnetization to switch between equivalent easy axes through an anisotropy obstacle. This switching happens much faster than when the time average magnetic remanence is zero [8].

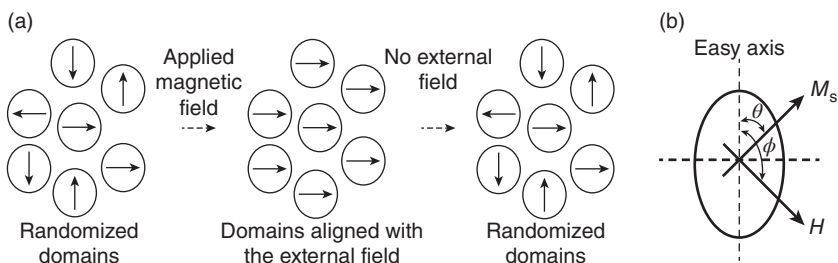


Figure 11.1 (a) Traits of superparamagnetic particles in the presence and absence of an externally applied magnetic field. Source: Hajalilou et al. [8]/with permission of Springer Nature, and (b) schematic diagram of a particle showing the angle between the easy axis and applied field H (ϕ) and the resulting magnetization (θ).



By considering the term “superparamagnetism,” the first factor that discriminates against other magnetic materials is its magnetic properties, i.e. saturation magnetization (M_s) and coercivity (H_c), permeability, and *remanent* magnetization of the sample. Nevertheless, the main question is how can one distinguish it from paramagnetic or ferromagnetic materials? How do their M - H or B - H hysteresis curves look like? Do they preserve their characteristics at any temperature or particle/grain size? Why are they called superparamagnetic materials? And several other questions may be asked. Herewith, before we consider “superparamagnetism,” we would like to describe the particle/grain distribution based on their size by considering single-domain (there is only one domain with one spin inside it) and multi-domain (MD) regions. It is well known that the variation of coercivity with grain size determines the transition from a single-domain region to multi-domain regions and vice versa, where this is considered a critical grain size (Figure 11.2). This critical size is mainly dependent on different factors such as type of materials and synthesis condition. In the following text, two examples will be taken into account to clarify these statements. In fact, once the size of particles reduces to the critical value (D_{cir}), every particle becomes a single magnetic domain. In this case, the nanoparticles have a large magnetic moment in the presence of an externally applied magnetic field, but they become paramagnetic in the absence of an applied field. This is called superparamagnetic behavior. Such materials represent a high saturation magnetization even comparable to that of ferromagnetic materials. In other words, when the particle size is further reduced to a critical diameter D_{cir} , the coercivity decreases to zero (Figure 11.2). At this stage, thermal effects are strong enough to overcome the magnetocrystalline anisotropy energy and spontaneously demagnetize a previously saturated assembly of particles.

Below a certain temperature, which is called “transition temperature,” the thermal energy can no longer be comparable with anisotropy energy, and the particles retain a ferromagnetic state.

It is believed that the coercivity is strongly dependent on the grains/particles size [8, 15], as illustrated in Figure 11.2. It means that the grains/particles can be ranged in the single-domain (SD) or multi-domain (MD) state, depending on the size of grains/particles. When they are ultra-small (normally less than 10 nm), in terms of

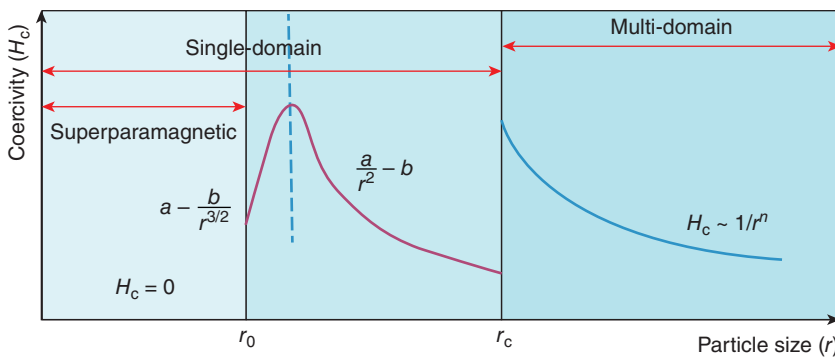


Figure 11.2 Coercivity versus particle size.



their size, they can be stated in superparamagnetic regime, where the coercivity (H_c) is zero. Sometimes, even though their sizes are small and present H_c , they are still in SD regime. In this state, coercivity follows two steps: $a - b/r^{3/2}$ and $a/r^2 - b$. In the first stage, the coercivity increases with the increase in particle size (r), which follows the $a - b/r^{3/2}$ relation. Then, it reaches the maximum value, which is considered a critical radius of grains/ particles in the single-domain regime. Thereafter, the coercivity decreases with the further increase in r until r_c . In fact, by increasing the grains/ particles, the grain boundaries are the most crucial factors contributing to coercivity in the case of large-grained polycrystalline nanomaterials ($d > L_{\text{exch}}$). Therefore, fine-grained soft magnetic materials are often magnetically harder than coarse-grained soft ones with identical compositions. As a result, coercivity would have a tendency to decline since the grain size increases, according to the well-accepted $1/d$ law. Such a phenomenon can occur in the multi-domain regime as well [15].

It has been proven that the grains in multi-domain regimes possess greater domain walls and, thus, an enhancement is achieved in the contribution of wall movement to magnetization and demagnetization, which needs less energy than domain rotation [16]. In other words, in the single-domain state, the magnetization direction is only varied by rotation of the magnetic moment ensemble of all magnetically coupling atoms of the particle rather than the domain wall movement [17]. In an assumption that the single-domain particles have a fixed magnetization direction, they contain an energy barrier deriving from the so-called uniaxial anisotropy. This energy in the presence of an externally applied magnetic field (H) is the sum of its Zeeman energies (second term of the equation) and magnetic anisotropy (first term of the equation) as follows [18]:

$$E = KV \sin^2(\phi - \theta) - \mu_0 M_s V H \cos \phi \quad (11.1)$$

where θ is the angle between magnetization (M) and H , θ is the angle between the easy direction of magnetization and H , V is the volume of the particles, M_s is the saturation magnetization of the sample, and K is the anisotropy parameter. The preferred magnetic moment direction is either 0° or 180° due to the anisotropy barrier. For the particle to switch magnetization direction from 0° to 180° , a barrier (ΔE_a) with the energy $K_a V$ (with V as the particle volume and K_a as the anisotropy energy per volume, which is material dependent) has to be overcome, as shown in Figure 11.3 [20]. A strong external magnetic field is required for the rotation of the magnetic direction.

The anisotropy energy ($K_a V$) (that declines with the particle size) would become smaller than the prevailing thermal energy $k_B T$ (k_B is the Boltzmann constant, and T is absolute temperature) if the size of a single-domain particle is further reduced. Due to quantum mechanical reasons, the magnetic moments of all atoms in the particle still couple, and the material would be ferri- or ferromagnetic in bulk. However, at this point, the total particle magnetic moment is not fixed in the “energy valley” to either a 0° or 180° direction anymore; it can experience random fluctuation (Figure 11.3) [17, 21, 22]. This is called the superparamagnetic effect [17]. The temperature above which the thermal energy is enough to transform



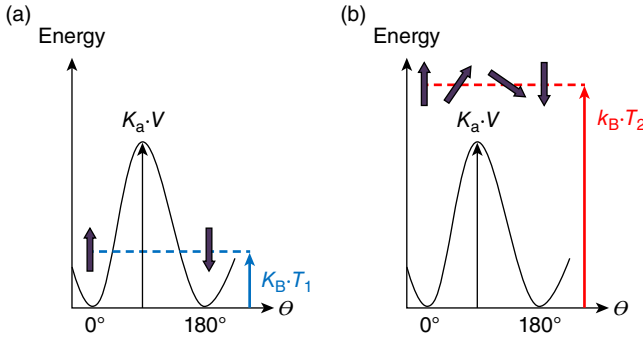


Figure 11.3 The uniaxial anisotropy in a single-domain magnetic particle signifies an energy barrier that is proportional to the particle volume. It hinders with particle magnetization to switch its direction if the thermal energy of the particle (at T_1) is not sufficient (a). Free fluctuation of the magnetization direction of particles at T_2 occurs due to sufficient thermal energy above a certain temperature (T_B), which overcomes the anisotropy barrier (b). Source: Gobrecht et al. [19]/with permission of Walter de Gruyter.

a single-domain particle with a fixed magnetic moment direction to a particle with a randomly fluctuating magnetic moment is called blocking temperature (T_B) in the ZFC and FC curves [17]. Above T_B , the magnetic moment of single-domain particle points in a certain direction only for a very short time τ , which is given by

$$\tau = \tau_0 \exp \left(\frac{-\delta E}{KT} \right) \quad (11.2)$$

In 1949, Néel, in the case of magnetism in single-domain grains in the context of geophysics study, proposed an expression for the frequency f at which the magnetization direction fluctuates [23]. It is given by an Arrhenius' equation-like function as follows [20, 22]:

$$f = f_0 \exp \left(\frac{K_a V}{k_B T} \right) \quad (11.3)$$

The estimated value of f_0 was found to be 10^9 s^{-1} [17, 24].

In the parallel evolution of microstructure changes on the magnetic characteristics of soft ferrite of Ni-ferrite nanoparticles, the concept of transition from single-domain to multi-domain is evident in Figure 11.4. In fact, it was found that the particles would grow by increasing the sintering temperature to reduce the free energy (ΔG) due to the reduction in total grain boundary energy [25].

Now by referring to their corresponding B - H curves (Figure 11.5a) and plotting the coercivity versus grain size, it can be seen that by increasing the sintering temperature (which is accompanied by grain growth), the saturation magnetization increases. On the other hand, the coercivity of the samples first increases sharply and thereafter decreases with the increase in the grain size. From this curve (Figure 11.5b) with the assistance of grain size distribution, one can determine the critical grain size for the desired sample. In fact, this value implies the transition from the single-domain region to the multi-domain region. Critical grain size in the case of the Ni-ferrite sample was found to be 211 nm. Furthermore, the grain size



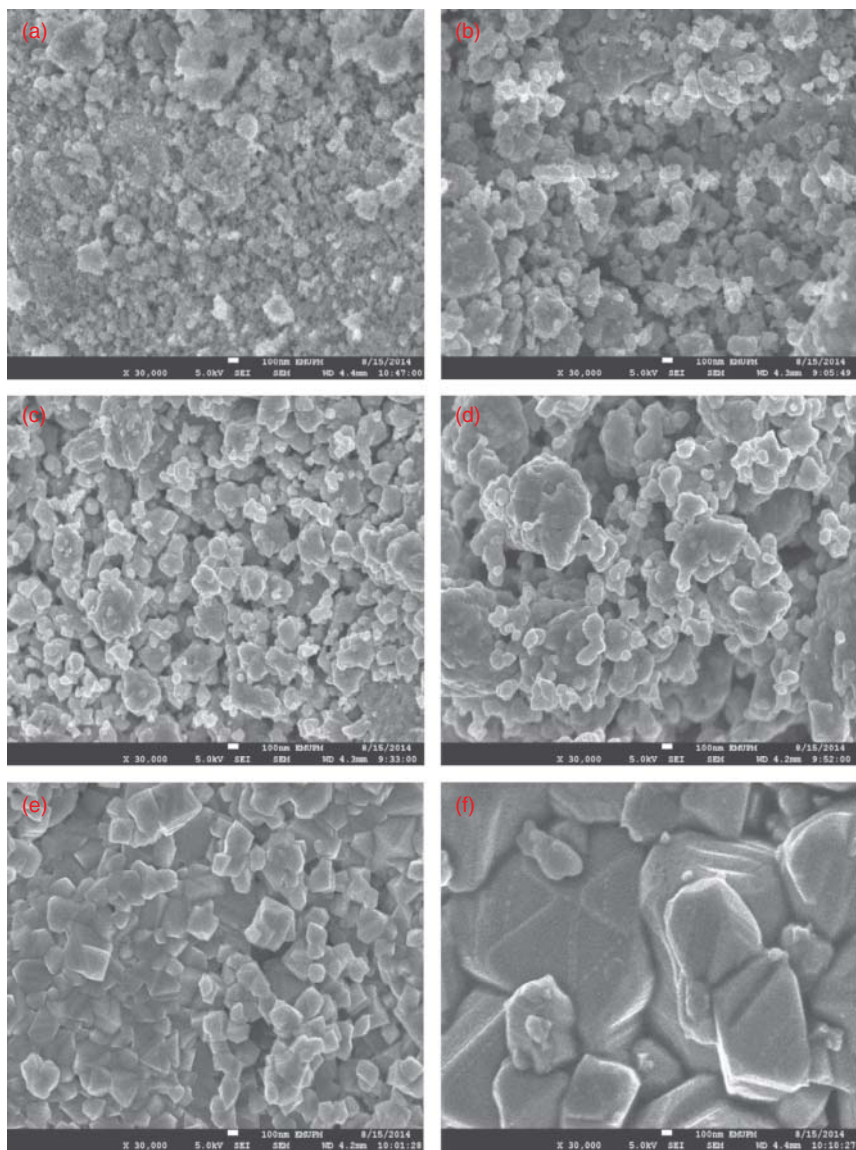


Figure 11.4 FeSEM images of (a) 30-hours-activated samples sintered at (b) 900 °C, (c) 1000 °C, (d) 1100 °C, (e) 1200 °C, and (f) 1300 °C with their corresponding particle size distribution histograms. Source: [25], A. Hajalilou et al. (2015), ELSEVIER.

distribution histogram obviously indicates that the transition from single-domain to multi-domain areas increases by grain growth in such a way that all the grains are distributed in multi-domain areas in the sample sintered at 1300 °C.

Hard magnetic Ba-ferrite nanoparticles are considered to further discuss the foregoing phenomenon. The parallel evolution of a microstructure relationship with magnetic characteristics in the Ba-ferrite samples revealed some interesting



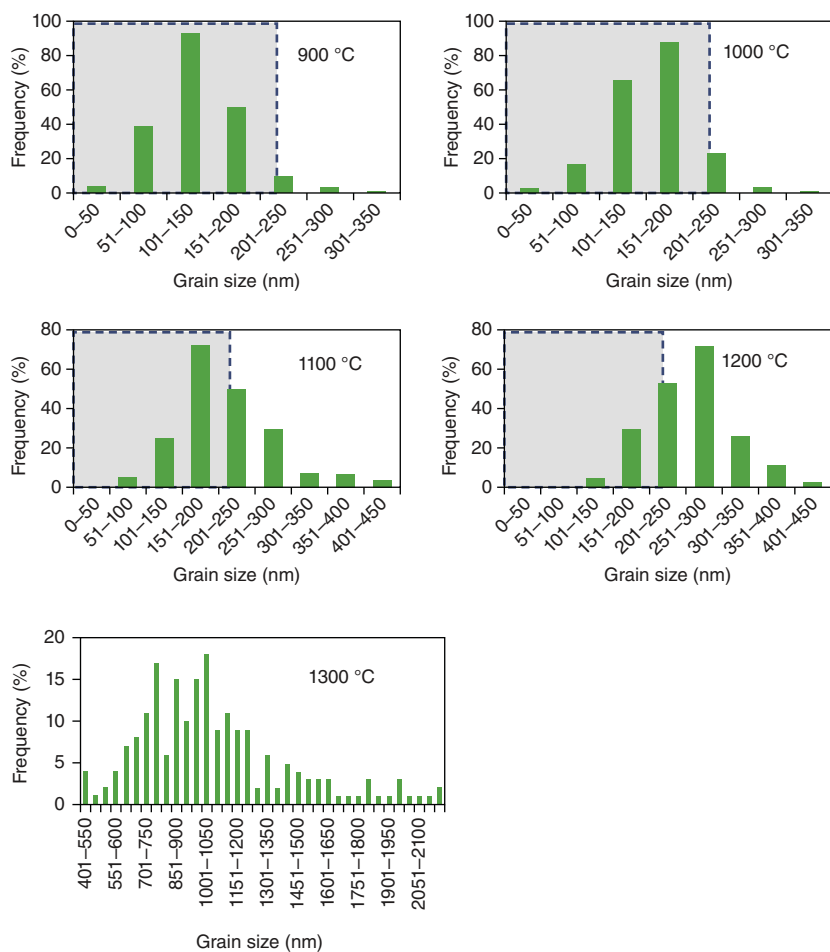
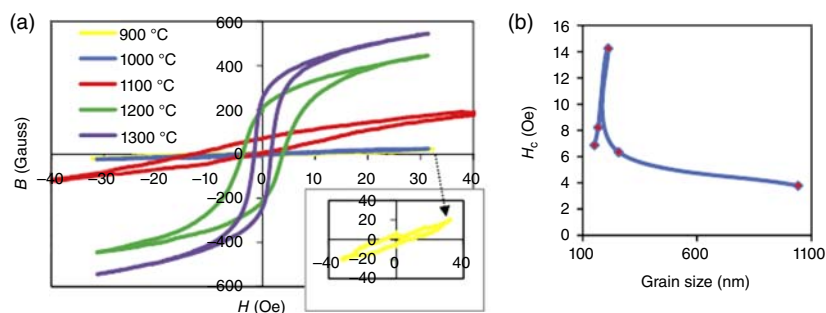


Figure 11.4 (Continued)

Figure 11.5 (a) $B-H$ hysteresis curve for Ni-ferrite samples and (b) their corresponding coercivity as a function of grain size. Source: Hajalilou et al. [25]/with permission of Elsevier.

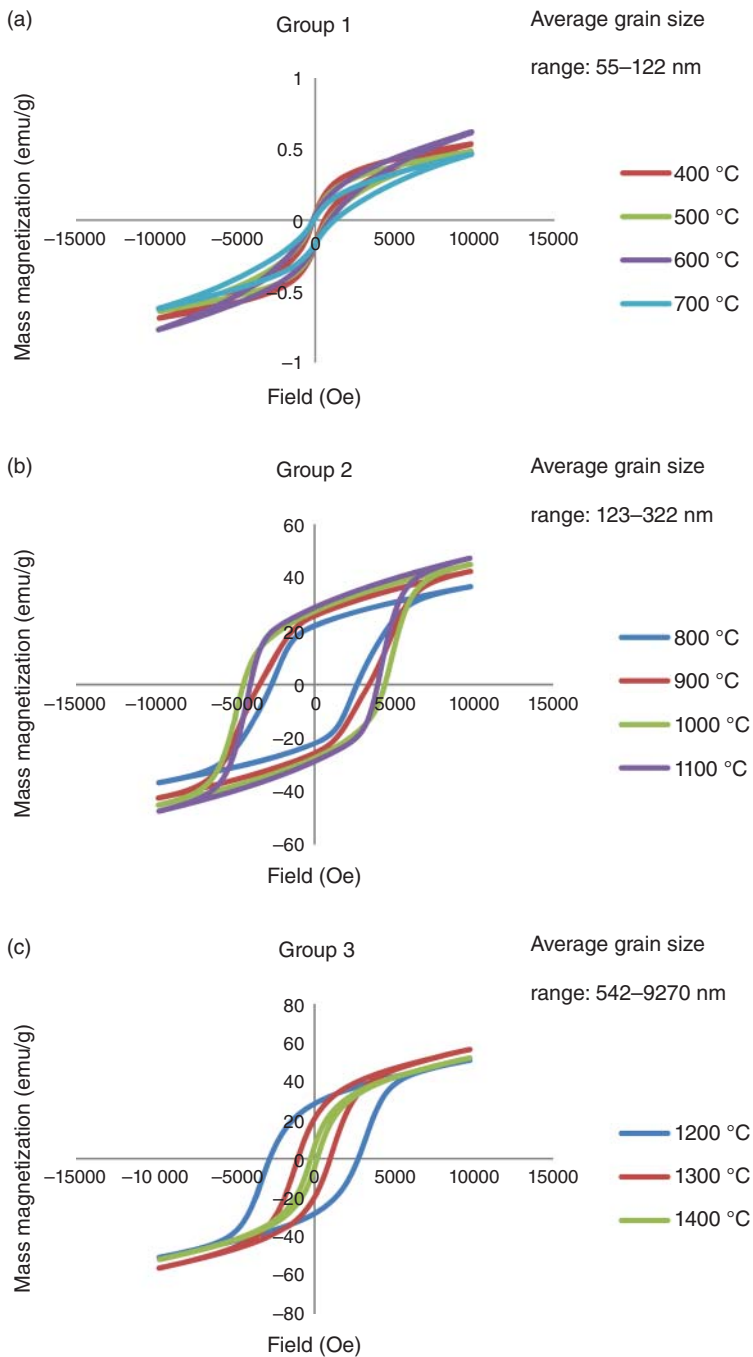


Figure 11.6 B – H hysteresis curves for Ba-ferrite samples (a–c) and their corresponding coercivity versus grain size in the plot (d). Source: Shafie et al. [26]/Springer Nature.



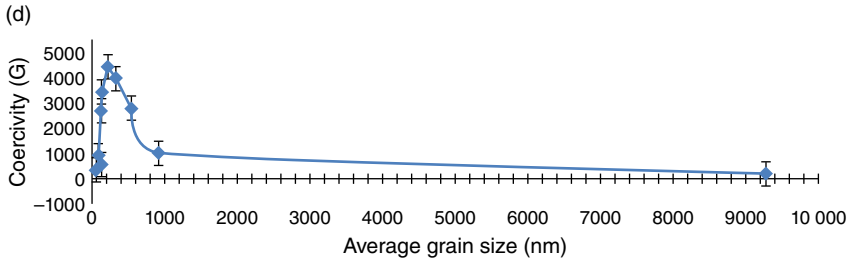


Figure 11.6 (Continued)

results, and the critical grain size was found to be about 219 nm. Three different groups of B - H curves with grain size distribution are shown in Figure 11.6a-c. By plotting coercivity (obtained from the B - H hysteresis curves) versus grain size (obtained from the field emission scanning electron microscopy [FeSEM] images) (Figure 11.6d), the critical grain size was determined, suggesting the transition from the single-domain to the multi-domain region [26].

A rough estimate of the critical diameter for the single domain formation can be made by assuming the thickness of a domain wall about 100 nm, but more rigorous estimations can be derived [27-29]. Taking into account that a particle with a uniaxial anisotropy whose anisotropy energy is given by

$$E = KV \sin^2 \theta \quad (11.4)$$

where K is the anisotropy energy density (J/m^3), V is the particle volume, and θ is the angle between the magnetization vector and the easy axis, the system thus has two minimal energy states separated by an energy barrier of height KV between them as shown in Figure 11.7. In this circumstance, it can be shown that for a spherical

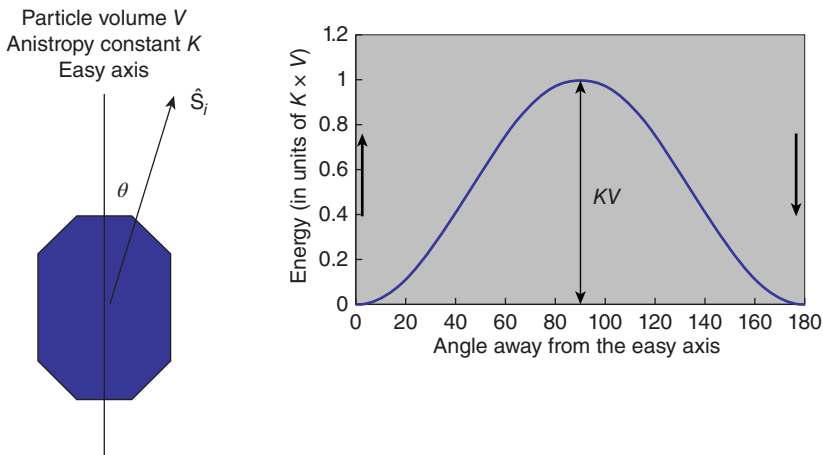


Figure 11.7 Anisotropy energy as a function of magnetization direction in a nanoparticle with uniaxial anisotropy.



particle with a large anisotropy, which satisfies the condition $K > \frac{\mu_0 M_s^2}{6}$, the critical diameter (D_{cir}) for single-domain particles is expressed by:

$$D_{\text{cir}} \approx \frac{18\sqrt{A_{\text{ex}}K}}{\mu_0 M_s^2} \quad (11.5)$$

The term A_{ex} is the exchange stiffness, defined by $zJ_{\text{ex}}S^2/a$, where z is the number of nearest neighbors, J_{ex} is the exchange integral, S^2 is the square of spin and a is the atomic spacing. In most materials, A_{ex} is equal to $10^{-11} \text{ J m}^{-1}$ and so, for instance, for Co particles with $K \sim 7 \times 10^5 \text{ J/m}^3$ and $M_s = 1.3 \times 10^6 \text{ A/m}$, $D_{\text{cir}} \sim 22 \text{ nm}$. This equation indicates that D_{cir} increases with anisotropy since from $t = \pi a (\frac{W}{3K})^{1/2}$, where K is the anisotropy energy density and W is the exchange energy/unit volume, the domain wall thickness is reduced so that the energy of a domain wall is larger, and it becomes energetically unfavorable to form one at a larger particle size. The opposite is true for saturation magnetization.

11.3 SPM Description Based on Magnetization Hysteresis Loop ($M-H$ or $B-H$)

Superparamagnetic can be described based on the equations that are employed for paramagnetic particles, e.g. the Langevin function [17, 22, 24], with only a difference that the magnetic moment of individual particles is much larger in the case of SPM. Thus, the hysteresis loop, $M-H$ or $B-H$, of SPM is more similar to that of a paramagnetic particle, but much steeper with higher magnetization. This is why they are named superparamagnetic. In this case, the coercivity of nanoparticles is almost zero or negligible (Figure 11.8). In fact, the Langevin function describes magnetization as a function of an applied magnetic field in paramagnetic materials. It induces the

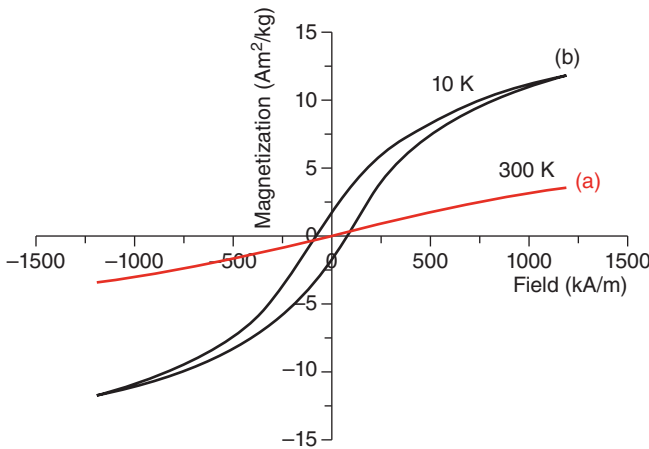


Figure 11.8 Schematic representation of the $M-H$ hysteresis curve of the superparamagnetic nanoparticles (a) with no coercivity at room temperature and (b) with coercivity at 10 K.



gradual orientation of randomly directed atomic magnetic moments in a paramagnetic material in the presence of an externally applied magnetic field. To describe an ensemble of nanoparticles through the Langevin function, each nanoparticle acts as a “large atom.” The magnetic moment of such a “large atom” is 103–105 times higher than the moment of the atoms it is composed of [17, 24]. Indeed, the Langevin equation is employed to nonlinear least fitting of the initial magnetization curve of the samples as:

$$M(H) = M_s \left[\coth \left(\frac{\mu H}{k_B T} \right) - \frac{k_B T}{\mu H} \right] \quad (11.6)$$

Herewith, k_B is the Boltzmann constant, T is the absolute temperature, $M(H)$ is the magnetization for an applied field H , and M_s is the saturation magnetization [6, 30, 31]. The SPM nanoparticles may have hysteresis (notable coercivity) or higher saturation magnetization, thus exhibiting behavior similar to that of ferromagnetic materials. Since the properties of SPM materials depend crucially on the spontaneous magnetic moment of magnetic grains, it is implicitly understood that temperature is below the Curie (T_C) or Neel temperature (T_N) of magnetic nanoparticles.

11.4 SPM Detection Based on ZFC and FC Magnetization Curves

Based on the Arrhenius equation as $\tau = \tau_0 \exp \frac{\Delta E}{k_B T}$, to determine the blocking temperature (T_B) as a value for T , the time scale of the experimental technique should be taken into account [4, 20, 32, 33]. For the magnetization measurement, a typical period of time (by convention) is 100 seconds. It averages out over the time of measurement if the considered particle magnetization direction fluctuates at the given experimental temperature with a frequency higher than 0.01 s^{-1} . The particle would act superparamagnetically, and no magnetization is measured. At a given temperature above T_B , the absence of hysteresis in the magnetization curve indicates the superparamagnetic characteristic of the magnetic nanoparticles [24, 34, 35].

As discussed, superparamagnetism can be characterized in terms of hysteresis curves, M - H or B - H , and $M(T)$ curves based on ZFC and FC experiments (Figure 11.9). In the case of M - H or B - H , as mentioned, there is no hysteresis, meaning that both retentivity and coercivity are zero. On the other hand, in the case of the $M(T)$ curve (Figure 11.9), the curve reveals that superparamagnetism is destroyed by cooling. The corresponding region to this temperature is considered as blocking temperature (T_B) and has a linear dependency on volume and the magnitude of the crystal field anisotropy. Below T_B , the particles have stable magnetization and represent hysteresis, suggesting a relaxation time for demagnetization of longer than 100 seconds. Considering the same criterion for stability for uniaxial particles, the T_B is given as:

$$T_B = \frac{KV}{25k_B} \quad (11.7)$$



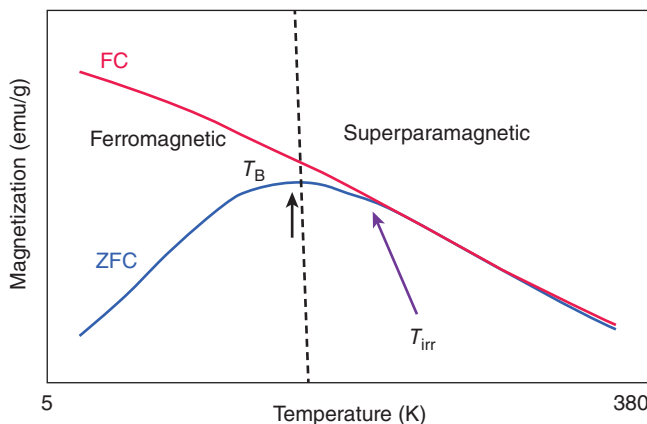


Figure 11.9 Schematic representation of magnetization versus temperature for the ZFC–FC curve.

where V is the volume of particles, k_B is the Boltzmann constant, and K is the anisotropy constant. According to this equation, Ni, as an example, with characteristics of ($K = 4.5 \times 10^3 \text{ J/m}^3$ and particle size = 20 nm) yields the T_B as -55 K . Above T_B , the thermal energy will be sufficient to suppress ferromagnetic characteristics and the particles, therefore, become superparamagnetic. Below T_B , the magnetization will be relatively stable and will represent ferromagnetic behavior.

References

- 1 Rezanezhad, A., Hajalilou, A., Eslami, F. et al. (2021). Superparamagnetic magnetite nanoparticles for cancer cells treatment via magnetic hyperthermia: effect of natural capping agent, particle size and concentration. *Journal of Materials Science: Materials in Electronics* 32: 24026–24040.
- 2 Hajalilou, A. and Mazlan, S.A. (2016). A review on preparation techniques for synthesis of nanocrystalline soft magnetic ferrites and investigation on the effects of microstructure features on magnetic properties. *Applied Physics A* 122: 680.
- 3 Hajalilou, A., Kianvash, A., Lavvafi, H., and Shameli, K. (2018). Nanostructured soft magnetic materials synthesized via mechanical alloying: a review. *Journal of Materials Science: Materials in Electronics* 29: 1690–1717.
- 4 Hajalilou, A., Ferreira, L.P., Melo Jorge, M.E. et al. (2021). Superparamagnetic Ag–Fe₃O₄ composites nanoparticles for magnetic fluid hyperthermia. *Journal of Magnetism and Magnetic Materials* 537: 168242.
- 5 Ogholbeyg, A.B., Kianvash, A., Hajalilou, A. et al. (2018). Cytotoxicity characteristics of green assisted-synthesized superparamagnetic maghemite ($\gamma\text{-Fe}_2\text{O}_3$) nanoparticles. *Journal of Materials Science: Materials in Electronics* 29: 12135–12143.
- 6 Etemadifar, R., Kianvash, A., Arsalani, N. et al. (2018). Green synthesis of superparamagnetic magnetite nanoparticles: effect of natural surfactant and heat



- treatment on the magnetic properties. *Journal of Materials Science: Materials in Electronics* 29: 17144–17153.
- 7 Jakubovics, J.P. (1987). *Magnetism and Magnetic Materials*. London: Institute of Metals, Carlton House Terrace.
 - 8 Hajalilou, A., Mazlan, S.A., Lavvafi, H., and Shameli, K. (2016). *Field Responsive Fluids as Smart Materials*. Springer.
 - 9 Fannin, P., Marin, C., and Malaescu, I. (2003). The influence of particle concentration and polarizing field on the resonant behaviour of magnetic fluids. *Journal of Physics: Condensed Matter* 15: 4739.
 - 10 Tackett, R., Parsons, J., Machado, B. et al. (2010). Evidence of low-temperature superparamagnetism in Mn_3O_4 nanoparticle ensembles. *Nanotechnology* 21: 365703.
 - 11 Knobel, M., Nunes, W., Socolovsky, L. et al. (2008). Superparamagnetism and other magnetic features in granular materials: a review on ideal and real systems. *Journal of Nanoscience and Nanotechnology* 8: 2836–2857.
 - 12 Mikhaylova, M., Kim, D.K., Bobrysheva, N. et al. (2004). Superparamagnetism of magnetite nanoparticles: dependence on surface modification. *Langmuir* 20: 2472–2477.
 - 13 Woods, S., Kirtley, J., Sun, S., and Koch, R. (2001). Direct investigation of superparamagnetism in Co nanoparticle films. *Physical Review Letters* 87: 137205.
 - 14 Majumder, D. and Karan, S. (2013). Magnetic properties of ceramic nanocomposites. *Ceramic Nanocomposites* 51–91.
 - 15 Hajalilou, A., Hashim, M., Kamari, H.M., and Masoudi, M.T. (2015). Effects of milling atmosphere and increasing sintering temperature on the magnetic properties of nanocrystalline $\text{Ni}_{0.36}\text{Zn}_{0.64}\text{Fe}_2\text{O}_4$. *Journal of Nanomaterials* 16: 232.
 - 16 Hajalilou, A., Hashim, M., Ebrahimi-Kahrizsangi, R., and Sarami, N. (2015). Influence of CaO and SiO_2 co-doping on the magnetic, electrical properties and microstructure of a Ni–Zn ferrite. *Journal of Physics D: Applied Physics* 48: 145001.
 - 17 Khomutov, G.B. and Koksharov, Y.A. (2009). Organized ensembles of magnetic nanoparticles: preparation, structure, and properties. *Magnetic Nanoparticles* 117–195.
 - 18 Zhang, S. and Zhao, D. (ed.) (2017). *Advances in Magnetic Materials: Processing, Properties, and Performance*. CRC press.
 - 19 Gobrecht, H., Bucka, H., Bergmann, L. et al. (2019). *Aufbau der Materie*. Walter de Gruyter GmbH & Co KG.
 - 20 Mørup, S., Hansen, M.F., and Frandsen, C. (2010). Magnetic interactions between nanoparticles. *Beilstein Journal of Nanotechnology* 1: 182–190.
 - 21 Mørup, S. and Frandsen, C. (2004). Thermoinduced magnetization in nanoparticles of antiferromagnetic materials. *Physical Review Letters* 92: 217201.
 - 22 Mandel, K. (2013). Synthesis and characterisation of superparamagnetic nanocomposite particles for water purification and resources recovery. PhD dissertation. Julius-Maximilians-University, Würzburg.
 - 23 Néel, L. (1949). Théorie du traînage magnétique des ferromagnétiques en grains fins avec applications aux terres cuites. *Annales Geophysicae* 5: 99–136.



- 24 Park, Y., Adenwalla, S., Felcher, G., and Bader, S. (1995). Superparamagnetic relaxation of Fe deposited on MgO (001). *Physical Review B* 52: 12779.
- 25 Hajalilou, A., Hashim, M., Ebrahimi-Kahrizsangi, R., and Kamari, H.M. (2015). Influence of evolving microstructure on electrical and magnetic characteristics in mechanically synthesized polycrystalline Ni-ferrite nanoparticles. *Journal of Alloys and Compounds* 633: 306–316.
- 26 Shafie, M., Hashim, M., Ismail, I. et al. (2014). Magnetic M–H loops family characteristics in the microstructure evolution of BaFe₁₂O₁₉. *Journal of Materials Science: Materials in Electronics* 25: 3787–3794.
- 27 Kittel, C. (1946). Theory of the structure of ferromagnetic domains in films and small particles. *Physical Review* 70: 965.
- 28 O’Handley, R.C. (2000). *Modern Magnetic Materials: Principles and Applications*. Wiley.
- 29 C. Binns, Tutorial section on nanomagnetism, in: *Frontiers of Nanoscience* 6, 2014, pp. 1–32. Elsevier
- 30 Hajalilou, A., Hashim, M., and Masoudi, M.T. (2015). A comparative study of in-situ mechanochemically synthesized Mn_{0.5}Zn_{0.5}Fe₂O₄ ferrite nanoparticles in the MnO/ZnO/Fe₂O₃ and MnO₂/Zn/Fe₂O₃ systems. *Ceramics International* 41: 8070–8079.
- 31 Abdollah, H., Mansor, H., Reza, E.-K., and Taghi, M.M. (2015). Effect of milling atmosphere on structural and magnetic properties of Ni–Zn ferrite nanocrystalline. *Chinese Physics B* 24: 048102.
- 32 Jalili, H., Aslibeiki, B., Hajalilou, A. et al. (2022). Bimagnetic hard/soft and soft/hard ferrite nanocomposites: structural, magnetic and hyperthermia properties. *Ceramics International* 48: 4886–4896.
- 33 Kavkhani, R., Hajalilou, A., Abouzari-Lotf, E. et al. (2022). CTAB assisted synthesis of MnFe₂O₄@SiO₂ nanoparticles for magnetic hyperthermia and MRI application. *Materials Today Communications* 31: 103412.
- 34 Moskowitz, B.M. (1991). Hitchhiker’s guide to magnetism. *Environmental Magnetism Workshop (IRM), Institute for Rock Magnetism University of Minneapolis, Minneapolis, Minnesota*. pp. 48.
- 35 Coey, J.M. (2010). *Magnetism and Magnetic Materials*. Cambridge University Press.



12

Mössbauer Spectroscopy

12.1 Introduction to Mössbauer Spectroscopy

Mössbauer spectroscopy is a high-resolution technique employed to scrutinize nucleic environments. Indeed, it is a nuclear resonance spectroscopic technique Based on the Mössbauer effect, recoil-free γ -ray emission, and absorption in solids. The technique requires a source of γ rays, an absorber, and the means of modulating the energy of the emitted γ rays [1]. It is as well called γ -ray spectroscopy. It has a very fine resolution for detecting changes at the nuclear energy levels. Since its discovery in 1957, it has been evidenced to be a fragile, precise, and versatile technique with extensive utilization in various scientific disciplines, including but not limited to physics, chemistry, life science, materials science, biology, etc. [2–4]. It gives information about the structural, magnetic, chemical, and time-dependent behavior of materials [3, 4]. Particularly, it provides resolution of the magnetic hyperfine field in the probed nucleus in an experimental time window of the order of 10^{-8} s [5]. Furthermore, Mössbauer spectroscopy of a metal complex gives information about the oxidation state and spin state of metals, type of ligand coordinated to metal, and geometry of metal.

The qualitative analysis of the spectra is established based on the inspection of the type of absorption spectrum. In particular, the presence of six resonance lines (sextet) indicates the presence of a magnetic hyperfine field, which represents a spontaneous magnetic order in the material, as seen within the measurement time of the technique ($\sim 10^{-8}$ s). On the other hand, the presence of two resonance lines in the spectrum (a doublet) designates the lack of a magnetically blocked state, which can represent either the lack of a magnetic order (paramagnetism) or thermal instability (concerning the measurement time of the technique) of the net moment of a magnetically ordered material (superparamagnetism) [5].

The Mössbauer effect has, however, been detected in several isotopes (at least 88 γ -ray transitions in 72 isotopes of 42 different elements) such as ^{57}Fe , ^{61}Ni , ^{119}Sn , ^{121}Sb , ^{129}I , ^{151}Eu , ^{161}Dy , ^{186}Os , and ^{191}Ir [2, 4]. The isotope ^{57}Fe has the profitable combination of low γ -ray energy and a long lifetime in its first excited state (E.S). Furthermore, ^{57}Fe Mössbauer is a popular tool that is used to observe and examine the magnetic hyperfine parameters because there are many materials for practical use that contain iron. The natural abundance of ^{57}Fe isotope in such materials is



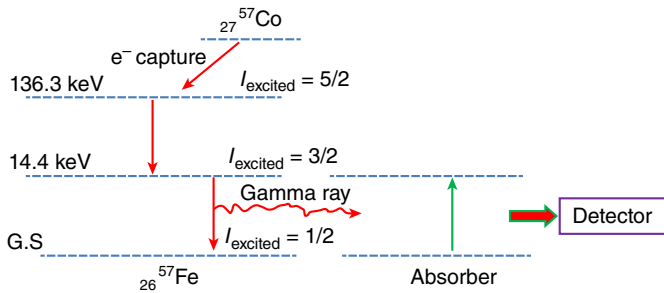


Figure 12.1 Schematic representation of $_{27}^{57}\text{Co}$ decaying to $_{26}^{57}\text{Fe}$.

2.12% [1]. ^{57}Co isotope in the Rh matrix is usually the preferred source of γ rays. It has a half-life of 270 days and decays to ^{57}Fe in the excited state. The 14.41 keV excited state is critical for Mössbauer spectroscopy, and γ rays from this state can resonantly be absorbed by ^{57}Fe nuclei in another material. Its decay scheme is shown in Figure 12.1. The figure indicates that the $_{27}^{57}\text{Co}$ nucleus is not stable, and it decays naturally by capturing electrons. It decays into ^{57}Fe , which is also unstable and located in the second excited state (E.S) with an energy of 136.3 keV. Thus, it will decay to the first excited state of ^{57}Fe with the energy of 14.4 keV, which is followed by decaying to a ground state (G.S) of ^{57}Fe and will emit γ rays. The emitted γ rays will be absorbed by the absorber, and the released signals will be detected by the detector.

In general, the basic information that one should know about Mössbauer spectroscopy are:

- It is γ -ray spectroscopy.
- Transition is done between the ground and the excited state of the nucleus.
- Mössbauer active nuclei are those that have $I > 0$, which have different values of I in the ground and excited states; I is the spin value.
- Principle: the principle involves a radioactive nucleus like ${}_Z\text{X}^A$ (Z : atomic number, and A : atomic mass); when it captures an electron, its atomic number reduces to $Z - 1$, and it gets converted to another nucleus, as shown in Figure 12.2.

An example is given in Figure 12.3 to further clarify the principle of Mössbauer spectroscopy. When ^{57}Co captures an electron, it will get converted to ^{57}Fe ; when it comes from the excited state (E.S) to the ground state (G.S), γ ray is emitted, which is called “ γ -ray fluorescence.” When the γ ray strikes another nucleus, it will transit from “G.S” to “E.S” and will absorb the emitted γ ray, which is called “ γ -ray resonance.” This happens within the nucleus where we want to get information. It simply means that the γ -ray fluorescence is in the state of the source, and the γ -ray resonance occurs in a sample.



Figure 12.2 Schematic representation of electron capture by radioactive nucleus.



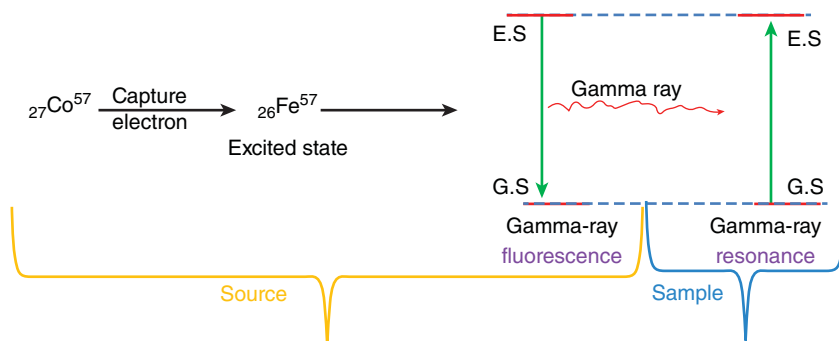


Figure 12.3 Schematic representation of emission and absorption in the iron atom.

12.2 Observed Effects in Mössbauer

12.2.1 Mössbauer Effect

The Mössbauer effect is the recoil-free emission of a γ -ray photon by a nucleus and its subsequent recoilless absorption by an identical nucleus. Rudolf Mössbauer discovered the effect which was named after him in 1957 and was awarded the Nobel Prize in 1961. It is based on the fluorescence and resonance of γ radiation, as shown in Figure 12.3. In fact, the Mössbauer effect is the recoilless emission and absorption of γ rays by identical nuclei in the source and absorber, respectively, without the loss of energy. This is attributed to the recoil of a nucleus and without thermal broadening [2]. It should be noted that the atoms in the source emitting the γ rays must be of the same isotope as atoms in the sample absorbing them.

The observation of γ -ray resonance, which is induced by nuclear transitions, was difficult before the discovery of the effect, mainly due to two key effects: the recoil of nuclei when emitting or absorbing γ rays and the extremely small hyperfine interactions between the nucleus and its environment. In other words, before the discovery of the Mössbauer Effect, it was thought that atoms could be considered free as far as nuclear reactions were concerned because the energy of nuclear events is so much larger than those associated with chemical bonding. The Mössbauer effect is based on the fact that this is not necessarily so. Mössbauer figured out that small recoiling energy tend to be generated due to a much larger nucleus' effective mass once the atoms are within a solid matrix. The γ -ray energy is so small that the recoil of the nucleus is too low to be transmitted as a phonon due to the quantum property of the lattice vibration, which produces a recoil-free γ -ray emission and absorption. Such recoil-free emission and absorption of γ rays are referred to as the Mössbauer effect, which allows observation of γ -ray resonance and produces Mössbauer spectra.

12.2.2 Recoil Effect

When γ -ray strikes the sample (Figure 12.4), the energy of γ rays will be reutilized in two ways: for making the transition from G.S to E.S, which is called resonance, and



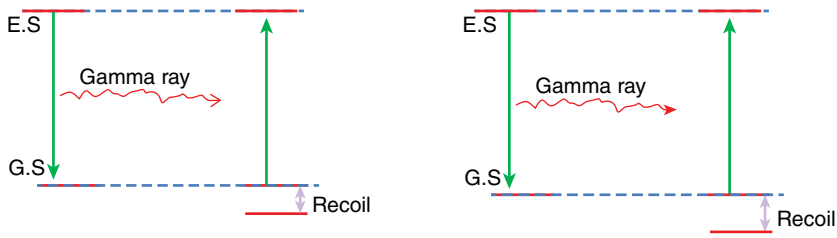


Figure 12.4 Schematic representation of the recoil phenomenon.

to overcome the recoil energy. Whenever this transition takes place, some amount of the nucleus will be pushed backward, because something is moving out in a forward direction (like a gun). So, the amount of energy that is wasted for this process or required for the recoil of the nucleus is called recoil energy. When this occurs, the nucleus suffers recoil and the γ ray is emitted with energy $E_\gamma = E - E_R$, where E_R is the recoil energy and is given by

$$E_R = \frac{E_\gamma^2}{2Mc^2} \quad (12.1)$$

where M is the mass of the nucleus, c is the velocity of light, and E_γ is the energy between G.S and E.S.

The γ rays of slightly higher energy than the resonance energy are needed to overcome recoil energy. Based on this equation, if the mass is higher, the recoil energy will be less. Recoil energy can be minimized if the nucleus is bounded very strongly (by keeping it in a crystalline solid). At this condition, $E_R = 0$.

The uncertainty in energy (line width [LW]) (Γ) for the nuclear excited state is given by

$$\Gamma = \frac{1}{\tau} \quad (12.2)$$

where τ is the mean lifetime of the nuclear state. Thus, if $2E_R \gg \Gamma$, resonant absorption of the emitted γ ray cannot occur for a free atom, see Figure 12.5.

When the nuclei are embedded in a rigid lattice, however, the whole solid may take up the recoil momentum. The recoil energy is proportional to $1/M_s$, where M_s is the mass of the solid and much larger than the mass of a single nucleus (M). The recoil energy is then negligible, and the emitted photons have energy close to E . Hence, M in equation (12.1) can be replaced by an effective mass, which is much larger. This gives rise to a much-reduced value of E_R . The emitted photons can therefore be resonantly absorbed by identical nuclei. In real solids, the nuclei are bound in the lattice but are free to vibrate about their mean positions, which causes thermal broadening. The emission and absorption of γ rays can be accompanied by the excitation of quantized phonons. For low recoil energies, there is a finite probability, f , that no phonons will be excited. In this case, $E_R = 0$ and there is no thermal broadening.

The portion of the decay that does not involve phonons is called the recoil-free fraction. This is the essence of the Mössbauer effect, which is the absorption of recoil momentum by the entire lattice of the solid. Since the lattice is much more massive



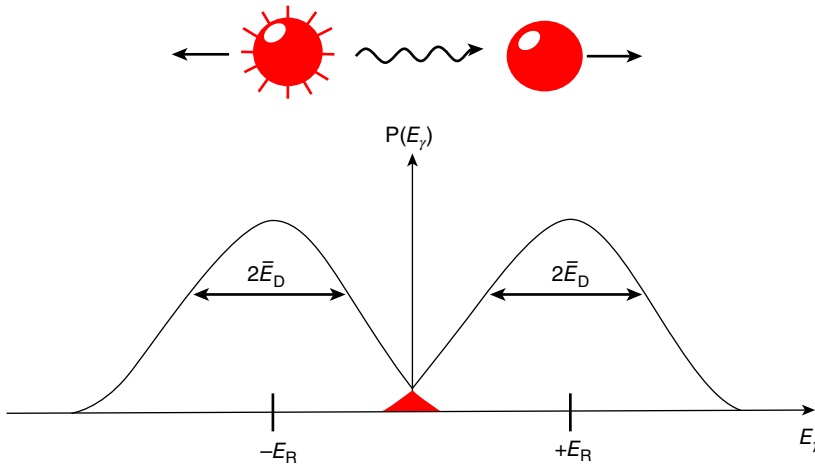


Figure 12.5 The recoil of free nuclei is due to the conservation of momentum when emitting or absorbing γ rays. Because of the recoil, the resonant overlap is too small, which prevents resonance.

than the nucleus, its recoil kinetic energy is effectively zero. The probability, f , for the low-temperature approximation is expressed by:

$$f = \exp \left(-\frac{E_R}{k\theta_d^2} \left(\frac{3}{2} + \frac{\pi^2 T^2}{\theta_d^2} \right) \right) \quad (12.3)$$

It indicates that temperature (T) has a reverse relation with probability; as the temperature is lower, the probability is higher [6]. Whenever a high-energy particle is released from a body at rest, the releasing body feels a back-rick, i.e. it is pushed backward; this is called the recoil effect (just like a gun). So, the energy of γ rays is slightly less than the natural energy of transition. Similarly, for a nucleus at rest to absorb γ ray, the energy of γ ray should be slightly greater than the natural energy. So, for free nuclei, this nuclear resonance (absorption and emission of γ rays by identical nuclei) is unobservable. But when nuclei are present in a solid crystal, there is very little loss as recoil energy. If the emitting and absorbing nuclei were in an identical chemical environment, the nuclear transition energies would be equal to nuclei resonance. But if the chemical environment is different, it will cause a shift in nuclear energy levels. To bring the nuclei in resonance, the energy of γ rays is slightly changed by the Doppler effect.

12.2.3 Doppler Effect

In this effect, the energy is changed by vibrating. That is, one can vibrate the source with a certain velocity. Then, due to this vibration, the energy of γ ray fluctuates. At a certain moment, this energy becomes exactly equal to the energy of the absorbent. So, the absorbent can absorb γ radiation. Then, the Doppler effect is given as follows:

$$E' = E \left(1 + \frac{V}{c} \right) \quad (12.4)$$



where E is the energy of γ radiation, V is the velocity of source vibration (mm/s), c is the velocity of light, and E' is energy changes. The shift in frequency ($\Delta\nu$) is given by

$$\Delta\nu = \nu \left(\frac{V}{c} \right) \quad (12.5)$$

where ν is equal to c/λ . For example, in Mössbauer spectra, a source emitting at 14.4 keV (3.48×10^{18} Hz) had to be moved toward the absorber at 2.2 mm/s for resonance. The shift of frequency between source and absorber is

$$\Delta\nu = 3.48 \times 10^{18} \times \frac{2.2}{3 \times 10^{11}} = 2.55 \times 10^7 \text{ Hz} = 25.5 \times 10^6 \text{ Hz} = 25.5 \text{ MHz} \quad (12.6)$$

12.3 Hyperfine Interactions

In Mössbauer spectroscopy, nuclei are used as probes of the local environment. Thus, electrostatic and magnetic interactions of a nucleus with its surroundings give rise to a shift and splitting of the nuclear energy levels. The interactions of the nuclei with their surroundings are known as hyperfine interactions. Indeed, hyperfine interactions are the interactions between a nuclear and its surrounding environment, which can vary the energy level of nuclear transitions and therefore influence the shape of Mössbauer spectra. In other words, a nucleus may interact with electric and magnetic fields from its surrounding environments. Such interactions are known as hyperfine interactions and can shift energy levels and lift their degeneracy. Hyperfine interactions are extremely small compared to the energy level of a nucleus. Before the discovery of the Mössbauer effect, it was difficult to observe these small interactions because of the large background energies. The extremely high-energy resolution of the Mössbauer effect enables observation of these interactions. In the Mössbauer effect, there are three types of hyperfine interaction, namely the electric monopole interaction (which is also known as isomer shift), the magnetic dipole interaction (magnetic splitting), and the electric quadrupole interaction (quadrupole splitting [QS]). The nuclear Hamiltonian (H) can be written as [2]:

$$H = H_0 + E_0 + M_1 + M_2 \quad (12.7)$$

where E_0 , M_1 , and M_2 are the electric monopole interaction, the magnetic dipole interaction, and the electric quadrupole interaction, respectively. H_0 represents all other terms except for the hyperfine interactions. In the following sections, these interactions are briefly described. A more detailed discussion can be found in Refs. [2, 3].

12.3.1 Electric Monopole Interaction

This interaction arises due to the finite size of the nucleus and the electric charge density from the s-electrons within it, resulting in a Coulombic interaction between them [3]. This interaction has the effect of shifting all energy levels by varying amounts and is known as the isomer shift (δ) (Figure 12.6a). It simply means



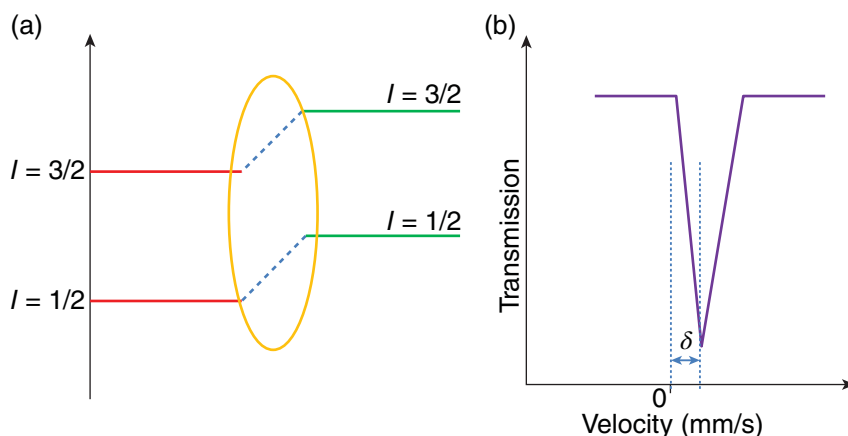


Figure 12.6 Schematic representation of (a) isomer shifts in isolated ^{57}Fe , and (b) transmission versus velocity creating a one deep.

that the isomer shift of absorption lines in a Mössbauer spectrum arises due to interaction between nuclear charge density and the surrounding “s” electron cloud. In other words, the shift occurs due to the difference in the s-electron density at nuclear sites between the source and absorber. Consequently, the centroid of the Mössbauer spectrum is shifted from zero velocity (Figure 12.6b), meaning that the deep absorption peak change from its original position. Figure 12.6 clearly indicates the isomer shift for isolated ^{57}Fe ; the energy level of ground state ($I = 1/2$) and first excited level ($I = 3/2$) is increased. δ cannot be measured directly due to the fact that Mössbauer spectroscopy is a relative method. A suitable reference for a specific source or an absorber is therefore needed.

The isomer shift (δ) is given by formula according to Greenwood and Gibb as [2]:

$$\delta = K [R_e^2 - R_g^2] \{ \psi_s^2(S) - \psi_s^2(A) \} \quad (12.8)$$

R_e and R_g are the radius of the excited and ground state of emitting and absorbing nuclei, respectively. $\psi_s(S)$ and $\psi_s(A)$ are the electron density of source and absorber, respectively. K is equal to $\frac{2\pi}{5}Ze^2$, Z is the atomic number, and e is the electronic charge. By assuming that the change in nuclear radius ($\Delta R = R_e - R_g$) is constant, for a fixed Mössbauer source, the isomer shift is modified as:

$$\delta = K_0 - K|\psi_a(0)|^2 \quad (12.9)$$

where K_0 and K are the relevant constants. This indicates that the isomer shift alters as a function of s-electron density ($|\psi_a(0)|^2$) at absorber nuclei, which can be affected by s-, p-, d-, and f-electrons as well as by covalency and formation of bonds [2].

Isomer shift mainly depends on (i) s-electron density (indirectly p and d-electron density), (ii) spin state; high and low spin states (HS, LS), (iii) nature of ligand (back bonding), and (iv) electronegativity of ligands, which are briefly described as follows.



12.3.1.1 S-Electron Density (Indirectly p and d-Electron Density)

Since s electron wave functions have their maxima at the nucleus, it affects the isomer shift to a large extent by screening of the s electrons caused by p or d electrons. Thus, it reduces s electron density, for example, in the case of ^{57}Fe , when the nuclei are under compression in the model of transition. It means the radius of nuclei in the excited state is lesser/lower than that of the ground state. This difference of R is negative ($\Delta R = -\text{ive}$). In this circumstance, the isomer shift will be affected negatively with s electron density. This means that

$$\delta \propto -(\psi_s^2(S) - \psi_s^2(A)) \quad (12.10)$$

This indicates that if there is an increase in s electron density, the isomer shift decreases. If there is an increase in d electron, which causes more shielding of s electron, the isomer shift increases.

In the case of ^{119}Sn , the nucleus is under expansion mode; this means that the radius of nuclei in the excited state is larger than that of the ground state. Thus, $\Delta R = +\text{ive}$. In this circumstance, isomer shift will be affected positively with s electron density. This means that

$$\delta \propto +(\psi_s^2(S) - \psi_s^2(A)) \quad (12.11)$$

This indicates that increase in s electron density, the isomer shift increases. On the other hand, the isomer shift decreases once d electron density increases. For example,

$$\text{Sn(II)} = 5\text{S}^2 5\text{P}^0, \text{ so } \delta \text{ is positive, (+ive)}$$

$$\text{Sn(IV)} = 5\text{S}^0 5\text{P}^0, \delta \text{ is negative, (-ive)}$$

Generally, Sn(II) compounds show the isomer shift $>2.1 \text{ mm/s}$, while Sn(IV) shows the isomer shift $< 2.1 \text{ mm/s}$.

In the case of iron, Fe^{2+} and Fe^{3+} ions, however, have similar s-electrons and have different values of isomer shift (δ). This difference in δ is associated with the additional d-electron in the Fe^{2+} ion that declines the net attractive Coulomb potential for the 3s-electrons. This gives rise to a reduction in the charge density at the nucleus. Thus, the isomer shift in Mössbauer spectroscopy of iron compound is given as:

$$\text{Fe(II)} > \text{Fe(III)} > \text{Fe(IV)} \quad (12.12)$$

The isomer shift depends on s-electron density. Since the iron atomic number is 26, we have

$$\text{Fe(26)}: 3\text{d}^6 4\text{s}^2 \quad (12.13)$$

$$\text{Fe}^{2+}: 3\text{d}^6 4\text{s}^0 \quad (12.14)$$

$$\text{Fe}^{3+}: 3\text{d}^5 4\text{s}^0 \quad (12.15)$$

$$\text{Fe}^{2+}: 3\text{d}^4 4\text{s}^0 \quad (12.16)$$

$$\text{Fe}^{2+} > \text{Fe}^{3+} > \text{Fe}^{4+} \quad (12.17)$$



One can observe that the s-electron is zero, so with the large number of d-electron, the isomer shift is also large. This indicates that the isomer shift can probe the valence state of a compound. The difference in isomer shift between Fe^{2+} and Fe^{3+} ions was found to be 0.9 mm/s, which is larger than the natural line width (LW) of the Fe^{2+} ion and therefore can be observed by Mössbauer experiments [7]. The isomer shift is quoted by velocity units (in mm/s) rather than in energy units. Furthermore, 1 mm/s is equivalent to $4 : 8 \times 10^{-8}$ keV for ^{57}Fe isotope [2]. Values of isomer shifts of absorbers are usually quoted with respect to a standard reference absorber such as α -iron.

12.3.1.2 Dependency of Isomer Shift on Spin State

This dependency is described by given ^{57}Fe as an example, for $\text{Fe(VI)} < \text{Fe(IV)} < \text{Fe(III)} < \text{Fe(III)} < \text{Fe(II)} < \text{Fe(II)}$, once the spin value reaches to low (LS) or high (HS), thus, accordingly,

$$\text{HS} < \text{HS to LS} < \text{LS} < \text{HS} < \text{LS} < \text{HS} \quad (12.18)$$

We conclude that isomer shift (HS) > isomer shift (LS). For comparison, we can see in the case of Fe(II) in the high and low states (Figure 12.7) that there is no electron in an easy orbital in the case of low spin (LS).

We know that “eg” orbitals lie directly on the axis, so the electron in it will provide better shielding of s electron as compared to t_{2g} orbital. Thus, we can say that the presence of electrons in easy orbital (eg) will provide more shielding, and hence, there is less s electron density and high isomer shift.

12.3.1.3 Dependency of Isomer Shift on Strong Field Ligands

Strong field ligands are also known as π -acceptance ligands such as CO and CN^- . In these ligands, they have a tendency on the back donation of electron density; the electron can be donated from metal to π -acceptance ligands. So, there will be a decrease in d electron density because it is donated to the ligand. Thus, the s electron density will increase on metal, which results in a lower isomer shift. For example, the sequence of isomer shift is:

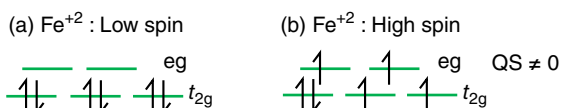
$$[\text{Fe}(\text{CN})_5\text{NO}]^{-2} < [\text{Fe}(\text{CN})_6]^{-3} < [\text{Fe}(\text{CN})_5(\text{NH}_3)]^{-3} \quad (12.19)$$

12.3.1.4 Dependency of Isomer Shift on Electronegativity of Ligands

Once the electronegativity of ligands is higher, the s electron will be less on metal, which results in more isomer shift. For example, the sequence of isomer shift is:

$$\text{FeBr}_2 < \text{FeCl}_2 < \text{FeF}_2 \quad (12.20)$$

Figure 12.7 Schematic representation of the spin value of Fe(II) in (a) low and (b) high spin states.



12.3.2 Electric Quadrupole Interaction (Quadrupole Splitting)

A deep γ -ray absorption or transmission versus velocity curve may be observed in the Mössbauer spectra (Figure 12.6b). Sometimes, this deep is not a single deep and is split into two parts (Figure 12.8a). These types of peaks are characteristics of “Quadrupole splitting (QS).” It is a phenomenon that arises due to the interaction between the electric quadrupole moment of the nucleus and the electric field gradient (EFG). It occurs only when nuclei have (i) spin value (I) greater than $3/2$, ($I > 3/2$) and (ii) asymmetric charge distribution (Figure 12.8b). These produce an electric quadrupole moment called QS or efg. This arises due to inhomogeneous electric field distribution. The more asymmetric the charge distribution is, the higher QS (efg) will occur. On the other hand, for ideal cubic symmetry, the QS is zero; this means that no quadrupole splitting is observed.

Asymmetry in the molecule may be of two types: (i) ligand contribution (non-cubic ligand constitution/different ligands). In this case, the energy of quadrupole splitting (ΔE_Q) is small. For example, in $[\text{Fe}(\text{CN})_5\text{NO}]^{2-}$, there is more asymmetry, but $[\text{Fe}(\text{CN})_6]^{4-}$ is symmetric and no splitting is observed. Another example is Fe(II) with low spin (LS) in the cases of $[\text{K}_4\text{Fe}(\text{CN})_6]$ and $\text{Na}_2[\text{Fe}(\text{CN})_5\text{NO}]$. $[\text{K}_4\text{Fe}(\text{CN})_6]$ has a cubic structure and no quadrupole splitting (QS) is observed, while $\text{Na}_2[\text{Fe}(\text{CN})_5\text{NO}]$ has a tetragonal structure and QS is observed and (ii) valency electron contribution (noncubic valency electron distribution of the atom). In this case, the energy of quadrupole splitting (ΔE_Q) is large. For example, the readers are referred to Figure 12.7.

A nucleus with spin has a nonspherical charge distribution and therefore possesses a nonzero quadrupole moment (Q), which signifies the deviation of the nuclear charge from spherical symmetry. Such nuclei can interact with an inhomogeneous electric field described by the EFG at the nucleus. The EFG is a 3×3 second rank tensor that has contributions from the unfilled electron shells, valency electrons, and surrounding lattice charges and can be given as [3]:

$$V_{ij} = \frac{\partial^2 V}{\partial_i \partial_j}(i, j = x, y, z) \quad (12.21)$$

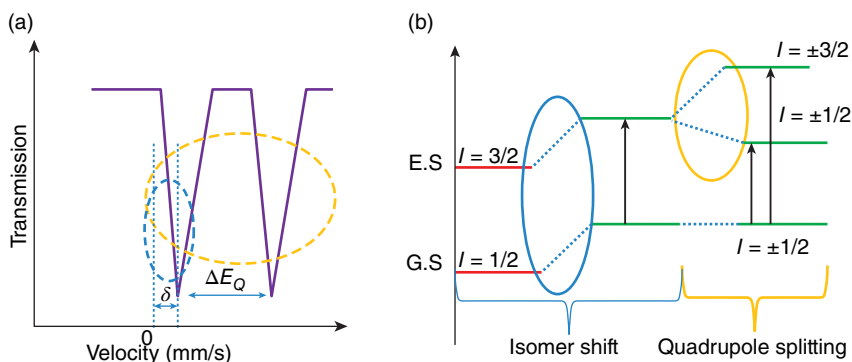


Figure 12.8 Schematic representation of quadrupole splitting; (a) Transmission versus velocity indicating a deep presented in Figure 12.6b into two deeps, and (b) Isomer shift followed by quadrupole splitting.



where V_{ij} is the EFG tensor components and V is the electrostatic potential at the nucleus. The diagonal elements of V_{ij} are dependent since they must satisfy the Laplace equation:

$$V_{xx} + V_{yy} + V_{zz} = 0 \quad (12.22)$$

In other words, the EFG tensor is traceless. A unique axis system known as the principal axis frame of the EFG is defined such that the off-diagonal terms disappear and

$$|V_{zz}| \geq |V_{yy}| \geq |V_{xx}| \quad (12.23)$$

Moreover, it is convenient to introduce the asymmetry parameter

$$\eta = \frac{V_{xx} - V_{yy}}{V_{zz}} \quad (12.24)$$

which denotes the deviation of the EFG from uniaxial symmetry. Based on equation (12.23), the value of η is limited to $0 \leq \eta \leq 1$. In fact, the electric field gradient is specified by two independent parameters, namely field gradient tensor $V_{zz} = (\partial V^2 / \partial Z^2)$ along the z -axis and an asymmetry parameter $\eta = (V_{xx} - V_{yy}) / V_{zz}$ with $0 \leq \eta \leq 1$ [8]. The Hamiltonian of the interaction between the nuclear electric quadrupole moment (Q) and the gradient of the electric field is given by:

$$H_Q = \vec{Q} \cdot \vec{\nabla} E \quad (12.25)$$

The eigenvalues of the above Hamiltonian are given as:

$$E_Q = \frac{eQV_{zz}}{4I(2I-1)} (3m_I^2 - I(I+1)) \left(1 + \frac{\eta^2}{3}\right)^{1/2} \quad (12.26)$$

$m_I = I, I-1, \dots, -I$ is the magnetic quantum number [9]. In the case of ^{57}Fe with spins $3/2$ and $1/2$, equation (12.26) can be reduced to:

$$E_Q = \pm \frac{eQV_{zz}^2}{4} \left(1 + \frac{\eta^2}{3}\right)^{1/2} \quad (12.27)$$

This gives a doublet corresponding to the transitions $\pm 3/2 \rightarrow \pm 1/2$ and $\pm 1/2 \rightarrow \pm 1/2$ [9]. For a nonzero field gradient, the excited energy level with $I = 3/2$ splits into two energy sublevels corresponding to $m_I = \pm 3/2$ and $m_I = \pm 1/2$ as shown in Figure 12.8. This means that the Mössbauer spectrum appears as two peaks separated by quadrupole splitting, $\nabla = eV_{zz}Q/2$ [10]. The quadrupole splitting (Δ) is a result of the interaction of the nuclear quadrupole moment with the gradient of the electric field $\vec{\nabla} E$ due to other charges in the crystal [8]. A nuclear quadrupole moment shows the deviation of the nucleus from spherical symmetry. A nonspherical charge distribution has been stated for nuclei in states with an angular momentum quantum number $I > 1/2$ [2]. This yields a nuclear quadrupole moment. An asymmetric charge distribution around the nucleus or a ligand arrangement will give rise to an asymmetrical electric field at the nucleus. The electric quadrupole interaction will lead to splitting into the nuclear energy levels and forms a two-line shape of a Mössbauer spectrum (Figure 12.8a). The quadrupole splitting also reflects the local structure in the vicinity and the symmetry of the bonding environment of a Mössbauer atom [4].



12.3.3 Magnetic Dipole Interaction (Magnetic Splitting)

In this case, several deeps can be observed on Mössbauer spectra. Such deeps arise due to the magnetic dipole moment of the nucleus' interaction with an internal magnetic field. Internal magnetic field comes from ferro, ferri, and antiferromagnetic properties (dipole properties of the nucleus). This magnetic field is a direct conclusion of local magnetic properties. It depends on the value and direction of local magnetic fields. Because of magnetic splitting, a nucleus with spin I splits into $2I + 1$ states. For example, for $I = 1/2$, we have $m_I = +1/2, -1/2$, and for $I = 3/2$, we have $m_I = +3/2, +1/2, -1/2, -3/2$.

The magnetic field at the nucleus generates the magnetic hyperfine interaction, which originates from the dipole interaction between the nuclear spin moment and a magnetic field. The magnetic field can originate either within the atom, within the crystal via exchange interactions, or as a result of applying an external magnetic field.

A nucleus with a nonzero spin has a magnetic moment, which interacts with internal hyperfine fields acting at the nucleus [11]. It simply means that the magnetic hyperfine structure arises from the interaction of the nuclear magnetic dipole moment ($\vec{\mu}$) with the magnetic field (\vec{H}) at the site of the nucleus. The Hamiltonian for the magnetic hyperfine dipole interaction is given as [2]:

$$H_M = -\vec{\mu} \cdot \vec{B}_{hf} = -g_n \mu_N \vec{I} \cdot \vec{B}_{hf} \quad (12.28)$$

Or

$$H_d = -\vec{\mu} \cdot \vec{H} = -g_n \mu_N \vec{I} \cdot \vec{H} \quad (12.29)$$

where g_n is the nuclear g -factor, μ is the nuclear magneton (or nuclear magnetic moment), μ_N is the nuclear Bohr magneton, and \vec{I} is the nuclear spin. \vec{B}_{hf} also indicates the total magnetic field. The corresponding eigenvalues or energy levels of the above magnetic Hamiltonian (E_M) can be given as:

$$E_M = -M_I g_n \mu_N B_{hf} \quad (12.30)$$

Or

$$E_M = -\frac{\mu H m_I}{I} = \mu_n g_n H m_I \quad (12.31)$$

where m_I is the magnetic quantum number representing the z component of I [3]. The magnetic field splits the nuclear level of spin I into $(2I + 1)$ equispaced nondegenerate substates, which, coupled with the selection rule ($\Delta m_I = 0, \pm 1$), produces six-line Mössbauer spectra for a $3/2 \rightarrow 1/2$ transition (Figure 12.9), where $m_I = I, I - 1, \dots, -I$ is the nuclear azimuthal spin quantum number. It can be seen that this interaction splits a nuclear state $|I\rangle$ into $2I + 1$ equally spaced state. For example, the ^{166}Er nucleus has excited and ground states of $|I = 2\rangle$ and $|I = 0\rangle$, respectively. In the presence of the magnetic dipole interaction, the excited state will split into five levels, while the ground state does not split. The allowed transitions obey the selection rules for the dipole transition with $\Delta I = 2, \Delta m = 0$, and ± 1 , giving five possible Mössbauer transitions.



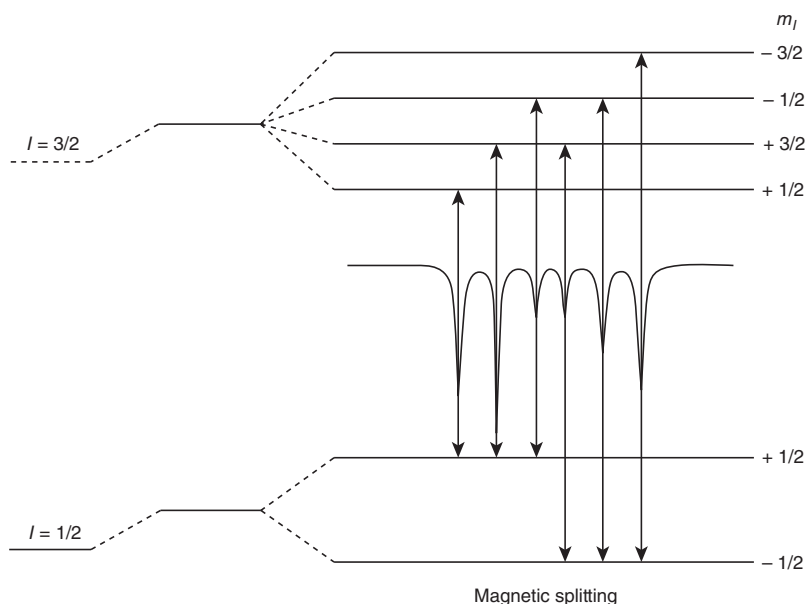


Figure 12.9 Schematic representation of hyperfine interactions: magnetic splitting. Source: Greenwood [2]/with permission of Springer Nature.

Moreover, in ^{166}Er Mössbauer spectra, the relative intensities are 1 : 1 : 1 : 1 : 1. In another example, the ^{155}Gd nucleus has excited and ground states of $|I = 5/2\rangle$ and $|I = 3/2\rangle$, respectively. Under the influence of the magnetic dipole interaction, the excited state splits into six levels, and the ground state splits into four levels. The allowed transitions are $\Delta m_I = 0, \pm 1$, and ± 2 , giving 12 possible Mössbauer transitions with the relative intensities of 10 : 6 : 3 : 1 : 4 : 6 : 6 : 4 : 1 : 3 : 6 : 10 (Figure 12.10).

The magnetic field splits the nuclear levels with spins I into $2I + 1$ equally spaced nondegenerate sublevels (Figure 12.10). The splitting between adjacent levels is

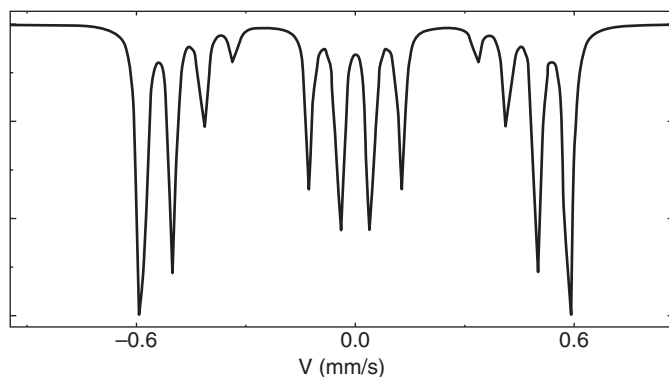


Figure 12.10 Simulated spectrum of ^{155}Gd with $B_{\text{hf}} = 20 \text{ T}$, $eQV_{zz} = 0$, $\eta = 0$ and line width of $\Gamma = 0.05 \text{ mm/s}$. Source: Chipaux [12]/with permission of Elsevier.



$g_n \mu_n H$ [2]. In Mössbauer spectroscopy, the preferential absorption of γ ray occurs between the sublevels of the excited nuclear state and the sublevels of the ground state [8] consistent with the selection rules $\Delta m = 0, \pm 1$. This leads to six absorption lines called Zeeman lines with a centroid that is close to the velocity $v \geq 0$ channel in the spectrum as shown in Figure 12.10.

The hyperfine field (H) is generated by the polarizing effects of unpaired electron spins (I). The spin direction flips after a while by one or more mechanisms associated with electronic spin relaxation [2]. In paramagnetic materials, the spin relaxation is rapid. This results in the magnetic field having a zero time average value. Hence, no magnetic field can be recorded. However, in the ferromagnetic, antiferromagnetic, and ferrimagnetic materials, the relaxation rates are effectively low, and the splitting of energy levels can be seen [13]. There are also intermediate possibilities where the electronic spins are relaxing on a time scale that is similar to that of nuclear transitions. This results in complicated spectra. Examples of such materials are superparamagnets, which can embrace both unusual fast and slow relaxations [2].

12.4 Mössbauer Spectroscopy Applied to Magnetism

The versatility of Mössbauer spectroscopy enables it to be not only employed in the field of materials science, i.e. physics, chemistry, and engineering, but also almost in all-natural sciences, medical sciences, and engineering fields. As mentioned, it is widely employed to evaluate the chemical, structural, and magnetic properties of various types of materials. Indeed, Mössbauer spectroscopy is typically employed to characterize magnetic nanoparticles (MNPs), including, but not limited to, phase identification and phase transition identification, magnetic ordering temperature determination, phase percentage, and ion distribution. For example, the characteristic of the hyperfine parameters detected in a Mössbauer spectrum yields phase identification. This is more similar to X-ray diffraction. Furthermore, the cation distribution in Mössbauer spectroscopy is comparable with that in X-ray diffraction. The determination of the temperature dependence of hyperfine parameters can identify the phase transitions. The temperature variation of the internal magnetic field measurement (H_{int}) yields the determination of the magnetic ordering temperature. Assuming that: $H_{\text{int}} \propto M$, where M is the magnetization of a sample, the ordering temperature can be determined by extrapolating to H_{int} at zero. It also offers the desired information about the relative site populations of cations in magnetic materials.

Types of magnetic ordering such as ferromagnetic, ferrimagnetic, and antiferromagnetic in polycrystalline materials can be determined via Mössbauer spectroscopy with the assistance of hyperfine transition intensity variations. The spin distribution of magnetic materials with low magnetic anisotropy will align parallel/antiparallel to the external field. The hyperfine transitions will be absent if the wave vector (k) is parallel to the applied field, owing to their $\sin 2\theta$ angular dependence. In the case of ferrimagnets, the magnetic fields within the sublattices align either parallel or



antiparallel to the external field. The hyperfine interactions will thus vary (enhance or decline) with the increase in an external field. These behaviors can be taken into account to determine the ferrimagnetic ordering. This is while the application of an external magnetic field will have little effect on the relative line intensities in polycrystalline antiferromagnets due to weak spin polarization. The random orientation of external and internal magnetic fields will result in broadening the absorption lines. The angular dependence of absorption line intensities would give a variety of information about the magnetic structure, depending on the polarized γ -ray sources are being used on single crystals of ordered magnetic materials [3].

However, the Mössbauer spectroscopy can be used to evaluate the magnetic behavior of several types of materials. In the following text, its application in the evaluation of, especially, superparamagnetic nanoparticles, is taken into an account by giving some relevant examples prepared with different methods mentioned in the Chapter 3.

12.4.1 Superparamagnetic Characterization

Not all compounds that contain unpaired valence electrons will display magnetic hyperfine splitting. More complicated spectra are being produced once the electronic spins relax on a time scale comparable with the nuclear transition. The spin relaxation in paramagnetic materials is rapid, which yields H or B with a time average of zero, and thus, no magnetic splitting is perceived [13]. The electronic spin–lattice interactions and electronic spin–spin interactions of neighboring ions are two main processes that lead to a spin–flipping in paramagnetic ions. Spin–lattice relaxation includes a transfer of Zeeman energy of the spin system to phonon modes of the lattice via spin–orbit coupling. On the other hand, the spin–spin process comprises energy transfer between interacting spins via dipole and exchange spin relaxation. The magnetic hyperfine spectra observed for magnetically ordered materials are interpreted using spin waves. The spin-wave time average is time-dependent, and an inward collapse of the hyperfine spectrum will occur if the spin relaxation frequency is of the order of the Larmor frequency. If the fluctuation rate of the spin waves is slow in comparison with the precession frequency of the nucleus in the field H , the full six-line pattern will emerge. On the other hand, in the case of rapid fluctuation rate, the nucleus will experience only a time-averaged zero field and an asymmetric quadrupole pattern will be observed. In short, superparamagnetic assemblages and paramagnetic materials will display two-line quadrupole Mössbauer patterns due to rapid spin relaxation, while materials with stable magnetizations will display the six-line magnetic hyperfine splitting.

As discussed in Chapter 10, superparamagnetism is a phenomenon in which the magnetic moment direction of a nanoparticle (NP) changes spontaneously due to thermal fluctuations [14–17]. If the frequency rate (R) of magnetic moment is greater than the Larmor frequency of ^{57}Fe nuclei, superparamagnetism causes the Zeeman structure of the Mössbauer spectrum to collapse into doublet or singlet lines below Curie temperature (T_C) [14]. Due to superparamagnetism, the magnetic moment of NPs experiences thermally stimulated excitations around the energy minimum [18].



As a result, sextet lines become asymmetrically broadened, and magnetic hyperfine field values decrease. Thermally stimulated excitations make the Mössbauer spectrum parameters less trustworthy and complicate the paradigm for interpreting spectra. Lowering the temperature can mitigate the deleterious effects of superparamagnetic relaxation on the Mössbauer spectrum structure. Indeed, low-temperature measurements are required to accurately analyze more completed Mössbauer spectra of irradiated ferrite nanoparticles (NPs) [19]. In light of this, low temperature (LT) ^{57}Fe Mössbauer spectroscopy is a useful tool for detecting and describing the superparamagnetic activity [19]. When it comes to Fe ions, which are often ferric and/or ferrous, the distribution of ionic charges in the lattice dominates the quadrupolar interactions, which reflect local symmetry. The isomer shift, on the other hand, reflects the electron density at the nuclei. This interaction comprises information about the Mössbauer ion's charge state, i.e. ^{57}Fe , as well as its local coordination [20].

In addition, low-temperature ^{57}Fe Mössbauer measurements in a large external magnetic field allow for precise cation distribution characterization in ferrites [21–28]. This is because in a nonzero external magnetic field, the subspectra corresponding to Fe cations at tetrahedral (A) and octahedral (B) sites, which are overlapped in a zero field, become separated. Also, because of the absence of magnetic relaxation effects, such as superparamagnetism, associated with the nanoscale structure of the magnetic materials, Mössbauer spectra obtained at low temperatures are therefore easier to interpret [21, 23, 24, 29]. The ^{57}Fe Mössbauer spectra of MgFe_2O_4 NPs at low temperatures (6.4 K) and in the field (5.5 T) are demonstrated in Figure 12.11, which are mechanically activated for various times (t_m)

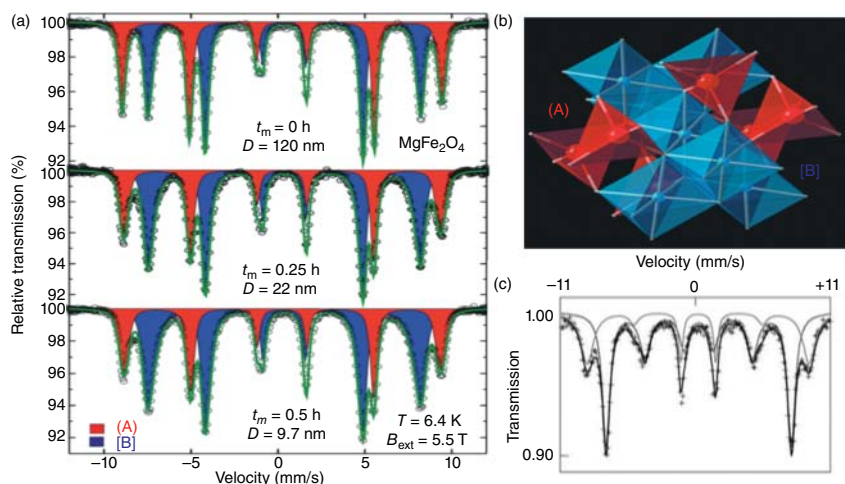


Figure 12.11 (a) ^{57}Fe Mössbauer spectra of MgFe_2O_4 NPs recorded at 6.4 K. The process is accomplished at different milling times (t_m), which results in obtaining different crystallite sizes (D). The spectra were collected in the presence of a 5.5 T external magnetic field applied perpendicular to the γ -ray direction. The spectra's velocity scale was calibrated against ^{57}Fe in Rh (b) Spinel structure structural units: tetrahedra (A) and octahedra [B]. Source: Šepelák et al. [21]/with permission of Royal Society of Chemistry, and (c) 4 K and 6 T in-field ^{57}Fe Mössbauer spectra of the ball-milled ZnFe_2O_4 NPs. Source: Harris and Šepelák [19]/with permission of Elsevier.



through the high-energy ball milling (HEBM) method [21]. The spectra of MgFe_2O_4 are constituted of two well-resolved sextets indicative of tetrahedrally coordinated ferric ions, $\text{Fe}^{3+}(\text{A})$ (isomer shift $\text{IS}(\text{A}) = 0.24(1) \text{ mm/s}$) and octahedrally coordinated ferric ions, $\text{Fe}^{3+}(\text{B})$ ($\text{IS}(\text{B}) = 0.35(1) \text{ mm/s}$) and are independent of crystallite size [30]. As exhibited in Figure 12.11b, based on the cation site occupancy, the chemical formula of crystalline spinel ferrites may be expressed as $(\text{M}_{1-\lambda}\text{Fe}_\lambda)[\text{M}_\lambda\text{Fe}_{2-\lambda}]\text{O}_4$, where parenthesis and square brackets signify tetrahedral (A) and octahedral (B) sites, respectively. The symbol λ is the so-called inversion degree, which is defined as the proportion of ferric ions that occupy the (A) sites. One may easily extract quantitative information on the cation distribution in the material from the intensity ratio of the (A) and [B] Mössbauer spectrum components ($I(\text{A})/I(\text{B}) = \lambda/(2-\lambda)$). The inversion degree (λ) of bulk MgFe_2O_4 with a mean crystallite size of 120 nm is obtained at about 0.90(4). This implies that the MgFe_2O_4 sample without ball milling (mechanically activated) is partly inverse spinel, $(\text{Mg}_{0.10}\text{Fe}_{0.90})[\text{Mg}_{0.90}\text{Fe}_{1.10}]\text{O}_4$. The milling process, on the other hand, causes the intensities of the (A) and [B] spectral components in MgFe_2O_4 NPs to redistribute. This indicates that more concentrations of Fe^{3+} occupy the A sites, and fewer concentrations of Fe^{3+} fill the B sites. The most striking feature is that the inversion degree of MgFe_2O_4 grows monotonically as the crystallite size decreases, reaching a maximum of 0.75(6) for $D = 9.7 \text{ nm}$. The most striking feature is that the inversion degree of MgFe_2O_4 grows monotonically as the crystallite size decreases, reaching a maximum of 0.75(6) for $D = 9.7 \text{ nm}$. As a result, high-energy ball milling of MgFe_2O_4 causes a nonequilibrium redistribution of Fe^{3+} and Mg^{2+} cations between the two nonequivalent spinel lattice positions, which can be represented as $(\text{Mg}_{0.10}\text{Fe}_{0.90})[\text{Mg}_{0.90}\text{Fe}_{1.10}]\text{O}_4 \rightarrow (\text{Mg}_{0.25}\text{Fe}_{0.75})[\text{Mg}_{0.75}\text{Fe}_{1.25}]\text{O}_4$. Likewise, the cation distribution is different in other ferrites synthesized by either wet-chemical or solid-state routes such as HEBM [31–33]. In addition, as shown in Figure 12.11a, due to a change in the local atomic environments of $\text{Fe}^{3+}(\text{A})$ and $\text{Fe}^{3+}(\text{B})$ ions, the milling process induces a substantial broadening of the (A) and [B] Mössbauer lines in MgFe_2O_4 NPs. The existence of distorted FeO_4 tetrahedra and FeO_6 octahedra in the nanostructured spinel could explain this variation. This finding is in line with recent spectroscopic studies of complex oxides, which indicated that mechanically induced cation redistribution was accompanied by deformation of the corresponding polyhedral structure units [26, 34, 35]. ^{57}Fe Mössbauer spectroscopy provides a unique opportunity to analyze the spin arrangement in a magnetic sample, in addition to providing information regarding local coordination, magnetic, and charge states of iron ions. The average spin canting angle (Ψ) can be computed from the ratio of the intensities of lines 2 and 1, I_2/I_1 , of the magnetically split six-line spectra with $\Psi = 90^\circ - \arcsin\{[3(I_2/I_1)/2]/[1 + 3(I_2/I_1)/4]\}^{1/2}$ when an external magnetic field (Bext) is applied perpendicularly to the γ -ray direction [22]. The intensity ratio $I_{2,1}$ for bulk MgFe_2O_4 is around 4/3. The spins are aligned with the external magnetic field of 5.5, indicating that the bulk ferrite has a Néel-type collinear spin arrangement of $(\text{Mg}_{0.1}\text{Fe}_{0.9}\uparrow)[\text{Mg}_{0.9}\text{Fe}_{1.1}\downarrow]\text{O}_4$. With a reduction in crystallite size due to increased milling time, the degree of noncollinearity of the spins increases. Furthermore, the average spin canting angles (Ψ) are obtained at $\sim 17^\circ$ and $\sim 22^\circ$ for the ball-milled MgFe_2O_4 NPs for 15 and 30 minutes, respectively.



Thus, the nanosized MgFe_2O_4 particles present magnetic disorder due to spin canting in addition to the nonequilibrium cation distribution. Taking into account the presence of disordered interfaces/near-surface layers in nanocrystalline milled and of structurally ordered grains/particles in the nonball-milled oxides [21, 23, 35, 36], it can be stated that all of the phenomena, i.e. the canted spin arrangement, the deformed polyhedra, and the non-equilibrium cation distribution, are found in nanostructured MgFe_2O_4 's interface/surface areas.

In another study [19], the 4 K and 6 T in-field ^{57}Fe Mössbauer spectra of high-energy ball-milled ZnFe_2O_4 NPs are demonstrated in Figure 12.11c. The results revealed that the occupation of Fe^{3+} cations on (A) sites is around 0.69, implying that the nanoferrite's crystal-chemical formula is $(\text{Zn}_{0.31}\text{Fe}_{0.69})[\text{Zn}_{0.69}\text{Fe}_{1.31}]\text{O}_4$ [37]. The difference between the cation distribution from Mössbauer measurements and the corresponding XPS experiments is due to the fact that XPS measurements only reflect the structure of the near-surface layers, whereas Mössbauer measurements characterize the structural disorder in the entire volume (interior) of the zinc ferrite (ZnFe_2O_4) NPs.

Figure 12.12 displays the 14 K recorded Mössbauer spectra of irradiated cobalt-nickel ferrite ($\text{Co-Ni Fe}_2\text{O}_4$) NPs accompanied by their $P(H)$ functions [38]. Three local maxima are evident in the $P(H)$ functions. Irradiated cobalt-nickel ferrite NPs have spectrum structures that are comparable to those of nonirradiated cobalt-nickel ferrite NPs [39, 40]. One of the sextets is associated with the Fe^{3+} ions in the oxygen tetrahedron, and two other sextets are attributed to the Fe^{3+} ions in

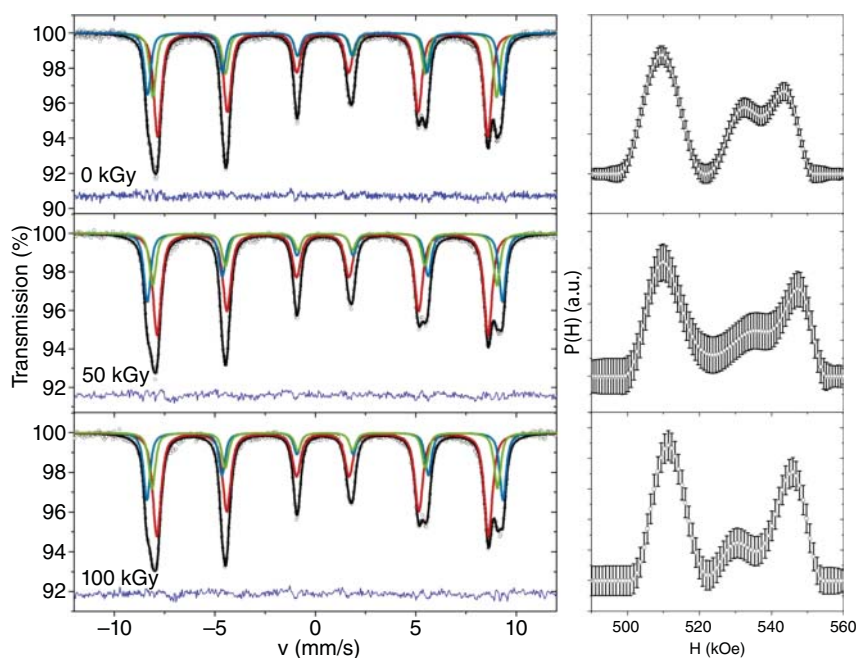


Figure 12.12 14 K Mössbauer spectra of $\text{Co}_{0.5}\text{Ni}_{0.5}\text{Fe}_2\text{O}_4$ NPs at different γ irradiation dose rates. Source: Srinivasamurthy et al. [38]/with permission of Elsevier.



the oxygen octahedron. The presence of two sextets in nonirradiated samples is due to the B site, which causes asymmetric coordination between Fe^{3+} ions and the oxygen environment. The hyperfine magnetic field values of the sextet S_{B1} are higher than those of the sextet S_{B2} . This implies that the sextet S_{B2} associates with Fe^{3+} having Ni^{2+} or Co^{2+} in their local environment. The concentration of Fe^{3+} ions in A and B sites is proportional to the sextet area (A) values. The A values of the sextet S_A increase when the irradiation dose is increased. Simultaneously, the areas of sextet S_A are lower than those seen in nonirradiated cobalt-nickel ferrites. Other hyperfine metrics such as quadrupole and isomer shifts as well as hyperfine magnetic fields are similar to nonirradiated materials. It has been found that increasing the dose from 50 to 100 kGy does not result in any significant changes in the Mössbauer spectrum characteristics in cobalt-nickel ferrite samples. As a result of the irradiation of cobalt-nickel ferrite NPs, the concentration of Fe^{3+} ions in the A site increases. This is more probably associated with the creation of some internal defects such as dislocation, grain boundaries, surface defects, and point defects in the ferrite NP structure due to γ -ray irradiation, where the cation redistribution in ferrite NPs is the outcome of this phenomenon.

In another study, 5 K Mössbauer spectroscopy in the absence and presence of 5 T (in-field) was considered to investigate the magnetic core-shell structure of the copper ferrite NPs synthesized with hydrothermal, and solvothermal methods, and to evaluate the cation distributions at the tetrahedral (A site) and octahedral (B site) sites [41]. Low temperature (LT) Mössbauer analyses, based on their corresponding spectra fitted with four sextets and a weak doublet, provide a more accurate description of the cation distribution, as shown in Figure 12.13a,b. Table 12.1 lists the various hyperfine interaction parameters as well as the relative area under the curves. More accurate data are obtained in the case of the recoil-free fraction ratio at the A and B sites (f_{MA}/f_{MB}) being ~ 1 at low temperature [42]. The results obtained suggest that the magnetically disordered shell region was considerably thinner for the MNPs synthesized with the solvothermal method. Such a thinner shell (dead layer) cannot cause a reduction in the saturation magnetization (M_s) [43].

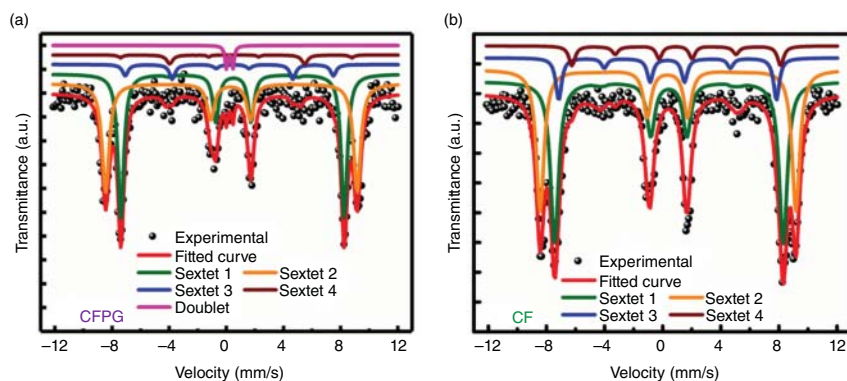


Figure 12.13 The (a) hydrothermal and (b) solvothermal methods MNPs in-field Mössbauer spectra at 5 K. Source: Kurian and Mathew [41]/with permission of Elsevier.



Table 12.1 LT in-field Mössbauer spectra were used to determine the cation distributions and spin canting angles of the core and shell areas of the CFPG and CF MNPs.

Samples	Sites	θ_{sc} (°)	Cation distribution (at ~5 K and ~5 T)
CFPG	A–core	1.1	$(\text{Cu}_{0.05}\text{Fe}_{0.95})_A[\text{Cu}_{0.95}\text{Fe}_{1.05}]_B\text{O}_4$
	B–core	8.1	
	A–shell	52.0	$(\text{Cu}_{0.24}\text{Fe}_{0.76})_A[\text{Cu}_{0.76}\text{Fe}_{1.24}]_B\text{O}_4$
	B–shell	56.1	
CF	A–core	7.7	$(\text{Cu}_{0.06}\text{Fe}_{0.94})_A[\text{Cu}_{0.94}\text{Fe}_{1.06}]_B\text{O}_4$
	B–core	15.6	
	A–shell	20.1	$(\text{Cu}_{0.39}\text{Fe}_{0.61})_A[\text{Cu}_{0.61}\text{Fe}_{1.39}]_B\text{O}_4$
	B–shell	33.3	

Source: Kurian et al. [41]/with permission of Elsevier.

The subspectra of A and B sites overlapped in the LT Mössbauer spectra of nanoferrites in the absence of an external magnetic field, while they become distinguishable in the presence of an applied external magnetic field. This means that the magnetic splitting of the A and B sites changes in opposite directions in the presence of an external field. In such a way that the applied field is removed from the hyperfine interaction field at the For LT in-field Mössbauer spectra, this results in nicely resolved sextets belonging to the A and B sites, allowing for an accurate quantitative estimate of cation distributions and spin canting angles [44].

Figure 12.14 indicates that the Mössbauer spectra of the Fe_3O_4 (magnetite) samples at 6 K split into several 6-line hyperfine patterns [45]. The spectra are remarkably similar to one another and to bulk crystal spectra (top spectrum). This demonstrates that their composition is nearly stoichiometric magnetite. They show

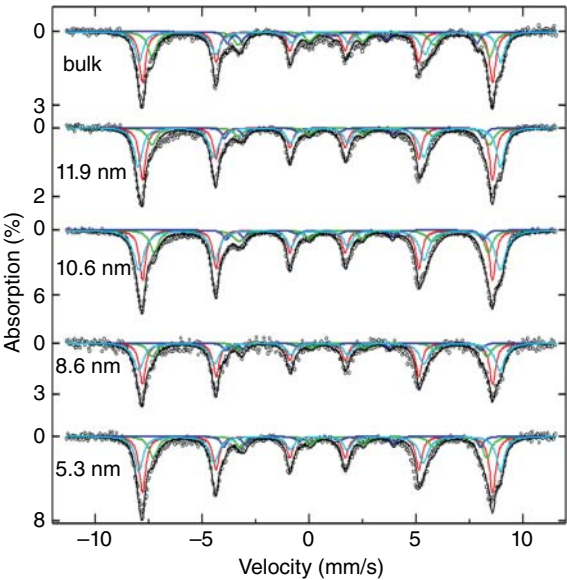


Figure 12.14 6 K Mössbauer spectra of bulk and NPs of Fe_3O_4 samples. Source: Hah et al. [45]/with permission of Elsevier.



lines indicative of Fe^{2+} at about -3.0 , -0.5 , and 3.0 mm/s in particular. In other words, the magnetite NPs can be oxidized to other phases of the iron oxide phase, i.e. $\gamma\text{-Fe}_2\text{O}_3$ (maghemite), which is not observed in this case. The spectra are matched to a model proposed by Berry et al. [46], in which one Fe^{3+} occupies the A (tetrahedral) site, while two Fe^{3+} and two Fe^{2+} occupy the B (octahedral) sites. Furthermore, the model is simplified by assuming only one Fe^{3+} on the B sites due to their hyperfine fields being detected close to equal. This assumption is considered to have a better comparison between NPs and micro-sized magnetite particles. For both Fe^{3+} sites, the quadrupole interaction is assumed to be zero. Because the monoclinic distortion creates distinct quadrupole shifts and dipolar fields along the monoclinic axis than in the perpendicular plane, the two Fe^{2+} s differ. The difference between the f -factors for the different iron sites was neglected due to its small value [47]. The hyperfine parameters were assumed to be the same for all the nanoparticles and are given in Table 12.2a, which are in agreement with the values reported by Berry et al. [46]. As expected, the EFG of the B(Fe^{2+}i) site is of opposite sign and roughly half the magnitude of the B(Fe^{2+}ii). The B(Fe^{2+}ii) sites have a positive EFG, resulting in a positive dipolar hyperfine field. Such behavior declines the core polarization field, resulting in a smaller hyperfine field. On the other hand, the negative EFG at the Bi sites leads to a negative dipolar field, which results in the attainment of a larger hyperfine field. The occupation (expressed as a percent) in each site for NPs and bulk (micro-sized particles) are provided in Table 12.2b. The fits demonstrate that the fraction of the Fe^{2+} atoms on the Bi and Bii sites in the NPs is declined in comparison with the micro-sized particles. This is while the Fe^{3+} fraction increases. The spectra in Figure 12.14 clearly show that vacancies have replaced some of the Fe^{2+} ions in the NPs, which is consistent with the appearance of vacancies replacing some of the Fe^{2+} ions in the NPs.

Table 12.2 (a) LT hyperfine parameters and (b) site populations (%) of iron atoms.

(a)						
Site	B_{hf} (kG)		δ (mm/s)		$\frac{1}{2} e^2 Qq$ (mm/s)	
A(Fe ³⁺)	507		0.41		0	
B(Fe ³⁺)	524		0.50		0	
B(Fe ²⁺ i)	489		0.91		−0.71	
B(Fe ²⁺ ii)	362		1.26		1.62	
(b)						
Particle size (nm)	A (Fe ³⁺)	B (Fe ³⁺)	B (Fe ²⁺ i)	B (Fe ²⁺ ii)	$R_2 = I^{3+}/I^{2+}$	x
Bulk	36	32	23	9	2.09	0.01
11.9 nm	36	40	16	8	3.25	0.11
10.6 nm	34	41	19	6	2.80	0.08
5.3 nm	38	35	19	8	3.02	0.09

Source: Hah et al. [45]/with permission of Elsevier.



12.4.2 Mössbauer Spectroscopy Applied to Characterize the Effect of Synthesis Method on the MNPs Behavior

It is believed that the synthesis method can significantly influence the characteristics of as-synthesized MNPs, such as saturation magnetization, coercivity, and remanence [48–58]. This mainly arises from the influence of the synthesis methods on the intrinsic properties of the particles, i.e. shape, size, and distribution [48, 59–64]. In this regard, Mössbauer spectroscopy can yield useful information about the MNPs. Here, the synthesis of iron oxide NPs with hydrothermal – H sample and coprecipitation – P sample is considered as an example. Figure 12.15 shows TEM images of the P and H samples along with their particle size distribution

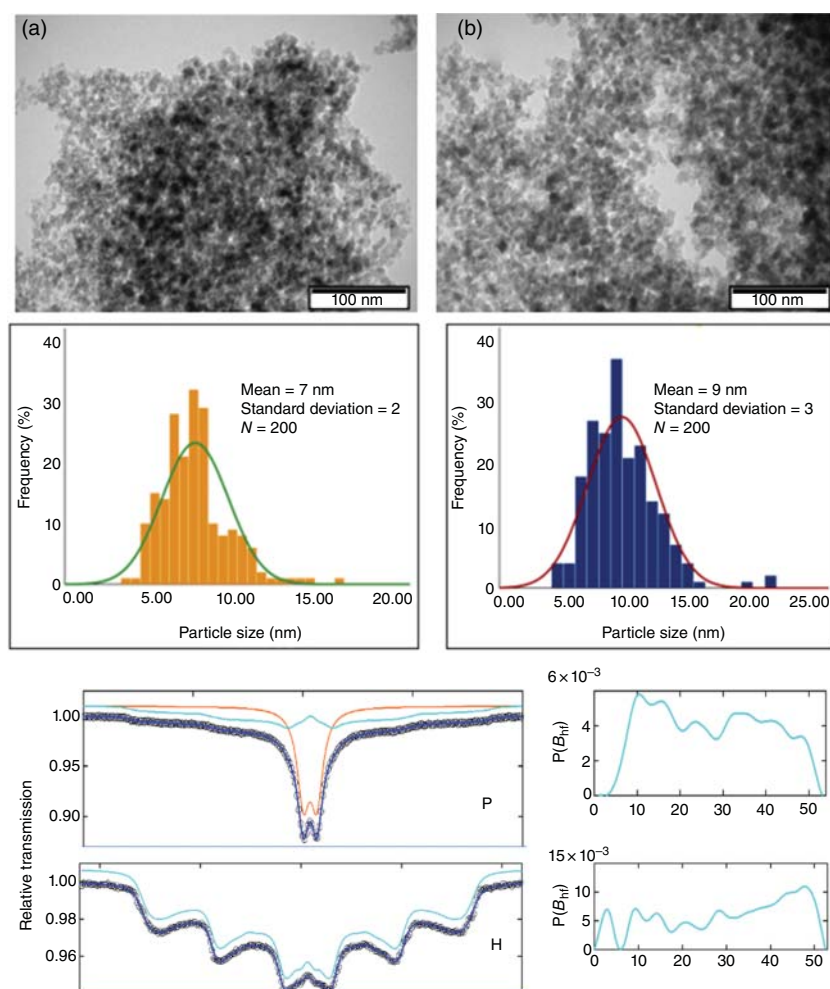


Figure 12.15 For (a) P and (b) H samples, TEM images and particle size distribution histograms are shown, which are accompanied by their corresponding Mössbauer spectra, accordingly. Source: Hajalilou et al. [43], Elsevier.



histograms. In both samples, the transmission electron microscopy (TEM) pictures reveal irregularly shaped particles that have agglomerated to some extent. The particle size distribution ranged from 2 to 18 nm, with an average particle size of 7 nm (Figure 12.15a). However, the particle size ranged from 2 to 24 nm for the H sample, with an average size of 9 nm (Figure 12.15b).

The spectra were fitted using at least one magnetic field distribution, with the results for the hyperfine parameters reported in Table 12.3. Two hyperfine sextets can be seen in a typical room temperature (RT) Mössbauer spectra for magnetite (Fe_3O_4) NPs with diameters greater than 20 nm. The first one with isomer shift values (δ) of Fe^{3+} in tetrahedral locations (position A of the spinel structure (AB_2O_4)) are about 0.28–0.30 mm/s. The second is the existence of Fe^{3+} and Fe^{2+} in octahedral coordination, which leads to a reduced magnetic field and a δ of roughly 0.65 mm/s (B) [43].

Between the two groups of samples, a distinct difference is instantly discernible. Part of the iron nuclei in P as-prepared samples are well fitted to a broad quadrupole doublet (approximately 50%), indicating the presence of NPs in the superparamagnetic state. Superparamagnetic behavior is linked to NPs with relaxation durations shorter than the time scale of the Mössbauer measurement, which is in the order of 10^{-7} s, the lifetime of the intermediate state of ^{57}Fe , which emits the 14.4 keV γ -ray irradiation in Mössbauer spectroscopy. This matches the magnetic relaxation time of iron oxide nanoparticles (IONPs) with an average diameter of 8 nm, which has been reported to be in the region of $\sim 10^{-8}$ [65]. If a superparamagnetic percentage exists in the H samples group, it is residual and does not improve spectra fitting when taken into account. This difference in Mössbauer spectra corresponds to TEM findings that P-NPs are smaller than H-NPs.

The samples' magnetic components are well matched to a single broad distribution of hyperfine magnetic fields, with isomer shift values (δ) ranging from 0.33 to 0.38 mm/s.

The broad distribution is linked to the size dispersion of NPs and δ values greater than 0.30 mm/s. The normal value for maghemite, with all iron as Fe^{3+} indicates that a minor percentage of Fe^{2+} persists in the bigger NPs (these ions have a typical value of δ roughly 0.66 mm/s in octahedral locations of the spinel structure). The quadrupole doublet component dominates in the P sample, indicating a weak magnetic field, which can be attributed to the particles' tiny size in the first scenario.

Table 12.3 Mössbauer hyperfine fitting parameters for P and H samples.

Sample	Site	$\langle B_{\text{hf}} \rangle [\sigma]$ (T)	δ (mm/s)	ϵ (mm/s)	QS (mm/s)	Γ (mm/s)	I (%)
P	1 (blue)	27[13]	0.35(1)	0.01(2)	—	0.40	51.0
	2 (orange)	—	0.32(1)	—	0.61(5)	0.68(1)	49.0
H	1	30[15]	—	0.33(1)	−0.01(1)	0.60	100

I is the relative area, Γ is the line width, QS is the quadrupole splitting, ϵ is the quadrupole shift, δ is the isomer shift, and $\langle B_{\text{hf}} \rangle [\sigma]$ is the average hyperfine field and standard deviation of the distribution of magnetic splitting.

Source: Hajalilou et al. [43]/with permission of Elsevier.



Figure 12.16 shows the collected room temperature (RT) Mössbauer spectra of the tested NPs after three weeks of wetting in another investigation [66]. Even for particles of an identical size, the form of the RT Mössbauer spectra of the reference samples obtained by three different synthesis processes is noticeably different. This is linked to the crystal growth state as well as the surface change caused by the altered synthesis circumstances [67]. The Fe_3O_4 sample's spectrum consists of a superposition of two relatively sharp sextets and a tiny doublet in the middle. Only broad sextets are seen in the $\text{SiO}_2@\text{Fe}_3\text{O}_4$ sample. The spectrum of the $\text{Fe}_3\text{O}_4@\text{Fe}_3\text{O}_4$ sample is a superposition of a broad sextet and a highly intense doublet. This finding could be attributed to a variety of factors. To begin with, each synthesis results in a somewhat distinct particle morphology, which is determined by the average diameter, shape, and size distribution of the particles formed. The TEM micrographs revealed particle sizes ranging from 13 ± 2 nm for Fe_3O_4 to 12 ± 2 nm for both $\text{SiO}_2@\text{Fe}_3\text{O}_4$ and $\text{Fe}_3\text{O}_4@\text{Fe}_3\text{O}_4$. The second explanation has to do with the crystallinity of the NPs produced using various procedures.

Due to layer-by-layer development, one can expect well-defined growth and therefore monocrystal during $\text{Fe}_3\text{O}_4@\text{Fe}_3\text{O}_4$ synthesis from iron (III) acetylacetonate during chloride synthesis. The interaction between iron atoms and the SiO_2 shell or the SiO_2 shell's oxidative protection of the Fe_3O_4 core should be considered while making NPs with a silica shell. Such behaviors have an impact on MNPs' intrinsic features such as shape, size, and distribution as well as their magnetic properties, particularly the ferrimagnetic–superparamagnetic transition and surface activity of the investigated NPs [68]. The quantitative analysis of the reference spectra measured for Fe_3O_4 NPs suggests that the NPs are below superparamagnetic blocking temperature; therefore, sharp sextets and a small doublet are seen here (its relative intensity is much less than 50% of the spectra). The NPs are below superparamagnetic blocking temperature, according to a quantitative study of the reference spectra observed for Fe_3O_4 NPs, thus resulting in sharp sextets and a tiny doublet (its relative intensity is much less than 50% of the spectra). Each sextet line in the $\text{SiO}_2@\text{Fe}_3\text{O}_4$ sample is widened by the presence of smaller particles and a convoluted shape generated by the SiO_2 shell's influence on the Fe_3O_4 core. The typical surface doublet in the spectrum's center part is not apparent here. As a result of these spectra, the particles are considerably below the superparamagnetic fluctuation regime. The observed spectrum is a superposition of a very broad sextet and doublet with relative intensity above 50% of the entire area in the last case of the measured reference $\text{Fe}_3\text{O}_4@\text{Fe}_3\text{O}_4$ NPs. This indicates that the particles are in the superparamagnetic condition at room temperature, and the blocking temperature is near room temperature. As demonstrated in Figure 12.16, the shape of the Mössbauer spectra for all the NPs treated with various environmental solutions has only a little impact on their magnetic characteristics. There are no obvious differences in the spectra for all the used solutions in the case of $\text{SiO}_2@\text{Fe}_3\text{O}_4$. This indicates that the SiO_2 shell protects the magnetite core from the effects of a solution. In the case of Fe_3O_4 and $\text{Fe}_3\text{O}_4@\text{Fe}_3\text{O}_4$ NPs, however, a modest variation in the NPs can be seen in the relative intensities of the doublet and sextet. In comparison to the reference samples, the intensity of the doublet increases in both series of the examined samples. For all the solutions, the



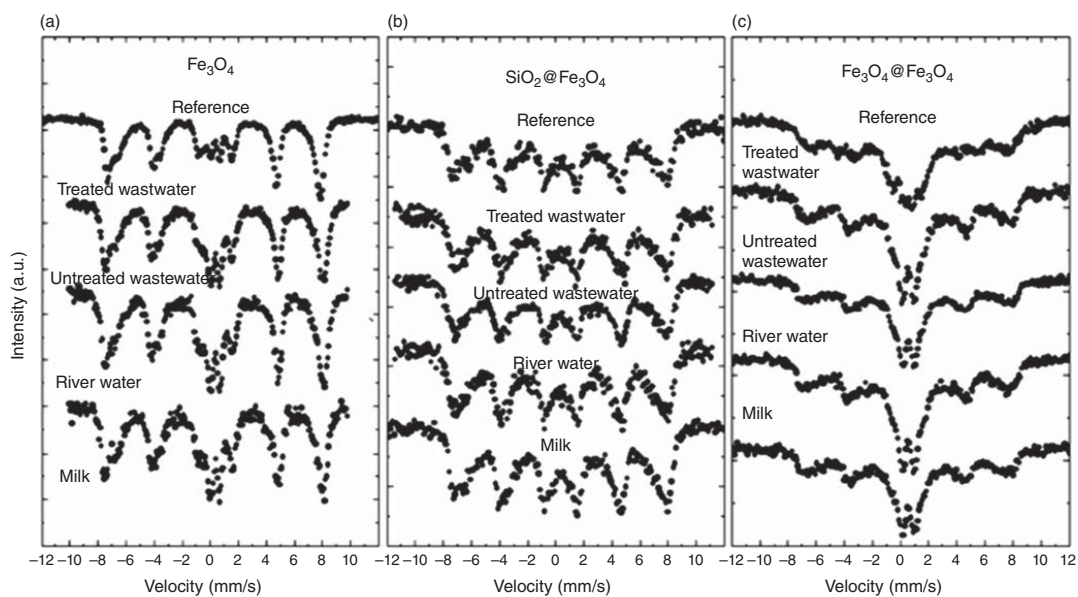


Figure 12.16 RT Mössbauer spectra of the (a) Fe_3O_4 ; (b) $\text{SiO}_2@\text{Fe}_3\text{O}_4$ NPs; (c) $\text{Fe}_3\text{O}_4@\text{Fe}_3\text{O}_4$ NPs wetted at different environmental solutions. Source: Klekotka et al. [66]/MDPI/Public Domain CC BY.



increase in the intensity of the doublet is nearly the same. Such behavior points to morphological and compositional changes in the investigated NPs, at least at the surface, as a result of organic substance absorption. This results in increased NP separation and a weakening of the dipole–dipole interaction as well as possible gradual oxidation of the Fe_3O_4 core.

Data from a variety of spinel ferrites [26, 28, 51, 54, 60–62, 69–79] clearly show that HEBM significantly alters the cation distribution in MNPs between the A and B sites. Because the identical nanomaterials from various laboratories exhibit variable degrees of cation redistribution, the impact of the HEBM process intensity on the level of structural disordering cannot be overlooked [24, 27, 28, 69, 70]. In this context, the Ca_2SnO_4 formation reaction from $2\text{CaO} + \text{SnO}_4$ mixture after four hours ball milling, in comparison with its corresponding non-ball milling state, introduces a good example of a system for the investigation of the local structural changes induced during the mechanosynthesis or HEBM process. This is attributed to the fact that the tin nucleus ^{119}Sn can be used as a local probe in both Mössbauer and nuclear magnetic resonance (NMR) measurement [23]. As illustrated in Figure 12.17a, the broad form of the NMR lines found for the as-synthesized Ca_2SnO_4 NPs contrasts with the relatively narrow lines for their

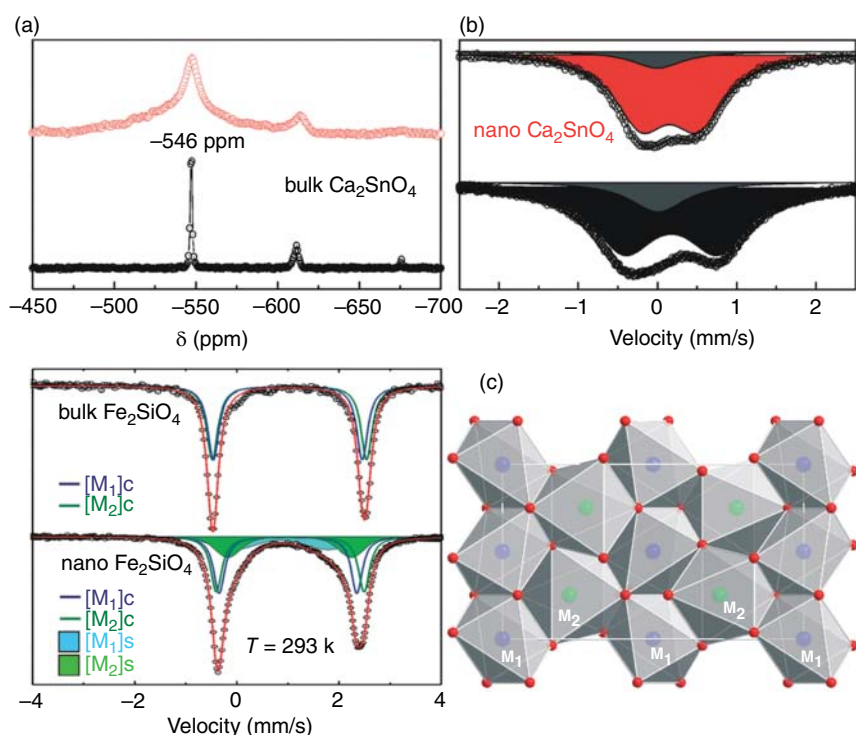


Figure 12.17 (a) ^{119}Sn MAS NMR spectra and (b) ^{119}Sn Mössbauer spectra of (top) the Ca_2SnO_4 NPs and (bottom) the Ca_2SnO_4 sample with micro-sized particles synthesized via the conventional thermal route. (c) (left) RT ^{57}Fe Mössbauer spectra of bulk $\alpha\text{-Fe}_2\text{SiO}_4$ and HEBM-synthesized $\alpha\text{-Fe}_2\text{SiO}_4$ NPs with the olivine structure. (right) Schematic presentation of the olivine structure. Source: Adapted from Šepelák et al. [23].



micro-sized analog. Because of the mechanically induced deformation of the SnO_6 octahedra, this suggests the existence of widely distributed local environments around the Sn nuclei. On the other hand, as shown in Figure 12.17b, the average quadrupole splitting for Ca_2SnO_4 NPs is much smaller than that anticipated for conventionally manufactured Ca_2SnO_4 NPs (micro-sized particles). This indicates that the Sn nuclei in the nanocrystalline material are subjected to smaller electric field gradients. As a result, the presence of distorted but more symmetric SnO_6 octahedra in the Ca_2SnO_4 NPs synthesized by the HEBM approach is demonstrated. Other mechanically alloyed complex oxides with the orthorhombic structure, such as fayalite ($\alpha\text{-Fe}_2\text{SiO}_4$), have also been shown to exhibit this dramatic local structural characteristic [80]. In this situation, ^{57}Fe Mössbauer spectroscopy can even be used to quantify the distribution of Fe^{2+} cations within the shell (with deformed but more symmetric octahedra) and core (with regular and asymmetric octahedra) of HEBM-synthesized NPs. The crystal-chemical formula highlighting the site occupancy at the atomic level in nanosized fayalite particles can be represented as $[\text{Fe}_{0.6}][\text{M}_1]\text{c}[\text{Fe}_{0.6}][\text{M}_2]\text{c} - [\text{Fe}_{0.4}][\text{M}_1]\text{s}[\text{Fe}_{0.4}][\text{M}_2]\text{sSiO}_4$, where $[\text{M}_1]\text{c}$, $[\text{M}_2]\text{c}$ and $[\text{M}_1]\text{s}$, $[\text{M}_2]\text{s}$ designate cation sites of octahedral coordination in the inner core and the surface shell of $\alpha\text{-Fe}_2\text{SiO}_4$ NPs, respectively, based on the data obtained from the ^{57}Fe Mössbauer observations, as shown in Figure 12.17c. It is worth noting that bulk fayalite crystallizes with the $[\text{Fe}][\text{M}_1][\text{Fe}][\text{M}_2]\text{SiO}_4$ olivine structure.

In another study [28], the high-field Mössbauer spectra of both bulk (micron size) and milled (nano size) nickel-ferrite (NiFe_2O_4) particles taken at 6.4 K are compared in Figure 12.18. Table 12.4 shows the results of the least squares fitting. The inversion degree of bulk nickel-ferrite determined from its high-field spectrum is around

Figure 12.18 6.4 K Mössbauer spectrum of the (a) bulk Ni ferrite sample and (b) nanosized Ni-ferrite NPs captured in a 5.5 T applied perpendicular to the gray direction. Source: Šepelák et al. [28]/with permission of Elsevier.

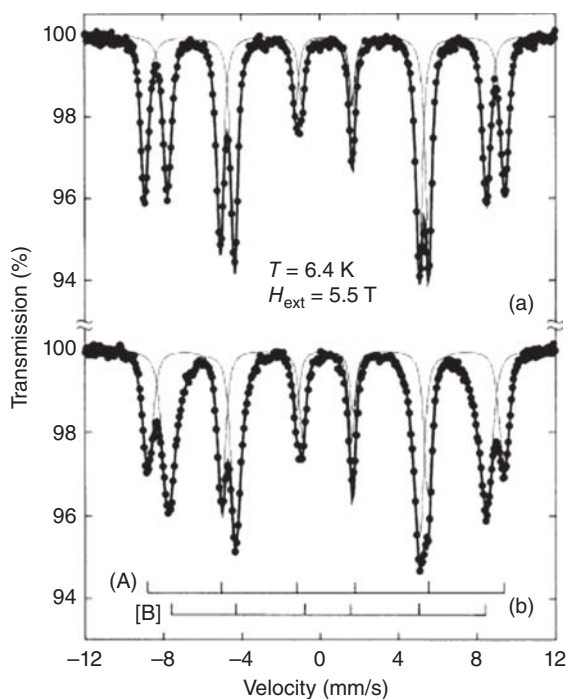


Table 12.4 Mössbauer spectra of the micro-sized (bulk) and nanosized Ni-ferrite particles with a cation distribution in the octa- and tetrahedral locations.

Sample	T (K)	$IS_{(A)}$ (mm/s)	$IS_{[B]}$ (mm/s)	$B_{(A)}$ (T)	$B_{[B]}$ (T)	$\theta_{(A)}$ (°)	$\theta_{[B]}$ (°)	x
Bulk $NiFe_2O_4$	6.4	0.25(4)	0.36(3)	51.51(2)	55.76(5)	0.1(1)	0.1(1)	0.99(4)
Milled $NiFe_2O_4$	6.4	0.25(7)	0.36(9)	50.94(8)	53.03(7) ^{a)}	24.4(8)	25.6(5)	0.72(1)
Milled and subsequently annealed (at 1198 K) $NiFe_2O_4$	239.0	0.14(3)	0.25(3)	49.23(6)	52.92(6)	0.3(1)	0.3(2)	0.99(7)

The average magnetic hyperfine field (B), average canting angle (θ), inversion degree (x), average isomer shift (IS), and the average canting angle (θ) are given in the table.

a) Average magnetic hyperfine field distribution.

Source: Šepelák et al. [28]/with permission of Elsevier.

$x = 0.99(4)$, as illustrated in Figure 12.18a. The ratio of areas of lines 2 and 5 ($I_{2,5}$) and lines 1 and 6 ($I_{1,6}$) in the high-field spectrum of the bulk sample is roughly 4/3. This means that along the external magnetic field of 5.5 T at 6.4 K, the spins are almost perfectly aligned ($\theta = 0.1(1)^\circ$). This yields a bulk ferrite with a virtually entirely inverted spinel structure as well as a Neel-type collinear spin arrangement of $(Fe\uparrow)[Ni\downarrow Fe\downarrow]O_4$.

Moreover, Mössbauer spectra measurements under a high field result in the attainment of two interesting results in the HEBM Ni-ferrite NPs: (i) the nanostructure formation with reduced iron cation fraction on (A) sites ($x = 0.72(1)$) and (ii) an observation of magnetically disordered structure in the milled NPs due to the spin canted effect included from the milling process. As given in Table 12.4, the average canting angles are found to be $\theta_{(A)} = 24.4(8)^\circ$ and $\theta_{[B]} = 25.6(5)^\circ$, which are computed from the altered subspectral area ratio $I_{2,5} = I_{1,6}$. The canted spin arrangements have been stated in several mechanically alloyed (HEBM) synthesized spinel ferrites, e.g. in milled zinc ferrite ($ZnFe_2O_4$) NPs [24, 70], $CdFe_2O_4$ [81], $MgFe_2O_4$ [26, 82], $CuFe_2O_4$ [83], $MnFe_2O_4$ [84], $NiFe_2O_4$ [27], and $CoFe_2O_4$ NPs [85]. The surface spin disorder is a key element in the relaxation behavior of magnetic oxide NPs, according to these studies. As an example, Kodama et al. [86, 87] proposed a model of spin distribution within nanoscale ferrite particles that included ferrimagnetically aligned core spins and a spin-glass-like surface layer. As a result of mechanically induced changes in spin canting and cation distribution, mechanically activated Ni-ferrite NPs are structurally and magnetically disordered.

In contrast to typical spinels, it is thought that mechanochemical or HEBM processing of inverse spinel ferrites is accompanied by a decrease in the concentration of Fe^{3+} cations on A sites, i.e. a decrease in the inversion degree. This is seen in Figure 12.19, where the 6.4 K and 5.5 T in-field ^{57}Fe Mössbauer spectra of Mg-ferrite ($MgFe_2O_4$) and Ni-ferrite ($NiFe_2O_4$) NPs synthesized through the HEBM technique are compared to those of their bulk counterparts [23]. It reveals



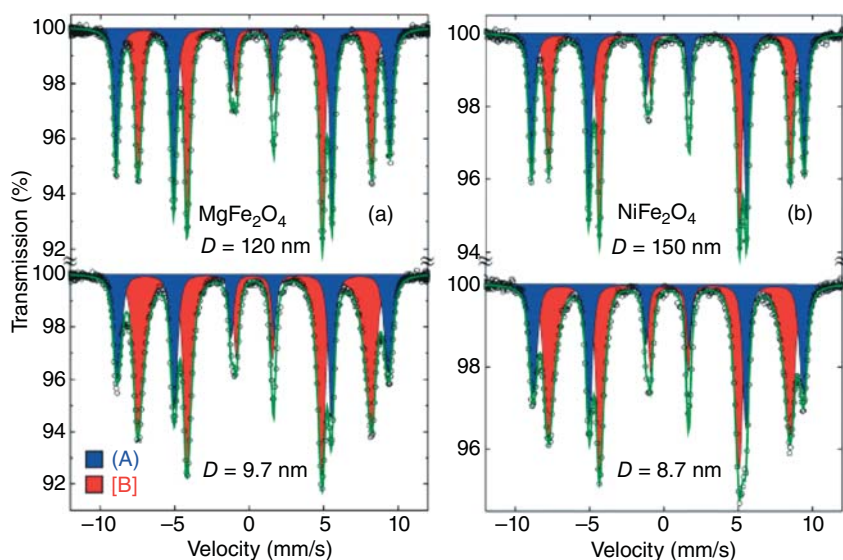


Figure 12.19 6.4 K ^{57}Fe Mössbauer spectra of the micro- and nano-sized synthesized samples via the HEBM method (a) MgFe_2O_4 and (b) NiFe_2O_4 . “The spectra with the perfectly resolved (A) and [B] subspectra were collected at in a 5.5 T in-field applied perpendicular to the γ -ray direction”. Source: Šepelák et al. [21]/with permission of Royal Society of Chemistry.

that nonball-milled Mg-ferrite and Ni-ferrite samples have a partially inverse $(\text{Mg}_{0.10}\text{Fe}_{0.90})[\text{Mg}_{0.90}\text{Fe}_{1.10}]\text{O}_4$ ($\lambda_c = 0.90$) and entirely inverse spinel structure $(\text{Fe})[\text{NiFe}]\text{O}_4$ ($\lambda_c = 1.00$), whereas the inversion degree (λ) of the ferrites NPs is around 0.7 [26–28]. Furthermore, the average spin canting angle (Ψ) can be simply calculated from the ratio of the intensities of lines 2 and 1, I_2/I_1 , of the magnetically split 6-line spectra when an external magnetic field is applied perpendicularly to the γ -ray direction. As demonstrated in Figure 12.19, the intensity ratio I_2/I_1 for bulk (micro-sized particles) Mg-ferrite and Ni-ferrite is around 4/3. Thus, the spins are aligned with the external magnetic field of 5.5 T, indicating that the bulk ferrites have a Néel-type collinear spin arrangement of the types $(\text{Mg}_{0.1}\text{Fe}_{0.9}\uparrow)[\text{Mg}_{0.9}\text{Fe}_{1.1}\downarrow]\text{O}_4$ and $(\text{Fe}\uparrow)[\text{Ni}\downarrow\text{Fe}\downarrow]\text{O}_4$. The noncollinearity degree of the spins enhances with the reduction in crystallite size, which obtains typically by increasing the milling time (t_m) in the aimed ferrites [26, 27]. Of course, the optimization of crystallite size with milling time is required (Abdollah). The average spin canting angles are obtained at about 24° and 26° for the nanocrystalline with the average size less than 10 nm in the case of Mg-ferrite (MgFe_2O_4) and Ni-ferrite (NiFe_2O_4) samples, respectively. As a result of spin canting, nanoscale magnetic oxides generated using the HEBM process have magnetic disorder in addition to cation disorder. In other investigations, Hamdeh et al. investigated the effect of high-energy ball milling on cation inversion in Zn ferrite NPs generated by an aerogel technique in 1995 [88] and 1997 [89]. They measured a Zn cation inversion of 0.55 that leads to ferrimagnetic activity up to 250 K based on the ^{57}Fe



Mössbauer spectroscopy and Rietveld refinement of X-ray diffraction pattern (XRD) measurements. Soon after, Šepelák et al. demonstrated that the cation inversion was a metastable state that could be completely reversed by heat treatments above 600 K [25, 90, 91]. Chinnasamy et al. [92, 93], investigated the effect of high-energy ball milling on Zn-ferrite and found that after 20 h of milling, induced ferrimagnetism was seen. In high-energy ball milling of Zn-ferrite aerogels, Oliver et al. [70] in collaboration with the Hamdeh group and Harris, used extended X-ray absorption fine structure (EXAFS) to measure an inversion parameter, which was found about 0.45. Hofmann et al. [94], Stewart et al. [95], and Figueroa et al. [96] performed variations of mechanical activation of zinc-ferrite and measured cation inversion of ~ 0.40 , following the work of Oliver et al. and other research teams. Li et al. [97], on the other hand, reported a 0.58 inversion. The main finding in all of these cases was a higher Néel temperature.

Figure 12.20a exhibits the RT transmission Mössbauer spectra of hematite ($\alpha\text{-Fe}_2\text{O}_3$) NPs obtained through HEBM after various milling times. The corresponding fitted spectra results are given in Table 12.5. The spectrum for the nonmilled sample was adjusted by introducing only one sextet with a hyperfine field (B_{hyp}) of 51.3 T, isomer shift of 0.37 mm/s, and quadrupolar shift of -0.2 mm/s relative to $\alpha\text{-Fe}$. These values indicate that the initial powder comprises only the hematite crystalline phase. A line broadening and intensity reduction in the spectra characteristics are observed by increasing milling time. Thus, a new sextet is taken into account to fit them properly. The new component might be associated with the hematite NPs obtained from the milling process, and the first sextet is attributed to

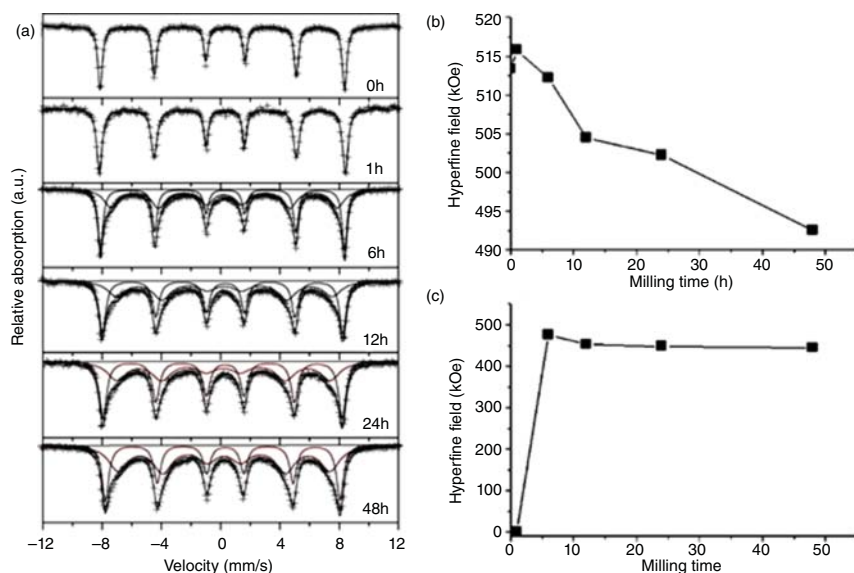


Figure 12.20 (a) RT Mössbauer spectra of the hematite NPs synthesized at different milling times. (b) The hyperfine field's evolution as a function of milling time in the NPs and (c) in the micro-sized hematite particles. Source: Lemine et al. [98]/with permission of Elsevier.



Table 12.5 The Mössbauer spectra fitting of the hematite NPs produced at different milling periods yielded the following results.

Milling times (h)	First sextet			Second sextet		
	B_{hyp} (kOe)	IS (mm/s)	Relative area (%)	B_{hyp} (kOe)	IS (mm/s)	Relative area (%)
0	513.4	0.36	100	—	—	0
1	515.8	0.36	100	—	—	0
6	512.2	0.37	48	475.7	0.382	52
12	504.5	0.37	52	452.7	0.4	48
24	502.2	0.36	52	447.7	0.34	48
48	492.2	0.37	40	444	0.37	60

Source: Lemine et al. [98]/with permission of Elsevier.

the micro-sized hematite particles. With milling times, the relative abundance of the micro-sized component (first sextet) decreases, while the nanosized component increases (second sextet). The increase in the new component is consistent with the concept that when the crystallite size decreases, the disordered regions become more visible [99]. Furthermore, as shown in Figure 12.20b, the B_{hyp} of the new component falls, whereas the B_{hyp} of the other sextet approaches the value of bulk hematite at all times, as shown in Figure 12.20c. The dynamic effects can be used to explain these phenomena. Small grains formed upon applying prolonged milling are mainly single magnetic domains and single crystals. Even in firmly packed powder, the magnetic interaction between such particles is weak because magnetic domains remain antiferromagnetic (or very weakly ferromagnetic below Morin transition). As a result, even at room temperature, the domain magnetization might relax. As a result of this process, the magnetic dipole interaction between the nucleus and the electronic shell is reduced, resulting in impressive line broadening, the latter dependent on the hyperfine line in particular. The entirely collapsed magnetic hyperfine structure, which is easily apparent for hematite particles truly distributed in the nonmagnetic carrier, is not visible due to the powder's strong compaction. Furthermore, the consistency of the overall change (isomer shift) versus milling time appears to confirm the dynamic effect concept. It means that during milling, the electron density on the iron nucleus remains nearly unaltered. As the Morin transition is caused by defects, the mixed state is observed around Morin transitions, i.e. regions of either antiferromagnetic order or with the canted structure. The temperature of the Morin transition can be changed by applying pressure or an external field. In as-ball-milled NPs, extensive imperfections such as grain boundary, dislocation, surface, and point defects lower the Morin transition temperature.

Figure 12.21a,b shows the ^{57}Fe Mössbauer spectra of the mechanically alloyed mixture of hematite ($\alpha\text{-Fe}_2\text{O}_3$) with Ca and CaO powder particles. Both samples' spectra present a sextet associated with hematite with a magnetic hyperfine field



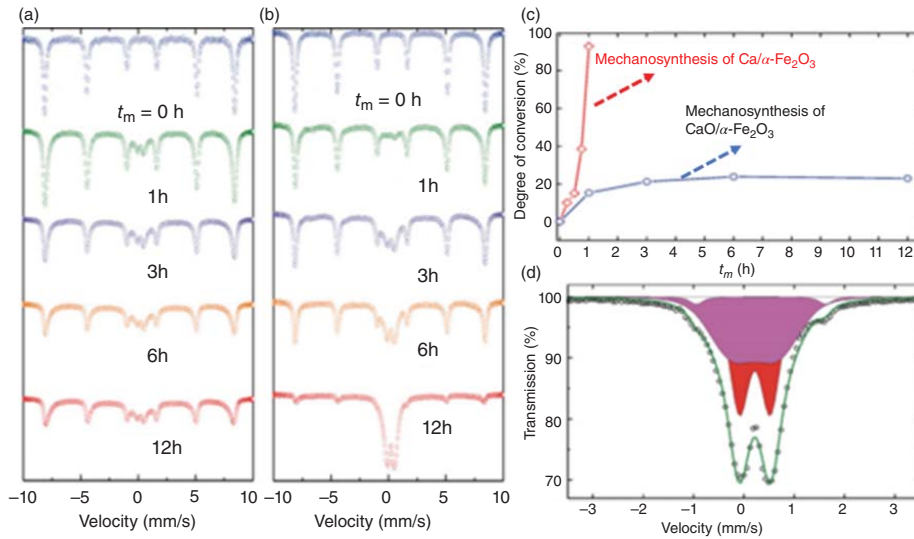


Figure 12.21 RT ^{57}Fe Mössbauer spectra of (a) the $\text{CaO}/\alpha\text{-Fe}_2\text{O}_3$ mixtures and (b) the $\text{Ca}/\alpha\text{-Fe}_2\text{O}_3$ powders milled for various times (t_m). (c) Evolution of the conversion degree of the Ca-ferrite NPs synthesized via the HEBM method at different milling times. The conversion degree is computed from the intensity of the Mössbauer sextet corresponding to hematite, I_{sext} , relative to the total spectral intensity, I_{tot} , according to $(1 - I_{\text{sext}}/I_{\text{tot}}) \times 100\%$. (d) The central part of the RT ^{57}Fe Mössbauer spectrum of the Ca-ferrite NPs produced from the $\text{Ca}/\text{Fe}_2\text{O}_3$ mixture. The other two colored subspectra in the orthorhombic structure of the ferrite belong to Fe^{3+} cations in non-equivalent octahedral positions. The Fe^{3+} ions in the non-milled $\alpha\text{-Fe}_2\text{O}_3$ phase are responsible for the small (7%) white (without space) subspectrum. The fit of the spectrum resulted in a Lorentzian width (Γ) of 0.30 mm/s. Source: Berchmans et al. [100]/with permission of Elsevier.



of 51.6(4) T. When the samples are subjected to the milling process, the Ca-ferrite (CaFe_2O_4) NPs are produced. The sextet becomes unbalanced toward the inside of each line as the milling time is increased, gradually collapses, and is gradually replaced by a central doublet. This is very similar to the NPs spectra reported in Ref. [101]. In this connection, it is worth noting that even when the particle size of the material reaches the nanoscale range, the Mössbauer spectrum of hematite shows only a broadened sextet, i.e. no superparamagnetic doublet. As a result, nonball-milled hematite in the Mössbauer spectra can be easily recognized [102, 103]. ^{57}Fe Mössbauer spectroscopy can be used to estimate the yield of this mechanochemical reaction because the spectrum components related to the educt (hematite) and product (Ca ferrite) phases are clearly resolved in the spectra. As shown in Figure 12.21a,b, the intensity of the Mössbauer sextet corresponding to hematite, I_{sext} , decreases in comparison to the total spectral intensity. During milling, the reactants gradually convert to the ferrite phase, as indicated by I_{tot} . It is evident that the Ca-ferrite NPs are produced after only 1 h ball milling in the case of the metal/oxide system, while it forms after 12 h milling at the same condition in the case of the oxide/oxide precursor system. Furthermore, as shown in Figure 12.21c, the conversion degree of the mechanically activated reaction reaches about 93% in the former case, while the yield of the reaction only reaches about 23% in the latter.

^{57}Fe Mössbauer spectroscopy offers information on the local symmetry, charge states, and magnetic state of iron ions in mechanically activated Ca-ferrite NPs in addition to the reaction yield. The existence of at least two crystallographically nonequivalent iron sites in the structure is indicated by the slightly asymmetrical center doublet in the spectrum of ferrite NPs shown in Figure 12.21d. Two quadrupole doublets corresponding to the ferrite phase and one sextet relating to the unreacted hematite phase are thus used to match this spectrum. The estimated isomer shifts of the doublet components ($\text{IS}_1 = 0.216(7)$ mm/s, $\text{IS}_2 = 0.210(1)$ mm/s) are both typical for ferric (Fe^{3+}) ions in octahedrally coordinated sites by oxygen [30]. The quadrupole splitting of the spectrum components ($\text{QS}_1 = 0.613(7)$ mm/s, $\text{QS}_2 = 0.924(2)$ mm/s) shows that the electric field gradients acting on Fe^{3+} nuclei in the two nonequivalent octahedral locations of the as-synthesized NPs are different. These values are higher than those stated for the micron-sized (bulk) Ca-ferrite particles manufactured conventionally ($\text{QS}_1 = 0.30$ mm/s, $\text{QS}_2 = 0.75$ mm/s) [104, 105]. Mechanically alloyed complex oxides, on the other hand, tend to have higher electric field gradients [24]. Due to polyhedra distortion, they are created by an asymmetric electronic charge distribution around the iron ions.

Figure 12.22a exhibits the Mössbauer spectra of the $2\text{CaO} + \text{SnO}_2$ mixture ball milled for various times in HEBM in comparison with the spectrum of Ca_2SnO_4 synthesized with the conventional ceramic route [106]. The spectrum of the starting powder is evaluated by a doublet with a quadrupole splitting $\text{QS} = 0.354(1)$ mm/s and an average isomer shift $\text{IS} = -0.016(2)$ mm/s corresponding to octahedrally coordinated Sn^{4+} cations in SnO_2 . The doublet is observed as a singlet in the spectrum due to a relatively large Lorentzian line width of $0.398(6)$ mm/s, typical of ^{119}Sn Mössbauer spectroscopy. Indeed, the Mössbauer spectroscopy merely indicates a broadening of the doublet in the early stages of milling (for $t_m \leq 0.25$ h).



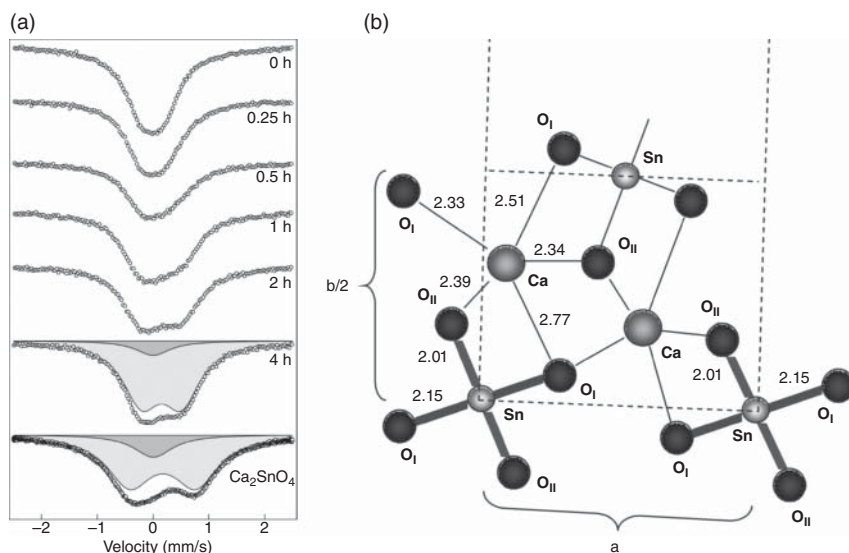


Figure 12.22 (a) Mössbauer spectra of the Ca_2SnO_4 with micro-sized particles (bottom) were obtained via the conventional ceramic route, and (top) the NPs obtained from ball milling of the $2\text{CaO} + \text{SnO}_2$ mixture at various times. Source: Šepelák et al. [106]/American Chemical Society. (b) Different lengths of Sn–OI and Sn–OII bonds in SnO_6 octahedra are highlighted in this projection of the orthorhombic structure of Ca_2SnO_4 on the (001) plane interatomic distances are in angstroms. Source: Trömel [107]/with permission of John Wiley & Sons.

However, the splitting of the doublet gradually increases with the increase in the milling time to $t_m \geq 0.5$ h. An asymmetric doublet structure is formed as a result of this. A superposition of two subspectra fits the spectrum of the 4-milled sample well; one minor singlet ($\text{IS}_2 = 0$ mm/s, $\text{QS}_2 = 0$ mm/s) attributed to Sn cations in CaSnO_3 and one dominant doublet with hyperfine parameters $\text{IS}_1 = 0.153(3)$ mm/s and $\text{QS}_1 = 0.722(4)$ mm/s corresponding to octahedrally coordinated Sn cations in Ca_2SnO_4 . This indicates that the Mössbauer spectroscopy is also able to reveal the existence of a small amount of the perovskite phase in the mechanically activated NPs.

Furthermore, from the spectra of the samples, it is evident that the average quadrupole splitting for the mechanically produced Ca_2SnO_4 NPs ($\text{QS} = 0.722(4)$ mm/s) is considerably smaller than that estimated for the Ca_2SnO_4 samples synthesized via the conventional ceramic route ($\text{QS} = 1.192(2)$ mm/s). This implies the existence of smaller electric field gradients acting on Sn nuclei in the nanostructured materials in comparison to those experienced by Sn nuclei in Ca_2SnO_4 with micro-sized particles. Considering the coordinates of tin and oxygen atoms in the orthorhombic structure of the micro-sized Ca_2SnO_4 sample ($\text{Sn} \equiv (0/0/0)$, $\text{O}_I \equiv (0.228/0.049/0.5)$, $\text{O}_{II} \equiv (0.36/0.31/0)$) as defined by XRD [107, 108]. The relatively large QS value obtained (i.e. large electric field gradients) for the micro-sized Ca_2SnO_4 particles can be described by a highly asymmetric charge distribution around Sn nuclei deriving from the different bond lengths of



$d(\text{Sn-O}_\text{I}) = 2.15 \text{ \AA}$ and $d(\text{Sn-O}_\text{II}) = 2.01 \text{ \AA}$ in SnO_6 octahedra. Figure 12.22b presents such a phenomenon, where the orthorhombic structure of Ca_2SnO_4 is projected on the (001) plane [107, 108]. Consequently, the smaller QS value for mechanically activated Ca_2SnO_4 NPs can be described by the existence of distorted but more symmetric SnO_6 octahedra in its structure, i.e. octahedra with bond lengths for which $d(\text{Sn-O}_\text{I}) - d(\text{Sn-O}_\text{II}) < 0.14 \text{ \AA}$. This is in line with the NMR measurements, which reveal a broad distribution of local environments around the Sn nuclei in the mechanically activated Ca_2SnO_4 NPs. From the above-mentioned information, the Mössbauer data cannot be ascertained whether the Sn-O_I and Sn-O_II bonds in the NPs are longer or shorter than those in the micro-sized Ca_2SnO_4 particles. In short, the short-range structural information attained from Mössbauer and NMR measurements can be summarized by stating that the surface shell regions of mechanically activated Ca_2SnO_4 NPs are disordered due to broadly distorted but symmetric octahedral environments around Sn nuclei (SnO_6 octahedra with more converging Sn-O_I and Sn-O_II bond lengths). Note that because of the relatively structureless Mössbauer spectrum of the ball-milled NPs, no effort is needed to separate the surface effects from the bulk effects in NPs and to quantitatively estimate the CaSnO_3 phase fraction.

In another study, ^{57}Fe Mössbauer spectroscopy is considered to evaluate the effect of milling conditions on the Ni-ferrite NPs obtained from the $\alpha\text{-Fe}_2\text{O}_3/\text{NiO}$ mixture. [103]. Figure 12.23a: a–g exhibits the Mössbauer spectra of the milled powder particles, wherein their spectra are compared with the micro-sized Ni ferrite particles synthesized via the conventional ceramic route (Figure 12.23h). Figure 12.24a shows the spectrum of the initial hematite/nickel oxide ($\alpha\text{-Fe}_2\text{O}_3/\text{NiO}$) mixture, which shows a sextet with a magnetic hyperfine field of $52.26(4) \text{ T}$ attributable to hematite. As the milling time increases, the sextet becomes lopsided toward the inside of each line. Furthermore, as illustrated in Figure 12.23a: a–g, they eventually collapse and are gradually replaced by a center doublet and a newly widened sextet. Figure 12.23g shows that the spectral components in the spectrum of the 8-h-milled sample are understood to induce from ^{57}Fe in small particles with relaxation times $\delta < \delta_L$ (dominating superparamagnetic doublet) and $\tau > \tau_L$ (minor sextet structure), where τ_L is the Larmor precession time of the nuclear magnetic moment ($\tau_L \approx 1 \times 10^{-8} - 1 \times 10^{-9} \text{ s}$) [22]. The broad shape of these spectral components, in contrast to the comparatively small magnetically split lines for the micro-sized Ni-ferrite particles, is revealed by comparing lines g and h in Figure 12.23. This demonstrates that the Fe^{3+} nuclei in the newly produced material are subjected to a wide range of magnetic fields. The Mössbauer spectrum of the micro-sized Ni-ferrite sample is fitted by a superposition of two subspectra corresponding to $\text{Fe}^{3+}(\text{A})$ and $\text{Fe}^{3+}(\text{B})$ ions, as demonstrated in Figure 12.23b: a,b. The sample's inversion degree, calculated from the subspectral intensity ratio $I_{(\text{A})}/I_{(\text{B})}$, is around $0.996(3)$. The spins are almost completely aligned $\Psi_{(\text{A})} = 0.2(1)^\circ$, $\Psi_{(\text{B})} = 0.3(2)^\circ$ along the external magnetic field of 5.5 T due to the fact that the intensity ratio I_2/I_1 is equal to $4/3$ for both (A) and (B) subspectra. Hence, the micro-sized ferrite particles present a totally inverse spinel structure with a Néel-type collinear spin arrangement of $(\text{Fe}\uparrow)[\text{NiFe}\downarrow]\text{O}_4$. Figure 12.23c compares the [B] site hyperfine field



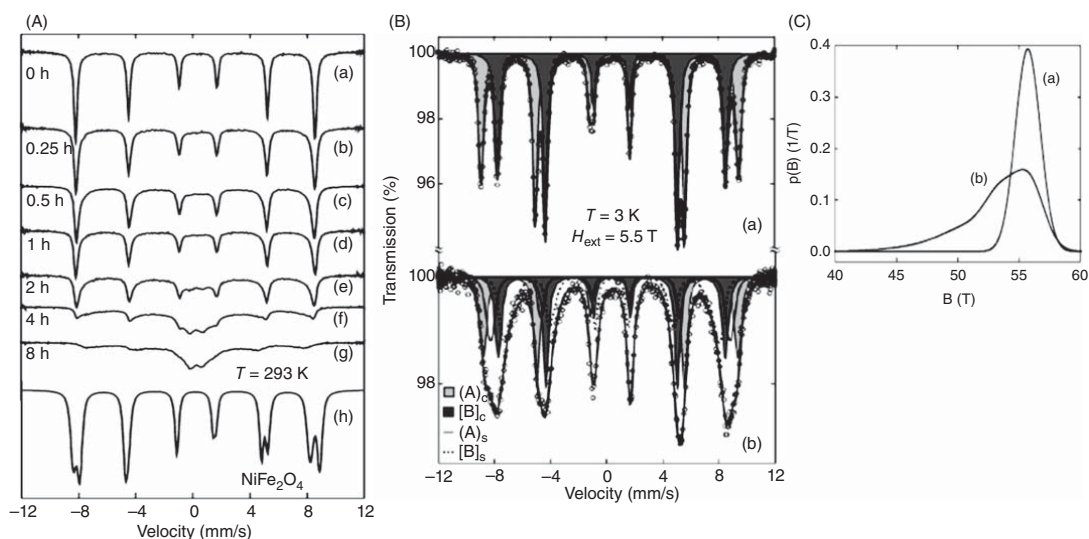


Figure 12.23 (A) RT Mössbauer spectra of the ball-milled hematite/nickel oxide mixture for different times and compared with the micro-sized Ni ferrite particles. (B) 3 K and 5.5 T in-field Mössbauer spectra of the Ni-ferrite particles synthesized via (a) the conventional ceramic method, and (b) NPs synthesized via HEBM. “(A)_c, [B]_c and (A)_s, and [B]_s represents cation sites of tetrahedral and octahedral coordination in the inner core and the surface shell of NiFe₂O₄ NPs, respectively”. (C) “[B] site HFDs obtained from the high-field Mössbauer spectra of the (a) micron-sized and (b) nanosized NiFe₂O₄ particles. The [B] site HFD of the mechanically activated NPs is a superposition of the core ([B]_c) and shell ([B]_s) contributions”. Source: Šepelák et al. [103]/American Chemical Society.



distributions (HFDs) originating from the high-field Mössbauer spectra of the NPs and micro-sized ferrite particles. It is important to note that the HFDs provide the most detailed information on the local magnetic fields acting on iron nuclei at a certain lattice location. Obviously, the B site iron nuclei in the micron-sized Ni-ferrite particles encounter the local fields from a relatively narrow interval ranging from about 53 to 58 T. In comparison, nanosized ferrite particles have a broad dispersion spanning from 45 to 58 T. This extensive HFD indicates that the mechanically activated Ni-ferrite NPs' macroscopic magnetic state is severely perturbed.

Figure 12.24a,b presents the TEM images of the ball-milled α -Fe₂SiO₄ NPs at low and high magnifications [80]. The particles with an almost spherical shape are distributed in the range of 5–25 nm with an average size of 13(2) nm. Furthermore, by closely looking at their high magnification image, it is evident that the nanoparticles are composed of a disordered shell structure with a thickness of 1 nm in size and an ordered structure of the core of around 12 nm. The TEM images also present lattice fringes attributed to the crystallographic plane (111) ($d = 3.556 \text{ \AA}$) of the α -Fe₂SiO₄ phase. They run the length of the particle core, revealing its single crystalline nature. The mechanochemical reaction is followed by ⁵⁷Fe Mössbauer spectroscopic analysis, as illustrated in Figure 12.24c, to determine the evolution of the product phase during milling in greater detail. It indicates that the sextets corresponding to α -Fe₂O₃ in the milled NPs. Furthermore, as the milling time is increased, Fe collapses and is eventually replaced by a center doublet characteristic of Fe²⁺ ions. Indeed, the milling process creates a complex series of heterogeneous solid-state transformations, including redox reaction ($2\text{Fe}^{3+} + 2\text{Fe}^0 \rightarrow 3\text{Fe}^{2+}$) and formation reaction ($2\alpha\text{-Fe}_2\text{O}_3 + 2\text{Fe} + 3\text{SiO}_2 \rightarrow 3\alpha\text{-Fe}_2\text{SiO}_4$), which are completed after only four hours. On the other hand, the Fe₂SiO₄ particles synthesized via the conventional ceramic route need several stages, a homogeneous mixture of the initial powder precursors, proper and fully compacting of the as-prepared powders, and finally heat treating them at high temperatures under controlled oxygen fugacity.

The evaluation of the Mössbauer spectra is considered to determine their local ionic configuration and also to fully understand the surface/interface effects from the core/bulk effects in the as-synthesized NPs from their corresponding micro-sized particles counterpart, as demonstrated in Figure 12.24d. The superposition of two doublets with the hyperfine parameters listed in Table 12.6 fits the spectra of micro-sized silicate particles effectively. These characteristics match those found in the olivine crystal structure of α -Fe₂SiO₄, in which Fe²⁺ cations fill two unequal octahedral positions, [M₁] and [M₂], in equal proportions, while Si⁴⁺ cations are coordinated by four O²⁻ ions to form SiO₄ tetrahedra (T). As a result, in micro-sized α -Fe₂SiO₄ particles, the crystal-chemical formula, emphasizing site occupancy at the atomic level, can be represented as [Fe]_[M₁][Fe]_[M₂]Si_(T)O₄. The core-shell morphology of the mechanically activated NPs needs to fit their Mössbauer spectrum by a superposition of four subspectra shown in Figure 12.24d, bottom. Two subspectra are attributed to the Fe²⁺ ions in the surface shell/interface regions of NPs (denoted [M₁]s and [M₂]s), and Fe²⁺ nuclei in the well-crystallized core of



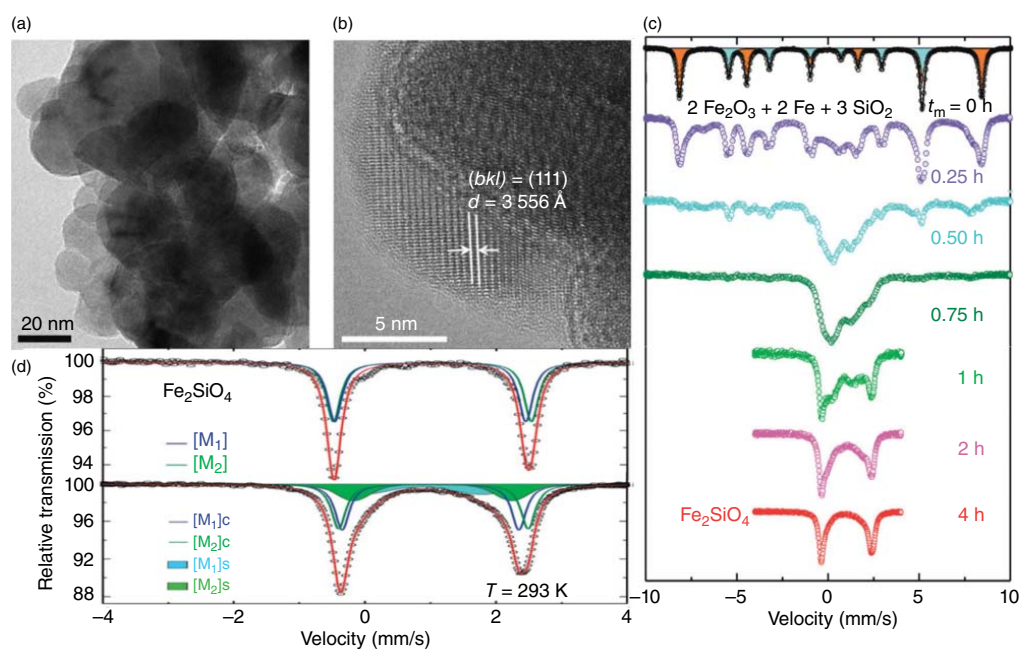


Figure 12.24 (a) Bright-field and (b) high-resolution TEM images of the ball-milled $2\alpha\text{-Fe}_2\text{O}_3$ NPs indicating the surface shell thickness of about 1 nm. (c) ^{57}Fe Mössbauer spectra of the ball-milled $2\alpha\text{-Fe}_2\text{O}_3 + 2\text{Fe} + 3\text{SiO}_2$ mixture at different times. (d) ^{57}Fe Mössbauer spectra of the micron-sized $\alpha\text{-Fe}_2\text{O}_3$ particles (top) and the nanosized $\alpha\text{-Fe}_2\text{O}_3$ particles (bottom), where $[\text{M}_1]c$, $[\text{M}_2]c$, and $[\text{M}_1]s$, $[\text{M}_2]s$ designate cation sites of octahedral coordination in the core-shell structure of the $\alpha\text{-Fe}_2\text{O}_3$ NPs. Source: [81], V. Šepelák et al. (2012), Royal Society of Chemistry.



Table 12.6 Data attained by fitting the Mössbauer spectra of the nanosized and micro-sized Fe_2SiO_4 particles.

Material	Octahedral site of Fe^{2+}	IS (mm/s)	QS (mm/s)	σ (mm/s)	I (%)
Bulk Fe_2SiO_4	$[\text{M}_1]$	0.99(5)	2.91(4)	0.042(1)	50.1(3)
	$[\text{M}_2]$	1.02(8)	3.02(1)	0.041(1)	49.9(4)
Nano Fe_2SiO_4	$[\text{M}_1]\text{c}$	1.00(1)	2.69(6)	0.045(2)	30.0(4)
	$[\text{M}_2]\text{c}$	1.04(5)	2.89(1)	0.046(2)	30.0(5)
	$[\text{M}_1]\text{s}$	0.86(3)	1.86(5)	0.77(2)	20.0(7)
	$[\text{M}_2]\text{s}$	1.03(3)	2.41(8)	0.40(1)	20.0(6)

Source: Šepelák et al. [80]/with permission of Royal Society of Chemistry.

Fe_2SiO_4 NPs are accounted for by two components (denoted $[\text{M}_1]\text{c}$ and $[\text{M}_2]\text{c}$). Comparison of $\sigma_{[\text{M}_1]\text{c}}$, $\sigma_{[\text{M}_2]\text{c}}$, $\sigma_{[\text{M}_1]\text{s}}$, and $\sigma_{[\text{M}_2]\text{s}}$ in Table 12.6 indicates that the Mössbauer lines corresponding to Fe atoms at surfaces/interfaces are significantly wider than those related to nanoparticles' cores. This clearly demonstrates a wide range of electric field gradients acting on the Fe^{2+} nuclei in the NPs' near-surface layers/interface regions. The pattern suggests that the ferrous ions in the nanofayalite's surface/interface regions are surrounded by highly deformed octahedra. The electric field gradients acting on Fe nuclei in the shell are less than those faced by Fe nuclei in the core of Fe_2SiO_4 NPs, which is another noteworthy feature. The surface shell regions of mechanically activated NPs are disordered, according to Mössbauer measurements, due to extensively deformed but more symmetric octahedra ($[\text{M}_1]\text{s}$ and $[\text{M}_2]\text{s}$ octahedra with a reduced dispersion of Fe—O bond lengths). Recent Mössbauer and NMR studies of mechanically activated Sn-containing oxide NPs support this conclusion [106].

From the intensity ratio $(I_{[\text{M}_1]\text{s}} + I_{[\text{M}_2]\text{s}})/(I_{[\text{M}_1]\text{c}} + I_{[\text{M}_2]\text{c}} + I_{[\text{M}_1]\text{s}} + I_{[\text{M}_2]\text{s}})$, the volume fraction (w) of the disordered surface/interface areas in nanoolivine is predicted to be around 40%. Therefore, the Fe ions distribution in the mechanically activated Fe_2SiO_4 NPs can be written as $[\text{Fe}_{0.6}]_{[\text{M}_1]\text{c}}[\text{Fe}_{0.6}]_{[\text{M}_2]\text{c}}[\text{Fe}_{0.4}]_{[\text{M}_1]\text{s}}[\text{Fe}_{0.4}]_{[\text{M}_2]\text{s}}\text{Si}_{(\text{T})}\text{O}_4$. The shell thickness is $t = 1.02(1)$ nm ($w = 100 [1 - (1 - 2t/D)^3]$) in the case of spherical NPs with an average diameter of 13 nm. This value is comparable to that reported in other oxide NPs produced through the HEBM technique and is in good accord with the HRTEM data presented in Figure 12.24a,b [102, 106, 109, 110]. As has been found with ball-milled ferrites NPs, the presence of deformed octahedra in nanofayalite should result in magnetic characteristics fluctuation. The Néel temperature of nanofayalite ($T_N = 65.0(1)$ K) is quite similar to that of the conventionally synthesized bulk $\alpha\text{-Fe}_2\text{SiO}_4$ (64.5 K) [111].

Figure 12.25a,b show the Mössbauer spectra of the precipitation-assisted synthesis of Co-ferrite (CoFe_2O_4) and Mn-ferrite (MnFe_2O_4) NPs in the presence and absence of a gelatinous medium, which is heat-treated at two different temperatures of 175 and 230 °C [112]. Their corresponding fitting parameters are listed in Table 12.7a,b. The Co-ferrite NPs spectra are all well fitted with a single sextet determined by



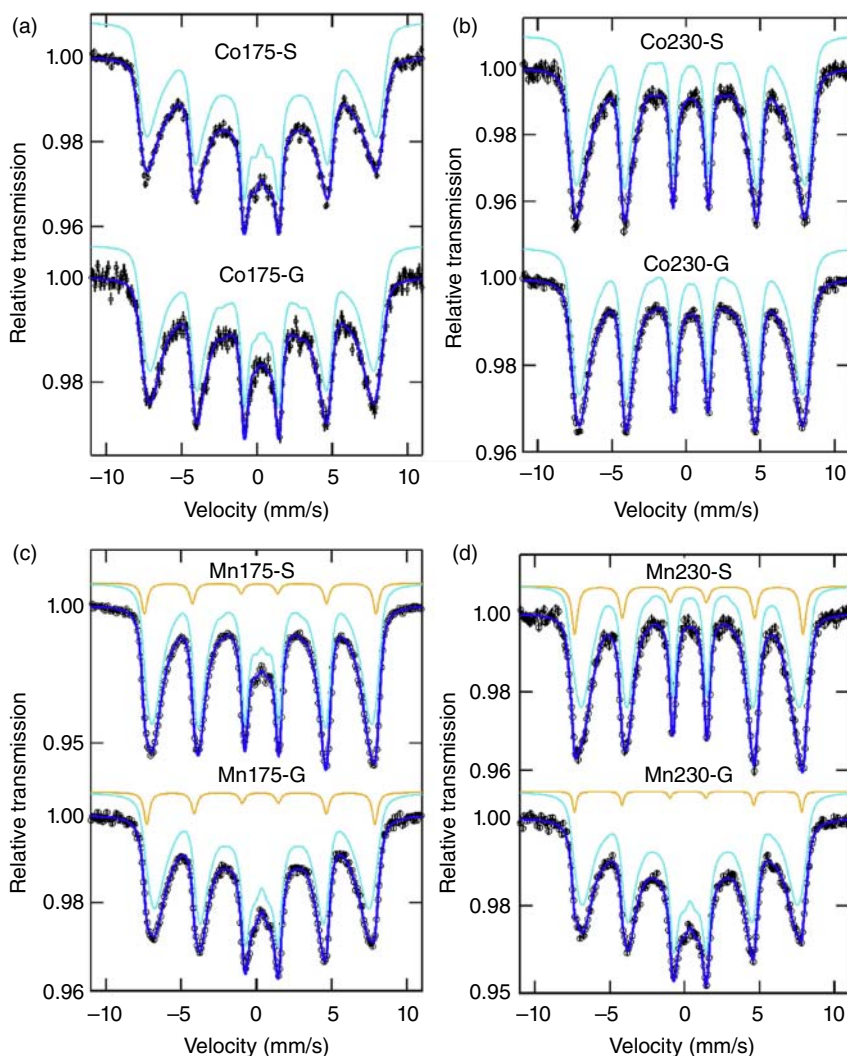


Figure 12.25 RT ^{57}Fe Mössbauer spectra of the Co-ferrite NPs and Mn-ferrite NPs synthesized at 175 °C (a) and 230 °C (b), without (c) and within (d) gelatinous medium, respectively. Source: Cruz et al. [112]/with permission of Elsevier.

a large distribution of hyperfine fields (B_{hf}) and an isomer shift value, d , around 0.31(1) mm/s, typical of Fe^{3+} ions. No relevant differences are detected between the NPs synthesized with or without a gelatinous medium, as exhibited in Figure 12.25a and Table 12.7a. Higher mean hyperfine fields (and less distributed) are determined for the NPs heated at 230 °C compared to the NPs heated at 175 °C due to a better crystallinity of the NPs obtained at relatively a higher temperature.

Two magnetic subspectra are used to adequately fit the Mn-ferrite NPs spectra. Site 1 suits to almost all iron ions, as evidenced by a “ d ” value of 0.36(1) mm/s and a wide B_{hf} distribution, which is characteristic of Fe^{3+} ions in octahedral sites. A tiny



Table 12.7 Mössbauer hyperfine fitting parameters of all the NPs obtained at different conditions, as mentioned above.

(a)							
Sample		$\langle B \rangle [\sigma] / T$	$\delta / (\text{mm/s})$	$\epsilon / (\text{mm/s})$	$\Gamma / (\text{mm/s})$		
Co175-S		33[15]	0.314(4)	0.003(7)	0.40		
Co175-G		36[14]	0.327(6)	0.004(10)	0.40		
Co230-S		42[10]	0.309(3)	−0.012(7)	0.39		
Co230-G		41[10]	0.319(2)	−0.005(4)	0.40		
(b)							
Sample	Site	B_{hf} / T	$\langle i_{\text{hf}} \rangle [\sigma] / T$	$\delta / (\text{mm/s})$	$\epsilon / (\text{mm/s})$	$\Gamma / (\text{mm/s})$	$I / \%$
Mn	1	—	38[13]	0.361(2)	−0.002(3)	0.40	93.3
175-S	2	47.8(1)	—	0.23(1)	0.05(1)	0.45(3)	6.7
Mn	1	—	33[14]	0.358(3)	−0.009(6)	0.47	94.1
175-G	2	47.1(1)	—	0.28(1)	0.04(2)	0.44(6)	5.9
Mn	1	—	43[6]	0.345(4)	0.005(8)	0.37	86.7
230-S	2	47.3(1)	—	0.27(2)	0.03(2)	0.46(5)	13.3
Mn	1	—	32[15]	0.360(4)	−0.004(7)	0.47	97.5
230-G	2	47.1(1)	—	0.23(1)	0.02(2)	0.38(6)	2.5

I is the relative area, Γ is the line width, QS is the quadrupole splitting, ϵ is the quadrupole shift, δ is the isomer shift, and $\langle B_{\text{hf}} \rangle [\sigma]$ is the average hyperfine field and standard deviation of the distribution of magnetic splitting and (b) the corresponding data related to the MnFe_2O_4 NPs.

Source: Cruz et al. [112]/with permission of Elsevier.

number of Fe^{3+} ions in tetrahedral sites is related to the second subspectrum, which has a “ d ” value equal to or less than 0.28 mm/s. Mn-ferrite NPs should have a nearly normal spinel behavior ($\gamma = 0.20$), with iron ions in octahedral sites and Mn^{2+} ions primarily in tetrahedral sites. Table 12.7b shows Mössbauer fitting parameters that are in good agreement with this finding. Mössbauer spectra in Figure 12.25b reveal that the thermal treatment temperature is a determinant for the NPs synthesized by the conventional ceramic route (Mn175-S and Mn230-S) but not for the samples attained by the gelatin-assisted synthesis route. In keeping with the particle size distribution of this sample, the subspectrum corresponding to site 1 of Mn230-S has the highest mean hyperfine magnetic field and the narrowest standard deviation ($\langle B_{\text{hf}} \rangle = 43$ [6] T) (largest NPs distribution and highest mean size values). A minor spinel inversion degree may be deduced for all samples based on the area of the relative sites and assuming the same f value (Lambe–Mössbauer factor) for both, with Mn230-G having the lowest value ($\gamma \sim 0.05$), corresponding to a quasinormal spinel. Consequently, it can be concluded that using the gelatinous medium can control the size and distribution of the as-synthesized NPs, which, affects the cation distribution of Mn and Fe ions in MnFe_2O_4 NPs. Such behavior arises from the surfactant behavior of gelatin.



12.5 Phase Formation Evaluation Through Mössbauer Spectroscopy

The XRD is the most applicable and useful for the structural and phase formation of MNPs. But, in some cases, for example, in iron oxide NPs, the detection and distinguishing of some phases from each other have become very difficult due to the existence of some impurities in the product (normally less than 10% cannot be detected by XRD). Iron oxides can be found in a variety of natural forms, the most common of which are magnetite (Fe_3O_4), maghemite ($\gamma\text{-Fe}_2\text{O}_3$), and hematite ($\alpha\text{-Fe}_2\text{O}_3$). $\gamma\text{-Fe}_2\text{O}_3$ is formed naturally in the earth's crust as a result of atmospheric agents reacting with magnetite or by heating other iron oxides [113]. Fe_3O_4 and $\gamma\text{-Fe}_2\text{O}_3$ possess the spinel structure, where the cation distribution is written as $\text{Fe}^{3+}[\text{Fe}^{2+}\text{Fe}^{3+}]\text{O}_4$ and $\text{Fe}^{3+}[\text{xFe}^{3+}]\text{O}_3$, respectively, Fe cations without brackets are on tetrahedral (A sites) of the cubic spinel lattice, while those with brackets are on octahedral (B sites). In $\gamma\text{-Fe}_2\text{O}_3$ the sign x denotes the unoccupied B sites. Although the structures of Fe_3O_4 and $\gamma\text{-Fe}_2\text{O}_3$ are identical, there are Fe vacancies in the B sites of $\gamma\text{-Fe}_2\text{O}_3$. On the other hand, in the hexagonal $\alpha\text{-Fe}_2\text{O}_3$ phase, there is only one crystalline lattice site for Fe^{3+} [55, 114]. Since the magnetite XRD peaks almost overlap with the $\gamma\text{-Fe}_2\text{O}_3$ phase and the magnetic NPs can easily be oxidized to $\text{Fe}_{3-x}\text{O}_4$ [43], other accurate and sensitive techniques such as Mössbauer spectroscopy are required to be taken into consideration. The Mössbauer spectra of the as-synthesized iron-oxide NPs could be thoroughly investigated to determine all the present forms of iron oxide phases in the as-synthesized sample.

For example, in the case of synthesis of magnetite NPs, the XRD pattern revealed a good match of the peaks with reference magnetite peaks (Figure 12.26a). This means that all the diffraction peaks of the produced Fe_3O_4 NPs are attributed to a single-phase spinel structure with the space group Fd-3m and can be matched to the Joint Committee on Powder Diffraction Standards (JCPDS) card no. 85-1436 [115], thus showing the production of the required iron oxide phase. For comparison with the as-synthesized samples, Fe_3O_4 micro-sized particles are examined using XRD as a standard sample. There is no extra secondary phase in the samples, and the peaks are well matched. However, as observed from their Mössbauer spectra, they contain about 2.1% hematite, which is undetectable by XRD examination. This suggests that the Mössbauer spectroscopy is complementary to the XRD technique. In this context, the collected data from Mössbauer spectra of the formed NPs and their coated ones with Ag NPs are shown in Figure 12.26b. The hyperfine parameters associated with their respective spectra characteristics are provided in Table 12.8 by fitting the spectra using at least one magnetic field distribution. The results show that the NPs contain a significant amount of oxidized magnetite, with the samples being better characterized as $\text{Fe}_{3-x}\text{O}_4$. Two hyperfine sextets can be seen in typical RT Mössbauer spectra for magnetite NPs with diameters greater than 20 nm. The first one is attributed to Fe^{3+} in A sites of the spinel structure (AB_2O_4), having isomer shift values (δ) of about 0.28–0.30 mm/s, and the second one is associated with the presence of Fe^{3+} and Fe^{2+} in octahedral coordination (B) with a smaller magnetic field and δ around 0.65 mm/s. The left and right spectrum asymmetry (unimportant or



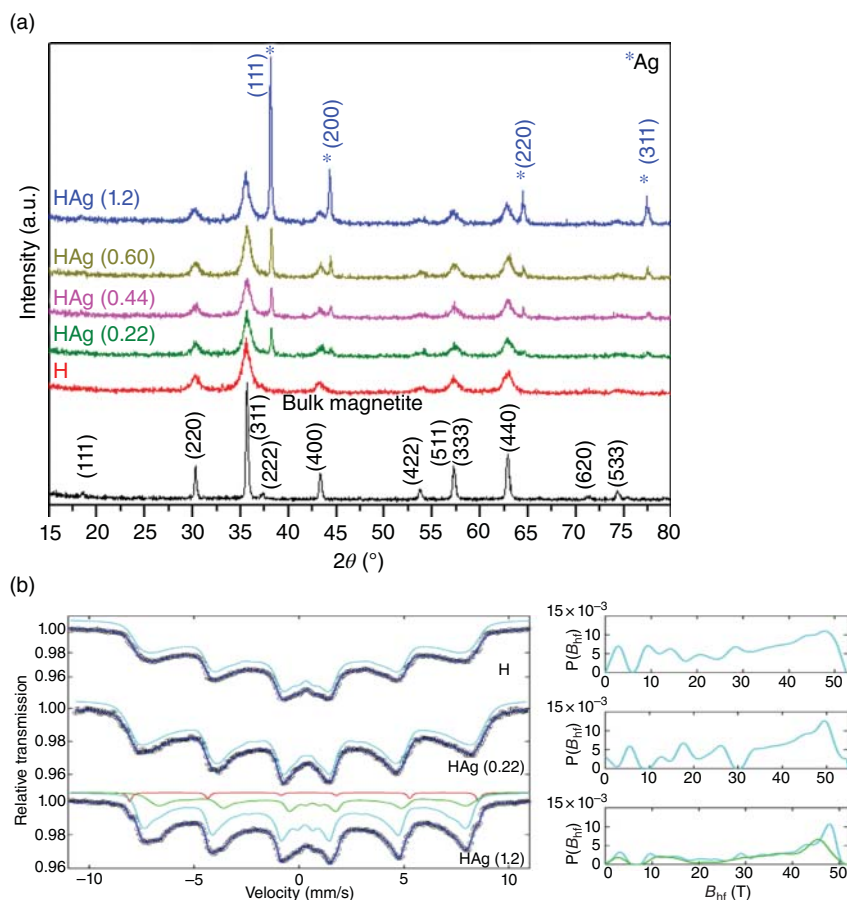


Figure 12.26 (a) XRD patterns of the as-synthesized magnetite NPs compared to their corresponding micron-sized counterpart, and (b) Mössbauer spectra of the magnetite NPs synthesized via the hydrothermal route (H) and coated with two different amounts of Ag NPs; HAg (0.22) and HAg (1.2). Source: Hajalilou et al. [43]/with permission of Elsevier.

nonexistent in the other spectra) in sample HAg(1.2) is clear evidence of a greater contribution from Fe^{2+} in octahedral sites, despite the presence of only 2% hematite. This enhancement is associated with the reducing characteristics of the environment during Ag NPs coating.

Figure 12.27a displays the RT Mössbauer spectrum recorded for the as-synthesized iron oxide NPs [116]. Two magnetically separated subspectra, S1 and S2, are used to suit the spectrum. The presence of pure single phase Fe_3O_4 is not indicated by the subspectral area and magnetic hyperfine field (B_{hf}). The area of the A site subspectrum (S1) for a pure single-phase Fe_3O_4 should be half that of the B site subspectrum (S2). Furthermore, because the magnetic hyperfine fields of both Fe sites in $\gamma\text{-Fe}_2\text{O}_3$ are equivalent, this spectrum does not correspond to a single-phase $\gamma\text{-Fe}_2\text{O}_3$. Furthermore, due to the overlapping of the Mössbauer lines of these phases, the hyperfine field of $\alpha\text{-Fe}_2\text{O}_3$ is identical to that of $\gamma\text{-Fe}_2\text{O}_3$,



Table 12.8 RT Mössbauer hyperfine fitting parameters for (a) P, PAg (0.22) and PAg (1.2) and (b) H, HAg (0.22) and HAg (1.2) samples, where I is the relative area, Γ is the line width, QS is the quadrupole splitting, ϵ is the quadrupole shift, δ is the isomer shift, and $\langle B_{hf} \rangle [\sigma]$ is the average hyperfine field and standard deviation of the distribution of magnetic splitting.

Sample	Site	$\langle B_{hf} \rangle [\sigma]$ (T)	B_{hf} (T)	δ (mm/s)	ϵ (mm/s)	Γ (mm/s)	I (%)
H	1	30[15]	—	0.33(1)	−0.01(1)	0.60	100
HAg (0.22)	1	34[12]	—	0.36(1)	−0.01(1)	0.60	100
HAg (1.2)	1 (blue)	33[15]	—	0.29(1)	−0.01(1)	0.40	71.6
	2 (green)	33[14]	—	0.65(1)	−0.01(1)	0.40	26.3
	3 (red)	—	51.5(1)	0.36(1)	−0.22(1)	0.24(2)	2.1

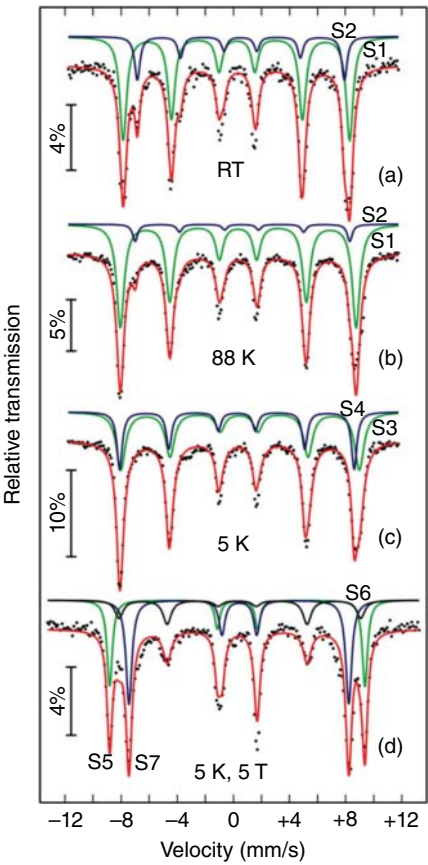


Figure 12.27 Transmission Mössbauer spectra of the as-synthesized iron oxide (Fe_3O_4 , γ - Fe_2O_3 , and α - Fe_2O_3) powder measured at (a) RT, (b) 88 K, (c) 5 K, and (d) 5 K in presence of an applied magnetic field of 5 T. Source: Nagar et al. [116]/with permission of Elsevier.



ruling out the idea of none of these phases are present. Because the presence of this phase can be seen in the XRD pattern, the contribution from $\alpha\text{-Fe}_2\text{O}_3$ must also be considered. Therefore, the detected Mössbauer spectrum is attributed to a contribution of all Fe_3O_4 , $\gamma\text{-Fe}_2\text{O}_3$, and $\alpha\text{-Fe}_2\text{O}_3$ phases. However, preparation parameters such as oxygen gas pressure, the temperature gradient in the plasma chamber, and others determine the degree of homogeneity and relative amount of the different phases. In other words, these parameters determine the Fe vacancy content in Fe_3O_4 and the nucleation and growth of each phase [117, 118].

The 5 K and 5 T in-field Mössbauer spectrum reveal that the iron vacancies are only available at the B site, not at both the A and B sites, suggesting the $\gamma\text{-Fe}_2\text{O}_3$ phase formation. The relative percentage of the Fe_3O_4 , $\gamma\text{-Fe}_2\text{O}_3$, and $\alpha\text{-Fe}_2\text{O}_3$ phases can be qualitatively defined from the relative area of the subspectra. Figure 12.27a indicates that the sextet with the smaller hyperfine field (S2) is associated with the iron atoms in B site in magnetite, where it has double the area contribution in comparison to the iron atoms in the A site. The B site subspectrum (S2) of the magnetite NPs presents an area of 23% of the total area based on the fitting parameters indicated in Table 12.9. This means that 66% of the relative area is ascribed to both the hematite and maghemite while about 34% is the sum of A and B sites in the magnetite phase. The significant overlapping of the hyperfine field values of the hematite and maghemite phases prevents the individual regions of these two phases from being estimated. The maximum inaccuracy in estimating the spectral area is expected to be around 5%. Upon cooling below 120 K, magnetite undergoes a change known as the Verwey transition [117], which has the orthorhombic structure. The exact temperature of the transition is determined based on the sample purity. The extra electron on Fe^{2+} is localized below the transition temperature in comparison to Fe^{3+} . On the other hand, this extra electron rapidly exchanges between Fe^{2+} and Fe^{3+} ions on the B site above the transition temperature. At room temperature, this exchange frequency is substantially higher than the Larmor frequency, resulting in an average intermediate valency. As a result, the iron ions in the B site have a different hyperfine field than the A site ions [119]. This frequency reduces as the temperature drops, and the electrons get confined at a lower temperature, resulting in the magnetic hyperfine fields of both A and B sites becoming equal. This is clearly evident in the 88 K Mössbauer spectrum, where the relative spectral area of S2, which associates with the iron ions in the B site of Fe_3O_4 NPs is very small in comparison to that at RT, as exhibited in Figure 12.27a. Figure 12.27c exhibits the 5 K Mössbauer spectrum. It strongly suggests that the extra electron of Fe^{2+} is localized, resulting in a single hyperfine field for the iron ions in the magnetite phase in A and B sites. Consequently, the spectrum in Figure 12.27a,b is fitted in a different method. At 5 K, the hyperfine fields of both sites (A and B sites) of Fe_3O_4 and $\gamma\text{-Fe}_2\text{O}_3$ are equal as well as for the $\gamma\text{-Fe}_2\text{O}_3$ phase. The hyperfine field of Fe_3O_4 (subspectrum S4), on the other hand, differs slightly from that of $\gamma\text{-Fe}_2\text{O}_3$ and $\alpha\text{-Fe}_2\text{O}_3$ (subspectrum S3). The areas of the two subspectra in Figure 12.27c relate to the relative amount of Fe_3O_4 (36%, S4) and $\gamma\text{-Fe}_2\text{O}_3$ and $\alpha\text{-Fe}_2\text{O}_3$ (64%, S3), with a maximum estimated error in the area of roughly 5%.



Table 12.9 Mössbauer spectral parameters.

Temperature/ magnetic field	Subspectrum	δ (mm/s)	2ϵ (mm/s)	B_{hf} (T)	Spectral area (%)	FWHM (mm/s)	R_{23}
300 K $B_{\text{ext}} = 0$ T	S1	0.35	0.03	50.0	78	0.60	2.4
	S2	0.63	0.03	45.8	23	0.46	1.5
88 K $B_{\text{ext}} = 0$ T	S3	0.45	0.01	52.0	91	0.65	2.2
	S4	0.73	0.06	47.4	9	0.43	1.4
5 K $B_{\text{ext}} = 0$ T	S5	0.55	0.07	52.7	64	0.78	2.3
	S6	0.36	0.00	51.8	36	0.47	1.9
5 K $B_{\text{ext}} = 5$ T	S7	0.40	0.01	56.4	33	0.44	0.0
	S8	0.42	0.21	53.4	22	0.70	4.0
	S9	0.51	0.05	48.6	45	0.51	0.0

Isomer shift (δ) relative to ^{57}Co source (Rh matrix) at room temperature, quadrupole splitting (QS), magnetic hyperfine field B_{hf} , relative spectral area, spectral linewidth (FWHM), and the 2nd to 3rd Mössbauer line intensity ratio (R_{23}).

Source: Cruz et al. [112]/with permission of Elsevier.

Figure 12.27d presents the 5 K and 5 T in-field Mössbauer spectrum. Three subspectra (S5, S6, and S7) are used to match the spectrum, and all of the Mössbauer parameters obtained are listed in Table 12.9. For the fitting, it is assumed that the second and fifth line intensity is only due to the $\alpha\text{-Fe}_2\text{O}_3$ phase, where the antiferromagnetically arranged Fe^{3+} spins align perpendicular to the applied field (spin flop) [120]. As a result, the intensity ratio between the 2nd and 3rd Mössbauer lines (R_{23}) of the subspectrum (S6) is 4.0 when measured perpendicular to the γ -ray direction. In this applied magnetic field of 5 T, the observed hyperfine field of $\alpha\text{-Fe}_2\text{O}_3$ practically does not change [120]. Moreover, the subspectrum S6 is assigned to the $\alpha\text{-Fe}_2\text{O}_3$ phase because the Mössbauer line positions are expected to remain identical compared to the zero-field scenario, except for a slight broadening in the line. Hence, the 22% area of the sextet spectrum is because of the existing amount of $\alpha\text{-Fe}_2\text{O}_3$ phase in the NPs. The results revealed that applying an external magnetic field of 5 T increases the saturation magnetization (M_s), and as a result, affects the effective hyperfine field of the A site (B site) in both Fe_3O_4 and $\gamma\text{-Fe}_2\text{O}_3$. This indicates that the magnitude of magnetic splitting of the A and B sites subspectra are just interchanged in comparison to the zero-field measurements. As a result, the contribution from the A sites and B sites of Fe_3O_4 and $\gamma\text{-Fe}_2\text{O}_3$ (larger effective hyperfine field) is allocated to subspectrum S5, and the contribution from the B sites of Fe_3O_4 and $\gamma\text{-Fe}_2\text{O}_3$ is attributed to subspectrum S7 in Figure 12.27d (smaller effective hyperfine field). This means that the B-site Fe magnetic moments align along the B_{ext} direction at 5 K due to the negative hyperfine interaction constant for iron, while the A-site moments align opposite the B_{ext} direction (due to the negative hyperfine interaction constant for iron). Furthermore, the areas determined for the subspectra S5 and S7 are 33% and 45% of the overall area of the spectrum, respectively. The subspectrum corresponding to the B site of Fe_3O_4 contributes 23% of the entire subspectrum S7, according to the results of least-squares fitting of the Mössbauer spectrum recorded at RT (Figure 12.27a). When this area is combined with half of the area given by



$\gamma\text{-Fe}_2\text{O}_3$ (belonging to the B site), the inner sextet S7 has a total area of 45%. As a result, the area attributed to the B-site sextet of $\gamma\text{-Fe}_2\text{O}_3$ is $45\% - 23\% = 22\%$, and therefore, the $\gamma\text{-Fe}_2\text{O}_3$ phase contributes a total area of 44% to the entire spectrum. By considering the subspectrum S5 (A sites of Fe_3O_4 and $\gamma\text{-Fe}_2\text{O}_3$), the same area can be obtained for the $\gamma\text{-Fe}_2\text{O}_3$ phase. As a result, the percentages of Fe_3O_4 , $\alpha\text{-Fe}_2\text{O}_3$, and $\gamma\text{-Fe}_2\text{O}_3$ in the sample are 34%, 22%, and 44%, respectively. Furthermore, an intermediate B-site vacancy state between Fe_3O_4 and $\gamma\text{-Fe}_2\text{O}_3$ cannot exist since, otherwise, the distribution of B sites in Figure 12.27d would be significantly wider, resulting in a bigger linewidth for B sites in Figure 12.27d. The defect/disorder-containing phases of $\alpha\text{-Fe}_2\text{O}_3$ or the interface between $\alpha\text{-Fe}_2\text{O}_3$ and other phases is responsible for the observed modest shoulder (not considered in fitting) with smaller (but not bigger) hyperfine fields (at roughly 7 mm/s). The foregoing results are quite close to the measured areas of 64% and 36% of the Mössbauer spectrum obtained at 5 K for the inner sextet S7 (which associates with $\gamma\text{-Fe}_2\text{O}_3$ and $\alpha\text{-Fe}_2\text{O}_3$) and the outer sextet S5 (which associates with Fe_3O_4), respectively (although there is a strong overlap of the lines). The f -factors of A- and B-site Fe atoms were assumed to be identical in all of these area calculations for calculating the concentrations of $\gamma\text{-Fe}_2\text{O}_3$ and Fe_3O_4 . The f -factor of the A-site Fe atoms is somewhat larger than that of the B-site Fe atoms, but this does not significantly alter the results [121].

Figure 12.28a demonstrates the RT Mössbauer spectra of the magnetite NPs synthesized in different environments, which are employed in magnetic hyperthermia. The fitted parameters are given in Table 12.10 as well [122]. All spectra are well resolved considering two iron sites and using two distributions of the hyperfine magnetic field (B_{hf}), as anticipated for magnetite NPs with mean diameters <20 nm. Different isomer shift (δ) values are observed at two iron sites. The one with a higher mean-field (site 1) offers δ values from 0.27(1) to 0.31(1) mm/s and is designated to Fe^{3+} , while the one with lower B_{hf} (site 2) has δ values around 0.68(5) mm/s (except sample M-ag) and is a characteristic of $\text{Fe}^{2.5+}$ in bulk magnetite (mixture of Fe^{2+} and Fe^{3+}) [123]. Nevertheless, it is obvious that none of the samples comprise the relative amount of Fe^{3+} (site 1) and $\text{Fe}^{2.5+}$ (site 2) except for the sextets of iron in bulk magnetite, $[\text{Fe}^{3+}]_{\text{tet}}[\text{Fe}^{2+}, \text{Fe}^{3+}]_{\text{oct}}\text{O}_4$. According to the XRD data, the samples are better characterized as $\text{Fe}_{3-x}\text{O}_4$, indicating a high degree of oxidation. Despite having a high δ value at site 2, sample M-td had the smallest fraction of this site. The mean value of B_{hf} is also lower than the values seen in the other samples. This phenomenon is attributed to the ultrafine-sized particles with the lower mean particle size and distribution based on their corresponding TEM images. The degree of oxidation (x) in $\text{Fe}_{3-x}\text{O}_4$ NPs can be computed from the relative amount of each iron site (I); using Eq. (12.32) [124]. The results obtained are given in Table 12.10. It must be noted that this equation is not always true, e.g. since the δ value found for site 2 is far from 0.68 mm/s for the M-ag sample. From the results obtained, it is possible to deduce that the synthesis environment has the main role in the oxidation degree of the NPs, where the NPs synthesized in gelatin medium (M-gel) present the lower oxidation degree according to the following equation.

$$x = \frac{1.8 - I(\text{Fe}^{2.5+})/I(\text{Fe}^{3+})}{5.4 + 5I(\text{Fe}^{2.5+})/I(\text{Fe}^{3+})} \quad (12.32)$$



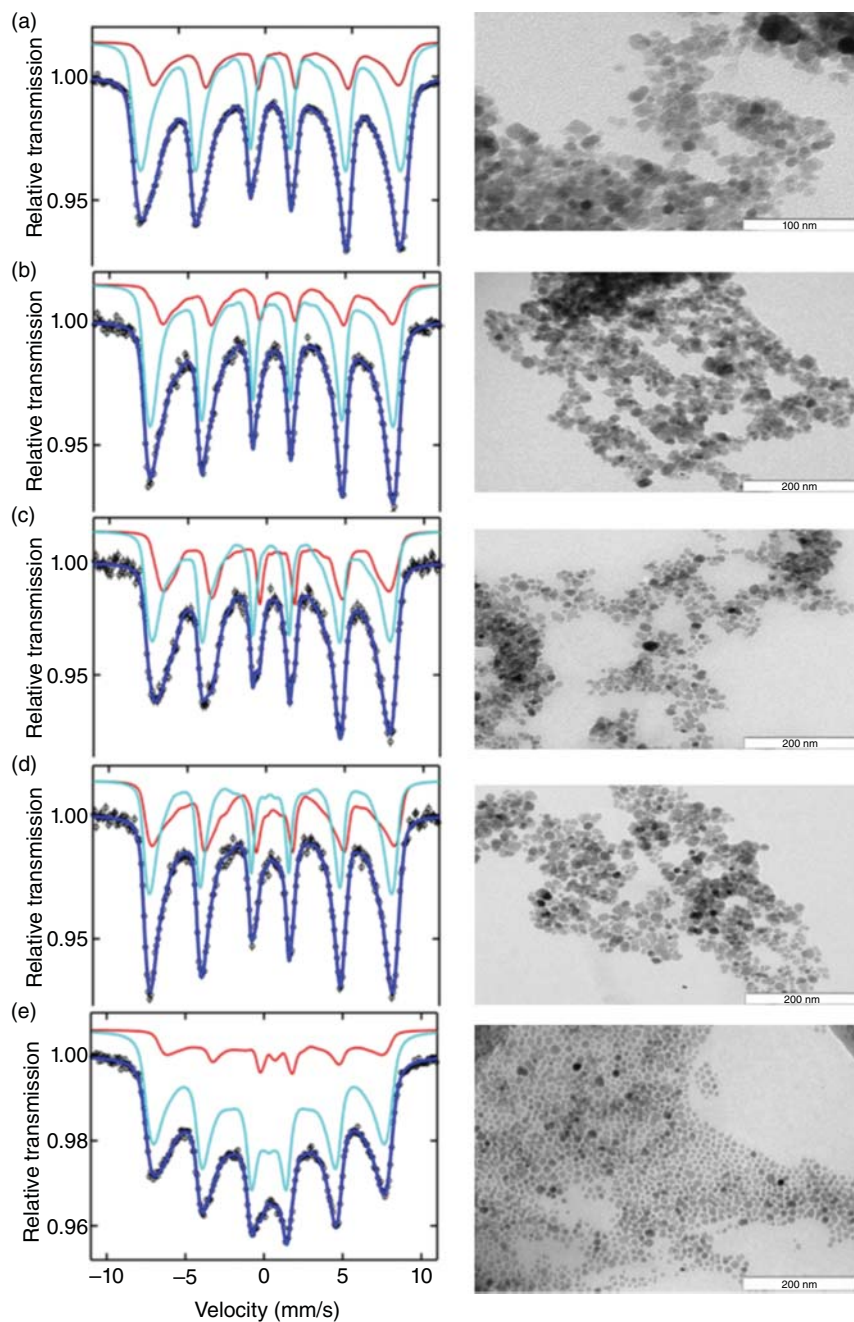


Figure 12.28 ^{57}Fe Mössbauer spectra of the magnetite NPs synthesized by the different methods: (a) M, (b) M-sf, (c) M-geI, (d) M-ag, and (e) M-td, and their corresponding TEM images in the right-hand side". Source: [124], A.F. Alves et al. (2016), Springer Nature.



Table 12.10 Mössbauer hyperfine fitting parameters for the as-synthesized magnetite NPs, where I is the relative area, Γ is line width, ε is quadrupole shift, δ is isomer shift, $\langle B_{\text{hf}} \rangle [\sigma]$ is the average hyperfine field and standard deviation of the magnetic field distribution, and x is the oxidation degree computed from Eq. (12.32).

Sample	Site	$\langle B_{\text{hf}} \rangle (\sigma)$ (T)	δ (mm/s)	ε (mm/s)	Γ (mm/s)	I (%)	x
M	1	42 (8)	0.30 (1)	−0.01 (1)	0.40	71.0	0.19
	2	38 (10)	0.64 (1)	0.05 (1)	0.35	29.0	
M-sf	1	43 (9)	0.31 (1)	−0.01 (1)	0.38	73.9	0.20
	2	40 (9)	0.69 (2)	0.02 (3)	0.41	26.1	
M-gel	1	42 (8)	0.27 (1)	0.01 (1)	0.32	59.4	0.13
	2	37 (11)	0.63 (2)	−0.05 (3)	0.32	40.6	
M-ag	1	43 (10)	0.27 (1)	−0.03 (2)	0.35	49.6	—
	2	39 (12)	0.49 (2)	−0.08 (3)	0.35	50.4	
M-td	1	33 (14)	0.31 (1)	0.01 (1)	0.55	81.4	0.24
	2	31 (13)	0.73 (2)	−0.09 (3)	0.45	18.6	

Source: Alves et al. [122]/with permission of Springer Nature.

12.6 Chemical Composition Evaluation Based on the Mössbauer Spectroscopy Spectra

The magnetic properties of totally localized ferrites, according to Néel's molecular field theory, are primarily determined by the strength of magnetic interactions between atoms in various A and B sites as well as the cation distribution. [125]. In a ferrimagnetic material, the anti-parallel A–B magnetic (super) exchange is the strongest, and both B–B and A–A (super) exchanges tend to be negative [125]. Because the inter-ionic distances and angles (proportional inversely to lengths and directly to angles) determine the intensities of these magnetic exchanges and superexchanges, the lengths and angles of cation–cation (Me–Me), cation–anion (Me–O), and Me–O–Me bonds must be investigated. Figure 12.29 exhibits the unique Me–Me (b, c, d, e, and f) and Me–O (p, q, r, s) bonds and Me–O–Me ($\theta_1, \theta_2, \theta_3, \theta_4, \theta_5$) angles in the spinel AB_2O_4 structure established with VESTA software [127]. The bond lengths and angles of the $\text{Mg}_{1-x}\text{Ni}_x\text{Fe}_2\text{O}_4$ NPs system can be calculated from the lattice parameter (a) and oxygen parameter (u); based on the XRD refinement results, one can estimate the bond lengths and angles of the $\text{Mg}_{1-x}\text{Ni}_x\text{Fe}_2\text{O}_4$ NPs system in accordance with the equations proposed by Lakhani et al. [128].

Figure 12.30a demonstrates the 78 K Mössbauer spectra of the $\text{Mg}_{1-x}\text{Ni}_x\text{Fe}_2\text{O}_4$ NPs. The spectra reveal two well-resolved Zeeman sextets assigned to the Fe^{3+} ions in the tetrahedral (A) and octahedral (B) sublattices, indicating ferrimagnetic behavior. The fine lines in the pictures indicate the spectrum fitting analytical results, while the dots represent the experimental data. The peak width (Γ), magnetic hyperfine field (H_{hf}), quadrupole splitting (Δ), isomer shift (IS), and the specified inversion factor are all provided in Table 12.11 as predicted hyperfine parameters recovered



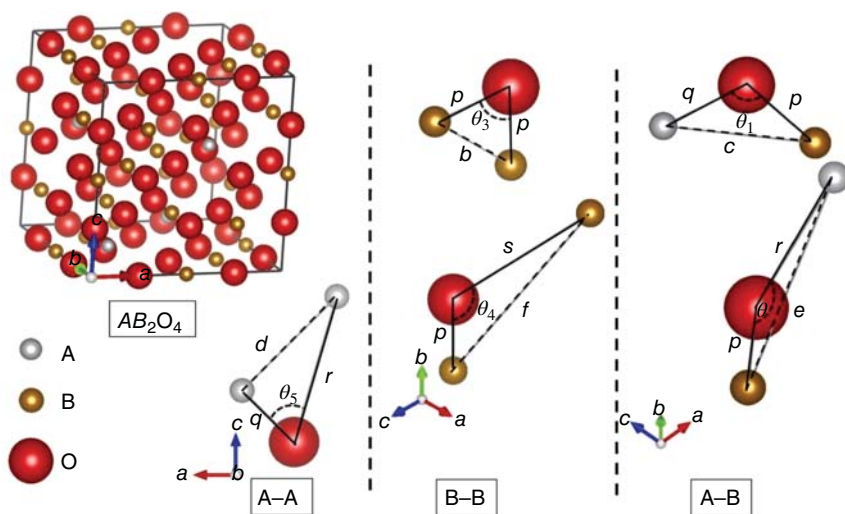


Figure 12.29 “The unique Me–Me and Me–O bonds and Me–O–Me angles in the spinel ferrite crystal structure with the A site at 8a ($1/8, 1/8, 1/8$) and B site at 16d ($1/2, 1/2, 1/2$)”. Source: Kassem et al. [126]/with permission of Elsevier.

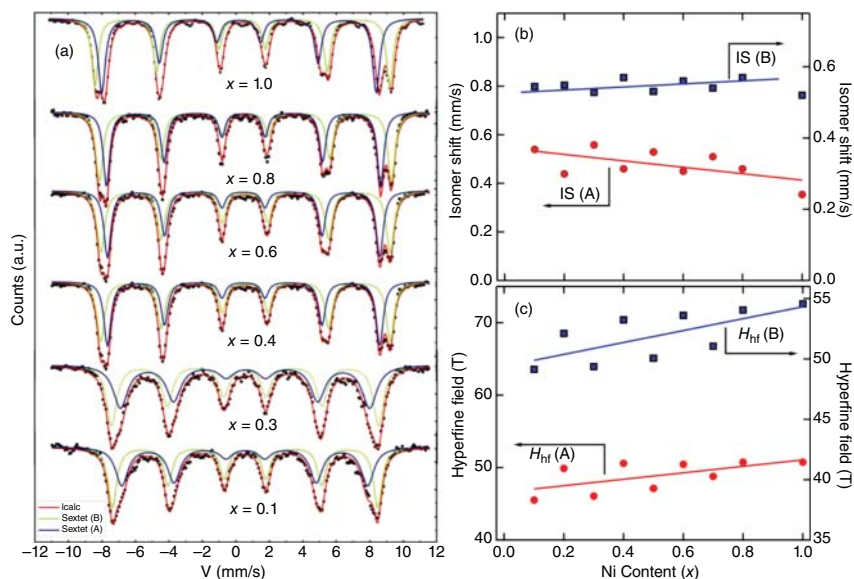


Figure 12.30 (a) 78 K Mössbauer spectra of $Mg_{1-x}Ni_xFe_2O_4$ NPs, and the dependency of (b) isomer shift and (c) hyperfine magnetic field on the Ni content. Source: Kassem et al. [126]/with permission of Elsevier.



Table 12.11 Mössbauer hyperfine parameters; the inversion factor (δ_{Moss}), peak width (Γ), magnetic hyperfine field (H_{hf}), isomer shift (IS), and quadrupole splitting (Δ) of $\text{Mg}_{1-x}\text{Ni}_x\text{Fe}_2\text{O}_4$ NPs.

x (Ni^{2+})	Site	IS (mm/s)	δ (mm/s)	H_{hf} (T)	Γ (mm/s)	Area (%)	δ_{Moss}
0.1	Sextet (A)	0.54	−0.017	45.52	0.45	45.22	0.905
	Sextet [B]	0.5444	0.0001	49.139	0.304	54.22	
0.2	Sextet (A)	0.4389	−0.0065	49.894	0.3	46.37	0.927
	Sextet [B]	0.5485	0.015	52.12	0.33	53.63	
0.3	Sextet (A)	0.558	−0.023	46.08	0.52	47.97	0.959
	Sextet [B]	0.528	0.008	49.37	0.368	52.03	
0.4	Sextet (A)	0.46	−0.0068	50.605	0.3	47.41	0.948
	Sextet [B]	0.57	0.0129	53.244	0.309	52.59	
0.5	Sextet (A)	0.531	−0.005	50.06	0.29	48.05	0.961
	Sextet [B]	0.529	−0.0013	47.14	0.41	51.95	
0.6	Sextet (A)	0.45	0.0044	50.45	0.25	47.73	1
	Sextet [B]	0.56	0.0112	53.613	0.27	52.27	
0.7	Sextet (A)	0.51	−0.025	48.79	0.378	48.8	0.990
	Sextet [B]	0.54	0.0054	51.065	0.279	51.2	
0.8	Sextet (A)	0.46	0.0006	50.757	0.23	49.6	0.992
	Sextet [B]	0.57	0	54.058	0.251	50.4	
1.0	Sextet (A)	0.354	0.005	50.75	0.50	50	1
	Sextet [B]	0.52	0.008	54.56	0.47	50	

Source: Kassem et al. [126]/with permission of Elsevier.

via spectral fitting. The Fe^{3+} ions at the B site present a larger hyperfine field in the sextet [129, 130]. Both the calculated Isomer shift (IS) and the hyperfine field (H_{f}) values are compatible with the high spin d^5 (Fe^{3+}) state, with $\text{IS} \approx 0.05 - 0.6$ mm/s and $H_{\text{hf}} \approx 22\langle S_z \rangle$, where $\langle S_z \rangle = 5/2$ [129, 131]. Figure 12.30b,c indicate the dependency of IS and H_{hf} on the Ni-content. The longer B—O bond compared to the A—O bond accounts for the higher IS for the B site compared to the A site, $\gamma = p/q > 1$. With Ni substitution, the shift in bond lengths explains the modest general drop in IS for the A site and the slight general increase for the B site. The existence of multiple hyperfine fields at the octahedral Fe^{3+} nuclei induced by the three cations (Fe^{3+} , Ni^{2+} , and Mg^{2+}) in the B site results in the attainment of wider B site sextet line width compared to the A site [84]. The H_{hf} enhances in general behaviors at both A and B sites, when nonmagnetic Mg^{2+} is replaced by magnetic Ni^{2+} , as shown in Figure 12.30c and Table 12.11, which can be explained by the likely additional positive transfer field from the further included Ni^{2+} magnetic ions. Additionally, the studied quadrupole splitting (Δ) slightly changes around zero in both A and B sites as previously discovered in the presence of strong magnetic interactions. The distribution of quadrupole interactions caused by chemical instability causes a noticeable expansion of the individual Zeeman lines but no shift in quadrupole line [132]. The relative areas of the corresponding sextets with the bulk (core and surface) yield



the Fe^{3+} ions concentrations at the A and B as well as the inversion factor (δ_{Moss}), as given in Table 12.11. It is evident that the Mössbauer spectroscopy yields a similar values of inversion factor and cation distribution to the values attained from the XRD refinement. This is more noticeable in the case of high Ni concentrations [126].

References

- 1 Coey, J.M. (2010). *Magnetism and Magnetic Materials*. Cambridge University Press.
- 2 Greenwood, N.N. (2012). *Mössbauer Spectroscopy*. Springer Science & Business Media.
- 3 Gonser, U. (1975). *Mössbauer Spectroscopy*. Berlin Heidelberg: Springer-Verlag.
- 4 Dickson, D.P. and Berry, F.J. (2005). *Mössbauer Spectroscopy*. Cambridge University Press.
- 5 Rancourt, D.G. (1998). Mössbauer spectroscopy in clay science. *Hyperfine Interactions* 117: 3–38.
- 6 Housley, R. and Hess, F. (1966). Analysis of Debye-Waller-factor and Mössbauer-thermal-shift measurements. I. General theory. *Physical Review* 146: 517.
- 7 Chen, Y.-L. and Yang, D.-P. (2007). *Mössbauer Effect in Lattice Dynamics: Experimental Techniques and Applications*. Wiley.
- 8 Wertheim, G.K. (1964). *Mössbauer Effect: Principles and Applications*. New York: Academic Press.
- 9 Danon, J. (1968). *Lecture Notes on the Mössbauer Effect*, Gordon and Breach. London, UK: Science Publishers Ltd.
- 10 Msomi, J.Z. (2007). Synthesis, structural and magnetic properties of bulk and nanosized $(\text{Zn}, \text{Cd}, \text{Cu})_{0.5}\text{Ni}_{0.5}\text{Fe}_2\text{O}_4$ and NiFe_2O_4 ferrites. PhD thesis. University of KwaZulu Natal.
- 11 Cadogan, J. and Ryan, D. (2006). Mössbauer spectroscopy. In: *Handbook of Applied Solid State Spectroscopy*, 201–256. Springer.
- 12 Chipaux, R. (1990). MOSPLV, a program for simulation of complex Mössbauer spectra in polycrystalline samples. *Computer Physics Communications* 60: 405–415.
- 13 Kalska-Szostko, B. (2000). Mössbauer spectroscopy on selected magnetic compounds. Doctoral dissertation. Acta Universitatis Upsaliensis.
- 14 Mørup, S., Hansen, M.F., and Frandsen, C. (2019). 1.04 magnetic nanoparticles. In: *Comprehensive Nanoscience and Nanotechnology*, 89–140. Amsterdam, The Netherlands: Elsevier.
- 15 Hajalilou, A., Mazlan, S.A., Lavvafi, H., and Shameli, K. (2016). *Field Responsive Fluids as Smart Materials*. Springer.
- 16 Hajalilou, A., Etemadifar, R., Abbasi-Chianeh, V., and Abouzari-Lotf, E. (2018). Electrophoretically-deposited nano- Fe_3O_4 @carbon 3D structure on carbon fiber as high-performance supercapacitors. *Journal of Electronic Materials* 47: 4807–4812.



- 17 Hajalilou, A., Abouzari-Lotf, E., Etemadifar, R. et al. (2018). Fabrication by electrophoretic deposition of nano- Fe_3O_4 and $\text{Fe}_3\text{O}_4@\text{SiO}_2$ 3D structure on carbon fibers as supercapacitor materials. *JOM* 70: 1404–1410.
- 18 Gawas, S.G., Meena, S.S., Bhatt, P., and Verenkar, V.M. (2018). Nanoscale-driven structural changes and associated superparamagnetism in magnetically diluted Ni–Zn ferrites. *Materials Chemistry Frontiers* 2: 300–312.
- 19 Harris, V.G. and Šepelák, V. (2018). Mechanochemically processed zinc ferrite nanoparticles: evolution of structure and impact of induced cation inversion. *Journal of Magnetism and Magnetic Materials* 465: 603–610.
- 20 Walker, L., Wertheim, G.K., and Jaccarino, V. (1961). Interpretation of the Fe^{57} isomer shift. *Physical Review Letters* 6: 98.
- 21 Šepelák, V., Bégin-Colin, S., and Le Caër, G. (2012). Transformations in oxides induced by high-energy ball-milling. *Dalton Transactions* 41: 11927–11948.
- 22 Long, G.J. and Grandjean, F. (2013). *Mössbauer Spectroscopy Applied to Inorganic Chemistry*. Springer Science & Business Media.
- 23 Šepelák, V., Düvel, A., Wilkening, M. et al. (2013). Mechanochemical reactions and syntheses of oxides. *Chemical Society Reviews* 42: 7507–7520.
- 24 Šepelák, V. and Becker, K. (2000). Mössbauer studies in the mechanochemistry of spinel ferrites. *Journal of Materials Synthesis and Processing* 8: 155–166.
- 25 Šepelák, V., Tkáčová, K., Boldyrev, V. et al. (1997). Mechanically induced cation redistribution in ZnFe_2O_4 and its thermal stability. *Physica B: Condensed Matter* 234: 617–619.
- 26 Šepelák, V., Baabe, D., Litterst, F., and Becker, K. (2000). Structural disorder in the high-energy milled magnesium ferrite. *Journal of Applied Physics* 88: 5884–5893.
- 27 Šepelák, V., Baabe, D., and Becker, K. (2000). Mechanically induced cation redistribution and spin canting in nickel ferrite. *Journal of Materials Synthesis and Processing* 8: 333–337.
- 28 Šepelák, V., Baabe, D., Mienert, D. et al. (2003). Evolution of structure and magnetic properties with annealing temperature in nanoscale high-energy-milled nickel ferrite. *Journal of Magnetism and Magnetic Materials* 257: 377–386.
- 29 Winkler, E., Zysler, R., Mansilla, M.V. et al. (2008). Surface spin-glass freezing in interacting core–shell NiO nanoparticles. *Nanotechnology* 19: 185702.
- 30 Menil, F. (1985). Systematic trends of the ^{57}Fe Mössbauer isomer shifts in (FeO_n) and (FeF_n) polyhedra. Evidence of a new correlation between the isomer shift and the inductive effect of the competing bond $\text{T-X} (\rightarrow \text{Fe})$ (where X is O or F and T any element with a formal positive charge). *Journal of Physics and Chemistry of Solids* 46: 763–789.
- 31 Millot, N., Bégin-Colin, S., Perriat, P., and Le Caër, G. (1998). Structure, cation distribution, and properties of nanocrystalline titanomagnetites obtained by mechanosynthesis: comparison with soft chemistry. *Journal of Solid State Chemistry* 139: 66–78.
- 32 Millot, N., Colin, S.B., Perriat, P. et al. (1999). Characterization of ferrites synthesized by mechanical alloying and soft chemistry. *Nanostructured Materials* 12: 641–644.



- 33 Guigue-Millot, N., Begin-Colin, S., Champion, Y. et al. (2003). Control of grain size and morphologies of nanograined ferrites by adaptation of the synthesis route: mechanosynthesis and soft chemistry. *Journal of Solid State Chemistry* 170: 30–38.
- 34 Šepelák, V., Indris, S., Heitjans, P., and Becker, K. (2007). Direct determination of the cation disorder in nanoscale spinels by NMR, XPS, and Mössbauer spectroscopy. *Journal of Alloys and Compounds* 434: 776–778.
- 35 Šepelák, V., Bergmann, I., Indris, S. et al. (2011). High-resolution ^{27}Al MAS NMR spectroscopic studies of the response of spinel aluminates to mechanical action. *Journal of Materials Chemistry* 21: 8332–8337.
- 36 Šepelák, V., Bergmann, I., Indris, S. et al. (2010). Nanocrystalline complex oxides prepared by mechanochemical reactions. In: *AIP Conference Proceedings*, 96–101. American Institute of Physics.
- 37 Nachbaur, V., Tauvel, G., Verdier, T. et al. (2009). Mecanosynthesis of partially inverted zinc ferrite. *Journal of Alloys and Compounds* 473: 303–307.
- 38 Srinivasamurthy, K., Manjunatha, K., El-Denglawey, A. et al. (2021). Dosimetry induced modifications in structural, magnetic and Mössbauer spectroscopy studies of ^{60}Co γ -irradiated $\text{Co}_{0.5}\text{Ni}_{0.5}\text{Fe}_2\text{O}_4$. *Radiation Physics and Chemistry* 189: 109781.
- 39 Matsnev, M. and Rusakov, V. (2012). SpectrRelax: an application for Mössbauer spectra modeling and fitting. In: *AIP Conference Proceedings*, 178–185. American Institute of Physics.
- 40 Srinivasamurthy, K., Angadi, V.J., Kubrin, S. et al. (2018). Evidence of enhanced ferromagnetic nature and hyperfine interaction studies of Ce-Sm doped Co-Ni ferrite nanoparticles for microphone applications. *Ceramics International* 44: 18878–18885.
- 41 Kurian, J., Lahiri, B., Mathew, M.J., and Philip, J. (2021). High magnetic fluid hyperthermia efficiency in copper ferrite nanoparticles prepared by solvothermal and hydrothermal methods. *Journal of Magnetism and Magnetic Materials* 538: 168233.
- 42 Kurian, J. and Mathew, M.J. (2018). Structural, optical and magnetic studies of CuFe_2O_4 , MgFe_2O_4 and ZnFe_2O_4 nanoparticles prepared by hydrothermal/solvothermal method. *Journal of Magnetism and Magnetic Materials* 451: 121–130.
- 43 Hajalilou, A., Ferreira, L., Jorge, M.M. et al. (2021). Superparamagnetic Ag- Fe_3O_4 composites nanoparticles for magnetic fluid hyperthermia. *Journal of Magnetism and Magnetic Materials* 537: 168242.
- 44 Dey, S., Dey, S., Ghosh, B. et al. (2013). Role of inhomogeneous cation distribution in magnetic enhancement of nanosized $\text{Ni}_{0.35}\text{Zn}_{0.65}\text{Fe}_2\text{O}_4$: a structural, magnetic, and hyperfine study. *Journal of Applied Physics* 114: 093901.
- 45 Hah, H., Gray, S., Johnson, C. et al. (2021). Mössbauer spectroscopy of superparamagnetic Fe_3O_4 nanoparticles. *Journal of Magnetism and Magnetic Materials* 539: 168382.
- 46 Berry, F.J., Skinner, S., and Thomas, M.F. (1998). ^{57}Fe Mössbauer spectroscopic examination of a single crystal of Fe_3O_4 . *Journal of Physics: Condensed Matter* 10: 215.



- 47 Sawatzky, G., Van Der Woude, F., and Morrish, A. (1969). Recoilless-fraction ratios for Fe^{57} in octahedral and tetrahedral sites of a spinel and a garnet. *Physical Review* 183: 383.
- 48 Kavkhani, R., Pourzaki, M., Kianvash, A. et al. (2021). Effect of sintering temperature and soaking time on the magnetic properties and transmission behavior of nano crystalline $\text{Mg}_{0.8}\text{Mn}_{0.2}\text{Al}_{0.1}\text{Fe}_{1.9}\text{O}_4$. *Journal of Sol-Gel Science and Technology* 99: 444–454.
- 49 Rezanezhad, A., Rezaie, E., Ghadimi, L.S. et al. (2020). Outstanding supercapacitor performance of Nd–Mn co-doped perovskite LaFeO_3 @nitrogen-doped graphene oxide nanocomposites. *Electrochimica Acta* 335: 135699.
- 50 Ghadimi, L.S., Arsalani, N., Ahadzadeh, I. et al. (2019). Effect of synthesis route on the electrochemical performance of CoMnFeO_4 nanoparticles as a novel supercapacitor electrode material. *Applied Surface Science* 494: 440–451.
- 51 Adli, R.G., Kianvash, A., Hosseini, M.G. et al. (2019). Facile and scalable synthesis of ultrafine MnCo_2O_4 nanoparticles via mechanical alloying as supercapacitive materials. *JOM* 71: 2396–2404.
- 52 Rezaie, E., Rezanezhad, A., Hajalilou, A. et al. (2019). Electrochemical behavior of $\text{SrFe}_{12}\text{O}_{19}/\text{CoFe}_2\text{O}_4$ composite nanoparticles synthesized via one-pot hydrothermal method. *Journal of Alloys and Compounds* 789: 40–47.
- 53 Rezaie, E., Rezanezhad, A., Ghadimi, L.S. et al. (2018). Effect of calcination on structural and supercapacitance properties of hydrothermally synthesized plate-like $\text{SrFe}_{12}\text{O}_{19}$ hexaferrite nanoparticles. *Ceramics International* 44: 20285–20290.
- 54 Adli, R.G., Kianvash, A., Hosseini, M.G. et al. (2018). Mechanochemically synthesized $\text{NiCo}_2\text{O}_4/\text{Vulcan}/\text{PANI}$ nanocomposite and investigation of its electrochemical behavior as a supercapacitor. *Ceramics International* 44: 20049–20057.
- 55 Etemadifar, R., Kianvash, A., Arsalani, N. et al. (2018). Green synthesis of superparamagnetic magnetite nanoparticles: effect of natural surfactant and heat treatment on the magnetic properties. *Journal of Materials Science: Materials in Electronics* 29: 17144–17153.
- 56 Mirzazadeh, A., Kianvash, A., and Hajalilou, A. (2018). Plating of Cu and Ni metals on Mg-ferrite sintered bodies by an electroless method and an investigation of magnetic behavior. *Journal of Materials Science: Materials in Electronics* 29: 5753–5760.
- 57 Hajalilou, A., Abouzari-Lotf, E., Abbasi-Chianeh, V. et al. (2018). Inclusion of octahedron-shaped ZnFe_2O_4 nanoparticles in combination with carbon dots into carbonyl iron based magnetorheological suspension as additive. *Journal of Alloys and Compounds* 737: 536–548.
- 58 Namvari, M., Kianvash, A., and Hajalilou, A. (2018). Influence of Ca–La and Cr-addition on the structure and magnetic characteristics of nanocrystalline Sr-hexaferrite powder. *Journal of Materials Science: Materials in Electronics* 29: 1435–1443.
- 59 Hajalilou, A., Mazlan, S.A., Abbasi, M., and Lavvafi, H. (2016). Fabrication of spherical CoFe_2O_4 nanoparticles via sol–gel and hydrothermal methods and investigation of their magnetorheological characteristics. *RSC Advances* 6: 89510–89522.



- 60 Hajalilou, A., Hashim, M., Ebrahimi-Kahrizsangi, R., and Kamari, H.M. (2015). Influence of evolving microstructure on electrical and magnetic characteristics in mechanically synthesized polycrystalline Ni-ferrite nanoparticles. *Journal of Alloys and Compounds* 633: 306–316.
- 61 Hajalilou, A., Kamari, H.M., and Shameli, K. (2017). Dielectric and electrical characteristics of mechanically synthesized Ni-Zn ferrite nanoparticles. *Journal of Alloys and Compounds* 708: 813–826.
- 62 Hajalilou, A., Kianvash, A., Lavvafi, H., and Shameli, K. (2018). Nanostructured soft magnetic materials synthesized via mechanical alloying: a review. *Journal of Materials Science: Materials in Electronics* 29: 1690–1717.
- 63 Hajalilou, A. and Mazlan, S.A. (2016). A review on preparation techniques for synthesis of nanocrystalline soft magnetic ferrites and investigation on the effects of microstructure features on magnetic properties. *Applied Physics A* 122: 1–15.
- 64 Rezanezhad, A., Hajalilou, A., Eslami, F. et al. (2021). Superparamagnetic magnetite nanoparticles for cancer cells treatment via magnetic hyperthermia: effect of natural capping agent, particle size and concentration. *Journal of Materials Science: Materials in Electronics* 32: 24026–24040.
- 65 Mikhaylova, M., Jo, Y., Kim, D.-K. et al. (2004). The effect of biocompatible coating layers on magnetic properties of superparamagnetic iron oxide nanoparticles. *Hyperfine Interactions* 156: 257–263.
- 66 Klekotka, U., Zambrzycka-Szelewa, E., Satuła, D., and Kalska-Szostko, B. (2021). Stability studies of magnetite nanoparticles in environmental solutions. *Materials* 14: 5069.
- 67 Kalska-Szostko, B., Wykowska, U., and Satuła, D. (2015). Magnetic nanoparticles of core-shell structure. *Colloids and Surfaces A: Physicochemical and Engineering Aspects* 481: 527–536.
- 68 Kalska-Szostko, B., Cydzik, M., Satuła, D., and Giersig, M. (2011). Mössbauer studies of core-shell nanoparticles. *Acta Physica Polonica A* 119: 3–5.
- 69 Druska, P., Steinike, U., and Šepelák, V. (1999). Surface structure of mechanically activated and of mechanosynthesized zinc ferrite. *Journal of Solid State Chemistry* 146: 13–21.
- 70 Oliver, S., Harris, V., Hamdeh, H., and Ho, J. (2000). Large zinc cation occupancy of octahedral sites in mechanically activated zinc ferrite powders. *Applied Physics Letters* 76: 2761–2763.
- 71 Hajalilou, A., Mazlan, S.A., and Shameli, K. (2016). A comparative study of different concentrations of pure Zn powder effects on synthesis, structure, magnetic and microwave-absorbing properties in mechanically-alloyed Ni-Zn ferrite. *Journal of Physics and Chemistry of Solids* 96: 49–59.
- 72 Hajalilou, A., Hashim, M., Abbasi, M. et al. (2015). A comparative study on the effects of different milling atmospheres and sintering temperatures on the synthesis and magnetic behavior of spinel single phase $\text{Ni}_{0.64}\text{Zn}_{0.36}\text{Fe}_2\text{O}_4$ nanocrystals. *Journal of Materials Science: Materials in Electronics* 26: 7468–7483.

- 73 Hajalilou, A., Hashim, M., Kamari, H.M., and Masoudi, M.T. (2015). Effects of milling atmosphere and increasing sintering temperature on the magnetic properties of nanocrystalline $\text{Ni}_{0.36}\text{Zn}_{0.64}\text{Fe}_2\text{O}_4$. *Journal of Nanomaterials* 16: 232.
- 74 Abdollah, H., Mansor, H., Reza, E.-K., and Taghi, M.M. (2015). Effect of milling atmosphere on structural and magnetic properties of Ni-Zn ferrite nanocrystalline. *Chinese Physics B* 24: 048102.
- 75 Hajalilou, A., Hashim, M., Ebrahimi-Kahrizsangi, R., and Sarami, N. (2015). Influence of CaO and SiO_2 co-doping on the magnetic, electrical properties and microstructure of a Ni-Zn ferrite. *Journal of Physics D: Applied Physics* 48: 145001.
- 76 Hajalilou, A., Hashim, M., and Kamari, H.M. (2015). Structure and magnetic properties of $\text{Ni}_{0.64}\text{Zn}_{0.36}\text{Fe}_2\text{O}_4$ nanoparticles synthesized by high-energy milling and subsequent heat treatment. *Journal of Materials Science: Materials in Electronics* 26: 1709–1718.
- 77 Masoudi, M.T., Saidi, A., Hashim, M., and Hajalilou, A. (2015). Comparison of structure and magnetic properties of Mn-Zn ferrite mechanochemically synthesized under argon and oxygen atmospheres. *Canadian Journal of Physics* 93: 1168–1173.
- 78 Hajalilou, A., Hashim, M., Kamari, H.M. et al. (2014). Synthesis of ZrC nanoparticles in the ZrO_2 -Mg-C-Fe system through mechanically activated self-propagating high-temperature synthesis. *Acta Metallurgica Sinica (English Letters)* 27: 1144–1151.
- 79 Hajalilou, A., Hashim, M., Ebrahimi-Kahrizsangi, R. et al. (2014). Carbo-silicothermic reduction of rutile to produce nano-sized particles of TiC and its composite with SiO_2 . *Metallurgical and Materials Transactions B* 45: 1615–1621.
- 80 Šepelák, V., Myndyk, M., Fabián, M. et al. (2012). Mechano-synthesis of nanocrystalline fayalite, Fe_2SiO_4 . *Chemical Communications* 48: 11121–11123.
- 81 Chinnasamy, C., Narayanasamy, A., Ponpandian, N. et al. (2001). Ferrimagnetic ordering in nanostructured CdFe_2O_4 spinel. *Journal of Applied Physics* 90: 527–529.
- 82 Šepelák, V., Schultze, D., Krumeich, F. et al. (2001). Mechanically induced cation redistribution in magnesium ferrite and its thermal stability. *Solid State Ionics* 141: 677–682.
- 83 Jiang, J., Goya, G., and Rechenberg, H. (1999). Magnetic properties of nanostructured CuFe_2O_4 . *Journal of Physics: Condensed Matter* 11: 4063.
- 84 Mahmoud, M., Hamdeh, H., Ho, J. et al. (2000). Mössbauer studies of manganese ferrite fine particles processed by ball-milling. *Journal of Magnetism and Magnetic Materials* 220: 139–146.
- 85 Lin, D., Nunes, A., Majkrzak, C., and Berkowitz, A. (1995). Polarized neutron study of the magnetization density distribution within a CoFe_2O_4 colloidal particle II. *Journal of Magnetism and Magnetic Materials* 145: 343–348.
- 86 Kodama, R.H., Berkowitz, A.E., McNiff, E. Jr., and Foner, S. (1996). Surface spin disorder in NiFe_2O_4 nanoparticles. *Physical Review Letters* 77: 394.

- 87 Kodama, R.H. and Berkowitz, A.E. (1999). Atomic-scale magnetic modeling of oxide nanoparticles. *Physical Review B* 59: 6321.
- 88 Hamdeh, H., Ho, J., Oliver, S. et al. (1995). Ferrimagnetic zinc ferrite fine powders. *IEEE Transactions on Magnetics* 31: 3808–3810.
- 89 Hamdeh, H.H., Ho, J.C., Oliver, S.A. et al. (1997). Magnetic properties of partially-inverted zinc ferrite aerogel powders. *Journal of Applied Physics* 81: 1851–1857.
- 90 Šepelák, V., Wißmann, S., and Becker, K. (1998). A temperature-dependent Mössbauer study of mechanically activated and non-activated zinc ferrite. *Journal of Materials Science* 33: 2845–2850.
- 91 Šepelák, V. and Becker, K. (2004). Comparison of the cation inversion parameter of the nanoscale milled spinel ferrites with that of the quenched bulk materials. *Materials Science and Engineering A* 375, 864: 861–A377.
- 92 Chinnasamy, C., Narayanasamy, A., Ponpandian, N. et al. (2000). Magnetic properties of nanostructured ferrimagnetic zinc ferrite. *Journal of Physics: Condensed Matter* 12: 7795.
- 93 Chinnasamy, C., Narayanasamy, A., Ponpandian, N., and Chattopadhyay, K. (2001). The influence of Fe^{3+} ions at tetrahedral sites on the magnetic properties of nanocrystalline ZnFe_2O_4 . *Materials Science and Engineering A* 304: 983–987.
- 94 Hofmann, M., Campbell, S., Ehrhardt, H., and Feyerherm, R. (2004). The magnetic behaviour of nanostructured zinc ferrite. *Journal of Materials Science* 39: 5057–5065.
- 95 Stewart, S.J., Figueroa, S., López, J.R. et al. (2007). Cationic exchange in nanosized ZnFe_2O_4 spinel revealed by experimental and simulated near-edge absorption structure. *Physical Review B* 75: 073408.
- 96 Figueroa, S. and Stewart, S. (2009). First XANES evidence of a disorder–order transition in a spinel ferrite compound: nanocrystalline ZnFe_2O_4 . *Journal of Synchrotron Radiation* 16: 63–68.
- 97 Li, F., Wang, L., Wang, J. et al. (2004). Site preference of Fe in nanoparticles of ZnFe_2O_4 . *Journal of Magnetism and Magnetic Materials* 268: 332–339.
- 98 Lemine, O., Sajieddine, M., Bououdina, M. et al. (2010). Rietveld analysis and Mössbauer spectroscopy studies of nanocrystalline hematite $\alpha\text{-Fe}_2\text{O}_3$. *Journal of Alloys and Compounds* 502: 279–282.
- 99 Lemine, O., Alyamani, A., Sajieddine, M., and Bououdina, M. (2009). Characterization of $\alpha\text{-Fe}_2\text{O}_3$ nanoparticles produced by high energy ball milling. In: *Proceedings of the 1st WSEAS International Conference on Nanotechnology*, 66–69.
- 100 Berchmans, L., Myndyk, M., Da Silva, K. et al. (2010). A rapid one-step mechanosynthesis and characterization of nanocrystalline CaFe_2O_4 with orthorhombic structure. *Journal of Alloys and Compounds* 500: 68–73.
- 101 Hirabayashi, D., Sakai, Y., Yoshikawa, T. et al. (2006). Mössbauer characterization of calcium–ferrite oxides prepared by calcining Fe_2O_3 and CaO . *Hyperfine Interactions* 167: 809–813.

- 102 Šepelák, V., Feldhoff, A., Heitjans, P. et al. (2006). Nonequilibrium cation distribution, canted spin arrangement, and enhanced magnetization in nano-sized MgFe_2O_4 prepared by a one-step mechanochemical route. *Chemistry of Materials* 18: 3057–3067.
- 103 Šepelák, V., Bergmann, I., Feldhoff, A. et al. (2007). Nanocrystalline nickel ferrite, NiFe_2O_4 : mechanosynthesis, nonequilibrium cation distribution, canted spin arrangement, and magnetic behavior. *The Journal of Physical Chemistry C* 111: 5026–5033.
- 104 Tsipis, E., Pivak, Y., Waerenborgh, J. et al. (2007). Oxygen ionic conductivity, Mössbauer spectra and thermal expansion of $\text{CaFe}_2\text{O}_{4-\delta}$. *Solid State Ionics* 178: 1428–1436.
- 105 Hudson, A. and Whitfield, H. (1967). Mössbauer effect studies on calcium ferrites. Part I. Temperatures above the Néel point. *Journal of the Chemical Society A: Inorganic, Physical, Theoretical* 376–378.
- 106 Šepelák, V., Becker, K.D., Bergmann, I. et al. (2009). A one-step mechanochemical route to core-shell Ca_2SnO_4 nanoparticles followed by ^{119}Sn MAS NMR and ^{119}Sn Mössbauer spectroscopy. *Chemistry of Materials* 21: 2518–2524.
- 107 Trömel, M.Z. (1969). Die Kristallstruktur der Verbindungen vom Sr_2PbO_4 -Typ. *Zeitschrift für anorganische und allgemeine Chemie* 371: 237–247.
- 108 Trömel, M.Z. (1967). Kristallstrukturdaten für Ca_2SnO_4 und Cd_2SnO_4 . *Naturwissenschaften* 54 (1): 17–18.
- 109 Šepelák, V., Becker, S.M., Bergmann, I. et al. (2012). Nonequilibrium structure of Zn_2SnO_4 spinel nanoparticles. *Journal of Materials Chemistry* 22: 3117–3126.
- 110 Da Silva, K.L., Menzel, D., Feldhoff, A. et al. (2011). Mechanosynthesized BiFeO_3 nanoparticles with highly reactive surface and enhanced magnetization. *The Journal of Physical Chemistry C* 115: 7209–7217.
- 111 Dachs, E., Geiger, C.A., von Seckendorff, V., and Grodzicki, M. (2007). A low-temperature calorimetric study of synthetic (forsterite + fayalite) $\{(\text{Mg}_2\text{SiO}_4 + \text{Fe}_2\text{SiO}_4)\}$ solid solutions: an analysis of vibrational, magnetic, and electronic contributions to the molar heat capacity and entropy of mixing. *The Journal of Chemical Thermodynamics* 39: 906–933.
- 112 Cruz, M., Ferreira, L., Ramos, J. et al. (2017). Enhanced magnetic hyperthermia of CoFe_2O_4 and MnFe_2O_4 nanoparticles. *Journal of Alloys and Compounds* 703: 370–380.
- 113 Ogholbeyg, A.B., Kianvash, A., Hajalilou, A. et al. (2018). Cytotoxicity characteristics of green assisted-synthesized superparamagnetic maghemite ($\gamma\text{-Fe}_2\text{O}_3$) nanoparticles. *Journal of Materials Science, Materials in Electronics* 29: 12135–12143.
- 114 S. Kanagesan, M. Hashim, S. Tamilselvan, N. Alitheen, I. Ismail, A. Hajalilou, K. Ahsanul, Synthesis, characterization, and cytotoxicity of iron oxide nanoparticles, *Advances in Materials Science and Engineering*, 2013 (2013), 710432, <https://doi.org/10.1155/2013/710432>.

- 115 Hajalilou, A., Mazlan, S.A., Shilan, S.T., and Abouzari-Lotf, E. (2017). Enhanced magnetorheology of soft magnetic carbonyl iron suspension with binary mixture of Ni-Zn ferrite and Fe_3O_4 nanoparticle additive. *Colloid and Polymer Science* 295: 1499–1510.
- 116 Nagar, H., Kulkarni, N.V., Karmakar, S. et al. (2008). Mössbauer spectroscopic investigations of nanophase iron oxides synthesized by thermal plasma route. *Materials Characterization* 59: 1215–1220.
- 117 Schmidbauer, E. and Keller, M. (2006). Magnetic hysteresis properties, Mössbauer spectra and structural data of spherical 250 nm particles of solid solutions Fe_3O_4 - γ - Fe_2O_3 . *Journal of Magnetism and Magnetic Materials* 297: 107–117.
- 118 Verwey, E. and Haayman, P. (1941). Electronic conductivity and transition point of magnetite (“ Fe_3O_4 ”). *Physica* 8: 979–987.
- 119 McNab, T., Fox, R., and Boyle, A. (1968). Some magnetic properties of magnetite (Fe_3O_4) microcrystals. *Journal of Applied Physics* 39: 5703–5711.
- 120 Bødker, F., Hansen, M.F., Koch, C.B. et al. (2000). Magnetic properties of hematite nanoparticles. *Physical Review B* 61: 6826.
- 121 Pascal, C., Pascal, J., Favier, F. et al. (1999). Electrochemical synthesis for the control of γ - Fe_2O_3 nanoparticle size. Morphology, microstructure, and magnetic behavior. *Chemistry of Materials* 11: 141–147.
- 122 Alves, A.F., Mendo, S.G., Ferreira, L.P. et al. (2016). Gelatine-assisted synthesis of magnetite nanoparticles for magnetic hyperthermia. *Journal of Nanoparticle Research* 18: 27.
- 123 Oh, S.J., Cook, D., and Townsend, H. (1998). Characterization of iron oxides commonly formed as corrosion products on steel. *Hyperfine Interactions* 112: 59–66.
- 124 Vandenbergh, R.E. and De Grave, E. (2013). Application of Mössbauer spectroscopy in earth sciences. In: *Mössbauer Spectroscopy*, 91–185. Springer.
- 125 Cullity, B.D. and Graham, C.D. (2011). *Introduction to Magnetic Materials*. Wiley.
- 126 Kassem, M., El-Fadl, A.A., Hassan, A. et al. (2021). Structure and cationic distribution dependent soft magnetic properties of single-domain $\text{Mg}_{1-x}\text{Ni}_x\text{Fe}_2\text{O}_4$ ($0 \leq x \leq 1.0$) nanocrystals. *Materials Science and Engineering B* 274: 115494.
- 127 Momma, K. and Izumi, F. (2008). VESTA: a three-dimensional visualization system for electronic and structural analysis. *Journal of Applied Crystallography* 41: 653–658.
- 128 Lakhani, V., Pathak, T., Vasoya, N., and Modi, K. (2011). Structural parameters and X-ray Debye temperature determination study on copper-ferrite-aluminates. *Solid State Sciences* 13: 539–547.
- 129 Ugendar, K., Babu, V.H., Reddy, V.R., and Markaneyulu, G. (2019). Cationic ordering and magnetic properties of rare-earth doped NiFe_2O_4 probed by Mössbauer and X-ray spectroscopies. *Journal of Magnetism and Magnetic Materials* 484: 291–297.

- 130 Amer, M. and El Hiti, M. (2001). Mössbauer and X-ray studies for $\text{Ni}_{0.2}\text{Zn}_x\text{Mg}_{0.8-x}\text{Fe}_2\text{O}_4$ ferrites. *Journal of Magnetism and Magnetic Materials* 234: 118–125.
- 131 Hodges, J., Short, S., Jorgensen, J. et al. (2000). Evolution of oxygen-vacancy ordered crystal structures in the perovskite series $\text{Sr}_n\text{Fe}_n\text{O}_{3n-1}$ ($n = 2, 4, 8$, and ∞), and the relationship to electronic and magnetic properties. *Journal of Solid State Chemistry* 151: 190–209.
- 132 Mahmoud, M. and Sattar, A. (2004). Mössbauer study of Cu–Zn ferrite substituted with rare earth ions. *Journal of Magnetism and Magnetic Materials* 277: 101–105.

13

Application of Magnetic Nanoparticles

13.1 Introduction

Magnetic nanoparticles have been an intensive subject of research. These particles have unique and unexpected chemical and physical properties, a large surface-to-volume ratio, and a large number of defects that exist at/or close to the surface of the particles. Such properties can be controlled by modifying the intrinsic properties of the nanoparticles, i.e. shape, size, and distribution. These properties affect magnetic saturation, coercivity, magnetization, and magnetic loss [1–15]. This allows engineering magnetic nanoparticles with specific properties for various applications, including high-density recording, color imaging, ferrofluids, high-frequency devices, magnetic refrigerators, energy storage devices, and drug delivery [1–8]. In medical science, they have been widely used in cancer therapy and drug delivery and as contrast agents in magnetic resonance imaging (MRI). Also, emerging applications of magnetic nanoparticles are appearing in various fields, including defense and energy (solar cells, capacitors, batteries, etc.). Therefore, the selection of the synthesis route is an important factor for engineering magnetic nanoparticles with the desired shape, size, and distribution that are tailor-made for specific applications.

13.2 Magnetic Nanoparticles: Application in Engineering

Here we give an overview of the applications of magnetic nanoparticles in several fields:

13.2.1 Mechanical and Materials Engineering: Magnetic Nanoparticles in Magnetorheological Fluids (MRF)

Magnetorheological fluids (MRF) are typically composed of micron-sized soft magnetic particles suspended in an aqueous carrier or nonmagnetic fluid. Their rheological properties such as shear viscosity and yield stress are intensely dependent on both the MRF's constituent and an applied magnetic field strength [7, 16–21].

Magnetic Nanoparticles: Synthesis, Characterization, and Applications, First Edition.

Abdollah Hajalilou, Mahmoud Tavakoli, and Elahe Parvini.

© 2023 WILEY-VCH GmbH. Published 2023 by WILEY-VCH GmbH.

Indeed, the fluid represents usually Newtonian behavior in the absence of an externally applied field. However, a unique phase transition from a liquid-like to a solid-like state within milliseconds occurs in the presence of a magnetic field [7, 16–21]. This is due to the alignment of dispersed magnetic particles in the field direction, which results in a chain-like structure. The rheological effect is typically influenced by the state of magnetic particles, i.e. type, shape, size, and distribution as well as the carrier fluid type and surfactant [7]. Thus, a broad range of engineering applications is anticipated by optimum control of the states [7, 22].

Several types of micron-sized soft magnetic species like Ni–Zn ferrite, carbonyl iron (CI), and Fe_3O_4 are widely used as magnetic particles [7]. Among them, CI is more popular due to its favorable magnetic properties, e.g. high saturation magnetization (M_s) and low coercivity (H_c). On the other hand, a higher density of CI (about 7.87 g/cm^3) compared with a continuous medium restricts its magnetorheological (MR) applications due to the sedimentation issue. In other words, a large density difference between the magnetic particles and the continuous medium causes a serious dispersion problem such as sedimentation in MRF. Generally, three main techniques have been proposed and undertaken to address this problem: inclusion of nanoparticles as an additive into MR suspension [7, 9–21], bi-dispersing of nano and micron-sized particles [23], and coating of the employed micron-sized magnetic particles [17]. Each of these methods presents some advantages and disadvantages. For instance, the coating process reduces the density of magnetic particles remarkably. Also, it is difficult to control the coating thickness, which is mainly dependent on various parameters such as the reactive agent molar ratio and temperature. Therefore, the introduction of magnetic nanoparticles such as Fe_3O_4 as an additive into MR suspension is prevailing owing to the prevention effect against the mutual contacts of magnetic particles, which leads to an improvement of the rheological effects in the case of hard baking. In the case of the bi-dispersing state of particles, since the use of magnetic particles in MR suspension is 50 : 50 (50 wt% nanoparticles, and 50 wt% micron-sized particles), the strength of the formed chain-like structure is not as much as strong compared to the nanoparticles-additive-based MR suspension. The mechanism of the inclusion of nanoparticles into MR suspension is given in Ref. [19]. In brief, once the magnetic nanoparticles are added to the MR suspension, they fill the cavity and pores of the micron-sized magnetic particles and make a strong chain-like structure in the presence of an applied magnetic field, as shown in Figure 13.1.

13.2.2 Environmental Engineering: Magnetic Nanoparticles in Wastewater Treatment

Recently, the application of magnetic nanomaterials has been explored in wastewater treatment. This is related to one of the major applications of nanomaterials, i.e. adsorption. Adsorption is a process of accumulation of adsorbate from bulk gas, solid, or liquid on the adsorbent surface (Figure 13.2). Adhesion of atoms, ions, or molecules on the surface of the adsorbent could also be considered as adsorption. Adsorbate is the substance that adsorbs on the surface, whereas adsorbent is the

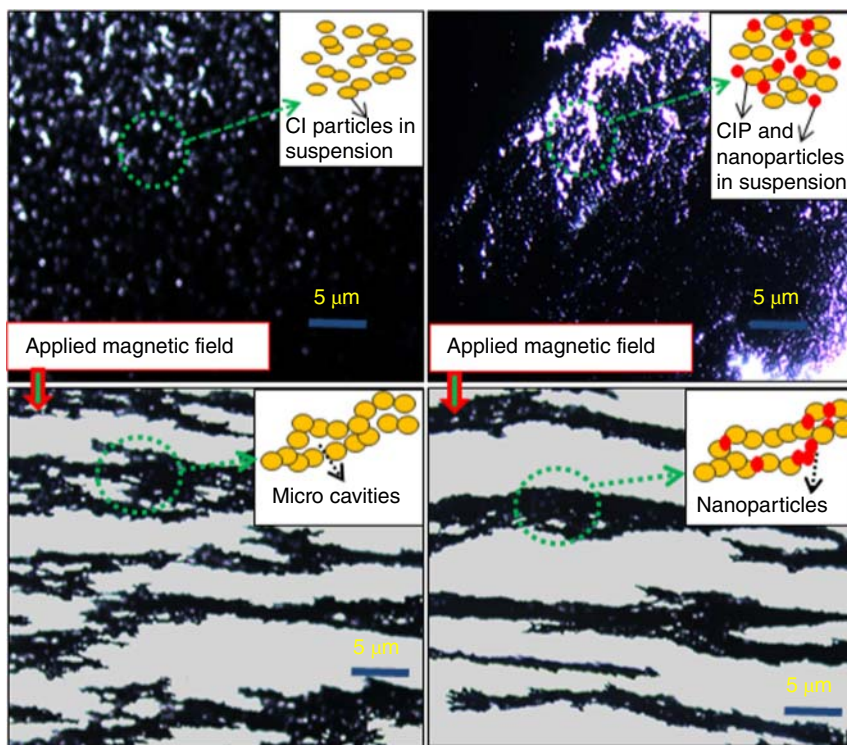
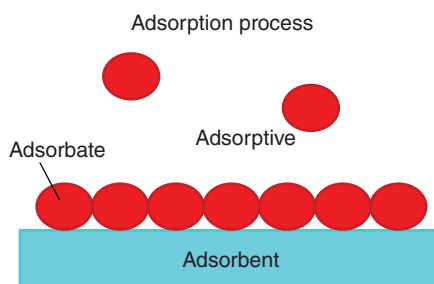


Figure 13.1 Presentation of chain formation mechanism by optical microscopy images taken from MR suspensions in the presence and absence of nanoparticle additives under an applied magnetic field. Source: [19], A. Hajalilou et al. (2016), ELSEVIER.

Figure 13.2 Adsorbent and adsorbate in the adsorption process.



substance that adsorbs the adsorbate. Any kind of metal oxide including iron oxide nanoparticles (IONPs) is known as an effective and low-cost adsorbent in wastewater treatment. IONPs possess higher adsorption capacity and faster kinetic because of having a high surface area, high diffusion of the intraparticle, and a large number of surface reaction sites such as vacancies, defects, edges, and corners. Modification of the IONP structure by introducing vacancies creates a new site of adsorption [24]. It has become the attention of many researchers to evaluate and reveal the underlying mechanism responsible for the contaminant removal in wastewater.

As discussed in Chapter 5, there are two types of the adsorption process, which are chemical adsorption and physical adsorption. Chemical adsorption involves the covalent bond of adsorbate with the surface of the adsorbent. For specific adsorption, it could happen due to the affinity of certain species to the surface of the adsorbent. The specific adsorption involves direct coordination of the adsorbate on the surface of the adsorbent. There is no solvent molecule between adsorbed species and the adsorbent. In contrast, physical adsorption occurs due to the contribution of weak forces such as electrostatic interaction, hydrogen bonding, and van der Waals interactions. Non-specific adsorption is dominated by electrostatic interaction. At least 1 mol of hydrogen is interposed between the adsorbent and adsorbate surface. The adsorbate will attach to the surface of the adsorbent until the surface is fully saturated.

Organic anion and organic compounds could be removed from the wastewater by introducing chelating agents such as surfactant on the IONP surface. The adsorption of the organic ligand is usually dominated by electrostatic effects, and ligand exchange and hydrogen bonds may be involved [25]. Filius et al. reported the entire adsorption of the organic compound due to the electrostatic forces and hydrogen bonding with the surface of hydroxyl groups [26].

IONPs coated with cetyltrimethylammonium bromide (CTAB) as an adsorbent were used to adsorb and remove amaranth (AM) from an aqueous solution in one study [27]. The adsorption and desorption of AM were found to be quite efficient using the new magnetic separation. The Langmuir equation well matches the adsorption data in an aqueous solution of AM at 25 °C, with a maximum adsorption amount of 1.05 mg/mg and a Langmuir adsorption equilibrium constant of 0.901/mg. Using methanol for desorption of adsorbed AM, the influence of temperature, pH of the aqueous medium, electrolyte content, the composition of adsorbent solvent, and interfering ions on the recovery process were also investigated. Because there was no internal diffusion resistance, both adsorption and desorption of AM were quick, taking only five minutes. According to the findings, the CTAB-coated IONPs might be used to remove the anionic dye from wastewater. In spiked samples of Karoon River water, the AM was successfully eliminated [27]. The mechanism of the wastewater is schematically illustrated in Figure 13.3.

Nowadays, magnetic nanoparticles, such as IONPs are considered as potential adsorbents. One reason for this is due to the extremely small size of IONPs, which yields a large surface area per unit volume. In addition, the highly active surface sites give rise to high adsorption capability on the surface of IONPs. The use of IONPs

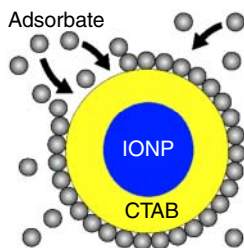


Figure 13.3 CTAB-coated iron oxide nanoparticles (IONPs) in wastewater treatment.

as adsorbents accelerates wastewater treatment by using the capability of IONPs as one of the magnetic materials that can be easily separated from the wastewater after treatment by supplying an external magnetic field [28].

Removal of *p*-chlorophenol (4-CP)-contaminated wastewater by using a combination of pulsed discharged plasma process with IONPs was studied by Lei et al. [29]. The degradation of 4-CP was completed by Fenton's reaction that occurs on the surface of IONPs. Fenton's reaction is a process of energizing electron-producing hydroxyl radicals due to the ionization of H_2O molecules. The hydroxyl molecule combined forming hydrogen peroxide that reacts with ferrous ions at the surface of IONPs contributed to the production of ferric ions that take the role in degrading 4-CP substances. As the amount of IONPs was increased, the removal efficiency of 4-CP also increased.

Many factors affect the removal efficiency of contamination. Panasiuk studied the effect of the Fe(II)/Fe(III) ratio of IONPs and the concentration of contamination substances on the performance of IONPs in wastewater treatment [30]. It was found that the effectiveness of phosphorus removal using IONPs declined as the Fe(II)/Fe(III) ratio enhanced. Also, as the concentration of phosphorus in the wastewater increased, the effectiveness of IONPs in removing phosphorus substances was reduced. This is because the same amount of IONPs cannot afford to adsorb a high amount of phosphorus as the amount of phosphorus content in the wastewater increases. Importantly, the IONPs were able to recover after the second and third time of the adsorption process. Zhang et al. found that the removal efficiency of IONPs almost remains constant even after reusing over six cycles [31]. IONPs modified with graphene oxide and Mg_3Al-OH -layered composites were able to remove the high capacity of heavy metal Pb(II) and hydrophobic organic pesticide 2,4-dichlorophenoxyacetic acid (2,4-D) from an aqueous solution. The effectiveness of IONPs in removing the substances was increased as the amount of graphene oxide increased in the composites.

IONPs can remove some metals in wastewater from industries and synthetic wastewater, but it has a high dependency on the amount of IONPs, size of particles, contact time between IONPs and wastewater, and pH value of the solution [32]. Owing to the competition of proton and heavy metals from the oxide surface site at a low pH value, only a small percentage of removal of heavy metals was detected. It was stated that the type of chelator results in either inhibiting or enhancing the heavy metal removal by surface modification of IONPs. In Ref. [33], the surface of IONPs was modified with polypyrrole-magnetite (PPy- Fe_3O_4) NPs via an *in situ* chemical oxidative polymerization route and employed for highly toxic hexavalent chromium (Cr(VI)) elimination in synthetic wastewater. The magnetic separation efficiency at 0.2 l/min indicated that increasing Fe_3O_4 content in the nanocomposite from 40.5% to 58.5% increased the separation efficiency from 81–98% to 66–84% with and without 30 g of stainless-steel wool packing under a magnetic field, respectively. Continuous operation results indicated that with a 5 l working volume and 20 mg/l of Cr(VI) aqueous solution, a 30 minutes initial residence time was enough to obtain 100% Cr(VI) removal and magnetic separation efficiency. These findings present the feasibility of the magnetic adsorption separation device in

treating a large volume of wastewater in both semi-continuous and continuous operation modes based on permanent magnets.

In similar research, magnetic biochar that was prepared from eucalyptus leaf residue was employed to eliminate heavy metals such as Ni(II), Cu(II), total Cr, Cr(VI), and Cu(II) in electroplating wastewater [34]. These heavy metals were effectively removed from wastewater with removal rates of 100%, 100%, 97.63%, and 97.11%, respectively. These results show very well the effectiveness of IONPs in wastewater treatment.

13.2.3 Surface Engineering

Surface engineering refers to manipulating the surface of nanoparticles for a specific application. Since magnetic nanoparticles, such as IONPs are widely utilized in medical science, it is often required to modify their surface in order to reduce their toxicity and increase their biocompatibility and stability. As discussed in Chapter 5, several techniques can be applied to modify the surface of magnetic nanoparticles. For surface modification of magnetic nanoparticles for medical aspects, one should consider two main factors: first, the coating or the shell layer should not cause a large increase in the particles size; and second, it should not cause a large decrease in magnetic properties due to a thick coating layer or shell [17, 35]. Both of these factors can limit the application of MNPs, e.g. in magnetic hyperthermia.

13.2.4 Tissue Engineering (TE)

TE is an interdisciplinary field that targets repair, replacement, retaining, or increasing tissue and organ-level functions. Some of the current obstacles to TE approaches include a lack of techniques for capturing appropriate physiological architectures, ineffective cell growth, existing limitations in biomaterials, and unstable and insufficient production of growth factors to stimulate cell communication and proper response. One can add to this list the inability to control cellular functions and their various characteristics, including electrochemical, mechanical, and biological, and concerns of biomolecular detection and biosensors. Magnetic nanoparticles are at the forefront of nanotechnology, and their distinctive size-dependent properties have proven promising materials in overcoming several issues encountered by TE today [36]. This is because magnetic nanoparticles have been employed to assemble more complex tissue structures than those that are obtained by conventional scaffold-based TE strategies. Moreover, intracellular delivery of magnetic nanoparticles allowed cell positioning by appropriate use of magnetic field and created cellular cluster. They are also utilized to control the cell's function [37].

Despite remarkable progress in the use of nanoparticles over the last decades, the full potential of the applications of nanoparticles in remedying TE issues has yet to be realized. Several papers, e.g. Refs. [36–41], have considered those issues.

13.3 Magnetic Nanoparticle Application in Energy

Recent advances in electrical cars, mobile devices, the Internet of Things (IoTs), and the Internet of Medical Things (IoMTs) require the fabrication of novel energy storage devices that are light, compact, efficient, and environmentally friendly.

13.3.1 Supercapacitors and Batteries

Supercapacitors, which are also known as ultra-capacitors or electrochemical capacitors, are among the most applicable candidates to settle down the forgoing-mentioned issues by having long cycle life, high power density, safe operation, and low-cost maintenance. These properties make them an attractive option as storage devices in electronics [1, 2, 35, 42]. Three main types of supercapacitors are (i) double-layer capacitors (DLCs), (ii) pseudocapacitors, and (iii) hybrid supercapacitors. The DLCs generally have more power density but less energy density than batteries, and they store charge between electrode and electrolyte [43]. Carbon-based materials such as graphene and carbon xerogels are among the most employed materials for this purpose. Pseudocapacitors accumulate energy via reduction and oxidation reactions. Pseudocapacitors typically have higher capacitance than double-layer ones. Conducting polymers, metal hydroxides, and metal oxides are the most popular materials for pseudocapacitors. Contrarily, hybrid supercapacitors contain faradic and non-faradic reactions, which support high cycle life. Composite materials like polymer/carbon/metal oxides have been developed for this purpose.

More recently, several magnetic nanoparticles such as iron oxides and metal oxides have been used in supercapacitor and battery applications as electrode or energy storage materials [1, 2, 35, 42–47]. Most of them are considered nanomaterials due to their higher surface-to-volume ratio aspect, but the effects of magnetic catachrestic such as saturation magnetization (M_s) and coercivity (H_c) on the electrochemical have not been taken into account frequently. Thus, close communication between chemists and physicists' researchers together with materials scientists is required to grasp this phenomenon.

13.3.2 Solar Cells

Magnetic nanoparticles have drawn great attention in solar or photovoltaic cell fields due to their several advantages as they behave like a magnetic dipole with a permanent magnetic moment that could be easily manipulated by an external magnetic field when the size of particles is less than 20 nm. Furthermore, their magnetization appears to be zero on average yet with the absence of an external magnetic field, due to the fact that remanence and coercivity of the nanoparticle are small enough to be negligible. All these features make magnetic nanoparticles potential for being incorporated into photovoltaic devices because of their small size and their large magnetic

susceptibility [48]. The strategy is based on a quantum physical principle, which suggests that electrons have a kind of internal rotation, known as spin. According to the quantum physics laws, this spin has a value of $1/2$. The positively charged hole also has a spin of $1/2$. The two spins can either add up if they are in the same direction or cancel out each other if they are in opposite directions. The electron–hole pair can hence have an overall spin of 0 or 1. Pairs with a spin of 1 exist for longer than those with an overall spin of 0.

The researchers set out to find a material that was able to convert the spin 0 states into a spin 1 state. This required nanoparticles of heavy elements, which flip the spin of the electron or the hole so that the spins of the two particles are aligned in the same direction. The iron oxide magnetite (Fe_3O_4) is in fact able to do just this. Adding magnetite nanoparticles to the substrate increased the efficiency of the solar cells by up to 11% [49]. The effect of doping various magnetic materials nanoparticles, including ferromagnetic and superparamagnetic Fe_3O_4 , ZnFe_2O_4 , and NiFe_2O_4 nanoparticles, into organic solar cells (OSCs) are studied by impedance spectroscopy (IS). It was found that the solar cell performance increases by the charge carrier's effective lifetime extension [50]. The photovoltaic solar cell's performance directly relies on the magnetic moment and alignment of the superparamagnetic single-domain magnetic nanoparticles. Alignment of the magnetic nanoparticles within the organic solar cells' active layer gives rise to dipole–dipole interaction, which results in further improvement of photovoltaic performance because of efficient charge collection at the short-circuit condition [50]. A negative influence on the device performance was found in the case of ferromagnetic nanoparticle doping. However, in dark conditions, devices doped with CoFe_2O_4 showed higher forward current presumably owing to leakage current through the large MNPs aggregation or electron-polaron hopping [50].

13.4 Magnetic Nanoparticles Application in Medical Science

The goal of the field of nanomedicine or biomedicine is to develop nanoparticles with a particular characteristic for application in the health sector. Magnetic nanoparticles are desirable candidates in MRI as contrast agents, magnetic sorting and separation, biomarker labeling, drug delivery, magnetic hyperthermia, cellular activity control, and gene transfer. The main reason for the interest in magnetic nanoparticles is the possibility of manipulating these particles by penetration of a magnetic field through the tissues. This is a major positive point as compared to the optical control of nanoparticles, e.g. laser-based manipulation, whose penetration through tissues usually suffers great loss. A magnetic field can be used to physically move the particles to the desired region of the body. Moreover, a low magnetic background induced by biological substances results in the achievement of a high signal-to-noise ratio and low electrical and magnetic interference.

13.4.1 Magnetic Resonance Imaging (MRI)

MRI is a powerful diagnostic tool for the detection of diseases. The imaging depends on the magnetic moment of protons in the region of the body [51–56]. When a large static magnetic field, e.g. 1.5–7 T, is applied to the protons, nuclear spins are aligned in the direction of the applied magnetic field, either parallel or anti-parallel. Thus, the nuclear spins cause an induced net moment in the region. The net moment undergoes processional movement with respect to the magnetic field direction. The precession frequency (ω), which is defined as Larmor frequency, is given as:

$$\omega = \gamma \cdot B_0 \quad (13.1)$$

where B_0 is the external magnetic field strength and γ is the gyro-magnetic ratio, an intrinsic parameter of the material.

If the static magnetic field is constantly applied, an equilibrium status will be obtained with the net moment processing around the field. In MRI, radiofrequency (RF) pulses are introduced into the system to interrupt the equilibrium state. After the application of an RF pulse, some nuclear spins will flip their direction from parallel to anti-parallel or vice versa as shown in Figure 13.4. At this time, the moment can be decomposed into the transverse component and longitudinal component with respect to the external magnetic field. It takes a certain amount of time for nuclear spins to come back to the equilibrium status, which is called the relaxation time. There are two types of relaxation time, namely T_1 and T_2 . T_1 relaxation time is a measure of time cost for longitudinal components to relax back. T_2 relaxation time is a measure of the time cost of the transverse component to relax back to its original state. Relaxation time is characteristic of biological matters due to the different content of water or hydrogen atoms. By coding different relaxation time lengths, contrasted images can be formed which makes the technique capable to examine a particular biological part of interest.

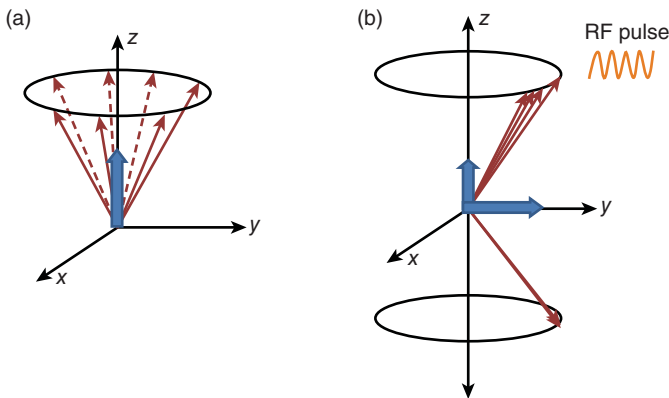


Figure 13.4 Schematic representation of the alignment of the magnetic moment of protons in magnetic resonance imaging (a) without and (b) with RF pulse input. Source: Adapted from Refs. [57, 58].

Magnetic nanoparticles are utilized as T_2 contrast agents in MRI. A dipolar field from the magnetic moment of particles poses an inhomogeneous field surrounding the protons nearby. The field accelerates the de-phasing of protons and shortens the time for spins to relax back to the state of zero net transverse moments.

Magnetite particles have been mostly studied and are available for clinical use. However, they are not necessarily the optimal candidate for MRI contrast agents [59]. Figure 13.5 show the changes in MRI signal intensity for Mn ferrite NPs (MF_1) and Mn ferrite@SiO₂ (MFS_1) samples with time and sample concentration. The MF_1 exhibits a higher ability as a T_2 contrast agent with an apparent decrease in MR signals with time and a higher decrease in contrast as concentration increases. The relaxivity r_2 value of MF_1 was found to be $1.04 \mu\text{g}/\text{ml}^{-1} \text{ s}^{-1}$ higher than MFS_1 , which was $0.32 \mu\text{g}/(\text{ml s})^{-1}$. This indicates that the ability of MF_1 to induce local magnetic inhomogeneity was higher than MFS_1 , and it has the potential to be used as an MRI T_2 contrast agent. For comparison, a study measuring synthesized manganese-ferrite in nanocomposites (14 nm particle size) at 3 T showed an r_2 value of $74 \text{ mmol}^{-1} \text{ s}^{-1}$. Another study of synthesized manganese ferrite nanoparticles coated with silica showed an r_2 value of $60.65 \text{ mmol}^{-1} \text{ s}^{-1}$ (14 nm particle size) when measured at 4.7 T. When compared with commercial T_2 MRI contrast agents, ferumoxides (Feridex) developed by AMAG Pharma (hydrodynamic diameter ~ 200 nm) reported an r_2 value of $98.3 \text{ mmol}^{-1} \text{ s}^{-1}$ while Resovist (Ferucarbotran) developed by Schering AG (hydrodynamic diameter > 50 nm) declared r_2 value of $151 \text{ mmol}^{-1} \text{ s}^{-1}$ at 1.5. Thus, by comparing the r_2 values reported in this study with other manganese-based nanoparticles and commercial T_2 MRI contrast agents, we conclude that MF_1 can be used as an MRI T_2 contrast agent.

According to the principle, the strength of the dipolar field affects how well the particles enhance the contrast. The dipolar field of a nanoparticle is given as:

$$H = \sum_{ij} \frac{3\vec{n}(\vec{m}_j \cdot \vec{n}) - \vec{m}_j}{|r_{ij}|^3} \quad (13.2)$$

where m_j and m_i are the moments of the i th and j th atom, n is the field direction, and r_{ij} is the distance between i th and j th atom. The spatial distribution of the dipolar field also affects the effectiveness of increasing contrast. Therefore, high magnetic moment particles with different morphologies are new candidates with a strong dipolar field of variable spatial distribution.

13.4.2 Drug Delivery

Transporting a medicine to a specific site of the body, e.g. a cancerous tumor, is called a drug delivery system. In this regard, several factors should be considered: types of the used magnetic nanoparticles, their toxicity, healthy tissues surrounding the tumor site, and side effects.

Numerous strategies have been suggested for targeting drugs and carrier systems to their locus of interest. For loco-regional therapy, the system is delivered as close as possible to the target site (first-order targeting). Application of drugs and carriers takes place either intravascularly or into a cavity as it is currently done in cancer

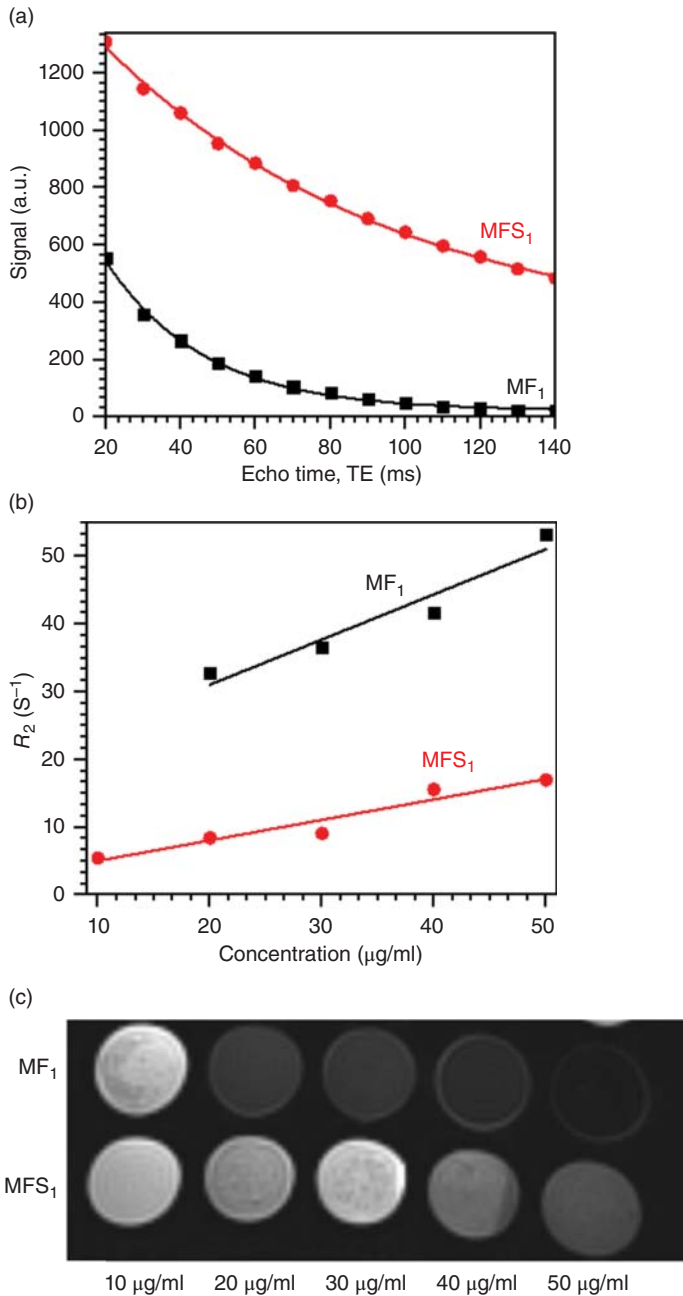


Figure 13.5 (a) Signal relaxation curve as a function of TE for different magnetic nanoparticles (MNPs) at concentration of 30 µg/ml. (b) Transverse relaxation rate, R_2 versus samples concentration (c) T_2 -weighted MRI of nanoparticles with different formulation in 1% agarose phantom at 3.0 T (using multi-echo spin echo (SE) sequence [time to repeat (TR)/time to echo (TE) = 3000/30 ms]). Source: [62], R. Kavkhani et al. (2022), ELSEVIER.

therapy employing cytostatic drugs. Receptor-oriented drug/carrier systems take benefit from the interaction between the coupling of antibodies and/or hormones to the local receptors (second-order targeting) [60, 61].

Distribution of ultrafine magnetic particles, ranging in 5–500 nm, as a carrier in colloidal systems varies the distribution pattern of drugs within the body [60]. For example, the use of superparamagnetic IONPs allows for minimizing systemic side effects while maintaining therapeutic concentrations locally, which may lead one step closer to the “Magic Bullet,” an expression introduced by Paul Ehrlich as early as 1906 [62]. Drug targeting can be accomplished in three routes, namely passive, active, or physical targeting. In the first mode of targeting, the drug distribution within the body takes place through the drug and carrier characteristics that are unchanged (“Prodrugs”) [63]. Active targeting is obtained with mechanisms that allow direct targeting of drugs and/or carriers to specific cells, tissues, or organ systems through specific recognition mechanisms. Physical targeting allows the distribution of drugs and carrier systems through external influences, such as magnets in the case of superparamagnetic IONPs or heat [60, 64].

13.4.3 An Introduction to Hyperthermia (Therapy) in Cancer Treatment (Methods, Mechanisms, Constraints, and Role of Nanotechnology)

Hyperthermia, in general, means the increase of body temperature from physiological (37°C) to more than that of the normal state. A high temperature of a body typically causes illness, such as fever or heat shock, but an increase in body temperature with a controlled condition, in some cases, is used to treat diseases, especially cancer. The idea of using heat to treat cancer has been considered for a long time ago, but the efforts of recent years have led to the development of new technologies such as magnetic hyperthermia or its combination with other methods like chemotherapy and radiotherapy.

Hyperthermia is generally used in two modes for cancer treatment, namely local (topical) and regional forms. In the first method, a very high temperature is used to remove a small part of the cells or tissues like a tumor. This type of hyperthermia is usually called local hyperthermia. In the second method, the temperature of a part of the body or even the whole body is raised a few degrees higher than the normal body temperature; this type of treatment improves the performance of other cancer treatments such as radiotherapy and chemotherapy. This form of hyperthermia is called regional hyperthermia or whole-body hyperthermia. Both general methods are commonly used as an accompanied treatment. Of course, some hyperthermia methods, like radiofrequency degradation, may also be used as the main treatment, but the lack of heat distribution in all tumor cells, the inadequate amount of heat produced, and the unwanted thermal effect on healthy cells are the most important challenges for such methods. Thus, recently, nanotechnology has put forward new horizons for solving such problems. Magnetic nanoparticles by representing a potentiality in accumulation in tumor tissue, distribution in all areas of the tumor, and the ability to generate more heat, are concerned. In fact, magnetic hyperthermia has been shown to have good results in the treatment of cancer cells [65–68]. This type of therapy

was clinically approved in Europe for glioblastoma treatments in 2011, and clinical treatments were already performed on prostate cancer and brain tumors [69]. Regardless of technical considerations and challenges, this method requires more investigation to optimize the employed parameters and improve its performance.

In brief, magnetic nanoparticles would produce heat under alternative magnetic field radiation and under a process called magnetic displacement. The induced heat can be used in various applications to detect and remedy cancer or tumor in the body. Magnetic hyperthermia (hyperthermia) for treating tumors is referred to as heat generation by magnetic nanoparticles through the application of an alternating external magnetic field with RF frequency. The results of clinical and pre-clinical studies with magnetic nanoparticles for cancer treatment through hyperthermia indicate the ability of this method to overcome the problems facing the hyperthermia treatment [69–71], such as a lack of proper distribution of heat in the tumor area and damaging of living cells, which prevents the proper functioning of the method for treating cancer. In normal hyperthermia treatment, the temperature and physiological conditions of the patient require strict control; hence, other hyperthermic methods such as magnetic hyperthermia or a combination of magnetic hyperthermia with chemigraphy or radiography are required. An induction of magnetic fluid hyperthermia with magnetic nanoparticles under an AC magnetic field is also one of the developed methods. Although the use of iron oxide in tumor heating was first reported by Gilchrist in 1957, it has grown steadily in recent years. Still, some other challenges are under meticulous investigation, which will be discussed in Sections 13.4.3.1 and 13.4.3.2.

13.4.3.1 Magnetic Loss Processes Contributed to Magnetic Heating

Heat dissipation in magnetic particles in the presence of an alternating magnetic field can be accomplished based on (i) hysteresis relaxation: Néel and Brownian relaxation and (ii) hysteresis loss, which are described as follows.

Néel and Brownian Relaxation In cancer treatment through magnetic hyperthermia, the superparamagnetic nanoparticles are typically dispersed in a non-magnetic liquid. During the treatment, these nanofluids are subjected to an alternating magnetic field. In the presence of an externally applied magnetic field, the magnetic nanoparticles oscillate and convert the magnetic energy to heat. Two main mechanisms are responsible for this relaxation: Néel and Brownian relaxations. The Néel mechanism is due to the rotation of the magnetic moment inside the particles. The Brownian relaxation mechanism is due to the physical rotation of the particle around itself. To better understand the role of each mechanism, one might consider nanoparticles in fixed and moving states. If the particle is in a fixed state, there is no contribution of Brownian to the relaxation. Therefore, the particles only transfer the stored energy to the surrounding environment via Néel relaxation. In the case of considering moving states of particles (free particles), both mechanisms contribute to the relaxations, as shown in Figure 13.6. For each of these relaxation mechanisms, the relaxation time is considered the Néel relaxation time (τ_N) and Brownian relaxation time (τ_B). The combination of them yields an

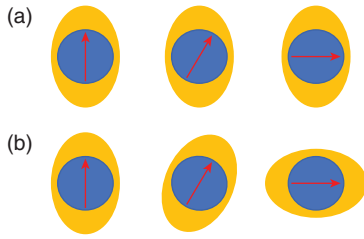


Figure 13.6 Schematic representation of (a) Néel, and (b) Brownian relaxations.

effective relaxation time (τ_{eff}). The Brownian relaxation time (τ_B) is determined by the hydrodynamics properties of the fluid and the Néel relaxation time (τ_N) by the magnetic anisotropic energy of the superparamagnetic nanoparticles.

It should also be noted that the Brownian relaxation mechanism generates heat through the viscosity friction among the particles and between particles and liquid, which is also known as viscous energy loss.

Hysteresis Loss To better understand how the heat is formed in the magnetic nanoparticles, it is first necessary to consider the properties of magnetic materials (as discussed in Chapters 1 and 2). In brief, the magnetic properties of materials can be investigated by examining the response of particles to an externally applied field (Figure 13.7).

As shown in the hysteresis diagram of ferromagnetic materials, external energy is required to overcome the domino walls, which are created by intrinsic properties of a matter, anisotropy, boundaries, and impurities in materials. If an AC alternating external magnetic field in magnetic fluid hyperthermia is applied to ferromagnetic or ferrimagnetic materials, a continuous stream of energy is transmitted to the material that heats the material. This is the physical basis of magnetic hyperthermic treatments in the ferro- and ferrimagnetic materials, which is expressed by:

$$P = \mu_0 f \int H dM \quad (13.3)$$

where P is the heat generated in a volume unit by a ferromagnetic particle, f is the frequency, and the integral indicates the area of the hysteresis loop.

Furthermore, the magnetic losses increase the temperature by using various magnetic resonance processes. This increase in temperature depends on different factors such as the field strength, frequency used, and the employed magnetic particles'

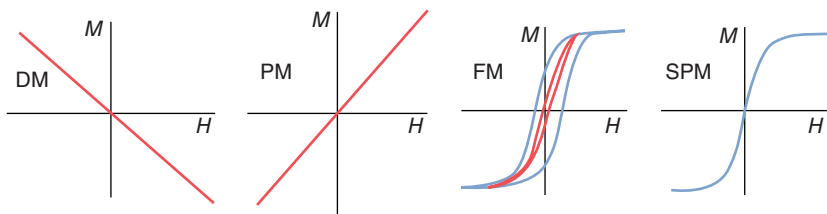


Figure 13.7 Magnetization is a function of an applied magnetic field in Diamagnetic (DM), Paramagnetic (PM), Ferromagnetic (FM), and Superparamagnetic (SPM) materials. Source: Hajalilou et al. [7]/with permission of Springer Nature.

properties. Structural properties include particle shape, size and distribution, crystallinity, and concentration.

13.4.3.2 Challenges of Magnetic Hyperthermia for Therapeutic Uses

While promising advances were made in the field of magnetic hyperthermia, further progress requires addressing several existing challenges that require further research as listed below.

Considering the Intrinsic Characteristics of Magnetic Nanoparticles to Achieve a Maximum Specific Absorption Rate (SAR) When the ferrofluid is exposed to an AC magnetic field, the amount of energy absorbed is considered specific absorption rate (SAR). Achieving the possible maximum SAR in magnetic nanoparticles allows us to use a smaller amount of injectable ferrofluid. The SAR value mainly depends on parameters such as magnetization, size of particles, their distribution, and the power and frequency of the alternating magnetic field used. The existing parameters must be manipulated to obtain the maximum SAR in such a way that the hyperthermia is effective with the minimum possible amount of magnetic nanoparticles, thus enabling their easier removal from the body. Furthermore, by reducing the dose of employed magnetic nanoparticles, their toxicity reduces as well. Therefore, by engineering the shape, size, and other properties related to magnetic particles, one can improve the magnetic properties of the approved nanoparticles for *in vivo* applications, thus improving hyperthermic efficiency by obtaining high SAR, with a reduced amount of particles.

In terms of the type of magnetic nanoparticles, since the superparamagnetic particles possessing a particle size below 10 nm have much more colloid stability, they are more likely to be considered in hyperthermic studies. Such particles however have limited heat generation compared to the larger particles. One possible solution to address this is manipulating the shape of particles, e.g. from spherical to cubic or rod shape or their organization in chain-like structure, which can improve their SAR value.

In terms of the dose of used magnetic nanoparticles, it is always attempted to use the smallest amount of nanoparticles to obtain the required heat. The unit watts per gram (W/g) are used for expressing the specific loss power (SLP) by nanoparticles for the induction of minimum heat needed for the tumor. In some cases, microscopic magnetic implants are currently employed around and inside the tumor area (seeds) to treat some types of cancer in the clinical. However, still, most of the effort is on the potential for heat generation by magnetic nanoparticles that can be directly injected into the blood. These materials include a wide range of nanoparticles consisting of single-domain nanoparticles and superparamagnetic nanoparticles of less than 10 nm. Apart from several studies on the use of specific magnetic alloys or the use of transition metals such as Co, Ni, Zn, and Mg in most studies, iron oxide compounds, i.e. magnetite (Fe_3O_4) and maghemite ($\gamma\text{-Fe}_2\text{O}_3$), are broadly utilized in cancer treatment through hyperthermia. Because these two compounds have good chemical stability and lack harmful effects as compared to metals or alloys such as cobalt.

Improvement of the Used Magnetic Nanoparticles Characteristics: Remove or Reduce the Toxic Effects of Used Nanomaterials Different types of magnetic nanostructures of iron and cobalt alloys with better magnetic properties compared to IONPs are available, but unfortunately, these structures are not biocompatible and are not usable for *in vivo* applications. Some possible solutions include reducing the concentration of the nanoparticles and coating those nanoparticles with biocompatible materials such as gold or silica (Figure 13.8) [59].

Most cases of hyperthermia studies only consider the cause of cell death due to increased heat, and the intrinsic toxicity of the magnetic nanoparticles has been less taken into account. Furthermore, the investigation of cell toxicity is taken into account in short-term periods. A pharmacokinetic and comprehensive study of the toxicity of the magnetic nanoparticles should be further investigated.

Effect of an Externally Applied Magnetic Field The effect of applied magnetic field characteristics, i.e. frequency and amplitude used, on cells, tissues, and biological fluids must be carefully considered as well. For example, using low frequency or amplitude may not generate enough heat, while high frequency or amplitude may cause heat loss or can destroy the healthy cells as well. Thus, the optimal condition should be considered.

Creating and Maintaining a Therapeutic Temperature with Controlled Distribution

Although it is possible to distribute the magnetic nanoparticles in cells and tumor tissues, it is still a challenge to induce and maintain a higher temperature in the body. In this regard, the blood flow-cooling action should be considered in magnetic hyperthermia. In tumor regions, which usually have an irregular and leaky vascular structure, blood flow varies in different regions. Moreover, even the blood flow velocity differs from that of normal blood flow during the treatment process. Therefore, it should be noted that the transfer of heat convection by the bloodstream ultimately reduces the tumor's temperature, especially if the tumor is in regions with high blood flow such as the liver, kidney, and lung.

Other cases that can provide a proper and homogenous distribution of temperature across all tumor areas without damaging healthy cells during magnetic hyperthermia are through precise targeting of nanoparticles with appropriate targeting biomolecules [72].

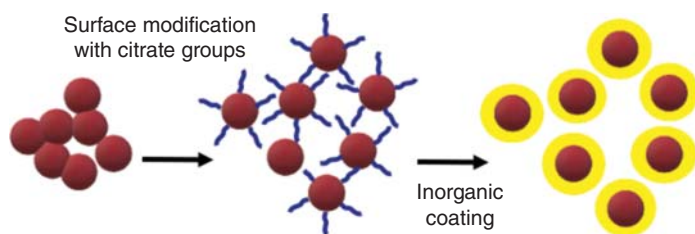


Figure 13.8 A schematic diagram of how to coat the magnetic nanoparticles with inorganic materials to make core-shell magnetic particles.

Several improved strategies employing nanoparticle engineering have been in practice for upgrading the selectivity of metastatic cells and to have direct access to poorly manageable tumor regions. Targeted nanoparticle therapy paves the way toward tumor biomarkers and tissue-specific cancer stages and provides effective strategies for non-accessible tumor regions, thus leading to tangible modification in the history of the cancer world [73–75]. In fact, magnetic nanoparticle formulations for cross-dwelling biological dams like blood–brain barrier and vascular endothelium as well as escape from the reticular dystrophy system need a comprehensive targeting strategy.

One of the other challenges in hyperthermia treatment is the availability of an accurate strategy for temperature monitoring during hyperthermia. Currently, hyperthermia is used for general therapies with invasive methods in which a thermometer sensor is used for subcutaneous ultrasound or fluoroscopic conduction in the target area. The ability to control the distribution of energy within living tissues has been very much taken into account by the development of electronic devices and modeling systems in the past decades and has made remarkable progress. Indeed, several solutions have been proposed to create a non-invasive method for thermometry. In one solution, computational models are used to check the temperature at different points of the tumor [76–79]. These models take into account various factors such as blood circulation, field characteristics, magnetic nanostructures, heat generated by the nanoparticles, and the body's cells. Developing such models are essential for reducing the thermal doses of healthy cells and reducing the field exponent on the patient.

In another innovative approach, magnetic nanoparticles coated with thermosensitive fluorescence polymers were used [80, 81]. When exposed to the heat, the fluorescence color of the structure is abandoned and becomes visible with a spectrofluorometer. The use of infrared thermal cameras outside of the magnetic field is also used as a non-invasive method [82, 83].

One technical challenge that is under investigation is how to selectively raise the temperature of a specific area of the body. Generally, the blood flow prevents the rising temperature and the blood flow rate in the tumor tissue is about 100 g/min. Therefore, to reach a temperature higher than 42 °C, in some areas of the tumor, at least a power density of 20–40 W/kg should be employed in the target area.

At present, the optimal temperature distribution for hyperthermia in clinical applications is yet unknown. The distribution of temperature obtained in various hyperthermia methods has low homogeneity, and the total amount of heat produced is also limited. This is due to the physiological and physical characteristics of the electrical tissue binderies, the varying speed and order of blood flow in different areas, characteristics of the magnetic nanoparticles, carrier fluid, and employed conditions. With the advances made in hyperthermia tools and techniques, today a majority of deep tumors can be heated up to 42 °C at specific points [84–86]. However, with clinical applications, an achievement of a specific temperature in tumors via magnetic hyperthermia is still uncertain. In summary, there is still a need for obtaining a high and homogeneous temperature in the tumor as far as possible.

Control of Drug Release Through Magnetic Nanoparticles Recently, there have been several publications demonstrating magnetic nanoparticle-based hyperthermia to generate local heat resulting in the release of drugs either bound to the magnetic nanoparticle or encapsulated within polymeric matrices. Indeed, drug delivery strategies aim to maximize a drug's therapeutic index by increasing the concentration of the drug at target sites while minimizing delivery to off-target tissues. Because biological tissues are minimally responsive to magnetic fields, there has been a great deal of interest in using magnetic nanoparticles in combination with applied magnetic fields to selectively control the accumulation and release of drugs in target tissues while minimizing the impact on surrounding tissue. In particular, spatially variant magnetic fields have been used to encourage the accumulation of drug-loaded magnetic nanoparticles at target sites, while time-variant magnetic fields have been used to induce drug release from thermally sensitive nanocarriers. In this review, we discuss nanoparticle formulations and approaches that have been developed for magnetic targeting and/or magnetically induced drug release, as well as ongoing challenges in using magnetism for therapeutic applications [87–90].

Create Thermal Resistance in Cells One of the challenges faced by hyperthermia is the creation of thermal resistance in cancer cells treated with hyperthermia. Hyperthermia can kill cells in two forms: apoptosis, when the heat treatment is slow, and, necrotic when the heating rate is high. Typically, in apoptosis treatments, some cells can resist the apoptosis process. Factors such as early heating should be considered to use precise thermal planning. Based on the data from the studies, the dose–response curve for hyperthermia is similar to dose–response curves obtained in radiotherapy and chemotherapy, and it is possible to create thermal resistance if no proper heating program is used.

Combining Other Treatments with Hyperthermia Magnetic hyperthermia becomes more effective in the conjunction with other treatments such as chemotherapy or radiotherapy. For example, radiation therapy causes the denaturation of malignant cells. Therefore, when hyperthermia is accompanied by radiation, the heat released from the magnetic particles causes changes in the cell cycle, which can result in more rapid denaturation of the malignant cells by agglutination of the cell nucleus proteins. The thermal enhancement ratio is defined as the sensitivity of the cells to radiation (ionizing radiation) at 37°C relative to the sensitivity of the cells at higher temperatures. Since the internal part of the tumor due to the lack of blood circulation has inadequate oxygen, radiotherapy treatment usually has little effect on these areas. When the temperature rises, the blood levels of these areas increase, and the effectiveness of radiotherapy increases. Thus, the use of other therapies, such as chemotherapy with magnetic hyperthermia and radiotherapy, can also increase the effectiveness of the treatment. Furthermore, hyperthermia seems to cause more cancer cells to become susceptible to radiation and chemotherapy drugs [91–93]. Many clinical studies have been conducted on the combination of hyperthermia and radiation therapy or chemotherapy on various types of cancers such as sarcoma, melanoma, head and neck cancer, rectum, liver, cervix, mesothelioma,

breast, bladder, lung, brain, and so on [94, 95]. Many of these studies show the effect of hyperthermia on reducing tumor size as a pre or simultaneous treatment with chemotherapy and physiotherapy [91–96].

13.5 Other General Applications of Magnetic Nanoparticles

The magnetic nanoparticles have found a wide variety of applications in cases where a high permeability is required. This includes high-frequency microwave absorption [4, 7, 10, 97], core material in various transformers, recording heads and tapes, TV deflection units, and inductors [97–99].

References

- 1 Adli, R.G., Kianvash, A., Hosseini, M.G. et al. (2018). Mechanochemically synthesized NiCo_2O_4 /Vulcan/PANI nanocomposite and investigation of its electrochemical behavior as a supercapacitor. *Ceramics International* 44: 20049–20057.
- 2 Hajalilou, A., Etemadifar, R., Abbasi-Chianeh, V., and Abouzari-Lotf, E. (2018). Electrophoretically-deposited nano- Fe_3O_4 @carbon 3D structure on carbon fiber as high-performance supercapacitors. *Journal of Electronic Materials* 47: 4807–4812.
- 3 Hajalilou, A., Hashim, M., Ebrahimi-Kahrizsangi, R., and Sarami, N. (2014). Synthesis and structural characterization of nano-sized nickel ferrite obtained by mechanochemical process. *Ceramics International* 40: 5881–5887.
- 4 Hajalilou, A., Kamari, H.M., and Shameli, K. (2017). Dielectric and electrical characteristics of mechanically synthesized Ni–Zn ferrite nanoparticles. *Journal of Alloys and Compounds* 708: 813–826.
- 5 Hajalilou, A., Kianvash, A., Lavvafi, H., and Shameli, K. (2018). Nanostructured soft magnetic materials synthesized via mechanical alloying: a review. *Journal of Materials Science: Materials in Electronics* 29: 1690–1717.
- 6 Hajalilou, A. and Mazlan, S.A. (2016). A review on preparation techniques for synthesis of nanocrystalline soft magnetic ferrites and investigation on the effects of microstructure features on magnetic properties. *Applied Physics A* 122: 1–15.
- 7 Hajalilou, A., Mazlan, S.A., Lavvafi, H., and Shameli, K. (2016). *Field Responsive Fluids as Smart Materials*. Springer.
- 8 Kanagesan, S., Hashim, M., Tamilselvan, S. et al. (2013). Synthesis, characterization, and cytotoxicity of iron oxide nanoparticles. *Advances in Materials Science and Engineering* 2013: 1–7.
- 9 Hajalilou, A., Hashim, M., Ebrahimi-Kahrizsangi, R., and Kamari, H.M. (2015). Thermal evolution of the Ni-ferrite nanoparticles obtained by mechanical alloying as probed by differential scanning calorimetry. *Journal of Thermal Analysis and Calorimetry* 119: 995–1000.

- 10 Hajalilou, A., Hashim, M., Ebrahimi-Kahrizsangi, R., and Kamari, H.M. (2015). Influence of evolving microstructure on electrical and magnetic characteristics in mechanically synthesized polycrystalline Ni-ferrite nanoparticles. *Journal of Alloys and Compounds* 633: 306–316.
- 11 Hajalilou, A., Hashim, M., Ebrahimi-Kahrizsangi, R., and Sarami, N. (2015). Influence of CaO and SiO₂ co-doping on the magnetic, electrical properties and microstructure of a Ni–Zn ferrite. *Journal of Physics D: Applied Physics* 48: 145001.
- 12 Hajalilou, A., Hashim, M., and Masoudi, M.T. (2015). A comparative study of in-situ mechanochemically synthesized Mn_{0.5}Zn_{0.5}Fe₂O₄ ferrite nanoparticles in the MnO/ZnO/Fe₂O₃ and MnO₂/Zn/Fe₂O₃ systems. *Ceramics International* 41: 8070–8079.
- 13 Ismail, M.A.N., Hashim, M., Hajalilou, A. et al. (2014). Magnetic properties of mechanically alloyed cobalt-zinc ferrite nanoparticles. *Journal of Superconductivity and Novel Magnetism* 27: 1293–1298.
- 14 Mirzazadeh, A., Kianvash, A., and Hajalilou, A. (2018). Plating of Cu and Ni metals on Mg-ferrite sintered bodies by an electroless method and an investigation of magnetic behavior. *Journal of Materials Science: Materials in Electronics* 29: 5753–5760.
- 15 Ogholbeyg, A.B., Kianvash, A., Hajalilou, A. et al. (2018). Cytotoxicity characteristics of green assisted-synthesized superparamagnetic maghemite (γ-Fe₂O₃) nanoparticles. *Journal of Materials Science: Materials in Electronics* 29: 12135–12143.
- 16 Hajalilou, A., Abouzari-Lotf, E., Abbasi-Chianeh, V. et al. (2018). Inclusion of octahedron-shaped ZnFe₂O₄ nanoparticles in combination with carbon dots into carbonyl iron based magnetorheological suspension as additive. *Journal of Alloys and Compounds* 737: 536–548.
- 17 Hajalilou, A., Kianvash, A., Shameli, K., and Lavvafi, H. (2017). Carbonyl iron based magnetorheological effects with silver nanoparticles via green-assisted coating. *Applied Physics Letters* 110: 261902.
- 18 Hajalilou, A., Mazlan, S.A., Abbasi, M., and Lavvafi, H. (2016). Fabrication of spherical CoFe₂O₄ nanoparticles via sol-gel and hydrothermal methods and investigation of their magnetorheological characteristics. *RSC Advances* 6: 89510–89522.
- 19 Hajalilou, A., Mazlan, S.A., and Shila, S.T. (2016). Magnetic carbonyl iron suspension with Ni–Zn ferrite additive and its magnetorheological properties. *Materials Letters* 181: 196–199.
- 20 Hajalilou, A., Mazlan, S.A., Shilan, S.T., and Abouzari-Lotf, E. (2017). Enhanced magnetorheology of soft magnetic carbonyl iron suspension with binary mixture of Ni–Zn ferrite and Fe₃O₄ nanoparticle additive. *Colloid and Polymer Science* 295: 1499–1510.
- 21 Shilan, S.T., Mazlan, S.A., Ido, Y. et al. (2016). A comparison of field-dependent rheological properties between spherical and plate-like carbonyl iron particles-based magneto-rheological fluids. *Smart Materials and Structures* 25: 095025.

- 22 Rezaie, E., Hajalilou, A., Rezanezhad, A. et al. (2020). Magnetorheological studies of polymer nanocomposites, Chapter 13. In: *Rheology of Polymer Blends and Nanocomposites* (ed. S. Thomas, C. Sarathchandran and N. Chandran), 263–294. Elsevier.
- 23 Ekwebelam, C. and See, H. (2009). Microstructural investigations of the yielding behaviour of bidisperse magnetorheological fluids. *Rheologica Acta* 48: 19–32.
- 24 Auffan, M., Rose, J., Bottero, J.-Y. et al. (2009). Towards a definition of inorganic nanoparticles from an environmental, health and safety perspective. *Nature Nanotechnology* 4: 634–641.
- 25 Schindler, P. (2018). Co-adsorption of metal ions and organic ligands: formation of ternary surface complexes. *Reviews in Mineralogy and Geochemistry* 23 (1): 281–307.
- 26 Filius, J.D., Hiemstra, T., and Van Riemsdijk, W.H. (1997). Adsorption of small weak organic acids on goethite: modeling of mechanisms. *Journal of Colloid and Interface Science* 195: 368–380.
- 27 Zargar, B., Parham, H., and Hatamie, A. (2009). Fast removal and recovery of amaranth by modified iron oxide magnetic nanoparticles. *Chemosphere* 76: 554–557.
- 28 Hu, J., Chen, G., and Lo, I.M. (2005). Removal and recovery of Cr(VI) from wastewater by maghemite nanoparticles. *Water Research* 39: 4528–4536.
- 29 Lei, L., Hao, X., Zhang, X., and Zhou, M. (2007). Wastewater treatment using a heterogeneous magnetite (Fe_3O_4) non-thermal plasma process. *Plasma Processes and Polymers* 4: 455–462.
- 30 Panasiuk, O. (2010). Phosphorus removal and recovery from wastewater using magnetite.
- 31 Zhang, F., Song, Y., Song, S. et al. (2015). Synthesis of magnetite–graphene oxide-layered double hydroxide composites and applications for the removal of Pb(II) and 2,4-dichlorophenoxyacetic acid from aqueous solutions. *ACS Applied Materials & Interfaces* 7: 7251–7263.
- 32 Oskay, E. (2003). Treatment of wastewater using magnetite. Dokuz Eylül University Graduate School of Natural and Applied Sciences, Turkey.
- 33 Muthui, M.A. (2013). Magnetic adsorption separation process for industrial wastewater treatment using polypyrrole-magnetite nanocomposite.
- 34 Wang, S.-y., Tang, Y.-k., Li, K. et al. (2014). Combined performance of biochar sorption and magnetic separation processes for treatment of chromium-contained electroplating wastewater. *Bioresource Technology* 174: 67–73.
- 35 Hajalilou, A., Abouzari-Lotf, E., Etemadifar, R. et al. (2018). Fabrication by electrophoretic deposition of nano- Fe_3O_4 and $\text{Fe}_3\text{O}_4/\text{SiO}_2$ 3D structure on carbon fibers as supercapacitor materials. *JOM Journal of the Minerals, Metals and Materials Society* 70: 1404–1410.
- 36 Hasan, A., Morshed, M., Memic, A. et al. (2018). Nanoparticles in tissue engineering: applications, challenges and prospects. *International Journal of Nanomedicine* 13: 5637.

- 37 Lee, E.A., Yim, H., Heo, J. et al. (2014). Application of magnetic nanoparticle for controlled tissue assembly and tissue engineering. *Archives of Pharmacal Research* 37: 120–128.
- 38 Ito, A. and Kamihira, M. (2011). Tissue engineering using magnetite nanoparticles, Chapter 9. In: *Progress in Molecular Biology and Translational Science* (ed. A. Villaverde), 355–395. Academic Press.
- 39 Ito, A. and Honda, H. (2007). Magnetic nanoparticles for tissue engineering. *Nanotechnologies for the Life Sciences*: Online.
- 40 Ito, A. and Kamihira, M. (2011). Tissue engineering using magnetite nanoparticles. *Progress in Molecular Biology and Translational Science* 104: 355–395.
- 41 Ito, A., Takizawa, Y., Honda, H. et al. (2004). Tissue engineering using magnetite nanoparticles and magnetic force: heterotypic layers of cocultured hepatocytes and endothelial cells. *Tissue Engineering* 10: 833–840.
- 42 Rezaie, E., Rezanezhad, A., Ghadimi, L.S. et al. (2018). Effect of calcination on structural and supercapacitance properties of hydrothermally synthesized plate-like $\text{SrFe}_{12}\text{O}_{19}$ hexaferrite nanoparticles. *Ceramics International* 44: 20285–20290.
- 43 Adli, R.G., Kianvash, A., Hosseini, M.G. et al. (2019). Facile and scalable synthesis of ultrafine MnCo_2O_4 nanoparticles via mechanical alloying as supercapacitive materials. *JOM Journal of the Minerals Metals and Materials Society* 71: 2396–2404.
- 44 Rezaie, E., Hajalilou, A., and Su, Y. (2021). Perovskites for supercapacitors. In: *Handbook of Supercapacitor Materials* (eds. A. Khan, A.M. Asiri, R. Boddula, A. Kolosov), 131–185. Wiley. <https://doi.org/10.1002/9783527824779.ch5>.
- 45 Adli, R.G., Su, Y., Hosseini, M.G., and Hajalilou, A. (2021). Metal oxides for supercapacitors. In: *Handbook of Supercapacitor Materials* (eds. A. Khan, A.M. Asiri, R. Boddula, A. Kolosov), 245–283. Wiley. <https://doi.org/10.1002/9783527824779.ch9>.
- 46 Rezaie, E., Rezanezhad, A., Hajalilou, A. et al. (2019). Electrochemical behavior of $\text{SrFe}_{12}\text{O}_{19}/\text{CoFe}_2\text{O}_4$ composite nanoparticles synthesized via one-pot hydrothermal method. *Journal of Alloys and Compounds* 789: 40–47.
- 47 Ghadimi, L.S., Arsalani, N., Ahadzadeh, I. et al. (2019). Effect of synthesis route on the electrochemical performance of CoMnFeO_4 nanoparticles as a novel supercapacitor electrode material. *Applied Surface Science* 494: 440–451.
- 48 Wu, D. (2018). Magnetic field effects induced by incorporation of magnetic nanoparticles on bulk heterojunction polymer solar cells. University of Akron.
- 49 González, D.M., Körstgens, V., Yao, Y. et al. (2015). Improved power conversion efficiency of P3HT: PCBM organic solar cells by strong spin–orbit coupling-induced delayed fluorescence. *Advanced Energy Materials* 5 (8): 1401770.
- 50 Kovalenko, A., Yadav, R.S., Pospisil, J. et al. (2016). Towards improved efficiency of bulk-heterojunction solar cells using various spinel ferrite magnetic nanoparticles. *Organic Electronics* 39: 118–126.
- 51 Grover, V.P., Tognarelli, J.M., Crossey, M.M. et al. (2015). Magnetic resonance imaging: principles and techniques: lessons for clinicians. *Journal of Clinical and Experimental Hepatology* 5: 246–255.

- 52 Pankhurst, Q.A., Connolly, J., Jones, S.K., and Dobson, J. (2003). Applications of magnetic nanoparticles in biomedicine. *Journal of Physics D: Applied Physics* 36: R167.
- 53 Haacke, E.M., Brown, R.W., Thompson, M.R., and Venkatesan, R. (1999). *Magnetic Resonance Imaging: Physical Principles and Sequence Design*. New York: Wiley-Liss.
- 54 Ogawa, S., Lee, T.-M., Kay, A.R., and Tank, D.W. (1990). Brain magnetic resonance imaging with contrast dependent on blood oxygenation. *Proceedings of the National Academy of Sciences of the United States of America* 87: 9868–9872.
- 55 Huettel, S.A., Song, A.W., and McCarthy, G. (2004). *Functional Magnetic Resonance Imaging*. Sunderland, MA: Sinauer Associates.
- 56 Kwong, K.K., Belliveau, J.W., Chesler, D.A. et al. (1992). Dynamic magnetic resonance imaging of human brain activity during primary sensory stimulation. *Proceedings of the National Academy of Sciences of the United States of America* 89: 5675–5679.
- 57 Currie, S., Hoggard, N., Craven, I.J. et al. (2013). Understanding MRI: basic MR physics for physicians. *Postgraduate Medical Journal* 89: 209–223.
- 58 Maher, K. (2006). *Basic Physics of Nuclear Medicine*. Wikibooks Contributors.
- 59 Kavkhani, R., Hajalilou, A., Abouzari-Lotf, E. et al. (2022). CTAB assisted synthesis of $\text{MnFe}_2\text{O}_4@\text{SiO}_2$ nanoparticles for magnetic hyperthermia and MRI application. *Materials Today Communications* 31: 103412.
- 60 Neuberger, T., Schöpf, B., Hofmann, H. et al. (2005). Superparamagnetic nanoparticles for biomedical applications: possibilities and limitations of a new drug delivery system. *Journal of Magnetism and Magnetic Materials* 293: 483–496.
- 61 Sezaki, H. and Hashida, M. (1984). Macromolecule-drug conjugates in targeted cancer chemotherapy. *Critical Reviews in Therapeutic Drug Carrier Systems* 1: 1–38.
- 62 Ehrlich, P. (1906). *Collected Studies on Immunity*. Wiley.
- 63 Davis, S. (1997). Biomedical applications of nanotechnology—implications for drug targeting and gene therapy. *Trends in Biotechnology* 15: 217–224.
- 64 Davis, S. and Illum, L. (1986). Colloidal carriers and drug targeting. *Acta Pharmaceutica Technologica* 32: 4–9.
- 65 Kobayashi, T. (2011). Cancer hyperthermia using magnetic nanoparticles. *Biotechnology Journal* 6: 1342–1347.
- 66 Yin, P.T., Shah, S., Pasquale, N.J. et al. (2016). Stem cell-based gene therapy activated using magnetic hyperthermia to enhance the treatment of cancer. *Biomaterials* 81: 46–57.
- 67 Moise, S., Byrne, J.M., El Haj, A.J., and Telling, N.D. (2018). The potential of magnetic hyperthermia for triggering the differentiation of cancer cells. *Nanoscale* 10: 20519–20525.
- 68 Hajalilou, A., Ferreira, L.P., Jorge, M.E.M. et al. (2021). Superparamagnetic $\text{Ag-Fe}_3\text{O}_4$ composites nanoparticles for magnetic fluid hyperthermia. *Journal of Magnetism and Magnetic Materials* 537: 168242.
- 69 Maier-Hauff, K., Ulrich, F., Nestler, D. et al. (2011). Efficacy and safety of intratumoral thermotherapy using magnetic iron-oxide nanoparticles combined with

- external beam radiotherapy on patients with recurrent glioblastoma multiforme. *Journal of Neuro-Oncology* 103: 317–324.
- 70 Conde-Leboran, I., Baldomir, D., Martinez-Boubeta, C. et al. (2015). A single picture explains diversity of hyperthermia response of magnetic nanoparticles. *The Journal of Physical Chemistry C* 119: 15698–15706.
 - 71 Wilczewska, A.Z., Niemirowicz, K., Markiewicz, K.H., and Car, H. (2012). Nanoparticles as drug delivery systems. *Pharmacological Reports* 64: 1020–1037.
 - 72 Kruger, C.A. and Abrahamse, H. (2018). Utilisation of targeted nanoparticle photosensitiser drug delivery systems for the enhancement of photodynamic therapy. *Molecules* 23: 2628.
 - 73 Pankhurst, Q., Thanh, N., Jones, S., and Dobson, J. (2009). Progress in applications of magnetic nanoparticles in biomedicine. *Journal of Physics D: Applied Physics* 42: 224001.
 - 74 Chang, D., Lim, M., Goos, J.A. et al. (2018). Biologically targeted magnetic hyperthermia: potential and limitations. *Frontiers in Pharmacology* 9: 831.
 - 75 Malik, A., Tahir Butt, T., Zahid, S. et al. (2017). Use of magnetic nanoparticles as targeted therapy: theranostic approach to treat and diagnose cancer. *Journal of Nanotechnology* 2017: 1098765.
 - 76 Nabil, M. and Zunino, P. (2016). A computational study of cancer hyperthermia based on vascular magnetic nanoconstructs. *Royal Society Open Science* 3: 160287.
 - 77 Chiang, J., Wang, P., and Brace, C.L. (2013). Computational modelling of microwave tumour ablations. *International Journal of Hyperthermia* 29: 308–317.
 - 78 González, F.J. (2021). Thermal simulations of cancerous breast tumors and cysts on a realistic female torso. *Journal of Biomechanical Engineering* 143: 061001.
 - 79 Kandala, S.K., Sharma, A., Mirpour, S. et al. (2021). Validation of a coupled electromagnetic and thermal model for estimating temperatures during magnetic nanoparticle hyperthermia. *International Journal of Hyperthermia* 38: 611–622.
 - 80 Herrera, A.P., Rodríguez, M., Torres-Lugo, M., and Rinaldi, C. (2008). Multifunctional magnetite nanoparticles coated with fluorescent thermo-responsive polymeric shells. *Journal of Materials Chemistry* 18: 855–858.
 - 81 Chanana, M., Jahn, S., Georgieva, R. et al. (2009). Fabrication of colloidal stable, thermosensitive, and biocompatible magnetite nanoparticles and study of their reversible agglomeration in aqueous milieu. *Chemistry of Materials* 21: 1906–1914.
 - 82 Tattersall, G.J. (2016). Infrared thermography: a non-invasive window into thermal physiology. *Comparative Biochemistry and Physiology Part A: Molecular & Integrative Physiology* 202: 78–98.
 - 83 Usamentiaga, R., Venegas, P., Guerediaga, J. et al. (2014). Infrared thermography for temperature measurement and non-destructive testing. *Sensors* 14: 12305–12348.
 - 84 Franckena, M. (2010). Hyperthermia for the treatment of locally advanced cervix cancer.

- 85 Stauffer, P.R. and van Rhooen, G.C. (2016). Overview of bladder heating technology: matching capabilities with clinical requirements. *International Journal of Hyperthermia* 32: 407–416.
- 86 Lyons, B.E., Obana, W.G., Borcich, J.K. et al. (1986). Chronic histological effects of ultrasonic hyperthermia on normal feline brain tissue. *Radiation Research* 106: 234–251.
- 87 Liu, J.F., Jang, B., Issadore, D., and Tsourkas, A. (2019). Use of magnetic fields and nanoparticles to trigger drug release and improve tumor targeting. *Wiley Interdisciplinary Reviews: Nanomedicine and Nanobiotechnology* 11: e1571.
- 88 Kumar, C.S. and Mohammad, F. (2011). Magnetic nanomaterials for hyperthermia-based therapy and controlled drug delivery. *Advanced Drug Delivery Reviews* 63: 789–808.
- 89 Bear, J.C., Patrick, P.S., Casson, A. et al. (2016). Magnetic hyperthermia controlled drug release in the GI tract: solving the problem of detection. *Scientific Reports* 6: 1–11.
- 90 Caetano, B., Guibert, C., Fini, R. et al. (2016). Magnetic hyperthermia-induced drug release from ureasil-PEO- γ -Fe₂O₃ nanocomposites. *RSC Advances* 6: 63291–63295.
- 91 Mortezaee, K., Narmani, A., Salehi, M. et al. (2021). Synergic effects of nanoparticles-mediated hyperthermia in radiotherapy/chemotherapy of cancer. *Life Sciences* 269: 119020.
- 92 Spirou, S.V., Basini, M., Lascialfari, A. et al. (2018). Magnetic hyperthermia and radiation therapy: radiobiological principles and current practice. *Nanomaterials* 8: 401.
- 93 Yang, S.-J., Huang, C.-H., Wang, C.-H. et al. (2020). The synergistic effect of hyperthermia and chemotherapy in magnetite nanomedicine-based lung cancer treatment. *International Journal of Nanomedicine* 15: 10331.
- 94 Jha, S., Sharma, P.K., and Malviya, R. (2016). Hyperthermia: role and risk factor for cancer treatment. *Achievements in the Life Sciences* 10: 161–167.
- 95 Sezer, A.D. (2012). *Recent Advances in Novel Drug Carrier Systems*. London, UK: IntechOpen <https://www.intechopen.com/books/2509>.
- 96 Umemura, M., Islam, M.R., Fukumura, H. et al. (2019). Simultaneous hyperthermia-chemotherapy effect by arterial injection of Fe (Salen) for femur tumor. *Cancer Science* 110: 356–365.
- 97 Hajalilou, A., Mazlan, S.A., and Shameli, K. (2016). A comparative study of different concentrations of pure Zn powder effects on synthesis, structure, magnetic and microwave-absorbing properties in mechanically-alloyed Ni–Zn ferrite. *Journal of Physics and Chemistry of Solids* 96: 49–59.
- 98 Shafie, M., Hashim, M., Ismail, I. et al. (2014). Magnetic M–H loops family characteristics in the microstructure evolution of BaFe₁₂O₁₉. *Journal of Materials Science: Materials in Electronics* 25: 3787–3794.
- 99 Masoudi, M.T., Saidi, A., Hashim, M., and Hajalilou, A. (2015). Comparison of structure and magnetic properties of Mn–Zn ferrite mechanochemically synthesized under argon and oxygen atmospheres. *Canadian Journal of Physics* 93: 1168–1173.

Index

a

absorption 25, 99, 107, 129, 173, 181, 233, 235–237, 239, 242, 246, 247, 258, 262, 309, 313

π -acceptance ligands 241

active drug targeting 306

adsorbate 108, 296–298

adsorption 42, 105–108, 296–299

alternating current (AC) susceptibility measurement 170

imaginary component 169

in MNPs 177–188

information obtained from 173–174

probe of high-frequency magnetic dynamics 172–173

probe of low-frequency magnetic dynamics 172

real component 169

to probe transitions in colloidal suspensions 188–190

amaranth (AM) removal 298

anisotropy barrier (KV) 138, 141, 142, 184, 222, 223, 227

anisotropy energy 11, 12, 20, 138, 144, 147, 165, 176, 184, 185, 189, 200–222, 227, 228

anisotropy energy density 138, 144, 189, 227, 228

anti-ferromagnetic (AFM) materials 2, 166, 198, 201–203

antiferri susceptibility 173

antiferromagnetism 4, 5, 140

apoptosis treatments 312

arrested precipitation 32

asymmetry in molecule 242

b

ball-milled $2\alpha\text{-Fe}_2\text{O}_3$ NPs

bright-field and high-resolution TEM images 269–270

ball milling 30, 31, 46, 47, 66, 249, 258, 261, 262, 265, 266

Bardeen–Cooper–Schrieffer theory 123

B–H hysteresis loop 19–22, 61, 71, 73

block copolymers (BCPs) 182, 183

blocking temperature (TB) 137, 138, 223

vs. applied pressure, and density 146–147

field dependence 144–146

heat treatment effect 147–148

particle size distribution 141–144

volume of particles 144

Bohr magneton 1, 2, 9, 163, 244

Bohr magneton unit 2

Boltzmann constant 3, 36, 144, 174, 184, 185, 189, 222, 229, 230

Branched polyethyleneimine (BPEI) 46

Brownian relaxation mechanism 307, 308

Brownian rotation 220

c

Ca-ferrite NPs 264, 265
 canonical spin glass 182, 201
 capping agents 41, 42, 46
 carbon nanotubes (CNTs)/Fe₃O₄
 composite NPs 186
 carbonyl iron (CI) 103, 296
 cetyltrimethyl ammonium bromide
 (CTAB) 42, 103–105, 111, 298
 coated IONPs, in wastewater
 treatment 298
 chemical adsorption 107, 108, 298
 chemical composition evaluation
 281–284
 chemical functionalization 105–106
 chemical vapor deposition (CVD) 30
 chemisorption 108
 cluster glass 138, 201
 CNT-SQUID sensors 120
 Co-ferrite nanoparticles 43, 143
 co-precipitation method 44, 102, 103
 coercivity (H_c) 22, 142, 221
 CoFe₂O₄/Fe₃O₄ NPs 139
 Coherent polycrystal model 39
 colloidal nanoparticle formation 33
 conventional critical slowing down
 model 176, 179, 180
 Cooper pairs 122–126
 corona discharge 99–101
 covalently-attached poly(*N*-isopropyl
 acrylamide) (pNIPAM) coated
 cobalt ferrite NPs 190
 critical temperature (T_c) 3, 10, 78, 81,
 121, 122, 124
 crystalline magnetic materials 39, 61,
 62, 163
 Cu and Ni metal plating on Mg-ferrite
 103
 Curie law 3
 Curie temperature 5, 8, 10, 18, 50, 70,
 73, 74, 86, 140, 146, 220, 247
 Curie temperature separation technique
 (CTST) 50
 Cyano-Bridged Magnetic Nanoparticles
 system 182

d

diamagnetism 3, 4
 dipolar coupling 157
 dipolar interactions 140, 142, 159, 165,
 182
 direct current (DC) SQUID 117,
 119–120, 169, 219
 direct exchange interaction 158–162,
 208
 Doppler effect 237–238
 double-layer capacitors (DLC) 301
 droplet model 201
 dynamic susceptibility 172, 173
 Dzyaloshinsky–Moriya interaction
 166

e

eddy current loss 23–24, 37, 61, 80, 81
 eddy current loss factor 23
 Edwards–Anderson (EA) model 202
 electric field gradient (EFG) 242, 243,
 253, 259, 265, 266, 271
 electric monopole interaction 238–241
 electrochemical capacitors 301
 electrochemical etching 30
 electron hopping 24
 electron-lattice interaction 123–124
 electrostatic stabilization 42, 46
 exchange anisotropy 10, 13
 exchange coupling 4
 exchange interactions 74, 78, 158, 159,
 163, 164, 175, 186, 198, 208, 244

f

Faraday's Law of electromagnetic
 induction 23
 FC magnetization curves 143, 219,
 229–230
⁵⁷Fe Mössbauer spectra 199, 233, 248
 of CaO/α-Fe₂O₃ mixtures and
 powders 263–264
 of Co-ferrite NPs and Mn-ferrite NPs
 271–272
 of high-energy ball-milled ZnFe₂O₄
 NPs 248, 250

- of magnetite NPs 279–280
- of MgFe_2O_4 NPs 248, 249
- of MgFe_2O_4 and NiFe_2O_4 261, 262
- Ni ferrite NPs 267
- Fe_3O_4 NPs 46, 139, 187, 188, 255–257, 274, 277, 299
- Fe_3O_4 @C nanoparticles formation 103
- Fe_3O_4 @ mSiO_2 core-shell structures synthesis 111
- Fe_3O_4 @ SiO_2 nanoparticles 111
- Fe_3O_4 (F) NPs 139
- Fe_3O_4 /Co Fe_2O_4 NPs 139
- ferrimagnetism 4–5, 9, 164, 262
- ferrites 59
 - materials 18
- ferromagnetic dominance
 - strong 70
- ferromagnetism 4, 5, 69, 70, 162, 175
- ferromagnetism dominance
 - moderately strong 70
 - weak 69
- field cooled (FC) curve 137–138
- field cooled cooling (FCC) 11, 12, 136, 137, 141
- field cooled warming (FCW) 136, 142
- field cooling (FC) 136–137, 199
- field strength 21, 23, 61, 295, 303, 308
- finite size effects on magnetic properties 206–207
- flux density 4, 19, 21, 22, 24, 61, 137
- flux quantization 121, 125
- fractal-cluster model 201
- free energy (ΔG) 35, 36, 64, 85, 104, 140, 209, 210, 223
- free energy changes 35
- free nuclei, recoil of 237
- functionalization
 - chemical 105–106
 - defined 104–105
 - physical 106–108
 - types 105

g

- gamma ferric oxide 88, 89
- gamma-ray fluorescence 234
- gamma-ray resource 234
- gamma-ray spectroscopy 233
- grain boundaries 5, 13, 14, 24, 38, 39, 41, 62–64, 66, 67, 70, 71, 86, 222, 251
- grain boundary diffusion 63, 64, 84, 86
- grain boundary segregation 64
- grain growth coarsening 64
- green chemistry 45

h

- hard ferrites 71–80
- hard magnetic Ba-ferrite nanoparticles 224
- hard magnetic materials 17–19
- heating rate 62, 64, 88, 89, 312
- Herzer's random anisotropy model 38, 39, 78
- heterogenous-nuclei 33
- hierarchical model 201, 209, 210
- high-energy ball milling (HEBM)
 - process 31, 46, 47, 249, 258–262, 264, 265, 271
- high-frequency electron paramagnetic resonance (HF-EPR) 128–130
- high-frequency magnetic dynamics 172–173
- high-temperature SQUID sensors 120
- homogeneous freezing 185
- homogenous-nuclei 33
- HTS vs. LTS dc SQUID 119
- hybrid supercapacitors 301
- hydrothermal method 43, 148
- hyperfine interactions 238
 - electric monopole interaction 238–241
 - electric quadrupole interaction 242–244
 - magnetic dipole interaction 244–246
- hyperthermia 306
 - local 306

hyperthermia (*contd.*)

- magnetic loss 307–309
 - hysteresis loss 308–309
 - Neel and Brownian relaxation 307–308
- and radiation therapy 312
- regional/whole-body 306
- for therapeutic uses, challenges of 309–313
- drug release control 312
- externally applied magnetic field effect 310
- maximum specific absorption rate 309
- therapeutic temperature creation and maintenance 310–312
- thermal resistance in cells 312
- used nanomaterials, toxic effects removal/reduction of 310

hysteresis loop 25

- defined 19
- domains orientation 20–21
- process of 19–20

i

indirect exchange interaction 160–162

inhomogeneous freezing 185

initial permeability 14, 21, 40, 61, 91

inorganic compounds 31

inversion degree 249

of MgFe_2O_4 249

of ferrites NPs 261

 SiO_2 synthesis 104, 110, 176, 256

iron atom, emission and absorption of 235

iron oxide nanoparticles (IONPs) 43, 297, 299

from industrial wastes

- Curie temperature separation technique (CTST) 50

- magnetic separation technique (MST) 50

- oxidation of Wuestite 50–51

surface modification

- with CTAB 103–105
- with hexanoic acid and oleic acid 102
- with phosphatidylcholine 102
- with polyethylene and 3-amino propyltriethoxysilane 103
- with silica and 3-(4-methoxybenzylideneamino)-2-thioxothiazolidin-4-one 102

synthesis with H and P samples

- collected room temperature Mössbauer spectra 256
- Mössbauer hyperfine fitting parameters 255
- particle size distribution histograms 254
- superparamagnetic behavior 255
- TEM images 254

irradiated cobalt-nickel ferrite NPs 250, 251

irreversibility temperature (Tirr) 142, 146

isomer shift 238–242, 248, 249, 251, 255, 260, 262, 263, 265, 272–274, 276, 278, 279, 281–283

j

Josephson junction effect 117, 121

Josephson tunneling (JT) phenomenon 125–127

k

Kondo effect 201

l

Langevin function 228, 229

Langevin model 3

Larmor frequency 247, 277, 303

laser ablation 30–31

lattice diffusion 63–64, 86

Linkjoin Technology MATS 2010 Static Hyteresisgraph 22

lock-in amplifier 171–172

- loco-regional therapy 304
 low-frequency magnetic dynamics 172
- m**
- M–H hysteresis loops 21, 81
 Mössbauer effect 233, 235
 Mössbauer spectra
 of Co ferrite (CoFe_2O_4) and Mn ferrite (MnFe_2O_4) NPs, precipitation-assisted synthesis of 271
 of hematite NPs 262, 263
 of $\text{Mg}_{1-x}\text{Ni}_x\text{Fe}_2\text{O}_4$ NPs 281, 282
 of micron-sized (bulk) and nanosized Ni-ferrite particles 259, 260
 of ball-milled hematite/nickel oxide mixture 267, 268
 of Ca_2SnO_4 with micron-sized particles 265, 266
 of nanosized and micron-sized Fe_2SiO_4 particles 271
 6K Mössbauer spectra
 of Fe_3O_4 (magnetite) samples 252
 14K Mössbauer spectra
 of $\text{Co}_{0.5}\text{Ni}_{0.5}\text{Fe}_2\text{O}_4$ NPs 250
 Mössbauer spectroscopy 233–235
 applications 246
 basic information 234
 chemical composition evaluation based on 281–284
 electric quadrupole interaction 238, 242–243
 hyperfine interactions 238–246
 isomer shift dependency
 on electronegativity of ligands 241
 on spin state 241
 on strong field ligands 241
 magnetic nanoparticle behaviour, synthesis method effect on 254–273
 magnetic ordering, types of 246
 phase formation evaluation 274–281
 qualitative analysis 233
- S electron density 240–241
 superparamagnetic characterization 247–253
 vs. X-ray diffraction 246
 maghemite ($\gamma\text{-Fe}_2\text{O}_3$) 139, 274, 309
 magnetic anisotropy 10–13, 144, 165, 174, 222, 246
 magnetic biochar, for heavy metals removal 300
 magnetic characteristic measurements
 B–H hysteresis loop 22
 M–H hysteresis loop 21–22
 magnetic dipole interaction 238, 244–246, 263
 magnetic dipole-dipole interaction 157–158, 190
 magnetic ferrite ceramics 59
 magnetic iron oxide nanocomposites, morphologies of 108
 magnetic losses
 Eddy current loss 23–24
 hysteresis loop 25–26
 residual loss 25
 magnetic marker monitoring method 127
 magnetic materials
 extrinsic or extensive properties 13–14
 hard 19
 intrinsic properties 8–13
 soft 18
 magnetic nanomaterials 45, 60, 128–131
 in wastewater treatment 296
 magnetic nanoparticles
 dipolar interactions 165
 in drug delivery 304–306
 exchange interactions 158–162
 general applications of 313
 in hyperthermia 306–313
 in magnetorheological fluids 295–296
 in medical science 295, 302
 magnetic resonance imaging 303–304

- magnetic nanoparticles (*contd.*)
 - magnetic dipole-dipole interaction 157–158
 - in solar cells 301–302
 - spin-orbit interaction 165–166
 - in surface engineering 300
 - super-exchange interaction 163–165
 - supercapacitors and batteries 301
 - surface modification of
 - with alkoxysilanes 104
 - with surfactant 103–105
 - in tissue engineering 300
 - magnetic ordering temperature 4, 140, 246
 - magnetic phase transitions 169, 181
 - magnetic separation technique (MST) 50
 - magnetic splitting 238, 244–247, 252, 278
 - magnetic thermotherapy 307
 - magnetism
 - antiferromagnetism 4
 - diamagnetism 3
 - ferrimagnetism 4
 - ferromagnetism 4–5
 - paramagnetism 3
 - magnetism types 140
 - magnetism-microstructure parallel evolution
 - in hard ferrites 71–80
 - in soft ferrites 80–83
 - in yttrium iron garnet 68–71
 - magnetization 1, 61, 148–149
 - curves 229–230
 - hysteresis loop 228–229
 - magnetocrystalline anisotropy 8, 10–12, 25, 67, 78, 144, 165–166, 221
 - magnetocrystalline anisotropy constant (K_1) 67
 - magnetocrystalline anisotropy energy 11, 20, 144, 221
 - magnetocrystalline anisotropy energy density 144
 - magnetoencephalography (MEG) 130, 131
 - magnetorheological (MR) fluids 295–296
 - magnetostriction 5, 8, 12–13, 25, 67
 - magnetostriction constant (λ) 67
 - materials science, SQUID usage in 128
 - mechanical alloying (MA) process 36, 46–47
 - Meissner effect 122
 - memory dip 209
 - memory effect 201, 208–210
 - microemulsion 42, 43, 102
 - microwave-assisted chemistry techniques 45
 - Mn–Zn ferrites 18, 31, 37, 81
 - $\text{MnFe}_2\text{O}_4\text{SiO}_2$ nanoparticles 111
 - monodispersed colloidal suspensions 190
 - monodispersed nanoparticles 35
 - Morin transition 263
 - MPMS sample magnetometer 135
 - multi-sample sintering scheme 89–90
- n**
- Néel temperature 4, 140, 229, 262, 271
 - nanostructured magnetic materials
 - Curie temperature separation technique (CTST) 50
 - finite size effects on magnetic properties 206–207
 - importance of the synthesis and/or preparation methods 31
 - magnetic behaviors on particle/grain shape 40–41
 - magnetic behaviors on particle/grain size 38–40
 - magnetic separation technique (MST) 50
 - mechanical alloying (MA) process 46–47
 - memory effect 208–210
 - oxidation of Wuestite 50–51
 - particle size and shape 32–33

- questions related to the selected synthesis route 33–38
- reentrant spin glass (RSG) behavior 203–206
- spin-canted effect 197–199
- spin-glass-like behavior 200–203
- standard ceramic route 46
- surface effect 207–208
- synthesis process of 30–31
- wet-chemical synthesis route 41–43
- Neel relaxation mechanism 141, 190, 307–308
- Neel rotation 220
- Neel–Brown model 144, 174, 175, 178–180, 184–186
- Ni–Zn ferrites 17, 24, 37, 61, 66, 81, 85
- nickel ferrite (NiFe_2O_4) nano particles, high-field Mössbauer spectra of 259
- non-covalent functionalization 105–106
- non-irradiated cobalt-nickel ferrite NPs 250–251
- non-specific adsorption 298
- nonmagnetic TiO_2 nanoparticle 84
- nonzero imaginary susceptibility 173
- nuclear quadrupole moment 243
- nucleation rate 34, 36
- o**
- one-electron Green function 160
- orbital magnetic moment 1–2
- orbital-spin coupling 165
- Ostwald ripening 32
- p**
- paramagnetism 3–4, 140, 233
- parylene coating 99, 101
- p-chlorophenol (4-CP) contaminated wastewater removal 299
- penetration depth 122
- permeability 3, 8, 11, 13–14, 18, 19, 21, 23, 37, 40, 61, 66–67, 69–70, 81, 87, 88, 91, 143, 165, 198, 221, 313
- phonon 123, 235–236, 247
- phosphatidylcholine (PC) 102
- photolysis 99, 101
- physical adsorption 105–108, 298
- physical drug targeting 306
- physical functionalization 106–108
- physical vapor deposition (PVD) 30
- physisorption 108
- Planck's constant 1, 174
- plasma surface treatment 99
- polaron hopping mechanism 24
- polyaniline/ Fe_3O_4 nanostructures 182
- polycrystalline materials 12, 41, 61, 63–64, 66, 78, 89, 246
- polydispersed nanoparticles 35
- polymer-coated iron oxide nanoparticles 109
- polymer-coated magnetic nanoparticles 109
- porous ceramics 64
- power-law (P-L) model 176–177, 184
- pseudocapacitors 301
- q**
- quadrupole splitting (QS) 238, 242–243, 259, 265–266, 281, 283
- quantum physical principle 302
- r**
- radio frequency (RF) SQUID 117–118
- recoil effect 235–237
- recoil energy 236–237
- recoil-free fraction 236, 251
- recoil phenomenon 236
- reentrant spin glass (RSG) behavior 203–206
- relaxation time 137–138, 141, 144, 174–178, 180, 182, 184, 186, 188–190, 202, 220, 229, 255, 267, 303, 307–308
- remanence (M_r) 8, 20, 22, 148
- remanence magnetization (B_r) 8, 87–88
- residual loss 23, 25, 61
- room-temperature (RT) transmission Mössbauer spectra

room-temperature (RT) transmission Mössbauer spectra (*contd.*)
 of Fe_3O_4 sample 256, 257
 of hematite ($\alpha\text{-Fe}_2\text{O}_3$) NPs 262
 of magnetite NPs 279
 Ruderman–Kittel interaction 160
 Ruderman–Kittel–Kasuya–Yosida (RKKY) effect 159–161, 201

S

saturation induction (Bs) 22, 68, 81, 87
 saturation magnetization (Ms) 3, 8, 10, 19, 21, 22, 25, 37, 40, 81, 88–89, 102–103, 142, 179, 197–198, 206, 221–223, 228–229, 251, 254, 278, 296, 301
 scanning SQUID microscopes 127
 second phase (Zener) drag 64
 shape anisotropy 10, 12, 25, 81
 Sherrington–Kirkpatrick (SK) model 202
 sigmoid-shaped ferromagnetic hysteresis curve 61
 sigmoid-shaped hysteresis loop 73
 silanization 104–105, 108
 silica coating 110
 silica-coated iron oxide nanoparticles 110
 single-phase Ni-ferrite 81
 single-sample sintering scheme 89–90
 sintered Ba ferrite samples 71, 79
 sintering
 characteristics of 60
 defined 62
 densifying mechanism 63
 final stage 62
 intermediate stage 62
 magnetic-microstructure parallel evolution 65
 multi-sample sintering scheme 89–91
 necking formation 62
 single-sample sintering scheme 89–91
 soaking time 84–88

slanting-sigmoid hysteresis loop 73
 ^{119}Sn MAS NMR spectra 258
 ^{119}Sn Mössbauer spectra 258
 soaking time 61–62, 64, 84–89
 soft ferrites 13–14, 80–81, 223
 soft magnetic materials 17–18, 37–39, 81, 148, 222
 sol-gel method 30, 43–45
 solar cells 295, 301–302
 solute drag 64
 solvothermal method 45, 251
 sonochemical 42, 44
 specific adsorption 298
 spin-canted effect 197–199
 spin glass (SG) phenomena 140, 169, 172
 canonical spin glass 201
 surface spin glass 201
 spin-lattice relaxation 189, 247
 spin magnetic moment 1
 spin-orbit interaction 165–166
 spin relaxation 247
 in paramagnetic materials 246
 spinel ferrites 8, 11–12, 17, 24, 39, 62, 80, 84–85, 162, 249, 258, 260, 282
 SQUID VSM magnetometer, principle in 121
 Stöber method 110–111
 steric stabilization 42–43, 46
 Stoner–Wohlfarth (SW) system 165
 stress anisotropy 10, 13
 supercapacitors 301
 superconducting material
 characteristics 127
 superconducting quantum interference device (SQUID) magnetometry
 advantage and disadvantage of 128–131
 blocking temperature 138–140
 categories 117
 description 117
 direct current (DC) 119–120
 dual junction (DC) loop 118
 field cooling (FC) curve 136–137
 magnetic ordering temperature 140

- magnetization 148–149
 - magnetization (M) vs. temperature (T) 141–148
 - Néel temperature 140
 - setup and detection mechanism 135, 136
 - spin glass (SG) 140–141
 - superparamagnetic (SPM) 140–141
 - types of magnetism 140
 - zero field cooled (ZFC) curve 136–137
 - superconducting transitions 169
 - superconductivity 123, 135
 - Bardeen–Cooper–Schrieffer (BCS) theory 123
 - coherence characteristics 125
 - Cooper pairs 123, 124
 - electron-lattice interaction 123–124
 - energy gap 124
 - flux quantization 125
 - superconductors 117, 121–122, 124–126, 128, 169, 172
 - super-exchange interaction 78, 87, 162, 163–165
 - superparamagnetic (SPM) 140–141
 - effect 222
 - iron oxide nanoparticles 103
 - super-spin-glass phase transition 169
 - superparamagnetic nanoparticles (SPMNP) 138, 174, 181, 228, 247, 307–309
 - superparamagnetism 169, 247–253
 - based on size of particles and magnetic measurements 219–228
 - magnetization hysteresis loop 228–229
 - ZFC and FC magnetization curves 229–230
 - superspins 143, 176, 179–181, 184, 202, 208
 - super spin glass (SSG) behavior 176
 - surface anisotropy 10, 13, 176, 197
 - surface diffusion 63–64, 66, 84–85
 - surface effect 198, 207–208
 - surface engineering 104, 111, 300
 - surface modification
 - aims of 99
 - based on organic reaction 108
 - based on polymerization 109
 - benefits of 99, 100
 - corona discharge 100–101
 - with inorganic layers 110–111
 - of magnetic nanoparticles
 - with alkoxysilanes 104
 - non-seeded method 101
 - with surfactant 103–105
 - of nanomaterials
 - functionalization methods 105–108
 - Parylene coating 101
 - photolysis 101
 - plasma treatment 99–100
 - surface spin glass 201
 - surface tension 104, 106
 - surfactants 103
 - advantages of 104
 - amphiphilic nature of 104
 - types 104
- t**
- thermal decomposition 45, 88, 89
 - thermal energy (KT) 4, 45, 47, 74, 78, 122, 140, 141, 158, 188, 210, 220–223, 230
 - thermal enhancement ratio 312
 - thermal plasma 30
 - tissue engineering (TE) 300, 305
 - transition temperature 121–122, 140, 173, 176, 177, 201–202, 204, 221, 263, 277
 - transmission Mössbauer spectra of
 - as-synthesized iron oxide 276
 - T_1 relaxation time 303
 - T_2 relaxation time 303
- u**
- ultra-capacitors 301
 - ultrasonic cutting 30
 - uniaxial anisotropy 203, 222–223, 227

v

vapor transport 63–64

vibrating sample magnetometer (VSM)
21–22, 117, 121

Vogel–Fulcher (VF) model 175
scaling law 188

vortex dynamics 169

w

Wuestite oxidation 50–51

y

yttrium barium copper oxides (YBCOs)
120

yttrium iron garnet (YIG) 5, 68–72,
163–164

z

Zeeman energies 165, 222, 247

Zeeman lines 246, 283

zero field cooled (ZFC) 136
curve 137, 229–230

magnetization curves 229–230

ZFC $M(T)$ curve 142